frontiers | Research Topics

Hydrogenase: Structure, function, maturation, and application

Edited by
Stefan Frielingsdorf, Francesca Valetti, Constanze Pinske and Chris Greening

Published in
Frontiers in Microbiology

ISSN 1664-8714
ISBN 978-2-8325-3647-6
DOI 10.3389/978-2-8325-3647-6

About Frontiers

Frontiers is more than just an open access publisher of scholarly articles: it is a pioneering approach to the world of academia, radically improving the way scholarly research is managed. The grand vision of Frontiers is a world where all people have an equal opportunity to seek, share and generate knowledge. Frontiers provides immediate and permanent online open access to all its publications, but this alone is not enough to realize our grand goals.

Frontiers journal series

The Frontiers journal series is a multi-tier and interdisciplinary set of open-access, online journals, promising a paradigm shift from the current review, selection and dissemination processes in academic publishing. All Frontiers journals are driven by researchers for researchers; therefore, they constitute a service to the scholarly community. At the same time, the *Frontiers journal series* operates on a revolutionary invention, the tiered publishing system, initially addressing specific communities of scholars, and gradually climbing up to broader public understanding, thus serving the interests of the lay society, too.

Dedication to quality

Each Frontiers article is a landmark of the highest quality, thanks to genuinely collaborative interactions between authors and review editors, who include some of the world's best academicians. Research must be certified by peers before entering a stream of knowledge that may eventually reach the public - and shape society; therefore, Frontiers only applies the most rigorous and unbiased reviews. Frontiers revolutionizes research publishing by freely delivering the most outstanding research, evaluated with no bias from both the academic and social point of view. By applying the most advanced information technologies, Frontiers is catapulting scholarly publishing into a new generation.

What are Frontiers Research Topics?

Frontiers Research Topics are very popular trademarks of the *Frontiers journals series*: they are collections of at least ten articles, all centered on a particular subject. With their unique mix of varied contributions from Original Research to Review Articles, Frontiers Research Topics unify the most influential researchers, the latest key findings and historical advances in a hot research area.

Find out more on how to host your own Frontiers Research Topic or contribute to one as an author by contacting the Frontiers editorial office: frontiersin.org/about/contact

Hydrogenase: Structure, function, maturation, and application

Topic editors

Stefan Frielingsdorf — Technical University of Berlin, Germany
Francesca Valetti — University of Turin, Italy
Constanze Pinske — Martin Luther University of Halle-Wittenberg, Germany
Chris Greening — Monash University, Australia

Citation

Frielingsdorf, S., Valetti, F., Pinske, C., Greening, C., eds. (2023). *Hydrogenase: Structure, function, maturation, and application*. Lausanne: Frontiers Media SA. doi: 10.3389/978-2-8325-3647-6

Table of contents

frontiers | Frontiers in Microbiology

TYPE Editorial
PUBLISHED 22 September 2023
DOI 10.3389/fmicb.2023.1284540

OPEN ACCESS

EDITED AND REVIEWED BY
David Emerson,
Bigelow Laboratory for Ocean Sciences,
United States

*CORRESPONDENCE
Stefan Frielingsdorf
✉ stefan.frielingsdorf@tu-berlin.de

RECEIVED 28 August 2023
ACCEPTED 12 September 2023
PUBLISHED 22 September 2023

CITATION
Frielingsdorf S, Pinske C, Valetti F and Greening C (2023) Editorial: Hydrogenase: structure, function, maturation, and application. *Front. Microbiol.* 14:1284540. doi: 10.3389/fmicb.2023.1284540

Editorial: Hydrogenase: structure, function, maturation, and application

Stefan Frielingsdorf[1]*, Constanze Pinske[2], Francesca Valetti[3] and Chris Greening[4]

[1]Institute of Chemistry, Biophysical Chemistry, Technische Universität Berlin, Berlin, Germany, [2]Institute for Biology, Microbiology, Martin-Luther University Halle-Wittenberg, Halle (Saale), Germany, [3]Department of Life Sciences and Systems Biology, University of Torino, Turin, Italy, [4]Department of Microbiology, Monash University, Clayton, VIC, Australia

KEYWORDS

hydrogenase, metalloenzyme, hydrogen, metabolism, biotechnology, metal cofactor maturation

Editorial on the Research Topic
Hydrogenase: structure, function, maturation, and application

Molecular hydrogen (H_2) is an important molecule in the metabolism of diverse microorganisms (Greening et al., 2015). Many microorganisms use H_2 as an electron donor to support aerobic respiration, anaerobic respiration, and carbon fixation. Others produce H_2 as a means to dispose reducing equivalents through fermentative and photobiological processes. Furthermore, exchange of H_2 between different species shapes the ecology and biogeochemistry of diverse ecosystems globally (Schwartz et al., 2013). The enzymes that split or evolve H_2 are called hydrogenases and these metalloproteins can be divided into three phylogenetically unrelated classes distinguishable by the metal composition of their active sites, namely [Fe]-, [FeFe]-, and [NiFe]-hydrogenases (Lubitz et al., 2014). Following a century of hydrogenase research, it is now possible to isolate, handle, and investigate these fragile enzymes. There have been numerous advances in understanding the regulation, function, structures, and maturation of these enzymes, as well as their involvement in important processes such as microbial pathogenesis and greenhouse gas cycling (Lubitz and Tumas, 2007; Greening et al., 2019; Benoit et al., 2020; Ehhalt and Rohrer, 2022). The employment of hydrogenases and hydrogenase-based applications could also potentially facilitate the world's transition to a sustainable H_2-based energy economy in the future.

Hydrogenases mediate a seemingly simple reaction, i.e., the splitting of H_2 into a proton and a hydride, followed by the complete separation of protons and electrons. However, the reaction mechanisms of the different enzyme types are not yet fully understood. Likewise, the intricate maturation of the metal cofactors is a constant resource of unprecedented biological chemistry (Bortolus et al., 2018; Britt et al., 2020; Schulz et al., 2020; Arlt et al., 2021; Stripp et al., 2021; Pagnier et al., 2022; Arriaza-Gallardo et al., 2023; Caserta et al., 2023). Additionally, features such as the frequent membrane association and O_2 sensitivity of hydrogenases has so far hindered *in vitro* harnessing of their function. New structural, spectroscopic, and electrochemical data and methods will enable new insights into their maturation and reactions. In addition, the discovery and characterization of diverse hydrogenases occurring in different microorganisms provide opportunities to discover new physiological roles,

structural adaptations, and potential applications of these enzymes (Peters et al., 2015; Dragomirova et al., 2018; Schuchmann et al., 2018; Pinske, 2019; Winkler et al., 2021). Attempts to employ hydrogenases for industrial purposes have been made, however, there is presumably still a long way to go until processes involving hydrogenases (biological H_2 production or biological fuel cells) will become economically feasible (Rögner, 2015; Ji et al., 2023; Xuan et al., 2023).

This Research Topic comprises 11 articles that aimed to bring together recent advances in hydrogenase research, including structure, function, maturation, and application. In terms of structural investigation, Dragelj et al. theoretically and experimentally analyzed an isolated large subunit of a [NiFe]-hydrogenase. They confirmed that [NiFe] large subunits dimerize in the absence of their small subunit (Hartmann et al., 2018; Kwon et al., 2018; Caserta et al., 2020), and showed that the [NiFe]-cofactor is stabilized by the dimerization. In the realm of structure-function relationships, Kisgeropoulos et al. investigated the effect of amino acid exchanges of the primary proteinaceous proton acceptor in [FeFe]-hydrogenase. The data expand previous work (Cornish et al., 2011; Morra et al., 2012; Duan et al., 2018; Artz et al., 2020), demonstrating that the pK_a of the proton acceptor is one factor controlling the catalytic bias of the enzyme. Three further articles dealt with functional aspects of hydrogenases. Morra reviewed the identification and characterization of novel [FeFe]-hydrogenases, described their functional roles, and recent findings regarding their O_2 tolerance. Kpebe et al. reported on the essential role of a bifurcating [FeFe]-hydrogenase in the sulfate reducer *Solidesulfovibrio fructosivorans*, showing that during ethanol oxidation, the hydrogenase confurcates electrons from NADH and reduced ferredoxin to produce H_2, which is later on used for energy conservation using sulfate as electron acceptor. The function of a bidirectional [NiFe]-hydrogenase in *Synechocystis* sp. PCC 6803 was investigated by Burgstaller et al.. They showed that this hydrogenase is essential for growth on arginine and glucose in the presence of light and O_2, and interestingly this function seems to be unrelated to H_2 catalysis. Instead, an H_2-independent role for the transfer of electrons into the photosynthetic electron transfer chain is proposed, which is an important hypothesis that may also be relevant for certain multisubunit hydrogenases in other species.

On the subtopic of hydrogenase maturation, Haase and Sawers investigated residues that contribute to [NiFe]-hydrogenase maturation. They found a histidine residue in a HypC-type chaperone that is important for efficient binding to its maturation partner HypD (Blokesch and Böck, 2002). In addition, this residue is important for selectivity, ensuring that only the correct large [NiFe]-hydrogenase subunit is matured. It should be emphasized that understanding cofactor maturation and incorporation is of high importance for any future application of hydrogenases, which is demonstrated in the following article. In an interdisciplinary approach in the fields of maturation and application, Fan et al. significantly improved the [NiFe]-cofactor incorporation in the course of heterologous production of a [NiFe]-hydrogenase from *Cupriavidus necator* in *Escherichia coli*. Previously, cofactor insertion was not functional, resulting in production of inactive hydrogenases (Fan et al., 2021).

Another four articles explore the application of hydrogenases. Hogendoorn et al. isolated the novel strain "*Candidatus* Hydrogenisulfobacillus filiaventi" R50 gen. nov., sp., nov. which was characterized as a chemolithoautotrophic thermoacidophilic aerobic H_2-oxidizing bacterium. This strain excretes about half of the fixed CO_2 in the form of amino acids, which makes it a promising candidate for the industrial production of organic compounds from CO_2, using H_2 as energy source. H_2 oxidation in this strain is facilitated by two [NiFe]-hydrogenases from the groups 1b and 1h, with the latter conferring high affinity toward H_2 (Søndergaard et al., 2016). Kobayashi et al. engineered the acetogenic bacterium *Moorella thermoacetica* for enhanced acetate, ethanol and acetone production. They found that H_2 supplementation under mixotrophic conditions increases NADH levels but can inhibit growth due to an unbalanced redox status. This study emphasized the role of a reversible electron-bifurcating group A3 [FeFe]-hydrogenase for balancing the cellular redox state. These observations may also be exploited for biohydrogen production by that strain. Another way to produce H_2 was analyzed by Barahona et al.. In order to enhance nitrogenase-driven H_2 production in *Rhodobacter capsulatus*, they used a sensory hydrogenase coupled to the production of a fluorescence signal. By inducing genome-wide mutations and using high-throughput fluorescence-activated cell sorting, they were able to generate mutants with elevated H_2 evolution capabilities. Finally, Schumann et al. reviewed current state-of-the-art and future perspectives for efficient light-driven H_2 production using phototrophic microorganisms. This technology potentially enables conversion of solar energy into a chemical compound that enables storage and transport. However, as discussed by the authors, extensive engineering is required for this technology to be efficient and scalable.

Taken together, the Research Topic advances our knowledge especially on the function and application of hydrogenases and provides important perspectives for future H_2-based biologically green technologies.

Author contributions

SF: Writing—original draft, Writing—review and editing. CP: Writing—review and editing. FV: Writing—review and editing. CG: Writing—review and editing.

Funding

Funded by the Deutsche Forschungsgemeinschaft (DFG, German Research Foundation) under Germany's Excellence Strategy—EXC 2008–390540038—UniSysCat (SF).

Acknowledgments

We thank the Frontiers in Microbiology editorial team for their support. Even more importantly, we

thank all reviewers for their critical comments and constructive suggestions.

Conflict of interest

The authors declare that the research was conducted in the absence of any commercial or financial relationships that could be construed as a potential conflict of interest.

Publisher's note

References

Arlt, C., Nutschan, K., Haase, A., Ihling, C., Tänzler, D., Sinz, A., et al. (2021). Native mass spectrometry identifies the HybG chaperone as carrier of the $Fe(CN)_2CO$ group during maturation of *E. coli* [NiFe]-hydrogenase 2. *Sci. Rep.* 11, 24362. doi: 10.1038/s41598-021-03900-w

Arriaza-Gallardo, F. J., Zheng, Y.-C., Gehl, M., Nomura, S., Fernandes Queiroz, J. P., and Shima, S. (2023). [Fe]-hydrogenase, cofactor biosynthesis and engineering. *Chem. Bio. Chem.* 2023:e202300330. doi: 10.1002/cbic.202300330

Artz, J., Mulder, D., Ratzloff, M., Peters, J., and King, P. (2020). *The Hydricity and Reactivity Relationship in [FeFe]-Hydrogenases.* doi: 10.21203/rs.3.rs-77874/v1

Benoit, S. L., Maier, R. J., Sawers, R. G., and Greening, C. (2020). Molecular hydrogen metabolism: a widespread trait of pathogenic bacteria and protists. *Microbiol. Mol. Biol. Rev.* 84, 19. doi: 10.1128/MMBR.00092-19

Blokesch, M., and Böck, A. (2002). Maturation of [NiFe]-hydrogenases in *Escherichia coli*: the HypC cycle. *J. Mol. Biol.* 324, 287–296. doi: 10.1016/S0022-2836(02)01070-7

Bortolus, M., Costantini, P., Doni, D., and Carbonera, D. (2018). Overview of the maturation machinery of the H-cluster of [FeFe]-hydrogenases with a focus on HydF. *Int. J. Mol. Sci.* 19. doi: 10.3390/ijms19103118

Britt, R. D., Rao, G., and Tao, L. (2020). Biosynthesis of the catalytic H-cluster of [FeFe] hydrogenase: the roles of the Fe-S maturase proteins HydE, HydF, and HydG. *Chem. Sci.* 11, 10313–10323. doi: 10.1039/D0SC04216A

Caserta, G., Hartmann, S., van Stappen, C., Karafoulidi-Retsou, C., Lorent, C., Yelin, S., et al. (2023). Stepwise assembly of the active site of [NiFe]-hydrogenase. *Nat. Chem. Biol.* 19, 498–506. doi: 10.1038/s41589-022-01226-w

Caserta, G., Lorent, C., Ciaccafava, A., Keck, M., Breglia, R., Greco, C., et al. (2020). The large subunit of the regulatory [NiFe]-hydrogenase from *Ralstonia eutropha* - a minimal hydrogenase? *Chem. Sci.* 11, 5453–5465. doi: 10.1039/D0SC01369B

Cornish, A. J., Gärtner, K., Yang, H., Peters, J. W., and Hegg, E. L. (2011). Mechanism of proton transfer in [FeFe]-hydrogenase from *Clostridium pasteurianum*. *J. Biol. Chem.* 286, 38341–38347. doi: 10.1074/jbc.M111.254664

Dragomirova, N., Rothe, P., Schwoch, S., Hartwig, S., Pinske, C., and Sawers, R. G. (2018). Insights into the redox sensitivity of *chloroflexi* Hup-hydrogenase derived from studies in *Escherichia coli*: merits and pitfalls of heterologous [NiFe]-hydrogenase synthesis. *Front. Microbiol.* 9, 2837. doi: 10.3389/fmicb.2018.02837

Duan, J., Senger, M., Esselborn, J., Engelbrecht, V., Wittkamp, F., Apfel, U.-P., et al. (2018). Crystallographic and spectroscopic assignment of the proton transfer pathway in [FeFe]-hydrogenases. *Nat. Commun.* 9, 4726. doi: 10.1038/s41467-018-07140-x

Ehhalt, D. H., and Rohrer, F. (2022). The tropospheric cycle of H_2: a critical review. *Tellus B Chem. Phys. Meteorol.* 61, 500. doi: 10.1111/j.1600-0889.2009.00416.x

Fan, Q., Caserta, G., Lorent, C., Lenz, O., Neubauer, P., and Gimpel, M. (2021). Optimization of culture conditions for oxygen-tolerant regulatory [NiFe]-hydrogenase production from *Ralstonia eutropha* H16 in *Escherichia coli*. *Microorganisms* 9, 61195. doi: 10.3390/microorganisms9061195

Greening, C., Biswas, A., Carere, C. R., Jackson, C. J., Taylor, M. C., Stott, M. B., et al. (2015). Genomic and metagenomic surveys of hydrogenase distribution indicate H_2 is a widely utilised energy source for microbial growth and survival. *ISME J.* 10, 761–77. doi: 10.1038/ismej.2015.153

Greening, C., Geier, R., Wang, C., Woods, L. C., Morales, S. E., McDonald, M. J., et al. (2019). Diverse hydrogen production and consumption pathways influence methane production in ruminants. *ISME J.* 13, 2617–2632. doi: 10.1038/s41396-019-0464-2

Hartmann, S., Frielingsdorf, S., Ciaccafava, A., Lorent, C., Fritsch, J., Siebert, E., et al. (2018). O_2-tolerant H_2 activation by an isolated large subunit of a [NiFe] hydrogenase. *Biochemistry* 57, 5339–5349. doi: 10.1021/acs.biochem.8b00760

Ji, H., Wan, L., Gao, Y., Du, P., Li, W., Luo, H., et al. (2023). Hydrogenase as the basis for green hydrogen production and utilization. *J. Energy Chem.* 85, 348–362. doi: 10.1016/j.jechem.2023.06.018

Kwon, S., Watanabe, S., Nishitani, Y., Kawashima, T., Kanai, T., Atomi, H., et al. (2018). Crystal structures of a [NiFe] hydrogenase large subunit HyhL in an immature state in complex with a Ni chaperone HypA. *Proc. Natl. Acad. Sci. U.S.A.* 115, 7045–7070. doi: 10.1073/pnas.1801955115

Lubitz, W., Ogata, H., Rüdiger, O., and Reijerse, E. (2014). Hydrogenases. *Chem. Rev.* 114, 4081–4148. doi: 10.1021/cr4005814

Lubitz, W., and Tumas, W. (2007). Hydrogen: an overview. *Chem. Rev.* 107, 3900–3903. doi: 10.1021/cr050200z

Morra, S., Giraudo, A., Di Nardo, G., King, P. W., Gilardi, G., and Valetti, F. (2012). Site saturation mutagenesis demonstrates a central role for cysteine 298 as proton donor to the catalytic site in CaHydA [FeFe]-hydrogenase. *PloS ONE* 7, e48400. doi: 10.1371/journal.pone.0048400

Pagnier, A., Balci, B., Shepard, E. M., Broderick, W. E., and Broderick, J. B. (2022). [FeFe]-hydrogenase *in vitro* maturation. *Angew. Chem. Int. Ed.* 61, e202212074. doi: 10.1002/anie.202212074

Peters, J. W., Schut, G. J., Boyd, E. S., Mulder, D. W., Shepard, E. M., Broderick, J. B., et al. (2015). [FeFe]- and [NiFe]-hydrogenase diversity, mechanism, and maturation. *BBA - Mol. Cell Res.* 1853, 1350–1369. doi: 10.1016/j.bbamcr.2014.11.021

Pinske, C. (2019). Bioenergetic aspects of archaeal and bacterial hydrogen metabolism. *Adv. Microb. Physiol.* 74, 487–514. doi: 10.1016/bs.ampbs.2019.02.005

Rögner, M. (2015). *Biohydrogen.* Berlin, Boston: Walter de Gruyter GmbH and Co. KG.

Schuchmann, K., Chowdhury, N. P., and Müller, V. (2018). Complex multimeric [FeFe] hydrogenases: biochemistry, physiology and new opportunities for the Hydrogen Economy. *Front. Microbiol.* 9, 2911. doi: 10.3389/fmicb.2018.02911

Schulz, A.-C., Frielingsdorf, S., Pommerening, P., Lauterbach, L., Bistoni, G., Neese, F., et al. (2020). Formyltetrahydrofolate decarbonylase synthesizes the active site CO ligand of O_2-tolerant [NiFe] Hydrogenase. *J. Am. Chem. Soc.* 142, 1457–1464. doi: 10.1021/jacs.9b11506

Schwartz, E., Fritsch, J., and Friedrich, B. (2013). "H_2-metabolizing prokaryotes," in *The Prokaryotes*, eds. E. Rosenberg, E. F. DeLong, S. Lory, E. Stackebrandt, and F. Thompson (Berlin: Springer Berlin Heidelberg), 119–199.

Søndergaard, D., Pedersen, C. N. S., and Greening, C. (2016). HydDB: A web tool for hydrogenase classification and analysis. *Sci. Rep.* 6, 34212. doi: 10.1038/srep34212

Stripp, S. T., Oltmanns, J., Müller, C. S., Ehrenberg, D., Schlesinger, R., Heberle, J., et al. (2021). Electron inventory of the iron-sulfur scaffold complex HypCD essential in [NiFe]-hydrogenase cofactor assembly. *Biochem. J.* 478, 3281–3295. doi: 10.1042/BCJ20210224

Winkler, M., Duan, J., Rutz, A., Felbek, C., Scholtysek, L., Lampret, O., et al. (2021). A safety cap protects hydrogenase from oxygen attack. *Nat. Commun.* 12, 756. doi: 10.1038/s41467-020-20861-2

Xuan, J., He, L., Wen, W., and Feng, Y. (2023). Hydrogenase and nitrogenase: key catalysts in biohydrogen production. *Molecules* 28, 31392. doi: 10.3390/molecules28031392

frontiers in Microbiology

MINI REVIEW
published: 02 March 2022
doi: 10.3389/fmicb.2022.853626

Fantastic [FeFe]-Hydrogenases and Where to Find Them

*Simone Morra**

Faculty of Engineering, University of Nottingham, Nottingham, United Kingdom

[FeFe]-hydrogenases are complex metalloenzymes, key to microbial energy metabolism in numerous organisms. During anaerobic metabolism, they dissipate excess reducing equivalents by using protons from water as terminal electron acceptors, leading to hydrogen production. This reaction is coupled to reoxidation of specific redox partners [ferredoxins, NAD(P)H or cytochrome c_3], that can be used either individually or simultaneously (*via* flavin-based electron bifurcation). [FeFe]-hydrogenases also serve additional physiological functions such as H_2 uptake (oxidation), H_2 sensing, and CO_2 fixation. This broad functional spectrum is enabled by a modular architecture and vast genetic diversity, which is not fully explored and understood. This Mini Review summarises recent advancements in identifying and characterising novel [FeFe]-hydrogenases, which has led to expanding our understanding of their multiple roles in metabolism and functional mechanisms. For example, while numerous well-known [FeFe]-hydrogenases are irreversibly damaged by oxygen, some newly discovered enzymes display intrinsic tolerance. These findings demonstrate that oxygen sensitivity varies between different [FeFe]-hydrogenases: in some cases, protection requires the presence of exogenous compounds such as carbon monoxide or sulphide, while in other cases it is a spontaneous built-in mechanism that relies on a reversible conformational change. Overall, it emerges that additional research is needed to characterise new [FeFe]-hydrogenases as this will reveal further details on the physiology and mechanisms of these enzymes that will enable potential impactful applications.

Keywords: hydrogenase, energy metabolism, oxygen sensitivity, H-cluster, metalloenzymes

OPEN ACCESS

Edited by:
Stefan Frielingsdorf, Technical University of Berlin, Germany

Reviewed by:
Eric Stephen Boyd, Montana State University, United States
Myriam Brugna, Aix-Marseille Université, France

***Correspondence:**
Simone Morra
simone.morra@nottingham.ac.uk

Specialty section:
This article was submitted to Microbiological Chemistry and Geomicrobiology, a section of the journal Frontiers in Microbiology

Received: *12 January 2022*
Accepted: *10 February 2022*
Published: *02 March 2022*

Citation:
Morra S (2022) Fantastic [FeFe]-Hydrogenases and Where to Find Them. Front. Microbiol. 13:853626. doi: 10.3389/fmicb.2022.853626

INTRODUCTION

Microbial hydrogen metabolism is thought to have appeared in the very early days of life on Earth, before oxygen began to accumulate in the atmosphere 2.4 billion years ago (Lyons et al., 2014). It has existed ever since, and it still plays a key role in numerous environments such as soil, wetlands, marine sediments, freshwaters, oceans, geothermal springs, and animal guts (Boyd et al., 2010; Greening et al., 2016; Piche-Choquette and Constant, 2019).

Hydrogenases are specialised metalloenzymes essential to microbial hydrogen metabolism. They are classified in three classes based on the metals found at the active site: [FeFe]-hydrogenases, [NiFe]-hydrogenases, and [Fe]-hydrogenases (also known as Hmd) (Vignais and Billoud, 2007).

[FeFe]-hydrogenases are found in the genome of numerous microorganisms, both Prokaryotes and Eukaryotes but not in Archaea (Peters et al., 2015). Their enzymatic features depend on

a biologically unusual iron sulphur centre, named H-cluster, composed of a cubane [4Fe4S]-subcluster linked to a [FeFe]-subcluster *via* a conserved cysteine residue. Concerted proton and electron transfer steps lead to H_2 production, *via* a mechanism that is under debate (Haumann and Stripp, 2018; Birrell et al., 2021). The ability of [FeFe]-hydrogenases to catalyse reversible H_2 production at high turnover rates and low overpotential has put them under the spotlight for potential exploitation in devices to produce green hydrogen (Morra et al., 2017; Evans et al., 2019; Brown and King, 2020). [FeFe]-hydrogenases have also inspired the synthesis of artificial catalysts that mimic their natural properties (Ahmed and Dey, 2019; Karayilan et al., 2019). Synthetic biology has also explored the potential of exploiting [FeFe]-hydrogenases *in vivo*, to improve or to instal H_2 production in several microbial hosts (Klein et al., 2010; Kelly et al., 2015; Noone et al., 2017; Kanygin et al., 2020; Wegelius et al., 2021).

This Mini Review will focus on [FeFe]-hydrogenases and highlight how recent research is revolutionising our understanding of these enzymes.

[FeFe]-HYDROGENASES DIVERSITY: A POORLY EXPLORED SPACE

In the post-genomic and multi-omics era, thousands of putative [FeFe]-hydrogenase sequences can be retrieved from public databases. The common factor to all [FeFe]-hydrogenases is the H-domain, a ∼40 kDa (350 amino acids) protein domain that hosts the H-cluster. In addition to sequence variability within this core domain, [FeFe]-hydrogenases display a highly modular genetic organisation, featuring several additional domains and subunits that lead to both monomeric and multi-subunit enzyme complexes. Research in this field has identified massive diversity and several classification schemes have been proposed (Meyer, 2007; Vignais and Billoud, 2007; Calusinska et al., 2010; Winkler et al., 2013). In addition to studying the hydrogenase gene phylogeny, recent studies have also included the analysis of flanking genes. Poudel et al. (2016) compiled 714 sequences and proposed three groups: (G1) monomeric HydA; (G2) trimeric HydABC; (G3) tetrameric HydABCD. Greening et al. (2016) curated 1,222 sequences and proposed a classification into three groups (**Figure 1**): (A) prototypical and bifurcating; (B) putative ancestral; (C) putative sensory; by analysing variations in the domain organisation and probable quaternary structure, group A can be further split into four subtypes.

However, only three model enzymes have been experimentally characterised to a high level of detail using various techniques, and they all belong to group A (subtype A1). These are: CpI (from the anaerobic nitrogen-fixing bacterium *Clostridium pasteurianum*) (Nakos and Mortenson, 1971; Peters et al., 1998; Therien et al., 2017); DvH (from the sulphate-reducing bacterium *Desulfovibrio vulgaris*) (Legall et al., 1971; Nicolet et al., 1999; Pohorelic et al., 2002); and CrHydA1 (from the eukaryotic green alga *Chlamydomonas reinhardtii*) (Happe and Naber, 1993; Happe and Kaminski, 2002; Mulder et al., 2010). DvH and DdH (from *Desulfovibrio desulfuricans*) sequences have been claimed to be identical (Nicolet et al., 1999), even if a closer inspection at genomes denotes numerous differences. Despite this, the nomenclature has been used interchangeably, and biophysical characterisation has been carried out on DvH sequence under the DdH name (Nicolet et al., 1999; Birrell et al., 2016; Rodriguez-Macia et al., 2020).

From the late 1990s, research has expanded to more [FeFe]-hydrogenases thanks to important technical advances, such as recombinant overexpression (Girbal et al., 2005; King et al., 2006; Kuchenreuther et al., 2010) and production of semi-synthetic hydrogenases (Berggren et al., 2013; Esselborn et al., 2013). Currently, approximately 40 [FeFe]-hydrogenases have been studied experimentally (**Figure 1** and **Supplementary Table 1**). A simple comparison of these numbers with the count of putative [FeFe]-hydrogenases makes it evident that only very little is currently known about these enzymes' diversity. Furthermore, the level of characterisation is highly variable, and in most cases only a very limited amount of information is available (**Supplementary Table 1**).

BEYOND HYDROGEN PRODUCTION: MULTIPLE FUNCTIONAL ROLES

[FeFe]-hydrogenases are well-known for their prototypical role in hydrogen production (**Figure 1**): the enzyme acts as a sink for reducing equivalents, allowing for dissipation of excess reducing power from energy metabolism. This role is well-characterised in some clostridial hydrogenases, such as CpI (Therien et al., 2017), and in algal hydrogenases, such as CrHydA1 (Happe and Kaminski, 2002). Other hydrogenases with very high sequence similarity are believed to acts in a similar way both within green algae (Florin et al., 2001; Winkler et al., 2002; Kamp et al., 2008; Meuser et al., 2011; Cornish et al., 2015) and Clostridia (Demuez et al., 2007; Morra et al., 2016b). However, H_2-producing hydrogenases do not cluster together in the phylogenetic tree, demonstrating that the function cannot simply be predicted from the sequence alone, as previously noted (Greening et al., 2016).

In addition to this flagship role, several new functions have been identified. During hydrogen uptake (**Figure 1**), the enzyme oxidises hydrogen and transfers the low potential electrons to a suitable cellular acceptor. This function has been proposed for relatively few [FeFe]-hydrogenases, such as the cytoplasmic CpII (Therien et al., 2017) and periplasmic DdH/DvH (Pohorelic et al., 2002).

Reactions of additional complexity are catalysed by multi-subunit [FeFe]-hydrogenases. AwHydA2 (from *Acetobacterium woodii*) (Schuchmann and Muller, 2013) and TkHydA2 (from *Thermoanaerobacter kivui*) (Schwarz et al., 2018) have been shown to form stable heterotetrameric complexes with two FeS subunits and a formate dehydrogenase (FdhF) subunit. These enzymes have been named HDCR (Hydrogen-Dependent Carbon dioxide Reductase) after their unprecedented ability to catalyse direct CO_2 reduction using H_2 as the sole reducing agent, in a single and efficient step (Schuchmann et al., 2018; Leo et al., 2021).

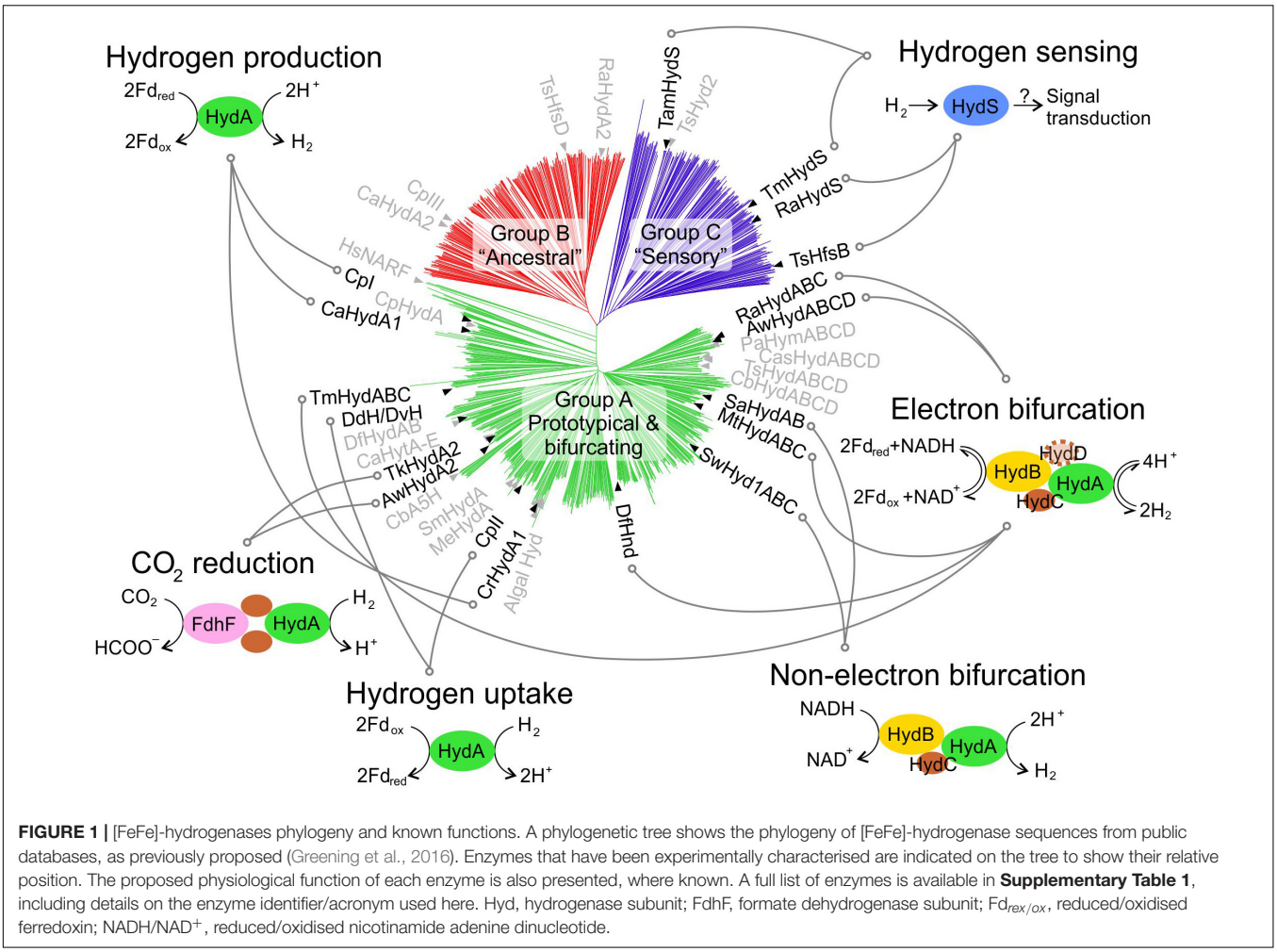

FIGURE 1 | [FeFe]-hydrogenases phylogeny and known functions. A phylogenetic tree shows the phylogeny of [FeFe]-hydrogenase sequences from public databases, as previously proposed (Greening et al., 2016). Enzymes that have been experimentally characterised are indicated on the tree to show their relative position. The proposed physiological function of each enzyme is also presented, where known. A full list of enzymes is available in **Supplementary Table 1**, including details on the enzyme identifier/acronym used here. Hyd, hydrogenase subunit; FdhF, formate dehydrogenase subunit; $Fd_{rex/ox}$, reduced/oxidised ferredoxin; $NADH/NAD^+$, reduced/oxidised nicotinamide adenine dinucleotide.

Following the discovery of TmHydABC (from *Thermotoga maritima*) (Schut and Adams, 2009), numerous other heterotrimeric and heterotetrameric [FeFe]-hydrogenases have been shown to perform flavin-based electron bifurcation (FBEB). These enzymes couple the thermodynamically favourable oxidation of ferredoxin to the unfavourable oxidation of NADH leading to H_2 production. The coupling is synergistic and provides a clear physiological advantage over "conventional" hydrogen production from ferredoxin only, as it allows simultaneous reoxidation of both NADH and ferredoxin from glycolysis, thus facilitating ATP production in the absence of aerobic respiration (Buckel and Thauer, 2018; Peters et al., 2018; Schuchmann et al., 2018).

Two [FeFe]-hydrogenases SwHyd1ABC (from *Syntrophomonas wolfei*) (Losey et al., 2017) and SaHydAB (from *Syntrophus aciditrophicus*) (Losey et al., 2020) have been discovered to catalyse H_2 production from NADH without the requirement of reduced ferredoxin. Despite overall sequence and predicted structural similarity to FBEB enzymes, closer inspection of the flavin-containing HydB subunit revealed differences that may explain the absence of synergistic bifurcation (Losey et al., 2020).

A sensory role has been proposed for a number of group C [FeFe]-hydrogenases, such as TmHydS (Chongdar et al., 2018) and TamHydS (Land et al., 2020). This function has been proposed based the presence of a PAS domain, that is known to take part in signal transduction of other proteins. Furthermore, the lack of a conserved cysteine near the H-cluster slows down the turnover rate, thus making unlikely an active metabolic role. Additional evidence supporting a sensory role has been reported for RaHydS (from *Ruminococcus albus*) (Zheng et al., 2014) and TsHfsB (from *Thermoanaerobacterium saccharolyticum*) (Shaw et al., 2009). However, given the little direct physiological evidence for such role, this assignment is considered putative.

Group B is currently much less characterised and a tentative denomination as "ancestral" has been proposed, but due to lack of evidence it is difficult to discuss further on their function. Some data are available for CpIII, showing that the gene is transcribed (Therien et al., 2017) and that the enzyme is active and displays a different catalytic bias to both CpI and CpII (Artz et al., 2020).

It is also notable that proteins with sequence similarity to [FeFe]-hydrogenases can be found in higher eukaryotes, including humans (HsNARF, **Figure 1**), where they lost H_2-linked functionality and evolved to other roles (Barton and Worman, 1999; Ding et al., 2020).

The impressive variety of functional roles for [FeFe]-hydrogenases is not surprising given the large number of organisms that rely on them, and their evolutionary history

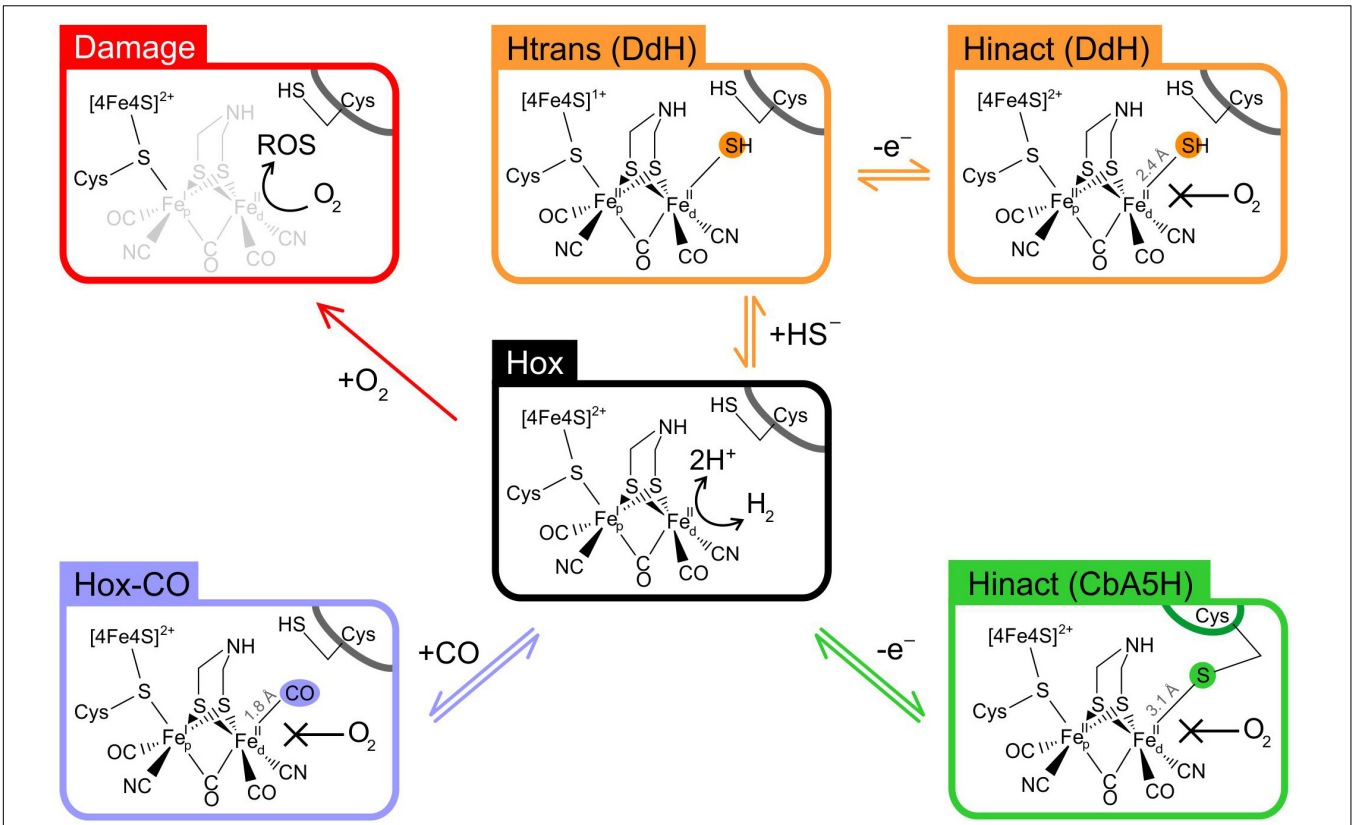

FIGURE 2 | Oxygen tolerance strategies in [FeFe]-hydrogenases. Schematic representation of the H-cluster in the oxidised active state Hox (centre). In the absence of any exogenous protectant, numerous [FeFe]-hydrogenases undergo irreversible inactivation due to H-cluster damage with loss of Fe atoms (red pathway); carbon monoxide acts as a protective agent due to its ability to form Hox-CO, by binding reversibly to the H-cluster at the same site as O_2 (purple pathway); in DdH, a similar mechanism occurs when sulphide binds to the H-cluster forming Hinact, *via* the Htrans intermediate (orange pathway); in CbA5H, a conformational change in the protein structure allows for a conserved cysteine to directly bind to the H-cluster, forming Hinact (green pathway). Fe_p, proximal iron atom; Fe_d, distal iron atom; Cys, cysteine residue.

that allowed adaptation to numerous ecological niches. However, such diversity does not only occur across different organisms, but also within them: several species possess multiple [FeFe]-hydrogenase genes annotated in the genome, often in addition to other H_2-activating enzymes such as [NiFe]-hydrogenases and nitrogenases (Calusinska et al., 2010; Baffert et al., 2019). The apparent redundancy of hydrogen-related enzymes may provide advantages by quickly adapting the metabolism in response to the environmental changes. However, a comprehensive investigation on multiple hydrogenases within an organism is currently missing.

Thermoanaerobacterium saccharolyticum has four putative [FeFe]-hydrogenases and a putative [NiFe]-hydrogenase genes. A systematic knockout study revealed that the *hfs* genes encoding for TsHfsB and TsHfsD [FeFe]-hydrogenases are essential for H_2 production, while deletion of the other genes had no effect on this function. Moreover, deletion of *hfs* genes downregulated the expression of all the other genes (*hyd* and *ech*), suggesting a regulatory or sensory role for TsHfsB. Consequently, group B TsHfsD may be the main enzyme for H_2 production in this organism (Shaw et al., 2009).

Within green algae, it is common to find two closely related [FeFe]-hydrogenase genes that are likely originating from gene duplication (Meuser et al., 2011). For example, *Chlamydomonas reinhardtii* encodes for CrHydA1 and CrHydA2, whose expression profile is very similar (Forestier et al., 2003). The two isoenzymes differ for their affinity for the ferredoxin PetF and for catalytic bias, suggesting different functional roles (Engelbrecht et al., 2021).

The well-known solvent producer *Clostridium acetobutylicum* has two [FeFe]-hydrogenases (CaHydA1 and CaHydA2), a [NiFe]-hydrogenase and nitrogenase. It has been suggested that CaHydA1 is the main enzyme for hydrogen production during acidogenesis (Demuez et al., 2007), but more recently a ΔCaHydA1 mutant strain has shown abundant H_2 production (Du et al., 2021) suggesting a significant contribution from other enzymes. On the other hand, the [NiFe]-hydrogenase has been shown to play a key role in hydrogen cycling during solventogenesis (i.e., H_2 reoxidation to provide reducing power for the acid-to-solvent conversion) (Germane et al., 2018).

In the case of *Clostridium pasteurianum* (three [FeFe]-hydrogenases, a [NiFe]-hydrogenase and nitrogenase), it has

been proposed that CpI is the key H_2 producer under non-nitrogen-fixing conditions (Adams, 1990), while CpII and the [NiFe]-hydrogenase would act as H_2 uptake enzymes during nitrogen fixation. This would allow for reducing equivalents to be recovered from the highly uncoupled reaction of nitrogenase, ultimately improving the efficiency of this energy-consuming process (Therien et al., 2017).

Gene expression studies of multiple [FeFe]-hydrogenases in *Clostridium butyricum*, *Clostridium beijerinckii*, and Clostridium *perfringens* have shown that all genes are transcribed and regulation is actively occurring, suggesting different functional roles that have not yet been determined (Morra et al., 2014; Calusinska et al., 2015; Arizzi et al., 2021).

OXYGEN SENSITIVITY: NOT AN INSURMOUNTABLE PROBLEM

For long time it has been assumed that [FeFe]-hydrogenases were extremely sensitive to O_2, with their catalytic activity disappearing irreversibly and very quickly, in contrast to [NiFe]-hydrogenases that often display reversible inhibition or complete tolerance (Goldet et al., 2009; Lautier et al., 2011; Kubas et al., 2017). While this is certainly true for some of the most studied model [FeFe]-hydrogenases, the characterisation of novel enzymes has recently revealed that the phenomenon of oxygen sensitivity is highly variable across the class, and several examples of oxygen-stable enzymes exist (**Figure 2**).

Studies on model enzymes CrHydA1 and CpI have shown that the H-cluster suffers severe and irreversible structural damage when exposed to oxygen, resulting in loss of several Fe atoms and their non-protein ligands (Stripp et al., 2009; Swanson et al., 2015; Esselborn et al., 2019). The exact degradation mechanism is still under debate, but there is agreement that this requires O_2 binding to the distal iron atom (Fe_d) followed by electron and proton transfer, leading to the formation of reactive oxygen species (ROS) that in turn would cause the actual damage (**Figure 2**). Protection from oxygen can occur in the presence of carbon monoxide *via* competition, as CO is able to bind to Fe_d faster than oxygen, forming Hox-CO (Lemon and Peters, 1999; Goldet et al., 2009).

Oxygen sensitivity of [FeFe]-hydrogenases is an obvious practical limitation to working with such enzymes and raises concerns over their prospective exploitation for potential applications (Ghirardi, 2015; Karayilan et al., 2019). As such, several attempts have been made to improve oxygen tolerance of model [FeFe]-hydrogenases, adopting both rational and random mutagenesis approaches but the improvements reported are limited (Lautier et al., 2011; Bingham et al., 2012; King et al., 2014).

More progress has been made by looking at other [FeFe]-hydrogenases. For example, it has been known for decades that DdH and DvH can be purified under air as an inactive state (named Hinact) that can be reactivated by a reductive treatment (Pierik et al., 1998; Roseboom et al., 2006). However, the first attempts to generate Hinact *in vitro* were unsuccessful, and the exact protection mechanism has been elusive for years. Only recently it was shown that DdH requires the addition of exogenous sulphide to form Hinact, *via* the intermediate species Htrans. It has been demonstrated that Hinact in DdH (**Figure 2**) is an overoxidized H-cluster with sulphide bound to Fe_d, thus preventing O_2 binding by direct competition and protecting the enzyme from damage. Given the importance of sulphur metabolism in *Desulfovibrio*, it has been suggested that this mechanism may play a physiological role *in vivo*. Interestingly, sulphide dependent Hinact formation is not an exclusive feature of DdH, as it occurs in CrHydA1 as well; however, this mechanism is not effective on CpI, highlighting variability between different [FeFe]-hydrogenases (Rodriguez-Macia et al., 2018; Rodriguez-Macia et al., 2020).

Also recently, it has been shown that CbA5H from *C. beijerinckii* is able to form Hinact in a fully reversible manner; the enzyme can be inactivated and reactivated multiple times without any loss of activity (Morra et al., 2016a). Further characterisation showed that Hinact formation in CbA5H does not require exogenous sulphide and spectro-electrochemical titrations showed that the Hox/Hinact transition in CbA5H is a 1-electron process that occurs at an unusually low potential, without forming Htrans (Corrigan et al., 2020). Xray crystallography has recently confirmed that Hinact in CbA5H is indeed independent of exogenous sulphide, as a sulphur atom from a conserved cysteine can bind directly Fe_d, following a conformational change within the enzyme (**Figure 2**). This is particularly fascinating since the immediate surroundings of the H-cluster in CbA5H are conserved and do not differ from other [FeFe]-hydrogenases. Hence, it has been proposed that the protection mechanism depends on three non-conserved amino acids, situated far away from the H-cluster, that allow for the local conformational change to occur. This finding highlights the complexity of the interplay between the H-cluster and the protein residues as a fundamental part of [FeFe]-hydrogenase function, challenging the common assumption of [FeFe]-hydrogenases being a rigid scaffold that simply hosts a metal cluster responsible for their peculiar features (Winkler et al., 2021).

Protection from oxygen is not limited to few fortunate cases, as it has been shown that two other [FeFe]-hydrogenases are likely to display similar protection mechanisms: DfHnd, the heterotetrameric bifurcating [FeFe]-hydrogenase from *Desulfovibrio fructosovorans* forms Hinact and is protected from oxygen damage (Kpebe et al., 2018); also CpIII can form a species whose spectroscopy is reminiscent of Hinact (Artz et al., 2020).

Overall, recent research has highlighted that oxygen sensitivity/tolerance in [FeFe]-hydrogenases is much more complex than previously assumed. Different enzymes display completely different reactivity toward oxygen, with a growing number of them being able to tolerate it. It emerges that long term protection from oxygen damage in [FeFe]-hydrogenases invariably requires a nucleophilic species (CO, H_2S or a cysteine thiol) to directly bind Fe_d thus competing for O_2 binding (**Figure 2**). While carbon monoxide protection seems to be a universal feature of all hydrogenases, sulphur-based protection appears to vary significantly between different enzymes. This clearly highlights that the protein environment plays a crucial role in determining the enzyme's fate when

exposed to O_2, but the exact determinants for such a diversity are not comprehensively understood. Also, the physiological implications of oxygen tolerance in [FeFe]-hydrogenases have not been fully addressed yet.

CONCLUSION AND FUTURE PERSPECTIVES

Recent characterisation of novel [FeFe]-hydrogenases has highlighted a broad functional spectrum that exceeds their prototypical role in hydrogen production. Involvement in hydrogen sensing, electron bifurcation and CO_2 reduction demonstrate how diverse [FeFe]-hydrogenase functions are, and how crucial they are to support cellular metabolism under different conditions. It has also become clear that several [FeFe]-hydrogenases have evolved strategies to cope with oxygen, making them oxygen tolerant.

Despite the major advancements summarised here, the current understanding of [FeFe]-hydrogenase diversity is still limited because few enzymes have been characterised in detail so far. Studying novel [FeFe]-hydrogenases and populating the phylogenetic tree with experimental evidence from this unexplored space will be essential to improve our understanding of [FeFe]-hydrogenase function.

Research in this field has shown that relying mainly on few model enzymes and extrapolating information, in the assumption that they represent a vast enzyme class, inevitably leads to severe biases. Providing accurate predictions purely based on primary sequence data and phylogenetic positioning will always be a risky task but it is reasonable to expect that expanding our knowledge to additional enzymes will make comparisons between closely related sequences more reliable. Improving our understanding of [FeFe]-hydrogenase function will provide numerous benefits, for example when interpreting-omics data, as this task heavily relies on previous information being available and correctly annotated in databases. Also, the availability of additional enzymes will inevitably expand the portfolio of [FeFe]-hydrogenases with desirable features for a given application, either *in vitro* in a technological device, or *in vivo* within an engineered organism, or as an inspirational example for artificial catalysts, thus increasing the chances for success in future applications.

AUTHOR CONTRIBUTIONS

The author confirms being the sole contributor of this work and has approved it for publication.

FUNDING

SM gratefully acknowledges support from the University of Nottingham *via* the Nottingham Research Fellowship scheme.

SUPPLEMENTARY MATERIAL

The Supplementary Material for this article can be found online at: https://www.frontiersin.org/articles/10.3389/fmicb.2022.853626/full#supplementary-material

REFERENCES

Adams, M. W. W. (1990). The structure and mechanism of iron-hydrogenases. *Biochim. Biophys. Acta* 1020, 115–145. doi: 10.1016/0005-2728(90)90044-5

Ahmed, M. E., and Dey, A. (2019). Recent developments in bioinspired modelling of NiFe - and FeFe -hydrogenases. *Curr. Opin. Electrochem.* 15, 155–164. doi: 10.1021/acs.accounts.0c00315

Arizzi, M., Morra, S., Gilardi, G., Pugliese, M., Gullino, M. L., and Valetti, F. (2021). Improving sustainable hydrogen production from green waste: FeFe -hydrogenases quantitative gene expression RT-qPCR analysis in presence of autochthonous consortia. *Biotechnol. Biofuels* 14:17. doi: 10.1186/s13068-021-02028-3

Artz, J. H., Zadvornyy, O. A., Mulder, D. W., Keable, S. M., Cohen, A. E., Ratzloff, M. W., et al. (2020). Tuning Catalytic Bias of Hydrogen Gas Producing Hydrogenases. *J. Am. Chem. Soc.* 142, 1227–1235. doi: 10.1021/jacs.9b08756

Baffert, C., Kpebe, A., Avilan, L., and Brugna, M. (2019). Hydrogenases and H-2 metabolism in sulfate-reducing bacteria of the Desulfovibrio genus. *Adv. Microbial. Physiol.* 74, 143–189. doi: 10.1016/bs.ampbs.2019.03.001

Barton, R. M., and Worman, H. J. (1999). Prenylated prelamin A interacts with Narf, a novel nuclear protein. *J. Biol. Chem.* 274, 30008–30018.

Berggren, G., Adamska, A., Lambertz, C., Simmons, T. R., Esselborn, J., Atta, M., et al. (2013). Biomimetic assembly and activation of FeFe -hydrogenases. *Nature* 499:66. doi: 10.1038/nature12239

Bingham, A. S., Smith, P. R., and Swartz, J. R. (2012). Evolution of an FeFe hydrogenase with decreased oxygen sensitivity. *Int. J. Hydrogen Energy* 37, 2965–2976. doi: 10.1016/j.ijhydene.2011.02.048

Birrell, J. A., Rodriguez-Macia, P., Reijerse, E. J., Martini, M. A., and Lubitz, W. (2021). The catalytic cycle of FeFe hydrogenase: A tale of two sites. *Coordinat. Chem. Rev.* 449:214191. doi: 10.1016/j.ccr.2021.214191

Birrell, J. A., Wrede, K., Pawlak, K., Rodriguez-Macia, P., Rudiger, O., Reijerse, E. J., et al. (2016). Artificial Maturation of the Highly Active Heterodimeric FeFe Hydrogenase from Desulfovibrio desulfuricans ATCC 7757. *Israel J. Chem.* 56, 852–863. doi: 10.1002/ijch.201600035

Boyd, E. S., Hamilton, T. L., Spear, J. R., Lavin, M., and Peters, J. W. (2010). FeFe -hydrogenase in Yellowstone National Park: evidence for dispersal limitation and phylogenetic niche conservatism. *Isme J.* 4, 1485–1495. doi: 10.1038/ismej.2010.76

Brown, K. A., and King, P. W. (2020). Coupling biology to synthetic nanomaterials for semi-artificial photosynthesis. *Photosynth. Res.* 143, 193–203. doi: 10.1007/s11120-019-00670-5

Buckel, W., and Thauer, R. K. (2018). Flavin-Based Electron Bifurcation, Ferredoxin, Flavodoxin, and Anaerobic Respiration With Protons (Ech) or NAD(+) (Rnf) as Electron Acceptors: A Historical Review. *Front. Microbiol.* 9:401. doi: 10.3389/fmicb.2018.00401

Calusinska, M., Hamilton, C., Monsieurs, P., Mathy, G., Leys, N., Franck, F., et al. (2015). Genome-wide transcriptional analysis suggests hydrogenase- and nitrogenase-mediated hydrogen production in Clostridium butyricum CWBI 1009. *Biotechnol. Biofuels* 8:27. doi: 10.1186/s13068-015-0203-5

Calusinska, M., Happe, T., Joris, B., and Wilmotte, A. (2010). The surprising diversity of clostridial hydrogenases: a comparative genomic perspective. *Microbiol. Sgm* 156, 1575–1588. doi: 10.1099/mic.0.032771-0

Chongdar, N., Birrell, J. A., Pawlak, K., Sommer, C., Reijerse, E. J., Rudiger, O., et al. (2018). Unique Spectroscopic Properties of the H-Cluster in a Putative Sensory FeFe Hydrogenase. *J. Am. Chem. Soc.* 140, 1057–1068. doi: 10.1021/jacs.7b11287

Cornish, A. J., Green, R., Gartner, K., Mason, S., and Hegg, E. L. (2015). Characterization of Hydrogen Metabolism in the Multicellular Green Alga Volvox carteri. *PLos One* 10:e0125324. doi: 10.1371/journal.pone.0125324

Corrigan, P. S., Tirsch, J. L., and Silakov, A. (2020). Investigation of the Unusual Ability of the FeFe Hydrogenase from Clostridium beijerinckii to Access an O-2-Protected State. *J. Am. Chem. Soc.* 142, 12409–12419. doi: 10.1021/jacs.0c04964

Demuez, M., Cournac, L., Guerrini, O., Soucaille, P., and Girbal, L. (2007). Complete activity profile of Clostridium acetobutylicum FeFe -hydrogenase and kinetic parameters for endogenous redox partners. *FEMS Microbiol. Lett.* 275, 113–121. doi: 10.1111/j.1574-6968.2007.00868.x

Ding, D., Valdivia, A. O., and Bhattacharya, S. K. (2020). Nuclear prelamin a recognition factor and iron dysregulation in multiple sclerosis. *Metabolic Brain Dis.* 35, 275–282. doi: 10.1007/s11011-019-00515-z

Du, G. Q., Che, J., Wu, Y. D., Wang, Z. Z., Jiang, Z. Y., Ji, F., et al. (2021). Disruption of hydrogenase gene for enhancing butanol selectivity and production in Clostridium acetobutylicum. *Biochem. Engin. J.* 5:171.

Engelbrecht, V., Liedtke, K., Rutz, A., Yadav, S., Gunzel, A., and Happe, T. (2021). One isoform for one task? The second hydrogenase of Chlamydomonas reinhardtii prefers hydrogen uptake. *Int. J. Hydrogen Energy* 46, 7165–7175. doi: 10.1016/j.ijhydene.2020.11.231

Esselborn, J., Kertess, L., Apfel, U. P., Hofmann, E., and Happe, T. (2019). Loss of Specific Active-Site Iron Atoms in Oxygen-Exposed FeFe -Hydrogenase Determined by Detailed X-ray Structure Analyses. *J. Am. Chem. Soc.* 141, 17721–17728. doi: 10.1021/jacs.9b07808

Esselborn, J., Lambertz, C., Adamska-Venkatesh, A., Simmons, T., Berggren, G., Nothl, J., et al. (2013). Spontaneous activation of FeFe -hydrogenases by an inorganic 2Fe active site mimic. *Nat. Chem. Biol.* 9, 607–609. doi: 10.1038/nchembio.1311

Evans, R. M., Siritanaratkul, B., Megarity, C. F., Pandey, K., Esterle, T. F., Badiani, S., et al. (2019). The value of enzymes in solar fuels research - efficient electrocatalysts through evolution. *Chem. Soc. Rev.* 48, 2039–2052. doi: 10.1039/c8cs00546j

Florin, L., Tsokoglou, A., and Happe, T. (2001). A novel type of iron hydrogenase in the green alga Scenedesmus obliquus is linked to the photosynthetic electron transport chain. *J. Biol. Chem.* 276, 6125–6132. doi: 10.1074/jbc.M008470200

Forestier, M., King, P., Zhang, L. P., Posewitz, M., Schwarzer, S., Happe, T., et al. (2003). Expression of two Fe -hydrogenases in Chlamydomonas reinhardtii under anaerobic conditions. *Europ. J. Biochem.* 270, 2750–2758. doi: 10.1046/j.1432-1033.2003.03656

Germane, K. L., Liu, S. C., Gerlach, E. S., Savage, A. M., Renberg, R. L., Zu, T. N. K., et al. (2018). Hydrogen-Cycling during Solventogenesis in Clostridium acetobutylicum American Type Culture Collection (ATCC) 824 Requires the NiFe -Hydrogenase for Energy Conservation. *Ferment. Basel* 4:16.

Ghirardi, M. L. (2015). Implementation of photobiological H-2 production: the O-2 sensitivity of hydrogenases. *Photosynth. Res.* 125, 383–393. doi: 10.1002/mbo3.37

Girbal, L., Von Abendroth, G., Winkler, M., Benton, P. M. C., Meynial-Salles, I., Croux, C., et al. (2005). Homologous and heterologous overexpression in Clostridium acetobutylicum and characterization of purified clostridial and algal Fe-only hydrogenases with high specific activities. *Appl. Environ. Microbiol.* 71, 2777–2781. doi: 10.1128/AEM.71.5.2777-2781.2005

Goldet, G., Brandmayr, C., Stripp, S. T., Happe, T., Cavazza, C., Fontecilla-Camps, J. C., et al. (2009). Electrochemical Kinetic Investigations of the Reactions of FeFe -Hydrogenases with Carbon Monoxide and Oxygen: Comparing the Importance of Gas Tunnels and Active-Site Electronic/Redox Effects. *J. Am. Chem. Soc.* 131, 14979–14989. doi: 10.1021/ja905388j

Greening, C., Biswas, A., Carere, C. R., Jackson, C. J., Taylor, M. C., Stott, M. B., et al. (2016). Genomic and metagenomic surveys of hydrogenase distribution indicate H-2 is a widely utilised energy source for microbial growth and survival. *ISME J.* 10, 761–777. doi: 10.1038/ismej.2015.153

Happe, T., and Kaminski, A. (2002). Differential regulation of the Fe-hydrogenase during anaerobic adaptation in the green alga Chlamydomonas reinhardtii. *Europ. J. Biochem.* 269, 1022–1032. doi: 10.1046/j.0014-2956.2001.02743.x

Happe, T., and Naber, J. D. (1993). Isolation, characterization and N-terminal amino acid sequence of hydrogenase from the green alga Chlamydomonas reinhardtii. *Europ. J. Biochem.* 214, 475–481. doi: 10.1111/j.1432-1033.1993.tb17944.x

Haumann, M., and Stripp, S. T. (2018). The Molecular Proceedings of Biological Hydrogen Turnover. *Accounts Chem. Res.* 51, 1755–1763. doi: 10.1021/acs.accounts.8b00109

Kamp, C., Silakov, A., Winkler, M., Reijerse, E. J., Lubitz, W., and Happe, T. (2008). Isolation and first EPR characterization of the FeFe -hydrogenases from green algae. *Biochim. Biophys. Acta Bioenerget.* 1777, 410–416. doi: 10.1016/j.bbabio.2008.02.002

Kanygin, A., Milrad, Y., Thummala, C., Reifschneider, K., Baker, P., Marco, P., et al. (2020). Rewiring photosynthesis: a photosystem I-hydrogenase chimera that makes H-2 in vivo. *Energy Environ. Sci.* 13, 2903–2914.

Karayilan, M., Brezinski, W. P., Clary, K. E., Lichtenberger, D. L., Glass, R. S., and Pyun, J. (2019). Catalytic Metallopolymers from 2Fe-2S Clusters: Artificial Metalloenzymes for Hydrogen Production. *Angew. Chem. Int. Edition* 58, 7537–7550. doi: 10.1002/anie.201813776

Kelly, C. L., Pinske, C., Murphy, B. J., Parkin, A., Armstrong, F., Palmer, T., et al. (2015). Integration of an [FeFe]-hydrogenase into the anaerobic metabolism of *Escherichia coli*. *Biotechnol. Rep.* 8, 94–104.

King, P., Ghirardi, M. L., and Seibert, M. (2014). Oxygen-resistant hydrogenases and methods for designing and making same. *USA Patent Appl.* 8:958.

King, P. W., Posewitz, M. C., Ghirardi, M. L., and Seibert, M. (2006). Functional studies of FeFe hydrogenase maturation in an *Escherichia coli* biosynthetic system. *J. Bacteriol.* 188, 2163–2172.

Klein, M., Ansorge-Schumacher, M. B., Fritsch, M., and Hartmeier, W. (2010). Influence of hydrogenase overexpression on hydrogen production of Clostridium acetobutylicum DSM 792. *Enzyme Microbial Technol.* 46, 384–390.

Kpebe, A., Benvenuti, M., Guendon, C., Rebai, A., Fernandez, V., Le Laz, S., et al. (2018). A new mechanistic model for an O-2-protected electron-bifurcating hydrogenase, Hnd from Desulfovibrio fructosovorans. *Biochim. Biophys. Acta Bioenerget.* 1859, 1302–1312. doi: 10.1016/j.bbabio.2018.09.364

Kubas, A., Orain, C., De Sancho, D., Saujet, L., Sensi, M., Gauquelin, C., et al. (2017). Mechanism of O-2 diffusion and reduction in FeFe hydrogenases. *Nat. Chem.* 9, 88–95. doi: 10.1038/nchem.2592

Kuchenreuther, J. M., Grady-Smith, C. S., Bingham, A. S., George, S. J., Cramer, S. P., and Swartz, J. R. (2010). High-Yield Expression of Heterologous FeFe Hydrogenases in *Escherichia coli*. *PLoS One* 5:e15491. doi: 10.1371/journal.pone.0015491

Land, H., Sekretareva, A., Huang, P., Redman, H. J., Nemeth, B., Polidori, N., et al. (2020). Characterization of a putative sensory FeFe -hydrogenase provides new insight into the role of the active site architecture. *Chem. Sci.* 11, 12789–12801. doi: 10.1039/d0sc03319g

Lautier, T., Ezanno, P., Baffert, C., Fourmond, V., Cournac, L., Fontecilla-Camps, J. C., et al. (2011). The quest for a functional substrate access tunnel in FeFe hydrogenase. *Faraday Dis.* 148, 385–407. doi: 10.1039/c004099c

Legall, J., Dervartanian, D. V., Spilker, E., Lee, J. P., and Peck, H. D. (1971). Evidence for the involvement of non-heme iron in the active site of hydrogenase from Desulfovibrio vulgaris. *Biochim. Biophys. Acta* 234, 526–30.

Lemon, B. J., and Peters, J. W. (1999). Binding of exogenously added carbon monoxide at the active site of the iron-only hydrogenase (CpI) from Clostridium pasteurianum. *Biochemistry* 38, 12969–12973. doi: 10.1021/bi9913193

Leo, F., Schwarz, F. M., Schuchmann, K., and Muller, V. (2021). Capture of carbon dioxide and hydrogen by engineered *Escherichia coli*: hydrogen-dependent CO2 reduction to formate. *Appl. Microbiol. Biotechnol.* 105, 5861–5872. doi: 10.1007/s00253-021-11463-z

Losey, N. A., Mus, F., Peters, J. W., Le, H. M., and Mcinerney, M. J. (2017). Syntrophomonas wolfei Uses an NADH-Dependent, Ferredoxin-Independent FeFe -Hydrogenase To Reoxidize NADH. *Appl. Environ. Microbiol.* 83, e01335–17. doi: 10.1128/AEM.01335-17

Losey, N. A., Poudel, S., Boyd, E. S., and Mcinerney, M. J. (2020). The Beta Subunit of Non-bifurcating NADH-Dependent FeFe -Hydrogenases Differs From Those of Multimeric Electron-Bifurcating FeFe -Hydrogenases. *Front. Microbiol.* 11:14. doi: 10.3389/fmicb.2020.01109

Lyons, T. W., Reinhard, C. T., and Planavsky, N. J. (2014). The rise of oxygen in Earth's early ocean and atmosphere. *Nature* 506, 307–315. doi: 10.1038/nature13068

Meuser, J. E., Boyd, E. S., Ananyev, G., Karns, D., Radakovits, R., Murthy, U. M. N., et al. (2011). Evolutionary significance of an algal gene encoding an FeFe -hydrogenase with F-domain homology and hydrogenase activity in Chlorella variabilis NC64A. *Planta* 234, 829–843. doi: 10.1007/s00425-011-1431-y

Meyer, J. (2007). FeFe hydrogenases and their evolution: a genomic perspective. *Cell. Mole. Life Sci.* 64, 1063–1084. doi: 10.1007/s00018-007-6477-4

Morra, S., Arizzi, M., Allegra, P., La Licata, B., Sagnelli, F., Zitella, P., et al. (2014). Expression of different types of FeFe -hydrogenase genes in bacteria isolated from a population of a bio-hydrogen pilot-scale plant. *Int. J. Hydrog. Energ.* 39, 9018–9027.

Morra, S., Arizzi, M., Valetti, F., and Gilardi, G. (2016a). Oxygen Stability in the New FeFe -Hydrogenase from Clostridium beijerinckii SM10 (CbA5H). *Biochemistry* 55, 5897–5900. doi: 10.1021/acs.biochem.6b00780

Morra, S., Mongili, B., Maurelli, S., Gilardi, G., and Valetti, F. (2016b). Isolation and characterization of a new FeFe -hydrogenase from Clostridium perfringens. *Biotechnol. Appl. Biochem.* 63, 305–311. doi: 10.1002/bab.1382

Morra, S., Valetti, F., and Gilardi, G. (2017). FeFe -hydrogenases as biocatalysts in bio-hydrogen production. *Rendiconti Lincei Scienze Fisiche E Naturali* 28, 183–194.

Mulder, D. W., Boyd, E. S., Sarma, R., Lange, R. K., Endrizzi, J. A., Broderick, J. B., et al. (2010). Stepwise FeFe -hydrogenase H-cluster assembly revealed in the structure of HydA(Delta EFG). *Nature* 465, 248–U143. doi: 10.1038/nature08993

Nakos, G., and Mortenson, L. (1971). Purification and properties of hydrogenase, an iron sulfur protein, from Clostridium pasteurianum W5. *Biochim. Biophys. Acta* 227:576. doi: 10.1016/0005-2744(71)90008-8

Nicolet, Y., Piras, C., Legrand, P., Hatchikian, C. E., and Fontecilla-Camps, J. C. (1999). Desulfovibrio desulfuricans iron hydrogenase: the structure shows unusual coordination to an active site Fe binuclear center. *Struct. Folding Design* 7, 13–23. doi: 10.1016/s0969-2126(99)80005-7

Noone, S., Ratcliff, K., Davis, R., Subramanian, V., Meuser, J., Posewitz, M. C., et al. (2017). Expression of a clostridial FeFe -hydrogenase in Chlamydomonas reinhardtii prolongs photo-production of hydrogen from water splitting. *Algal Res. Biomass Biofuels Bioprod.* 22, 116–121.

Peters, J. W., Beratan, D. N., Bothner, B., Dyer, R. B., Harwood, C. S., Heiden, Z. M., et al. (2018). A new era for electron bifurcation. *Curr. Opin. Chem. Biol.* 47, 32–38. doi: 10.1016/j.cbpa.2018.07.026

Peters, J. W., Lanzilotta, W. N., Lemon, B. J., and Seefeldt, L. C. (1998). X-ray crystal structure of the Fe-only hydrogenase (Cpl) from Clostridium pasteurianum to 1.8 angstrom resolution. *Science* 282, 1853–1858. doi: 10.1126/science.282.5395.1853

Peters, J. W., Schut, G. J., Boyd, E. S., Mulder, D. W., Shepard, E. M., Broderick, J. B., et al. (2015). FeFe - and NiFe -hydrogenase diversity, mechanism, and maturation. *Biochim. Biophys. Acta Mole. Cell Res.* 1853, 1350–1369. doi: 10.1016/j.bbamcr.2014.11.021

Piche-Choquette, S., and Constant, P. (2019). Molecular Hydrogen, a Neglected Key Driver of Soil Biogeochemical Processes. *Appl. Environ. Microbiol.* 85, e02418–18. doi: 10.1128/AEM.02418-18

Pierik, A. J., Hulstein, M., Hagen, W. R., and Albracht, S. P. J. (1998). A low-spin iron with CN and CO as intrinsic ligands forms the core of the active site in Fe -hydrogenases. *Europ. J. Biochem.* 258, 572–578. doi: 10.1046/j.1432-1327.1998.2580572.x

Pohorelic, B. K. J., Voordouw, J. K., Lojou, E., Dolla, A., Harder, J., and Voordouw, G. (2002). Effects of deletion of genes encoding Fe-only hydrogenase of Desulfovibrio vulgaris Hildenborough on hydrogen and lactate metabolism. *J. Bacteriol.* 184, 679–686. doi: 10.1128/JB.184.3.679-686.2002

Poudel, S., Tokmina-Lukaszewska, M., Colman, D. R., Refai, M., Schut, G. J., King, P. W., et al. (2016). Unification of FeFe -hydrogenases into three structural and functional groups. *Biochim. Biophys. Acta General Subj.* 1860, 1910–1921. doi: 10.1016/j.bbagen.2016.05.034

Rodriguez-Macia, P., Galle, L. M., Bjornsson, R., Lorent, C., Zebger, I., Yoda, Y., et al. (2020). Caught in the H-inact: Crystal Structure and Spectroscopy Reveal a Sulfur Bound to the Active Site of an O-2-stable State of FeFe Hydrogenase. *Angewandte Chem. Int. Edition* 59, 16786–16794. doi: 10.1002/anie.202005208

Rodriguez-Macia, P., Reijerse, E. J., Van Gastel, M., Debeer, S., Lubitz, W., Rudiger, O., et al. (2018). Sulfide Protects FeFe Hydrogenases From O-2. *J. Am. Chem. Soc.* 140, 9346–9350.

Roseboom, W., De Lacey, A. L., Fernandez, V. M., Hatchikian, E. C., and Albracht, S. P. J. (2006). The active site of the FeFe -hydrogenase from Desulfovibrio desulfuricans. II. Redox properties, light sensitivity and CO-ligand exchange as observed by infrared spectroscopy. *J. Biol. Inorg. Chem.* 11, 102–118. doi: 10.1007/s00775-005-0040-2

Schuchmann, K., Chowdhury, N. P., and Muller, V. (2018). Complex Multimeric FeFe Hydrogenases: Biochemistry, Physiology and New Opportunities for the Hydrogen Economy. *Front. Microbiol.* 9:2911. doi: 10.3389/fmicb.2018.02911

Schuchmann, K., and Muller, V. (2013). Direct and Reversible Hydrogenation of CO2 to Formate by a Bacterial Carbon Dioxide Reductase. *Science* 342, 1382–1385. doi: 10.1126/science.1244758

Schut, G. J., and Adams, M. W. W. (2009). The Iron-Hydrogenase of Thermotoga maritima Utilizes Ferredoxin and NADH Synergistically: a New Perspective on Anaerobic Hydrogen Production. *J. Bacteriol.* 191, 4451–4457. doi: 10.1128/JB.01582-08

Schwarz, F. M., Schuchmann, K., and Muller, V. (2018). Hydrogenation of CO2 at ambient pressure catalyzed by a highly active thermostable biocatalyst. *Biotechnol. Biofuels* 11:11. doi: 10.1186/s13068-018-1236-3

Shaw, A. J., Hogsett, D. A., and Lynd, L. R. (2009). Identification of the FeFe -Hydrogenase Responsible for Hydrogen Generation in Thermoanaerobacterium saccharolyticum and Demonstration of Increased Ethanol Yield via Hydrogenase Knockout. *J. Bacteriol.* 191, 6457–6464. doi: 10.1128/JB.00497-09

Stripp, S. T., Goldet, G., Brandmayr, C., Sanganas, O., Vincent, K. A., Haumann, M., et al. (2009). How oxygen attacks FeFe hydrogenases from photosynthetic organisms. *Proc. Natl. Acad. Sci. U.S.A.* 106, 17331–17336. doi: 10.1073/pnas.0905343106

Swanson, K. D., Ratzloff, M. W., Mulder, D. W., Artz, J. H., Ghose, S., Hoffman, A., et al. (2015). FeFe -Hydrogenase Oxygen Inactivation Is Initiated at the H Cluster 2Fe Subcluster. *J. Am. Chem. Soc.* 137, 1809–1816. doi: 10.1021/ja510169s

Therien, J. B., Artz, J. H., Poudel, S., Hamilton, T. L., Liu, Z. F., Noone, S. M., et al. (2017). The Physiological Functions and Structural Determinants of Catalytic Bias in the FeFe -Hydrogenases CpI and CpII of Clostridium pasteurianum Strain W5. *Front. Microbiol.* 8:11. doi: 10.3389/fmicb.2017.01305

Vignais, P. M., and Billoud, B. (2007). Occurrence, classification, and biological function of hydrogenases: An overview. *Chem. Rev.* 107, 4206–4272. doi: 10.1021/cr050196r

Wegelius, A., Land, H., Berggren, G., and Lindblad, P. (2021). Semisynthetic FeFe -hydrogenase with stable expression and H-2 production capacity in a photosynthetic microbe. *Cell Rep. Phys. Sci.* 2:100376. doi: 10.1016/j.xcrp.2021.100376

Winkler, M., Duan, J. F., Rutz, A., Felbek, C., Scholtysek, L., Lampret, O., et al. (2021). A safety cap protects hydrogenase from oxygen attack. *Nat. Commun.* 12:756. doi: 10.1038/s41467-020-20861-2

Winkler, M., Esselborn, J., and Happe, T. (2013). Molecular basis of FeFe -hydrogenase function An insight into the complex interplay between protein and catalytic cofactor. *Biochim. Biophys. Acta Bioenerg.* 1827, 974–985. doi: 10.1016/j.bbabio.2013.03.004

Winkler, M., Heil, B., and Happe, T. (2002). Isolation and molecular characterization of the Fe -hydrogenase from the unicellular green alga Chlorella fusca. *Biochim. Biophys. Acta Gene Struct. Exp.* 1576, 330–334. doi: 10.1016/s0167-4781(02)00239-7

Zheng, Y. N., Kahnt, J., Kwon, I. H., Mackie, R. I., and Thauer, R. K. (2014). Hydrogen Formation and Its Regulation in Ruminococcus albus: Involvement of an Electron-Bifurcating FeFe -Hydrogenase, of a Non-Electron-Bifurcating FeFe -Hydrogenase, and of a Putative Hydrogen-Sensing FeFe -Hydrogenase. *J. Bacteriol.* 196, 3840–3852. doi: 10.1128/JB.02070-14

Conflict of Interest: The author declares that the research was conducted in the absence of any commercial or financial relationships that could be construed as a potential conflict of interest.

frontiers in Microbiology

ORIGINAL RESEARCH
published: 29 March 2022
doi: 10.3389/fmicb.2022.872581

Exchange of a Single Amino Acid Residue in the HybG Chaperone Allows Maturation of All H_2-Activating [NiFe]-Hydrogenases in *Escherichia coli*

*Alexander Haase and R. Gary Sawers**

Institute of Microbiology, Martin-Luther-University Halle-Wittenberg, Halle, Germany

The biosynthesis of the $NiFe(CN)_2CO$ organometallic cofactor of [NiFe]-hydrogenase (Hyd) involves several discreet steps, including the synthesis of the $Fe(CN)_2CO$ group on a HypD-HypC scaffold complex. HypC has an additional function in transferring the $Fe(CN)_2CO$ group to the apo-precursor of the Hyd catalytic subunit. Bacteria that synthesize more than one Hyd enzyme often have additional HypC-type chaperones specific for each precursor. The specificity determinants of this large chaperone family are not understood. *Escherichia coli* synthesizes two HypC paralogs, HypC and HybG. HypC delivers the $Fe(CN)_2CO$ group to pre-HycE, the precursor of the H_2-evolving Hyd-3 enzyme, while HybG transfers the group to the pre-HybC of the H_2-oxidizing Hyd-2 enzyme. We could show that a conserved histidine residue around the amino acid position 50 in both HypC and HybG, when exchanged for an alanine, resulted in a severe reduction in the activity of its cognate Hyd enzyme. This reduction in enzyme activity proved to be due to the impaired ability of the chaperones to interact with HypD. Surprisingly, and only in the case of the $HybG_{H52A}$ variant, its co-synthesis with HypD improved its interaction with pre-HycE, resulting in the maturation of Hyd-3. This study demonstrates that the conserved histidine residue helps enhance the interaction of the chaperone with HypD, but additionally, and in *E. coli* only for HybG, acts as a determinant to prevent the inadvertent maturation of the wrong large-subunit precursor. This study identifies a new level of control exerted by a bacterium synthesizing multiple [NiFe]-Hyd to ensure the correct enzyme is matured only under the appropriate physiological conditions.

Keywords: hydrogen evolution, hydrogen oxidation, HypC chaperone, HybG chaperone, HypD, maturation, NiFe-hydrogenase

OPEN ACCESS

Edited by:
Stefan Frielingsdorf, Technical University of Berlin, Germany

Reviewed by:
Wolfgang Buckel, University of Marburg, Germany
Carole Baffert, Aix-Marseille Université, France

***Correspondence:**
R. Gary Sawers
gary.sawers@mikrobiologie.uni-halle.de

Specialty section:
This article was submitted to Microbial Physiology and Metabolism, a section of the journal Frontiers in Microbiology

Received: *09 February 2022*
Accepted: *01 March 2022*
Published: *29 March 2022*

Citation:
Haase A and Sawers RG (2022) Exchange of a Single Amino Acid Residue in the HybG Chaperone Allows Maturation of All H_2-Activating [NiFe]-Hydrogenases in Escherichia coli. Front. Microbiol. 13:872581. doi: 10.3389/fmicb.2022.872581

INTRODUCTION

During growth under anoxic conditions, *Escherichia coli* synthesizes three comparatively abundant [NiFe]-hydrogenases (Hyd) (Pinske and Sawers, 2016; Sargent, 2016). Of these three enzymes, two, Hyd-1 and Hyd-2, are principally functional in H_2 oxidation (Ballantine and Boxer, 1985; Sawers et al., 1985), while the third, Hyd-3, is a component of the H_2-evolving formate hydrogenlyase (FHL) complex (McDowall et al., 2014). All three enzymes have the same organometallic cofactor

[$NiFe(CN)_2CO$, or [NiFe]-cofactor] in their active site, which is required for reversible catalytic dihydrogen (H_2) activation by the enzyme (Böck et al., 2006; Lacasse and Zamble, 2016). The biosynthesis and insertion of this [NiFe]-cofactor into the large-subunit precursors of the respective Hyd enzymes requires the combined actions of six accessory proteins, the functions of which have been described previously (Böck et al., 2006). While the synthesis of this [NiFe]-cofactor is not the focus of this study, it is nevertheless important to stress that the $Fe(CN)_2CO$ component of the cofactor is assembled on a separate scaffold complex comprising the iron-sulfur protein HypD and either of the two small ∼10 kDa proteins called HypC or HybG. These latter two paralogs, which are the focus of this study, are structurally and functionally related and appear to have multifarious functions, being required for both biosynthesis and delivery of the $Fe(CN)_2CO$ group to the Hyd large-subunit precursors (Blokesch et al., 2001; Böck et al., 2006). They concomitantly acquire the iron ion and a CO_2 molecule, which potentially acts as a source of the CO ligand (Soboh et al., 2013; Arlt et al., 2021); the cellular sources of these are unknown. In complex with HypD, either HypC or HybG is required to aid the synthesis of the $Fe(CN)_2CO$ group (Blokesch et al., 2002, 2004). Once the synthesis of this group has been completed, the chaperones deliver $Fe(CN)_2CO$ to their designated large-subunit precursors (Arlt et al., 2021). The roles of HypC and HybG are schematically summarized in **Figure 1A**. Importantly, HypC specifically delivers the $Fe(CN)_2CO$ group to pre-HycE, the precursor of Hyd-3, and to a lesser extent to pre-HyaB, the precursor of Hyd-1, while HybG delivers the group specifically and preferentially to pre-HybC, and to pre-HyaB (Blokesch et al., 2001). The aim of this study is, therefore, to provide further insight into how the precursor specificity of the chaperones is delimited.

A recent study has demonstrated that HybG interacts with either HypD or pre-HybC, presumably shuttling $Fe(CN)_2CO$ from the HypD to pre-HybC (Arlt et al., 2021). These findings corroborate earlier proposals that the distinct precursor specificity shown by HybG and HypC for particular client proteins, as well as a common specificity for HypD, signifies a chaperone function for these small proteins (Drapal and Böck, 1998; Wolf et al., 1998; Jones et al., 2004). Because these proteins are small, it remains unclear whether common determinants on HypC and HybG govern their interaction with different precursors and with HypD, or whether different motifs play a role. Importantly, what prevents HybG from interacting with pre-HycE and activating Hyd-3, but allows it to interact with pre-HybC and pre-HyaB?

One answer to this question likely lies in the fact that the gene encoding HybG is located within the *hyb* structural gene operon, which encodes Hyd-2 (Menon et al., 1994). Typically, genes encoding HypC family members are located adjacent to those encoding HypD (Böck et al., 2006; Lacasse and Zamble, 2016), so the physical separation of the *hybG* gene from *hypD* on the *E. coli* genome presumably helps to limit HybG's ability to compete with HypC for HypD interaction.

Due to the lack of structural information on the HybG-pre-HybC or HypC-pre-HycE complexes, we must rely on the knowledge gained from *in vivo* studies performed with *E. coli* (Hartwig et al., 2015; Thomas et al., 2018), and from structural analyses of HypC and HypD from *Thermococcus kodakarensis* (Watanabe et al., 2007, 2012), to gain insight into potentially key residues or motifs involved in distinguishing client proteins.

The structure of HypC has revealed that, along with the essential *N*-terminal cysteine residue (C2), there is a highly conserved histidine residue at amino acid position 51 (H51; *E. coli* numbering) (**Figure 1B**), which is proximal to C2, and consequently has been suggested to have a role in stabilizing the binding of the $Fe(CN)_2CO$ group (Watanabe et al., 2007). The limited *in vivo* studies examining the role of this histidine residue have reported that its exchange for arginine in HypC essentially abolishes the Hyd-3-dependent H_2 evolution (Blokesch, 2004), while an *in vitro* study performed with the same variant reported that it was impaired in cofactor synthesis (Soboh et al., 2013). The examination of the crystal structure of the HypCD complex from *T. kodakarensis* located it to the interaction surface between the proteins (Watanabe et al., 2012; **Figure 1B**), which might also explain the biosynthesis-deficient phenotype observed when it is exchanged for another residue (Soboh et al., 2013).

In an attempt to resolve the function of this residue in the chaperone we have used HypC and HybG of *E. coli* as a model system and made a new variant by exchanging this residue for alanine in both proteins (position 52 in HybG). Using combined *in vitro* and *in vivo* experimental approaches, we show that this conserved histidine residue is indeed important to allow HypC and HybG to interact effectively with HypD. Unexpectedly, however, our studies also revealed that the $HybG_{H52A}$ variant gains the ability to interact with pre-HycE, thus identifying this histidine residue as a key determinant in ensuring that HybG normally does not mature Hyd-3 *in vivo*.

MATERIALS AND METHODS

Bacterial strains and plasmids. The *E. coli* strains used in this study included MC4100 *[* F–, *araD139*, Δ (*argF-lac*)*U169*, λ$^-$, *rpsL150*, *relA1*, *deoC1*, *flhD5301*, Δ (*fruK-yeiR*)*725*(*fruA25*), *rbsR22*, Δ (*fimB-fimE*) (Casadaban, 1976)*]*, and its isogenic mutant derivative SHH228 (like MC4100, but Δ*hypC* Δ*hybG*) (Hartwig et al., 2015). All of the plasmids used in this study are listed in **Table 1** and were introduced individually into strain SHH228 for either determination of Hyd-associated enzyme activities or protein purification. To construct plasmid phypCstrep carrying the native *hypC* gene with an additional *C*-terminal Strep-tag II coding sequence, genomic DNA isolated from *E. coli* strain MC4100 was used as a template for the PCR-amplification of the *hypC* gene using oligonucleotide primers hypC_*Bsa*I_IBA3_fwd (5′-GCACACGGTCTCAAATGTGCATAGGCGTTCCCGG-3′) and hypC_*Bsa*I_IBA3_rev (5′-GCACACGGTCTCAGCGCTGACATCCGGCTCAACGTCAAA-3′). The PCR product was digested with *Bsa*I and the resulting DNA fragment was ligated into the *Bsa*I-digested pASK-IBA3plus vector (IBA Lifesciences, Göttingen, Germany) to generate the plasmid phypCstrep. The

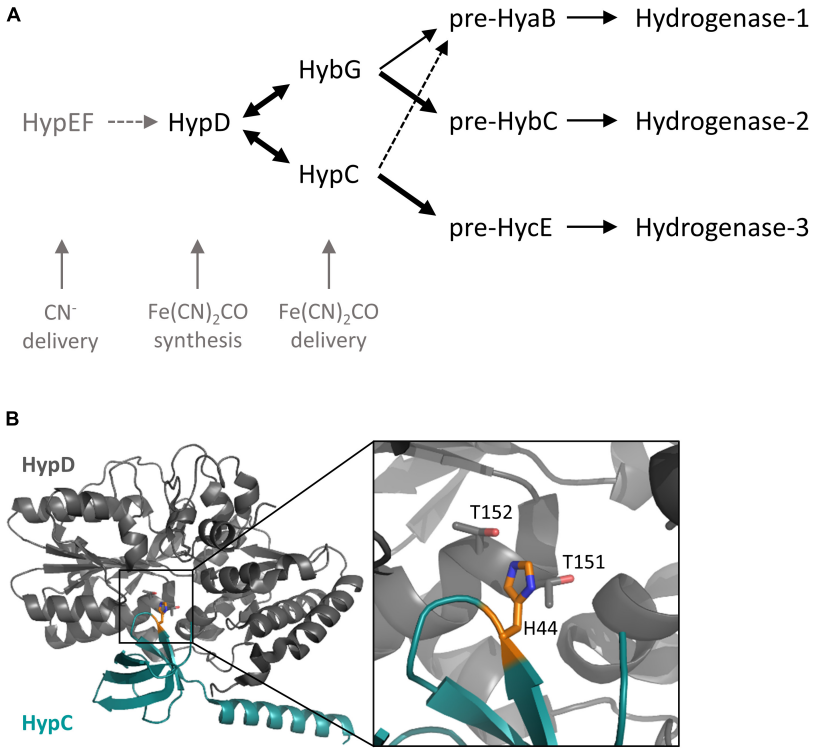

FIGURE 1 | The HypC chaperones involved in the maturation of hydrogenases in *E. coli*. **(A)** Schematic overview of the roles of HypC and HybG and their respective precursor specificities. The thickness of the arrow correlates with precursor preference. Dotted arrows indicate weak interaction, while double-headed arrows signify a reversible interaction. **(B)** Close-up of the location of the conserved histidine at the interface between HypC and HypD in the structure of scaffold complex determined for *Thermococcus kodakarensis* (PDB structure 3VYR; Watanabe et al., 2012). Note that the original residue numbering of $HypD_{Tk}$ and $HypC_{Tk}$ was retained in the structural analysis, so histidine 44 corresponds to H51 of *Escherichia coli* HypC, and threonine 151 and 152 of $HypD_{Tk}$ correspond to threonine T149 and T150 in HypD from *E. coli*. The location of the conserved histidine is indicated in orange and the structural representation was determined using PyMOL (The PyMOL Molecular Graphics System, version 2.5, Schrödinger, LLC).

plasmids phypC(H51A)strep, pT-hypDC(H51A)Strep, phybG(H52A)strep, and pT-hybG(H52A)-hypDEF were generated by PCR-based site-directed mutagenesis using the Q5® Site-Directed Mutagenesis Kit (New England Biolabs, United States). Plasmids phypC(H51A)strep and pT-hypDC(H51A)Strep were generated by changing codon 51 in the *hypC* gene on the plasmids phypCstrep and pT7-hypDCStrep (Blokesch et al., 2004), respectively, from CAC to GCC employing the oligonucleotides hypC_H51A_fw (5′-GGTACTGGTAGCCGTTGGCTTTGCCAT-3′) and hypC_H51A_rv (5′-CACTGGCCCACGCGCGGC-3′). Plasmids phybG(H52A)strep and pT7-hybG(H52A)-hypDEF were generated by changing codon 52 in the *hybG* gene on the plasmids phybGstrep (Soboh et al., 2014) and pT-hybG-hypDEF (Soboh et al., 2014), respectively, from CAT to GCC using the oligonucleotides hybG_H52A_fw (5′-GGTGCTGGTAGCCGTCGGATTTGC-3′) and hybG_H52A_rv (5′- CACTGGCCCAGTAGATCG-3′).

Growth Conditions

In preparation for routine microbiology and molecular biology experiments, such as cloning, strains were grown on LB-agar plates or in LB-broth at 37°C (Miller, 1972). Anaerobic growth for Hyd enzyme assays and enzyme activity-staining after native polyacrylamide gel electrophoresis (PAGE) was performed at 37°C as standing liquid cultures in the buffered rich medium TGYEP (1% w/v tryptone, 0.5% w/v yeast extract, 0.8% w/v glucose, 100 mM potassium phosphate, pH 6.5) (Begg et al., 1977). The growth medium was supplemented with trace element solution SLA (Hormann and Andreesen, 1989). When required, the antibiotics ampicillin, chloramphenicol, or kanamycin were added to a final concentration of 100, 25, or 50 μg ml^{-1}, respectively. Cells were harvested anaerobically when cultures had reached an OD_{600} nm of between 0.8 and 1.2 by centrifugation at 5,000 *g* for 15 min at 4°C. Cell pellets were either used immediately or stored at −20°C until use.

For anaerobic protein overproduction experiments, *E. coli* strain SHH228 (Δ*hypC* Δ*hybG*) was transformed with the indicated plasmids using standard procedures (Sambrook et al., 1989). Cultivation of cells was performed in modified TB medium (2.4% w/v yeast extract, 1.2% w/v peptone from casein, 0.04% w/v glycerol, 0.4% w/v glucose and 0.003% w/v magnesium sulfate heptahydrate) (Soboh et al., 2012). Depending on the plasmid used, the medium also included either 100 μg ml^{-1} ampicillin or 15 μg ml^{-1} chloramphenicol to maintain plasmid selection. Cultures were incubated anaerobically without

shaking at 37°C until an optical density at 600 nm (OD_{600}) of 0.4 was reached. To increase the amount of protein for purification purposes, the expression of the plasmid pASK-IBA3-borne *hypC* and *hybG* genes was induced by the addition of 0.2 μg ml^{-1} anhydrotetracycline (AHT), whereas for pT7-7- and pACYC-Duet1-based plasmids, gene expression was induced by the addition of 0.1 mM isopropyl β-D-1-thiogalactopyranoside (IPTG). Incubation of the cultures was continued at 30°C for 3 h, after which the cells were harvested by centrifugation at 5000 × *g* for 15 min at 4°C. The filling of bottles and tubes for the centrifugation of cultures and cell suspensions was performed under anoxic conditions in an anaerobic chamber (Coy Laboratories, Grass Lake, United States). Cell pellets, derived by centrifugation, were either used immediately or stored at – 20°C until use.

Measurement of Hydrogen Production

Two methods were used to determine H_2 production. One involved measuring cumulative H_2 production after anaerobic cultivation of strains, while the other determined continuous H_2 production in cell suspensions. Cumulative H_2 content was determined by growing strains in 15 ml Hungate tubes (initially filled with N_2) containing 8 ml of culture medium. The cultures were incubated for 20 h at 30°C and the H_2 concentration was measured by removing 200 μl aliquots from the headspace and analyzing the gas-phase using gas chromatography with a GC2010 Plus Gas Chromatograph (Shimadzu, Kyōto, Japan) as described (Pinske et al., 2015). Pure nitrogen was used as the carrier gas, and the amount of H_2 produced was calculated based on a standard curve prepared with pure H_2 gas. The experiment was repeated three times and each assay was performed in triplicate.

Continuous H_2 production by whole cells was determined using a modified Clark-type electrode equipped with an OXY/ECU module (Oxytherm, Hansatech Instruments, Norfolk, United Kingdom) to reverse the polarizing voltage to –0.7 V, essentially as described (Lindenstrauß et al., 2017). Cells were grown as described above, but only until the late-exponential phase was attained, and after the anaerobic centrifugation of cells to remove culture medium, the cell pellet was suspended in degassed 50 mM Tris, pH 7.0 and the centrifugation step was repeated. Subsequently, the cell pellet was suspended in 1 ml of degassed 50 mM Tris, pH 7.0 and 50 μl aliquots were added to the chamber of the electrode, which contained 1.95 ml of degassed 50 mM Tris, pH 7.0, equilibrated at 30°C. The reaction was started by adding 14 mM glucose, which was converted to formate intracellularly to act as a substrate of the FHL reaction and the amount of H_2 produced was determined using pure H_2 gas as described (Sargent et al., 1999). The assay was performed in triplicate using three biological replicates for each strain analyzed.

Preparation of Crude Extracts for Determination of Hyd Enzyme Activity

Cell paste was suspended in 2 ml of 50 mM MOPS, pH 7, including 5 μg DNase I ml^{-1} and 0.2 mM phenylmethylsulfonyl fluoride per 1 g wet weight. Cells were disrupted by sonication (20 W for 2 min with 0.5 s pulses). Cell debris and unbroken cells were removed by centrifugation for 20 min at 21,000 × *g* at 4°C. The supernatant (crude extract) was carefully decanted into a fresh tube and was used immediately. Protein concentration was determined as described before (Lowry et al., 1951).

Assay of Total H_2-Oxidizing Hyd Enzyme Activity

The total Hyd enzyme activity of the crude extracts was determined as H_2-dependent reduction of benzyl viologen (BV) as described (Ballantine and Boxer, 1985), except that the buffer used was 50 mM MOPS, pH 7.0. The wavelength used for the absorbance measurement was 600 nm and an ε_M value of 7,400 M^{-1} cm^{-1} was assumed for reduced BV. One unit of enzyme activity corresponded to the reduction of 1 μmol of substrate

TABLE 1 | Strains and plasmids used in this study.

Strain or plasmid	Relevant genotype or characteristic(s)	References
Strains		
MC4100	F$^-$ *araD139* (*argF-lac*)*U169 ptsF25 deoC1 relA1 flbB5301 rspL150*	Casadaban, 1976
SHH228	Like MC4100, but Δ*hypC* Δ*hybG*	Hartwig et al., 2015
Plasmids		
pASK-IBA3		
phypCstrep	pASK-IBA3, *hypC* with C-terminal Strep-tag II, Amp^R	This study
phypC(H51A)strep	Like phypCstrep, but codon 51 in *hypC* changed CAC → GCC, Amp^R	This study
pT-hypDCStrep	pT7-7, *hypD, hypCStrep*, Amp^R	Blokesch et al., 2004
pT-hypDC(H51A)Strep	Like pT-hypCDStrep, but codon 51 in *hypC* changed CAC → GCC, Amp^R	This study
phybGstrep	pASK-IBA3, *hybG* with C-terminal Strep-tag II, Amp^R	Soboh et al., 2014
phybG(H52A)strep	Like phybGstrep, but codon 52 in *hybG* CAT → GCC, Amp^R	This study
[a]pT-hybG-hypDEF	pT7-7, *hypD, hypE*, *hybGStrep*, *hypF*, Amp^R	Soboh et al., 2014
pT-hybG(H52A)-hypDEF	Like pT-hybG-hypDEF, but codon 52 in *hybG* CAT → GCC, Amp^R	This study
[b]pHycEH	pACYC-Duet1, MCS1: $_{His}$*hycE* (internal His-tag on HycE), MCS2; $_{Strep}$*hycH* (*N*-terminal Strep-tag II on HycH), Cm^R	Lindenstrauß et al., 2017

[a]*Note that the presence of the hypE and hypF genes had no influence on the function of HybG.*
[b]*The vector was used as a resource to purify His-tagged pre-HycE separately from Strep-tagged HycH.*

min^{-1}. Enzyme assays were performed in triplicate using three biological replicates.

Non-denaturing Polyacrylamide Gel Electrophoresis and Hyd Activity-Staining

Non-denaturing PAGE was performed according to Ballantine and Boxer (1985) using crude extracts (25 μg of protein). Prior to application onto the gel, crude extracts were incubated with a final concentration of 4% (v/v) Triton X-100 at 4°C for 15 min. Separating gels included 7.5% (w/v) polyacrylamide and 0.1% (w/v) Triton X-100. To visualize the activity of Hyd-1, Hyd-2, and Hyd-3, activity-staining after native PAGE was performed according to Pinske et al. (2012) using 50 mM MOPS, pH 7 buffer, which included 0.5 mM BV and 1 mM 2,3,5-triphenyltetrazolium chloride. Gels were incubated overnight at 25°C in an atmosphere of 9% N_2: 5% H_2. Experiments were repeated several times with the same results and a representative gel is shown.

Protein Purification

All steps for protein purification were carried out in an anaerobic chamber (Coy Laboratories, Grass Lake, United States). Wet cell paste was suspended in 2 ml buffer W (50 mM Tris, pH 8, containing 150 mM NaCl) per 1 g cell paste. Phenylmethylsulfonyl fluoride (PMSF) was added to a final concentration of 0.8 mM and DNAse I to a final concentration of 10 μg/ml to the cell suspension. Cells were disrupted by sonication (Sonotrode, 35 W with 0.5 s pulses for 5 min) on ice. Cell debris and unbroken cells were removed by centrifugation at 21,000 × *g* for 20 min at 4°C. The supernatant obtained after centrifugation was used immediately for anaerobic protein purification. Strep-tag-II-tagged HypC and HybG were purified individually or in complex with HypD, using Strep-tactin sepharoseXT Sepharose (IBA Lifesciences, Göttingen), exactly as described (Soboh et al., 2013; Arlt et al., 2021). His-tagged pre-HycE was purified using cobalt-charged TALON Superflow agarose (Cytiva), following the manufacturer's instructions.

Purified proteins were buffer-exchanged into anaerobic 50 mM Tris, pH 8, using 5 ml PD-10 columns containing G-25 matrix (Cytiva). The resulting protein samples were concentrated using Amicon centrifugal concentration filters (cut-off of 5 kDa for HypC and HybG proteins and 50 kDa for pre-HycE samples). Purified protein samples were stored at –80°C.

Protein Interaction Studies Using Pull-Down Assays and Western Blotting

To examine the interaction between Strep-tagged $HybG_{WT}$, $HybG_{H52A}$, $HypC_{WT}$, or $HypC_{H51A}$ with His-tagged pre-HycE 150 μg of each protein (5:1 mol excess of chaperone) was mixed and incubated at 30°C under anoxic conditions for 2 h. After incubation, the mixture was loaded onto either a 0.5 ml Strep-tactin sepharoseXT column or a 0.5 ml cobalt-charged TALON Superflow agarose column for the enrichment of the interaction partners. Columns were pre-equilibrated with buffer W (50 mM Tris/HCl, pH 8, containing 150 mM NaCl). After loading of sample, the columns were washed with 10 column volumes of buffer W to remove unbound proteins. Bound proteins were subsequently eluted with buffer W containing 50 mM biotin (Strep-tactin sepharoseXT columns), or with buffer W containing 300 mM imidazole (cobalt-charged NTA columns). Fractions of 0.5 ml were collected and aliquots from these were analyzed by electrophoresis on 12.5% (w/v) or 1% (w/v) denaturing polyacrylamide sodium dodecylsulfate (SDS)-PAGE (Laemmli, 1970). After the separation of polypeptides, they were transferred onto a nitrocellulose membrane as described (Towbin et al., 1979). After blocking the membrane, interaction partners were identified by challenging with polyclonal antiserum raised against HypC, HybG, or HycE (Pinske et al., 2015; Arlt et al., 2021). The detection was based on chemiluminescence using the Immuno-detection kit SuperSignal West Pico PLUS (Thermo Scientific, Brunswick, Germany) and an imager Amersham Imager 600 (GE Healthcare Bio-Sciences AB, Solingen, Germany).

RESULTS

An H52A-Exchange in HybG Results in Wild-Type Levels of H_2 Production

The HypC chaperone preferentially matures pre-HycE, the Hyd-3 large subunit precursor, while its paralogue HybG preferentially introduces the $Fe(CN)_2CO$ group of the [NiFe]-cofactor into pre-HyaB and pre-HybC, the respective precursors of Hyd-1 and Hyd-2 (Blokesch et al., 2001; Arlt et al., 2021). As the aim of this study was to determine the significance of the conserved His residue in HypC and HybG for their function, we decided to exchange the large, charged histidine residue in both proteins for a small, non-polar alanine residue. First, a series of eight plasmids carrying either the native *hypC* gene, the native *hybG* gene, or carrying *hypC* + *hypD,* or *hybG* + *hypD* together, was constructed (**Table 1**). Derivatives of these four plasmids were also constructed, in which codon 51 in *hypC* and codon 52 in *hybG* were mutated to decode as an alanine residue (see section "Materials and Methods"). It is important to note that in all experiments described in the current study, HypC and HybG both carried a *C*-terminal Strep-tag II. The presence of this StrepII-tag does not interfere with the functionality of either protein with respect to Hyd precursor maturation (Blokesch et al., 2004; Soboh et al., 2013; Thomas et al., 2018). Consequently, in the interest of convenience, we will henceforth generally refer to these proteins without mentioning the tag.

As the first experiment to examine the potential effects of exchanging the conserved histidine residues in HypC and HybG to alanine on the maturation of the Hyd-1, -2, and -3 enzymes, we first determined the total H_2-oxidizing Hyd enzyme activity (**Figure 2A**). Therefore, strain SHH228 (see **Table 1**), lacking genomic copies of both *hypC* and *hybG*, but retaining *hybD* (Hartwig et al., 2015), was transformed with each of the eight plasmids individually. After the anaerobic growth of the strains and preparation of crude extracts (see section "Materials and Methods" for details), the total Hyd enzyme activity was determined for each (**Figure 2A**). An extract derived from the parental strain MC4100 had a total Hyd activity of approximately 1.5 U mg^{-1} and served as a positive control, while an extract

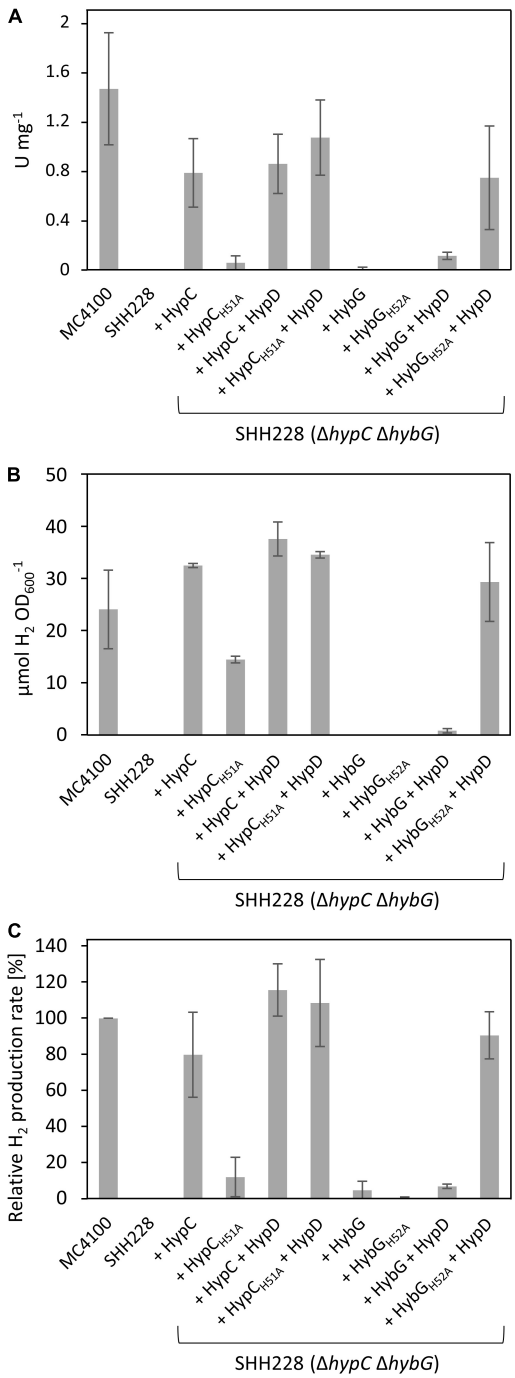

FIGURE 2 | H_2-oxidizing and H_2-evolving activities of *E. coli* strain SHH228 (Δ*hypC*Δ*hybG*) synthesizing different HypC and HybG variants. **(A)** Total H_2-oxidizing hydrogenase enzyme activity, measured as H_2-dependent BV reduction (see section "Materials and Methods") was determined in crude extracts derived from anaerobically grown SHH228 transformed with the following plasmids: phypCstrep, (HypC); phypC(H51A)strep, ($HypC_{H51A}$); pT-hypDCStrep, (HypD + HypC); pT-hypDC(H51A)Strep, (HypD + $HypC_{H51A}$); phybGstrep, (HybG); phybG(H52A)strep, ($HybG_{H52A}$); pT-hybG-hypDEF, (HypD + HybG); pT-hybG(H52A)-hypDEF, (HypD + $HybG_{H52A}$). MC4100 is the isogenic parental wild-type strain of SHH228 (Δ*hypC*Δ*hybG*). One unit of enzyme activity corresponded to the reduction of 1 μmol of substrate min^{-1}.

(Continued)

FIGURE 2 | (B) The total accumulated H_2 production after fermentative growth of the same strains as shown in part **(A)** was determined after 20 h of anaerobic growth in TGYEP, pH 6.5 (see section "Materials and Methods" for details). The amount of H_2 in an aliquot of 200 μl of the gas phase was determined. **(C)** H_2 evolution rates in freshly harvested exponentially growing cells were determined for the same strains as in parts **(A,B)** using whole cells and glucose as reductants (see section "Materials and Methods" for details). The data are presented as a percentage relative to the activity determined for MC4100, which was 46.3 ± 8.3 nmol H_2 min^{-1} mg^{-1} and represented the 100% value. All assays **(A–C)** show data as standard deviations from the mean, determined using at least three independent biological replicates, each assayed in duplicate or triplicate.

derived from SHH228 (*hypC hybG*) had no detectable activity and acted as the negative control (**Figure 2A**). The introduction of plasmid phypCstrep carrying the parental *hypC* gene restored approximately 50% of the parental total Hyd enzyme activity to the mutant. This is consistent with HypC being required for the maturation of Hyd-3 and with the fact that under these growth conditions, Hyd-3 constitutes the bulk of the total Hyd activity (Sawers et al., 1985; Pinske et al., 2011). In contrast, the isogenic plasmid phypC(H51A)strep with a mutation in codon 51 of *hypC* only restored the total Hyd activity to a level that was less than 5% of that measured for the positive control MC4100 (**Figure 2A**). This indicates that the H51A amino acid exchange in HypC severely compromised its ability to function in maturation of Hyd-3, which is also consistent with the reduced amount of $Fe(CN)_2CO$ group detected after purification of HypD associated with an $HypC_{H51R}$ variant reported earlier (Soboh et al., 2013).

As the *hypC* gene is typically found located adjacent to *hypD* in the genomes of microorganisms that synthesize [NiFe]-Hyd, and because HypC and HypD form the central scaffold complex during the maturation of these enzymes (Böck et al., 2006; Lacasse and Zamble, 2016), we wished to determine whether their multicopy co-expression might rescue the Hyd-deficient phenotype exhibited by SHH228 synthesizing $HypC_{H51A}$, despite this strain already possessing a genomic copy of *hypD*. Therefore, we determined the total Hyd enzyme activity of the strain co-expressing both genes from the same plasmid. When the native *hypC* gene was co-expressed with *hypD*, a similar total Hyd enzyme activity was determined compared to when *hypC* was expressed alone from plasmid phypCstrep (**Figure 2A**). When the same experiment was repeated using a plasmid co-expressing *hypD* (pT-hypDCstrep in **Table 1**) and the mutated *hypC* gene synthesizing $HypC_{H51A}$ [pT-hypDC(H51A)strep, **Table 1**], the total Hyd enzyme activity was recovered to a level close to that measured for the wild-type strain. This result suggests that $HypC_{H51A}$ is still functional in the maturation of Hyd-3, but is less efficient at completing maturation unless HypD and the HypC proteins are co-over-produced.

The *hybG* gene, encoding HybG, is located within the *hyb* operon (Menon et al., 1994) and does not have its own associated *hypD* gene. The introduction of a plasmid carrying only *hybG*, encoding Strep-tagged native HybG, into strain SHH228 (Δ*hypC* Δ*hybG*) failed to result in restoration of wild-type total Hyd activity to the mutant and activity was barely detectable (**Figure 2A**). It should be noted that the percentage contribution

of Hyd-1 plus Hyd-2 activity to the total H_2-oxidizing Hyd activity under fermentative conditions is only between 10–20% (Sawers et al., 1985; Pinske et al., 2011). This does not, however, explain the poor complementation achieved by re-introducing plasmid-borne native *hybG*. Therefore, to determine whether the co-expression of *hybG* with *hypD* might improve complementation and increase H_2-oxidizing Hyd activity, plasmid pT-hybG-hypDEF was tested. After fermentative growth, crude extracts derived from SHH228/pT-hybG-hypDEF revealed an increase in the total Hyd activity to around 10% of the total activity measured for the wild-type MC4100 (**Figure 2A**), which approximately represents an activity consistent with that expected for Hyd-1 plus Hyd-2 under these growth conditions (Pinske et al., 2011). Note that plasmid pT-hybG-hypDEF also carries the *hypE* and *hypF* genes. The presence of these genes does not affect the total Hyd enzyme activity determined compared to when only *hybG* + *hypD* or only *hypC* + *hypD* is present on the plasmid (Haase and Sawers, unpublished results).

The anticipated transformation of SHH288 with plasmid phybG(H52A)strep, which has a mutation in codon 52 in the *hybG* gene resulting in exchange of histidine for alanine and delivering $HybG_{H52A}$, failed to yield measurable Hyd activity (**Figure 2A**). Surprisingly, however, when *hypD* was co-expressed with this mutated *hybG* gene on pT-hybG(H52A)-hypDEF, the total Hyd activity measured was similar to that measured for *hypC-hypD* on pT-hypDCStrep in SHH228 (**Figure 2A**). This result suggests that this approximate 10-fold increase in total Hyd activity, relative to what was measured when pT-hybG-hypDEF was introduced into SHH228, was either due to an unexpected increase in the combined Hyd-1 and Hyd-2 activity, or because Hyd-3 activity was activated by the variant $HybG_{H52A}$ protein when it was co-over-produced with HypD.

An H52A Exchange in HybG Restores H_2 Production to a *hypC-hybG Escherichia coli* Mutant

In order to resolve this issue, we first tested the same set of strains for their ability to produce H_2 during glucose fermentation (**Figures 2B,C**). The amount of H_2 accumulated in stationary-phase cells after batch cultivation revealed that the positive control MC4100 accumulated approximately 25 μmol H_2 OD_{600} nm^{-1}, while the negative control SHH228 (Δ*hypC* Δ*hybG*) accumulated no detectable H_2 gas (**Figure 2B**). SHH228 transformed with pT-hybG(H52A)-hypDEF (synthesizing HypD plus $HybG_{H52A}$) accumulated H_2 to a level that was slightly more than that of the parental MC4100 strain, indicating that Hyd-3 was active. The same experiment performed with a plasmid bearing *hypD* and the parental *hybG* genes (pT-hybG-hypDEF) showed essentially no H_2 accumulation, as did SHH228 transformed with plasmids carrying only the parental *hybG* or only the mutated *hybG* genes lacking the additional *hypD* gene (**Figure 2B**). This supports the conclusion that the mutant $HybG_{H52A}$ chaperone, synthesized at a high level together with HypD, was capable of maturing Hyd-3 and thus accounted for the H_2 production by the strain. As further controls, when SHH228 co-over-produced either HypC or $HypC_{H51A}$ together with HypD, H_2 also accumulated to wild-type levels (**Figure 2B**). However, when the strain only synthesized $HypC_{H51A}$, H_2 accumulated to approximately 50% of parental levels.

To verify these results, the ability of the same set of strains to evolve H_2 in cell suspensions derived from exponentially grown cells was assessed using a hydrogen-electrode (**Figure 2C**). The results essentially reflected those obtained by measuring cumulative H_2 production, with the exception that SHH228 synthesizing $HypC_{H51A}$ from phypC(H51A)strep had an H_2-evolving activity that was only 10% of that of the wild-type strain MC4100 (**Figure 2C**). These results confirmed the poor complementation of the Hyd -deficient phenotype exhibited by this strain when the total Hyd activity was measured in extracts (compare **Figure 2A**). It is likely that in the cumulative H_2 assay, the cells had sufficient time to accumulate H_2 in the stationary phase, which probably accounts for the difference when the two assay methods for H_2 production by the strain are compared (compare **Figures 2B,C**).

The $HybG_{H52A}$ Variant Is Able to Mature Hyd 3

Bands corresponding to Hyd-1, Hyd-2, and Hyd-3 can be readily distinguished after native PAGE followed by staining the gel specifically for Hyd enzyme activity (Pinske et al., 2012). Moreover, this technique also allows the identification of an H_2:benzyl viologen oxidoreductase activity associated with the formate dehydrogenases (Fdh) N and O, which is a side-reaction of these enzymes (Soboh et al., 2011), but is a useful control for these experiments. As HybG typically cannot facilitate the maturation of Hyd-3 (Blokesch et al., 2001; Böck et al., 2006), we first looked at the extracts derived from both exponential-phase (**Figure 3A**) and stationary-phase cells (**Figure 3B**) for evidence of HybG-dependent synthesis of active Hyd-3. Regardless of whether the native *hybG* gene was expressed alone, or co-expressed with *hypD* from a plasmid, no manifestation of active Hyd-3 after native PAGE and staining for Hyd enzyme activity could be observed (**Figure 3**). In contrast, when $HybG_{H52A}$ was co-synthesized with HypD in strain SHH288 (Δ*hypC* Δ*hybG*), and in the absence of any HypC, Hyd-3 activity could be visualized (**Figure 3B**). Although the activity band was relatively weak, it was clearly visible, especially in the crude extract derived from stationary-phase cells. Moreover, the activity band had an intensity comparable to that in exponential-phase cells when the native *hypC* gene was expressed on its own from plasmid phypCstrep (**Figure 3A**). This result indicates that $HybG_{H52A}$ can mature the large subunit precursor (pre-HycE) of Hyd-3.

Hydrogenase-1 is more active in anaerobic stationary-phase cells, while Hyd-2 is more active in exponential-phase cells (Ballantine and Boxer, 1985; Sawers et al., 1985). The examination of the activity-stained bands in the other extracts revealed that, although Strep-tagged native HybG was capable of restoring maturation of both Hyd-1 and Hyd-2 in exponential- and stationary-phase cells (**Figures 3A,B**), the intensity of the respective activity bands was low. This possibly explains the poor phenotypic complementation by plasmid-borne *hybG* when introduced into SHH228 and the very low total Hyd activity

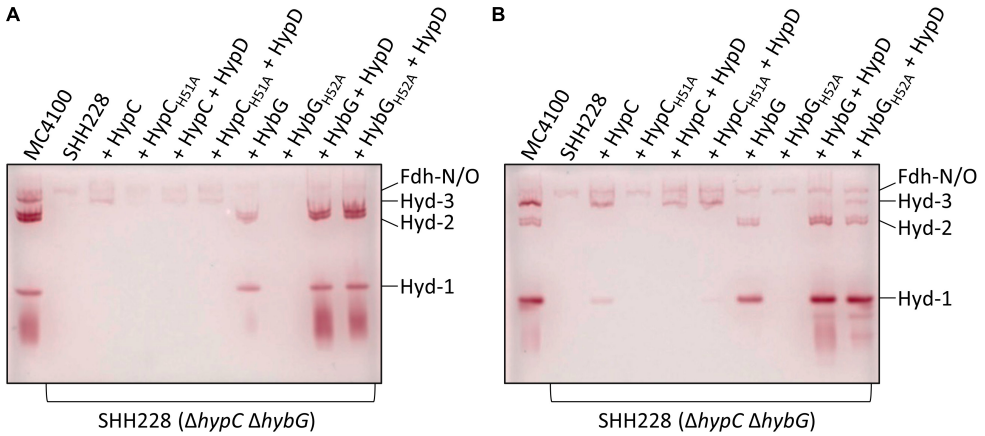

FIGURE 3 | Identification of hydrogenases 1, 2, and 3 by enzyme activity-staining. Protein complexes in crude extracts (25 μg of protein) derived from the indicated strains (see legend to **Figure 1A**) were separated in native polyacrylamide gel electrophoresis (PAGE) (7.5% w/v polyacrylamide) and subsequently stained for hydrogenase enzyme activity (see section "Materials and Methods"). Cells were grown anaerobically in TGYEP, pH 6.5, and harvested in the exponential phase (**A**; cultivation to OD_{600} 0.7) or in the stationary phase (**B**; cultivation at 30°C for 16 h). The migration positions of Hyd-1, Hyd-2, and Hyd-3 are shown on the right side of the gels. The activity-staining band labeled Fdh-N/O signifies the weak H_2-oxidizing activity associated with the formate dehydrogenases N and O and acted as a loading control.

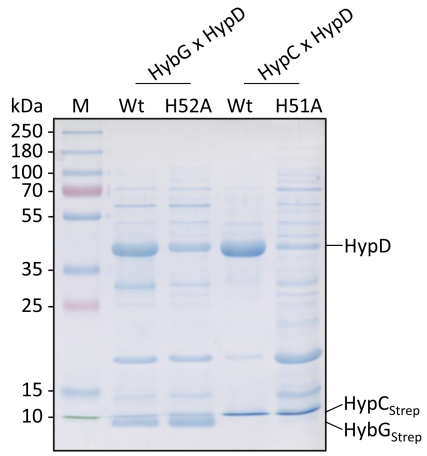

FIGURE 4 | Analysis of co-enrichment of untagged HypD with Strep-tagged HypC and HybG variants. Aliquots of elution fractions (10 μg protein) were separated by SDS-PAGE (12.5% w/v acrylamide) followed by staining with Coomassie Brilliant Blue. The migration positions of HypD, Strep-tagged HypC (HypC$_{Strep}$), and HybG (HybG$_{Strep}$) are indicated at the right side of the panel. Migration positions of molecular mass markers are shown on the left of the gel.

measured in **Figure 2A**. Strain SHH228, synthesizing the HybG$_{H52A}$ variant, showed no activity bands corresponding to either Hyd-1 or Hyd-2 when the cognate gene was expressed on its own from plasmid phybG(H52A)strep (**Figures 3A,B**). Notably, however, when either *hybG* allele was co-expressed with *hypD*, extracts derived from the corresponding cells revealed wild-type levels of activity-staining bands for Hyd-1 and Hyd-2 (**Figure 3**). These results suggest that the co-synthesis of HypD either resulted in the stabilization of the respective HybG chaperones when the cognate genes were co-expressed or facilitated interaction of the proteins to allow scaffold complex formation, thus improving the efficiency of maturation of both the large-subunit precursors, pre-HyaB and pre-HybC.

In this regard, crude extracts derived from stationary-phase cells of SHH288/phypCstrep, which synthesized Strep-tagged native HypC, revealed only a weak activity band that migrated at the position of Hyd-1, but no such similar activity band was observed in an extract derived from SHH288 co-expressing *hypC* and *hypD* (**Figure 3B**); the levels of Hyd-3 remained similar for both strains, providing an internal loading control. This underscores the preferential maturation of pre-HycE over pre-HyaB by HypC carrying $Fe(CN)_2CO$ (see also **Figure 1A**).

HybG$_{H52A}$ Interacts Better With Pre-HycE but Worse With HypD

HypC-HypD and HybG-HypD complexes can be readily isolated from anaerobically cultivated cells (Blokesch et al., 2004; Soboh et al., 2012) and it has been shown using structural analyses (Watanabe et al., 2012) and by native mass spectrometry (Arlt et al., 2021) that both sets of complexes form (1:1) heterodimers. To determine whether the exchange of the conserved histidine residue that is predicted to be important for the interaction with HypD (see **Figure 1A**; Watanabe et al., 2012; Miki et al., 2020) has an impact on this interaction, we enriched, by affinity chromatography in a single step HybG-HypD, HybG$_{H52A}$-HypD, HypC-HypD, and HypC$_{H51A}$-HypD complexes from anaerobically grown SHH228 cells. To do this, we took advantage of the StrepII-tag on the chaperones (see section "Materials and Methods"). The resulting complexes were separated by SDS-PAGE and visualized using Coomassie Blue staining (**Figure 4**). While the native HybG and HypC proteins each could be enriched together with high amounts of HypD and minimal contaminating polypeptides, the mutated chaperone proteins clearly interacted more poorly with HypD. The complexes

formed were less-well resolved, the affinity-enriched samples included considerably more contaminating proteins, and, based on densitometric analysis (ImageQuant TL program Cytiva), the apparent stoichiometries were significantly lower than those observed for the respective native chaperone (at least 50% lower for $HybG_{H52A}$:HypD and ∼85% lower for $HypC_{H51A}$:HypD).

Next, we purified separately Strep-tagged native HybG and $HybG_{H52A}$, as well as a His-tagged derivative of pre-HycE, the precursor of the Hyd-3 large subunit. These were then used in interactions experiments (see section "Materials and Methods") to test whether $HybG_{H52A}$ could form a complex with pre-HycE (**Figure 5**). The results show that when complexes were allowed to form between His-tagged pre-HycE and Strep-tagged native HybG and the mixture was subsequently separated on a cobalt-charged TALON Superflow agarose column, only low amounts of HybG co-eluted with pre-HycE (**Figure 5A**). When the same mixture was passed over a Strep-tactin sepharose column, no pre-HycE could be identified to co-elute with Strep-tagged HybG (**Figure 5B**). In contrast, when the same experiment was repeated with Strep-tagged $HybG_{H52A}$, more of the chaperone was shown to co-elute with His-tagged pre-HycE after cobalt-charged TALON agarose chromatography (**Figure 5C**), and pre-HycE could clearly be identified to co-elute with Strep-tagged $HybG_{H52A}$ after Strep-tactin sepharose affinity chromatography (**Figure 5D**).

In a similar experiment performed with Strep-tagged HypC, Strep-tagged $HypC_{H51A}$, and His-tagged pre-HycE, native HypC co-eluted strongly with His-tagged pre-HycE (**Figure 5E**), while $HypC_{H51A}$ interacted more poorly with pre-HycE (**Figure 5F**).

DISCUSSION

In *E. coli,* the scaffold protein HypD interacts with two distinct but related HypC-family chaperones, which in turn deliver the synthesized $Fe(CN)_2CO$ group to three separate large-subunit precursors. Although both chaperones interact (with different effectiveness) with pre-HyaB, the Hyd-1 large-subunit precursor, only HypC delivers the iron group to pre-HycE, while pre-HybC receives the group exclusively from HybG (Blokesch et al., 2001; Arlt et al., 2021). Here, we have resolved two key discriminatory functions associated with a conserved histidine residue within the HypC-family chaperone member, HybG. Although only semi-quantitative, the results of our interaction experiments give a first clear indication that an H52A residue exchange in HybG diminishes the ability of the chaperone to interact with its scaffold partner HypD. This result was corroborated when a similar exchange in HypC was made, which also resulted in a diminished interaction with HypD when compared with native HypC. An H-to-A residue exchange in either protein thus appears to weaken the interaction with the scaffold protein HypD, with which it functions to synthesize the $Fe(CN)_2CO$ group (Böck et al., 2006). This also provides a biochemical explanation for the previous observation that an exchange of H51 for an arginine residue in HypC impaired Hyd-3-dependent H_2 evolution by *E. coli* (Blokesch, 2004; Soboh et al., 2013). Based on the structural analysis of the HypC-HypD complex (see **Figure 1B**), this histidine residue is predicted to form part of the contact surface between HybG and HypD but has also been suggested possibly to aid the coordination of the $Fe(CN)_2CO$ group when the chaperone delivers the group to the large-subunit precursor (Watanabe et al., 2007, 2012). The findings made in the current study are consistent with this residue being important for the interaction with HypD but do not support a role for the residue in coordinating the organometallic iron group, because our experiments involving co-synthesis of either $HypC_{H51A}$ or $HybG_{H52A}$ with HypD revealed that efficient maturation of their cognate large-subunit precursors still occurred with both chaperone variants. For example, the observed reduction in Hyd-2 activity caused by the H52A exchange in HybG could be totally restored if the gene encoding $HybG_{H52A}$ was co-expressed with *hypD*. This suggests that the interaction between $HybG_{H52A}$ [bearing the $Fe(CN)_2CO$ group] and the pre-HybC large-subunit precursor is not strongly compromised by the exchange, and the observed reduction in Hyd-2 activity might be due simply to the poorer interaction of $HybG_{H52A}$ with HypD. Nevertheless, future quantitative assessment of binding affinities for these various interaction partners will be needed to verify this proposal.

This contrasts sharply, however, with the demonstration of improved interaction between $HybG_{H52A}$ and pre-HycE, which resulted in an unprecedented HybG-dependent maturation of Hyd-3. This result suggests that the histidine residue functions to prevent HybG from interacting with pre-HycE. When histidine is substituted by the much smaller alanine residue, this inhibition is relieved, allowing interaction and maturation to take place. A similar residue exchange in HypC (H51A) did not have any effect on Hyd-2 enzyme activity, only causing decreased H_2 production, because pre-HycE is HypC's principal interaction partner (Drapal and Böck, 1998; Blokesch et al., 2004; Böck et al., 2006). Thus, the $HypC_{H51A}$ variant does not become capable of interacting with pre-HybC to generate active Hyd-2, suggesting that pre-HycE has structural features at its chaperone interaction surface that differ from those of both pre-HybC and pre-HyaB. Future structural comparisons of these precursors will be highly beneficial, coupled with a chemical cross-linking analysis, to define these interacting residues.

Thus, two features of the HybG chaperone seem to be important in ensuring it only matures the H_2-oxidizing Hyd-1 and Hyd-2 enzymes *in vivo*. Firstly, expression of the *hybG* gene within the *hyb* operon, plus its physical separation from the *hypD* gene, ensures that HybG and pre-HybC are synthesized together. Nevertheless, HybG is produced in sufficient amounts also to allow maturation of pre-HyaB (precursor of Hyd-1) as well as pre-HybC, and it appears to be more effective at this than HypC (see also Blokesch et al., 2001). The fact that co-expressing the *hypD* gene with the mutated *hybG* gene improved complementation ability may be due to a form of translational coupling that compensates for the poorer HypD-$HybG_{H52A}$ complex formation by improving their chances of interacting in the cell. The consequence is that sufficient production of the $Fe(CN)_2CO$ group occurs to facilitate the maturation of all three Hyd large subunit precursors.

Secondly, the H52 residue, as well as being required for optimal interaction with HypD, acts to prevent HybG from interacting with pre-HycE. Non-native co-overexpression of the

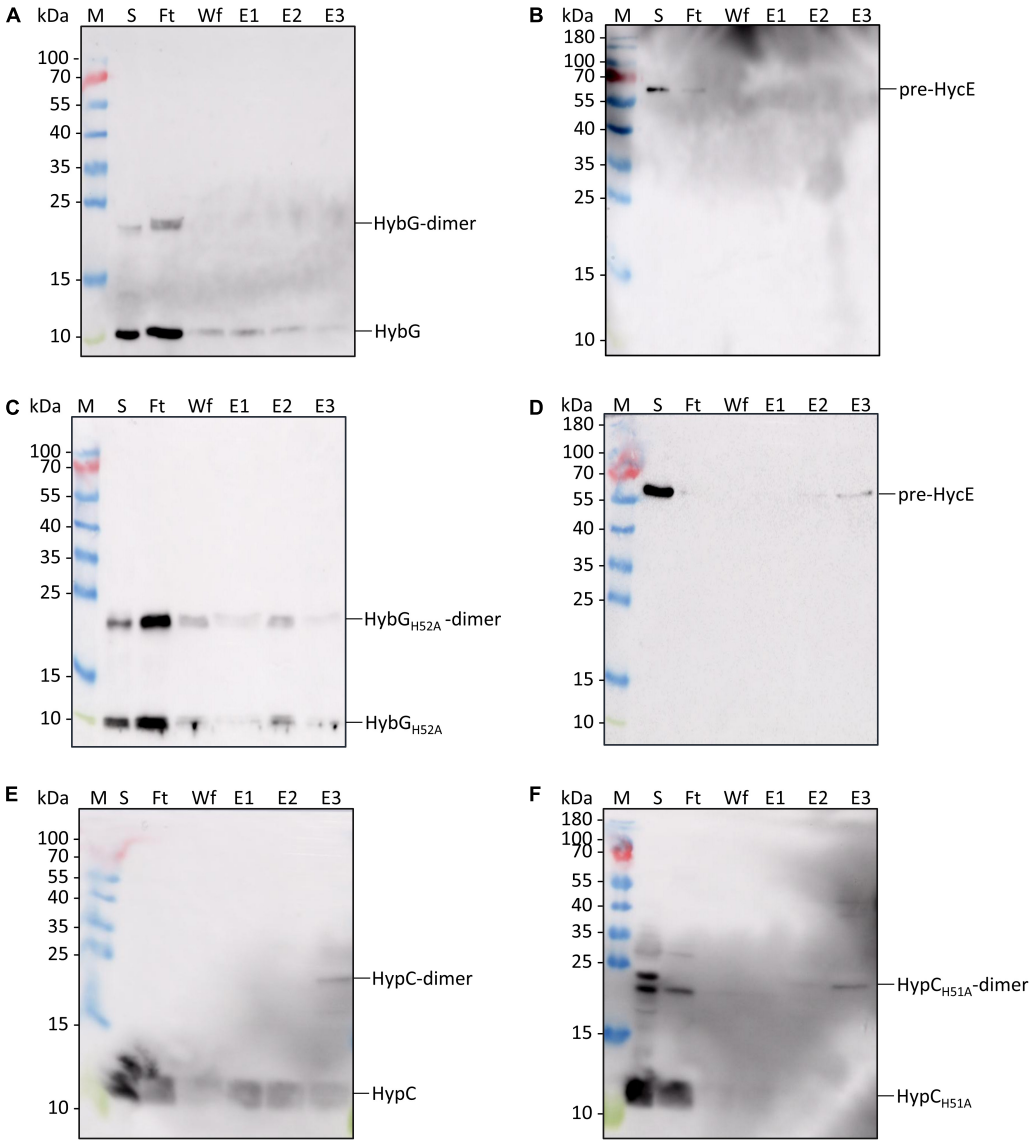

FIGURE 5 | Identification of interaction partners: HybG$_{H52A}$ forms a complex with pre-HycE. Purified Strep-tagged HypC$_{WT}$, HypC$_{H51A}$, HybG$_{WT}$, or HybG$_{H52A}$ was mixed with purified His-tagged pre-HycE and after affinity chromatography, aliquots of the original sample mixture (S), the unbound flow-through (Ft), the material washed from the column (Wf) and the eluted material (fractions E1, E2, and E3) were separated by SDS PAGE followed by western blotting. Membranes were treated with antiserum raised against HypC, HybG, or HycE, each diluted 1:4000. **(A)** Blot treated with anti-HybG antiserum after separation of a mixture of Strep-tagged HybG and His-tagged pre-HycE on a cobalt-charged TALON agarose column. HybG monomers and dimers (dimers are occasionally observed after SDS-PAGE; Arlt et al., 2021) are indicated on the right of the blot. Migration positions of molecular mass markers are shown on the left of the blot. **(B)** The same experiment as shown in panel **(A)** was performed, but after the separation of the mixture on a Strep-tactin sepharose column, His-tagged pre-HycE was detected with anti-HycE antiserum. **(C)** A mixture of purified Strep-tagged HybG$_{H52A}$ and pre-HycE was separated on a cobalt-charged TALON agarose column as described in part **(A)**. HybG$_{H52A}$ was detected with anti-HybG antiserum. **(D)** The same mixture as in part **(C)** was separated on a Strep-tactin sepharose column and pre-HycE was detected with anti-HycE antiserum. **(E)** Western blot in which a mixture of Strep-tagged HypC and His-tagged pre-HycE was separated on a cobalt-charged TALON agarose column and HypC was detected with anti-HypC antiserum. **(F)** Western blot in which a mixture of Strep-tagged HypC$_{H51A}$ and His-tagged pre-HycE was separated on a cobalt-charged TALON agarose column, with subsequent detection using anti-HypC antiserum.

native *hybG* and *hypD* genes still failed to result in inadvertent maturation of pre-HycE, but not when codon 52 of *hybG* coded for an alanine residue. The selective maintenance of H52 in HybG thus assures effective HybG-HypD scaffold complex formation, while at the same time guaranteeing that pre-HycE cannot be matured by HybG. This study thus identifies a new layer of control during Hyd maturation. Controlling which chaperone (HypC or HybG) preferentially interacts with HypD determines which Hyd precursor is matured in accordance with the demands set by the physiological conditions. This ultimately results in the balanced production of H_2-evolving and H_2-oxidizing enzyme activities.

DATA AVAILABILITY STATEMENT

The raw data supporting the conclusions of this article will be made available by the authors, without undue reservation.

AUTHOR CONTRIBUTIONS

AH and RGS conceived and designed the study, analyzed the data, and drafted the manuscript. AH performed all of the experiments. Both authors approved the manuscript.

FUNDING

This work was funded by the Deutsche Forschungsgemeinschaft as part of the research initiative SPP1927: "Iron-Sulfur for Life" granted to RGS.

ACKNOWLEDGMENTS

We thank Kerstin Nutschan and Constanze Pinske for discussion and Kerstin Nutschan for help in constructing plasmids.

REFERENCES

Arlt, C., Nutschan, K., Haase, A., Ihling, C., Tänzler, D., Sinz, A., et al. (2021). Native mass spectrometry identifies the HybG chaperone as carrier of the $Fe(CN)_2CO$ group during maturation of *E. coli* [NiFe]-hydrogenase 2. *Sci. Rep.* 11:24362. doi: 10.1038/s41598-021-03900-w

Ballantine, S. P., and Boxer, D. H. (1985). Nickel-containing hydrogenase isoenzymes from anaerobically grown *Escherichia coli* K-12. *J. Bacteriol.* 163, 454–459. doi: 10.1128/jb.163.2.454-459

Begg, Y., Whyte, J., and Haddock, B. A. (1977). The identification of mutants of *Escherichia coli* deficient in formate dehydrogenase and nitrate reductase activities using dye indicator plates. *FEMS Microbiol. Lett.* 2, 47–50.

Blokesch, M. (2004). *[NiFe]-Hydrogenasen von Escherichia coli: Funktionen der am Metalleinbau beteiligten Proteine*. Ph.D. thesis. Munich: Ludwig–Maximilians University.

Blokesch, M., Albracht, S. P., Matzanke, B. F., Drapal, N. M., Jacobi, A., and Böck, A. (2004). The complex between hydrogenase-maturation proteins HypC and HypD is an intermediate in the supply of cyanide to the active site iron of [NiFe]-hydrogenases. *J. Mol. Biol.* 344, 155–167. doi: 10.1016/j.jmb.2004.09.040

Blokesch, M., Magalon, A., and Böck, A. (2001). Interplay between the specific chaperone-like proteins HybG and HypC in maturation of hydrogenases 1, 2, and 3 from *Escherichia coli*. *J. Bacteriol.* 183, 2817–2822. doi: 10.1128/JB.183.9.2817-2822.2001

Blokesch, M., Paschos, A., Theodoratou, E., Bauer, A., Hube, M., Huth, S., et al. (2002). Metal insertion into NiFe-hydrogenases. *Biochem. Soc. Trans.* 30, 674–680. doi: 10.1042/bst0300674

Böck, A., King, P., Blokesch, M., and Posewitz, M. (2006). Maturation of hydrogenases. *Adv. Microb. Physiol.* 51, 1–71. doi: 10.1016/s0065-2911(06)51001-x

Casadaban, M. J. (1976). Transposition and fusion of the *lac* genes to selected promoters in *Escherichia coli* using bacteriophage lambda and Mu. *J. Mol. Biol.* 104, 541–555. doi: 10.1016/0022-2836(76)90119-4

Drapal, N., and Böck, A. (1998). Interaction of the hydrogenase accessory protein HypC with HycE, the large subunit of *Escherichia coli* hydrogenase 3 during enzyme maturation. *Biochemistry* 37, 2941–2948. doi: 10.1021/bi9720078

Hartwig, S., Thomas, C., Krumova, N., Quitzke, V., Türkowsky, D., Jehmlich, N., et al. (2015). Heterologous complementation studies in *Escherichia coli* with the Hyp accessory protein machinery from *Chloroflexi* provide insight into [NiFe]-hydrogenase large subunit recognition by the HypC protein family. *Microbiology* 161, 2204–2219. doi: 10.1099/mic.0.000177

Hormann, K., and Andreesen, J. R. (1989). Reductive cleavage of sarcosine and betaine by *Eubacterium acidaminophilum via* enzyme systems different from glycine reductase. *Arch. Microbiol.* 153, 50–59.

Jones, A. K., Lenz, O., Strack, A., Buhrke, T., and Friedrich, B. (2004). NiFe hydrogenase active site biosynthesis: identification of Hyp protein complexes in *Ralstonia eutropha*. *Biochemistry* 43, 13467–13477. doi: 10.1021/bi048837k

Lacasse, M. J., and Zamble, D. B. (2016). [NiFe]-hydrogenase maturation. *Biochemistry* 55, 1689–1701. doi: 10.1021/acs.biochem.6b00706

Laemmli, U. (1970). Cleavage of structural proteins during the assembly of the head of bacteriophage T4. *Nature* 227, 680–685. doi: 10.1038/227680a0

Lindenstrauß, U., Skorupa, P., McDowall, J. S., Sargent, F., and Pinske, C. (2017). The dual-function chaperone HycH improves assembly of the formate hydrogenlyase complex. *Biochem. J.* 474, 2937–2950. doi: 10.1042/BCJ20170431

Lowry, O., Rosebrough, N., Farr, A., and Randall, R. (1951). Protein measurement with the Folin phenol reagent. *J. Biol. Chem.* 193, 265–275.

McDowall, J. S., Murphy, B. J., Haumann, M., Palmer, T., Armstrong, F. A., and Sargent, F. (2014). Bacterial formate hydrogenlyase complex. *Proc. Natl. Acad. Sci. U.S.A.* 111, E3948–E3956. doi: 10.1073/pnas.1407927111

Menon, N. K., Chatelus, C. Y., Dervartanian, M., Wendt, J. C., Shanmugam, K. T., Peck, H. D. Jr., et al. (1994). Cloning, sequencing, and mutational analysis of the *hyb* operon encoding *Escherichia coli* hydrogenase 2. *J. Bacteriol.* 176, 4416–4423. doi: 10.1128/jb.176.14.4416-4423

Miki, K., Atomi, H., and Watanabe, S. (2020). Structural insight into [NiFe] hydrogenase maturation by transient complexes between Hyp proteins. *Acc. Chem. Res.* 53, 875–886. doi: 10.1021/acs.accounts.0c00022

Miller, J. (1972). *Experiments in Molecular Genetics*. Cold Spring Harbor, NY: Cold Spring Harbor Laboratory.

Pinske, C., Jaroschinsky, M., Linek, S., Kelly, C. L., Sargent, F., and Sawers, R. G. (2015). Physiology and bioenergetics of [NiFe]-hydrogenase 2-catalyzed H_2-consuming and H_2-producing reactions in *Escherichia coli*. *J. Bacteriol.* 197, 296–306. doi: 10.1128/JB.02335-14

Pinske, C., Jaroschinsky, M., Sargent, F., and Sawers, G. (2012). Zymographic differentiation of [NiFe]-hydrogenases 1, 2 and 3 of *Escherichia coli* K-12. *BMC Microbiol.* 12:134. doi: 10.1186/1471-2180-12-134

Pinske, C., Krüger, S., Soboh, B., Ihling, C., Kuhns, M., Braussemann, M., et al. (2011). Efficient electron transfer from hydrogen to benzyl viologen by the [NiFe]-hydrogenases of *Escherichia coli* is dependent on the co-expression of the iron-sulfur cluster-containing small subunit. *Arch. Microbiol.* 193, 893–903. doi: 10.1007/s00203-011-0726-5

Pinske, C., and Sawers, R. G. (2016). Anaerobic formate and hydrogen metabolism. *EcoSal Plus* 7. doi: 10.1128/ecosalplus.ESP-0011-2016

Sambrook, J., Fritsch, E. F., and Maniatis, T. (1989). *Molecular Cloning: a Laboratory Manual*, 2nd Edn. Cold Spring Harbor, NY: Cold Spring Harbor Laboratory.

Sargent, F. (2016). The model [NiFe]-hydrogenases of *Escherichia coli*. *Adv. Microb. Physiol.* 68, 433–507. doi: 10.1016/bs.ampbs.2016.02.008

Sargent, F., Stanley, N. R., Berks, B. C., and Palmer, T. (1999). Sec-independent protein translocation in *Escherichia coli*. A distinct and pivotal role for the TatB protein. *J. Biol. Chem.* 274, 36073–36082. doi: 10.1074/jbc.274.51.36073

Sawers, R. G., Ballantine, S. P., and Boxer, D. H. (1985). Differential expression of hydrogenase isoenzymes in *Escherichia coli* K-12: evidence for a third isoenzyme. *J. Bacteriol.* 164, 1324–1331. doi: 10.1128/jb.164.3.1324-1331

Soboh, B., Lindenstrauss, U., Granich, C., Javed, M., Herzberg, M., Thomas, C., et al. (2014). [NiFe]-hydrogenase maturation *in vitro*: analysis of the roles of the HybG and HypD accessory proteins. *Biochem. J.* 464, 169–177. doi: 10.1042/BJ20140485

Soboh, B., Pinske, C., Kuhns, M., Waclawek, M., Ihling, C., Trchounian, K., et al. (2011). The respiratory molybdo-selenoprotein formate dehydrogenases of *Escherichia coli* have hydrogen: benzyl viologen oxidoreductase activity. *BMC Microbiol.* 11:173. doi: 10.1186/1471-2180-11-173

Soboh, B., Stripp, S. T., Bielak, C., Lindenstrauß, U., Braussemann, M., Javaid, M., et al. (2013). The [NiFe]-hydrogenase accessory chaperones HypC and HybG of *Escherichia coli* are iron- and carbon dioxide-binding proteins. *FEBS Lett.* 587, 2512–2516. doi: 10.1016/j.febslet.2013.06.055

Soboh, B., Stripp, S. T., Muhr, E., Granich, C., Braussemann, M., Herzberg, M., et al. (2012). [NiFe]-hydrogenase maturation: isolation of a HypC-HypD complex carrying diatomic CO and CN^- ligands. *FEBS Lett.* 586, 3882–3887. doi: 10.1016/j.febslet.2012.09.019

Thomas, C., Waclawek, M., Nutschan, K., Pinske, C., and Sawers, R. G. (2018). The extended *C*-terminal α-helix of the HypC chaperone restricts recognition of large subunit precursors by the Hyp-scaffold machinery during [NiFe]-hydrogenase maturation in *Escherichia coli*. *J. Mol. Microbiol. Biotechnol.* 28, 87–97. doi: 10.1159/000489929

Towbin, H., Staehelin, T., and Gordon, J. (1979). Electrophoretic transfer of proteins from polyacrylamide gels to nitrocellulose sheets: procedure and some applications. *Proc. Natl. Acad. Sci. U.S.A.* 76, 4350–4354. doi: 10.1073/pnas.76.9.4350

Watanabe, S., Matsumi, R., Arai, T., Atomi, H., Imanaka, T., and Miki, K. (2007). Crystal structures of [NiFe] hydrogenase maturation proteins HypC, HypD, and HypE: insights into cyanation reaction by thiol redox signaling. *Mol. Cell* 27, 29–40. doi: 10.1016/j.molcel.2007.05.039

Watanabe, S., Matsumi, R., Atomi, H., Imanaka, T., and Miki, K. (2012). Crystal structures of the HypCD complex and the HypCDE ternary complex: transient intermediate complexes during [NiFe] hydrogenase maturation. *Structure* 20, 2124–2137. doi: 10.1016/j.str.2012.09.018

Wolf, I., Buhrke, T., Dernedde, J., Pohlmann, A., and Friedrich, B. (1998). Duplication of *hyp* genes involved in maturation of [NiFe] hydrogenases in *Alcaligenes eutrophus* H16. *Arch. Microbiol.* 170, 451–459. doi: 10.1007/s002030050666

Conflict of Interest: The authors declare that the research was conducted in the absence of any commercial or financial relationships that could be construed as a potential conflict of interest.

Publisher's Note: All claims expressed in this article are solely those of the authors and do not necessarily represent those of their affiliated organizations, or those of the publisher, the editors and the reviewers. Any product that may be evaluated in this article, or claim that may be made by its manufacturer, is not guaranteed or endorsed by the publisher.

frontiers | Frontiers in Microbiology

ORIGINAL RESEARCH
published: 29 April 2022
doi: 10.3389/fmicb.2022.894375

High-Yield Production of Catalytically Active Regulatory [NiFe]-Hydrogenase From *Cupriavidus necator* in *Escherichia coli*

*Qin Fan[1], Giorgio Caserta[2], Christian Lorent[2], Ingo Zebger[2], Peter Neubauer[1], Oliver Lenz[2] and Matthias Gimpel[1]**

[1] Chair of Bioprocess Engineering, Department of Biotechnology, Technische Universität Berlin, Berlin, Germany, [2] Department of Chemistry, Technische Universität Berlin, Berlin, Germany

OPEN ACCESS

Edited by:
Constanze Pinske, Martin Luther University of Halle-Wittenberg, Germany

Reviewed by:
Hideaki Ogata, Nara Institute of Science and Technology (NAIST), Japan
Simone Morra, University of Nottingham, United Kingdom

***Correspondence:**
Matthias Gimpel
matthias.gimpel@tu-berlin.de

Specialty section:
This article was submitted to Microbial Physiology and Metabolism, a section of the journal Frontiers in Microbiology

Received: *11 March 2022*
Accepted: *08 April 2022*
Published: *29 April 2022*

Citation:
Fan Q, Caserta G, Lorent C, Zebger I, Neubauer P, Lenz O and Gimpel M (2022) High-Yield Production of Catalytically Active Regulatory [NiFe]-Hydrogenase From Cupriavidus necator in Escherichia coli. Front. Microbiol. 13:894375. doi: 10.3389/fmicb.2022.894375

Hydrogenases are biotechnologically relevant metalloenzymes that catalyze the reversible conversion of molecular hydrogen into protons and electrons. The O_2-tolerant [NiFe]-hydrogenases from *Cupriavidus necator* (formerly *Ralstonia eutropha*) are of particular interest as they maintain catalysis even in the presence of molecular oxygen. However, to meet the demands of biotechnological applications and scientific research, a heterologous production strategy is required to overcome the low production yields in their native host. We have previously used the regulatory hydrogenase (RH) from *C. necator* as a model for the development of such a heterologous hydrogenase production process in *E. coli*. Although high protein yields were obtained, the purified enzyme was inactive due to the lack of the catalytic center, which contains an inorganic nickel-iron cofactor. In the present study, we significantly improved the production process to obtain catalytically active RH. We optimized important factors such as O_2 content, metal availability, production temperature and time as well as the co-expression of RH-specific maturase genes. The RH was successfully matured during aerobic cultivation of *E. coli* by co-production of seven hydrogenase-specific maturases and a nickel permease, which was confirmed by activity measurements and spectroscopic investigations of the purified enzyme. The improved production conditions resulted in a high yield of about 80 mg L^{-1} of catalytically active RH and an up to 160-fold space-time yield in *E. coli* compared to that in the native host *C. necator* [<0.1 U (L d) $^{-1}$]. Our strategy has important implications for the use of *E. coli* K-12 and B strains in the recombinant production of complex metalloenzymes, and provides a blueprint for the production of catalytically active [NiFe]-hydrogenases in biotechnologically relevant quantities.

Keywords: regulatory hydrogenase, difficult-to-express protein, *Escherichia coli*, [NiFe]-hydrogenase, *Cupriavidus necator*

INTRODUCTION

[NiFe]-hydrogenases are metalloenzymes that catalyze the reversible oxidation of molecular hydrogen (H_2) into protons and electrons, which makes them very attractive from both scientific and applied perspectives (Fontecilla-Camps et al., 2007; Lubitz et al., 2014). Their core module is composed of a large subunit harboring the catalytic nickel-iron [NiFe] center and a small subunit hosting one to three iron-sulfur clusters that mediates electron transfer between the active site and the physiological electron acceptor/donor (Ogata et al., 2016). The inorganic [NiFe] center is coordinated to the protein *via* four cysteine-derived thiolates, two of which are terminal nickel ligands whereas the other two serve as bridging ligands between the nickel and the iron. The iron is further coordinated by one carbonyl (CO) group and two cyanide (CN^-) residues (Fontecilla-Camps et al., 2007; Lubitz et al., 2014; Peters et al., 2015). Synthesis and incorporation of the [NiFe] cofactor into the apo-hydrogenase is a highly complex process that requires a set of at least six maturation proteins, named HypABCDEF (Forzi and Sawers, 2007; Lacasse and Zamble, 2016). The HypCD complex serves as central scaffold for the assembly of the $Fe(CN)_2CO$ moiety (Blokesch et al., 2004a; Bürstel et al., 2012; Watanabe et al., 2012). The cyanide ligands are synthesized from carbamoyl phosphate by a concerted action of HypE and HypF (Casalot and Rousset, 2001; Reissmann et al., 2003; Blokesch et al., 2004b; Rangarajan et al., 2008; Lacasse and Zamble, 2016). The source of the CO ligand in anaerobic hydrogenase biosynthesis is still unknown (Bürstel et al., 2011). Among others (Lenz et al., 2007), acetate (Roseboom et al., 2005) and CO_2 (Soboh et al., 2013) have been suggested as precursors, but compelling evidence is lacking. Under aerobic conditions, however, formyl-tetrahydrofolate serves as the CO precursor (Bürstel et al., 2016). The preformed $Fe(CN)_2CO$ fragment is then transferred from the HypCD complex into the apo-form of the large hydrogenase subunit (Arlt et al., 2021). Subsequently, the nickel is incorporated by HypA and HypB complex (Lacasse and Zamble, 2016). In *E. coli*, the SlyD protein is also involved in nickel insertion (Leach et al., 2007; Kaluarachchi et al., 2012; Pinske et al., 2015). Upon insertion of the complete [NiFe] cofactor, the hydrogenase large subunit usually undergoes proteolytic cleavage, in which the C-terminal extension is cleaved off (Senger et al., 2017; Pinske et al., 2019; Hartmann et al., 2020). This cleavage step allows oligomerization of the cofactor-containing large subunit with the small subunit, whose Fe-S clusters are incorporated by the universal Isc/Suf machinery.

Due to the complex maturation process, recombinant production of [NiFe]-hydrogenases is challenging, especially in heterologous systems, and makes scalability difficult (Fan et al., 2020). We have chosen the regulatory [NiFe]-hydrogenase (RH) from *Cupriavidus necator* (formerly *Ralstonia eutropha*) as a model for the development of a heterologous hydrogenase production system in *E. coli*. *C. necator* actually possesses four different [NiFe]-hydrogenases, all of which are O_2-tolerant, i.e., they perform H_2 conversion even in the presence of molecular oxygen (Fritsch et al., 2013; Schwartz et al., 2013; Lenz et al., 2015). The RH functions as H_2 sensor in the context of H_2-dependent transcriptional regulation of the genes encoding the two energy-conserving [NiFe]-hydrogenases of *C. necator* (Lenz et al., 1997, 2010). Like typical [NiFe]-hydrogenases, the RH consists of two subunits, a large subunit HoxC (52 kDa) containing the $NiFe(CN)_2CO$ center and a small subunit HoxB (36 kDa) harboring three [4Fe-4S] clusters (Pierik et al., 1998; Kleihues et al., 2000). Its H_2-oxidizing activity is absolutely insensitive to O_2 (Buhrke et al., 2005a; Ash et al., 2015). The maturation proteins required for cofactor assembly of the RH are encoded by the *hyp1* operon (*hypA1B1F1CDE*) of *C. necator* (Buhrke et al., 2001). In contrast to most other [NiFe]-hydrogenases, the RH large subunit HoxC does not undergo C-terminal processing, making RH a relatively simple [NiFe]-hydrogenase model. Recently, we succeeded to produce the RH heterologously in *E. coli* in a soluble form and purified the protein by a single affinity chromatography step (Fan et al., 2021a). By using an EnPresso B-based fed-batch-like growth mode, we obtained up to 250 mg L^{-1} of RH in shake flask cultures. This RH yield was about 250-fold higher than that from the native producer (Bernhard et al., 2001; Fan et al., 2021a). The productivity has been further improved using IPTG or lactose autoinduction (Fan et al., 2021b). Regrettably, the purified RH turned out to be inactive. While the small subunit appeared to be fully equipped with Fe-S clusters, the large subunit lacked the [NiFe] cofactor, indicating malfunctioning maturation in the heterologous host.

In this study, we aimed at the heterologous production of RH with catalytic activity by testing different *E. coli* strains with various genetic backgrounds and by varying the process conditions. By co-expression of the *hyp1* operon from *C. necator* and the supplementation of the growth medium with $NiCl_2$ we obtained RH with catalytic activity. The successful incorporation of the $NiFe(CN)_2CO$ cofactor was confirmed by IR and EPR spectroscopy. By co-expression of the *hoxN* and *hypX* genes, encoding a nickel permease and a dedicated maturase, respectively, catalytically active RH was also purified from aerobically grown *E. coli* BL21.

MATERIALS AND METHODS

Bacterial Strains, Media and Growth Conditions

While *E. coli* TG1 (Baer et al., 1984) was used for plasmid maintenance, the *E. coli* B strain BL21 Gold (Stratagene, Germany) and the K-12 strains W3110 (Bachmann, 1972) and MC4100 (Casadaban and Cohen, 1979) were used for RH production. Plasmid pQF8 (Fan et al., 2021a) was used for overproduction of structural RH subunits, $HoxB_{Strep}$ and HoxC, under control of the IPTG inducible $P_{lac-CTU}$ promoter. All strains and plasmids are listed in **Supplementary Tables 1, 2**.

Transformations and plasmid propagations were performed on solid and liquid TY medium (16 g L^{-1} tryptone, 10 g L^{-1} yeast extract, 5 g L^{-1} NaCl, for solid medium 2% agar-agar). The fed-batch-like EnPresso® B medium (EnPresso GmbH, Berlin, Germany) was used for RH production. The EnPresso B medium is based on a typical *E. coli* mineral salt medium supplemented with trace elements and Na_2SeO_3, Na_2MoO_4 and $Ni(NO_3)_2$ as

described previously (Soini et al., 2008). In this medium, glucose is enzymatically released from a non-metabolizable polymer contained therein. For preparation of a pre-culture, *E. coli* cells were inoculated from a single colony in 10 mL LB medium (10 g L^{-1} tryptone, 5 g L^{-1} yeast extract, 10 g L^{-1} NaCl) and shaken for 6–8 h at 37°C, 250 rpm (Infors HT, 25 mm offset, Switzerland). For main cultures, 50 mL EnPresso® B medium was inoculated to an OD_{600} of 0.2 in 250 mL baffled Ultra Yield® shake flask (Thomson Instrument Company, Oceanside, CA, United States) (20% v/v) supplemented with 25 μL of reagent A (1.5 U L^{-1}) for overnight cultivation at 30°C, 250 rpm (Infor HT, Switzerland). At the induction point booster and 75 μl reagent A (4.5 U L^{-1}) were added according to the manufacturer's instructions (EnPresso GmbH, Berlin, Germany) and RH production triggered by addition of 50 μM IPTG. The cells were cultivated under the same conditions for 24 h at 30°C or for 48 h/72 h at 18°C. If required all media were supplemented with 25 μg mL^{-1} chloramphenicol and 25 μg mL^{-1} kanamycin for selection.

For induction under O_2 limited conditions the cultivation protocol was altered as follows. To ensure a high cell density before, a first dose of booster and 75 μl reagent A (4.5 U L^{-1}) were added after overnight cultivation and growth continued for 12 h under the same conditions. After 12 h of boosted growth, cultures were transferred into 125 mL baffled PreSens shake flask (40% v/v) which was placed on an SFR shake flask reader (PreSens Precision Sensing GmbH, Regensburg, Germany) in a Kuhner LTX orbital shaker (50 mm offset, Adolf Kühner AG, Basel, Switzerland) with online monitoring of dissolved oxygen (DO) and pH. The oxygen level was controlled by manually reducing the shaking speed from 250 rpm to 100 rpm until a DO value almost close to 0% was reached to ensure O_2-limited (microaerobic) conditions. A 2nd dose of booster and reagent A was added together with 50 μM IPTG to induce RH production and cultivation continued at 30°C for 36 h or at 18°C for 48 h/66 h/72 h as indicated. Finally, cells were harvested by centrifugation at 8,000 × *g*, 4°C for 10 min. The cell pellets were frozen in liquid nitrogen and stored at −80°C until further use. To investigate an effect of metal ion addition on active RH production, appropriate concentrations of $NiCl_2$ or $FeSO_4$ were added to the cultures at the induction point and 8 mL boosted cultures were distributed onto the Deep Well OxoDish® OD24-DW deepwell plates with DO online monitoring and cultivated in an SDR SensorDish® Reader (both from PreSens Precision Sensing GmbH, Regensburg, Germany) which was placed in a Duetz plate holder (EnzyScreen BV, Heemstede, Netherlands) and placed and cultivated in the Kuhner LTX shaker (50 mm offset, Adolf Kühner AG, Basel, Switzerland). After 24 h of induction under O_2-limited cultivation conditions at 30°C cells were harvested from the 8 mL culture suspension as described above.

RH Purification, Spectroscopic Characterization and Activity Assay

RH purification has been described in detail previously (Fan et al., 2021a,b). All elution fractions were concentrated by ultra-filtration (14,000 × g, 4°C) using Amicon Ultra Ultracel 30 kDa cut-off concentrators (Merk Millipore, Germany). An aliquot of the final concentrate was used for SDS-PAGE. The gels were stained with colloidal Coomassie blue G250 solution and subsequently bands were quantified with ImageJ for determination of protein concentrations. A defined solution of bovine serum albumin served as standard. H_2-oxidizing activity of RH was measured spectrophotometrically using a Cary50 UV-vis spectrophotometer (Varian, Agilent, Santa Clara, California), and the H_2 uptake assay using methylene blue as an electron acceptor was used as described previously (Lenz et al., 2018). Measurements were performed with two biological replicates and the standard deviation was calculated from at least two independent technical replicates. For screening experiments of optimal nickel or iron concentrations, the H_2-oxidation activity was measured in soluble extract of the cell lysates separated from solid cell debris and insoluble fraction after sonication (3 min, 30 s on/off, sonotrode with 3 mm diameter, 30% amplitude) (UP200S, Hielscher GmbH, Germany). The reaction was started by the addition of 200 μl soluble extract to 1.8 mL reaction buffer followed by 100% H_2 gas saturation as described previously (Fan et al., 2021a). The RH concentration in the soluble extract was quantified in Western blot analysis using known concentration of HoxC as a control. Infrared (IR) and electron paramagnetic resonance (EPR) spectroscopy of RH were measured as described previously (Fan et al., 2021a).

Construction of Plasmids for *hyp* Gene Expression

Plasmid pGK16, a derivative of the medium copy plasmid pGK14 (Brantl, 1994) carrying a kanamycin resistance gene instead of the erythromycin resistance gene (Gimpel, unpublished) was used as basis for the construction of the *hyp* gene expression plasmids. First, the 267 bp *Sal*I/*Bgl*II fragment from plasmid pGW2 (Schollmeyer, 2020) harboring the P_{tac} promoter, a multiple cloning site and a transcription terminator was cloned into the corresponding pGK14 vector, yielding plasmid pQF11. Next, using Q5 DNA polymerase (New England Biolabs), PCR amplification of the complete *hyp1* operon from pRH-Hyp (Lenz et al., 2007) and *hyp1 (ΔF1)* operon from pRH-Hyp(ΔF1) (Lenz et al., 2007) was performed with oligonucleotides MG0164 (5′-TCATCTAGACGGAGTCTTTGGGAGATACTG-3′) and MG0168 (5′-ACTGCGGCCGCTTAACAAATGCGCGGAAGCT G-3′). The PCR products were digested with *Xba*I and *Not*I and cloned into the pQF11 cut with the same enzymes yielding pQF12 and pQF13. The plasmid pQF12, which contains the complete *hyp1* operon, was used as the basis for the integration of further maturation enzymes. The high-affinity nickel permease encoding *C. necator hoxN* gene was PCR amplified using primers MG0226 (ATCGCGGCCGCACAGGAGACTTCCAGCATGTTCCA) and MG0227 (ACTGCGGCCGCTTAACATGAACTTGTCGGCCAG GA) and plasmid pCH231 (Wolfram et al., 1995) as template. The resulting 0.9 kb fragment was digested with *Not*I and subsequently ligated into the corresponding pQF12 vector yielding plasmid pQF17. The primer pair MG0243 (AGTTCTAGAGCGAGTCGGCTATGCGCATATTGC)/MG024

4 (ATGTCTAGATCAAGATCGTTTCCCCGCAAGTGC) and plasmid pGE771 (Lauterbach and Lenz, 2013) as template were used to PCR-amplify a 1.8 kb fragment encoding the *C. necator* aerobic maturase HypX. The resulting fragment was digested with *Xba*I and ligated into the corresponding pQF17 vector, resulting in plasmid pQF18. The correctness of the amplified sequences was confirmed by sequencing (LGC Genomics, Berlin). A schematic map of all plasmids can be found in **Supplementary Figure 1**. Expression plasmids were introduced sequentially.

RESULTS

Heterologous Production of Catalytically Active RH in O_2-Limited *E. coli* Cultures

In a previous study we showed that high RH yields can be obtained with *E. coli* BL21 Gold carrying the RH overproduction plasmid pQF8 (strain BQF8RH; Fan et al., 2021a). However, the purified RH did not contain any [NiFe] cofactor (Fan et al., 2021a), which is consistent with major defects of *E. coli* BL21 in metal ion transport and metalloprotein biosynthesis (Pinske et al., 2011). This phenotype has been attributed to a non-sense mutation in the *fnr* gene whose gene product regulates nickel transport and *hyp* gene expression. Global deficiencies in anaerobic metabolism and metal ion transport seem to be common for *E. coli* B derivatives (Pinske et al., 2011). To overcome this obstacle, we transformed the two *E. coli* K-12 derivatives *E. coli* W3110 and *E. coli* MC4100 with plasmid pQF8, resulting into the recombinant strains WQF8RH and MQF8RH, respectively. All strains were cultivated under both aerobic and O_2-limiting conditions in shake-flasks containing EnPresso B medium, as described in section "Materials and Methods." O_2 limitation (DO value close to 0%) was initiated by reducing the shaking speed from 250 to 100 rpm after induction (**Supplementary Figure 3**). After 24 h of IPTG induction, cells were collected, disrupted, and the RH was purified by affinity chromatography. Furthermore, the H_2-oxidizing activity of all RH samples was determined.

Regardless of the aeration, similar RH protein yields were obtained (data not shown). However, considering the higher final cell densities (**Supplementary Figure 2A**), the obtained volumetric yields were 1.5–2.5-fold higher under aerobic conditions (**Figure 1A**). Interestingly, among the three strains tested, BQF8RH performed best under aerobic conditions but worst under O_2-limiting conditions (**Figure 1A** and **Supplementary Figure 2C**), suggesting that anaerobic conditions might be suboptimal for RH production in *E. coli* BL21. Presumably, the lack of certain anaerobic respiration-related proteins and/or enzymes in the B strains prevents rapid adaptation to anaerobic stress (Pinske et al., 2011) and leads to slower growth and lower protein production (Kim et al., 2014). However, the RH purified from BQF8RH showed no activity regardless of the growth conditions (**Figure 1B**). In contrast, RH preparations from both *E. coli* K-12 derivatives grown under O_2-limiting conditions exhibited a specific activity of 0.02 U mg^{-1}, while RH purified from aerobically grown cells was inactive (**Figure 1B**). The latter could be due to either the lack of the hydrogenase maturation apparatus or insufficient uptake of nickel ions under aerobic cultivation, both of which are modulated by the transcriptional regulator FNR under anaerobic conditions (Wu et al., 1989; Lutz et al., 1991; Messenger and Green, 2003). Thus, the lack of FNR in *E. coli* B-strains, as well as the reduced FNR levels in the presence of O_2, might prevent nickel uptake, [NiFe] cofactor assembly, and consequently the synthesis of catalytically active RH. Nevertheless, the RH activities obtained from both *E. coli* K-12 derivatives were quite low and corresponded to only 0.5–1% of those reported for the RH protein isolated from *C. necator,* which is in the range of 1.6–4.5 U mg^{-1} (Buhrke et al., 2005a,b; Caserta et al., 2020). This indicates that the hydrogenase maturation apparatus of *E. coli* K-12 is only able to mature *C. necator* RH to a very limited extent.

Co-expression of the *C. necator hyp* Genes Improves RH Maturation in *E. coli*

It has been reported previously that co-expression of the *C. necator hyp* genes markedly improve the activity of heterologously produced RH (Lenz et al., 2007). Thus, we constructed plasmids pQF12 and pQF13 carrying the entire *C. necator hyp1* operon [*hypA1B1(F1)CDE*] with or without *hypF1*, respectively, under control of the IPTG-inducible P_{tac} promoter. The plasmids were transferred into strains BQF8RH, WQF8RH, and MQF8RH, resulting in BQF8RH2 and BQF8RH3, WQF8RH2 and WQF8RH3, MQF8RH2 and MQF8RH3, respectively. The strains were cultivated under O_2-limiting conditions, RH was purified, and its H_2-oxidation activity was measured. Co-expression of the maturase genes did not significantly affect the RH yield, indicating that the cells tolerate the higher metabolic load (**Figures 1A,C**). RH purified from strains BQF8RH2 and BQF8RH3 still showed no activity, whereas co-expression of the maturase genes significantly increased the RH activity in the K12 derivatives (**Figure 1D**). RH purified from WQF8RH2 and MQF8RH2 displayed a specific activity of 0.03 U mg^{-1} and 0.07 U mg^{-1} (**Figure 1D**), which corresponds to a 1.5 and 3.5-fold increase, respectively, compared to the parental strains, which did not express the *C. necator hyp* genes. Remarkably, the strains WQF8RH3 and MQF8RH3, which co-express the *hyp1* operon without *hypF1*, showed even higher RH activities with a 2.5- and 6-fold increase, respectively (**Figure 1D**). These data highlight the positive effect of the co-expressed *C. necator* maturase genes on the catalytic activity of RH and underscore the previously observed requirement of the *hypF* gene of *E. coli* for RH maturation under anaerobic conditions (Lenz et al., 2007). Furthermore, *E. coli* MQF8RH3 was found to be most suitable for production of active RH as it showed the highest specific RH activity among the strains discussed so far. However, despite co-expression of the *C. necator hyp* genes, the activity of the heterologously produced RH remained very low.

Addition of Nickel Improves the RH Activity in *E. coli*

The comparatively low activity of the heterologously produced RH might result from an insufficient supply of nickel by the

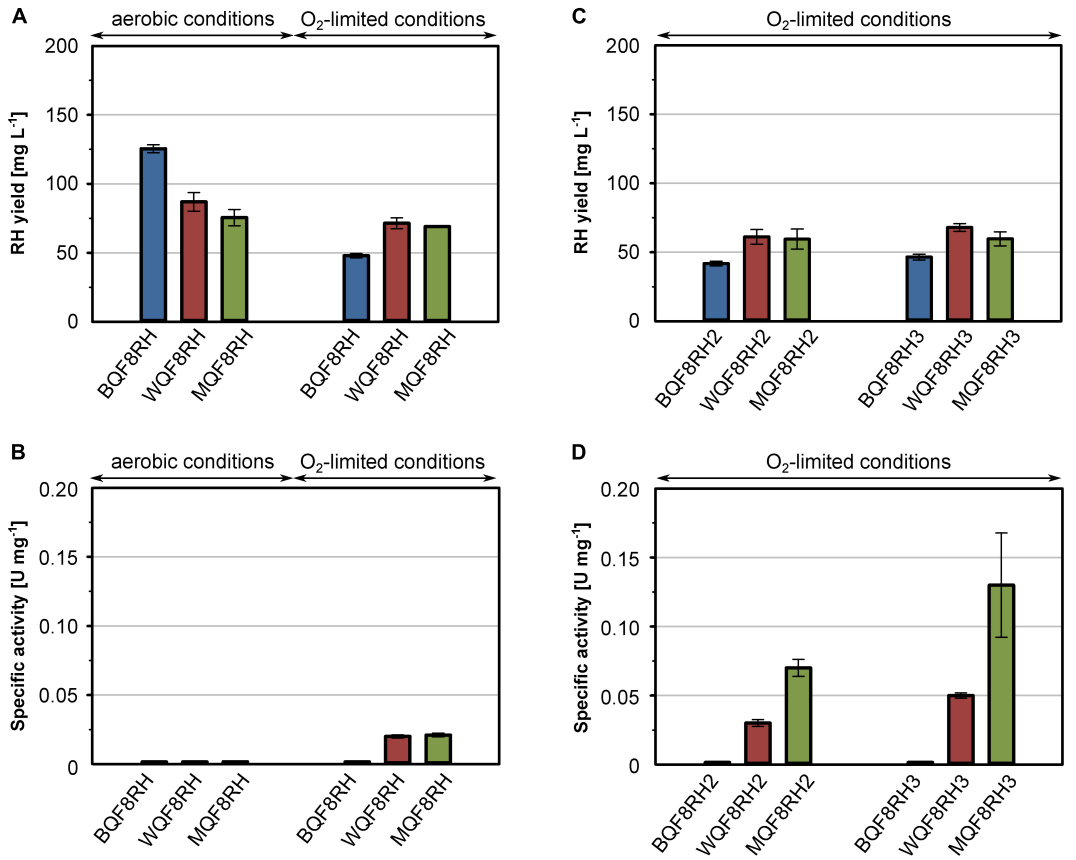

FIGURE 1 | Comparison of production strains, cultivation mode and *hyp* gene co-expression for heterologous RH production. *E. coli* strains BQF8RH, WQF8RH and MQF8RH (derivatives of *E. coli* strains BL21 Gold, W3110 and MC4100, respectively) carry plasmid pQF8 encoding the two RH subunits were used. For co-expression of the maturation genes of *C. necator*, strains BQF8RH, MQF8RH and WQF8RH were transformed with either plasmid pQF12 (encoding the entire *hyp1* operon) or plasmid pQF13 (encoding the modified *hyp1(ΔF1)* operon lacking *hypF1*) yielding strains BQF8RH2, WQF8RH2 or MQF8RH2 and BQF8RH3, WQF8RH3 or MQF8RH3, respectively. All strains were cultivated in 50 mL EnPresso B medium as described in section "Materials and Methods." For aerobic production, cultivation was performed in 250-mL Ultra Yield flasks (20% V/V) shaken at 250 rpm, whereas O_2-limited production was performed in 125-mL PreSens flasks (40% V/V) adjusted to a DO near 0% by manually decreasing the shaking speed. RH protein was purified by affinity chromatography **(A,C)** and specific activities measured from the purified samples **(B,D)**.

EnPresso B medium used for strain cultivation. Similar to LB, EnPresso B medium is a rich medium that most likely has a chelating effect on metal ions, thereby reducing their bioavailability (Rathnayake et al., 2013). To test this hypothesis, we added 500 μM nickel to the medium and cultivated the *E. coli* strains MQF8RH, MQF8RH2 and MQF8RH3 under microaerobic conditions. $NiCl_2$ supplementation did neither affect the bacterial growth nor the yield of the purified RH (**Figure 2A**), excluding toxic effects of the additional nickel. In contrast, the extra nickel resulted in a significant increase in RH activity when the *C. necator hyp* machinery was co-expressed (**Figure 2B**). In fact, we observed an increase from 0.07 U mg^{-1} to 0.28 U mg^{-1} for the RH isolated from MQF8RH2 and from 0.13 U mg^{-1} to 0.34 U mg^{-1} for the RH isolated from strain MQF8RH3 cultivated at 30°C (**Figure 2B**). An even higher activity of 0.5 U mg^{-1} was obtained when the same strains were cultured at 18°C for an extended time period of 66 h after IPTG induction (see section "Materials and Methods"), although the lower temperature decreased the volumetric RH yield (**Figure 2A**). Remarkably, the RH proteins isolated from strains MQF8RH2 and MQF8RH3 cultivated at 18°C had similar specific activities, suggesting that the presence of the *C. necator hypF1* gene no longer impacted enzyme maturation (**Figures 1D**, **2B**). The lower cultivation temperature is accompanied by an increased oxygen concentration, which could be the reason for the acquired functionality of HypF1. In conclusion, lowering the cultivation temperature and nickel supplementation markedly improved the specific activity of RH isolated from *E. coli* MC4100.

Escherichia coli BL21 Gold is known to be deficient in nickel uptake (Pinske et al., 2011). We thus tested whether the addition of $NiCl_2$ improves the activity of the RH purified from strains BQF8RH, BQF8RH2, and BQF8RH3 cultivated at 30°C. Indeed, we detected a low activity of 0.09 U mg^{-1} for the RH purified from strain BQF8RH3 (**Figure 2D**). Thus, nickel availability appears to be the major impediment to [NiFe] cofactor assembly

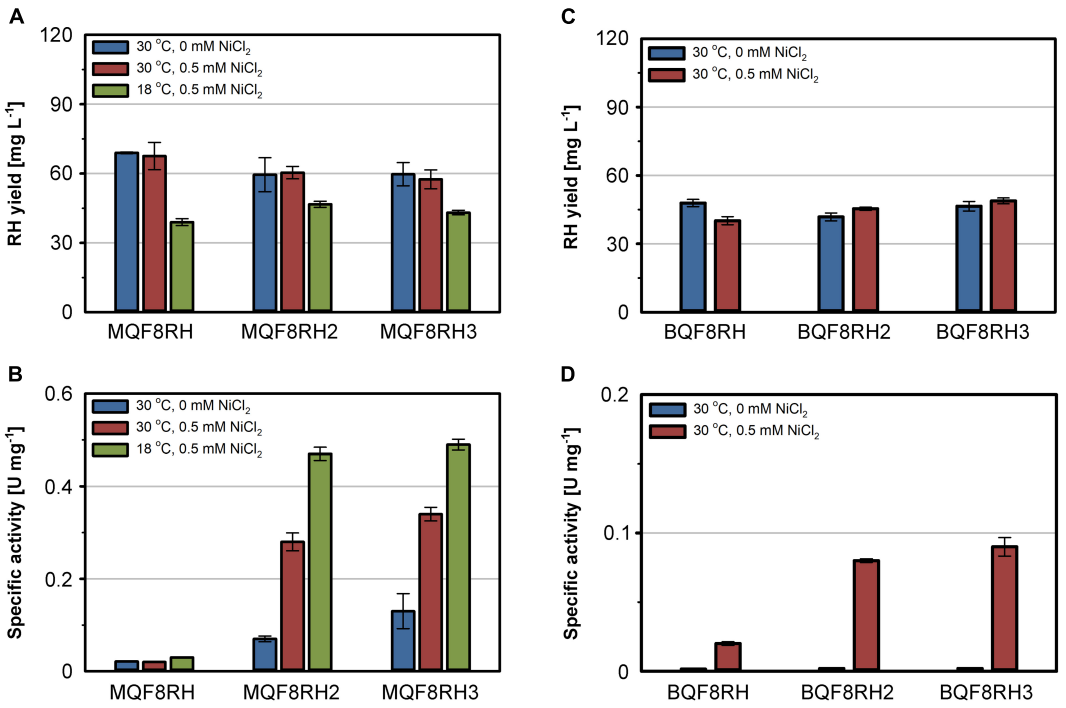

FIGURE 2 | Effect of $NiCl_2$ addition and cultivation temperature on RH yield and activity. Strains *E. coli* MQF8RH, MQF8RH2, MQF8RH3, BQF8RH, BQF8RH2 and BQF8RH3 were cultivated in 125 mL PreSens flask with 50 mL boosted EnPresso B medium under O_2-limited conditions. After induction, the temperature was either maintained at 30°C or shifted to 18°C. $NiCl_2$ (0.5 mM) was supplemented at the time point of the induction of RH gene expression as indicated. RH protein was purified by affinity chromatography **(A,C)** and specific activities measured from the purified samples **(B,D)**.

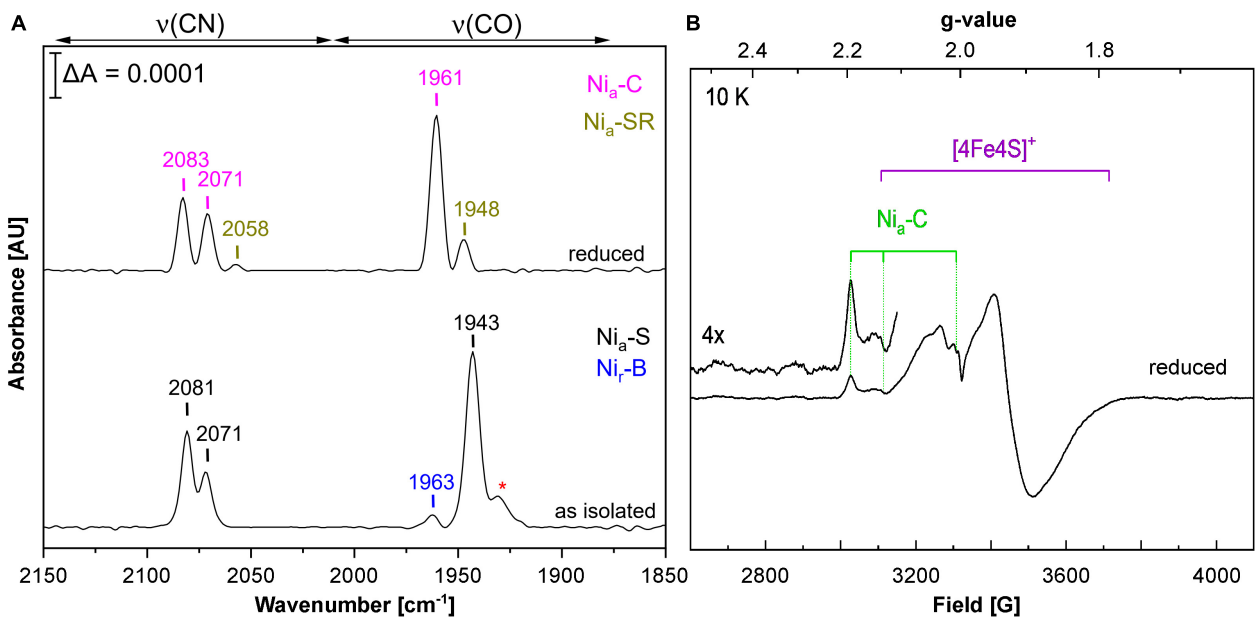

FIGURE 3 | Spectroscopic characterization of RH heterologously produced in *E. coli*. Spectroscopic data were recorded on RH purified from MQF8RH2 (30°C/0.5 mM $NiCl_2$). **(A)** IR spectra of as-isolated and H_2-reduced RH. The signals indicate the presence of CO and CN ligands of the $NiFe(CN)_2CO$ active site. Bands are labeled according to the different redox states of the RH (Ash et al., 2015; Roncaroli et al., 2015; Caserta et al., 2020), i.e., Ni_a-S (2,081, 2,071, 1,943 cm^{-1}), Ni_r-B (2,097, 2,089, 1,963 cm^{-1}), Ni_a-SR (2,073, 2,058, 1,948 cm^{-1}), and Ni_a-C (2,083, 2,071, 1,961 cm^{-1}). The red asterisk most likely indicates traces of Ni_r-S species (1,931 cm^{-1}). **(B)** EPR spectrum of sodium dithionite ($Na_2S_2O_4$)-reduced RH. The spectrum was recorded at 10 K and a microwave power of 1 mW.

in *E. coli* BL21 Gold. However, the RH activity was approximately fourfold lower than that of the K-12 strain MQF8RH3 cultivated under the same conditions.

Heterologously Produced RH Contains the Native NiFe (CO)$(CN)_2$ Cofactor

Using *E. coli* MC4100 as host, we obtained RH activities that were about half of those reported for the first RH preparations from *C. necator* (Bernhard et al., 2001). This prompted us to spectroscopically investigate the cofactor content of purified RH from *E. coli* strain MQF8RH3, which was cultivated under O_2-limiting conditions at 30°C and elevated nickel concentrations. By infrared spectroscopy, we monitored the CO and CN stretching vibrations of the CO and CN^- ligands of the $NiFe(CN)_2(CO)$ cofactor, which appear in a spectral region, in which no other protein-specific vibrations occur (De Lacey et al., 2007; Lubitz et al., 2014). The IR spectrum of the as-isolated, oxidized RH protein was dominated by the typical bands of the so-called Ni_a-S state, characterized by a CO stretching band at 1,943 cm^{-1} and two cyanide stretchings at 2,071 and 2,081 cm^{-1}. The IR signal amplitudes suggested a cofactor occupation of 5–10%. Treatment with H_2 gas resulted in reduced RH, whose IR spectrum is dominated by the Ni_a-C state with a CO stretching band at 1,961 cm^{-1} and two CN stretchings at 2,071 and 2,083 cm^{-1} (**Figure 3A**; Bernhard et al., 2001; Buhrke et al., 2005b; Roncaroli et al., 2015; Caserta et al., 2020). EPR spectroscopy, which allows the detection of paramagnetic states, confirmed the presence of signals related to the Ni_a-C-state (g_x = 2.19, g_y = 2.13, g_z = 2.01) as well as $[4Fe\text{-}4S]^{1+}$ cluster(s) signals in reduced RH treated with an excess of sodium dithionite (**Figure 3B**), which is in line with previous results obtained from RH isolated from *C. necator* (Roncaroli et al., 2015). These results demonstrate that the RH isolated from *E. coli* contains a canonical $NiFe(CN)_2(CO)$ cofactor that shares the same spectroscopic properties as the native RH isolated from *C. necator*.

Optimal Metal Ion Supplementation for RH Activity in *E. coli*

The nickel supplementation experiments described above were performed with a nickel concentration of 500 μM. To determine the optimal metal content in the growth medium, we devised a screening experiment with *E. coli* MQF8RH3 cultivated in 24-deepwell plates filled with EnPresso B medium containing different concentrations of nickel and iron. The cells were harvested, and the RH activity in crude cell extracts was determined as described in material and methods. The addition of up to 2 mM of either $NiCl_2$ or $FeSO_4$ had no effect on cell growth, as the final OD did not vary significantly (**Figure 4A**). As expected, $NiCl_2$ addition led to an increase of RH activity in the crude extracts. The highest activity of 0.5 U mg^{-1} was observed upon addition of 100 μM $NiCl_2$, which corresponds to an approximately threefold increase compared to the sample without nickel addition (**Figure 4B**). Further increase in nickel concentration diminished the RH activity (**Figure 4B**). In contrast, the addition of up to 500 μM $FeSO_4$ had only a negligible effect on the RH activity in the crude extract. A further increase even reduced the RH activity below 50% of the level achieved without iron addition. Thus, metal concentrations higher than 100 μM Ni and 500 μM Fe had a negative effect on RH activity and were avoided in subsequent experiments. Based on these screening experiments, we investigated the effect of nickel and iron on RH production and activity in larger medium volumes. *E. coli* MQF8RH3 was cultivated at 18°C in EnPresso B supplemented with different nickel:iron ratios [0:0, 100:0, 0:100, 100:100 (μM:μM)]. RH was purified and its activity was measured (**Figure 5**). The RH yield was the same under all conditions (**Figure 5A**). An activity of approx. 0.13 U mg^{-1} was observed without the addition of nickel or iron (**Figure 5B**), which is consistent with our data at 30°C (**Figure 2B**). The activity did not vary significantly upon addition of 100 μM $FeSO_4$, indicating that sufficient iron is present in the EnPresso B medium. In contrast, the addition of 100 μM $NiCl_2$ resulted in a fourfold increase of specific activity of 0.55 U mg^{-1}, which was similar to the value measured in the presence of 100 μM $NiCl_2$/100 μM $FeSO_4$ (0.57 U mg^{-1}, **Figure 5B**). Based on these results, we added 100 μM $NiCl_2$ but not further iron source to the growth media.

Improved RH Maturation by Co-production of HoxN and HypX From *C. necator*

The results described above clearly show a significant activity increase when the RH is isolated from O_2-limited *E. coli* cultures. Aerobic cultivation, by contrast, led to higher protein yields (**Figure 1A**). Therefore, we aimed to improve RH activity under aerobic conditions. Nickel supply is limited particularly under aerobic conditions as the endogenous nickel uptake system in *E. coli* in FNR-dependent and functional only under anaerobic conditions (Wu et al., 1989). Thus, we considered the gene encoding the high-affinity nickel permease HoxN, which mediates nickel uptake in *C. necator* under aerobic conditions (Eberz et al., 1989; Eitinger and Friedrich, 1991; Wolfram et al., 1995). Consequently, we extended plasmid pQF12 by adding *hoxN* gene from *C. necator* resulting into plasmid pQF17 (*hypA1B1F1CDE-hoxN)* (**Supplementary Figure 1**).

Additionally, we also considered that under aerobic conditions the formyltetrahydrofolate decarbonylase HypX from *C. necator* is responsible for the biosynthesis of the CO ligand of the $NiFe(CN)_2(CO)$ site (Bürstel et al., 2016; Schulz et al., 2020). Thus, we further extended plasmid pQF17 by implementing the *hypX* gene, yielding plasmid pQF18 (*hypA1B1F1CDEX-hoxN)*. The plasmids pQF17 and pQF18 were transferred to *E. coli* MQF8RH, resulting in strains MQF8RH7 and MQF8RH8, respectively. The new strains were grown in addition to strain MQF8RH2 in $NiCl_2$-supplemented (100 μM) and boosted EnPresso B medium under both aerobic and O_2-limited conditions. Cells were harvested after 48 h of IPTG induction, proteins purified and their specific activities quantified. While the presence of the new genes did not significantly affect the RH yield in the new strains (**Figure 6A**), the introduction

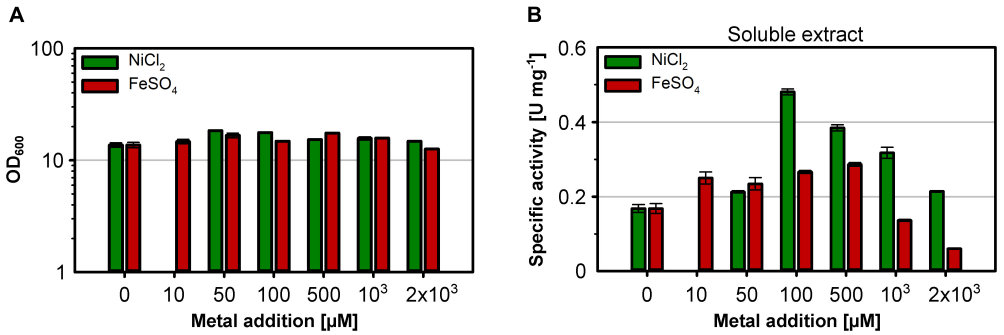

FIGURE 4 | Effect of the Ni and Fe concentration on cell growth and RH activity. *E. coli* strain MQF8RH3 was cultivated in 24-deepwell plates with 8 mL boosted EnPresso medium at 30°C under O_2-limited conditions. $NiCl_2$ or $FeSO_4$ were supplemented using the indicated concentrations varying from 0 to 2.0 mM. Cells were harvested 24 h after induction with 50 µM IPTG. **(A)** Optical density of the cell culture just before harvesting. **(B)** Soluble extracts were obtained by sonication and RH activity was measured. The specific RH activity was calculated based on the RH concentrations determined in the crude extracts by Western blotting (**Supplementary Figure 4**).

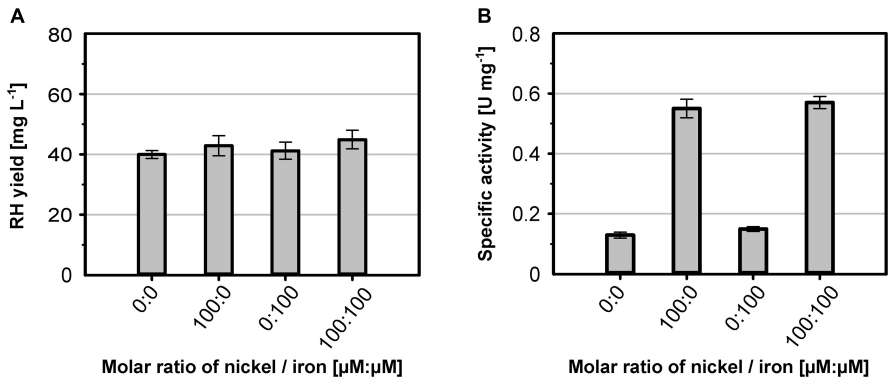

FIGURE 5 | Metal effect on soluble RH yield and activity. *E. coli* strain MQF8RH3 was cultivated in 125 mL PreSens flasks with 50 mL boosted EnPresso B medium at 18°C. The medium was supplemented with different molar ratios of $NiCl_2$ and $FeSO_4$ as indicated. **(A)** RH protein was purified by affinity chromatography, and the yield was quantified. **(B)** Specific activities measured from the purified RH samples.

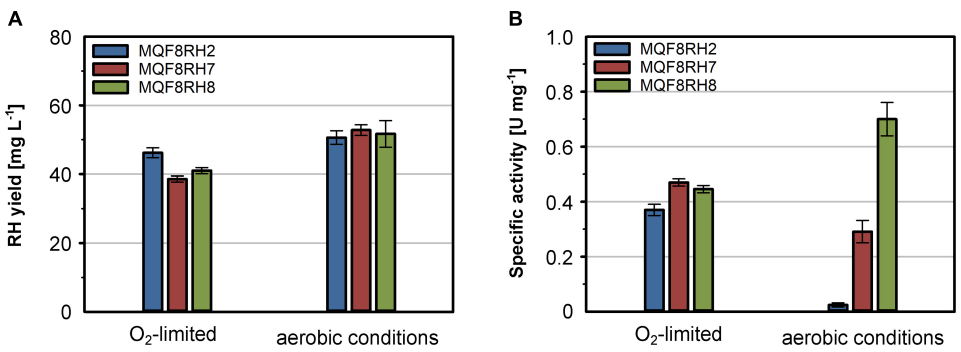

FIGURE 6 | Effect of *hoxN1* and *hypX* genes on the production of active RH. *E. coli* strains MQF8RH2 (RH-Hyp1), MQF8RH7 (RH-Hyp1-HoxN1) and MQF8RH8 (RH-Hyp1-HoxN1-HypX) were cultivated at 18°C in 50 mL boosted EnPresso B medium supplemented with 0.1 mM $NiCl_2$. After induction with 50 µM IPTG, RH production lasted for 48 h under either aerobic or O_2-limited conditions. **(A)** RH protein was purified by affinity chromatography, and the yield was quantified. **(B)** Specific activities measured from the purified RH samples.

of HoxN led to a slight increase of RH activity under O_2-limited conditions and about 12-fold higher activity under aerobic conditions (**Figure 6B**). These data clearly indicate that HoxN is functional in nickel uptake in the presence of high O_2 concentrations. The introduction of *hypX* did not improve the RH activity obtained from cells grown under O_2-limiting conditions, in line with a so far elusive HypX-independent CO ligand synthesis (Soboh et al., 2013; Arlt et al.,

2021). In contrast, the RH isolated from the aerobically grown strain MQF8RH8 showed a twofold higher specific activity (0.7 U mg^{-1}) than the RH purified from strain MQF8RH7 (**Figure 6B**). These data, surprisingly, evidenced the successful implementation of HypX in *E. coli* strains able to synthesize the active site CO ligand under aerobic conditions. Taken together, these findings demonstrate that co-expression of HypX and HoxN in addition to the *C. necator hyp1* operon enables biosynthesis of active RH even under aerobic conditions. Additionally, we successfully increased the space-time yield of catalytically active RH by a factor of about 27 compared to strain MQF8RH2 cultivated under the same conditions (12.5 *vs.* 0.45 U (L d) $^{-1}$). The reported RH activity under aerobic conditions represents the highest activity for a heterologous produced RH so far.

Production of Catalytically Active RH in *E. coli* BL21 Gold

The successful heterologous production of active RH through co-expression of the *hyp* and *hoxN* genes under aerobic conditions prompted us to revisit strain BQF8RH that so far showed the highest RH yield, although inactive (**Figure 1A**). Hence, we transformed strain BQF8RH with plasmid pQF18 and investigated the RH production in the resulting strain BQF8RH8 using the MC4100 derivative MQF8RH8 for comparison. Both strains were cultivated under aerobic conditions with or without the addition of $NiCl_2$. The added $NiCl_2$ neither affected cell growth (**Figure 7A**) nor the RH yield of the two strains (**Figure 7B**). As expected, the *E. coli* BL21 derivative BQF8RH8 showed an about 50% higher RH yield compared to the K12 derivative MQF8RH8. However, the prolongation of the aerobic induction period from 48 h to 72 h resulted in a twofold decrease in RH yield for both strains (**Figure 7B**). Clearly, nickel supplementation is necessary for production of catalytically active RH (**Figure 7C**) when the strains are cultivated under aerobic conditions. After 48 h of induction, the specific activities of the RH preparations from both MQF8RH8 and BQF8RH8 ranged similarly at about 0.6 U mg^{-1}. Despite the marked decrease in RH yield (**Figure 7B**), extension of the production period from 48 h to 72 h resulted in a threefold and fivefold increase in the specific RH activities of the samples isolated from strains MQF8RH8 and BQF8RH8 to 2 U mg^{-1} and even 3 U mg^{-1}, respectively (**Figure 7C**). Accordingly, the specific RH activity of strain BQF8RH8 was almost as high as that of RH isolated from the native host *C. necator* (Caserta et al., 2020). Considering protein yield and specific activity, the yield of active RH was similar (40 U L^{-1} of culture) for both

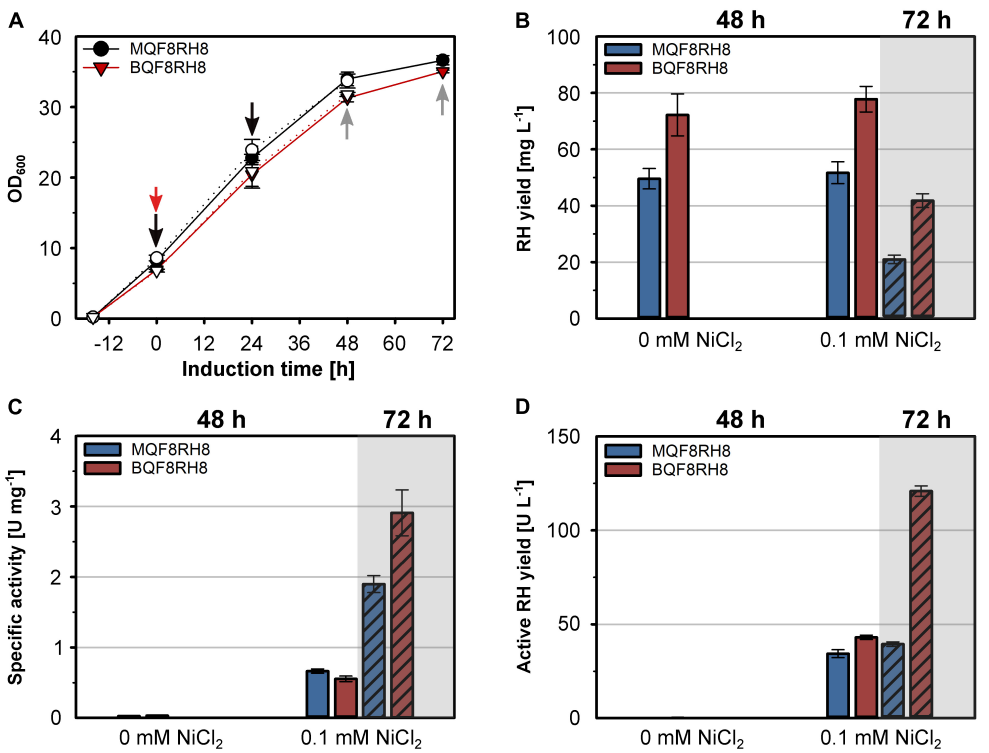

FIGURE 7 | Production of active RH in aerated cultures of *E. coli* BL21 Gold. *E. coli* strains MQF8RH8 and BQF8RH8 were cultured in 50 mL boosted EnPresso B medium at 18°C under aerobic conditions. RH gene expression was induced with 50 μM IPTG and cells harvested 48 h or 72 h (hatched columns) after induction. $NiCl_2$ was added at the time point of induction of gene expression as indicated. **(A)** Cell growth. The time point of induction is indicated by a red arrow, while the time points of booster addition and cell harvest are indicated by black and gray arrows, respectively. Open and filled symbols represent growth of *E. coli* with or without 0.1 mM $NiCl_2$, respectively. **(B)** RH protein was purified by affinity chromatography, and the yield was quantified. **(B)** specific activities measured from the purified RH samples. **(D)** Volumetric yield of RH calculated from the results in panels **(B,C)**.

induction periods of MQF8RH8 and for BQF8RH8 after 48 h of induction (**Figure 7D**). Remarkably, after an induction time of 72 h, we obtained an unprecedented yield of active RH of 120 U L^{-1} (**Figure 7D**) for strain BQF8RH8.

DISCUSSION

Here, we present a major improvement in the heterologous hydrogenase production in *E. coli* exemplified by the purification of catalytically active RH from *C. necator*. We optimized important factors such as the cultivation mode (anaerobic/aerobic), Ni and Fe content in the medium, production temperature, and co-expression of specific maturation genes, thereby systematically increasing the H_2-oxidizing activity. The RH activities as well as the protein yields obtained from all experiments conducted are summarized in **Supplementary Table 3**. Even though the RH is synthesized in an active form in its native host, *C. necator*, under aerobic conditions (Bernhard et al., 2001; Buhrke et al., 2005a; Ash et al., 2015), no active RH could be purified from aerobically grown *E. coli* strains without further genetic amendments. Under microaerobic/anaerobic growth conditions, however, little RH activity was observed, consistent with the fact that the hydrogenase maturation apparatus of *E. coli* is functional only under anaerobiosis (Messenger and Green, 2003; Forzi and Sawers, 2007; Lenz et al., 2007). Nevertheless, the very low activity suggests that the *E. coli* Hyp maturases are inefficient in outfitting the RH with the $NiFe(CN)_2CO$ cofactor. Indeed, the co-expression of the *hyp1* operon encoding the HypA1, B1, F1, C, D, and E proteins from *C. necator* further increased RH activity in *E. coli* (**Figure 1**). Although the Hyp proteins of *E. coli* and *C. necator* show an amino acid sequence identity of 18–45% (Wolf et al., 1998; Böck et al., 2006; Vignais and Billoud, 2007), this observation clearly demonstrates that they are not generally interchangeable with each other. The HypF protein plays an interesting role here. HypF1 from *C. necator* seems to be inactive under anaerobic conditions, and the *E. coli* HypF ortholog of *E. coli* takes over its function, consistent with a previous report (Lenz et al., 2007). Moreover, both HypF versions seem to compete with each other, as there is an increase in RH activity under anaerobic conditions in the absence of HypF1 of *C. necator*. The likely reason is that the inactive version of *C. necator* interferes with the interaction of the HypE protein with the *E. coli* HypF. Notably, the HypF1 of *C. necator* comprises only one of three domains present in canonical HypF proteins, such as that from *E. coli* (Wolf et al., 1998; Paschos et al., 2002). While canonical HypF proteins synthesize cyanide (CN) residue from carbamoyl phosphate and ATP, the truncated HypF likely requires carbamoyl adenylate for CN synthesis (Reissmann et al., 2003; Blokesch et al., 2004b). It is possible that carbamoyl adenylate is produced in sufficient quantities in living cells only under aerobic conditions. This assumption is supported by the higher RH activities obtained at lower temperature (**Figure 2**) which can be explained by a higher oxygenation of the medium compared to higher temperatures. Furthermore, lower temperatures might prevent misfolding of both the RH subunits and the maturases.

As nickel and iron are essential for RH activity, both metal ions must be provided in sufficient quantities. The availability of the metal ions depends both on their concentration in the medium, their bioavailability and the presence of specific cellular uptake systems. In *E. coli*, Fe^{2+} is predominantly transported across the membrane by the Feo system under microaerobic and anaerobic growth conditions, while Fe^{3+}, occurring predominantly under aerobic conditions, is taken up by the Fec system (Braun and Hantke, 2011; Kosman, 2013; Lau et al., 2016). Thus, the versatile iron uptake systems in *E. coli* allow for sufficient intracellular availability and iron homeostasis under both aerobic and anaerobic conditions. Kim et al. (2010, 2011) reported that iron rather than nickel needs to be added for the production of active *E. coli* hydrogenase 1 and *Hydrogenovibrio marinus* [NiFe]-hydrogenase in *E. coli* in a modified minimal medium. In the case of EnPresso B, the addition of iron had a negligible effect on the RH activity (**Figures 4**, **5**), indicating that this medium already contains sufficient iron. In contrast to iron, nickel is much less abundant and might be limiting in case of the overproduction of nickel-containing proteins such as [NiFe]-hydrogenase. In *E. coli*, nickel is taken up *via* the specific Nik system, which is synthesized only under anaerobic conditions. In Nik-deficient strains, such as *E. coli* BL21, nickel can be taken up by the magnesium transport system, which, however, has much lower specificity for nickel than the Nik transporter (Eitinger and Mandrand-Berthelot, 2000). In line with previous results that a high concentration (0.5 mM) of $NiCl_2$ added to the medium restores the activity of *E. coli* hydrogenases in strains with defects in nickel uptake (Waugh and Boxer, 1986; Wu et al., 1989), the activity of the RH improves significantly in all tested strains upon nickel addition (**Figures 2–5**). Interestingly, not only the Nik-deficient BL21 derivatives but also the MC4100 derivatives showed nickel dependence, indicating that the chelating properties of the medium limit the availability of nickel. The co-production of the high-affinity nickel permease HoxN from *C. necator* resulted in a substantial increase in RH activity both under anaerobic and aerobic growth conditions. Moreover, the presence of HoxN enables RH maturation even in the presence of molecular oxygen (**Figure 6**). Notably, the addition of up to 0.1 mM $NiCl_2$ to our EnPresso B medium had no effect on cell growth, even in the presence of HoxN.

It has been previously shown that under aerobic conditions the availability of CO is limiting for maturation of the $NiFe(CN)_2CO$ cofactor of hydrogenase (Bürstel et al., 2011). To address this potential problem in case of the production of hydrogenase in aerobically grown *E. coli*, we co-expressed the auxiliary *hypX* gene from *C. necator*, which is known to encode a CoA-dependent formyl-tetrahydrofolate (THF) decarbonylase (Schulz et al., 2020). This strategy improved the RH activity by threefold compared to a strain producing the HoxN permease alone (**Figure 6**). Remarkably, co-expression of *hoxN* and *hypX* genes in aerobically grown cells resulted in RH activities that were above those measured for RH isolated from anaerobically grown cells (**Figure 7**). Here, prolonged cultivation time from 48 h to 72 h significantly improved the specific RH activity, suggesting that the active site formation seems to be clearly dependent

on post-induction time. It is possible that the biosynthesis and incorporation of active site is a slow process, as it requires the involvement of multiple active maturases. This assumption is supported by the linear and continuous increase in specific RH activities with increasing induction time upon induction from 6 h to 72 h. Therefore, prolonging the induction time might serve as a further alternative strategy to maximize the cofactor occupancy in the active center and increase hydrogenase activity.

CONCLUSION

Commercial use of [NiFe]-hydrogenases is limited by the difficulty of producing these biocatalysts in scalable quantities. With some important exceptions, [NiFe]-hydrogenases are usually isolated from their native hosts (Fan et al., 2020). This is due to the fact that these complex metalloenzymes require a sophisticated maturation machinery. With this study we demonstrated that it is possible to produce a non-native [NiFe]-hydrogenase recombinantly in *E. coli* with high yield and a catalytic activity that—most importantly—is equivalent to that of hydrogenase purified from the native host. We purified the O_2-tolerant regulatory hydrogenase from *C. necator* from three *E. coli* derivatives with different genetic backgrounds under various growth conditions. Whereas Bernhard et al. and Caserta et al. obtained approx. 1 U L^{-1} (1.1 mg L^{-1} of RH with an activity of 1 U mg^{-1}) (Bernhard et al., 2001) and 0.4 U L^{-1} (0.1 mg L^{-1}, 4.5 U mg^{-1}) (Caserta et al., 2020), respectively, of purified RH from the native host, *C. necator*, our heterologous production process achieved 120 U L^{-1} (40 mg L^{-1} with 3 U mg^{-1}). This corresponds to an 100–300-fold higher yield of catalytically active RH. The highest yield was obtained from aerobically cultivated of *E. coli*, which significantly shortens the process time compared to the production in *C. necator*. Through strain improvement, i.e., the co-expression of specific maturation genes, and process optimization, we were even able to produce a catalytically active metalloprotein in the metabolically deficient *E. coli* BL21. Through optimally controlled expression of the required genes and optimized production conditions, the combinational strategy developed in this work offers a clear advantage over the native producer. Our strategy provides a useful roadmap for biotechnologically relevant production of [NiFe]-hydrogenases and can be applied in scale-up studies to achieve commercial feasibility of complex, difficult-to-produce metalloenzymes.

DATA AVAILABILITY STATEMENT

The raw data supporting the conclusions of this article will be made available by the authors, without undue reservation.

AUTHOR CONTRIBUTIONS

MG, QF, and OL participated in experimental design and interpretation of the results. QF carried out all molecular biological and biochemical experiments, and prepared the original draft. GC, CL, and IZ performed the spectroscopic IR and EPR measurements and the data evaluation. GC, CL, IZ, PN, and OL analyzed the data with major contributions from QF and MG. MG, PN, and OL revised the manuscript. All authors read and approved the final manuscript.

FUNDING

This work was supported by the Cluster of Excellence "Unifying Systems in Catalysis" (UniSysCat) coordinated by the Technische Universität Berlin and its graduate school, Berlin International Graduate School of Natural Sciences and Engineering (BIG-NSE), funded by the Deutsche Forschungsgemeinschaft (DFG) under Germany's Excellence Strategy (EXC 2008/1-390540038). QF obtained a grant from the China Government Scholarship program, 2017. GC and OL are grateful for EU financial support (Article 38.1.2, GC) within the European Union's Horizon 2020 Research and Innovation Program under grant agreement no 810856.

ACKNOWLEDGMENTS

We would like to appreciate Peter Hildebrandt for use of spectroscopic facilities and Janna Schoknecht for excellent technical assistance in activity measurements. We would also like to acknowledge support by the German Research Foundation and the Open Access Publication Fund of TU Berlin.

SUPPLEMENTARY MATERIAL

The Supplementary Material for this article can be found online at: https://www.frontiersin.org/articles/10.3389/fmicb.2022.894375/full#supplementary-material

REFERENCES

Arlt, C., Nutschan, K., Haase, A., Ihling, C., Tänzler, D., Sinz, A., et al. (2021). Native mass spectrometry identifies the HybG chaperone as carrier of the $Fe(CN)_2CO$ group during maturation of *E. coli* [NiFe]-hydrogenase 2. *Sci. Rep.* 11:24362. doi: 10.1038/s41598-021-03900-w

Ash, P. A., Liu, J., Coutard, N., Heidary, N., Horch, M., Gudim, I., et al. (2015). Electrochemical and infrared spectroscopic studies provide insight into reactions of the NiFe regulatory hydrogenase from *Ralstonia eutropha* with O_2 and CO. *J. Phys. Chem. B* 119, 13807–13815. doi: 10.1021/acs.jpcb.5b04164

Bachmann, B. J. (1972). Pedigrees of some mutant strains of *Escherichia coli* K-12. *Bacteriol. Rev.* 36, 525–557. doi: 10.1128/MMBR.36.4.525-557.1972

Baer, R., Bankier, A. T., Biggin, M. D., Deininger, P. L., Farrell, P. J., Gibson, T. J., et al. (1984). DNA sequence and expression of the B95-8 Epstein-Barr virus genome. *Nature* 310, 207–211. doi: 10.1038/310207a0

Bernhard, M., Buhrke, T., Bleijlevens, B., De Lacey, A. L., Fernandez, V. M., Albracht, S. P. J., et al. (2001). The H_2 sensor of *Ralstonia eutropha*. *J. Biol. Chem.* 276, 15592–15597. doi: 10.1074/jbc.M009802200

Blokesch, M., Albracht, S. P. J., Matzanke, B. F., Drapal, N. M., Jacobi, A., and Böck, A. (2004a). The complex between hydrogenase-maturation proteins HypC and

HypD is an intermediate in the supply of cyanide to the active site iron of [NiFe]-hydrogenases. *J. Mol. Biol.* 344, 155–167. doi: 10.1016/j.jmb.2004.09.040

Blokesch, M., Paschos, A., Bauer, A., Reissmann, S., Drapal, N., and Böck, A. (2004b). Analysis of the transcarbamoylation-dehydration reaction catalyzed by the hydrogenase maturation proteins HypF and HypE. *Eur. J. Biochem.* 271, 3428–3436. doi: 10.1111/j.1432-1033.2004.04280.x

Böck, A., King, P. W., Blokesch, M., and Posewitz, M. C. (2006). Maturation of hydrogenases. *Adv. Microb. Physiol.* 51, 1–71. doi: 10.1016/S0065-2911(06)51001-X

Brantl, S. (1994). The *copR* gene product of plasmid p1P501 acts as a transcriptional repressor at the essential *repR* promoter. *Mol. Microbiol.* 14, 473–483. doi: 10.1111/j.1365-2958.1994.tb02182.x

Braun, V., and Hantke, K. (2011). Recent insights into iron import by bacteria. *Curr. Opin. Chem. Biol.* 15, 328–334. doi: 10.1016/j.cbpa.2011.01.005

Buhrke, T., Bleijlevens, B., Albracht, S. P. J., and Friedrich, B. (2001). Involvement of *hyp* gene products in maturation of the H_2-sensing [NiFe] hydrogenase of *Ralstonia eutropha*. *J. Bacteriol.* 183, 7087–7093. doi: 10.1128/JB.183.24.7087-7093.2001

Buhrke, T., Lenz, O., Krauss, N., and Friedrich, B. (2005a). Oxygen tolerance of the H_2-sensing [NiFe] hydrogenase from *Ralstonia eutropha* H16 is based on limited access of oxygen to the active site. *J. Biol. Chem.* 280, 23791–23796. doi: 10.1074/jbc.M503260200

Buhrke, T., Löscher, S., Lenz, O., Schlodder, E., Zebger, I., Andersen, L. K., et al. (2005b). Reduction of unusual iron-sulfur clusters in the H_2-sensing regulatory NiFe hydrogenase from *Ralstonia eutropha* H16. *J. Biol. Chem.* 280, 19488–19495. doi: 10.1074/jbc.M500601200

Bürstel, I., Hummel, P., Siebert, E., Wisitruangsakul, N., Zebger, I., Friedrich, B., et al. (2011). Probing the origin of the metabolic precursor of the CO ligand in the catalytic center of [NiFe] hydrogenase. *J. Biol. Chem.* 286, 44937–44944. doi: 10.1074/jbc.M111.309351

Bürstel, I., Siebert, E., Frielingsdorf, S., Zebger, I., Friedrich, B., and Lenz, O. (2016). CO synthesized from the central one-carbon pool as source for the iron carbonyl in O_2-tolerant [NiFe]-hydrogenase. *Proc. Natl. Acad. Sci. U.S.A.* 113, 14722–14726. doi: 10.1073/pnas.1614656113

Bürstel, I., Siebert, E., Winter, G., Hummel, P., Zebger, I., Friedrich, B., et al. (2012). A universal scaffold for synthesis of the $Fe(CN)_2(CO)$ moiety of [NiFe] hydrogenase. *J. Biol. Chem.* 287, 38845–38853. doi: 10.1074/jbc.M112.376947

Casadaban, M. J., and Cohen, S. N. (1979). Lactose genes fused to exogenous promoters in one step using a Mu-lac bacteriophage: *in vivo* probe for transcriptional control sequences. *Proc. Natl. Acad. Sci. U.S.A.* 76, 4530–4533. doi: 10.1073/pnas.76.9.4530

Casalot, L., and Rousset, M. (2001). Maturation of the [NiFe] hydrogenases. *Trends Microbiol.* 9, 228–237. doi: 10.1016/S0966-842X(01)02009-1

Caserta, G., Lorent, C., Pelmenschikov, V., Schoknecht, J., Yoda, Y., Hildebrandt, P., et al. (2020). *In vitro* assembly as a tool to investigate catalytic intermediates of [NiFe]-hydrogenase. *ACS Catal.* 10, 13890–13894. doi: 10.1021/acscatal.0c04079

De Lacey, A. L., Fernández, V. M., Rousset, M., and Cammack, R. (2007). Activation and inactivation of hydrogenase function and the catalytic cycle: spectroelectrochemical Studies. *Chem. Rev.* 107, 4304–4330. doi: 10.1021/CR0501947

Eberz, G., Eitinger, T., and Friedrich, B. (1989). Genetic determinants of a nickel-specific transport system are part of the plasmid-encoded hydrogenase gene cluster in *Alcaligenes eutrophus*. *J. Bacteriol.* 171, 1340–1345. doi: 10.1128/jb.171.3.1340-1345.1989

Eitinger, T., and Friedrich, B. (1991). Cloning, nucleotide sequence, and heterologous expression of a high-affinity nickel transport gene from *Alcaligenes eutrophus*. *J. Biol. Chem.* 266, 3222–3227. doi: 10.1016/S0021-9258(18)49977-2

Eitinger, T., and Mandrand-Berthelot, M. A. (2000). Nickel transport systems in microorganisms. *Arch. Microbiol.* 173, 1–9. doi: 10.1007/s002030050001

Fan, Q., Caserta, G., Lorent, C., Lenz, O., Neubauer, P., and Gimpel, M. (2021a). Optimization of culture conditions for oxygen-tolerant regulatory [NiFe]-hydrogenase production from *Ralstonia eutropha* H16 in *Escherichia coli*. *Microorganisms* 9:1195. doi: 10.3390/microorganisms9061195

Fan, Q., Neubauer, P., and Gimpel, M. (2021b). Production of soluble regulatory hydrogenase from *Ralstonia eutropha* in *Escherichia coli* using a fed-batch-based autoinduction system. *Microb. Cell Fact.* 20:201. doi: 10.1186/s12934-021-01690-4

Fan, Q., Neubauer, P., Lenz, O., and Gimpel, M. (2020). Heterologous hydrogenase overproduction systems for biotechnology—An overview. *Int. J. Mol. Sci.* 21:5890. doi: 10.3390/ijms21165890

Fontecilla-Camps, J. C., Volbeda, A., Cavazza, C., and Nicolet, Y. (2007). Structure/function relationships of [NiFe]- and [FeFe]-hydrogenases. *Chem. Rev.* 107, 4273–4303. doi: 10.1021/cr050195z

Forzi, L., and Sawers, R. G. (2007). Maturation of [NiFe]-hydrogenases in *Escherichia coli*. *Biometals* 20, 565–578. doi: 10.1007/s10534-006-9048-5

Fritsch, J., Lenz, O., and Friedrich, B. (2013). Structure, function and biosynthesis of O_2-tolerant hydrogenases. *Nat. Rev. Microbiol.* 11, 106–114. doi: 10.1038/nrmicro2940

Hartmann, S., Frielingsdorf, S., Caserta, G., and Lenz, O. (2020). A membrane-bound [NiFe]-hydrogenase large subunit precursor whose C-terminal extension is not essential for cofactor incorporation but guarantees optimal maturation. *Microbiologyopen* 9, 1197–1206. doi: 10.1002/mbo3.1029

Kaluarachchi, H., Altenstein, M., Sugumar, S. R., Balbach, J., Zamble, D. B., and Haupt, C. (2012). Nickel binding and [NiFe]-hydrogenase maturation by the metallochaperone SlyD with a single metal-binding site in *Escherichia coli*. *J. Mol. Biol.* 417, 28–35. doi: 10.1016/j.jmb.2012.01.037

Kim, H. J., Jeong, H., Hwang, S., Lee, M.-S., Lee, Y.-J., Lee, D.-W., et al. (2014). Short-term differential adaptation to anaerobic stress via genomic mutations by *Escherichia coli* strains K-12 and B lacking alcohol dehydrogenase. *Front. Microbiol.* 5:476. doi: 10.3389/fmicb.2014.00476

Kim, J. Y., Jo, B., and Cha, H. (2010). Production of biohydrogen by recombinant expression of [NiFe]-hydrogenase 1 in *Escherichia coli*. *Microb. Cell Fact.* 9:54. doi: 10.1186/1475-2859-9-54

Kim, J. Y. H., Jo, B. H., and Cha, H. J. (2011). Production of biohydrogen by heterologous expression of oxygen-tolerant *Hydrogenovibrio marinus* [NiFe]-hydrogenase in *Escherichia coli*. *J. Biotechnol.* 155, 312–319. doi: 10.1016/j.jbiotec.2011.07.007

Kleihues, L., Lenz, O., Bernhard, M., Buhrke, T., and Friedrich, B. (2000). The H_2 sensor of *Ralstonia eutropha* is a member of the subclass of regulatory [NiFe] hydrogenases. *J. Bacteriol.* 182, 2716–2724. doi: 10.1128/JB.182.10.2716-2724.2000

Kosman, D. J. (2013). Iron metabolism in aerobes: managing ferric iron hydrolysis and ferrous iron autoxidation. *Coord. Chem. Rev.* 257, 210–217. doi: 10.1016/j.ccr.2012.06.030

Lacasse, M. J., and Zamble, D. B. (2016). [NiFe]-hydrogenase maturation. *Biochemistry* 55, 1689–1701. doi: 10.1021/acs.biochem.5b01328

Lau, C. K. Y., Krewulak, K. D., and Vogel, H. J. (2016). Bacterial ferrous iron transport: the Feo system. *FEMS Microbiol. Rev.* 40, 273–298. doi: 10.1093/femsre/fuv049

Lauterbach, L., and Lenz, O. (2013). Catalytic production of hydrogen peroxide and water by oxygen-tolerant [NiFe]-hydrogenase during H_2 cycling in the presence of O_2. *J. Am. Chem. Soc.* 135, 17897–17905. doi: 10.1021/ja408420d

Leach, M. R., Zhang, J. W., and Zamble, D. B. (2007). The role of complex formation between the *Escherichia coli* hydrogenase accessory factors HypB and SlyD. *J. Biol. Chem.* 282, 16177–16186. doi: 10.1074/jbc.M610834200

Lenz, O., Lauterbach, L., and Frielingsdorf, S. (2018). O_2-tolerant [NiFe]-hydrogenases of *Ralstonia eutropha* H16: Physiology, molecular biology, purification, and biochemical analysis. *Methods Enzymol.* 613, 117–151. doi: 10.1016/bs.mie.2018.10.008

Lenz, O., Lauterbach, L., Frielingsdorf, S., and Friedrich, B. (2015). "Oxygen-tolerant hydrogenases and their biotechnological potential," in *Biohydrogen*, ed. M. Rögner (Berlin: De Gruyter), 61–96. doi: 10.1515/9783110336733.61

Lenz, O., Ludwig, M., Schubert, T., Bürstel, I., Ganskow, S., Goris, T., et al. (2010). H_2 conversion in the presence of O_2 as performed by the membrane-bound [NiFe]-hydrogenase of *Ralstonia eutropha*. *ChemPhysChem* 11, 1107–1119. doi: 10.1002/cphc.200901002

Lenz, O., Strack, A., Tran-Betcke, A., and Friedrich, B. (1997). A hydrogen-sensing system in transcriptional regulation of hydrogenase gene expression in Alcaligenes species. *J. Bacteriol.* 179, 1655–1663. doi: 10.1128/JB.179.5.1655-1663.1997

Lenz, O., Zebger, I., Hamann, J., Hildebrandt, P., and Friedrich, B. (2007). Carbamoylphosphate serves as the source of CN^-, but not of the intrinsic CO

in the active site of the regulatory [NiFe]-hydrogenase from *Ralstonia eutropha*. *FEBS Lett.* 581, 3322–3326. doi: 10.1016/j.febslet.2007.06.027

Lubitz, W., Ogata, H., Ru, O., and Reijerse, E. (2014). Hydrogenases. *Chem. Rev.* 114, 4081–4148. doi: 10.1021/cr4005814

Lutz, S., Jacobi, A., Schlensog, V., Böhm, R., Sawers, G., and Böck, A. (1991). Molecular characterization of an operon (*hyp*) necessary for the activity of the three hydrogenase isoenzymes in *Escherichia coli*. *Mol. Microbiol.* 5, 123–135. doi: 10.1111/j.1365-2958.1991.tb01833.x

Messenger, S. L., and Green, J. (2003). FNR-mediated regulation of *hyp* expression in *Escherichia coli*. *FEMS Microbiol. Lett.* 228, 81–86. doi: 10.1016/S0378-1097(03)00726-2

Ogata, H., Lubitz, W., and Higuchi, Y. (2016). Structure and function of [NiFe] hydrogenases. *J. Biochem.* 160, 251–258. doi: 10.1093/jb/mvw048

Paschos, A., Bauer, A., Zimmermann, A., Zehelein, E., and Böck, A. (2002). HypF, a carbamoyl phosphate-converting enzyme involved in [NiFe] hydrogenase maturation. *J. Biol. Chem.* 277, 49945–49951. doi: 10.1074/jbc.M204601200

Peters, J. W., Schut, G. J., Boyd, E. S., Mulder, D. W., Shepard, E. M., Broderick, J. B., et al. (2015). [FeFe]- and [NiFe]-hydrogenase diversity, mechanism, and maturation. *Biochim. Biophys. Acta Mol. Cell Res.* 1853, 1350–1369. doi: 10.1016/j.bbamcr.2014.11.021

Pierik, A. J., Schmelz, M., Lenz, O., Friedrich, B., and Albracht, S. P. J. (1998). Characterization of the active site of a hydrogen sensor from *Alcaligenes eutrophus*. *FEBS Lett.* 438, 231–235. doi: 10.1016/S0014-5793(98)01306-4

Pinske, C., Bönn, M., Krüger, S., Lindenstrauß, U., and Sawers, R. G. (2011). Metabolic deficiences revealed in the biotechnologically important model bacterium *Escherichia coli* BL21(DE3). *PLoS One* 6:e22830. doi: 10.1371/journal.pone.0022830

Pinske, C., Sargent, F., and Sawers, R. G. (2015). SlyD-dependent nickel delivery limits maturation of [NiFe]-hydrogenases in late-stationary phase *Escherichia coli* cells. *Metallomics* 7, 683–690. doi: 10.1039/c5mt00019j

Pinske, C., Thomas, C., Nutschan, K., and Sawers, R. G. (2019). Delimiting the function of the C-terminal extension of the *Escherichia coli* [NiFe]-hydrogenase 2 large subunit precursor. *Front. Microbiol.* 10:2223. doi: 10.3389/fmicb.2019.02223

Rangarajan, E. S., Asinas, A., Proteau, A., Munger, C., Baardsnes, J., Iannuzzi, P., et al. (2008). Structure of [NiFe] hydrogenase maturation protein HypE from *Escherichia coli* and its interaction with HypF. *J. Bacteriol.* 190, 1447–1458. doi: 10.1128/JB.01610-07

Rathnayake, I., Megharaj, M., Krishnamurti, G., Bolan, N., and Naidu, R. (2013). Heavy metal toxicity to bacteria–Are the existing growth media accurate enough to determine heavy metal toxicity? *Chemosphere* 90, 1195–1200. doi: 10.1016/j.chemosphere.2012.09.036

Reissmann, S., Hochleitner, E., Wang, H., Paschos, A., Lottspeich, F., Glass, R. S., et al. (2003). Taming of a poison: biosynthesis of the NiFe-hydrogenase cyanide ligands. *Science* 299, 1067–1070. doi: 10.1126/science.1080972

Roncaroli, F., Bill, E., Friedrich, B., Lenz, O., Lubitz, W., and Pandelia, M.-E. (2015). Cofactor composition and function of a H_2-sensing regulatory hydrogenase as revealed by Mössbauer and EPR spectroscopy. *Chem. Sci.* 6, 4495–4507. doi: 10.1039/c5sc01560j

Roseboom, W., Blokesch, M., Böck, A., and Albracht, S. P. J. (2005). The biosynthetic routes for carbon monoxide and cyanide in the Ni-Fe active site of hydrogenases are different. *FEBS Lett.* 579, 469–472. doi: 10.1016/j.febslet.2004.12.013

Schollmeyer, J. (2020). *Bioprocess Development for the Production of a S-methyl-5′-thio-Adenosine Phosphorylase in Escherichia coli*. Master thesis. Berlin: TU Berlin.

Schulz, A. C., Frielingsdorf, S., Pommerening, P., Lauterbach, L., Bistoni, G., Neese, F., et al. (2020). Formyltetrahydrofolate decarbonylase synthesizes the active site CO ligand of O_2-tolerant [NiFe] hydrogenase. *J. Am. Chem. Soc.* 142, 1457–1464. doi: 10.1021/jacs.9b11506

Schwartz, E., Fritsch, J., and Friedrich, B. (2013). "H_2-metabolizing prokaryotes," in *The Prokaryotes: Prokaryotic Physiology and Biochemistry*, eds E. Rosenberg, E. F. DeLong, S. Lory, E. Stackebrandt, F. Thomson (Heidelberg, Berlin: Springer), 119–199. doi: 10.1007/978-3-642-30141-4_65

Senger, M., Stripp, S. T., and Soboh, B. (2017). Proteolytic cleavage orchestrates cofactor insertion and protein assembly in [NiFe]-hydrogenase biosynthesis. *J. Biol. Chem.* 292, 11670–11681. doi: 10.1074/jbc.M117.788125

Soboh, B., Stripp, S. T., Bielak, C., Lindenstrauß, U., Braussemann, M., Javaid, M., et al. (2013). The [NiFe]-hydrogenase accessory chaperones HypC and HybG of *Escherichia coli* are iron- and carbon dioxide-binding proteins. *FEBS Lett.* 587, 2512–2516. doi: 10.1016/j.febslet.2013.06.055

Soini, J., Ukkonen, K., and Neubauer, P. (2008). "High cell density media for *Escherichia coli* are generally designed for aerobic cultivations - consequences for large-scale bioprocesses and shake flask cultures. *Microb. Cell Fact.* 7:26. doi: 10.1186/1475-2859-7-26

Vignais, P. M., and Billoud, B. (2007). Occurrence, classification, and biological function of hydrogenases: an overview. *Chem. Rev.* 107, 4206–4272. doi: 10.1021/cr050196r

Watanabe, S., Matsumi, R., Atomi, H., Imanaka, T., and Miki, K. (2012). Crystal structures of the HypCD complex and the HypCDE ternary complex: transient intermediate complexes during [NiFe] hydrogenase maturation. *Structure* 20, 2124–2137. doi: 10.1016/j.str.2012.09.018

Waugh, R., and Boxer, D. H. (1986). Pleiotropic hydrogenase mutants of *Escherichia coli* K12: growth in the presence of nickel can restore hydrogenase activity. *Biochimie* 68, 157–166. doi: 10.1016/S0300-9084(86)81080-X

Wolf, I., Buhrke, T., Dernedde, J., Pohlmann, A., and Friedrich, B. (1998). Duplication of *hyp* genes involved in maturation of [NiFe] hydrogenases in *Alcaligenes eutrophus* H16. *Arch. Microbiol.* 170, 451–459. doi: 10.1007/s002030050666

Wolfram, L., Friedrich, B., and Eitinger, T. (1995). The *Alcaligenes eutrophus* protein HoxN mediates nickel transport in *Escherichia coli*. *J. Bacteriol.* 177, 1840–1843. doi: 10.1128/JB.177.7.1840-1843.1995

Wu, L. -F., Mandrand-Berthelot, M. -A., Waugh, R., Edmonds, C. J., Holt, S. E., and Boxer, D. H. (1989). Nickel deficiency gives rise to the defective hydrogenase phenotype of *hydc* and *fnr* mutants in *Escherichia coli*. *Mol. Microbiol.* 3, 1709–1718. doi: 10.1111/j.1365-2958.1989.tb00156.x

Conflict of Interest: PN is a shareholder of EnPresso GmbH.

The remaining authors declare that the research was conducted in the absence of any commercial or financial relationships that could be construed as a potential conflict of interest.

Publisher's Note: All claims expressed in this article are solely those of the authors and do not necessarily represent those of their affiliated organizations, or those of the publisher, the editors and the reviewers. Any product that may be evaluated in this article, or claim that may be made by its manufacturer, is not guaranteed or endorsed by the publisher.

frontiers | Frontiers in Microbiology

ORIGINAL RESEARCH
published: 12 May 2022
doi: 10.3389/fmicb.2022.897066

Reversible Hydrogenase Activity Confers Flexibility to Balance Intracellular Redox in *Moorella thermoacetica*

*Shunsuke Kobayashi[1†], Junya Kato[1†], Keisuke Wada[2], Kaisei Takemura[1], Setsu Kato[1], Tatsuya Fujii[3], Yuki Iwasaki[3], Yoshiteru Aoi[1], Tomotake Morita[2], Akinori Matsushika[1,3], Katsuji Murakami[3] and Yutaka Nakashimada[1]**

[1]Graduate School of Integrated Sciences for Life, Hiroshima University, Higashihiroshima, Japan, [2]National Institute of Advanced Industrial Science and Technology (AIST), Tsukuba, Japan, [3]National Institute of Advanced Industrial Science and Technology (AIST), Higashihiroshima, Japan

OPEN ACCESS

Edited by:
Constanze Pinske, Martin Luther University of Halle-Wittenberg, Germany

Reviewed by:
Gary Sawers, Martin Luther University of Halle-Wittenberg, Germany
Wolfgang Buckel, University of Marburg, Germany

***Correspondence:**
Yutaka Nakashimada
nyutaka@hiroshima-u.ac.jp

[†]These authors have contributed equally to this work and share first authorship

Specialty section:
This article was submitted to Microbial Physiology and Metabolism, a section of the journal Frontiers in Microbiology

Received: *15 March 2022*
Accepted: *19 April 2022*
Published: *12 May 2022*

Citation:
Kobayashi S, Kato J, Wada K, Takemura K, Kato S, Fujii T, Iwasaki Y, Aoi Y, Morita T, Matsushika A, Murakami K and Nakashimada Y (2022) Reversible Hydrogenase Activity Confers Flexibility to Balance Intracellular Redox in Moorella thermoacetica. Front. Microbiol. 13:897066. doi: 10.3389/fmicb.2022.897066

Hydrogen (H_2) converted to reducing equivalents is used by acetogens to fix and metabolize carbon dioxide (CO_2) to acetate. The utilization of H_2 enables not only autotrophic growth, but also mixotrophic metabolism in acetogens, enhancing carbon utilization. This feature seems useful, especially when the carbon utilization efficiency of organic carbon sources is lowered by metabolic engineering to produce reduced chemicals, such as ethanol. The potential advantage was tested using engineered strains of *Moorella thermoacetica* that produce ethanol. By adding H_2 to the fructose-supplied culture, the engineered strains produced increased levels of acetate, and a slight increase in ethanol was observed. The utilization of a knockout strain of the major acetate production pathway, aimed at increasing the carbon flux to ethanol, was unexpectedly hindered by H_2-mediated growth inhibition in a dose-dependent manner. Metabolomic analysis showed a significant increase in intracellular NADH levels due to H_2 in the ethanol-producing strain. Higher NADH level was shown to be the cause of growth inhibition because the decrease in NADH level by dimethyl sulfoxide (DMSO) reduction recovered the growth. When H_2 was not supplemented, the intracellular NADH level was balanced by the reversible electron transfer from NADH oxidation to H_2 production in the ethanol-producing strain. Therefore, reversible hydrogenase activity confers the ability and flexibility to balance the intracellular redox state of *M. thermoacetica*. Tuning of the redox balance is required in order to benefit from H_2-supplemented mixotrophy, which was confirmed by engineering to produce acetone.

Keywords: acetogen, metabolic engineering, ethanol production, hydrogen inhibition, hydrogen production, redox balance, mixotrophy

INTRODUCTION

There is a growing interest in chemical production derived from sources other than fossil fuels. Due to increasing levels of carbon dioxide (CO_2) in the atmosphere, low-carbon emissions are required to eliminate environmental threats, such as global warming. Technology to capture and utilize CO_2 as a resource is in progress worldwide, and bioprocessing of renewable feedstocks

is one promising candidate. However, economic cost is a bottleneck in bioprocessing applications of bulk chemicals. A means to reduce the cost is to maximize carbon conversion of feedstock to the product.

Acetogens are a group of microorganisms capable of autotrophic growth on CO_2 and hydrogen (H_2) and are thus promising chassis for utilizing CO_2 by bioprocesses (Ljungdhal, 1986; Wood, 1991; Drake, 1994; Drake et al., 2008). The main product is acetate, but some acetogens produce other valuable chemicals, such as ethanol. These by-products can be utilized for industrial production from waste materials, such as off-gas from steel mills. This process, called gas fermentation, has attracted worldwide attention (Bengelsdorf et al., 2016; Liew et al., 2016; Bengelsdorf and Dürre, 2017; Teixeira et al., 2018; Omar et al., 2019; Jin et al., 2020; Kopke and Simpson, 2020; Bourgade et al., 2021; Fackler et al., 2021). On the other hand, acetogens are also capable of heterotrophic growth on various carbohydrate substrates and are good candidates for bioconversion of biomass to useful chemicals. Utilization of acetogens is especially effective for carbon utilization because processing by acetogens emits much less CO_2 due to the nature of their CO_2 fixation pathway. When acetogens metabolize hexose to acetate, two molecules of CO_2 are produced, then reassimilated into the CO_2 fixation pathway by utilizing reducing equivalents from glycolysis. Therefore, acetogens can theoretically convert one hexose molecule to three acetate molecules (Fontaine et al., 1942; Schuchmann and Müller, 2014, 2016).

Autotrophic and heterotrophic metabolism can be combined for mixotrophic growth, which enables the enhancement of carbon utilization and conversion of extra CO_2 using H_2 as the source of reducing power (Fast et al., 2015; Maru et al., 2018). Mixotrophy is a general trait of acetogens and is effective in fermentation, especially for products that are more reduced than acetate. A previous report succeeded in increasing overall metabolite yields by supplying H_2 to sugar-based cultures of *Clostridium ljungdahlii* (Jones et al., 2016). In this case, a shift in the metabolite profile was observed by providing H_2, with ethanol as the primary metabolite, over less-reduced products. H_2 supply for the industrial applications of mixotrophic fermentation would be supported by the development of technology to provide CO_2-free H_2 using renewable energy-based approaches, such as water splitting, biomass gasification, and ammonia reforming (Hosseini and Wahid, 2016; Aryal et al., 2018). Thus, together with this technology development to provide H_2, mixotrophic fermentation would contribute to the low-carbon emitting and economically feasible bioprocesses.

In addition to natural by-products, acetogens can also be engineered to produce chemicals other than acetate. Genetic engineering of acetogens is challenging because of their genetic barrier, such as restriction–modification systems and physical barriers by gram-positive cell walls; however, development of engineering tools has substantially improved the efficiency of engineering acetogens (Minton et al., 2016; Jin et al., 2020; Bourgade et al., 2021). It is also possible to apply metabolic engineering for pathway optimization to enhance the production of target metabolites. Metabolic engineering has begun to highlight the potential of acetogens for chemical production from CO_2.

Moorella thermoacetica is a thermophilic acetogen (Drake and Daniel, 2004; Pierce et al., 2008). Due to its thermophilic nature, *M. thermoacetica* can be used to establish an advantageous bioprocess for the recovery of products, especially volatile chemicals (Taylor et al., 2009; Abdel-Banat et al., 2010; Basen and Müller, 2017; Redl et al., 2017). However, *M. thermoacetica* is categorized as a homoacetogen that produces acetate exclusively. Therefore, the metabolic pathway must be modified to produce other chemicals for industrial applications (Iwasaki et al., 2013, 2017; Kita et al., 2013). We previously succeeded in engineering *M. thermoacetica* to produce ethanol and acetone from sugars and syngas, as well as to enhance yields, by adjusting the carbon flux (Rahayu et al., 2017; Kato et al., 2021; Takemura et al., 2021a). Disruption of the major acetate production pathway enables near-exclusive ethanol production from sugars.

In this study, we attempted to apply H_2-supplemented mixotrophy to enhance ethanol yield. Unexpectedly, we found that H_2 supplementation inhibited the growth of a high-ethanol-producing strain. Metabolomic analysis revealed that the engineered strain balanced the intracellular redox status by producing H_2 to oxidize NADH during heterotrophic growth. Reversible hydrogenase activity, which oxidizes H_2 in the wild-type strain under standard conditions, plays a vital role in the redox maintenance of metabolically engineered strains. It is necessary to avoid this reverse reaction to fulfill H_2-supplemented-mixotrophic bioproduction.

MATERIALS AND METHODS

Bacterial Strains and Growth Conditions

Moorella thermoacetica ATCC 39073 and its derivatives were used in this study (**Table 1**). Modified ATCC1754 PETC medium comprising 1.0 g of NH_4Cl, 0.1 g of KCl, 0.2 g of $MgSO_4{\cdot}7H_2O$, 0.8 g of NaCl, 0.1 g of KH_2PO_4, 0.02 g of $CaCl_2{\cdot}2H_2O$, 2.0 g of $NaHCO_3$, 10 ml of trace elements, 10 ml of Wolfe's vitamin solution (Tanner, 1989), and 1.0 mg of resazurin/L of deionized water was used as the basal medium (Tanner et al., 1993). The pH of the solution was adjusted to 6.9. The medium was prepared anaerobically by boiling and cooling under an N_2–CO_2 (80:20) mixed-gas atmosphere. After cooling, the medium was dispensed into 125 ml glass culture vials (serum bottles) under an N_2–CO_2 mixed-gas atmosphere. The vials were crimp-sealed and autoclaved.

Before starting the culture, fructose, yeast extract, and L-cysteine·HCl·H_2O were added to reach final concentrations of 2.0, 1.0, and 1.2 g/l, respectively. The final volume was adjusted to 50 ml with water. To provide H_2, the headspace pressure in the vials was adjusted to 0.12 MPa by using N_2–CO_2

TABLE 1 | Strains used in this study.

Strain name	Relevant characteristics	References
Wild type	ATCC 39073	ATCC
Mt-*aldh*	*pyrF*::*aldh*	Rahayu et al., 2017
Mt-Δ*pduL2*::*aldh*	Δ*pduL2*::*aldh*	Rahayu et al., 2017
Mt-Δ*pduL1*Δ*pduL2*::*aldh*	Δ*pduL1* Δ*pduL2*::*aldh*	Rahayu et al., 2017
pduL2::acetone	Δ*pduL2*::*ctfAB-thl-adc*	Kato et al., 2021

(80:20) mixed-gas. H_2 gas was then injected at the desired pressure. For example, when 0.01 MPa of H_2 was tested, the total pressure was adjusted to 0.13 MPa by the H_2 gas injection. Cells were grown at 55°C with shaking at 180 rpm.

Analytical Methods

We sampled and analyzed 1 ml of the culture medium at each time point and calculated the dry cell weight using the optical density (OD) at 600 nm [OD_{600}; 1 g (dry cell weight)/L = 0.383 OD_{600}; Iwasaki et al., 2017]. The culture supernatant was analyzed for the amount of fructose, formate, acetate, ethanol, and acetone using high-performance liquid chromatography (HPLC; LC-2000 Plus HPLC; Jasco, Tokyo, Japan) equipped with a refractive index detector (RI-2031 Plus; Jasco), Shodex RSpak KC-811 column (Showa Denko, Kanagawa, Japan), and Shodex RSpak KC-G guard column (Showa Denko) at 60°C. Ultrapure water containing 0.1% (v/v) phosphoric acid was used as the mobile phase at a flow rate of 0.7 ml/min, and crotonate was used as the internal standard (Miura et al., 2014). The gas composition in the headspace of the culture vials was analyzed using GC-8A gas chromatograph (Shimadzu, Kyoto, Japan) equipped with a thermal conductivity detector and a stainless steel column packed with activated carbon at 70°C. Argon was used as the carrier gas (Miura et al., 2014). The total gas pressure in the headspace was measured using a differential pressure gauge (DMC-104 N11; Okano Works, Tokyo, Japan).

Metabolome Analysis

Strains were grown to reach the exponential phase between 0.5 and 0.7 OD_{600}. The culture was immediately filtered to collect cells equivalent to a total count of 20 OD_{600} (volume [mL] × OD_{600} ≈ 20). Filtration was performed using hydrophilic PTFE, 1 μm pore size, and a 90-mm-diameter filter disk (Omnipore; Merck KGaA, Darmstadt, Germany). Harvested cells were immediately immersed in pre-chilled methanol containing 100 μM ribitol and 100 μM (+)-10-camphorsulfonate to quench the metabolic activity. This procedure was quickly performed, within 45 s after opening culture vials, to avoid metabolites from artifacts, such as those caused by oxygenation, degradation, and other modifications. Subsequently, intracellular metabolites were extracted using the chloroform–water–methanol method (Bolten et al., 2007). The supernatant was then concentrated using a centrifugal concentrator (CC-105; Tomy, Tokyo, Japan). According to a previous study, pre-treatment and analysis of the dried samples were performed (Wada et al., 2022).

RESULTS

H_2 Supplementation Increases Carbon Utilization in Mixotrophic Growth by Producing Acetate, Not Ethanol, in Engineered Strains

Moorella thermoacetica can convert one hexose molecule to three acetate molecules in theory (**Figure 1A**; Fontaine et al., 1942; Schuchmann and Müller, 2014, 2016). The engineered strains were designed to produce ethanol from acetyl-CoA in two steps (reducing reactions; Rahayu et al., 2017; **Table 1**). The reducing equivalents provided by glycolysis were assumed to be properly consumed (**Figures 1A,B**). In a model, the Ech complex, HydABC complex, and NfnAB complex would convert the reducing equivalents to NADH and NADPH. These NADH and NADPH would be consumed by the Wood–Ljungdahl pathway to convert CO_2 to acetate in the wild-type strain, whereas reduction of acetyl-CoA would consume the NADH and NADPH in the ethanol-producing strains. Therefore, the redox conditions in the engineered strains producing ethanol should be balanced. In fact, we previously observed that all engineered strains (**Table 1**) grew and produced ethanol on hexose sugars. However, one molecule of CO_2 is released to produce one molecule of ethanol because of the requirement for extra reducing equivalents (approximately 33% of the carbon is released from hexose sugars in theory). Therefore we supplied H_2 to increase carbon utilization by mixotrophy.

We used a culture containing fructose as the carbohydrate substrate. H_2 was added to the headspace of the culture vial at a partial pressure of 0.08 MPa (equivalent to 40% of the gas phase). The gas phase also contained CO_2, and therefore extra CO_2 could be incorporated in addition to the released CO_2. Of the injected gas, CO_2 was 12% of the total, and the medium contained $NaHCO_3$ to supply CO_2. First, we tested the effect of H_2 on the wild-type strain. Acetate was produced as the end product and the carbon molar yield improved from 0.74 to 0.82, as expected (**Figures 2A,B**). The optical density increased similarly while fructose was consumed, and decreased after the complete consumption of fructose in both conditions, indicating no significant effect on the growth (**Figure 2C**). We then tested an ethanol-producing strain, Mt-*aldh*, in which the *aldh* gene encoding aldehyde dehydrogenase was expressed by a constitutive promoter. The main product was acetate, accompanied by a small amount of ethanol. This trend was similar in the H_2-supplied culture, and yield improvement was only observed for acetate production from 0.78 to 0.88 (**Figure 2A**). The change in ethanol production was not significant (0.02 and 0.03; **Figure 2B**). No significant effect on the growth was observed (**Figure 2D**). Although we expected to enhance the yield of reduced products, we reasoned that the abundant activity of the acetate production pathway in the Mt-*aldh* strain decreased the effect of H_2. We then tested another ethanol-producing strain, Mt-Δ*pduL2*::*aldh*, which showed less acetate production due to deletion of one of the two genes (*pduL2*) encoding phosphoacetyl transferase in the acetate production pathway. Despite the dominant production of ethanol over acetate, product yield enhancement was observed with only acetate from 0.19 to 0.25 (**Figures 2A,B**). The carbon molar yield for ethanol did not change (0.37). The rest was released as CO_2. The strain grew similarly in both conditions (**Figure 2E**). The effect of H_2 was in contrast to the results of a previous study, in which the supplementation of reducing power with H_2 was reflected in the production of more-reduced chemicals (Jones et al., 2016).

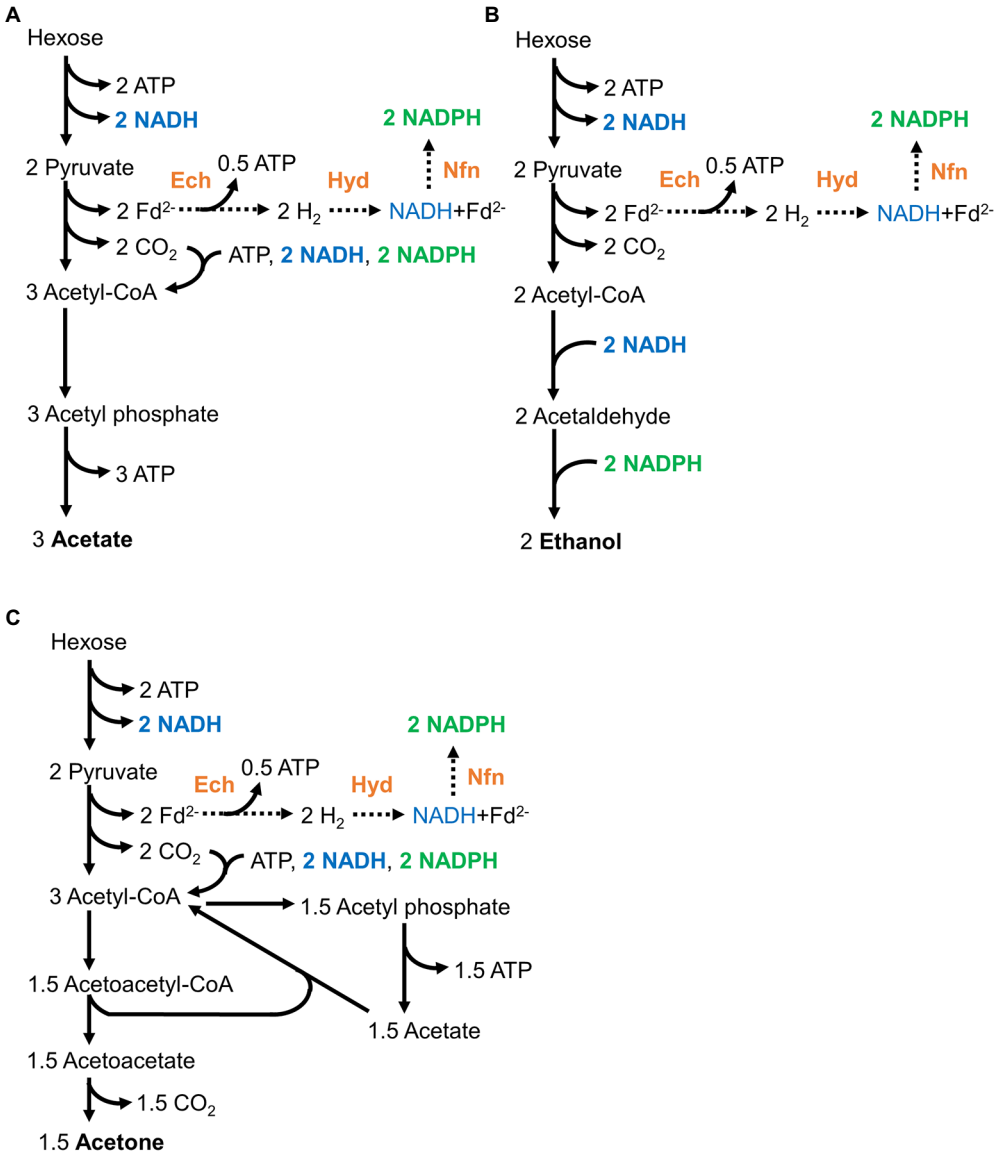

FIGURE 1 | Redox-balanced pathways for acetogenesis **(A)**, ethanol production **(B)**, and acetone production **(C)** from hexose in wild-type and engineered strains for ethanol production. NADH (shown in blue) and the reduced forms of ferredoxin are produced during glycolysis and the conversion of pyruvate to acetyl-CoA. The reduced ferredoxin is converted to NADPH (shown in green) *via* hydrogenases and electron-bifurcating enzymes, that is, the Ech complex, HydABC, and NfnAB complexes (shown in orange).

H_2 Supplementation Causes Growth Inhibition of the Engineered Strain, Which Exclusively Produces Ethanol

We tested the Mt-Δ*pduL1*Δ*pduL2*::*aldh* strain, which produces almost exclusively ethanol, because of the complete knockout of both two genes (*pduL1* and *pduL2*) encoding phosphoacetyl transferase. In this case, we observed an enhancement in the ethanol yield. The carbon molar yield for ethanol was increased from 0.47 to 0.54 (**Figure 2B**). Approximately 50% of the carbon from fructose was released as CO_2 in the absence of H_2, and H_2 supplementation supported capture and conversion of CO_2. However, the supplemented fructose was not completely consumed in the H_2-supplied condition after 60 h of cultivation, whereas the same strain in the H_2-unsupplied condition, or the other strains in both conditions, consumed fructose completely (**Figures 2C–F**). Only 40.2% of the supplemented fructose was consumed in the H_2-supplied condition, and the growth was significantly reduced in a correlated manner (**Figure 2F**). The volumetric amount of ethanol was also significantly less in the H_2-supplied condition, showing only 45.5% against the no-H_2 condition (17.6 mM in the absence of H_2 and 8.0 mM in the presence of H_2), reflecting the amount of consumed fructose. Therefore, although the Mt-Δ*pduL1*Δ*pduL2*::*aldh* strain showed increased carbon molar

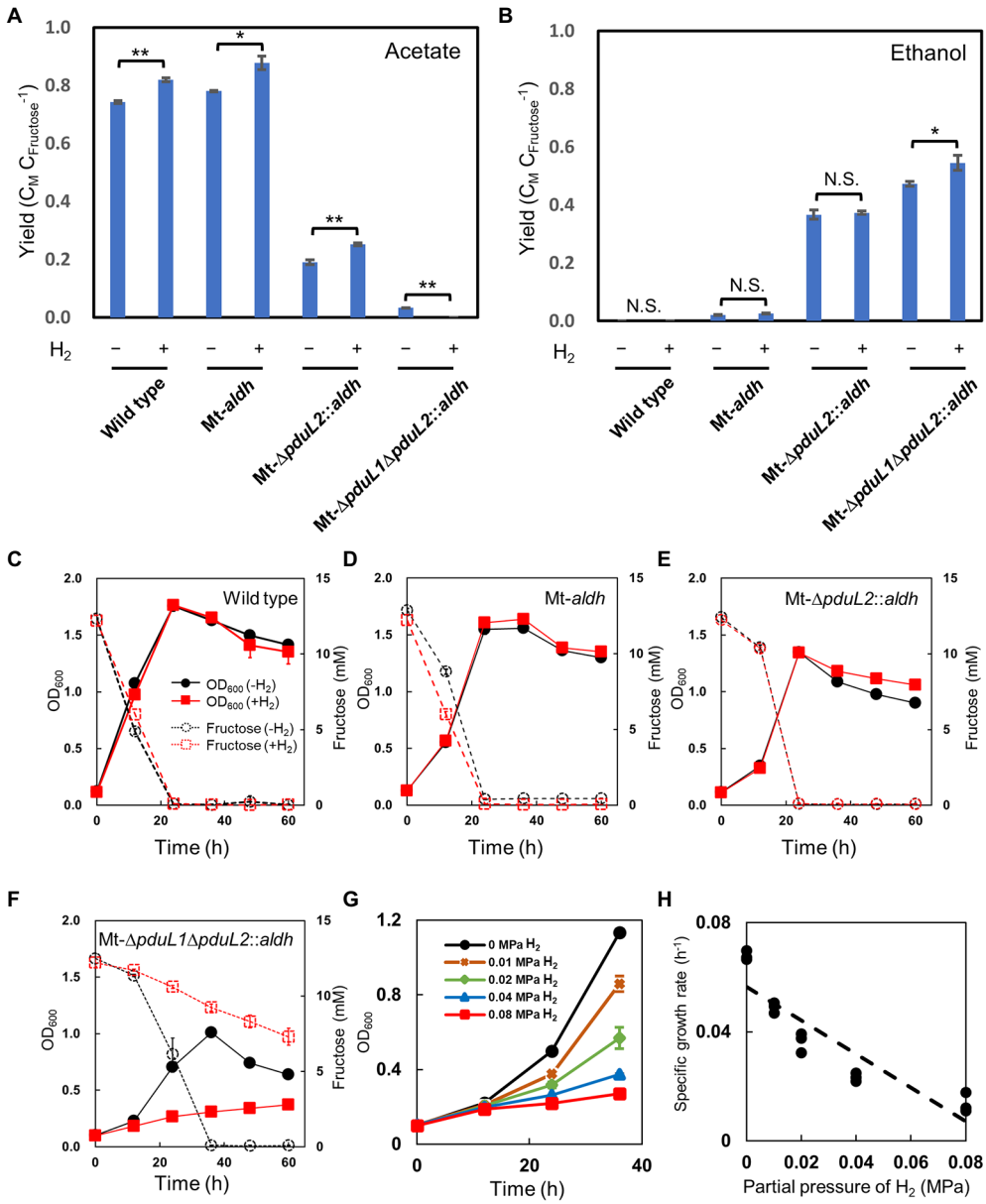

FIGURE 2 | Effect of H_2 supplementation on the wild-type strain and the engineered strains for ethanol production in mixotrophic conditions. **(A,B)** Product profiles shown as carbon molar yields (C_M $C_{Fructose}^{-1}$; $C_{Metabolite}$ $C_{Fructose}^{-1}$). Fructose was used as the carbohydrate substrate. The amount of acetate and ethanol production was compared with and without supplementation of H_2 (0.08 MPa partial pressure, 40% in the headspace) after 60 h when all the supplied fructose was consumed in the no H_2-supplied condition. *t*-test was performed to evaluate the significance. N.S., not significant; value of *p<0.05; value of **p<0.01. **(C-F)** Profiles for cell growth and fructose consumption. The culture was same as in **(A,B)**. Cell density was shown as OD_{600} (optical density at 600 nm) by solid lines. Fructose concentration was shown by dotted lines. Black, no H_2-supplied condition; red, H_2-supplied condition. **(G)** Growth profiles of the Mt-Δ*pduL1*Δ*pduL2*::*aldh* strain with various H_2 partial pressures. The profiles of the exponential phase were compared. The standard deviation (SD) of three biological replicates is shown by error bars. Some error bars are smaller than the symbols. **(H)** Specific growth rate plotted against H_2 partial pressure. All data shown were obtained in the culture for **(G)**.

yield for ethanol under H_2-supplemented mixotrophic conditions, growth inhibition emerged as an unexpected bottleneck.

We also tested the addition of different amounts of H_2 to the Mt-Δ*pduL1*Δ*pduL2*::*aldh* strain. In addition to the condition of partial pressure 0.08 MPa, we tested 0.04, 0.02, and 0.01 MPa, because the pressure of H_2 is correlated with dissolved H_2 in the culture medium. All cases with H_2 at any concentration showed growth inhibition effects. Interestingly, the effect of growth inhibition was dose-dependent, showing more potent inhibition by a higher concentration of H_2 in the culture medium, rather than by a certain threshold.

This tendency was clear when the growth rate was plotted against the H_2 pressure, showing a linear correlation (**Figure 2H**).

Metabolome Analysis Identifies Specific and Significant Enhancement of Intracellular NADH Level by H_2 Supplementation in the Ethanol-Producing Strain

To investigate the H_2-dependent growth inhibition mechanism of the ethanol-producing strain, we assessed intracellular metabolism by metabolome analysis. We used H_2 at 0.02 MPa, because a high dose of H_2 (such as 0.08 MPa) inhibited the growth almost completely, and hence might have significant effects on multiple metabolic pathways. We sampled the cells from the exponential phase and analyzed intracellular metabolites using GC–MS and LC–MS following the sample preparation method we developed. We succeeded in quantifying 19 intracellular metabolites, including seven cofactors (**Figures 3A,B**).

We then compared the Mt-Δ*pduL1*Δ*pduL2*::*aldh* strain and the wild-type strain, with or without H_2 supplementation. Among all analyzed metabolites, NADH levels were striking in the Mt-Δ*pduL1*Δ*pduL2*::*aldh* strain under H_2-supplied conditions. The NADH level increased by approximately four times compared to that in the no H_2 condition, whereas H_2 supplementation did not affect the NADH level in the wild-type strain. There was no such significant difference specific to H_2 supplementation in the other metabolites in the Mt-Δ*pduL1*Δ*pduL2*::*aldh* strain or metabolites in the wild-type strain (**Figure 3B**).

When the overall metabolite profiles were compared in the Mt-Δ*pduL1*Δ*pduL2*::*aldh* and wild-type strains in the no H_2 condition, the levels of glucose-6-phosphate, fructose-6-phosphate, fructose-1,6-bisphosphate, 3-phosphoglyceric acid, glutamate, and ATP were lower, and the levels of acetyl-CoA, AMP, and NADPH were higher in the Mt-Δ*pduL1*Δ*pduL2*::*aldh* strain. The ATP level was lowered in the Mt-Δ*pduL1*Δ*pduL2*::*aldh* due to the knockout of acetate production coupled with substrate-level phosphorylation, but the ATP level was enough to maintain the growth (**Figure 2F**). In contrast, the AMP level was higher in the Mt-Δ*pduL1*Δ*pduL2*::*aldh*, and this may be related with the change of ATP level. The higher level of acetyl-CoA probably reflects a difference of conversion rate of acetyl-CoA to ethanol and acetate. The higher level of NADPH in the Mt-Δ*pduL1*Δ*pduL2*::*aldh* strain suggests that the redox balance in this strain was altered by metabolic engineering. Metabolome analysis indicated that the Mt-Δ*pduL1*Δ*pduL2*::*aldh* strain suffered redox imbalances due to both metabolic engineering and H_2 supplementation.

Hydrogen Production by the Ethanol-Producing Strain

Metabolomic analysis suggested a strong relationship between growth inhibition by H_2 and increased levels of intracellular NADH. In *M. thermoacetica*, NAD^+ is reduced to NADH by the electron-bifurcating hydrogenase HydABC complex (Wang et al., 2013). The HydABC complex reduces NAD^+ and ferredoxin using electrons from H_2. This reaction is reversible and produces H_2 from NADH and reduced ferredoxin *in vitro*. Therefore, we measured the amount of H_2 in the headspace of culture vials (**Figure 4**). The amount of H_2 in the headspace was traced in conditions with or without H_2 supplementation, and the wild-type strain and the Mt-Δ*pduL1*Δ*pduL2*::*aldh* strain were compared. H_2 was supplied at 0.02 MPa of a partial pressure, in addition to fructose as a carbohydrate substrate, which was the same condition for our metabolome analysis. There was almost no H_2 production by the wild-type strain, and the supplied H_2 was consumed over time (**Figure 4A**). In contrast, the Mt-Δ*pduL1*Δ*pduL2*::*aldh* strain apparently did not consume H_2 under the same conditions (**Figure 4B**). Moreover, when H_2 was not supplied, the H_2 level increased in the culture vial of the Mt-Δ*pduL1*Δ*pduL2*::*aldh* strain, in contrast to that in the wild-type strain. H_2 production is usually attributed to the disposal of excess electrons from metabolism. In this case, this was most likely due to the increased level of NADH. However, H_2 formation would require a sufficiently low level of H_2 as the product. Therefore, the Mt-Δ*pduL1*Δ*pduL2*::*aldh* strain would have produced H_2 for the clearance of the excess electrons from catabolizing fructose, and H_2 supplementation would inhibit the H_2 production, causing the growth inhibition due to the redox imbalance.

NADH Consumption by DMSO Reduction Prevents the Growth Inhibition by H_2

The results of the H_2 measurement strongly indicated that the Mt-Δ*pduL1*Δ*pduL2*::*aldh* strain produced H_2 using excess reducing equivalents and balanced the intracellular redox. Our metabolome analysis showed imbalanced redox in the Mt-Δ*pduL1*Δ*pduL2*::*aldh* strain, manifested as an increased level of intracellular NADH. If a high level of intracellular NADH is the direct cause of growth inhibition, the Mt-Δ*pduL1*Δ*pduL2*::*aldh* strain should recover its growth in the presence of H_2 by lowering the intracellular NADH level. *M. thermoacetica* uses dimethyl sulfoxide (DMSO) as an electron acceptor, and the reported cases of bacterial DMSO reduction are NADH-dependent reactions (Zinder and Brock, 1978; De Bont et al., 1981; Drake and Daniel, 2004; Takemura et al., 2021b; Rosenbaum et al., 2022). We attempted to oxidize intracellular NADH *via* DMSO reduction by supplementing the culture medium with DMSO. We set up a culture of the Mt-Δ*pduL1*Δ*pduL2*::*aldh* strain with H_2 supplied at 0.08 MPa of partial pressure in addition to fructose, which showed strong growth inhibition (**Figures 2F–H**). At 24 h, the culture was supplied with 10 mM DMSO. The Mt-Δ*pduL1*Δ*pduL2*::*aldh* strain showed very slow growth with H_2 supplementation, but the growth rate dramatically increased upon DMSO supplementation (**Figure 5A**). The fructose supplied was completely consumed after 55 h (**Figure 5B**). The supplied DMSO was readily consumed within 20 h after the DMSO addition, consistent with the recovery of growth and fructose consumption

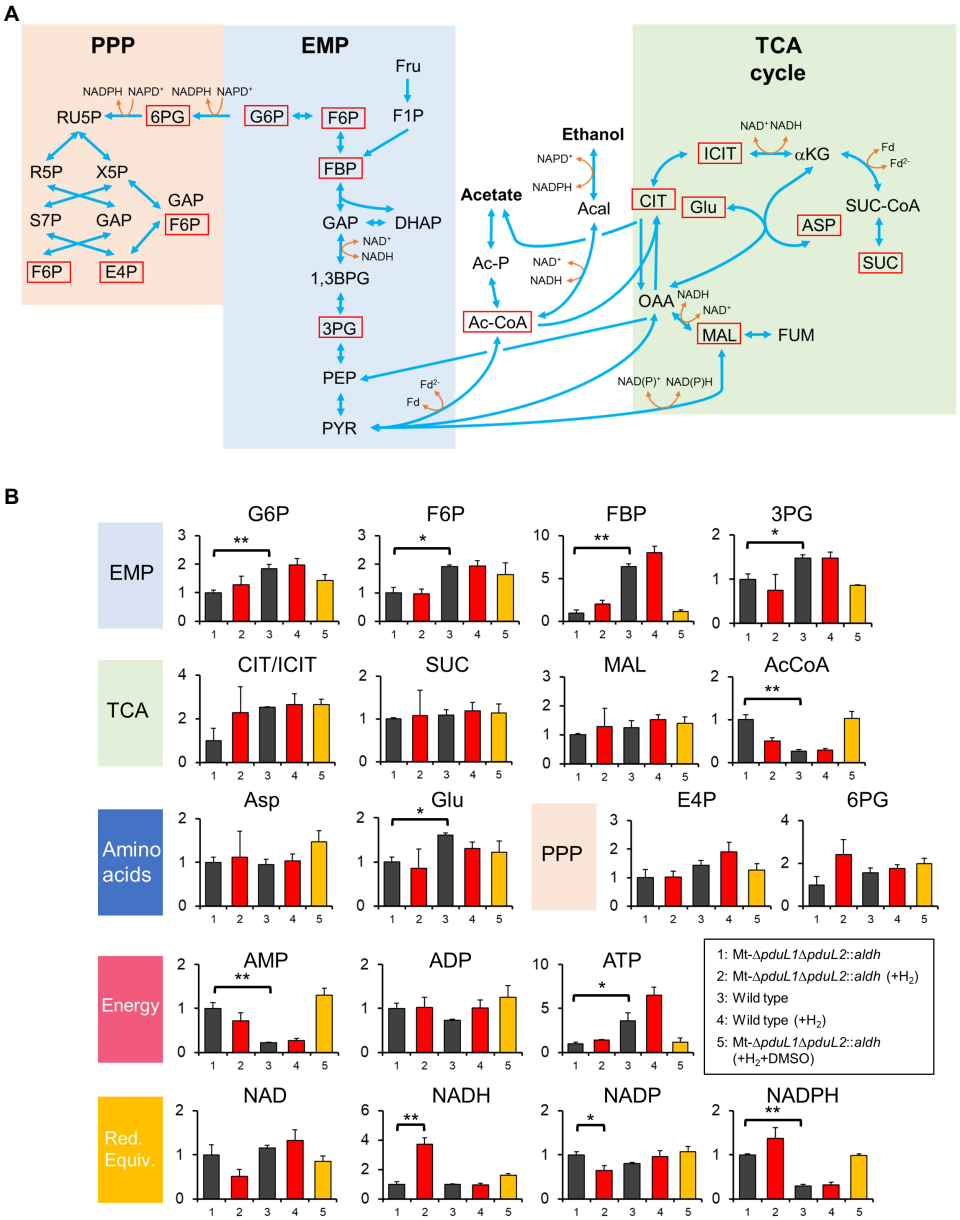

FIGURE 3 | Metabolome analysis of the Mt-Δ*pduL1*Δ*pduL2*::*aldh* strain and the wild-type strain with and without H_2 supplementation. **(A)** Metabolic pathways for the *Moorella thermoacetica* strains based on KEGG database (https://www.genome.jp/kegg-bin/show_organism?org=mta) and a previous study on a metabolic model (Islam et al., 2015). Metabolites quantified except for cofactors are shown by red squares. EMP, Embden–Meyerhof–Parnas pathway; PPP, pentose phosphate pathway; Fru, fructose; F1P, fructose 1-phosphate; G6P, glucose-6-phosphate; F6P, fructose 6-phosphate; FBP, fructose-1,6-bisphosphate; GAP, glyceraldehyde 3-phosphate; DHAP, dihydroxyacetone phosphate; 1,3BPG, 1,3-bisphosphoglyceric acid; 3PG, 3-phosphoglyceric acid; PEP, phosphoenolpyruvic acid; PYR, pyruvate; X5P, xylulose 5-phosphate; RU5P, ribulose 5-phosphate; R5P, ribose 5-phosphate; S7P, sedoheptulose 7-phosphate; E4P, erythrose 4-phosphate; Ac-CoA, Acetyl-CoA; Ac-P, acetyl phosphate; Acal, acetaldehyde; CIT, citrate; ICIT, isocitrate; αKG, alpha-ketoglutarate; SUC-CoA, succinyl-CoA; SUC, succinate; Glu, glutamate; OAA, oxaloacetic acid; MAL, malate; FUM, fumarate; ASP, aspartate; GAP, glyceraldehyde 3-phosphate. **(B)** Relative concentrations of intracellular metabolites for the Mt-Δ*pduL1*Δ*pduL2*::*aldh* strain and the wild-type strain in the absence (black) and presence of H_2 (0.02 MPa, red) on fructose as the carbohydrate substrate. The experiment with DMSO supplementation in addition to H_2 is shown in orange. All the cell samples were collected at around 0.6 of OD_{600}. DMSO was added at 0.4 of OD_{600}. For each sample, values were normalized to the Mt-Δ*pduL1*Δ*pduL2*::*aldh* strain without H_2 supplementation. The vertical axis represents a unitless ratio of metabolite concentrations. Error bars represent the SD of at least two biological replicates. Red. Equiv. represents reducing equivalents. *t*-test was performed to evaluate the significance between data sets 1 and 2, data sets 3 and 4, and data sets 1 and 3. Significant differences are shown. value of $*p<0.05$; value of $**p<0.01$.

(**Figure 5C**). The addition of DMSO also improved total ethanol production, whereas acetate production remained minor (**Figures 5D,E**).

We analyzed the effect of DMSO on the intracellular metabolome in the presence of H_2 (**Figure 3B**). We used the same culture conditions as in the metabolome analysis (H_2

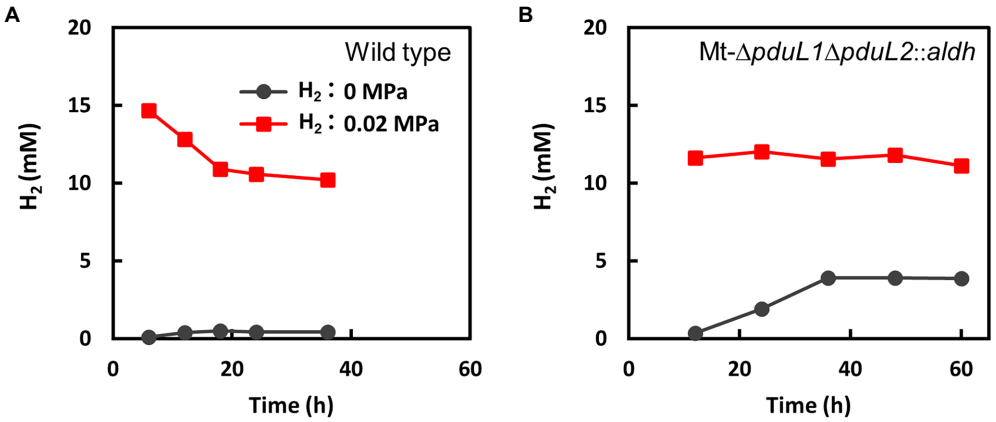

FIGURE 4 | Monitoring the consumption and evolution of H_2 by the wild-type strain **(A)** and the Mt-Δ*pduL1*Δ*pduL2*::*aldh* strain **(B)**. The total amount of H_2 was divided by the volume of the culture medium. Black, no H_2-supplied condition; red, H_2-supplied condition (0.02 MPa). Error bars, which are smaller than symbols, are the SD of three biological replicates.

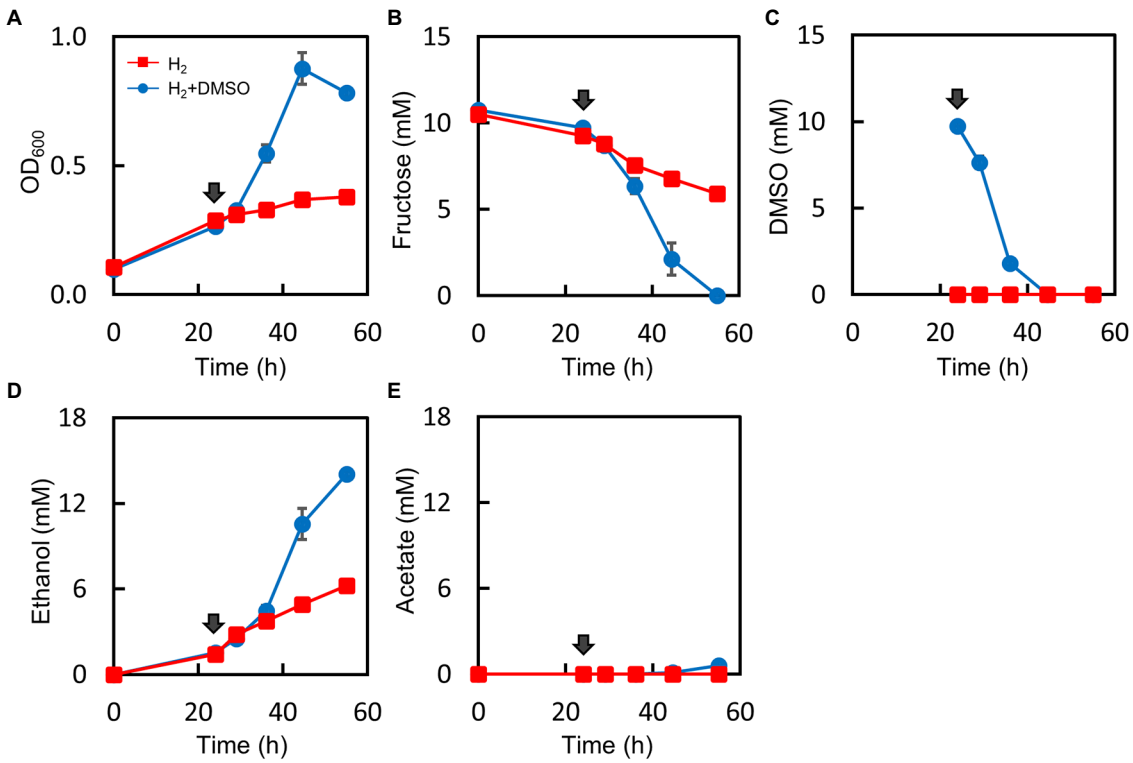

FIGURE 5 | Effect of DMSO supplementation on the culture profile in the H_2-supplemented mixotrophic condition of the Mt-Δ*pduL1*Δ*pduL2*::*aldh* strain. H_2 (0.08 MPa) was supplied to the fructose-supplemented culture, and DMSO (10 mM) was added to one group of the culture medium after 24 h (shown by arrows). The DMSO-supplied condition is shown in blue, whereas the no-DMSO condition is shown in red. Each graph shows the culture profiles for **(A)**, OD_{600}; **(B)**, Fructose concentration; **(C)**, DMSO concentration; **(D)**, Ethanol production; **(E)**, Acetate production. Error bars represent the SD of three biological replicates.

partial pressure = 0.02 MPa), except for DMSO supplementation, which was provided when the cells entered the exponential phase. As expected, the intracellular level of NADH was lower than that in the H_2 condition. Therefore, growth recovery correlated with intracellular NADH levels.

H_2 Enhances Target Metabolite Production by a Metabolically Engineered Strain With Balanced Redox

We found that the ethanol production pathway designed to balance the redox reaction requires tuning the imbalanced

redox by producing H_2. This means that our ethanol-producing strains need to be re-engineered to balance the redox reaction to benefit from H_2-supplemented mixotrophy. However, it is possible that artificial modifications in the genome can affect metabolic activities in an unpredictable manner. We previously succeeded in engineering *M. thermoacetica* to produce acetone (Kato et al., 2021; **Table 1**). The acetone synthesis pathway does not require any oxidoreductases to convert acetyl-CoA to acetone, which has the same redox balance as that of the native acetate pathway (**Figure 1C**). Therefore, acetone production has completely the same redox balance as acetate production, and the redox balance should not be affected. On the other hand, the pduL2::acetone strain has the same elements of genetic modification as an ethanol-producing strain, Mt-Δ*pduL2*::*aldh*, using a *pyrF* marker for selection and a constitutive G3PD (glyceraldehyde 3-phosphate dehydrogenase) promoter to express *aldh*, disrupting the acetate pathway. Therefore, we examined whether the introduction of an oxidoreductase affected the redox balance by testing the H_2-supplemented mixotrophic acetone production of the pduL2::acetone strain.

We set up cultures of the pduL2::acetone strain with fructose as the carbohydrate substrate and tested the effect of H_2 supplementation, as was performed for ethanol-producing strains. H_2 was supplied at 0.08 MPa of partial pressure, the highest dose used for the ethanol-producing strains. The pduL2::acetone strain grew in the presence of H_2 in the same manner as in its absence (**Figure 6A**). The optical density increased while fructose was consumed, and decreased after the complete consumption of fructose in both cases. Furthermore, the produced acetone and acetate increased with H_2 supplementation (**Figure 6B**), in contrast to ethanol production. Acetone production was enhanced by 13%, and the total carbon molar yield (the sum of acetate and acetone) was greater than one, indicating that extra CO_2 was converted to these metabolites. CO_2 was externally provided in the headspace gas and from $NaHCO_3$ in the medium, in addition to CO_2 released from metabolism. Engineering to introduce a non-reductive pathway did not erase the effect of mixotrophy. Therefore, we concluded that introducing oxidoreductase reactions to convert acetyl-CoA to ethanol caused H_2 production by extra electrons and H_2 inhibition.

DISCUSSION

Metabolic engineering to divert acetate to more reduced chemicals lowers carbon utilization and releases more CO_2 in acetogens due to the loss of the reducing power to fix and convert CO_2 for oxidoreductase reactions. One strategy for overcoming this issue is H_2-supplemented mixotrophy. However, our engineered strains, Mt-*aldh* and Mt-Δ*pduL2*::*aldh*, produced an increased amount of acetate instead of ethanol. Growth inhibition was observed in the Mt-Δ*pduL1*Δ*pduL2*::*aldh* strain. Therefore, the strategy for enhancing carbon utilization by H_2 is not effective for metabolically engineered strains in terms of ethanol production.

Growth inhibition due to H_2 supplementation has been reported in several studies. For example, one classical case involves *Clostridium cellobioparum*, an H_2 producer. When H_2 was added to the culture, *C. cellobioparum* growth was inhibited in an H_2 dose-dependent manner (Chung, 1976). This trend was similar to that of our ethanol-producing strain, Mt-Δ*pduL1*Δ*pduL2*::*aldh*. The study also reported that the removal of H_2 recovered the growth using a catalyst, gassing out, or co-culture with methanogenic microorganisms.

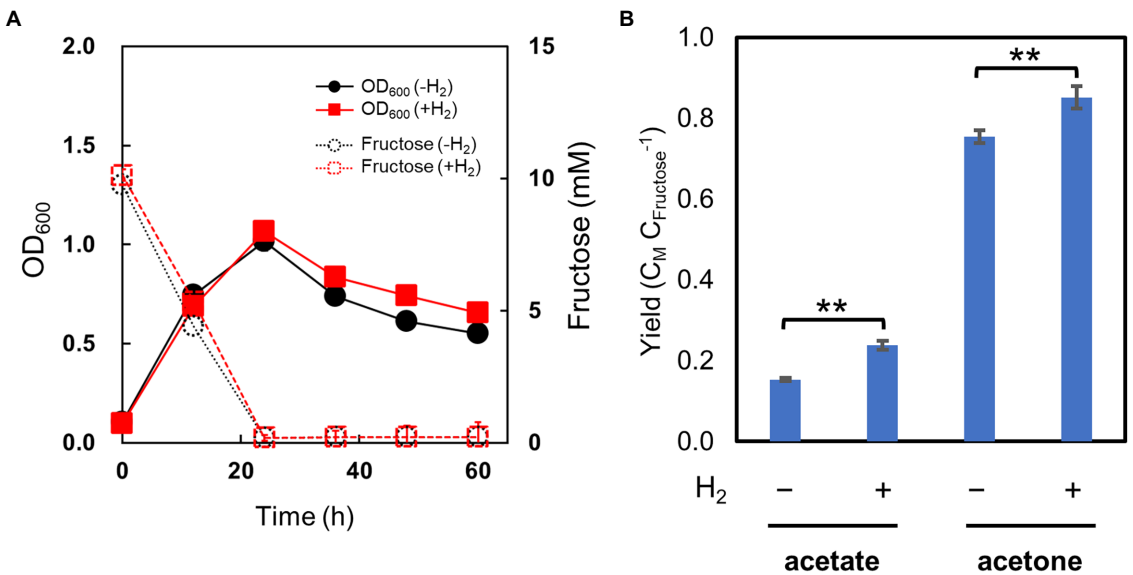

FIGURE 6 | Culture profiles of the metabolically engineered strain of *Moorella thermoacetica* for acetone production in the H_2-supplemented mixotrophic condition. **(A)** shows cell growth (solid lines) and fructose consumption (dotted lines) in the absence (black) and presence (red) of H_2. **(B)** shows carbon molar yields for acetate and acetone production. Error bars represent the SD of three biological replicates, some of which are smaller than symbols.

C. cellobioparum is a resident of the bovine rumen, living together with methanogens; therefore, the H_2 level remains low and does not affect their growth *in situ* (Hungate, 1967; Hungate et al., 1970). Another example was observed in the case of a thermophilic microorganism for H_2 bioproduction, *Caldicellulosiruptor saccharolyticus* (Willquist et al., 2011). A high level of H_2 produced by *C. saccharolyticus* inhibits its own growth, demanding continuous stripping of the produced H_2 from fermentation. Interestingly, the desired by-product for high H_2 yields is acetate, because more-reduced products, such as ethanol, drain electrons from H_2 production. When H_2 levels increase, *C. saccharolyticus* produces lactate and ethanol instead of H_2 to oxidize NADH and maintain the NADH/NAD ratio. In contrast, our metabolically engineered ethanol-producing strain of *M. thermoacetica* produced H_2 instead of ethanol to oxidize NADH. *M. thermoacetica* has been reported to evolve H_2 under certain conditions, such as in a CO-supplemented culture with glucose (Martin et al., 1983). The intracellular activity level of hydrogenases is significantly enhanced by CO, but not by other gas phases, including H_2 (Kellum and Drake, 1984). *M. thermoacetica* does not evolve H_2 in a standard culture under heterotrophic conditions, as seen in our experiment.

Metabolomic analysis revealed that the Mt-Δ*pduL1*Δ*pduL2*::*aldh* strain could maintain NADH levels in the absence of H_2. This was due to H_2 production for NADH oxidation, and might also be due to NADPH production using the NfnAB complex. The NfnAB complex transfers electrons from reduced ferredoxin and NADH to $NADP^+$ (Huang et al., 2012). However, because the Mt-Δ*pduL1*Δ*pduL2*::*aldh* strain possesses a high NADPH level, the conversion of reduced ferredoxin and NADH to NADPH would be inhibited or difficult. It is unclear why the basal level of NADPH in the Mt-Δ*pduL1*Δ*pduL2*::*aldh* strain was higher than that in the wild-type strain. One possibility is the slow conversion of acetyl-CoA to ethanol, because metabolome analysis showed that the intracellular level of acetyl-CoA was higher in the Mt-Δ*pduL1*Δ*pduL2*::*aldh* strain (**Figure 3B**). The reaction speed may have limited the consumption of cofactors NADH and NADPH, and the cofactors of the reduced forms accumulated. Although NADH production can be balanced by H_2 formation, NADPH production cannot be balanced. The Mt-Δ*pduL1*Δ*pduL2*::*aldh* strain could grow and produce ethanol in non-H_2-supplemented conditions, but NADH could not be balanced upon H_2 supplementation due to the blockage of H_2 production. Another possibility is unregulated NADPH production by the pentose phosphate pathway caused by unknown mechanisms due to metabolic engineering. Although a high level of NADPH remained, even in the presence of DMSO to consume NADH under H_2-supplemented conditions (**Figure 3B**), the NADPH level did not inhibit growth. Growth inhibition was caused by high NADH levels. We assume that the target reaction influenced by NADH level is glyceraldehyde 3-phosphate dehydrogenase, because this is NADH-dependent (Thauer, 1972; Huang et al., 2012). In studies on ethanol tolerance, glyceraldehyde 3-phosphate dehydrogenase was found to be inhibited by high levels of NADH in *Clostridium thermocellum* (Tian et al., 2017).

Finally, we confirmed that the increased acetate formation, but not ethanol formation, was due to the redox balance itself in the Mt-Δ*pduL2*::*aldh* strain. An engineered strain for acetone production produced higher levels of acetate and acetone with H_2 supplementation. Therefore, our strategy for gene manipulation itself did not affect redox balance, and the usefulness of H_2-supplemented mixotrophy was confirmed. The introduction of oxidoreductases affected the redox balance in ethanol-producing strains; hence, H_2 supplementation only enhanced acetate or inhibited growth. Although the metabolic pathway was designed to be redox-balanced by choosing oxidoreductases with appropriate cofactors (**Figure 1**), fine-tuning and a different design for properly balanced redox is required to derive benefits from H_2-supplemented mixotrophy for ethanol production. In contrast, if H_2 production is the aim of engineering, a metabolic design to increase the intracellular NADH level is one strategy to exploit the hydrogenase reaction.

DATA AVAILABILITY STATEMENT

The original contributions presented in the study are included in the article/supplementary material, and further inquiries can be directed to the corresponding author.

AUTHOR CONTRIBUTIONS

JK and YN conceived and designed the experiments. ShK, JK, and KW performed the experiments. ShK, JK, KW, KT, SeK, TF, YI, YA, TM, AM, and KM analyzed the data. ShK, JK, and KW visualized the data. JK prepared the manuscript. YN supervised the project. All authors have contributed to the manuscript and approved the submitted version.

FUNDING

Part of this work was supported by JSPS KAKENHI Grant Number 18K04853 and JST-Mirai Program Grant Number JPMJMI18E5, Japan.

ACKNOWLEDGMENTS

We thank Hikaru Miyaoka for providing technical assistance.

REFERENCES

Abdel-Banat, B. M., Hoshida, H., Ano, A., Nonklang, S., and Akada, R. (2010). High-temperature fermentation: how can processes for ethanol production at high temperatures become superior to the traditional process using mesophilic yeast? *Appl. Microbiol. Biotechnol.* 85, 861–867. doi: 10.1007/s00253-009-2248-5

Aryal, N., Kvist, T., Ammam, F., Pant, D., and Ottosen, L. D. M. (2018). An overview of microbial biogas enrichment. *Bioresour. Technol.* 264, 359–369. doi: 10.1016/j.biortech.2018.06.013

Basen, M., and Müller, V. (2017). "Hot" acetogenesis. *Extremophiles* 21, 15–26. doi: 10.1007/s00792-016-0873-3

Bengelsdorf, F. R., and Dürre, P. (2017). Gas fermentation for commodity chemicals and fuels. *Microb. Biotechnol.* 10, 1167–1170. doi: 10.1111/1751-7915.12763

Bengelsdorf, F. R., Poehlein, A., Linder, S., Erz, C., Hummel, T., Hoffmeister, S., et al. (2016). Industrial acetogenic biocatalysts: a comparative metabolic and genomic analysis. *Front. Microbiol.* 7:1036. doi: 10.3389/fmicb.2016.01036

Bolten, C. J., Kiefer, P., Letisse, F., Portais, J. C., and Wittmann, C. (2007). Sampling for metabolome analysis of microorganisms. *Anal. Chem.* 79, 3843–3849. doi: 10.1021/ac0623888

Bourgade, B., Minton, N. P., and Islam, M. A. (2021). Genetic and metabolic engineering challenges of C1-gas fermenting acetogenic chassis organisms. *FEMS Microbiol. Rev.* 45:fuab008. doi: 10.1093/femsre/fuab008

Chung, K. T. (1976). Inhibitory effects of H_2 on growth of *clostridium cellobioparum*. *Appl. Environ. Microbiol.* 31, 342–348. doi: 10.1128/aem.31.3.342-348.1976

De Bont, J. A. M., Van Dijken, J. P., and Harder, W. (1981). Dimethyl sulphoxide and dimethyl sulphide as a carbon, Sulphur and energy source for growth of *Hyphomicrobium* S. *Microbiology* 127, 315–323. doi: 10.1099/00221287-127-2-315

Drake, H.L. (1994). *Acetogenesis*. Boston, MA: Springer.

Drake, H. L., and Daniel, S. L. (2004). Physiology of the thermophilic acetogen *Moorella thermoacetica*. *Res. Microbiol.* 155, 869–883. doi: 10.1016/j.resmic.2004.10.002

Drake, H. L., Gossner, A. S., and Daniel, S. L. (2008). Old acetogens, new light. *Ann. N. Y. Acad. Sci.* 1125, 100–128. doi: 10.1196/annals.1419.016

Fackler, N., Heijstra, B. D., Rasor, B. J., Brown, H., Martin, J., Ni, Z., et al. (2021). Stepping on the gas to a circular economy: accelerating development of carbon-negative chemical production from gas fermentation. *Annu. Rev. Chem. Biomol. Eng* 12, 439–470. doi: 10.1146/annurev-chembioeng-120120-021122

Fast, A. G., Schmidt, E. D., Jones, S. W., and Tracy, B. P. (2015). Acetogenic mixotrophy: novel options for yield improvement in biofuels and biochemicals production. *Curr. Opin. Biotechnol.* 33, 60–72. doi: 10.1016/j.copbio.2014.11.014

Fontaine, F. E., Peterson, W. H., Mccoy, E., Johnson, M. J., and Ritter, G. J. (1942). A new type of glucose fermentation by *Clostridium thermoaceticum*. *J. Bacteriol.* 43, 701–715. doi: 10.1128/JB.43.6.701-715.1942

Hosseini, S. E., and Wahid, M. A. (2016). Hydrogen production from renewable and sustainable energy resources: promising green energy carrier for clean development. *Renew. Sustain. Energy Rev.* 57, 850–866. doi: 10.1016/j.rser.2015.12.112

Huang, H., Wang, S., Moll, J., and Thauer, R. K. (2012). Electron bifurcation involved in the energy metabolism of the acetogenic bacterium *Moorella thermoacetica* growing on glucose or H_2 plus CO_2. *J. Bacteriol.* 194, 3689–3699. doi: 10.1128/JB.00385-12

Hungate, R. E. (1967). Hydrogen as an intermediate in the rumen fermentation. *Arch. Mikrobiol.* 59, 158–164. doi: 10.1007/BF00406327

Hungate, R. E., Smith, W., Bauchop, T., Yu, I., and Rabinowitz, J. C. (1970). Formate as an intermediate in the bovine rumen fermentation. *J. Bacteriol.* 102, 389–397. doi: 10.1128/jb.102.2.389-397.1970

Islam, M. A., Zengler, K., Edwards, E. A., Mahadevan, R., and Stephanopoulos, G. (2015). Investigating *Moorella thermoacetica* metabolism with a genome-scale constraint-based metabolic model. *Integr. Biol.* 7, 869–882. doi: 10.1039/c5ib00095e

Iwasaki, Y., Kita, A., Sakai, S., Takaoka, K., Yano, S., Tajima, T., et al. (2013). Engineering of a functional thermostable kanamycin resistance marker for use in *Moorella thermoacetica* ATCC39073. *FEMS Microbiol. Lett.* 343, 8–12. doi: 10.1111/1574-6968.12113

Iwasaki, Y., Kita, A., Yoshida, K., Tajima, T., Yano, S., Shou, T., et al. (2017). Homolactic acid fermentation by the genetically engineered thermophilic homoacetogen *Moorella thermoacetica* ATCC 39073. *Appl. Environ. Microbiol.* 83, e00247–e00217. doi: 10.1128/AEM.00247-17

Jin, S., Bae, J., Song, Y., Pearcy, N., Shin, J., Kang, S., et al. (2020). Synthetic biology on acetogenic bacteria for highly efficient conversion of C1 gases to biochemicals. *Int. J. Mol. Sci.* 21:7639. doi: 10.3390/ijms21207639

Jones, S. W., Fast, A. G., Carlson, E. D., Wiedel, C. A., Au, J., Antoniewicz, M. R., et al. (2016). CO_2 fixation by anaerobic non-photosynthetic mixotrophy for improved carbon conversion. *Nat. Commun.* 7:12800. doi: 10.1038/ncomms12800

Kato, J., Takemura, K., Kato, S., Fujii, T., Wada, K., Iwasaki, Y., et al. (2021). Metabolic engineering of *Moorella thermoacetica* for thermophilic bioconversion of gaseous substrates to a volatile chemical. *AMB Express* 11:59. doi: 10.1186/s13568-021-01220-w

Kellum, R., and Drake, H. L. (1984). Effects of cultivation gas phase on hydrogenase of the acetogen *clostridium thermoaceticum*. *J. Bacteriol.* 160, 466–469. doi: 10.1128/jb.160.1.466-469.1984

Kita, A., Iwasaki, Y., Sakai, S., Okuto, S., Takaoka, K., Suzuki, T., et al. (2013). Development of genetic transformation and heterologous expression system in carboxydotrophic thermophilic acetogen *Moorella thermoacetica*. *J. Biosci. Bioeng.* 115, 347–352. doi: 10.1016/j.jbiosc.2012.10.013

Kopke, M., and Simpson, S. D. (2020). Pollution to products: recycling of 'above ground' carbon by gas fermentation. *Curr. Opin. Biotechnol.* 65, 180–189. doi: 10.1016/j.copbio.2020.02.017

Liew, F., Martin, M. E., Tappel, R. C., Heijstra, B. D., Mihalcea, C., and Kopke, M. (2016). Gas fermentation-a flexible platform for commercial scale production of low-carbon-fuels and chemicals from waste and renewable feedstocks. *Front. Microbiol.* 7:694. doi: 10.3389/fmicb.2016.00694

Ljungdhal, L. G. (1986). The autotrophic pathway of acetate synthesis in acetogenic bacteria. *Annu. Rev. Microbiol.* 40, 415–450. doi: 10.1146/annurev.mi.40.100186.002215

Martin, D. R., Lundie, L. L., Kellum, R., and Drake, H. L. (1983). Carbon monoxide-dependent evolution of hydrogen by the homoacetate-fermenting bacterium *Clostridium thermoaceticum*. *Curr. Microbiol.* 8, 337–340. doi: 10.1007/bf01573705

Maru, B. T., Munasinghe, P. C., Gilary, H., Jones, S. W., and Tracy, B. P. (2018). Fixation of CO_2 and CO on a diverse range of carbohydrates using anaerobic, non-photosynthetic mixotrophy. *FEMS Microbiol. Lett.* 365:fny039. doi: 10.1093/femsle/fny039

Minton, N. P., Ehsaan, M., Humphreys, C. M., Little, G. T., Baker, J., Henstra, A. M., et al. (2016). A roadmap for gene system development in *Clostridium*. *Anaerobe* 41, 104–112. doi: 10.1016/j.anaerobe.2016.05.011

Miura, T., Kita, A., Okamura, Y., Aki, T., Matsumura, Y., and Tajima, T., et al. (2014). Evaluation of marine sediments as microbial sources for methane production from brown algae under high salinity. *Bioresour. Technol.* 169, 362–366. doi: 10.1016/j.biortech.2014.07.013

Omar, B., El-Gammal, M., Abou-Shanab, R., Fotidis, I. A., Angelidaki, I., and Zhang, Y. (2019). Biogas upgrading and biochemical production from gas fermentation: impact of microbial community and gas composition. *Bioresour. Technol.* 286:121413. doi: 10.1016/j.biortech.2019.121413

Pierce, E., Xie, G., Barabote, R. D., Saunders, E., Han, C. S., Detter, J. C., et al. (2008). The complete genome sequence of *Moorella thermoacetica* (f. *Clostridium thermoaceticum*). *Environ. Microbiol.* 10, 2550–2573. doi: 10.1111/j.1462-2920.2008.01679.x

Rahayu, F., Kawai, Y., Iwasaki, Y., Yoshida, K., Kita, A., Tajima, T., et al. (2017). Thermophilic ethanol fermentation from lignocellulose hydrolysate by genetically engineered *Moorella thermoacetica*. *Bioresour. Technol.* 245, 1393–1399. doi: 10.1016/j.biortech.2017.05.146

Redl, S., Sukumara, S., Ploeger, T., Wu, L., Olshoj Jensen, T., Nielsen, A. T., et al. (2017). Thermodynamics and economic feasibility of acetone production from syngas using the thermophilic production host *Moorella thermoacetica*. *Biotechnol. Biofuels* 10:150. doi: 10.1186/s13068-017-0827-8

Rosenbaum, F. P., Poehlein, A., Daniel, R., and Müller, V. (2022). Energy-conserving dimethyl sulfoxide reduction in the acetogenic bacterium *Moorella thermoacetica*. *Environ Microbiol.* doi: 10.1111/1462-2920.15971 [Epub ahead of print].

Schuchmann, K., and Müller, V. (2014). Autotrophy at the thermodynamic limit of life: a model for energy conservation in acetogenic bacteria. *Nat. Rev. Microbiol.* 12, 809–821. doi: 10.1038/nrmicro3365

Schuchmann, K., and Müller, V. (2016). Energetics and application of heterotrophy in acetogenic bacteria. *Appl. Environ. Microbiol.* 82, 4056–4069. doi: 10.1128/AEM.00882-16

Takemura, K., Kato, J., Kato, S., Fujii, T., Wada, K., Iwasaki, Y., et al. (2021b). Enhancing hydrogen-dependent autotrophic growth of the thermophilic acetogen *Moorella thermoacetica* by supplementation of dimethyl sulfoxide as an electron acceptor. SSRN [preprint] Available at: https://papers.ssrn.com/sol3/papers.cfm?abstract_id=3995298. (Accessed April 14, 2022)

Takemura, K., Kato, J., Kato, S., Fujii, T., Wada, K., Iwasaki, Y., et al. (2021a). Autotrophic growth and ethanol production enabled by diverting acetate

flux in the metabolically engineered *Moorella thermoacetica*. *J. Biosci. Bioeng.* 132, 569–574. doi: 10.1016/j.jbiosc.2021.08.005

Tanner, R. S. (1989). Monitoring sulfate-reducing bacteria: comparison of enumeration media. *J. Microbiol. Methods* 10, 83–90. doi: 10.1016/0167-7012(89)90004-3

Tanner, R. S., Miller, L. M., and Yang, D. (1993). *Clostridium ljungdahlii* sp. nov., an acetogenic species in clostridial rRNA homology group I. *Int. J. Syst. Bacteriol.* 43, 232–236. doi: 10.1099/00207713-43-2-232

Taylor, M. P., Eley, K. L., Martin, S., Tuffin, M. I., Burton, S. G., and Cowan, D. A. (2009). Thermophilic ethanologenesis: future prospects for second-generation bioethanol production. *Trends Biotechnol.* 27, 398–405. doi: 10.1016/j.tibtech.2009.03.006

Teixeira, L. V., Moutinho, L. F., and Romão-Dumaresq, A. S. (2018). Gas fermentation of C1 feedstocks: commercialization status and future prospects. *Biofuels Bioprod. Biorefin.* 12, 1103–1117. doi: 10.1002/bbb.1912

Thauer, R. K. (1972). CO_2-reduction to formate by NADPH. The initial step in the total synthesis of acetate from CO_2 in *clostridium thermoaceticum*. *FEBS Lett.* 27, 111–115. doi: 10.1016/0014-5793(72)80421-6

Tian, L., Perot, S. J., Stevenson, D., Jacobson, T., Lanahan, A. A., Amador-Noguez, D., et al. (2017). Metabolome analysis reveals a role for glyceraldehyde 3-phosphate dehydrogenase in the inhibition of *C. thermocellum* by ethanol. *Biotechnol. Biofuels* 10:276. doi: 10.1186/s13068-017-0961-3

Wada, K., Saika, A., Ushimaru, K., Sato, S., Fukuoka, T., and Morita, T. (2022). Metabolomic evaluation of the central metabolic pathways of mannosylerythritol lipid biosynthesis in *Moesziomyces antarcticus* T-34. *J. Oleo Sci.* 71, 119–125. doi: 10.5650/jos.ess21229

Wang, S., Huang, H., Kahnt, J., and Thauer, R. K. (2013). A reversible electron-bifurcating ferredoxin- and NAD-dependent [FeFe]-hydrogenase (HydABC) in *Moorella thermoacetica*. *J. Bacteriol.* 195, 1267–1275. doi: 10.1128/JB.02158-12

Willquist, K., Pawar, S. S., and Van Niel, E. W. (2011). Reassessment of hydrogen tolerance in *Caldicellulosiruptor saccharolyticus*. *Microb. Cell Factories* 10:111. doi: 10.1186/1475-2859-10-111

Wood, H. G. (1991). Life with CO or CO_2 and H_2 as a source of carbon and energy. *FASEB J.* 5, 156–163. doi: 10.1096/fasebj.5.2.1900793

Zinder, S. H., and Brock, T. D. (1978). Dimethyl sulphoxide reduction by micro-organisms. *J. Gen. Microbiol.* 105, 335–342. doi: 10.1099/00221287-105-2-335

Conflict of Interest: The authors declare that the research was conducted in the absence of any commercial or financial relationships that could be construed as potential conflicts of interest.

Publisher's Note: All claims expressed in this article are solely those of the authors and do not necessarily represent those of their affiliated organizations, or those of the publisher, the editors and the reviewers. Any product that may be evaluated in this article, or claim that may be made by its manufacturer, is not guaranteed or endorsed by the publisher.

frontiers | Frontiers in Microbiology

ORIGINAL RESEARCH
published: 31 May 2022
doi: 10.3389/fmicb.2022.896190

Synechocystis sp. PCC 6803 Requires the Bidirectional Hydrogenase to Metabolize Glucose and Arginine Under Oxic Conditions

Heinrich Burgstaller[1], *Yingying Wang*[1], *Johanna Caliebe*[1,2], *Vanessa Hueren*[1], *Jens Appel*[1,2], *Marko Boehm*[1,2], *Sinje Leitzke*[1], *Marius Theune*[1,2], *Paul W. King*[3] *and Kirstin Gutekunst*[1,2]*

[1] *Plant Cell Physiology and Biotechnology, Botanical Institute, University of Kiel, Kiel, Germany,* [2] *Molecular Plant Physiology, Bioenergetics in Photoautotrophs, University of Kassel, Kassel, Germany,* [3] *National Renewable Energy Laboratory, Biosciences Center, Golden, CO, United States*

OPEN ACCESS

Edited by:
Constanze Pinske, Martin Luther University of Halle-Wittenberg, Germany

Reviewed by:
Tobias Goris, German Institute of Human Nutrition Potsdam-Rehbruecke (DIfE), Germany
Peter Lindblad, Uppsala University, Sweden

***Correspondence:**
Kirstin Gutekunst
kirstin.gutekunst@uni-kassel.de

Specialty section:
This article was submitted to Microbial Physiology and Metabolism, a section of the journal Frontiers in Microbiology

Received: *14 March 2022*
Accepted: *27 April 2022*
Published: *31 May 2022*

Citation:
Burgstaller H, Wang Y, Caliebe J, Hueren V, Appel J, Boehm M, Leitzke S, Theune M, King PW and Gutekunst K (2022) Synechocystis sp. PCC 6803 Requires the Bidirectional Hydrogenase to Metabolize Glucose and Arginine Under Oxic Conditions. Front. Microbiol. 13:896190. doi: 10.3389/fmicb.2022.896190

The cyanobacterium *Synechocystis* sp.PCC 6803 possesses a bidirectional NiFe-hydrogenase, HoxEFUYH. It functions to produce hydrogen under dark, fermentative conditions and photoproduces hydrogen when dark-adapted cells are illuminated. Unexpectedly, we found that the deletion of the large subunit of the hydrogenase (HoxH) in *Synechocystis* leads to an inability to grow on arginine and glucose under continuous light in the presence of oxygen. This is surprising, as the hydrogenase is an oxygen-sensitive enzyme. In wild-type (WT) cells, thylakoid membranes largely disappeared, cyanophycin accumulated, and the plastoquinone (PQ) pool was highly reduced, whereas Δ*hoxH* cells entered a dormant-like state and neither consumed glucose nor arginine at comparable rates to the WT. Hydrogen production was not traceable in the WT under these conditions. We tested and could show that the hydrogenase does not work as an oxidase on arginine and glucose but has an impact on the redox states of photosynthetic complexes in the presence of oxygen. It acts as an electron valve as an immediate response to the supply of arginine and glucose but supports the input of electrons from arginine and glucose oxidation into the photosynthetic electron chain in the long run, possibly *via* the NDH-1 complex. Despite the data presented in this study, the latter scenario requires further proof. The exact role of the hydrogenase in the presence of arginine and glucose remains unresolved. In addition, a unique feature of the hydrogenase is its ability to shift electrons between NAD(H), NADP(H), ferredoxin, and flavodoxin, which was recently shown *in vitro* and might be required for fine-tuning. Taken together, our data show that *Synechocystis* depends on the hydrogenase to metabolize organic carbon and nitrogen in the presence of oxygen, which might be an explanation for its prevalence in aerobic cyanobacteria.

Keywords: hydrogenase, diaphorase, photosynthetic complex I (NDH-1), photosynthesis, respiration, arginine, photomixotrophy

INTRODUCTION

The bidirectional NiFe-hydrogenase of the cyanobacterium *Synechocystis* is composed of a diaphorase sub-complex (HoxEFU), which reacts with its redox partners NAD(P)(H), ferredoxin, and flavodoxin and a hydrogenase sub-complex (HoxYH), which catalyzes the production and consumption of hydrogen (H_2) (Gutekunst et al., 2014; Artz et al., 2020). HoxEFUYH is the only hydrogenase encoded in this organism. It is localized in the cytoplasm and is found to associate dynamically with thylakoid membranes (Burroughs et al., 2014). The production of H_2 occurs under fermentative growth conditions as a means for balancing redox poise. Furthermore, at the onset of photosynthesis in dark-adapted cells, HoxEFUYH catalyzes hydrogen production (photohydrogen) during the brief anaerobic phase of growth. Under these conditions, surplus electrons from the photosynthetic electron chain that are not accepted by the Calvin–Benson–Bassham (CBB) cycle are transferred to the hydrogenase and utilized for H_2 production. In this situation, the enzyme works as an electron valve to protect the photosynthetic electron chain from over reduction (Appel et al., 2000; Cournac et al., 2004). Photohydrogen is subsequently oxidized by HoxEFUYH, and the electrons are most likely transferred to the photosynthetic electron chain *via* PQ (Dutta and Vermaas, 2016). As soon as oxygen accumulates due to H_2O splitting at photosystem II (PSII), hydrogen is neither produced nor oxidized. The current model assumes that exposure to oxygen blocks the active site of the NiFe-hydrogenase *via* a hydroxy (OH^-) group that bridges Ni and Fe in the active site of HoxH and thereby prevents H_2-turnover (Pandelia et al., 2010; McIntosh et al., 2011; Caserta et al., 2020). Due to its susceptibility to inactivation, the enzyme is considered oxygen sensitive. Therefore, it is remarkable that the enzyme is widespread in cyanobacteria, which seldomly encounter anoxic conditions in their natural environment. It is also worthy to note that the enzyme is constitutively expressed in *Synechocystis* under standard laboratory conditions, i.e., continuous light and constant O_2 supersaturation. Distinct subcomplexes of the enzyme (HoxEFU, HoxFUYH, and HoxFU) have been detected in addition to the complete HoxEFUYH pentameric enzyme *in vivo* (Eckert et al., 2012). However, it is still unknown whether these subcomplexes fulfill specific functions.

Synechocystis can grow on a variety of different nitrogen sources. For example, cells can consume either inorganic nitrogen in the form of nitrate and ammonium or organic nitrogen such as urea or arginine and glutamine (Flores and Herrero, 1994). Nitrate is reduced intracellularly to nitrite and ammonium, which is subsequently incorporated into biomass (Forchhammer and Selim, 2020). It has previously been shown that the hydrogenase is essential for growth in a dark-light cycle under mixotrophic conditions when nitrate is replaced by arginine as the nitrogen source (Gutekunst et al., 2014). The replacement of nitrate with arginine has a dramatic effect on the metabolism and phenotype of *Synechocystis*. Arginine can readily be taken up by the cells and metabolized as a cellular nitrogen source and in the production of cyanophycin (Stephan et al., 2000; Schriek et al., 2007). Cyanophycin consists of equimolar amounts of aspartic acid and arginine and can be quickly metabolized when required. Besides the accumulation of cyanophycin, cells cultivated on arginine also disassemble and restructure the thylakoid membranes, have reduced photosynthetic activity, and appear yellow due to a reduced chlorophyll content (Stephan et al., 2000). The addition of nitrate in combination with arginine partly rescues this phenotype (Stephan et al., 2000). The Δ*psbO* mutant has a compromised water-splitting apparatus at PSII and displays reduced H_2O oxidizing capacities. It grows better than the wild-type (WT) on arginine, stays green, and displays only minor morphological changes (Stephan et al., 2000). The difference between the WT and the Δ*psbO* mutant strain is even more pronounced at higher light intensities. While nitrate needs to be reduced by ferredoxin and is an important electron sink of the photosynthetic electron chain, arginine needs to be oxidized to be utilized for biosynthetic reactions. *Synechocystis* encodes enzymes for two distinct arginine oxidation pathways: the arginine deiminase pathway and the arginine dehydrogenase pathway (Schriek et al., 2007, 2009). The arginine deiminase pathway yields NH_4^+, NADH, and ATP, whereas the arginine dehydrogenase pathway yields NH_4^+, NAD(P)H, and succinate. The arginine deiminase in *Synechocystis* contains predicted transmembrane helices which implies that the enzyme could be membrane attached (Schriek et al., 2007). Arginine dehydrogenase has been clearly demonstrated to attach to the thylakoid membrane (Schriek et al., 2009). Electrons from arginine oxidation can either be fed directly into the plastoquinone (PQ)-pool *via* the arginine dehydrogenase or indirectly *via* succinate and the succinate dehydrogenase, which likewise transfers electrons into the PQ-pool (refer to photosynthetic electron transfer chain of **Figure 8**) (Schriek et al., 2009; Mullineaux, 2014). In contrast to nitrate, which accepts electrons from the photosynthetic electron chain, arginine reduces the PQ-pool. However, nitrate has the potential to relieve surplus electrons from photosynthesis, and arginine has the potential to overload the PQ pool and cause oxidative stress. This could be an explanation for the observation that the Δ*psbO* mutant with reduced H_20 splitting capacities is superior to the WT in metabolizing arginine especially in high light (Stephan et al., 2000; Schriek et al., 2009). The addition of glucose to cells cultured on arginine should enhance the supply of electrons by the activity of respiratory dehydrogenases that reduce the PQ pool (refer to photosynthetic electron transfer chain of **Figure 8**) (Lea-Smith et al., 2016; Wang et al., 2022). Photomixotrophic conditions on arginine should, therefore, lead to highly reducing conditions in the cells. The observation that Δ*hoxH* strain is unable to grow on arginine under mixotrophic dark-light conditions was interpreted as HoxEFUYH being required for electron dissipation *via* hydrogen production (Gutekunst et al., 2014). This interpretation appeared most obvious in cells during dark, fermentative H_2 production, or during transient hydrogen production at the onset of illumination (photohydrogen production). However, surprisingly, we found in this study that the Δ*hoxH* strain was unable to grow under photomixotrophic conditions on arginine, even under continuous illumination and O_2 saturating conditions. This is especially remarkable, as HoxH is known to be inactived in the presence of oxygen (McIntosh

et al., 2011). To address this conundrum, investigations were undertaken to ensure the growth phenotype arose from the absence of HoxH and to elucidate the physiological function of the enzyme under these growth conditions. Our results provide strong evidence that under oxic conditions, the hydrogenase has a physiological function beyond hydrogen cycling and is required for photomixotrophic growth on organic carbon and nitrogen.

MATERIALS AND METHODS

Construction of Mutants and Utilized Strains

All mutants that were constructed or utilized in this study are listed in **Supplementary Table 1**. All the primers used in this study are listed in **Supplementary Table 2**. All mutants were constructed in the non-motile GT WT of *Synechocystis* sp. PCC 6803 (Trautmann et al., 2012). Constructs for the deletion of the genes were generated by Gibson cloning (Gibson et al., 2009) assembling three fragments into the pBluescript SK(+) in a single step. After examination by sequencing, the plasmids were transformed into *Synechocystis* sp. PCC 6803 cells as described (Williams, 1988). In short, genes were replaced with antibiotic resistance cassettes *via* homologous recombination. The transformation efficiency is especially high in the exponential growth phase. Therefore, 250 ml *Synechocystis* cultures were inoculated in glass tubes (diameter of 3.5 cm) from a preculture with an OD_{750} of 0,15 on the day prior to transformation. On the day of transformation, the cells were harvested and resuspended in 600 μl BG11. A volume of 300 μl of the cell suspension was mixed with 6–18 μg plasmid DNA and incubated for 6 h at 30°C in darkness. Cells were plated on agar plates without antibiotics and kept in a climate chamber at 28°C and 50 μE m^2s^1. On the third day, antibiotics were added for selection pressure. After 2 weeks, single colonies appeared that were streaked on new BG11 agar plates with antibiotics for segregation six to eight times. Resulting transformants were either checked by PCR or Southern hybridization (**Supplementary Figures 3–7**).

Growth Conditions

Strains were either cultivated in BG11 medium which contains 17.6 mM nitrate or alternatively in BG110 medium without nitrate that was supplemented with 5 mM arginine. Notably, 10 mM glucose was added as indicated. DCMU was added at a concentration of 10 mM. For precultures, 50 ml of BG11 medium were inoculated with cells and antibiotics in the case of mutants in 100 ml Erlenmeyer flasks on a rotary at 28°C, 50 μE/m^2/s, and 100 rpm. After several days of growth, cultures were pelleted and washed twice in the medium of choice without antibiotics for growth experiments. Cells were inoculated into 200 ml BG-11 at an OD750 of 0.05 and placed into glass tubes with a diameter of 3.5 cm bubbled with air at 50 μE/m^2/s at 28°C, and growth was monitored every 24 h by measuring the optical density at 750 nm as described earlier (Makowka et al., 2020). The optical density (OD) of the culture was determined by photometrical analysis (UV 2501 PC Photometer, Shimadzu, Kyoto, Japan) at 750 nm, and its data were recorded and analyzed using the affiliated software UVProbe 2.33 (Shimadzu, Kyoto, Japan). Samples were diluted with BG11 medium by 1:10 when samples showed an OD_{750} value above 0.5.

Oxygen and Hydrogen Measurements

To measure the concentration of dissolved oxygen and hydrogen in the cultures, oxygen and hydrogen sensors from Unisense (Unisense, Aarhus, Denmark) were used according to the manufacturer's instructions. After a two-point calibration of the sensors, they were placed in the respective culture in glass tubes, and the measurement was started. Photosynthetic and respiratory activities were monitored *via* the oxygen evolution rate in the light and oxygen uptake rate in darkness. For this, calibrated sensors were put in a 25 ml culture (one sensor per culture, 3 repeats), which was illuminated for 15 min at 100 μmol photons m^{-2} s^{-1} followed by another 15 min in the darkness. For monitoring of oxygen and hydrogen concentrations during growth experiments, one hydrogen and one oxygen sensor were placed into the glass tubes with a diameter of 3.5 cm (Makowka et al., 2020). For the experiments shown in **Supplementary Figure 1**, one oxygen and one hydrogen sensor were placed into the glass tubes with cultures. The cultures with the sensors were incubated in dark and anoxic conditions from 0 to 0.73 h in order to prove their ability to produce fermentative hydrogen. As soon as the cells were illuminated, fermentative hydrogen was consumed. The cultures were purged with ambient air until they were saturated with O_2. The aeration was turned off, and the cultures were left under continuous light.

Hydrogenase Activity Measurements *via* Methyl Viologen

Hydrogenase activity was determined *via* methyl viologen (MV) as described before (Appel et al., 2020).

Expression of HoxH mRNA

After purification, 1 μg of RNA was subjected to a DNase digest. To check if the digest was complete, a test PCR with primers specific for *rnpB* was performed. If no PCR product was found, the RNA was reverse transcribed using the High Capacity RNA-to-cDNA Kit with the MuLV reverse transcriptase (Applied Biosystems, Warrington, UK). Subsequently, equal amounts of cDNA were used for the real-time PCR with the Power SYBR® Green PCR Master Mix (Applied Biosystems, Warrington, UK). In this case, the temperature program was step 1 95°C 10 min, step 2 95°C 15 s, step 3 60 °C 60 s, and additional 39 cycles between steps 2 and 3 in the PCR Cycler Rotor-Gene Q (Qiagen, Hilden, Germany). For the quantification, the $2^{-\Delta\Delta CT}$ method was used to analyze relative changes in transcript abundance (Livak and Schmittgen, 2001). The C_T value was determined for each sample. DNA was diluted 1:30, 1:300, and 1:3,000. The threshold was set for all samples to the normalized fluorescence 10^{-1}. A typical serial dilution is shown in **Supplementary Figure 8**. Data were analyzed using Rotor-Gene Q Software (version 2.0.2).

The C_T value was determined and normalized to the reference gene 16S rRNA under two different conditions (in BG11 and $BG11_0$ with arginine and glucose). From the C_T values, the

following ratio was determined:

$$ratio = \frac{2^{C_T(gene\ of\ intest\ condition\ 1)} - C_T(gene\ of\ interest\ condition\ 2)}{2^{C_T(refernence\ gene\ condition\ 1)} - C_T(reference\ gene\ condition\ 2)}$$

and is given in the different figures.

Protein Preparation, Protein Analysis, and Immunoblotting

Soluble protein extracts of various *Synechocystis* sp. PCC 6803 strains were generated by glass bead breakage and differential centrifugation as described (Appel et al., 2020). Protein concentrations were determined by Bradford assay (Carl Roth). Soluble protein samples were either separated on 10% (w/v) denaturing 1-D SDS-PAGE Bis/Tris gels using an MES running buffer or on 0.75 mm thick 12% (w/v) native 1-D BN-PAGE gels (Boehm et al., 2009). Prior to 1-D BN-PAGE, ß-dodecyl-D-maltoside (ß-DM) was added to a final concentration of 0.5% (w/v) from a 10% (w/v) stock to solubilize any remaining thylakoid membrane fragments and as a last step, 5% (v/v) Coomassie loading solution [750 mM ε-aminocaproic acid, 5% (w/v) Coomassie-G] was added. 2-D BN/SDS-PAGE and immunoblotting were performed as described by Appel et al. (2020). Primary antibodies used in this study were kindly provided by Prof. Peter Nixon (Imperial College, UK; purified, polyclonal antisera from rabbit against HoxE, HoxF, HoxU, HoxY, and HoxH).

Determination of Total Protein Amount Based on the OD_{750}

To determine if *Synechocystis* cells can be disrupted with similar efficiency, the protein concentration was measured in relation to the OD_{750}. Therefore, liquid cultures were cultivated in glass tubes for 4 days. Then, the OD_{750} of the cultures was measured, and the culture volume that corresponded to an OD_{750} of 0.1 and 0.3 was calculated, respectively. After centrifugation for 5 min at room temperature (RT), the pellet was resuspended in 500 µl ACA buffer (750 mM ε-aminocaproic acid, 50 mM Tris-HCl pH 7.5, and 0.5 mM EDTA), and the suspension was transferred to a new 2 ml reaction tube. In the next step, precisely 0.25 g of glass beads (0.17–0.18 mm, *Sigma Aldrich, Germany*) was added to the cell suspension. The mixture was vortexed at 4°C for 2 min using the following program: 12 cycles: 10 s "ON" followed by 10 s "OFF." The speed was set to maximum. Later, the glass beads were pelleted at 5,000 × *g* and 4°C for ∼1 min. To pellet the membrane fraction, the supernatant was transferred to a new 1.5 ml reaction tube and was centrifuged again at 12,000 × *g* and 4°C for 20 min. Then, the protein concentration was determined using the Bradford assay. To calculate the number of cells that were not broken up during the method described, the samples were examined under a light microscope. To simplify the counting, a *Neubauer* counting chamber was used. These chambers are divided into nine large squares, each with a 1 mm^2 area. The large squares are divided into 25 medium squares, and these are again divided into 16 small squares. Each of the smallest squares has an area of 0.0025 mm^2. Four of the medium squares were counted, and the total number of intact cells was extrapolated. The counting was repeated in triplicates, and the mean value was calculated. We found that it was possible to break cells quantitatively at low OD_{750} between 0.1 and 0.3. Therefore, total protein contents were determined at these cell densities.

Dual-KLAS/NIR

To measure the electron transfer around PSI (from plastocyanin to P700 to ferredoxin), cell suspensions were adjusted to an OD750 of 5.7 and illuminated for 600 ms with 1,350 µE/m^2/s. This illumination was repeated 20 times with an intermittent dark period of 30 s, and the average of the 20 measurements was calculated. Deconvolution of PC, $P700^+$, and ferredoxin from the original traces of the Dual-KLAS/NIR was performed as described (Theune et al., 2021). The Dual-KLAS/NIR measures at six different wavelengths in the near-infrared. From these wavelengths, four different signals are calculated. Since the absorption of the three components (i.e., plastocyanin, $P700^+$, and ferredoxin) contributes to a different extent to the four signals, the proportions of oxidized plastocyanin, $P700^+$, and reduced ferredoxin can be calculated by deconvolution (Klughammer and Schreiber, 2016).

Photochemical Quenching

Photochemical quenching (qP) measurements were conducted using a Multi-Color-PAM (Multiple Excitation Wavelength, Chlorophyll Fluorescence Analyzer, Heinz Walz, Effeltrich, DE). All cultures were brought to a chlorophyll concentration of 2.5 µg/ml and independently measured at least three times each day. A volume of 2 ml of each culture were measured in a cuvette. The actinic light was adjusted to 58 µE/m^2/s, and there were five repetitions of a sequence of 120 s of actinic light, a saturation flash (SAT), and then a dark phase of 30 s in one measurement. qP was calculated from $F_V/(F_M\text{-}F_0)$ (van Kooten and Snel, 1990).

Chlorophyll Content

To measure the chlorophyll *a* content, 3 × 100 µl of culture was centrifuged at 14,000 rpm (*Centrifuge 5424, Eppendorf*) for 5 min at RT. The cell pellet was resuspended in 1 ml of 100% methanol, vortexed for 3 min, and centrifuged again at 14,000 rpm (*Centrifuge 5424, Eppendorf*) for 5 min at RT to spin down cell debris. Using a spectrophotometer, the wavelengths 665, 666, and 750 nm were measured since chlorophyll *a* absorbs at the wavelengths 440–450 nm and 650–700 nm.

According to the following formula (Lichtenthaler, 1987), the chlorophyll *a* content was calculated as follows:

$$\text{Chl } a \text{ content } (\mu g/ml) = \frac{(\text{maximum of OD665 to OD666}) - \text{OD750}}{0.0809} \cdot \text{dilution}$$

Glucose Quantification

Glucose was quantified enzymatically by measuring the evolution of NADPH photometrically as a change of absorption at 340 nm in a sample volume of 5 µl (containing <5 mM glucose) in the presence of 0.5 units hexokinase, 0.5 units glucose-6-phosphate dehydrogenase, 2 mM ATP, 2 mM $NADP^+$, and 3 mM $MgCl_2$ in 91.3 mM Tris-HCl buffer in a total volume of 50 µl. Absorption

measurements were performed using a 96-well plate reader (Plate Reader Infinite M200Pro, Tecan, Austria).

Arginine or Cyanophycin Extraction and Quantification

One molecule of cyanophycin contains one molecule of arginine. Therefore, the concentration of cyanophycin equals the amount of arginine. Cyanophycin quantification was modified according to the study by Elbahloul et al. (2005) (Messineo, 1966). Step 1: cyanophycin extraction: 25 ml culture (OD_{750}:1.0) was collected by centrifugation (10 min, 4,000 *g*, RT), and 1 ml acetone was added to the pellet and incubated in a shaker at 1,400 *g* for 30 min. The sample was centrifuged at 13,000 *g* for 10 min, the supernatant was discarded, and the pellet was resuspended in 1.2 ml of 0.1 M HCl and incubated for 1 h at 60°C at 1,400 *g*. The sample was centrifuged at 13,000 *g* for 10 min at 4°C, the supernatant was transferred to a new reaction cup, and 300 μl of 0.1 M Tris-HCl, pH 9.0 was added. The sample was incubated at 4°C for 40 min, centrifuged at 18,000 *g* for 15 min, and the supernatant was discarded. The pellet was resuspended in 1 ml of 0.1 M HCl and used for the quantification. Arginine standards with concentrations of 0, 10, 20, 30, 40, 50, 60, and 70 μg were prepared. Step 2: cyanophycin quantification using the Sakaguchi reaction: 166 μl reagent A [300 mg KI (potassium iodide) in 100 ml distilled H_2O] was added to 166 μl sample/standard containing between 10 and 100 μg arginine (0.057–0.5 μM, 0.1 M HCl). A volume of 500 μl of reagent B (100 ml of 5 M KOH, 2 g potassium sodium tartrate, 0.1 g 2,4-dichloro-1-naphthol, 180 ml absolute ethanol, and 0.2 ml NaClO) was added, and the reaction was incubated for 1 h at RT. A volume of 166 μl of reagent C [5%(v/v) NaClO with distilled H_2O] was added, and the sample was incubated for exactly 10 min. The absorption at 520 nm was read immediately against a blank without arginine/cyanophycin.

Transmission Electron Microscopy

A volume of 30 ml of each *Synechocystis* culture were harvested at 8,000 *g* for 3 min and resuspended in 2 ml of the corresponding growth medium. The concentrated cells were fixed by adding 2 ml of a solution containing 5% glutaraldehyde (GA) and 2% paraformaldehyde (FA) in 0.2 M cacodylate buffer (pH 7.3). Samples were either stored at 4°C or directly observed with a transmission electron microscope (TEM, Tecnai G2 Spirit BioTWIN, Fei Company, Thermo Fisher Scientific, MS, USA).

Photosynthesis and Respiration Rate Measurements

The respiration and photosynthesis rates of *Synechocystis* cultures were determined as the oxygen uptake rate in darkness and oxygen evolution rate in the light, which was determined using a Unisense oxygen microsensor (Unisense, Denmark) according to the manufacturer's instruction.

RESULTS

Growth Behavior of Synechocystis WT and the Δ*hoxH* Mutant Strain Under Photomixotrophic Conditions on Arginine in the Presence of Oxygen

When WT and Δ*hoxH* were cultivated on arginine and glucose under continuous light, Δ*hoxH* displayed no growth, whereas the growth rate was similar to WT when cultured on nitrate, on arginine, or on glucose plus nitrate (**Figures 1A–D**).

Oxygen and hydrogen concentrations and OD_{750} were monitored in WT cells cultured on arginine and glucose for 96 h. Oxygen concentrations were close to saturation throughout the experiment, whereas, no hydrogen was detected (**Figure 1E**). As the cultures were purged with ambient air, in this setting, hydrogen might have been gassed out from the cultures. Therefore, hydrogen and oxygen concentrations in WT cultures on arginine and glucose were monitored during growth under continuous light without purging (**Supplementary Figure 1**). Again, no hydrogen was detected, whereas oxygen accumulated. These results show that oxygen is present, but no hydrogen is detected under conditions where HoxH is required for growth.

Morphology and Metabolic State of WT and Δ*hoxH* on Arginine and Glucose

Wild-type and Δ*hoxH* reduced their chlorophyll content relative to OD_{750} on arginine and glucose. WT cultures appeared yellow, and Δ*hoxH* cultures appeared colorless due to their low optical densities (**Figure 2**).

Quantification of glucose and arginine in the medium of WT and Δ*hoxH* cultures revealed that WT cells consumed both compounds, whereas consumption by Δ*hoxH* was negligible (**Figures 3A,B**). In agreement with this, the WT produced and stored large amounts of cyanophycin, which is composed of arginine and aspartic acid, whereas Δ*hoxH* did not (**Figure 3C**). Microscopic images confirmed that cyanophycin granules accumulated in WT cells only. Furthermore, they revealed that WT cells underwent dramatic morphological changes as they degraded their thylakoid membranes in contrast to Δ*hoxH* (**Figure 3D**). The morphological changes observed in WT cells are well in line with earlier observations that were made on WT cells cultivated on arginine (Stephan et al., 2000). In contrast, Δ*hoxH* cells cultured on arginine and glucose looked similar to Δ*hoxH* cells cultured on nitrate. The photosynthetic activities of WT and Δ*hoxH* cells were similar on nitrate and were strongly reduced in both when cultivated on arginine and glucose (**Figures 3E,F**). Dark respiration in Δ*hoxH* was decreased compared with the WT, which is in line with its lower glucose and arginine consumption rates under the growth in continuous light (**Figure 3G**). It is remarkable that Δ*hoxH* reduces its photosynthesis and respiratory activity even though the cells look normal and healthy with thylakoid membranes and

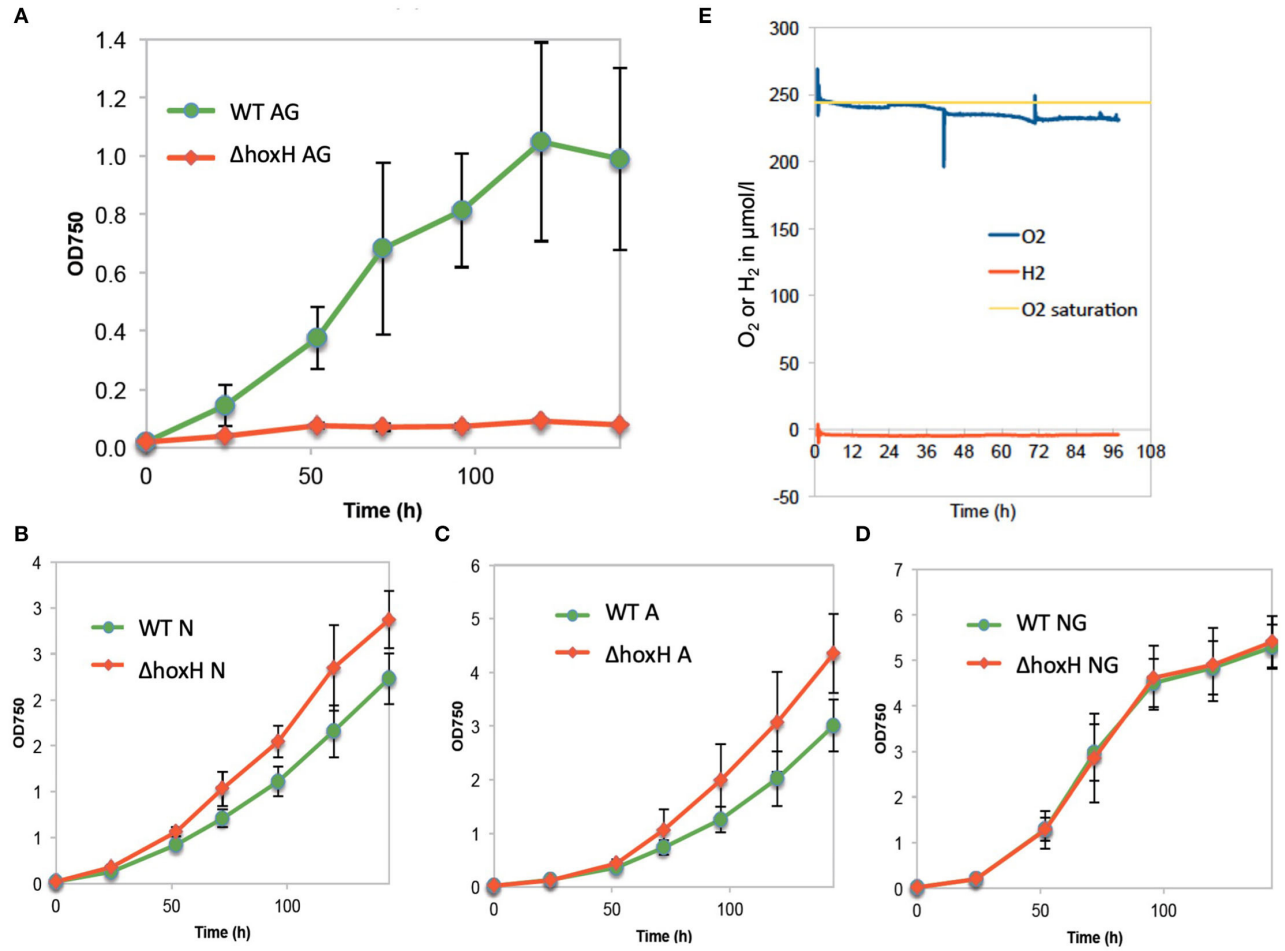

FIGURE 1 | Growth of wild type (WT) and ΔhoxH under different conditions and oxygen and hydrogen concentrations in cultures on arginine and glucose in continuous light (60 µE/m2/s). **(A)** Growth in arginine and glucose (AG), **(B)** growth in nitrate (N), **(C)** growth in arginine (A), **(D)** growth in nitrate and glucose (NG), **(E)** O_2 and H_2 concentration in the cultures cultivated on arginine and glucose.

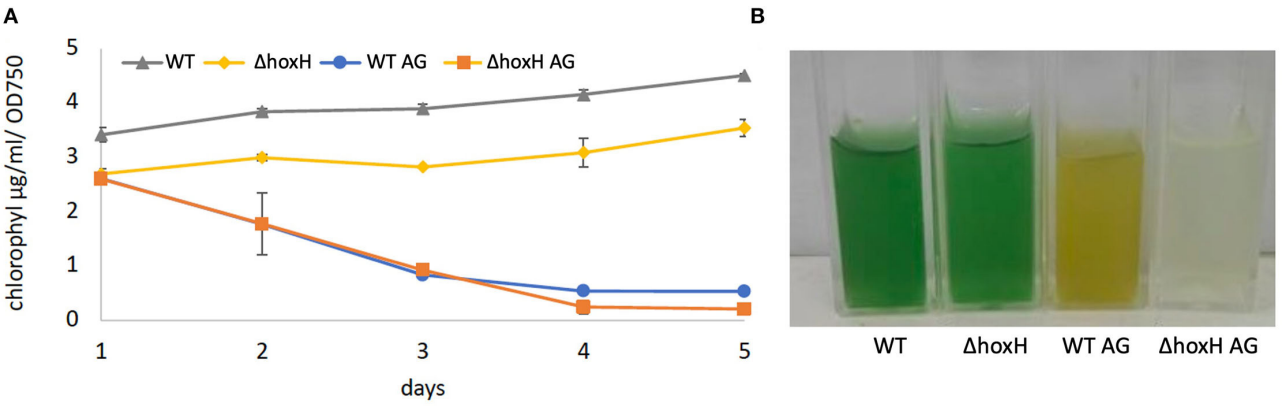

FIGURE 2 | (A) Chlorophyll content of WT and Δ*hoxH* during growth experiments under photoautotrophic conditions and on arginine and glucose. **(B)** The appearance of strains on day 3 after inoculation.

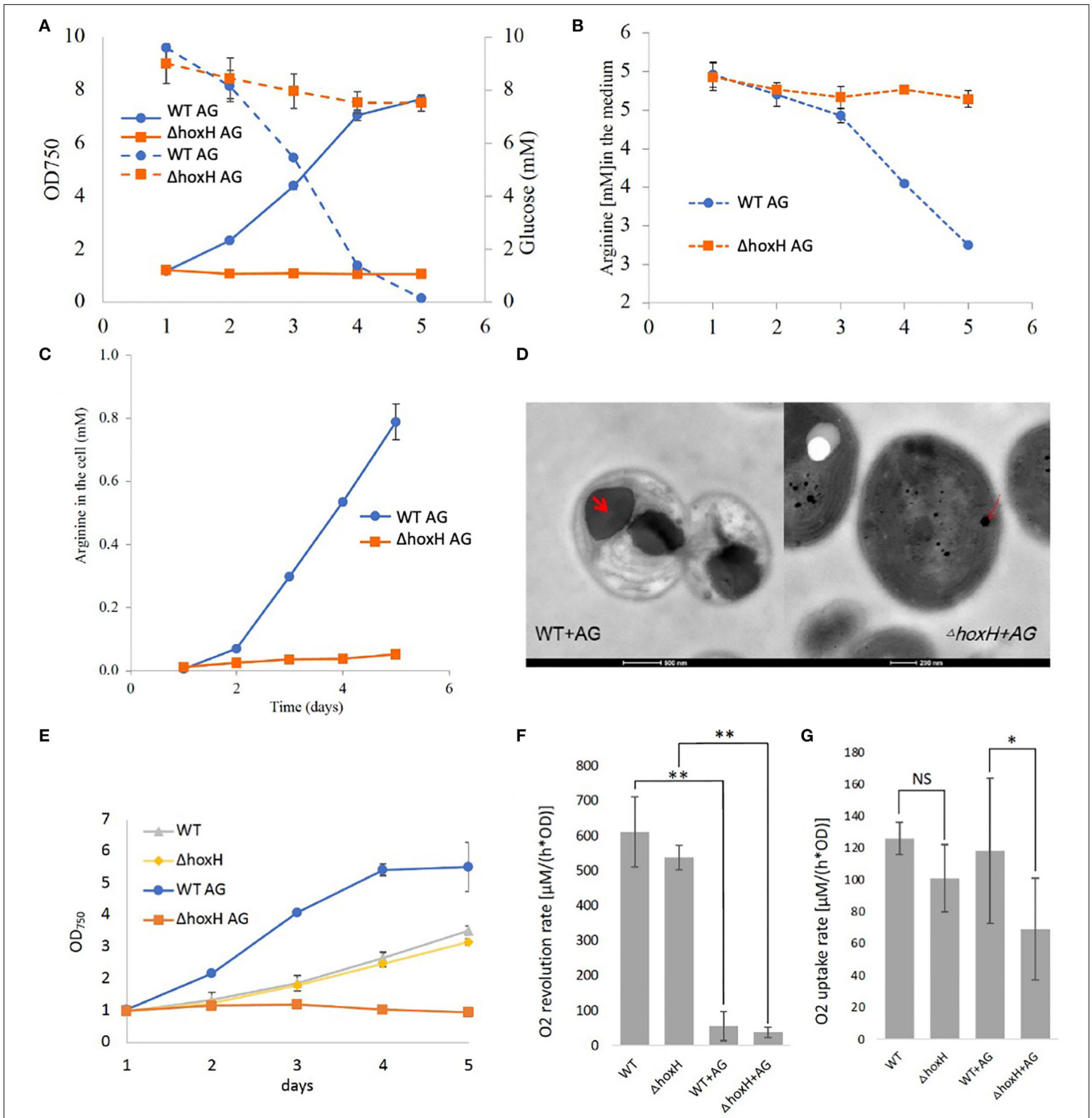

FIGURE 3 | Metabolism and morphology of WT and Δ*hoxH* on arginine and glucose. **(A)** Growth (solid line) and glucose consumption (dotted line). **(B)** Arginine consumption, **(C)** Cyanophycin content of cells displayed as arginine in the cells, **(D)** Transmission electron microscopy (TEM) images of WT and Δ*hoxH* that were cultivated on arginine and glucose. Cyanophycin granules are marked with a red arrow in the WT. **(E)** Growth experiment in which **(F)** dark respiration and **(G)** photosynthesis were determined by O_2 uptake and evolution on days 2–4. Stars on the column diagram indicate differences between mutant and WT by Tukey's HSD test (*$P < 0.05$, **$P < 0.01$). Throughout the figure 'NS' indicates 'not significant'. All error bars indicate standard deviation (s.d.) of four daily independent experiments.

only small amounts of cyanophycin granules. In view of the fact that Δ*hoxH* cells neither consumed glucose nor arginine in large quantities, were unable to grow and showed no morphological changes, it is assumed that Δ*hoxH* cells entered a dormant-like state and were unable to adapt in the same manner as WT cells.

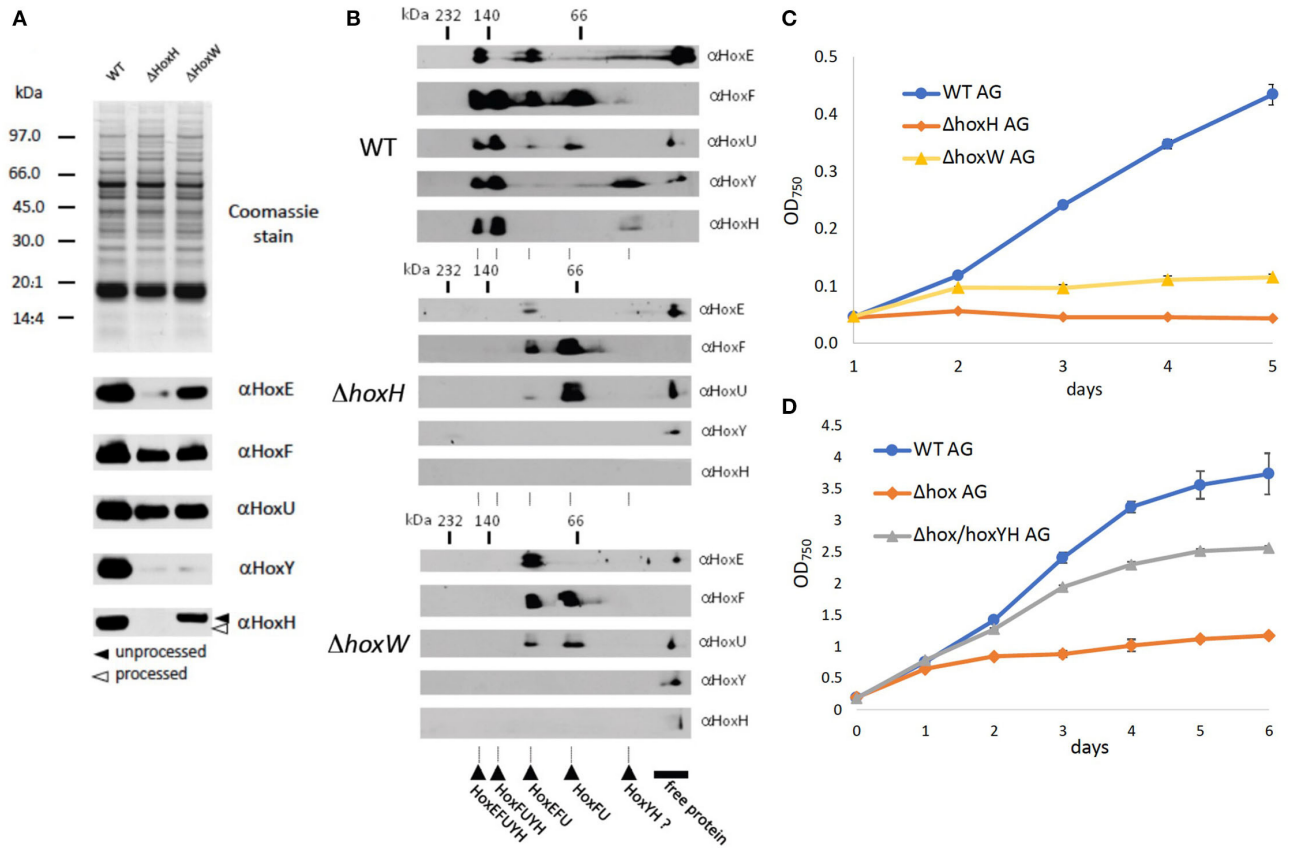

FIGURE 4 | Significance of the diaphorase and the hydrogenase on arginine and glucose. **(A)** SDS page and immunoblots of WT, Δ*hoxH,* and Δ*hoxW* with antibodies against all hox subunits **(B)** 2D Blue Native PAGE of WT, Δ*hoxH,* and Δ*hoxW* with antibodies against all hox subunits. The second dimension allows to check for the assembly of complexes. **(C)** Growth of WT, Δ*hoxH,* and Δ*hoxW* on arginine and glucose. **(D)** Complementation of Δ*hox* with *hoxYH* (Δ*hox*/hoxYH). Growth of WT, Δ*hox/hoxYH,* and Δ*hox* on arginine and glucose.

Importance of Diaphorase (HoxEFU) and Hydrogenase (HoxYH) Moiety on Arginine and Glucose

As no hydrogen was detected and hydrogenase is known to be oxygen-sensitive, one explanation for the function of Hox may be that the diaphorase is critical to growth under oxic conditions on arginine and glucose. To test this, levels of HoxEFU in Δ*hoxH* cell extracts were monitored by immunoblot. We also constructed a mutant strain Δ*hoxW* that is defective in the maturase HoxW that activates HoxH (Eckert et al., 2012). This mutant should in principle contain a fully assembled and functional HoxEFU diaphorase but lack a functional HoxH.

Immunoblots and 2D Blue Native PAGE revealed the presence and assembly of the diaphorase HoxEFU in both the Δ*hoxH* and Δ*hoxW* cells (**Figures 4A,B**). HoxE levels were slightly reduced in the Δ*hoxH* background but were fully present in Δ*hoxW* cells. HoxY levels were very low in both mutants, whereas HoxH was absent in Δ*hoxH* and only present in its unprocessed form in Δ*hoxW* cells (**Figure 4A**). In the WT the most prominent complexes that are visible in the second dimension are HoxEFUYH and HoxFUYH (**Figure 4B**). These complexes are missing in *hoxH* and *hoxW* deletion strains. However, complexes that contain the diaphorase subunits only, namely HoxEFU and HoxFU, are present in the WT and in both mutants.

As the diaphorase was apparently present and assembled in Δ*hoxW,* we tested the growth of this mutant on arginine and glucose and found it to be similar but slightly better than the growth of Δ*hoxH* cells (**Figure 4C**). In addition, when a Δ*hox* mutant, in which *hoxEFUYH* was deleted, was complemented with *hoxYH*, growth improved considerably, but not to WT levels (**Figure 4D**). These results indicate that the hydrogenase (HoxYH) is the critical component and that the diaphorase (HoxEFU) alone cannot support the growth of arginine and glucose. However, we cannot rule out that the holoenzyme of HoxEFUYH is required for the proper functioning of the diaphorase *in vivo*. The fact that the diminished growth of Δ*hox* (Δ*hoxEFUYH*) could be partly rescued by the introduction of *hoxYH*, furthermore, indicates that the hydrogenase indeed fulfills an important function

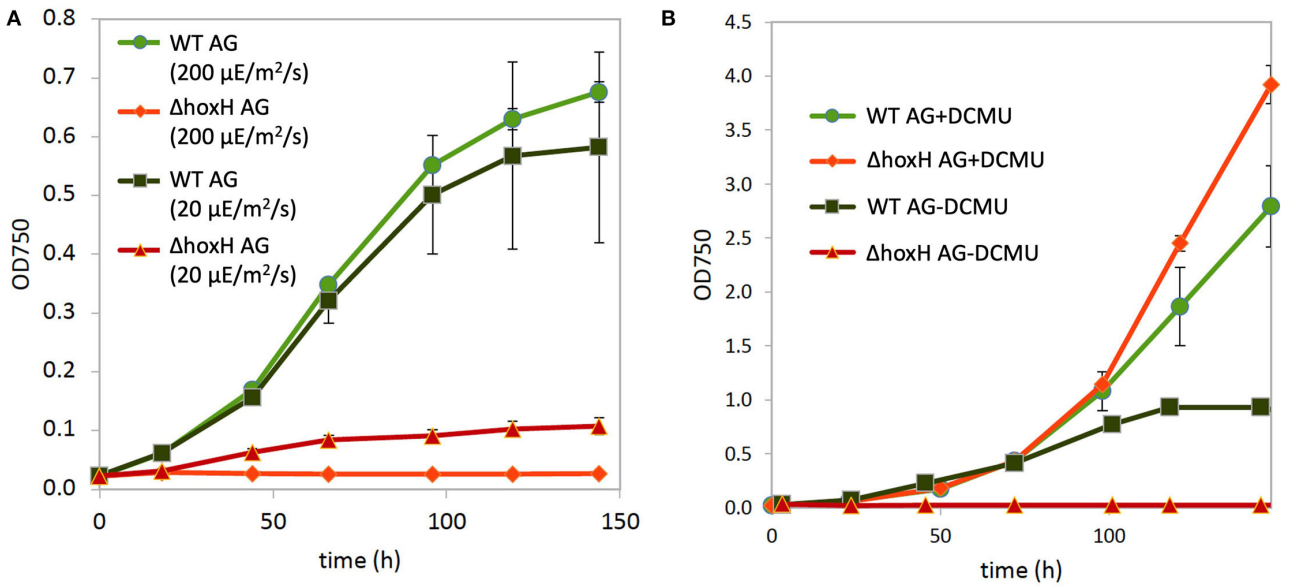

FIGURE 5 | Growth of WT and Δ*hoxH* on arginine and glucose. **(A)** Growth at high light (200 µE/m²/s) and low light (20 µE/m²/s). **(B)** Growth at medium light (60 µE/m²/s) in the absence and presence of the inhibitor DCMU, which blocks electron transfer from PSII to the plastoquinone (PQ) pool.

without the diaphorase under these conditions but that, in contrast, the holoenzyme HoxEFUYH is required for WT-like growth on arginine and glucose.

Transcription and Expression of the Hydrogenase Under Mixotrophic Conditions on Arginine

As the growth of the WT and Δ*hoxH* strains deviates from each other within the first day of cultivation, mRNA was isolated from cells cultured on nitrate (BG11) as control and on arginine and glucose ($BG11_0$AG) at 12, 24, 36, 48, and 72 h after inoculation. In cells cultured on arginine and glucose, the transcription of *hoxH* was upregulated 2-fold after 24 h and 5-fold after 36 h from inoculation (**Supplementary Figure 2A**). The expression levels of the *hoxEFUYH* operon 24 h after inoculation on arginine and glucose revealed that the entire *hox* operon was upregulated (**Supplementary Figure 2B**). Despite increased transcription, protein levels of Hox subunits (HoxE, F, U, Y, H) appeared to be unaffected (**Supplementary Figures 2C,D**).

Does the Hydrogenase Work as an Electron Valve for Photosynthesis on Arginine and Glucose?

Three main sources feed electrons into the PQ pool of the photosynthetic electron transport chain in cultures that are cultivated on arginine and glucose as follows: water splitting at PSII, the oxidation of the carbon skeleton of arginine, and the oxidation of glucose. This might lead to an over-reduced photosynthetic electron transfer chain with a highly reduced PQ pool. Therefore, the hydrogenase might work as an electron valve under these conditions. To test this, WT and Δ*hoxH* cells were cultivated on arginine and glucose under high light (200 µE/m²/s) and under low light (20 µE/m²/s) in order to determine if low light relieves the reductive stress to improve the growth of Δ*hoxH*. The WT strain grew well under both light intensities, whereas Δ*hoxH* which did not grow at all at 200 µE/m²/s but was able to grow under low light at 20 µE/m²/s (**Figure 5A**).

The addition of DCMU, which blocks electron transfer from PSII to the PQ pool, enhanced the growth of WT under medium light intensities (60 µE/m²/s), and the growth of Δ*hoxH* was completely rescued to WT levels (**Figure 6B**). These data show that the requirement for the hydrogenase on arginine and glucose is related to electron transport during photosynthesis.

To test if the hydrogenase has a direct and immediate impact on the photosynthetic electron transfer chain, the reduction and oxidation of plastocyanin (PC), P700, and ferredoxin were monitored upon the addition of arginine and glucose in WT and Δ*hoxH* *via* Dual-KLAS/NIR (**Figure 6**). PC and P700 are oxidized in WT and Δ*hoxH* at the onset of illumination (**Figures 6A–D**). Under photoautotrophic conditions, the first oxidation peak is reached ∼100 ms into the light pulse and is followed by a transient phase of stronger reduction of PC and P700 (**Figure 6A**). The reduction is caused by electrons coming in from PSII due to the reduced electron acceptor pool (Fdx and $NADP^+$) of PSI. After another 200 ms, this reduction phase reverts, and oxidation predominates again before the light is turned off after 600 ms (Theune et al., 2021). This second oxidation phase is governed by the activity of the flavodiiron proteins (mainly Flv1/3) that catalyze oxygen reduction at the acceptor side of PSI. In the absence of the flavodiiron proteins, this phase is missing (refer to **Figure 7B**) (SÈtif et al., 2020). In Δ*hoxH*, the reduction phase is faster and deeper for PC and

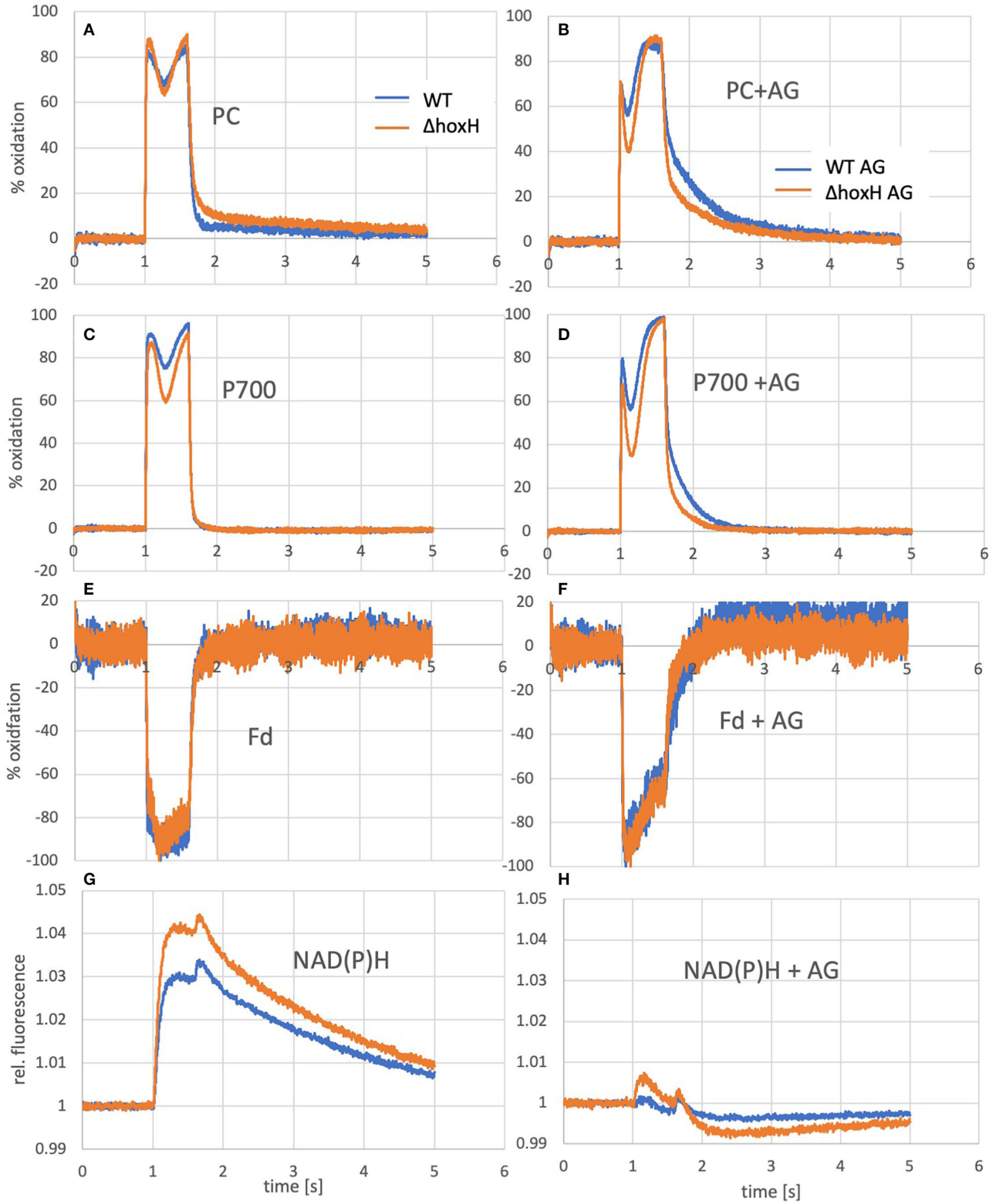

FIGURE 6 | Oxidation of PC and P700 and reduction of ferredoxin and NADPH of WT and Δ*hoxH* cultures as measured by the Dual-KLAS/NIR. On the left **(A, C, E, G)**, curves of cultures grown photoautotrophically are shown and on the right **(B, D, F, H)**, the same cultures are shown that were measured a few minutes after the addition of arginine and glucose.

P700 in contrast to the WT. This effect is more pronounced in the presence of arginine and glucose (**Figures 6B,D**). The first peak of oxidation becomes narrower and is reached after only 35 ms before reduction becomes stronger. Δ*hoxH* shows a deeper reduction trough in the light phase and a faster reduction in the dark phase. The mutant obviously suffers from a stronger acceptor side limitation. This is noticeable when comparing the reduction curves of NAD(P)H (**Figures 6G,H**). Under autotrophic conditions, NAD(P)H fluorescence shows a large increase in illumination, but in the presence of arginine and glucose, this peak is negligible. This indicates that the NAD(P)H pool is already mainly reduced on arginine and glucose. The same was observed for the ferredoxin pool, which was instantly fully reduced upon illumination on arginine and glucose (**Figures 6E,F**). Taken together, these data show that the hydrogenase works as a transient electron valve in an immediate response to the addition of organic carbon and nitrogen in the presence of oxygen.

However, as no hydrogen was traceable, the hypothesis was put forward that the hydrogenase might release electrons from the photosynthetic electron transport chain by reducing oxygen instead of protons. According to the current understanding, Ni and Fe in the active site of the hydrogenase are inactivated in the presence of oxygen by the formation of a bridging hydroxy group which prevents H_2-turnover (Pandelia et al., 2010; McIntosh et al., 2011; Caserta et al., 2020). The oxygen tolerance of the soluble NiFe-hydrogenase of *Ralstonia eutropha* is based on its oxidase activity which reactivates the enzyme by reducing the bound hydroxyl group to water (Lauterbach and Lenz, 2013). Based on this finding, the hypothesis was put forward that the oxygen-sensitive NiFe-hydrogenase of *Synechocystis* might also function as an oxidase and switch between H_2 production under anaerobic conditions and oxygen reduction under aerobic conditions. To test this hypothesis, two mutants were constructed. The first one lacked all of the terminal oxidases that are associated with the thylakoid membrane, namely, the respiratory terminal oxidase cytochrome C oxidase (*cyd*) and quinol oxidase (*cox*) but retained the alternative respiratory oxidase (*arto; ctaII*). In addition, flavodiiron proteins, namely, Flv2, Flv4, and Flv3, which have the potential to reduce oxygen, were deleted (Shimakawa et al., 2014; Brown et al., 2019). This resulted in the mutant strain Δ*flv24*Δ*flv3*Δ*cox*Δ*cyd*. The second mutant was the same as the first but also lacked the *hox* operon (*hoxEFUYH*), yielding the mutant strain Δ*flv24*Δ*flv3*Δ*cox*Δ*cyd*Δ*hox* (note that in this strain, the entire *hox* operon instead of *hoxH* was deleted). The redox status of photosynthetic components [plastocyanin (PC), P700 in PSI, and ferredoxin] were measured in these mutants and compared with the WT strain cultured on arginine and glucose on the second day after inoculation in the absence and in the presence of oxygen *via* Dual-KLAS/NIR (**Figure 7**). If the hydrogenase is functioning as an oxidase and transferring surplus electrons to oxygen, it was expected that the deletion of *hoxEFUYH* would result in more reduced photosynthetic components in the presence of oxygen. However, the ferredoxin pool and P700 were more reduced in Δ*flv24*Δ*flv3*Δ*cox*Δ*cyd* in comparison to Δ*flv24*Δ*flv3*Δ*cox*Δ*cyd*Δ*hox* indicating that acceptor side limitation at PSI was more severe in the presence of the hydrogenase (**Figures 7A–D**). Thus, our measurements show that the hydrogenase does not function as an oxidase.

We then examined the PSII fluorescence properties of WT and Δ*hoxH* cells cultured over a 5-day period on nitrate, or on arginine plus glucose, in order to monitor the redox state of the PQ pool. Both strains exhibited a similar PQ pool redox poise when cultivated on nitrate. When cultured on arginine plus glucose, the PQ pools of both strains were more reduced than in cells cultured on nitrate, becoming more pronounced in WT cells later in growth (**Figure 7G**). These data are well in line with the Dual-KLAS/NIR measurements during the growth on organic carbon and nitrogen in WT, Δ*flv24*Δ*flv3*Δ*cox*Δ*cyd,* and Δ*flv24*Δ*flv3*Δ*cox*Δ*cyd*Δ*hox* (**Figures 7A–F**). The fact that components of the photosynthetic electron transfer chain were more reduced in the WT in comparison to Δ*hoxH* on arginine and glucose (**Figure 7G**) is comprehensible considering that Δ*hoxH* did neither metabolize arginine nor glucose in large amounts and furthermore paused growth (**Figure 3**). Taken together, the results indicate that in the immediate response to the growth on arginine and glucose, the hydrogenase functions to dissipate electrons (**Figure 6**), however, in the long run for hours and days, hydrogenase supports feeding electrons into the PQ pool under these conditions, suggesting it has a dual function.

Significance of Components of the Respiratory Electron Chain for Growth on Arginine and Glucose

To evaluate the significance of components of the respiratory electron transfer chain for the growth on arginine and glucose, additional deletion mutants were constructed and tested. *Synechocystis* possesses three respiratory terminal oxidases: the quinol oxidase (*cox*) is localized in thylakoid membranes, cytochrome C oxidase (*cyd*) is localized in the thylakoid and cytoplasmic membranes, and the alternative respiratory oxidase (*arto*) is restricted to the cytoplasmic membranes (**Figure 8A**). Deletion of both thylakoid-associated oxidases (Δ*cyd*Δ*cox*) or all three of the terminal oxidases (Δ*cyd*Δ*cox*Δ*arto*) resulted in mutants that were still able to grow on arginine and glucose albeit at impaired rates (**Figure 8B**).

Three main respiratory dehydrogenases feed electrons from glucose oxidation into the PQ pool in *Synechocystis*: photosynthetic complex I (NDH-1) accepts electrons from reduced ferredoxin (Schuller et al., 2019), NDH-2 accepts electrons from NADH, and the succinate dehydrogenase (SDH) catalyzes the oxidation from succinate to fumarate. In the Δ*ndh2* mutant strain, all three homologs *ndbA/ndbB/ndbC* of the NADH dehydrogenase-like complex 2 (NDH2; *slr0851*, *slr1743*, and *sll1484*) were deleted. In the Δ*sdh* mutant, the two subunits *sdh1* and *sdh2* of the succinate dehydrogenase (SDH; *sll1625*, and *sll0823*)) were deleted. Additionally, in the Δ*ndh1* mutant, the subunits *ndh-D1* and *ndh-D2* of complex 1 (NDH1; *slr0331*, and *slr1291*) were deleted. Growth of all three mutant strains was impaired on arginine and glucose (**Figure 8C**), where the severest impairment was observed for Δ*ndh1* followed by

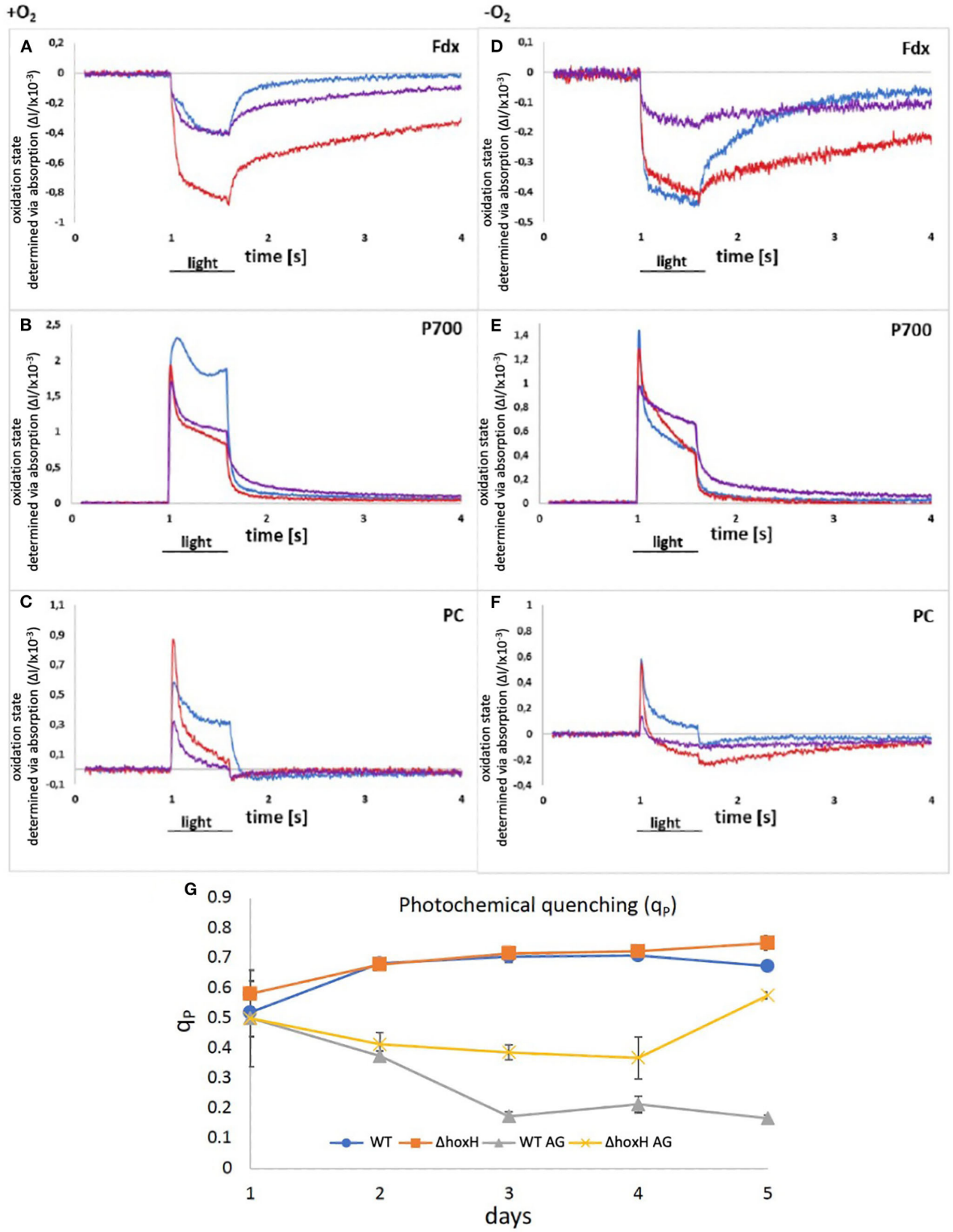

FIGURE 7 | (A–F) Redox states of components of the photosynthetic electron chain on arginine and glucose in the presence and absence of oxygen in WT, *Δflv24Δflv3Δcox Δcyd, and Δflv24Δflv3Δcox Δcyd Δhox.* The oxidation state was measured as absorption change ($\Delta I/I \times 10^{-3}$). Positive values show oxidation and negative values show a reduction of components. **(G)** Photochemical quenching (q_P) in WT and Δ*hoxH* on nitrate (WT and Δ*hoxH*) and on arginine and glucose (WT AG and Δ*hoxH* AG).

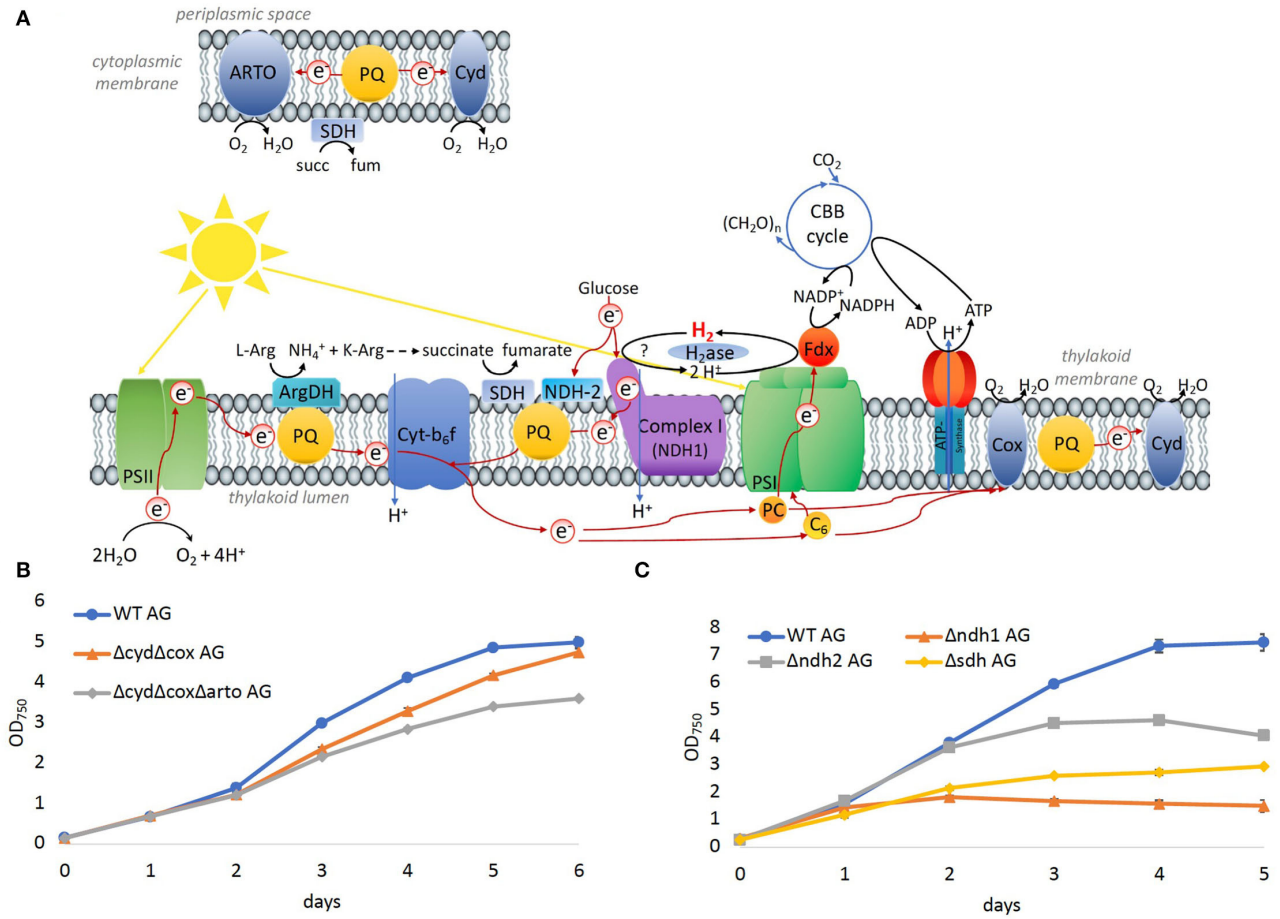

FIGURE 8 | Significance of the respiratory electron chain for growth on arginine and glucose. **(A)** Overview of photosynthetic and respiratory electrons chains in the thylakoid and cytoplasmic membrane. **(B)** Growth of WT and mutants in which terminal oxidases were deleted on arginine and glucose. **(C)** Growth of WT and dehydrogenases, that feed electrons into the PQ pool on arginine and glucose.

Δ*sdh*. Thus, the terminal oxidases appeared to be dispensable for growth on arginine and glucose, whereas SDH has a significant role, and hydrogenase and NDH-1 are essential.

DISCUSSION

An obvious question that suggests itself is why the bidirectional NiFe-hydrogenase, which is an oxygen-sensitive enzyme, is widespread in organisms that produce oxygen and rarely encounter anoxic conditions. Its presence has been regarded as a leftover from ancient times. However, the ancestors of cyanobacteria possessed several NiFe- and FeFe-hydrogenases (types 2a, 3b, 3c, 3d, and 4), whereas cyanobacteria kept only two NiFe-hydrogenases: the uptake NiFe-hydrogenase (type 2a) in association with N_2 fixation and the bidirectional NiFe-hydrogenase (type 3d) (Vignais and Billoud, 2007). The advantage for the uptake of hydrogenase, which consumes H_2, which is a by-product of N_2 fixation, is apparent. But why was the bidirectional enzyme kept? Cyanobacteria in microbial mats, in fact, encounter anoxic conditions at night due to intense respiration within the microbial mat community and produce fermentative hydrogen in darkness and photohydrogen on illumination (Burow et al., 2012a,b; Bolhuis et al., 2014; Nielsen et al., 2015). The function of the cyanobacterial bidirectional NiFe-hydrogenase is thus well-understood in microbial mats. However, the enzyme is also widespread in cyanobacteria from surface waters that stay oxygenated also at night (Barz et al., 2010; Beimgraben et al., 2014; Greening et al., 2015). Remarkably, it is absent from oligotrophic habitats as the open ocean but is found in freshwater and coastal waters that have a higher load of nutrients and occasionally encounter phytoplankton blooms (Barz et al., 2010). Excretion and lysis of organisms in senescent phytoplankton blooms and the bacterial breakdown of organic carbon to shorter sugars create mixotrophic conditions in these habitats that are typically accompanied by increased levels of dissolved organic nitrogen as arginine (Wetz and Wheeler, 2003, 2004; Teeling et al., 2012). The replacement of nitrate with arginine and addition of glucose in this study thus

somewhat mimics the situation of a senescent phytoplankton bloom in habitats where cyanobacterial NiFe-hydrogenases are found. The presented data indicate strongly that the hydrogenase has a function under oxic conditions which are most likely not based on hydrogen turnover but linked to photosynthesis and respiration to support a metabolic switch for growth in the presence of organic carbon and nitrogen. Please note that the concentrations of glucose and arginine that were utilized in this study are above those levels found in nature. We thus created artificial laboratory conditions so that the comparison with natural conditions must be performed cautiously. We did not find any evidence for the hypothesis that the hydrogenase works as an oxidase or functions as an electron valve during long-term growth. Rather, our results indicate that the hydrogenase supports to feed electrons into the photosynthetic electron transport chain. Since the Δ*hoxH* mutant does not consume significant amounts of glucose and arginine, it is not clear whether the hydrogenase is actively involved in feeding electrons into the photosynthetic electron transport chain in the WT, or if its absence in Δ*hoxH* rather prevents a metabolic switch and thereby results in less reduced photosynthetic components. The functional significance of hydrogenase is most likely linked to the tuning of the light reactions of photosynthesis (**Figure 5**). For example, *Synechocystis* possesses various complexes that fine-tune the intersystem electron transport chain including flavodiiron proteins, respiratory dehydrogenases, and terminal oxidases. Our results in this study demonstrate that most of these were dispensable for the growth on arginine and glucose and raise the question as to why hydrogenase is essential.

In-vitro experiments have revealed that the hydrogenase HoxEFU diaphorase sub-complex is able to exchange electrons between NAD(H), NAD(P)H, several ferredoxins and flavodoxin (Artz et al., 2020). This is a unique property of HoxEFU in having reactivity with more than four redox carriers. In contrast, FNR shuttles electrons between NADPH and ferredoxin, and the transhydrogenase (PntAB) transfers electrons from NADH to $NADP^+$ (Kämäräinen et al., 2016). Although the hydrogenase catalytic subunits, HoxYH, were not required for the HoxEFU activity with redox carriers *in vitro*, it cannot be ruled out that this function requires the presence of the HoxYH subunits *in vivo*. The data presented in this study add another dimension to Hox function by demonstrating that the hydrogenase subunit HoxH, but not the hydrogen reactivity of HoxH, is required for electron exchange with the PQ pool in cells grown on arginine and glucose. As the photosynthetic complex I was likewise required for growth on organic carbon and nitrogen, it is possible that the hydrogenase transfers electrons *via* NDH-1 into the PQ pool. This idea is further supported by the fact that respiration was diminished in Δ*hoxH* cells in comparison to the WT cells (**Figure 3F**). It has been shown that the cyanobacterial NDH-1 complex accepts electrons exclusively from reduced ferredoxin (Schuller et al., 2019). It is conceivable that the Hox hydrogenase complex might mediate an input of electrons *via* the NDH-1 complex into the photosynthetic electron transport chain and thereby tune photosynthesis and respiration in the presence of organic carbon and nitrogen. However, this idea requires further experimental support.

CONCLUSION

The cyanobacterial bidirectional NiFe-hydrogenase of *Synechocystis* is required for growth on organic carbon and nitrogen in the presence of oxygen and fulfills a function apart from hydrogen turnover. Its presence has an impact on the redox states of photosynthetic components in the presence of oxygen. It acts as an electron valve as an immediate response to the supply of arginine and glucose. The enzyme does not work as an oxidase and it does not have the role to dissipate electrons during long-term growth. Rather, hydrogenase supports the input of electrons into the photosynthetic electron transport chain. In the presence of the hydrogenase, *Synechocystis* performs a metabolic switch, which allows cells to grow on arginine and glucose but enters a dormant-like state in its absence. The exact manner by which hydrogenase influences the thylakoid membrane's electron transport chain remains unresolved. Our observations support a model for the more global occurrence of a bidirectional NiFe-hydrogenase in cyanobacteria that were found predominantly in oxygenated surface waters of nutrient-rich habitats. Its unique ability to shuttle electrons between NAD(H), NADP(H), ferredoxins, and flavodoxin might help to mediate an input of electrons *via* the NDH-1 complex into the photosynthetic electron chain. However, this view requires further experimental evidence.

DATA AVAILABILITY STATEMENT

The original contributions presented in the study are included in the article/**Supplementary Material**, further inquiries can be directed to the corresponding author/s.

AUTHOR CONTRIBUTIONS

HB, YW, JC, VH, JA, MB, SL, and MT performed experiments. HB, YW, JA, and KG contributed to conception and design of the study. HB, YW, JC, VH, JA, MB, SL, MT, PK, and KG analyzed and interpreted data. HB, YW, VH, and KG wrote the first draft of the manuscript. All authors contributed to manuscript revision, read, and approved the submitted version.

FUNDING

This study was supported by grants from the China Scholarship Council (CSC) (Grant # 201406320187), the German Ministry of Science and Education (BMBF FP309), and the German Science Foundation (DFG GU1522/2-1, GU1522/5-1, and FOR2816).

ACKNOWLEDGMENTS

We thank Cay Kruse for assistance with microscopy and the lab of Karl Forchhammer for help with the quantification of cyanophycin.

SUPPLEMENTARY MATERIAL

The Supplementary Material for this article can be found online at: https://www.frontiersin.org/articles/10.3389/fmicb.2022.896190/full#supplementary-material

REFERENCES

Appel, J., Hueren, V., Boehm, M., and Gutekunst, K. (2020). Cyanobacterial *in vivo* solar hydrogen production using a photosystem I–hydrogenase (PsaD-HoxYH) fusion complex. *Nat. Energy* 5, 458–467. doi: 10.1038/s41560-020-0609-6

Appel, J., Phunpruch, S., Steinmüller, K., and Schulz, R. (2000). The bidirectional hydrogenase of Synechocystis sp. PCC 6803 works as an electron valve during photosynthesis. *Arch. Microbiol.* 173, 333–338. doi: 10.1007/s002030000139

Artz, J. H., Tokmina-Lukaszewska, M., Mulder, D. W., Lubner, C. E., Gutekunst, K., Appel, J., et al. (2020). The structure and reactivity of the HoxEFU complex from the cyanobacterium Synechocystis sp. PCC 6803. *J. Biol. Chem.* 295, 9445–9454. doi: 10.1074/jbc.RA120.013136

Barz, M., Beimgraben, C., Staller, T., Germer, F., Opitz, F., Marquardt, C., et al. (2010). Distribution analysis of hydrogenases in surface waters of marine and freshwater environments. *PLoS ONE* 5, e13846. doi: 10.1371/journal.pone.0013846

Beimgraben, C., Gutekunst, K., Opitz, F., and Appel, J. (2014). hypD as a marker for [NiFe]-hydrogenases in microbial communities of surface waters. *Appl. Environ. Microbiol.* 80, 3776. doi: 10.1128/AEM.00690-14

Boehm, M., Nield, J., Zhang, P., Aro, E.-M., Komenda, J., and Nixon, P. J. (2009). Structural and mutational analysis of band 7 proteins in the cyanobacterium Synechocystis sp. strain PCC 6803. *J. Bacteriol.* 191, 6425–6435. doi: 10.1128/JB.00644-09

Bolhuis, H., Cretoiu, M. S., and Stal, L. J. (2014). Molecular ecology of microbial mats. *FEMS Microbiol. Ecol.* 90, 335. doi: 10.1111/1574-6941.12408

Brown, K. A., Guo, Z., Tokmina-Lukaszewska, M., Scott, L. W., Lubner, C. E., Smolinski, S., et al. (2019). The oxygen reduction reaction catalyzed by Synechocystis sp. PCC 6803 flavodiiron proteins. *Sustain. Energy Fuels* 3, 3191–3200. doi: 10.1039/C9SE00523D

Burow, L. C., Woebken, D., Bebout, B. M., McMurdie, P. J., Singer, S. W., Pett-Ridge, J., et al. (2012a). Hydrogen production in photosynthetic microbial mats in the Elkhorn Slough estuary, Monterey Bay. *ISME J.* 6, 863–874. doi: 10.1038/ismej.2011.142

Burow, L. C., Woebken, D., Marshall, I. P. G., Lindquist, E. A., Bebout, B. M., Prufert-Bebout, L., et al. (2012b). Anoxic carbon flux in photosynthetic microbial mats as revealed by metatranscriptomics. *ISME J.* 7, 1–13. doi: 10.1038/ismej.2012.150

Burroughs, N. J., Boehm, M., Eckert, C., Mastroianni, G., Spence, E. M., Yu, J., et al. (2014). Solar powered biohydrogen production requires specific localization of the hydrogenase. *Energy Environ. Sci.* 7, 3791–3800. doi: 10.1039/C4EE02502D

Caserta, G., Pelmenschikov, V., Lorent, C., Tadjoung Waffo, A. F., Katz, S., Lauterbach, L., et al. (2020). Hydroxy-bridged resting states of a [NiFe]-hydrogenase unraveled by cryogenic vibrational spectroscopy and DFT computations. *Chem. Sci.* 12, 2189–2197. doi: 10.1039/D0SC05022A

Cournac, L., Guedeney, G., Peltier, G., and Vignais, P. M. (2004). Sustained photoevolution of molecular hydrogen in a mutant of *Synechocystis* sp. strain PCC 6803 deficient in the Type I NADPH-dehydrogenase complex. *J Bacteriol.* 186, 1737–1746. doi: 10.1128/JB.186.6.1737-1746.2003

Dutta, I., and Vermaas, W. F. J. (2016). The electron transfer pathway upon H2 oxidation by the NiFe bidirectional hydrogenase of *Synechocystis* sp. PCC 6803 in the light shares components with the photosynthetic electron transfer chain in thylakoid membranes. *Int. J. Hydrogen Energy* 41, 11949–11959. doi: 10.1016/j.ijhydene.2016.01.172

Eckert, C., Boehm, M., Carrieri, D., Yu, J., Dubini, A., Nixon, P. J., et al. (2012). Genetic analysis of the hox hydrogenase in the cyanobacterium *Synechocystis* sp. PCC 6803 reveals subunit roles in association, assembly, maturation, and function. *J. Biol. Chem.* 287, 43502–43515. doi: 10.1074/jbc.M112.392407

Elbahloul, Y., Krehenbrink, M., Reichelt, R., and Steinbüchel, A. (2005). Physiological conditions conducive to high cyanophycin content in biomass of *Acinetobacter calcoaceticus* strain ADP1. *Appl. Environ. Microbiol.* 71, 858–866. doi: 10.1128/AEM.71.2.858-866.2005

Flores, E., and Herrero, A. (1994). "Assimilatory nitrogen metabolism and its regulation," in *The Molecular Biology of Cyanobacteria*, ed D. A. Bryant (Dordrecht: Springer Netherlands), 487–517.

Forchhammer, K., and Selim, K. A. (2020). Carbon/nitrogen homeostasis control in cyanobacteria. *FEMS Microbiol. Rev.* 44, 33–53. doi: 10.1093/femsre/fuz025

Gibson, D. G., Young, L., Chuang, R.-Y., Venter, J. C., Hutchison, C. A., and Smith, H. O. (2009). Enzymatic assembly of DNA molecules up to several hundred kilobases. *Nat. Methods* 6, 343–345. doi: 10.1038/nmeth.1318

Greening, C., Biswas, A., Carere, C. R., Jackson, C. J., Taylor, M. C., Stott, M. B., et al. (2015). Genomic and metagenomic surveys of hydrogenase distribution indicate H2 is a widely utilised energy source for microbial growth and survival. *ISME J.* 10, 1–17. doi: 10.1038/ismej.2015.153

Gutekunst, K., Chen, X., Schreiber, K., Kaspar, U., Makam, S., and Appel, J. (2014). The Bidirectional NiFe-hydrogenase in Synechocystis sp. PCC 6803 is reduced by flavodoxin and ferredoxin and is essential under mixotrophic, nitrate-limiting conditions. *J. Biol. Chem.* 289, 1930–1937. doi: 10.1074/jbc.M113.526376

H. K. Lichtenthaler (1987). Chlorophylls and carotenoids: Pigments of photosynthetic biomembranes. *Methods in Enzymol.* 148, 350–382. doi: 10.1016/0076-6879(87)48036-1

Kämäräinen, J., Huokko, T., Kreula, S., Jones, P. R., Aro, E.-M., and Kallio, P. (2016). Pyridine nucleotide transhydrogenase PntAB is essential for optimal growth and photosynthetic integrity under low-light mixotrophic conditions in *Synechocystis* sp. PCC 6803. *New Phytol.* 214. doi: 10.1111/nph.14353

Klughammer, C., and Schreiber, U. (2016). Deconvolution of ferredoxin, plastocyanin, and P700 transmittance changes in intact leaves with a new type of kinetic LED array spectrophotometer. *Photosyn. Res.* 128, 195–214. doi: 10.1007/s11120-016-0219-0

Lauterbach, L., and Lenz, O. (2013). Catalytic production of hydrogen peroxide and water by oxygen-tolerant [NiFe]-hydrogenase during H2 cycling in the presence of O2. *J. Am. Chem. Soc.* 135, 17897–17905. doi: 10.1021/ja408420d

Lea-Smith, D. J., Bombelli, P., Vasudevan, R., and Howe, C. J. (2016). Photosynthetic, respiratory and extracellular electron transport pathways in cyanobacteria. *Biochim. Biophys. Acta Bioenerget.* 1857, 247–255. doi: 10.1016/j.bbabio.2015.10.007

Livak, K. J., and Schmittgen, T. D. (2001). Analysis of relative gene expression data using real-time quantitative PCR and the 2(-Delta Delta C(T)) Method. *Methods* 25, 402–408. doi: 10.1006/meth.2001.1262

Makowka, A., Nichelmann, L., Schulze, D., Spengler, K., Wittmann, C., Forchhammer, K., et al. (2020). Glycolytic shunts replenish the calvin–benson–bassham cycle as anaplerotic reactions in cyanobacteria. *Mol. Plant.* 13, 471–482. doi: 10.1016/j.molp.2020.02.002

McIntosh, C. L., Germer, F., Schulz, R., Appel, J., and Jones, A. K. (2011). The [NiFe]-hydrogenase of the cyanobacterium Synechocystis sp. PCC 6803 works bidirectionally with a bias to H2 production. *J. Am. Chem. Soc.* 133, 11308–11319. doi: 10.1021/ja203376y

Messineo, L. (1966). Modification of the Sakaguchi reaction: Spectrophotometric determination of arginine in proteins without previous hydrolysis. *Arch. Biochem. Biophys.* 117, 534–540. doi: 10.1016/0003-9861(66)90094-4

Mullineaux, C. W. (2014). Co-existence of photosynthetic and respiratory activities in cyanobacterial thylakoid membranes. *Biochim. Biophys. Acta Bioenerget.* 1837, 503–511. doi: 10.1016/j.bbabio.2013.11.017

Nielsen, M., Revsbech, N. P., and Kühl, M. (2015). Microsensor measurements of hydrogen gas dynamics in cyanobacterial microbial mats. *Front. Microbiol.* 6, 726. doi: 10.3389/fmicb.2015.00726

Pandelia, M.-E., Ogata, H., and Lubitz, W. (2010). Intermediates in the catalytic cycle of [NiFe] hydrogenase: functional spectroscopy of the active site. *Chemphyschem* 11, 1127–1140. doi: 10.1002/cphc.200900950

Schriek, S., Kahmann, U., Staiger, D., Pistorius, E. K., and Michel, K.-P. (2009). Detection of an L-amino acid dehydrogenase activity in Synechocystis sp. PCC 6803. *J. Exp. Bot*. 60, 1035–1046. doi: 10.1093/jxb/ern352

Schriek, S., Rückert, C., Staiger, D., Pistorius, E. K., and Michel, K.-P. (2007). Bioinformatic evaluation of L-arginine catabolic pathways in 24 cyanobacteria and transcriptional analysis of genes encoding enzymes of L-arginine catabolism in the cyanobacterium *Synechocystis* sp. PCC 6803. *BMC Genom*. 8, 437. doi: 10.1186/1471-2164-8-437

Schuller, J. M., Birrell, J. A., Tanaka, H., Konuma, T., Wulfhorst, H., Cox, N., et al. (2019). Structural adaptations of photosynthetic complex I enable ferredoxin-dependent electron transfer. *Science* 363, 257–260. doi: 10.1126/science.aau3613

SÈtif, P., Shimakawa, G., Krieger-Liszkay, A., and Miyake, C. (2020). Identification of the electron donor to flavodiiron proteins in Synechocystis sp. PCC 6803 by *in vivo* spectroscopy. *Biochim. Biophys. Acta Bioenerget*. 1861:148256. doi: 10.1016/j.bbabio.2020.148256

Shimakawa, G., Shaku, K., Nishi, A., Hayashi, R., Yamamoto, H., Sakamoto, K., et al. (2014). Flavodiiron 2 and 4 proteins mediate an oxygen-dependent alternative electron flow in *Synechocystis* sp. PCC 6803 under CO2-limited conditions. *Plant Physiol*. 167, 472–480. doi: 10.1104/pp.114.249987

Stephan, D. P., Ruppel, H. G., and Pistorius, E. K. (2000). Interrelation between cyanophycin synthesis, l-arginine catabolism and photosynthesis in the cyanobacterium *Synechocystis* Sp. strain PCC 6803. *Zeitschrift Naturforschung* 55, 927–942. doi: 10.1515/znc-2000-11-1214

Teeling, H., Fuchs, B. M., Becher, D., Klockow, C., Gardebrecht, A., Bennke, C. M., et al. (2012). Substrate-controlled succession of marine bacterioplankton populations induced by a phytoplankton bloom. *Science* 336, 608–611. doi: 10.1126/science.1218344

Theune, M. L., Hildebrandt, S., Steffen-Heins, A., Bilger, W., Gutekunst, K., and Appel, J. (2021). *In-vivo* quantification of electron flow through photosystem I – Cyclic electron transport makes up about 35% in a cyanobacterium. *Biochim. Biophys. Acta Bioenerget*. 1862, 148353. doi: 10.1016/j.bbabio.2020.148353

Trautmann, D., Voss, B., Wilde, A., Al-Babili, S., and Hess, W. R. (2012). Microevolution in cyanobacteria: re-sequencing a motile substrain of *Synechocystis* sp. PCC 6803. *DNA Res*. 19, 435–448. doi: 10.1093/dnares/dss024

van Kooten, O., and Snel, J. F. H. (1990). The use of chlorophyll fluorescence nomenclature in plant stress physiology. *Photosyn. Res*. 25, 147–150. doi: 10.1007/BF00033156

Vignais, P. M., and Billoud, B. (2007). Occurrence, classification, and biological function of hydrogenases: an overview. *Chem. Rev*. 107, 4206–4272. doi: 10.1021/cr050196r

Wang, Y., Chen, X., Spengler, K., Terberger, K., Boehm, M., Appel, J., et al. (2022). Pyruvate:ferredoxin oxidoreductase and low abundant ferredoxins support aerobic photomixotrophic growth in cyanobacteria. *Elife* 11, e71339. doi: 10.7554/eLife.71339

Wetz, M. S., and Wheeler, P. A. (2003). Production and partitioning of organic matter during simulated phytoplankton blooms. *Limnol. Oceanogr*. 48, 1808–1817. doi: 10.4319/lo.2003.48.5.1808

Wetz, M. S., and Wheeler, P. A. (2004). Response of bacteria to simulated upwelling phytoplankton blooms. *Mar. Ecol. Prog. Ser*. 272, 49–57. doi: 10.3354/meps272049

Williams, J. G. K. (1988). "Construction of specific mutations in photosystem II photosynthetic reaction center by genetic engineering methods in Synechocystis 6803," in *Methods in Enzymology* (Academic Press), 167, 766–778. doi: 10.1016/0076-6879(88)67088-1

Conflict of Interest: The authors declare that the research was conducted in the absence of any commercial or financial relationships that could be construed as a potential conflict of interest.

Publisher's Note: All claims expressed in this article are solely those of the authors and do not necessarily represent those of their affiliated organizations, or those of the publisher, the editors and the reviewers. Any product that may be evaluated in this article, or claim that may be made by its manufacturer, is not guaranteed or endorsed by the publisher.

frontiers | Frontiers in Microbiology

TYPE Original Research
PUBLISHED 24 August 2022
DOI 10.3389/fmicb.2022.991123

OPEN ACCESS

EDITED BY
Chris Greening,
Monash University,
Australia

REVIEWED BY
Quanyu Zhao,
Nanjing Tech University,
China
Benjamin Duffus,
University of Potsdam,
Germany

*CORRESPONDENCE
Luis M. Rubio
lm.rubio@upm.es

SPECIALTY SECTION
This article was submitted to Microbial Physiology and Metabolism, a section of the journal Frontiers in Microbiology

RECEIVED 11 July 2022
ACCEPTED 09 August 2022
PUBLISHED 24 August 2022

CITATION
Barahona E, Isidro ES, Sierra-Heras L, Álvarez-Melcón I, Jiménez-Vicente E, Buesa JM, Imperial J and Rubio LM (2022) A directed genome evolution method to enhance hydrogen production in *Rhodobacter capsulatus*. *Front. Microbiol.* 13:991123. doi: 10.3389/fmicb.2022.991123

A directed genome evolution method to enhance hydrogen production in *Rhodobacter capsulatus*

Emma Barahona[1], Elisa San Isidro[1], Laura Sierra-Heras[1], Inés Álvarez-Melcón[1], Emilio Jiménez-Vicente[1], José María Buesa[1], Juan Imperial[1] and Luis M. Rubio[1,2]*

[1]Centro de Biotecnología y Genómica de Plantas, Universidad Politécnica de Madrid (UPM), Instituto Nacional de Investigación y Tecnología Agraria y Alimentaria (INIA-CSIC), Madrid, Spain, [2]Departamento de Biotecnología-Biología Vegetal, Escuela Técnica Superior de Ingeniería Agronómica, Alimentaria y de Biosistemas, Universidad Politécnica de Madrid, Madrid, Spain

Nitrogenase-dependent H_2 production by photosynthetic bacteria, such as *Rhodobacter capsulatus*, has been extensively investigated. An important limitation to increase H_2 production using genetic manipulation is the scarcity of high-throughput screening methods to detect possible overproducing mutants. Previously, we engineered *R. capsulatus* strains that emitted fluorescence in response to H_2 and used them to identify mutations in the nitrogenase Fe protein leading to H_2 overproduction. Here, we used ultraviolet light to induce random mutations in the genome of the engineered H_2-sensing strain, and fluorescent-activated cell sorting to detect and isolate the H_2-overproducing cells from libraries containing 5×10^5 mutants. Three rounds of mutagenesis and strain selection gradually increased H_2 production up to 3-fold. The whole genomes of five H_2 overproducing strains were sequenced and compared to that of the parental sensor strain to determine the basis for H_2 overproduction. No mutations were present in well-characterized functions related to nitrogen fixation, except for the transcriptional activator *nifA2*. However, several mutations mapped to energy-generating systems and to carbon metabolism-related functions, which could feed reducing power or ATP to nitrogenase. Time-course experiments of nitrogenase depression in batch cultures exposed mismatches between nitrogenase protein levels and their H_2 and ethylene production activities that suggested energy limitation. Consistently, cultivating in a chemostat produced up to 19-fold more H_2 than the corresponding batch cultures, revealing the potential of selected H_2 overproducing strains.

KEYWORDS

nitrogenase, flow cytometry, hydrogenase, biological hydrogen production, *hupA*, mutagenesis

Introduction

The nitrogen-fixing and photosynthetic purple non-sulfur bacterium (PNSB) *Rhodobacter capsulatus* evolves H_2 using two genetically distinct nitrogenases, a Mo-nitrogenase and an Fe-only nitrogenase, when cultured under anaerobic, illuminated conditions with organic compounds and in the total absence of nitrogen or in the presence of a poor nitrogen source (Scolnik and Haselkorn, 1984; Strnad et al., 2010). Nitrogenases are two-component enzymes (Bulen and LeComte, 1966) formed by a dinitrogenase (called MoFe protein in the Mo-nitrogenase and FeFe protein in the Fe-only nitrogenase) and a dinitrogenase reductase (called the Fe protein), which catalyze the reduction of N_2 into NH_3 in a reaction that also produces, at a minimum, one mol of H_2 per mol of reduced N_2 (Seefeldt et al., 2020).

$N_2 + 8\,H^+ + 8\,e^- + 16\,MgATP + 16\,H_2O \rightarrow H_2 + 2\,NH_3 + 16\,Mg\,ADP + 16\,P_i$.

The specific substrate-reducing activities of the *R. capsulatus* nitrogenases have been described (Schneider et al., 1991, 1997). The relative H_2 to NH_3 production varies with the component ratio and nitrogenase type, being much higher in lower electron fluxes and for the Fe-only nitrogenase compared to the Mo-nitrogenase, making potential H_2 production much higher than predicted from the above equation.

Rhodobacter capsulatus also expresses two hydrogenases: a cytosolic H_2-sensing [Ni-Fe] hydrogenase encoded by *hupU* and *hupV* (Vignais and Billoud, 2007), and a membrane-bound uptake [Ni–Fe] hydrogenase that catalyzes the reversible reaction $2H^+ + 2e^- \leftrightarrow H_2$ (Colbeau et al., 1993; Vignais et al., 2005). This latter enzyme is a heterodimer of the *hupA* and *hupB* gene products. The *hupC* gene product is a cytochrome b-type protein that anchors HupAB to the membrane and receives electrons from HupA (Vignais and Billoud, 2007). Transcription of *hupABC* is controlled by a promoter in response to H_2 and involves a HupUV H_2-sensor and a two-component regulatory system consisting of a histidine kinase HupT and a response regulator HupR. In the absence of H_2, HupT and HupUV interact to form a complex in which HupT has increased auto kinase activity. Autophosphorylated HupT transfers a phosphate group to HupR, which in this state is unable to activate transcription. In the presence of H_2, HupUV binds H_2 and HupT is released. Although trans-phosphorylation between HupT and HupR can occur, in this state HupT appears to function rather in a phosphatase mode, leaving HupR in the active, unphosphorylated state, which can now activate transcription (Vignais et al., 2005).

Diverse approaches have been used to increase H_2 production by genetic manipulation of microorganisms. Increase of H_2 production by hydrogenase obtained by directed mutagenesis or by removing genes related to their synthesis, regulation or assembly has been reported (Jahn et al., 1994; Masukawa et al., 2002; Liu et al., 2010). Nitrogenases are also excellent H_2-producing enzymes, and H_2 production *via* nitrogenase has also been improved, mainly in cyanobacteria (Bandyopadhyay et al., 2010; Masukawa et al., 2010; Skizim et al., 2012) and PNSB (Rey et al., 2007; Kim et al., 2008; Liu et al., 2010; Wang et al., 2010; Barahona et al., 2016; Zhang et al., 2016). An important limitation to improve H_2-producing enzymes is the scarcity of high-throughput screening methods for H_2 overproducing microorganisms. In this context, a combination of fluorescence-activated cell sorting (FACS), an engineered *R. capsulatus* strain that generates fluorescein in response to H_2, and the *in vivo* expression of random variants of the nitrogenase NifH protein in the engineered strain, has been used previously to detect and separate H_2 overproducing cells in screenings involving over a million variants per experiment (Barahona et al., 2016).

Here, we subjected *R. capsulatus* to directed genome evolution to increase H_2 production. Random UV mutagenesis of engineered H_2-sensing strains was combined with FACS to detect and isolate the resulting H_2-overproducing cells. Three rounds of mutagenesis/selection were performed to achieve 2- to 3-fold increase in H_2 production over the parental H_2-sensing strain. The effect of removing H_2 from the gas phase of *R. capsulatus* cultures to accelerate H_2 evolution was also investigated.

Materials and methods

Bacterial strains, growth media, and growth conditions

Bacterial strains used in this study are listed in Supplementary Table S1. *R. capsulatus* strains were cultivated either in rich YPS medium or RCV minimal medium (Weaver et al., 1975). RCV medium contained 30 mM DL-malate and 10 mM $(NH_4)_2SO_4$ as sole carbon and nitrogen source, respectively. When required for nitrogenase derepression, ammonium was omitted (RCV_0) and, when indicated, RCV was supplemented with 10 mM L-serine (in this work, called RCVS). For Petri dishes medium was solidified with 1.5% agar. The medium was supplemented with kanamycin (Km; 50 μg/ml) or rifampicin (Rif; 25 μg/ml) when required. Cultures were incubated at 30°C either under chemotrophic (aerobic) or phototrophic (anaerobic) conditions. Petri dishes were incubated at 30°C inside illuminated (300 lux) anaerobic jars in the presence of anaerobic gas generator bags (AnaeroGen™, Thermo Scientific, United States).

To determine growth curves of *R. capsulatus*-derived strains, precultures in RCV medium were diluted to an OD_{600} of 0.15 and transferred in triplicate to 24-multiwell plates. Cultures were grown at 30°C in presence of oxygen with shaking (700 rpm) using a SPECTROstar Nano instrument (BMG LABTECH, Germany) to determine the $OD_{600,}$ and growth was recorded every hour for 44 h.

To derepress nitrogenase in batch cultures, *R. capsulatus* cells precultured in RCV were transferred to 100-ml capped vials containing 60 ml of RCV_0 medium and adjusted to an initial OD_{600} of 0.18. Vials were sparged with N_2 to completely remove air. Cultures were grown at 30°C phototrophically (six 60 W light bulbs providing 300 lux at 25 cm of the vials) for 22 h.

Nitrogenase was also derepressed in continuous cultures. The system consisted of an illuminated 300 ml bioreactor containing 150 ml of RCV_0. The bioreactor was inoculated with anaerobically grown *R. capsulatus* cells to an initial OD_{600} of 0.3 and the reactor was made anaerobic by sparging N_2 for 1 h ($t = 0$ h). After 16 h of diazotrophic growth, the gas phase was renewed by sparging N_2 for 1 h. Then, a peristaltic pump was used to replace fresh medium for reactor contents at a flow of 2.5 ml/min until the end of the experiment. At $t = 39.5$ h, the bioreactor was opened again both to release any H_2 produced and to renew the N_2 atmosphere by sparging. H_2 measurements were taken at 0, 16, 17, 22.5, 25.5, 39.5, 40, 46, 49, and 63 h.

Ultraviolet light mutagenesis

Ultraviolet light (UV light) mutagenesis was performed on *R. capsulatus* wild-type, S1, and S2 strains to generate random mutations along the genome. Each strain was cultured for 48 h on two Petri dishes containing solid YPS medium. One of the two Petri dishes was exposed to UV light while the second plate was used as control. The procedure was carried out in the dark to prevent photoreactivation. After UV light exposure, a loop of cells from each Petri dish was resuspended in 1 ml YPS and vortexed vigorously. Serial dilutions (from 10^{-1} to 10^{-6}) were plated onto solid YPS to give 30–300 colonies/plate and incubated at 30°C for 48 h. Colony counts were performed to estimate survival rates. Nine UV treatment times were tested. At 30 s, and at 1, 3, 5, 6, and 8 min, there were no survival differences between UV-treated plates and non-treated controls. At 10 min, the survival rate in UV-treated plates was 90% of the control. At 13 min, the survival rate was 8% for *R. capsulatus* wild type and 10% for the S2 strain. No survivors were obtained after 15 min of UV illumination. Therefore, a 13-min exposure to UV light was used to generate libraries of random mutants. Each library contained *ca.* 3×10^9 colony-forming units.

Flow cytometry

Rhodobacter capsulatus cells grown under diazotrophic conditions in 100-ml capped vials, containing 60 ml of RCVS medium, were collected by centrifugation in Falcon tubes for 15 min at 4°C, 4,500×*g*, resuspended in 5 ml PBS supplemented with 10% glycerol, and incubated for 30 min at 4°C. Cells were then collected, resuspended in 1 ml of an 8:1:1 mixture of PBS, fluorescein di-β-D-galactopyranoside (FDG) and propidium iodide (PI), and incubated at 37°C for 30 min to facilitate FDG entrance into the cells. When cleaved by β-galactosidase, FDG releases fluorescein, which cannot diffuse across the cytoplasmic membrane (Plovins et al., 1994). Cells were collected by centrifugation, resuspended in RCV medium, and analyzed in a FACSVantage (sorter) flow cytometer using an argon ion laser to excite the fluorochrome (488 nm) and a 0.5 µm filament filter to separate very small particles. About 5×10^5 cells were analyzed in each experiment. The cell sorter was programmed with very stringent parameters to separate individual cells leading to clonal populations. Only a few cells from a subpopulation exhibiting 10–100-fold more fluorescence than the population average were sorted and recovered in 96-well microplates containing RCV medium. These stringent sorting conditions were chosen to ensure that just one highly fluorescent cell, or none, went into the receiving well. As a result, only a single microplate was filled in a 2-h experiment, and about one-half of the wells produced no growth when their contents were used as inoculum. Grown cultures were then diluted to normalize their OD and transferred to RCVS medium in 96-well microplates to derepress nitrogenase overnight and prepare for 4-methylumbelliferone β-D-galactopyranoside (MUG) assays.

4-Methylumbelliferone β-D-galactopyranoside activity assays

4-Methylumbelliferone β-D-galactopyranoside β-galactosidase activity assays were carried out as described in (Barahona et al., 2016). *R. capsulatus* cultures were incubated overnight under diazotrophic conditions inside a glove box in a 96-well plate (black/clear Optilux™ flat bottom; BD Biosciences) covered with a transparent adhesive sealer. Portions of 120 µl from each culture were transferred to a 96-well microplate containing 100 µl of Z-Buffer (Miller, 1972) in each well, then supplemented with 25 µl MUG solution (1 mg/ml solution in dimethyl sulfoxide) and incubated at room temperature for 2 h in darkness. MUG hydrolysis by β-galactosidase was quantified by fluorescence emission at 445 nm (372 nm excitation wavelength) in a Genios Pro (Tecan) microplate fluorometer.

In vivo nitrogenase acetylene reduction assay

To determine acetylene reduction activity in *R. capsulatus*, 1 ml portions of cultures grown under diazotrophic conditions were transferred to 9-ml sealed vials with a 94% N_2/6% acetylene gas phase and incubated at 30°C in presence of light for 30 min. Ethylene formation was detected in 50 µl samples withdrawn from the gas phase by using a Shimadzu GC-2014 gas chromatograph equipped with a 9-ft long, 1/8-in diameter Porapak R column. *In vivo* nitrogenase activity units are defined as nmol ethylene formed per min per ml of culture at an OD_{600} equal to 1 (nmol C_2H_4 min^{-1} OD_{600}^{-1}).

H_2 production measurements

To determine H_2 production in *R. capsulatus* cultures grown under diazotrophic conditions, 250 µl samples were withdrawn at

the indicated times from the gas phase of 100 ml capped vials. H_2 production in *R. capsulatus* continuous cultures was also determined in 250 µl gas phase samples withdrawn at the indicated times. Samples were injected in a Shimadzu GC-8A gas chromatograph equipped with a 6-ft long, 1/8-in diameter Molecular Sieve column 5A. Each measurement had two technical replicates per biological replicate. H_2 production activity is presented either as total H_2 released or as H_2 released per hour and ml of culture ($OD_{600} = 1$).

Immunoblot detection of NifH and NifDK proteins

For SDS-PAGE, cells from 1-ml culture samples were collected by centrifugation, resuspended in 2× Laemmli sample buffer supplemented with 0.1 M dithiothreitol (to a concentration equivalent to an OD_{600} of 4), and electrophoresed in 12% acrylamide/bisacrylamide (29:1) gels. For immunoblot analysis, proteins were transferred to nitrocellulose membranes for 40 min at 20 V using a Transfer-Blot® Semi Dry system (Bio-Rad). Immunoblot analyses were carried out with antibodies raised against a 1:1 mixture of *Azotobacter vinelandii* and *Rhodospirillum rubrum* NifH proteins (1:2,500 dilution) or with antibodies raised against *R. capsulatus* NifDK (1:2,000 dilution; antibody kindly donated by Yves Jouanneau, CNRS, Grenoble). Secondary HRP-conjugated anti-rabbit antibody (Invitrogen, United States) was used at 1:15,000 dilution.

Whole-genome DNA sequencing and data analysis

For second-generation genome sequencing, total DNA from bacterial cultures was isolated using the NZY Tissue gDNA isolation kit (NZYTech), following the manufacturer's instructions, and eluted in a final volume of 100 µl. A negative control that contained no sample was included in the DNA isolation process to check for cross-contamination during the experiments. DNA samples were quantified using the Qubit dsDNA HS Assay kit (Thermo Fisher Scientific) and sequenced by an external service provider (AllGenetics & Biology SL). Briefly, libraries were constructed using the Nextera XT DNA Library Prep kit (Illumina) according to the manufacturer's instructions, and they were dual indexed for post-sequencing demultiplexing. The fragment size distribution of the libraries was checked with an Agilent 2,100 Bioanalyzer using the Agilent DNA 1000 Kit. Libraries were quantified with the Qubit dsDNA HS Assay Kit and pooled in equimolar amounts. Pooled libraries were then sequenced with an Illumina MiSeq (2 × PE, 300 bp) sequencer.

For third-generation genome sequencing, total DNA extraction from S2– *R. capsulatus* culture was performed using DNeasy Blood & Tissue Kit (QIAGEN) according to PacBio guidelines for handling high-molecular-weight DNA for successful constructions of SMRTbell™ libraries. Quick Ampure XP bead clean-up was then performed to remove RNA contamination. DNA quality (i.e., integrity, purity, and concentration) necessary for library preparations was evaluated from gel images of DNA samples and by Qubit® fluorimetry. Barcoded libraries were prepared, and the size was selected by performing one 0.45 × (sample volume to beads volume ratio) clean followed by another 0.4 x clean using Ampure beads to remove DNA fragments smaller than 3–5 kb. Sequence data were demultiplexed and genomes assembled using PacBio's Microbial Assembly Tool.

Raw genome sequencing reads were processed to correct or eliminate erroneous reads. Error correction algorithms, from simple trimming processes using base quality scores to complex error correction approaches based on the frequency of erroneous reads in the set being assembled, were carried out. Subsequently, single-nucleotide polymorphisms (SNV) were mapped to the S2– *R. capsulatus* genome used as reference. Initial DNA sequence comparisons detected more than a thousand differences between the reference genome and UV-mutated derivatives, but most of those laid in regions of lower sequence coverage and were considered population polymorphisms. Thus, only SNVs present in more than 65% of the reads, and that were also present in subsequent strain derivatives (3 rounds of mutagenesis were performed), were considered for further analysis. All procedures were performed using Geneious version 6.1.8 software. SNVs were confirmed by performing Basic Local Alignment Search Tool (BLAST) against the reference genome.

Statistical analysis

Statistical analyses were carried out using Prism software. One-way ANOVA tests were performed to compare the means of multiple sets of data ($p < 0.05$). Adjusted p values were determined by the Bonferroni test.

Results

We sought to develop a method to generate and *in vivo* identify H_2 overproducing PNSB variants that could be easily implemented in the set-up of an academic R&D laboratory. This method starts by generating a huge library of random mutants that is subsequently screened in groups of half a million at a time by FACS using a fluorescence signal as proxy for H_2 production. The selection procedure favors speed and standardization, and balances, on one hand, a significant increase in fluorescence signal with, on the other hand, obtaining a manageable number of selected overproducing

strains. We found out that about 1% of the mutant population emitted 10-100-fold higher signal than average, and that a 2–3-h FACS experiment could sort out and collect 96 of them in a single plate. Because the number of isolated clones was relatively small, a growth test and secondary H_2 production proxy screening were then performed to validate the FACS selection before real H_2 production was determined. To "fix" advantageous mutations for H_2 production, we decided to pursue stepwise increments rather than performing a deeper–and much longer–screening of an individual mutagenic library. Thus, the 2–3 highest H_2 overproducing mutants were used in subsequent cycles of mutagenesis and screening. At the end, a collection of H_2 overproducing *R. capsulatus* mutants was analyzed by whole genome sequencing to gain insights into the genetic basis of their phenotypes and to establish the mutation genealogy.

First round of UV mutagenesis and screening for H_2-overproducing strains

Rhodobacter capsulatus S1 and S2 sensor strains contain a copy of *lacZ* (P*hupA*::*lacZ*) integrated in the chromosome between *hypF* and *hupA* (Supplementary Table S1). They express LacZ and catalyze the formation of fluorescein from fluorescein di-β-D-galactopyranoside (FDG) in response to endogenously produced H_2 (Barahona et al., 2016). In addition, S2 lacks the *hupAB* structural genes for the uptake-hydrogenase and is unable to consume H_2. Random genome-wide mutagenesis of S2 was performed as starting point to generate strains with enhanced *in vivo* H_2 production. S2 cells growing on solid YPS medium were exposed to UV light, serially diluted, and plated again to assess survival. About 3×10^9 colony-forming units (10% survival rate) were recovered after mutagenesis. Mutagenized cells (UV-S2) were pooled, derepressed for nitrogenase in RCVS medium, incubated with FDG, and analyzed by FACS flow cytometry (Figure 1A). Wild-type, S1, and S2 cells derepressed for nitrogenase and treated with FDG were used as controls. About 5×10^5 mutagenic events were processed per FACS sample. UV-S2 cells emitting 10 to 100-fold more fluorescence than the main population (1.4% of the total population in the P2 areas of Figure 1A) were sorted by the flow cytometer and some of them were collected into a 96-well microplate containing RCV medium. After incubation, growth was observed in 52% of the inoculated wells. Grown cultures were then transferred to RCVS medium inside an anaerobic glovebox for nitrogenase derepression and secondary MUG-based β-galactosidase activity determinations. Fourteen mutants exhibited at least 2.5-fold higher MUG-derived fluorescence than S2 (Figure 1B). Derepressed cultures showed statistically significant increases in H_2 production rates compared to S1 and S2 (see Round 1 box in Figure 2). S2-derived strains 2G, 11F, and 11G were selected as the highest H_2 producers and further analyzed in time-course H_2-production experiments (Figure 3A).

Additional rounds of mutagenesis and screening to further increase H_2 production

2G, 11F, and 11G strains were separately subjected to a second round of UV mutagenesis and FACS screening. The percentage of cells in selective P2 areas of FACS was 0.027, 0.5, and 0.01%, for UV-11F, UV-11G, and UV-2G, respectively (Figure 1A). As in round 1, cultures presenting over twice the β-galactosidase activity of their parental strains were monitored for H_2 production, and the highest H_2 producers were selected (Figure 1B). Selected strains were used in subsequent rounds of UV mutagenesis and screening while statistically significant increases in H_2 production rates were observed. Significant differences were observed between S1, S2, and mutants generated in mutagenic rounds 1 and round 2, but not between round 2 and round 3 mutants (Figure 2). Therefore, no further rounds of mutagenesis were performed after round 3. Supplementary Figure S1 shows the genealogy of *R. capsulatus* strains generated in this work.

The H_2 production rates of selected strains subject to subsequent rounds of UV mutagenesis are shown in Figure 3A. H_2 production rates of additional derivative strains can be found in Supplementary Figure S2. Rates were determined in time-course experiments after nitrogenase derepression, and statistically significant differences between S2 and derivative strains were observed at all investigated times. Strains 12A, 8D, and 12C stood out as the highest overproducers, with average production rates of 3,056, 2,830, and 3,180 nmol H_2 ml^{-1} h^{-1} $OD_{600}{}^{-1}$, respectively (compared to average S2 production of 1,388 nmol H_2 ml^{-1} h^{-1} $OD_{600}{}^{-1}$).

Mo-nitrogenase is the enzyme responsible for H_2 production in *R. capsulatus* growing photoheterotrophically in the absence of fixed N and when the growth medium contains Mo. *In vivo* nitrogenase activity in S2 and derivative strains was estimated by the acetylene-to-ethylene reduction method. Ethylene production was lower in S2 than in the derivative strains at all analyzed times, although differences were only statistically significant 22 h after derepression (Figure 3B). Correlations between H_2 and ethylene production activities were observed for all strains, indicating that H_2 overproduction phenotypes were not due to changes in nitrogenase substrate specificity (*i. e.* preference of H^+ over acetylene), as reported previously for *nifH* mutant experiments (Barahona et al., 2016). On the contrary, nitrogenase activities did not correlate with the accumulation of the NifH and NifDK components of Mo-nitrogenase, as S2 accumulated more Nif polypeptides than most of its derivative strains (Figure 3C). 8D, 3D, and 12C had slightly altered NifH and NifDK accumulation profiles compared to the other strains.

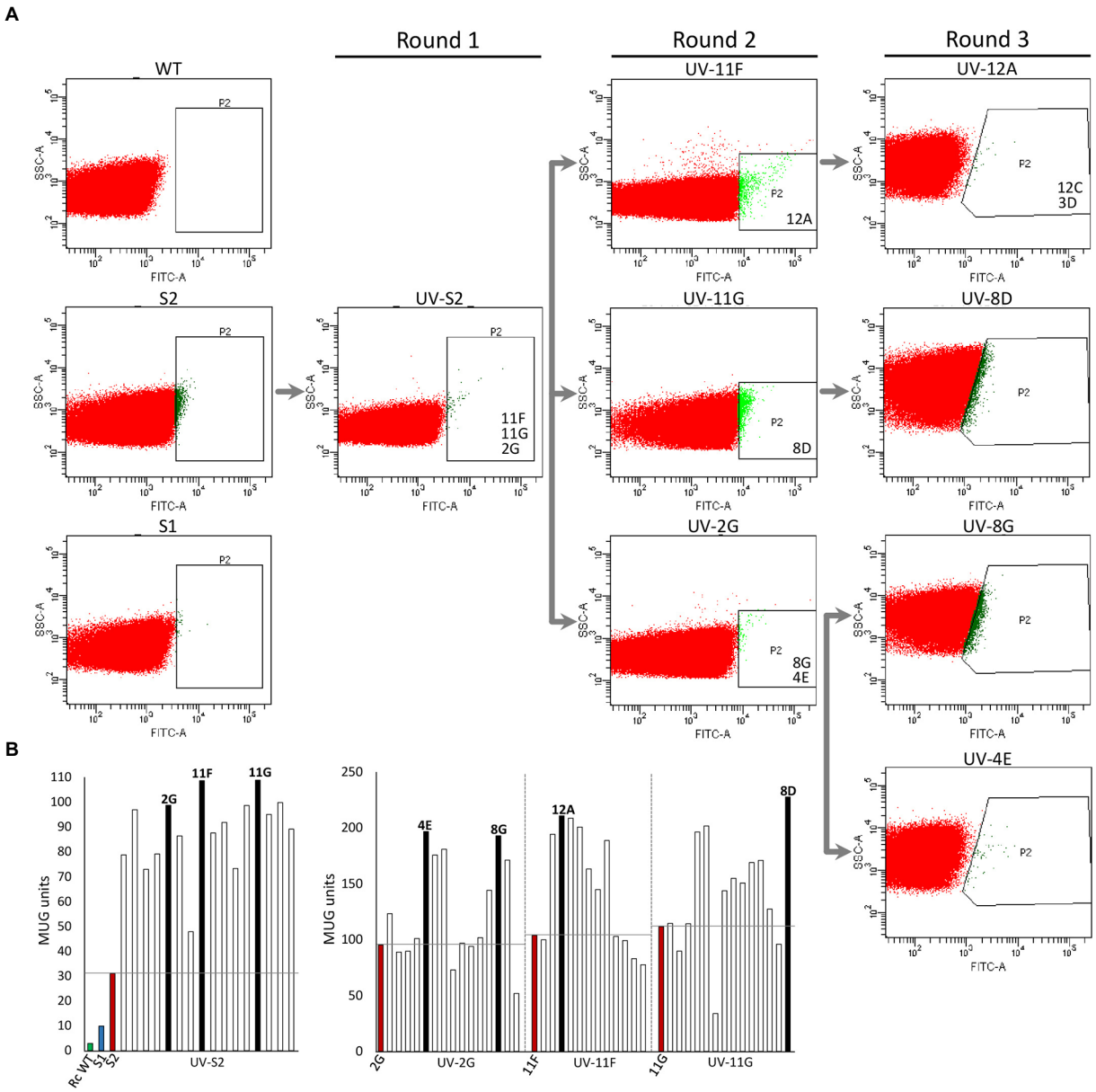

FIGURE 1
High-throughput selection of *Rhodobacter capsulatus* cells emitting fluorescence in response to H_2. **(A)** Fluorescence activated cell sorting. Dot-plot showing side-scattered light (SSC) versus fluorescence generated by fluorescein isothiocyanate (FITC) in *R. capsulatus* populations of wild type, S1, S2, UV-S2 (pool of S2 cells after UV treatment), and derivative strains obtained by further rounds of UV mutagenesis. P2 indicates areas used for cell sorting into 96-well plates. Strains analyzed in depth in this study (*e. g.* 11F, 11G, and 2G) are shown in the P2 area from which they were isolated. **(B)** Examples of beta-galactosidase activity (MUG hydrolysis in 96-well plate format) of clones sorted by FACS. Left, UV-S2. Right, UV-2G, UV-11F, and UV-11G sorted populations. Green and blue bars show wild-type and S1 and S2 activities, respectively. Red bars show activities of strain subject to each mutagenic treatment. Black bars represent activities of clones selected for further rounds of mutagenesis.

Improving H_2 production under continuous culture conditions with intermittent gas exchange

After maximum accumulation of nitrogenase polypeptides occurred, the rates of H_2 production decelerated over time in all strains and, finally, decreased between 38 and 39 h (Supplementary Figure S3). Consistently, acetylene reduction activities were lower at 39 h than at 22 h after nitrogenase derepression (data not shown). The slight decrease of NifH and NifDK accumulation over time (Figure 3C) cannot entirely account for the magnitude of this effect, and therefore, additional factors must be involved. One possibility is the limitation of electrons and ATP supply to nitrogenase. However, because aerobic non-diazotrophic growth also stopped at similar culture OD (Supplementary Figure S4), it appears that the observed decrease

was caused by more general, physiological causes. Typically, substrate limitation or waste accumulation are responsible for batch cultures entering the stationary growth phase. Therefore, continuous culture experiments were undertaken.

Continuous culture conditions were established that maintained culture density at $OD_{600} = 1.6$ (Figure 4A), and H_2 production by S2, 8D, and 12C strains was determined during 63-h experiments (Figures 4B,C). Periodic atmosphere changes to replenish N_2 and to remove accumulated H_2 were also implemented. Figure 4B shows that all accumulated H_2 disappeared after atmosphere regeneration at 17 and 40 h. H_2 production rates increased during the experiment and were always higher in 12C and 8D than S2 (Figure 4). At 63 h, strains 12C and 8D produced 63 ± 1 μmol H_2 h^{-1} ml^{-1} $OD_{600}{}^{-1}$ and 52 ± 2 μmol H_2 h^{-1} ml^{-1} $OD_{600}{}^{-1}$, respectively, compared to 12 ± 1 μmol H_2 h^{-1} ml^{-1} $OD_{600}{}^{-1}$ in the S2 strain. Comparison with their maximum H_2 production rates in batch cultures (*ca.* 1–3 μmol H_2 h^{-1} ml^{-1} $OD_{600}{}^{-1}$, see Figure 3A) indicated that continuous culture conditions effectively removed some limitations to H_2 production. The total volume of H_2 produced in 63 h by strains 8D and 12C was 4 and 5 l H_2 per L of culture, respectively (Figure 4C).

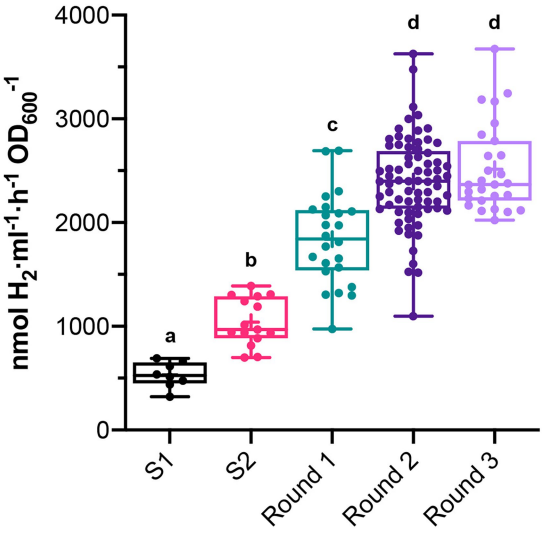

FIGURE 2
In vivo H_2 production in batch cultures of clones that had high β-galactosidase activity in previous MUG assays. Measurements were taken after each round of UV mutagenesis. *In vivo* H_2 production of S1 and S2 are shown as reference. Boxes show 25th to 75th percentiles, the median (line), and the mean (+). Whiskers show from minimum to maximum values. Each dot represents H_2 production of a different clone. Different letters indicate statistically significant differences ($p<0.05$ for S1 vs. S2, and $p<0.0001$ for the rest of group comparisons).

Identification of mutations in *Rhodobacter capsulatus* H_2 overproducing strains

Mutations present in 11F, 12A, 12C, 3D, and 8D strains were identified by whole genome sequencing (Illumina MiSeq, PE 2× 300 bp, 100× coverage) and mapped to the *R. capsulatus* S2 chromosomal DNA sequence. Due to the large number of differences in the DNA sequences of the mutants and S2, only SNVs that were present in more than 65% of the mutant reads, and that were also present in subsequent strain derivatives, were considered. These stringent criteria represent a conservative approach. Therefore, the chosen mutations might not encompass all possible changes but rather represent the minimum relevant changes caused by UV that, altogether, affect H_2 production phenotype. Mutations identified in the selected H_2 overproducing strains are listed in Table 1 and Supplementary Table S2. SNVs were identified that resulted in amino acid changes within functional gene sequences or changes in promoters and terminator regions. Point mutations leading to nucleotide deletions that create frameshifts were also observed. A total of 35 genomic changes, uniformly and randomly distributed across the genome, were identified among strains (Supplementary Table S2). These changes included two deletions and 31 SNVs, 21 of which resulted in amino acid changes. In seven cases, two mutations were localized very close in the same ORFs. As expected, parental variations were maintained in second- and third-round mutants (except for *eda* mutation in 11F).

Table 1 lists mutations in genes that could be relevant to H_2-overproducing phenotypes. Deletion of structural uptake hydrogenase genes (*hupAB*) was confirmed in S2 and all derivatives were sequenced in this study. Obviously, the absence of HupAB prevented consumption of H_2 produced by nitrogenase. 8D had a mutation in *ackA2*, encoding acetate kinase, which possibly affects carbon metabolism. 11F had a mutation in *rcc02232*, a gene linked to a nitrogen fixation gene cluster that encodes a FAD-dependent oxidoreductase, and possibly affects electron donation to nitrogenase. Importantly, this mutation was carried over to 12A, 12C, and 3D derivative strains. 12A had additional mutations in *rcc01477* (encoding another FAD-dependent oxidoreductase) and *araB* (encoding a ribulokinase involved in arabinose catabolism), with implications in carbohydrate metabolism and electron transfer. In addition to mutations carried over from 11F and 12A, 3D has a mutation in a *ndh* gene encoding a subunit of an NADH dehydrogenase, and thus involved in energy production. Most importantly, strain 12C has mutations in *metH3*, encoding a methionine synthase necessary for *S*-adenosylmethionine (SAM) biosynthesis, and in *nifA2*, a second, initially redundant, *nif*-specific transcriptional regulator located in *nif* cluster B (Demtröder et al., 2019). SAM is required for the biosynthesis of the iron-molybdenum cofactor of nitrogenase by NifB (Curatti et al., 2006). Notably, NifH and NifDK accumulation in 12C was not much lower than in the other analyzed strains (Figure 3C).

Discussion

Biohydrogen generation by photosynthetic bacteria, such as PNSB, exhibits low productivity making them unsuitable to

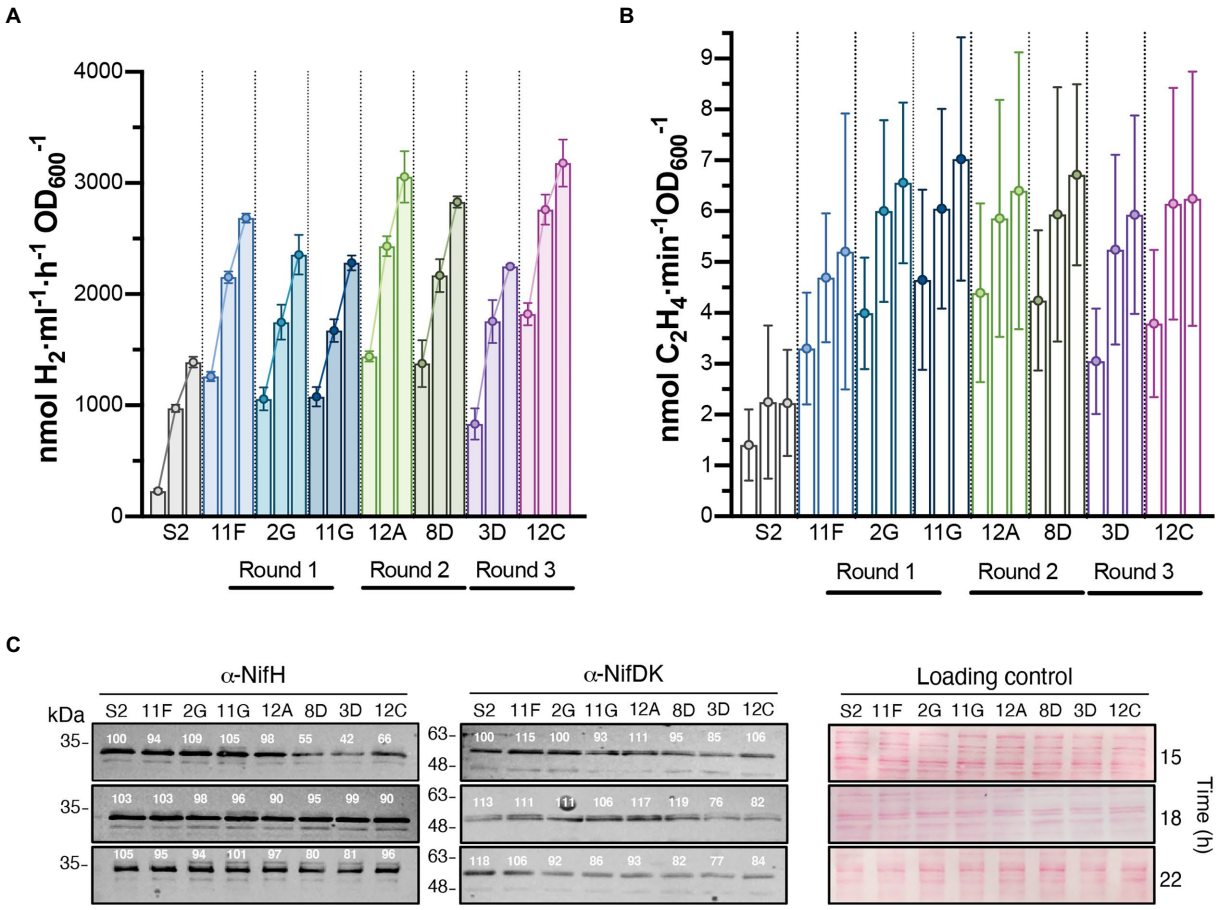

FIGURE 3
Time course of H_2 production in batch cultures of selected strains isolated after each round of UV mutagenesis. *In vivo* H_2 **(A)** and ethylene **(B)** production of S2 and the highest H_2 overproducing variants. The three bars of each strain represent activities at 15, 18, and 22h after the start of nitrogenase depression. Data represent the mean±SD of biological replicates (n=6 for H_2, n=4 for ethylene). Each biological replicate had 2 technical replicates. Statistically significant differences in H_2 production between S2 and H_2 overproducers existed at all measured times (p<0.0001). Differences in ethylene production between S2 and H_2 overproducers were statistically significant at 22h (p<0.05). **(C)** Immunoblot detection of nitrogenase NifH and NifDK components in cell-free soluble extracts from cultures shown in panel B. Normalized quantification of band intensity is indicated above each band. Ponceau staining of membranes is shown as loading control. Full uncropped gels are available as Supplementary Figure S5.

generate H_2 for large-scale applications (Chandrasekhar et al., 2015). However, their production has been insufficiently explored, being underdeveloped, and remains a promising renewable source of H_2 considering the energy input (sunlight) and purity of product output (Gupta et al., 2013; Chandrasekhar et al., 2015; Jiménez-Llanos et al., 2020; Chai et al., 2021). Several strategies to enhance photo-fermentative biohydrogen production have been described, such as immobilization of bacteria for continuous H_2 production (Fiβler et al., 1995; Elkahlout et al., 2019), modification of carbon substrates, nitrogen source, and micronutrients contained in the H_2 production medium (Liu et al., 2009; Laocharoen and Reungsang, 2014; Chen et al., 2017), and genetic modifications (Barahona et al., 2016; Feng et al., 2018b; Ma et al., 2021), among others.

Previously, we were able to increase H_2 production by *R. capsulatus* 10-fold through the development of a biotechnological tool for the detection of H_2-overproducing mutants expressing randomly generated nitrogenase variants (Barahona et al., 2016). The tool was based on the sensing hydrogenase of *R. capsulatus* and produced a fluorescent signal proportional to the amount of H_2 produced by each variant. Here, we have used it for genome-wide screening of mutations leading to enhanced H_2 production, thus expanding the impact of this tool.

This work focuses on methodology for non-designed enhancement of H_2 production activity through the detection of rare overproducers within a very large population of cells. One outcome from this work is that this method did not accumulate mutations on nitrogenase or hydrogenase genes, which would be obvious targets for a designed mutant strategy. It appears that a panoply of mutations, probably resulting in small production increments, underly the H_2 overproducing phenotype. As a result, the proposed methodology does not allow to unequivocally assign specific genotypes as responsible for the observed H_2 overproducing phenotype, and the putative contribution of each

TABLE 1 Mutations accumulated in *Rhodobacter capsulatus* H_2 overproducing strains.

Strain	Accumulated mutations	Relevant genes affected	Proposed function
S2	1 mutation	*hupAB*	Uptake hydrogenase (H_2 consumption)
11F	S2 + 7 mutations	*rcc02232*	FAD dependent oxidoreductase (Energy production)
12A	11F + 5 mutations	*rcc01477*	FAD-dependent oxidoreductase (Energy production)
		araB	Ribulokinase (Carbohydrate metabolism)
8D	S2 + 5 mutations	*ackA2*	Acetate kinase (Carbon metabolism)
3D	12A + 5 mutations	*ndh*	NADH dehydrogenase (Energy production)
12C	12A + 6 mutations	*metH3*	Methionine synthase (SAM biosynthesis)
		nifA2	Nif transcriptional regulator (Nitrogen fixation)

one of the identified mutations towards this phenotype will require further experimentation.

To identify genes and pathways involved in H_2 metabolism, we performed random DNA mutagenesis of *R. capsulatus* S2 using UV mutagenesis. Random mutagenesis of bacteria and algae using both physical (UV) and chemical (e.g. ethyl methane sulfonate) mutagens has been used extensively to improve microorganism activities useful at industrial scale (Joshi et al., 2013; Lee et al., 2014; Perin et al., 2015). UV radiation (250–290 nm) induces either formation of thymine dimers that cause transition of G and C to adenine A and thymine T and/or deletion of A–T base pairs in the DNA. *R. capsulatus* has an efficient photoreactivation system that repairs DNA damage induced by UV (Barbe et al., 1987). Thus, in this work, UV mutagenesis was performed in absence of visible light. Point mutations in *R. capsulatus* regulatory sequences and other key genes could result in enhanced H_2 production. The possibility of mutation bias resulting from the UV treatment cannot be ruled out as no other chemical random mutagenesis was performed in parallel. The survivors of mutagenic treatment were screened in groups of 5×10^5 CFU. About 0.01 to 1% of them exhibited enhanced fluorescence compared to the population average and the parental strain. The effectiveness of FACS high-throughput screening was confirmed by secondary β-galactosidase and H_2 production activities.

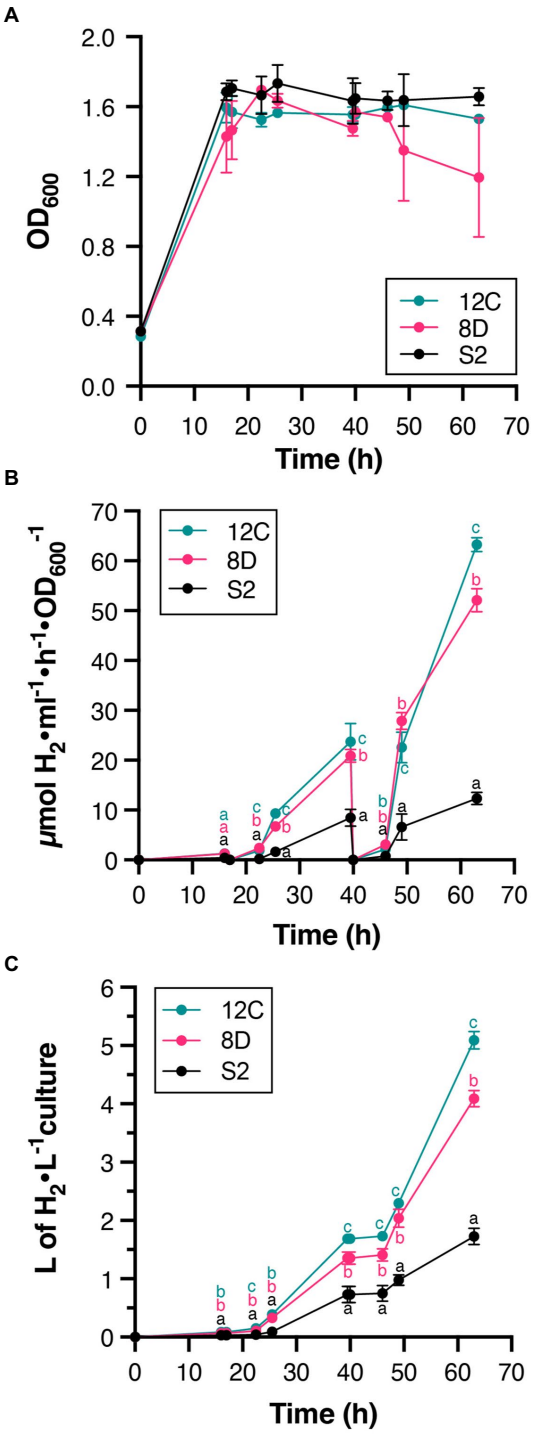

FIGURE 4
H_2 production in continuous cultures of S2, 8D, and 12C strains. **(A)** Stability of culture OD during the experiment. Continuous culture conditions were established once the OD_{600} reached 1.6. **(B)** Time course of *in vivo* H_2 accumulation. Note the disappearance of accumulated H_2 at times 17 and 40h due to complete regeneration of the gas phase. **(C).** The total amount of H_2 produced. Statistically significant differences in H_2 production between S2 and H_2 overproducers existed at all measured times. Different letters (a, b, or c) indicate statistically significant differences ($p<0.05$). In all panels, data represent the mean±SD of biological replicates ($n=4$ for S2, $n=2$ for 8D and 12C) with two technical replicates each.

The greatest differences in H_2 production were observed at 22 h, where all selected strains produced higher levels than S2. The highest H_2-overproducing strains were subject to subsequent rounds of UV mutagenesis and FACS to continue improving H_2 production. Thus, accumulation of mutations after each round could be closely linked to the enhancement of H_2 production. Differences in H_2 production rates were lower at 39 than 22 h, probably due to depletion of nutrients in batch cultures, as previously reported (Bianchi et al., 2010; Boran et al., 2010; Feng et al., 2018a). Overall, H_2 production was enhanced 6-fold by deleting the *hupAB* genes (uptake hydrogenase) and by performing random mutagenesis. In addition, continuous cultures of selected mutant strains were shown to produce 19-fold more H_2 than the corresponding batch cultures.

Nitrogenase variants greatly enhancing H_2 production have been previously obtained. The most active H_2 producers lost the ability to reduce acetylene into ethylene (Barahona et al., 2016; Zheng and Harwood, 2019). In contrast to the nitrogenase-focused approach, all variants analyzed by genome-wide screening exhibited higher acetylene reduction activities than the S2 parental strain, although nitrogenase structural proteins, NifH and NifDK, were expressed at similar levels. This observation suggests that changes selected in the genome of variants do not affect nitrogenase substrate specificity and could be altering either (i) other nitrogenase-related proteins, or proteins that are involved in nitrogen fixation-related pathways, or (ii) regulatory regions or factors. One aspect not investigated here was the possible contribution of the Fe-only nitrogenase to the H_2 overproduction phenotype. A comparative characterization of H_2 production by Mo- and Fe-only nitrogenases in a *hupB*$^-$ mutant of *R. capsulatus* indicated higher production from the Fe-only nitrogenase operating under N_2 atmosphere (Krahn et al., 1996). However, in our experiments, the Fe-only nitrogenase is repressed because the culture medium contains molybdate. Thus, mutations derepressing its expression in presence of molybdate would be required.

Regarding regulatory mutations, it is noteworthy that round 2 mutant 12C, one of the strongest H_2 overproducers, contains a mutation in *nifA2*. *R. capsulatus* contains two copies of the *nifA* transcriptional activator gene, *nifA1* and *nifA2*, and their gene products equally activate both *nif* and *anf* promoters (Demtröder et al., 2019). However, the regulation of *nifA2* differs from that of *nifA1* in that it is subject not only to NtrC nitrogen control, but also to the general, redox-responding RegAB regulatory system (Elsen et al., 2000).

Regarding mutations in nitrogenase-related functions or pathways, none of the mutations accumulated in selected H_2 overproducers targeted well-characterized functions related to nitrogen fixation. However, some of them affect genes with proposed functions that could be relevant to nitrogen fixation. Strain 11F –and hence 12A and its derivatives– contained a mutation in *rcc02232*, a proposed FAD oxidoreductase, while 12A and its derivatives accumulated an additional mutation in *rcc01477*, another proposed FAD oxidoreductase. FAD-dependent oxidoreductases play a role in energy-generating systems and here they may be part of an ancillary system, unknown until now, that can feed reducing power or ATP to the nitrogenase system. This possibility is further substantiated by the presence of a *ndh* mutation in 3D, 12A-derived strain. Although many NADH oxidases have been linked to oxidative stress control, regeneration of NAD^+ is also critical for cellular energy generation.

Another set of selected mutations is that of C metabolism-related functions. In strain 12A and derivatives, a mutation in *araB*, a ribulokinase, was selected, while strain 8D showed a mutation in *ackA2*, an acetate kinase. Gene *ackA2* has been implicated in a 1,2-propanediol degradation pathway that is overexpressed in mutants in the RegAB general redox regulatory system (Schindel and Bauer, 2016). AraB, on the other hand, catalyzes the conversion of ribulose to ribulose-5-phosphate (Agarwal et al., 2012). Ribulose-5-phosphate, besides constituting an energy vector, can feed into the pentose phosphate pathway. It has been reported that polysaccharide production substantially increases in *R. capsulatus* mutants lacking nitrogenase activity (Klein et al., 1991). This suggests that nitrogen fixation and polysaccharide production pathways may be competing for metabolites or reducing power. Were this the case, it is possible that a mutation in *araB* could result in higher energy availability to nitrogenase, thus explaining its higher H_2 production.

Finally, one of the mutations in the overproducing strain 12C is located within the *metH3* gene that codes for a methionine synthase. Methionine is a precursor of S-adenosyl-methionine (SAM), and SAM is required for NifB activity in the synthesis of the NifB-co cofactor, a precursor to the nitrogenase catalytic cofactor, FeMo-co (Buren et al., 2020). However, in the absence of data regarding alteration of SAM levels in strain 12C, the effect of this mutation is difficult to rationalize. This gene could simply be involved in the relative availability of sulfur that might affect the relative NH_3 vs. H_2 produced. Or its mutation might alter the relative expression of Mo– vs. Fe– only nitrogenase affecting H_2 produced.

At present it is difficult to rationalize the role of the above mutations that result in a nitrogenase able to efficiently evolve H_2 while not being affected in its ability to reduce N_2, within a specific framework. Further investigation of the phenotypes of these mutations will probably clarify some of the complex metabolic interactions that the proposed functions of the genes implicated suggest. This will probably unearth subtle redox and energy interactions in the nitrogen fixation process that have so far escaped detection but that are, nonetheless, important to determine the fate of electrons through nitrogenase. In this respect, it is important to keep in mind that alterations in the electron flux through nitrogenase can alter its preference for different substrates (*e. g.* protons or N_2). Purified nitrogenase allocates 25% of the electrons fed to it to proton reduction (Simpson and Burris, 1984), and this has been mechanistically explained (Seefeldt et al., 2020). However, *in vivo*, higher ratios of proton reduction have been observed, especially in symbiotic systems under stressful conditions for the legume symbiont (Schubert and Evans, 1976), an observation that is also commonly explained by the complexities of the nitrogenase catalytic mechanism: given that nitrogenase needs to store six electrons for the stepwise reduction of N_2 to NH_3, it is expected that

when the electron flux is suboptimal, electrons can leak out to protons and be lost as H_2. Hence, any mutations that negatively affect the efficiency of the flux of electrons through nitrogenase would probably result in a higher proportion of electrons allocated to protons, and thus a higher production of H_2. The selected mutations would fit within this category.

It is surprising that no nitrogenase mutations were identified in this screening. Future developments should include combining mutations identified in (Barahona et al., 2016) and this study, as well as exploiting the Fe-only nitrogenase activity by deregulating it or by changing culture conditions to express it.

Data availability statement

The datasets presented in this study can be found in online repositories. The names of the repository/repositories and accession number(s) can be found at: GenBank BioProject PRJNA859503.

Author contributions

LR initiated and directed this research. EB, EI, LS-H, and IÁ-M performed molecular biology. EB performed cellular biology, flow cytometry, and biochemical assays. EJ-V contributed biochemical assays. JB and EB performed fermentations. EB and JI performed mutant sequence analysis. EB and LR performed the experimental design and data analysis. EB, JI, and LR wrote the manuscript. All authors contributed to the article and approved the submitted version.

Funding

European Research Council starting grant 205442 funded the generation of hydrogen sensor strains. Fundación Iberdrola "Ayudas a la Investigación en Energía y Medio Ambiente 2018" funded DNA sequencing Universidad Politécnica de Madrid grant RP160050022 funded the rest of the work. EI and LS-H are recipient of Becas de Colaboración del Ministerio de Educación y Formación Profesional in the years 2018/19 and 2019/20, respectively.

Acknowledgments

We thank Laura Molero Martín for help with flow cytometry.

Conflict of interest

The authors declare that the research was conducted in the absence of any commercial or financial relationships that could be construed as a potential conflict of interest.

Publisher's note

Supplementary material

The Supplementary material for this article can be found online at: https://www.frontiersin.org/articles/10.3389/fmicb.2022.991123/full#supplementary-material

References

Agarwal, R., Burley, S. K., and Swaminathan, S. (2012). Structural insight into mechanism and diverse substrate selection strategy of L-ribulokinase. *Proteins* 80, 261–268. doi: 10.1002/prot.23202

Bandyopadhyay, A., Stockel, J., Min, H., Sherman, L. A., and Pakrasi, H. B. (2010). High rates of photobiological H_2 production by a cyanobacterium under aerobic conditions. *Nat. Commun.* 1:139. doi: 10.1038/ncomms1139

Barahona, E., Jimenez-Vicente, E., and Rubio, L. M. (2016). Hydrogen overproducing nitrogenases obtained by random mutagenesis and high-throughput screening. *Sci. Rep.* 6:38291. doi: 10.1038/srep38291

Barbe, J., Gibert, I., Llagostera, M., and Guerrero, R. (1987). DNA repair systems in the phototrophic bacterium *Rhodobacter capsulatus*. *J. Gen. Microbiol.* 133, 961–966. doi: 10.1099/00221287-133-4-961

Bianchi, L., Mannelli, F., Viti, C., Adessi, A., and De Philippis, R. (2010). Hydrogen-producing purple non-sulfur bacteria isolated from the trophic lake Averno (Naples, Italy). *Int. J. Hydrog. Energy* 35, 12216–12223. doi: 10.1016/j.ijhydene.2010.08.038

Boran, E., Özgür, E., van der Burg, J., Yücel, M., Gündüz, U., and Eroglu, I. (2010). Biological hydrogen production by *Rhodobacter capsulatus* in solar tubular photo bioreactor. *J. Clean. Prod.* 18, S29–S35. doi: 10.1016/j.jclepro.2010.03.018

Bulen, W. A., and LeComte, J. R. (1966). The nitrogenase system from Azotobacter: two-enzyme requirement for N_2 reduction, ATP-dependent H_2 evolution, and ATP hydrolysis. *Proc. Natl. Acad. Sci. U. S. A.* 56, 979–986. doi: 10.1073/pnas.56.3.979

Buren, S., Jimenez-Vicente, E., Echavarri-Erasun, C., and Rubio, L. M. (2020). Biosynthesis of nitrogenase cofactors. *Chem. Rev.* 120, 4921–4968. doi: 10.1021/acs.chemrev.9b00489

Chai, Y. H., Mohamed, M., Cheng, Y. W., Chin, B. L. F., Yiin, C. L., Yusup, S., et al. (2021). A Review on Potential of Biohydrogen Generation through Waste Decomposition Technologies. *Biomass Conv. Bioref.* 2, 1–26. doi: 10.1007/s13399-021-01333-z

Chandrasekhar, K., Lee, Y. J., and Lee, D. W. (2015). Biohydrogen production: strategies to improve process efficiency through microbial routes. *Int. J. Mol. Sci.* 16, 8266–8293. doi: 10.3390/ijms16048266

Chen, X., Lv, Y., Liu, Y., Ren, R., and Zhao, J. (2017). The hydrogen production characteristics of mixed photoheterotrophic culture. *Int. J. Hydrog. Energy* 42, 4840–4847. doi: 10.1016/j.ijhydene.2016.11.155

Colbeau, A., Richaud, P., Toussaint, B., Caballero, F. J., Elster, C., Delphin, C., et al. (1993). Organization of the genes necessary for hydrogenase expression in *Rhodobacter capsulatus*. Sequence analysis and identification of two *hyp* regulatory mutants. *Mol. Microbiol.* 8, 15–29. doi: 10.1111/j.1365-2958.1993.tb01199.x

Curatti, L., Ludden, P. W., and Rubio, L. M. (2006). NifB-dependent *in vitro* synthesis of the iron-molybdenum cofactor of nitrogenase. *Proc. Natl. Acad. Sci. U. S. A.* 103, 5297–5301. doi: 10.1073/pnas.0601115103

Demtröder, L., Pfänder, Y., Schäkermann, S., Bandow, J. E., and Masepohl, B. (2019). Nif A is the master regulator of both nitrogenase systems in *Rhodobacter capsulatus*. *Microbiology* 8:e921. doi: 10.1002/mbo3.921

Elkahlout, K. E., Sagir, E., Alipour, S., Koku, H., Gunduz, U., Eroglu, I., et al. (2019). Long-term stable hydrogen production from acetate using immobilized *Rhodobacter capsulatus* in a panel photobioreactor. *Int. J. Hydrog. Energy* 44, 18801–18810. doi: 10.1016/j.ijhydene.2018.10.133

Elsen, S., Dischert, W., Colbeau, A., and Bauer, C. E. (2000). Expression of uptake hydrogenase and molybdenum nitrogenase in *Rhodobacter capsulatus* is coregulated by the RegB-RegA two-component regulatory system. *J. Bacteriol.* 182, 2831–2837. doi: 10.1128/JB.182.10.2831-2837.2000

Feng, J., Yang, H., and Guo, L. (2018a). The photosynthetic hydrogen production performance of a newly isolated Rhodobacter capsulatus JL1 with various carbon sources. *Int. J. Hydrog. Energy* 43, 13860–13868. doi: 10.1016/j.ijhydene.2018.03.144

Feng, J., Yang, H., Wang, X., and Guo, L. (2018b). Enhanced hydrogen production performance of *cbbR* & *pycA* inactived *R. sphaeroides* mutant by improving the ammonium tolerance. *Int. J. Hydrog. Energy* 43, 18142–18150. doi: 10.1016/j.ijhydene.2018.07.196

Fiβler, J., Kohring, G. W., and Giffhorn, F. (1995). Enhanced hydrogen production from aromatic acids by immobilized cells of *Rhodopseudomonas palustris*. *Appl. Microbiol. Biotechnol.* 44, 43–46. doi: 10.1007/BF00164478

Gupta, S. K., Kumari, S., Reddy, K., and Bux, F. (2013). Trends in biohydrogen production: major challenges and state-of-the-art developments. *Environ. Technol.* 34, 1653–1670. doi: 10.1080/09593330.2013.822022

Jahn, A., Keuntje, B., Dörffler, M., Klipp, W., and Oelze, J. (1994). Optimizing photoheterotrophic H_2 production by Rhodobacter capsulatus upon interposon mutagenesis in the hupL gene. *Appl. Microbiol. Biotechnol.* 40, 687–690. doi: 10.1007/BF00173330

Jiménez-Llanos, J., Ramírez-Carmona, M., Rendón-Castrillón, L., and Ocampo-López, C. (2020). Sustainable biohydrogen production by chlorella sp. microalgae: a review. *Int. J. Hydrog. Energy* 45, 8310–8328. doi: 10.1016/j.ijhydene.2020.01.059

Joshi, S. M., Inamdar, S. A., Jadhav, J. P., and Govindwar, S. P. (2013). Random UV mutagenesis approach for enhanced biodegradation of sulfonated azo dye, green HE4B. *Appl. Biochem. Biotechnol.* 169, 1467–1481. doi: 10.1007/s12010-012-0062-5

Kim, E.-J., Lee, M.-K., Kim, M.-S., and Lee, J. K. (2008). Molecular hydrogen production by nitrogenase of *Rhodobacter sphaeroides* and by Fe-only hydrogenase of *Rhodospirillum rubrum*. *Int. J. Hydrog. Energy* 33, 1516–1521. doi: 10.1016/j.ijhydene.2007.09.044

Klein, G., Klipp, W., Jahn, A., Steinborn, B., and Oelze, J. (1991). The relationship of biomass, polysaccharide and H_2 formation in the wild-type and *nifA*/*nifB* mutants of *Rhodobacter capsulatus*. *Arch. Microbiol.* 155, 477–482. doi: 10.1007/Bf00244965

Krahn, E., Schneider, K., and Muller, A. (1996). Comparative characterization of H_2 production by the conventional Mo nitrogenase and the alternative "iron only" nitrogenase of *Rhodobacter capsulatus hup*$^-$ mutants. *Appl. Microbiol. Biot.* 46, 285–290. doi: 10.1007/s002530050818

Laocharoen, S., and Reungsang, A. (2014). Isolation, characterization and optimization of photo-hydrogen production conditions by newly isolated *Rhodobacter sphaeroides* KKU-PS5. *Int. J. Hydrog. Energy* 39, 10870–10882. doi: 10.1016/j.ijhydene.2014.05.055

Lee, B., Choi, G.-G., Choi, Y.-E., Sung, M., Park, M. S., and Yang, J.-W. (2014). Enhancement of lipid productivity by ethyl methane sulfonate-mediated random mutagenesis and proteomic analysis in *Chlamydomonas reinhardtii*. *Korean J. Chem. Eng.* 31, 1036–1042. doi: 10.1007/s11814-014-0007-5

Liu, T., Li, X., and Zhou, Z. (2010). Improvement of hydrogen yield by *hupR* gene knock-out and *nifA* gene overexpression in *Rhodobacter sphaeroides* 6016. *Int. J. Hydrog. Energy* 35, 9603–9610. doi: 10.1016/j.ijhydene.2010.06.072

Liu, B.-F., Ren, N.-Q., Ding, J., Xie, G.-J., and Guo, W.-Q. (2009). The effect of Ni^{2+}, Fe^{2+} and Mg^{2+} concentration on photo-hydrogen production by *Rhodopseudomonas faecalis* RLD-53. *Int. J. Hydrog. Energy* 34, 721–726. doi: 10.1016/j.ijhydene.2008.11.033

Ma, H., Yang, H., Zheng, X., Lie, T., and Yan, W. (2021). Promoting photo-fermentative hydrogen production performance by substituting the *rnf* promoter in *Rhodobacter capsulatus*. *Int. J. Hydrog. Energy* 46, 3742–3752. doi: 10.1016/j.ijhydene.2020.10.270

Masukawa, H., Inoue, K., Sakurai, H., Wolk, C. P., and Hausinger, R. P. (2010). Site-directed mutagenesis of the anabaena sp. strain PCC 7120 nitrogenase active site to increase photobiological hydrogen production. *Appl. Environ. Microbiol.* 76, 6741–6750. doi: 10.1128/AEM.01056-10

Masukawa, H., Mochimaru, M., and Sakurai, H. (2002). Disruption of the uptake hydrogenase gene, but not of the bidirectional hydrogenase gene, leads to enhanced photobiological hydrogen production by the nitrogen-fixing cyanobacterium *anabaena* sp. PCC 7120. *Appl. Microbiol. Biotechnol.* 58, 618–624. doi: 10.1007/s00253-002-0934-7

Miller, J. H. (1972). *Experiments in Molecular Genetics*. New York, NY: Cold Spring Harbor Laboratory.

Perin, G., Bellan, A., Segalla, A., Meneghesso, A., Alboresi, A., and Morosinotto, T. (2015). Generation of random mutants to improve light-use efficiency of *Nannochloropsis gaditana* cultures for biofuel production. *Biotechnol. Biofuels* 8:161. doi: 10.1186/s13068-015-0337-5

Plovins, A., Alvarez, A. M., Ibañez, M., Molina, M., and Nombela, C. (1994). Use of fluorescein-di-beta-D-galactopyranoside (FDG) and C12-FDG as substrates for beta-galactosidase detection by flow cytometry in animal, bacterial, and yeast cells. *Appl. Microbiol. Biotechnol.* 60, 4638–4641. doi: 10.1128/aem.60.12.4638-4641.1994

Rey, F. E., Heiniger, E. K., and Harwood, C. S. (2007). Redirection of metabolism for biological hydrogen production. *Appl. Environ. Microbiol.* 73, 1665–1671. doi: 10.1128/AEM.02565-06

Schindel, H. S., and Bauer, C. E. (2016). The RegA regulon exhibits variability in response to altered growth conditions and differs markedly between *Rhodobacter* species. *Microb. Genom.* 2:e000081. doi: 10.1099/mgen.0.000081

Schneider, K., Gollan, U., Dröttboom, M., Selsemeier-Voigt, S., and Müller, A. (1997). Comparative biochemical characterization of the iron-only nitrogenase and the molybdenum nitrogenase from *Rhodobacter capsulatus*. *Eur. J. Biochem.* 244, 789–800. doi: 10.1111/j.1432-1033.1997.t01-1-00789.x

Schneider, K., Müller, A., Schramm, U., and Klipp, W. (1991). Demonstration of a molybdenum- and vanadium-independent nitrogenase in a *nifHDK*-deletion mutant of *Rhodobacter capsulatus*. *Eur. J. Biochem.* 195, 653–661. doi: 10.1111/j.1432-1033.1991.tb15750.x

Schubert, K. R., and Evans, H. J. (1976). Hydrogen evolution: A major factor affecting the efficiency of nitrogen fixation in nodulated symbionts. *Proc. Natl. Acad. Sci. U. S. A.* 73, 1207–1211. doi: 10.1073/pnas.73.4.1207

Scolnik, P. A., and Haselkorn, R. (1984). Activation of extra copies of genes coding for nitrogenase in *Rhodopseudomonas capsulata*. *Nature* 307, 289–292. doi: 10.1038/307289a0

Seefeldt, L. C., Yang, Z. Y., Lukoyanov, D. A., Harris, D. F., Dean, D. R., Raugei, S., et al. (2020). Reduction of substrates by nitrogenases. *Chem. Rev.* 120, 5082–5106. doi: 10.1021/acs.chemrev.9b00556

Simpson, F. B., and Burris, R. H. (1984). A nitrogen pressure of 50 atmospheres does not prevent evolution of hydrogen by nitrogenase. *Science* 224, 1095–1097. doi: 10.1126/science.6585956

Skizim, N. J., Ananyev, G. M., Krishnan, A., and Dismukes, G. C. (2012). Metabolic pathways for photobiological hydrogen production by nitrogenase- and hydrogenase-containing unicellular cyanobacteria Cyanothece. *J. Biol. Chem.* 287, 2777–2786. doi: 10.1074/jbc.M111.302125

Strnad, H., Lapidus, A., Paces, J., Ulbrich, P., Vlcek, C., Paces, V., et al. (2010). Complete genome sequence of the photosynthetic purple nonsulfur bacterium *Rhodobacter capsulatus* SB 1003. *J. Bacteriol.* 192, 3545–3546. doi: 10.1128/JB.00366-10

Vignais, P. M., and Billoud, B. (2007). Occurrence, classification, and biological function of hydrogenases: an overview. *Chem. Rev.* 107, 4206–4272. doi: 10.1021/cr050196r

Vignais, P. M., Elsen, S., and Colbeau, A. (2005). Transcriptional regulation of the uptake [NiFe] hydrogenase genes in *Rhodobacter capsulatus*. *Biochem. Soc. Trans.* 33, 28–32. doi: 10.1042/BST0330028

Wang, D., Zhang, Y., Welch, E., Li, J., and Roberts, G. P. (2010). Elimination of Rubisco alters the regulation of nitrogenase activity and increases hydrogen production in *Rhodospirillum rubrum*. *Int. J. Hydrog. Energy* 35, 7377–7385. doi: 10.1016/j.ijhydene.2010.04.183

Weaver, P. F., Wall, J. D., and Gest, H. (1975). Characterization of *Rhodopseudomonas capsulata*. *Arch. Microbiol.* 105, 207–216. doi: 10.1007/BF00447139

Zhang, Y., Yang, H., Feng, J., and Guo, L. (2016). Overexpressing F0/F1 operon of ATPase in *Rhodobacter sphaeroides* enhanced its photo-fermentative hydrogen production. *Int. J. Hydrog. Energy* 41, 6743–6751. doi: 10.1016/j.ijhydene.2016.03.061

Zheng, Y., and Harwood, C. S. (2019). Influence of energy and electron availability on *in vivo* methane and hydrogen production by a variant molybdenum nitrogenase. *Appl. Environ. Microbiol.* 85, e02671–e02618. doi: 10.1128/aem.02671-18

frontiers | Frontiers in Microbiology

ORIGINAL RESEARCH
published: 28 September 2022
doi: 10.3389/fmicb.2022.903951

The Contribution of Proton-Donor pKa on Reactivity Profiles of [FeFe]-hydrogenases

*Effie C. Kisgeropoulos, Vivek S. Bharadwaj, David W. Mulder and Paul W. King**

National Renewable Energy Lab, Biosciences Center, Golden, CO, United States

OPEN ACCESS

Edited by:
Stefan Frielingsdorf, Technical University of Berlin, Germany

Reviewed by:
James Birrell, Max Planck Institute for Chemical Energy Conversion, Germany
Gustav Berggren, Uppsala University, Sweden

***Correspondence:**
Paul W. King
paul.King@nrel.gov

Specialty section:
This article was submitted to Microbiological Chemistry and Geomicrobiology, a section of the journal Frontiers in Microbiology

Received: *24 March 2022*
Accepted: *17 June 2022*
Published: *28 September 2022*

Citation:
Kisgeropoulos EC, Bharadwaj VS, Mulder DW and King PW (2022) The Contribution of Proton-Donor pKa on Reactivity Profiles of [FeFe]-hydrogenases. Front. Microbiol. 13:903951. doi: 10.3389/fmicb.2022.903951

The [FeFe]-hydrogenases are enzymes that catalyze the reversible activation of H_2 coupled to the reduction–oxidation of electron carriers. Members of the different taxonomic groups of [FeFe]-hydrogenases display a wide range of preference, or bias, for H_2 oxidation or H_2 production reactions, despite sharing a common catalytic cofactor, or H-cluster. Identifying the properties that control reactivity remains an active area of investigation, and models have emerged that include diversity in the catalytic site coordination environments and compositions of electron transfer chains. The kinetics of proton-coupled electron transfer at the H-cluster might be expected to be a point of control of reactivity. To test this hypothesis, systematic changes were made to the conserved cysteine residue that functions in proton exchange with the H-cluster in the three model enzymes: CaI, CpII, and CrHydA1. CaI and CpII both employ electron transfer accessory clusters but differ in bias, whereas CrHydA1 lacks accessory clusters having only the H-cluster. Changing from cysteine to either serine (more basic) or aspartate (more acidic) modifies the sidechain pKa and thus the barrier for the proton exchange step. The reaction rates for H_2 oxidation or H_2 evolution were surveyed and measured for model [FeFe]-hydrogenases, and the results show that the initial proton-transfer step in [FeFe]-hydrogenase is tightly coupled to the control of reactivity; a change from cysteine to more basic serine favored H_2 oxidation in all enzymes, whereas a change to more acidic aspartate caused a shift in preference toward H_2 evolution. Overall, the changes in reactivity profiles were profound, spanning 10^5 in ratio of the H_2 oxidation-to-H_2 evolution rates. The fact that the change in reactivity follows a common trend implies that the effect of changing the proton-transfer residue pKa may also be framed as an effect on the scaling relationship between the H-cluster di(thiolmethyl)amine (DTMA) ligand pKa and E_m values of the H-cluster. Experimental observations that support this relationship, and how it relates to catalytic function in [FeFe]-hydrogenases, are discussed.

Keywords: [FeFe]-hydrogenase, proton-coupled electron transfer, enzymatic reactivity, H-cluster, pKa and proton transfer, catalytic bias

INTRODUCTION

The [FeFe]-hydrogenase class of enzymes fulfill significant roles in H_2 metabolism and energy transduction. They catalyze the reversible reaction, $H_2 \leftrightarrow 2H^+ + 2e$- by performing either H_2 gas evolution (i.e., proton reduction) or H_2 oxidation. This is mediated by a complex metallocofactor, or H-cluster, consisting of a diiron site ($[2Fe]_H$) coordinated by a conserved cysteine to a [4Fe-4S] cubane ($[4Fe\text{-}4S]_H$; **Figure 1**). To achieve this reversibility, the enzyme must couple dynamic fluxes in both PT and ET to catalytic H_2 activation. As a result, the catalytic function of the H-cluster must be adapted to a changing energy landscape. [FeFe]-hydrogenases therefore represent an ideal model system for understanding the mechanisms that enzymes employ to control proton-coupled electron transfer (PCET) at metal sites to accomplish chemical transformation reactions. While most [FeFe]-hydrogenases possess neutral reactivity profiles, i.e., similar rates for both H_2 evolution and H_2 oxidation, there are instances where reactivity for either one or the other is favored. For example, the overall catalytic preference across the diversity of [FeFe]-hydrogenase from *Clostridium pasteurianum* spans an impressive seven orders of magnitude from CpI (neutral reactivity) to CpII (biased toward H_2 oxidation) and CpIII (biased toward H_2 evolution; Adams, 1990; Poudel et al., 2016; Artz et al., 2020b). The wide range in reactivity stands in contrast to the fact that all [FeFe]-hydrogenases studied so far share a common H-cluster cofactor.

Diversity in the amino acids that comprise the catalytic site environments, differential stabilization of catalytic intermediates, amino acid composition of proton transfer pathways, and differences in thermodynamic profiles of electron transfer relays have all been proposed to account for the observed differences in reactivity profiles of [FeFe]-hydrogenases (Cornish et al., 2011; Hexter et al., 2012; Ginovska-Pangovska et al., 2014; Artz et al., 2017; Caserta et al., 2018; Duan et al., 2018; Gauquelin et al., 2018; Rodríguez-Maciá et al., 2019; Senger et al., 2019; Lampret et al., 2020). It is conceivable these properties converge to control PCET chemistry at the H-cluster, and changes in the coupling of protons and electrons at the H-cluster may also have a role in the control of reactivity. Computational and experimental studies have shown that PT flux to the H-cluster involves defined, well-conserved structural elements (Long et al., 2014; Duan et al., 2018; Lampret et al., 2020) including a strictly conserved cysteine residue that forms an H-bonding network with the di(thiolmethyl)amine ligand (DTMA) and distal Fe (Fe_D) of $[2Fe]_H$ in catalytically active enzymes (**Figure 1**). Cysteine is a relatively basic residue (free cysteine pKa ~8) and mediates the proton exchange step with the H-cluster during catalysis. Electron transfer can also be a control point of catalytic reactivity due to variability in midpoint-potentials of accessory iron–sulfur clusters (referred to as F-clusters) and/or their electronic interactions with the H-cluster (Adams et al., 1989; Mulder et al., 2013; Artz et al., 2017; Rodríguez-Maciá et al., 2017, 2019, 2020; Caserta et al., 2018). Together these mechanisms exert control over the PT and ET fluxes in the enzyme and contribute to the control of the PCET kinetics at the H-cluster. For example, the fine-tuning of the thermodynamic equilibria between reaction intermediates (Artz et al., 2017), H-bonding effects on the electronic structure of the H-cluster (Mulder et al., 2014; Pham et al., 2018), or matching of proton transfer pKa values to the H-cluster DTMA ligand pKa (Lampret et al., 2020; Birrell et al., 2021) are all mechanisms that have been demonstrated to influence the catalytic cycle and overall reactivity profile of the [FeFe]-hydrogenases.

To address understanding of the PCET mechanism in [FeFe]-hydrogenases, this work summarizes the results on testing the hypothesis that the pKa of the conserved residue that mediates the coupling of PT to ET (or PCET) at the H-cluster can be tuned to control reactivity in [FeFe]-hydrogenases. Using [FeFe]-hydrogenases that differ in their intrinsic reactivity, we applied reverse engineering to replace the conserved cysteine with either a more basic (serine) or acidic (aspartate) residue (**Figure 1**). The enzymes examined include CaI from *Clostridium acetobutylicum* (neutral reactivity) and CpII from *C. pasteurianum* (H_2 oxidation bias), both of which have accessory F-clusters with different thermodynamic profiles (Adams et al., 1989), and HydA1 from *Chlamydomonas reinhardtii* (CrHydA1, neutral reactivity), which possesses only the catalytic H-cluster. Computational modeling was used to evaluate the pKa's of the native and enzyme variants, and the H_2 oxidation and evolution rates were measured to assess the reactivity profiles. The results of this work, in the context of previous biophysical studies of the reaction intermediates and redox profiles of related variants, are integrated into an overall thermodynamic model of reactivity control in [FeFe]-hydrogenase.

MATERIALS AND METHODS

Expression, Purification, and Activity Measurements of [FeFe]-hydrogenases

CaI, CpII, and CrHydAI [FeFe]-hydrogenases were expressed and purified as previously described (King et al., 2006; Mulder et al., 2014; Ratzloff et al., 2018; Artz et al., 2020b) and assayed for both H_2 evolution and H_2 oxidation (uptake) using standard biochemical assays (Duan et al., 2018; Artz et al., 2020b).

H_2 production was measured by gas chromatography (Agilent Technologies) using methyl viologen (MV) as the electron donor. The 2 ml reactions were set up in 13 ml anaerobic vials containing 1 µg to 1 mg of enzyme in 50 mM Tris (pH 8–8.3), 200–300 mM NaCl, 5% glycerol, and 10–100 mM sodium dithionite (DT); enzyme concentrations were varied as needed to measure kinetic parameters. Reactions were carried out at 37°C and initiated by the addition of MV to a final concentration of 5–80 mM. The reported rates were measured in the initial linear phase (varying from 5 to 40 min for the native enzymes and enzyme variants) of the reaction.

H_2 oxidation was monitored by UV–Vis using either methylene blue (MB) monitored at 664 nm ($\varepsilon = 95{,}000\ M^{-1}\ cm^{-1}$)

Abbreviations: PT, Proton transfer; ET, Electron transfer; H-bonding, hydrogen-bonding.

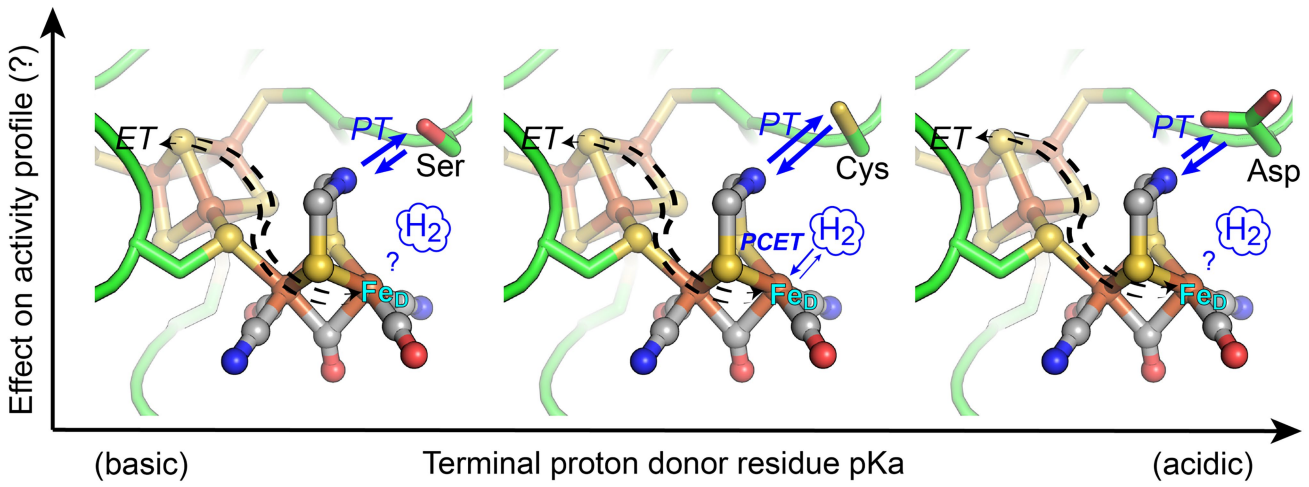

FIGURE 1 | Structural depiction of the [FeFe]-hydrogenase H-cluster active-site where coordination of orthogonal electron transfer (ET) and proton transfer (PT) pathways by proton-coupled electron transfer (PCET) at the distal Fe atom (Fe_D) of $[2Fe]_H$ results in catalytic activation of H_2. In this work, the conserved Cys residue (middle panel), which functions in proton exchange with the H-cluster di(thiolmethyl)amine (DTMA) ligand, was changed to either Ser (more basic pKa, left) or Asp (more acidic pKa, right). The activity profile of enzyme variants was measured to ascertain the extent that engineered variations to the pKa of the exchange step alter reactivity of [FeFe]-hydrogenases. Blue arrows indicate relative changes in the proton transfer direction bias for the variants. Structural representation from PDB 3C8Y, with substitution of Ser or Asp by alignment to PDB 6GLZ.

or benzyl viologen (BV) monitored at 600 nm ($\varepsilon = 10{,}000\ M^{-1}\ cm^{-1}$) as the electron acceptor (Cenens et al., 1988; Dörner and Boll, 2002; Duan et al., 2018). The 2 ml reactions were set up in 4 ml, septa-sealed cuvettes, with 1 µg to 1 mg of enzyme at various concentrations in 50 mM Tris pH 8–8.3, 300 mM NaCl, and 5% glycerol. The cuvettes were then either sparged continuously under H_2 for 5 min, or subjected to 10 vacuum/refill cycles with H_2 on a Schlenk line, and allowed to incubate under an overpressure of H_2 at room temperature for 5–10 min. The reaction was then initiated with the addition of the redox dye, to a final concentration of 38 µM (MB) or 10 mM (BV). No reduction of either dye was observed when added to cuvettes containing only buffer. The V_{max} values for CaI, CpI, and CrHydA1 are similar when either MV or MB is used as the acceptor (Adams and Mortenson, 1984; Artz et al., 2020b). The values for CpII are maximal using MB as the acceptor (Adams and Mortenson, 1984); therefore, MB was used for all CpII H_2 oxidation assays. Maximal rates were calculated over the initial 1–5 min of the reaction.

Structural Models and pKa Calculations of [FeFe]-hydrogenase Variants

Since experimentally characterized and holo-structures of CrHydA1, CpII, and CaI are not yet available, the open-source neural-network-based protein prediction tool AlphaFold2 was used for their structure prediction (Jumper et al., 2021). For each protein, only the amino acid sequence was used as input to AlphaFold2 and five models were generated. Since Alphafold2 does not incorporate ligands into its structure predictions, the top-ranked AlphaFold2 predicted structure for each [FeFe]-hydrogenase was aligned with the experimental X-ray crystal structure for CpI (PDB ID: 3C8Y) for the incorporation of the H-cluster into the predicted structures. The H-cluster-bound top-ranked models for each [FeFe]-hydrogenase were then used for pKa estimations for its titratable residues using the Propka ver. 3.1 software package (Bas et al., 2008; Søndergaard et al., 2011). Of particular interest are the pKa predictions for the conserved cysteine residue (and aspartic acid for the C→D variant) that functions in proton exchange with the H-cluster. Since Propka does not consider residues with bulk pKa values >10 as titratable, values for the serine residue in the C→S variants were not predicted in this study, and experimental values from related model systems were used (Bruice et al., 1962; Liepinsh and Otting, 1996). It may be noted that these pKa calculations are intended as estimates and not exact determinations of the pKa values. This will require more computationally intensive techniques such as constant pH molecular dynamics simulations which are not undertaken in this study.

RESULTS

pKa Calculations and Activity Profiles of Native [FeFe]-hydrogenases

The strictly conserved cysteine residue of catalytically active [FeFe]-hydrogenases (protein sequence number C298 CaI, C169 CpII, and C169 CrHydA1) is known to function in mediating the exchange of protons between the conserved proton transfer pathway and the H-cluster during catalysis (Cornish et al., 2011; Ginovska-Pangovska et al., 2014; Mulder et al., 2014; Lampret et al., 2020). The free-energy of proton transfer, ΔG^{PT}, is related to the pKa of the exchange site by Equation 1;

$$\Delta G^{PT} = 2.303 \cdot RT \cdot pKa \quad (1)$$

To examine the extent that the proton-transfer residue pKa controls H-cluster protonation and enzyme reactivity (**Figure 1**), we first evaluated the cysteine pKa values using computational approaches and established a baseline of activity values for the model [FeFe]-hydrogenases, CaI, CpII, and CrHydA1 (**Table 1**). Proton-transfer residue pKa values were calculated using Propka (Olsson et al., 2011; Søndergaard et al., 2011), a computational treatment for the empirical prediction of pKa values which also takes into account the influences of the protein environment (*vide infra*). For the [FeFe]-hydrogenases listed in **Table 1**, the determined cysteine pKa values ranged 11.5–12. It may be noted that the calculated values are more basic compared to the pKa value for a cysteine residue in bulk solution. This can be attributed to the fact that Propka considers the contributions from desolvation energies, H-bonding energies, electrostatic reorganization energies, and coulombic interactions that are all cumulatively added to the bulk pKa value of a given titratable residue. A greater degree of H-bonding shifts the pKa to be more basic, while a greater degree of desolvation makes conjugate bases more basic and conjugate acids more acidic (Bas et al., 2008). For the conserved cysteine in [FeFe]-hydrogenases, these collective effects contribute to an overall more basic pKa value.

Table 1 also shows H_2 evolution and H_2 oxidation rates for the model [FeFe]-hydrogenases. The corresponding reactivity preference, also referred to as catalytic bias (Abou Hamdan et al., 2012; Artz et al., 2020b; Fourmond et al., 2021; Mulder et al., 2021), can be discerned from the ratio of H_2 oxidation activity to H_2 evolution activity. A ratio approaching 1 is representative of the energy landscapes of the enzyme being leveled so that it no longer catalytically favors one direction or another. In such a case, the enzyme is described as having a "neutral" catalytic bias. As shown in **Table 1**, the dye-assays show that CaI, CpI, and CrHydA1 each have an H_2 oxidation-to-H_2 evolution ratio of <18, with CaI and CpI being slightly more neutral in bias than CrHydA1.

In contrast, and as shown previously (Adams and Mortenson, 1984; Chen and Blanchard, 1984; Adams, 1990; Artz et al., 2020b), CpII has a large bias toward H_2 oxidation, with an H_2 oxidation-to-H_2 evolution ratio that is two orders of magnitude greater than for CaI, CpI, or CrHydA1 (**Table 1**). It is noted that the calculated cysteine pKa values for all the enzymes examined here are generally basic and that all the catalytic [FeFe]-hydrogenases incorporate cysteine at the exchange site (an exception to cysteine occurs in the sensory [FeFe]-hydrogenases, see Poudel et al., 2016; Chongdar et al., 2018; Fasano et al., 2021). Thus, it does not appear that the pKa of the exchange step is used to control the reactivity or catalytic bias. The fact that the relative oxidation/evolution reaction profiles differ by as much as 10^3, with cysteines having similar pKa values, implies other factors, such as F-cluster reduction potentials, dynamic secondary interactions, and local electrostatics around the H-cluster (Adams et al., 1989; Caserta et al., 2018; Artz et al., 2020b), might be critical to the control of reactivity between enzyme types. It is also noted that the E_m of the H_{ox}/H_{red} transition is similar in value for CpI, CpII, and CrHydA1 (Adams et al., 1989; Silakov et al., 2009) and near the value of the H^+/H_2 couple (−413 mV vs. SHE at pH 7, 1 atm H_2), which is consistent with the minimal overpotential requirement of these enzymes for catalysis.

Cys→Ser Variant pKa and Activity Profiles

To probe how differences in reactivity of CaI, CpII, and CrHydA1 are influenced by the pKa of the nearby proton donor residue, we examined enzyme variants where the cysteine residue is

TABLE 1 | Overview of WT [FeFe]-hydrogenase activity[a] profiles.

Enzyme	[b]H_2 oxidation Activity	[c]H_2 evolution Activity	Oxidation/ Evolution ratio	Calc. Cysteine pKa	[d]E_m (mV) $H_{ox}/H_{red(H+)}$	References
CpII	110,000(MB) 34,000(MB) 17,600(MB)	16 10 3.5	6,900 3,400 5,000	11.7	−410	Artz et al., 2020b Adams, 1990 Chen and Blanchard, 1984
CpI	24,000(MB) 14,000(MV)	5,500 4,000	4 4	11.5	−400	Adams, 1990 Adams and Mortenson, 1984
CaI	10,057(MV)	2,234 ± 214	5	11.6	NA	Girbal et al., 2005 This work
CrHydA1	18,375(BV)	1,000	18	12.0	−400 (−362)	Duan et al., 2018 Yacoby et al., 2012

[a]*Activity reported as μmol H_2/min/mg enzyme for either H_2 oxidation or evolution.*

[b]*The V_{max} values for CpII H_2 oxidation assays are measured using 38 μM methylene blue (MB, E_m = +11 mV) as the acceptor (Adams, 1990). The V_{max} value of 10,057 for CaI was measured with methyl viologen (MV) E_m = −440 mV (Girbal et al., 2005), and the value of 18,357 for CrHydA1 (Duan et al., 2018) was measured with benzyl viologen (BV) E_m = −350 mV and at pH 10.*

[c]*H_2 evolution rates obtained using reduced MV (5–10 mM) as the electron acceptor. The CaI value of 2,234 ± 214 is from this work; the CrHydA1 value of 1,000 is from (Yacoby et al., 2012). The K_m values for MV are: CpII, 0.3 mM (Adams, 1990); CpI, 6 mM (Adams and Mortenson, 1984; Adams, 1990); CaI, 0.6–1 mM (Girbal et al., 2005); and CrHydA1, 0.8–0.9 mM (Von Abendroth et al., 2008).*

[d]*E_m is defined as the H_{ox}/H_{red} or $H_{ox}/H_{red}H$+ redox couples, which are not experimentally distinguished. CpI/CpII E_m values at pH 8 (Adams, 1990); CrHydAI E_m −400 mV at pH 8 (Silakov et al., 2009), or −362 mV at pH 8 (Sommer et al., 2017).*

either altered to a more basic serine (C→S) or more acidic aspartate (C→D) residue. Previous site-saturation studies at the cysteine position have shown that these two mutations retain H-cluster cofactor incorporation with decreased H_2 evolution activity (Knörzer et al., 2012; Morra et al., 2012; Mulder et al., 2014; Duan et al., 2018); however, the effects on H_2 oxidation and full activity profiles in the variants are less understood.

The Propka method used to calculate cysteine pKa values is not configured to calculate serine pKa values (see the section Materials and Methods for a detailed discussion). However, experimental measurements of the pKa of -OH moieties in mimics of the catalytic triad in chymotrypsin assign the pKa of serine to be ~13.6 (Bruice et al., 1962). In this enzyme, the serine-OH group is deprotonated by the Nε atom of a nearby histidine during catalytic esterification of aromatic amino acids (Bruice et al., 1962; Frey, 2001). The basicity of the histidine Nε atom, with a pKa of 12, is within the pKa range of the H-cluster DTMA ligand that was determined from the modeling of FTIR spectro-electrochemical data from CrHydA1 collected at different pH values ($H_{red}/H_{red}H^+$ pKa = 7.2 and, $H_{sred}/H_{sred}H^+$ pKa = 11.6; Sommer et al., 2017; Birrell et al., 2021). Based on these similarities to [FeFe]-hydrogenase, we have tentatively assigned the serine residue as having a pKa of ≥13.6. Other experimental studies have measured the pKa of the hydroxyl group on a serine amino acid to be >16 using NMR (Liepinsh and Otting, 1996), further indicating its highly basic nature.

Using redox-dye mediated assays on the purified CrHydA1 C169S variant, H_2 oxidation and evolution activities were determined and compared to CaI C298S (Cornish et al., 2011) and CpII C169S (Artz et al., 2020a; **Table 2**). The reactivity results show a collective shift toward H_2 oxidation reactivity for all the enzymes. Whereas CpII C169S maintained the highest H_2 oxidation preference among the C→S variants, the reactivity preference of CaI C298S likewise shifted over 100-fold toward H_2 oxidation compared to WT CaI. It is also noted that while all C→S variants exhibit a decrease in the absolute reactivity rates compared to WT counterparts, this decrease is consistently more pronounced for the H_2 evolution rates (**Table 2**), as has been observed for CpI (Cornish et al., 2011). This can be viewed as consistent with the basic pKa shift in relation to native Cys for the PT exchange step, and the transfer of protons from the H-cluster being more favored (discussed in more detail below).

Cys→Asp Variant pKa and Activity Profiles

The effect of introducing a more acidic proton donor residue near the H-cluster in CaI, CpII, and CrHydA1 was also examined using the C→D variant (**Table 3**). In contrast to the C→S variant, it could be expected that the more acidic pKa of the carboxyl group (pKa ≈ 4–6, **Table 3**) would cause a shift in the reactivity profile toward H_2 evolution, resulting in oxidation/

TABLE 2 | Activity[a] profiles of [FeFe]-hydrogenase C→S variants.

Enzyme	[b]H_2 oxidation activity	% of WT	[c]H_2 evolution activity	% of WT	Oxidation/ Evolution	Serine pKa[d]	References
CpII C169S	15,000$^{(MB)}$	14%	0.2	1.3%	75,000	≥13.6	Artz et al., 2020a
CaI C298S	1,600$^{(BV)}$	16%	1.2 ± 0.2	0.05%	1,300	≥13.6	Cornish et al., 2011, This work
CpI C299S	ND	ND	1.05	0.03%	–	≥13.6	Duan et al., 2018
CrHydA1 C169S	0.80 ± 0.1$^{(BV)}$ ND	0.004% ND	0.02 ± 0.01 0.92	0.002% 0.1%	40 –	≥13.6	This work Duan et al., 2018

[a]*Activity reported as μmol H_2/min/mg enzyme for either H_2 oxidation or evolution.*
[b]*H_2 oxidation rates obtained at pH 8–8.3 using the redox dyes indicated in superscripts as electron acceptors: MB = methylene blue (38 μM), or BV = benzyl viologen (10 mM). CaI C298S H_2 oxidation with BV, extrapolated from value of 16% measured for CpI C299S compared to WT (Cornish et al., 2011).*
[c]*H_2 evolution rates obtained using 10–80 mM reduced MV as the electron donor. The value for CaI C298S is from this work.*
[d]*Estimated based on Bruice et al. (1962).*

TABLE 3 | Activity[a] profiles of [FeFe]-hydrogenase C→D variants.

Enzyme	[b]H_2 oxidation Activity	% of WT	[c]H_2 evolution Activity	% of WT	Oxidation/ Evolution	Calc. Aspartate pKa	References
CpII C169D	19.5 ± 3.6$^{(MB)}$	0.02%	1.8 ± 0.4	11%	11	4.1	This work
CaI C298D	433$^{(MV)}$	4%	230	10%	2	4.3	Morra et al., 2012
CrHydA1 C169D	41 ± 17$^{(BV)}$ 225$^{(BV)}$	0.2% 1.2%	151 ± 41 582	15% 58%	0.3 0.4	6.6	This work Duan et al., 2018

[a]*Activity reported as μmol H_2/min/mg enzyme for either H_2 oxidation or evolution.*
[b]*H_2 oxidation rates were measured at pH 8–8.3 using the redox dyes indicated in superscripts; MB = methylene blue (38 μM), MV = methyl viologen, BV = benzyl viologen (10 mM).*
[c]*H_2 evolution rates were obtained using 5–10 mM MV as the electron donor.*

evolution ratios below 1. CrHydA1 C169D displayed a ratio <1 (oxidation/evolution ratio = 0.3) although this still falls within the definition for neutral bias given above, while CaI C298D also retains a neutral bias (Morra et al., 2012). Remarkably, CpII C169D had neutral reactivity, with an oxidation/evolution ratio of 11 (**Table 3**).

Although the WT activity profiles of CaI and CrHydAI are also considered neutral, the H_2 oxidation/evolution values for their C→D variants decreased relative to the WT, indicating a skewing toward H_2 evolution that was not present before. This is much more striking in the case of CpII, where the H_2 oxidation/evolution ratio for the C169D variant is shifted three orders of magnitude from WT in the direction of H_2 evolution, effectively neutralizing the CpII bias toward H_2 oxidation. As observed for the C→S variants, there is an overall decrease in the absolute H_2 reactivity rates of the C→D variants compared to WT counterparts, with the decrease now consistently more pronounced for the H_2 oxidation rates. From this, it appears that the pKa shift of the C→D substitution provides an overall leveling of the catalytic bias (oxidation/evolution ratio approaching 1).

TABLE 4 | Summary of exchange site pKa on [FeFe]-hydrogenase activity[a] profiles.

Enzyme	pKa[b]	Oxidation/ Evolution Reactivity Ratio	[c]Fold-Change Versus WT	[d]E_m (mV) $H_{ox}/H_{red(H+)}$
CpII C169S	≥13.6	75,000	$11^{(Ox)}$	NA
Ca1 C298S	≥13.6	1,300	$260^{(Ox)}$	NA
CrHydA1 C169S	≥13.6	40	$2.2^{(Ox)}$	−283
CpII	11.7	6,900	1	−410
CaI	11.6	5	1	NA
CrHydAI	12.0	18	1	−400 (−362)
CpII C169D	4.1	11	$627^{(Evol)}$	NA
CaI C298D	4.3	2	$2.5^{(Evol)}$	NA
CrHydA1 C169D	6.6	0.3	$60^{(Evol)}$	NA

[a]Activity reported as μmol H_2/min/mg enzyme for either H_2 oxidation or evolution.
[b]The pKa of the Serine -O(H) is estimated from values for Serine -O(H) in chymotrypsin analogues (Bruice et al., 1962; Frey, 2001).
[c]The amount (or fold) change in the variant oxidation/evolution reactivity ratios when compared to the corresponding WT ratio, the direction of the shift (either toward H_2 oxidation or H_2 evolution) is indicated in superscripts.
[d]E_m is defined as the redox couple between H_{ox} and H_{red} or $H_{red}H+$. CrHydA1 C169S E_m value at pH 8 (Mulder et al., 2017). CrHydA1 -400 mV (Silakov et al., 2009) and −362 mV (Sommer et al., 2017) determined from separate studies.

DISCUSSION

Here, we have tested the prediction that reactivity in [FeFe]-hydrogenases can be tuned through perturbing the pKa value of the amino acid in the secondary coordination sphere that mediates the proton exchange step with the H-cluster. Modulation of the proton exchange site pKa was achieved by mutation of Cys and led to pronounced shifts in the reactivity profiles of all the [FeFe]-hydrogenases that were tested, regardless of the presence of F-clusters or the intrinsic bias (**Table 4**; **Figure 1**). The native [FeFe]-hydrogenases establish a common baseline for comparison between the different enzymes as they exhibit similar properties, such as the pKa of the conserved cysteine residue (pKa = 11.5–12) and the E_m for the H_{ox}/H_{red} couple, which is relevant to the initial step for proton binding or H_2 activation (CpII, −410 mV; CpI, −400 mV; and CrHydAI, −400 mV; Adams, 1990; Silakov et al., 2009). The observed trends can be summarized as follows: the C→S substitution resulted in a more basic pKa that shifted reactivity toward H_2 oxidation, while the C→D substitution resulted in a more acidic pKa that shifted the reactivity toward that of H_2 evolution, resulting in an overall neutralization of the catalytic bias.

[FeFe]-hydrogenase Reactivity and the pKa, E_m Scaling Relationship

The selection of either Cys, Ser, or Asp as the proton exchange site residue imparts a profound control over reactivity, which we propose in part results from perturbing the balance between exchange site pKa (**Tables 1–3**) and the pKa of the DTMA ligand of the H-cluster (**Figure 2**), and changes to H-bonding at the DTMA in the variants (Duan et al., 2018; Pham et al., 2018). The change from Cys to Ser also coincides with previous observations (Mulder et al., 2017) of a positive shift in the measured H-cluster reduction potentials, consistent with changes to the H-cluster electronic structure. The values for CrHydA1 C169S compared to WT are −283 and −400 mV vs. NHE for reduction of H_{ox} to H_{red}, and −431 and −460 mV vs. NHE for reduction of H_{red} to H_{hyd} or H_{sred}, respectively (Silakov et al., 2009; Mulder et al., 2017; **Table 4**). Conversely, it has been shown that CaI C298D has a proportionately higher population of H_{ox} under reduction with either H_2 or sodium dithionite compared to WT CaI (Morra et al., 2016). This difference is consistent with a negative shift in the E_m value, and presumably a shift toward a more basic pKa value of the H-cluster DTMA ligand.

The differential stabilization of H-cluster oxidation states and E_m shifts can be explained within the framework of the linear-scaling relationships between the pKa and E_m of a transition metal catalyst (**Figure 2**; Bullock et al., 2014; Brereton et al., 2020; Puthenkalathil and Ensing, 2021). In this relationship, there is a direct correlation of the metal site pKa to the E_m value of the reduction potential, where a more acidic pKa is matched by a more positive reduction potential. For the serine variant of CrHydA1, substitution of the more basic serine would be predicted to induce a relative acidic shift in the H-cluster DTMA pKa value, and the E_m values of the H-cluster would be predicted to shift to more positive values. This is in fact the case (**Table 4**), which explains in part why the serine variants of CrHydA1 and CaI exhibit higher populations of the reduced states, predominantly H_{sred} and H_{hyd}, compared to the native enzyme under the same reducing conditions (Mulder et al., 2014, 2017; Pham et al., 2018; Ratzloff et al., 2018). The corresponding effect is also observed for the CaI aspartate variant, which maintains a high population of H_{ox} under reducing conditions (Morra et al., 2016). Thus, the effect of the cysteine variants on [FeFe]-hydrogenase reactivity can be modeled as a manifestation of combined changes to the

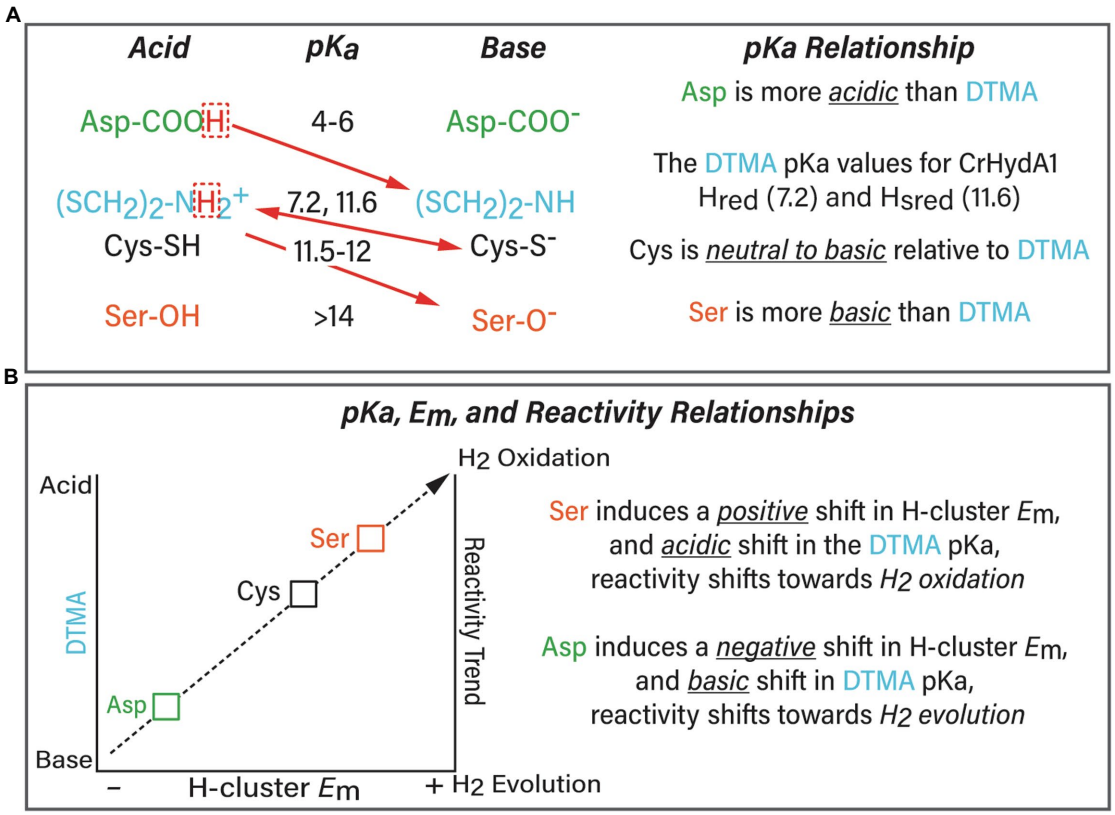

FIGURE 2 | (A) Summary of the relationship between the exchange site pKa (Asp, green; Cys, black; and Ser, orange) and pKa of the H-cluster DTMA ligand (blue). The preferred proton transfer direction is indicated with red arrows. The pKa values for Asp, Cys, and Ser were calculated in this study, and the measured pKa values for the bridging ligand di(thiolmethyl)amine (DTMA, blue) were taken from (Sommer et al., 2017; Birrell et al., 2021) for CrHydA1. The scaling model predicts that Asp induces a basic shift whereas Ser induces an acidic shift in DTMA pKa, this would create an even more favorable direction bias than indicated in the Figure. **(B)** Summary of the model of the pKa, E_m, and reactivity relationships based on the results of this work.

pKa relationship with DTMA, and to the E_m values of the H-cluster, which are summarized in **Figure 2**. The collective effect leads to a change in reactivity of [FeFe]-hydrogenase for H_2 oxidation (e.g., acidic H-cluster pKa and positive E_m shift) or H_2 evolution (e.g., basic H-cluster pKa and negative E_m shift; Artz et al., 2020b). The relationship between the exchange site pKa and the H-cluster DTMA pKa modeled in **Figure 2** predicts that there should be a corresponding negative shift in the value of E_m for C→D variants. This prediction is supported by IR spectra of the H_2, and dithionite reduced CaI C298D that clearly shows a high population of H_{ox}, and only minor populations of reduced states compared to the spectra of WT CaI, prepared under the same conditions (Morra et al., 2016).

Expanding the Model for Exchange Site Influence on Reactivity and the Special Case of CpII

It is also possible that the differences in reactivity arise from contributions other than pKa effects. In agreement with this, there are changes in the H-cluster electronic structures of Cys variants evidenced by changes in the FTIR and EPR spectra of catalytic intermediates compared to native enzymes (Mulder et al., 2013, 2014, 2017; Morra et al., 2016), that may occur from secondary sphere effects in the variants. Examples of these effects include the hydrophobicity, charge, electrostatics, and H-bonding networks that can control FeS cluster electronic structures and reduction potentials (Zuris et al., 2010; Hosseinzadeh and Lu, 2016). Indeed, the H_{hyd} state of the CrHydA1 C→S variant has been modeled as having a more contracted H-bonding network between the H-cluster Fe_D and the serine O-atom, when compared to the distance from Fe_D and the S-atom of cysteine in the native enzyme (Pham et al., 2018). The shorter N–H-O bond lengths vs. N–H-S accounted for shifts in the Fe-H/D frequencies in the NRVS spectra of H_{hyd}, and likely account for frequency shifts in νCO modes of redox intermediates in the FTIR spectra of the Cys-to-Ser variant versus wild-type (see Mulder et al., 2014, 2017).

Furthermore, whereas the model we set forth in **Figure 2** correlates trends in reactivity to changes in pKa, it does not completely account for differences in intrinsic reactivity between the different types of [FeFe]-hydrogenases we tested. Specifically, the fact that the cysteine variants of CpII have comparatively low H_2 evolution rates indicates that control of reactivity is not entirely embodied within the pKa relationship. The fact that cysteine has a basic pKa in all [FeFe]-hydrogenases, yet

CpII is strongly biased toward H_2 oxidation, implies that the H-cluster may be tuned differently compared to CpI/CaI, or CrHydA1. This could include effects such as dynamic secondary interactions and local electrostatics around the H-cluster, or differential stabilization of catalytic intermediates (Artz et al., 2020b). Mechanisms such as long-range potential effects from F-clusters may also contribute to the differences in reactivity of CpII vs. CpI/CaI and CrHydA1. These details indicate there are additional layers of control of H-cluster reactivity, for example, from the surrounding dielectric (Artz et al., 2020b), spin (de)localization, and other aspects of the electronic structure, the effects of which are being currently investigated by our group.

CONCLUSION

The outcome of these results identifies that the exchange site residue in proton transfer at the H-cluster can be used to control the reaction equilibria of [FeFe]-hydrogenases for H_2 activation. Together, the interplay of pKa and electronic effects integrate as a framework for rationalizing the overall free energy landscape surrounding the H-cluster in terms of a scaling relationship, useful for understanding how [FeFe]-hydrogenase control reactivity (**Figure 2**). Fine-tuning the H-cluster electronic structure by other outer non-coordinating residues is emerging from biophysical and structural studies of [FeFe]-hydrogenase diversity (Poudel et al., 2016; Caserta et al., 2018; Chongdar et al., 2018; Rodríguez-Maciá et al., 2019; Artz et al., 2020b; Lampret et al., 2020; Fasano et al., 2021) and informed by decades of studies on iron–sulfur clusters (Beinert et al., 1997; Bominaar et al., 1997; Brereton et al., 1998, 1999; Ye et al., 2019). Combining mutational studies with biochemical and biophysical analysis in the context of these findings will likely contribute to further insights into the exquisite control of catalysis and reactivity in [FeFe]-hydrogenases.

DATA AVAILABILITY STATEMENT

The original contributions presented in the study are included in the article/supplementary material; further inquiries can be directed to the corresponding author.

AUTHOR CONTRIBUTIONS

All authors analyzed data respective to their experiments. EK, DM, and PK performed protein expression, purification, and biochemical assays. VB conducted computational analyses on [FeFe]-hydrogenases. All authors contributed to the writing and/or editing the manuscript. All authors contributed to the article and approved the submitted version.

FUNDING

Funding was provided by the U.S. Department of Energy Office of Basic Energy Sciences, Division of Chemical Sciences, Geosciences, and Biosciences, Photosynthetic Systems Program.

LICENSES AND PERMISSIONS

REFERENCES

Abou Hamdan, A., Dementin, S., Liebgott, P.-P., Gutierrez-Sanz, O., Richaud, P., De Lacey, A. L., et al. (2012). Understanding and tuning the catalytic bias of hydrogenase. *J. Am. Chem. Soc.* 134, 8368–8371. doi: 10.1021/ja301802r

Adams, M. W. W. (1990). The structure and mechanism of iron-hydrogenases. *Biochim. Biophys. Acta* 1020, 115–145.

Adams, M. W., Eccleston, E., and Howard, J. B. (1989). Iron-sulfur clusters of hydrogenase I and hydrogenase II of *Clostridium pasteurianum*. *Proc. Natl. Acad. Sci.* 86, 4932–4936. doi: 10.1073/pnas.86.13.4932

Adams, M. W., and Mortenson, L. E. (1984). The physical and catalytic properties of hydrogenase II of *Clostridium pasteurianum*. A comparison with hydrogenase I. *J. Biol. Chem.* 259, 7045–7055. doi: 10.1016/S0021-9258(17)39835-6

Artz, J. H., Mulder, D. W., Ratzloff, M. W., Lubner, C. E., Zadvornyy, O. A., Levan, A. X., et al. (2017). Reduction potentials of [FeFe]-hydrogenase accessory iron–sulfur clusters provide insights into the energetics of proton reduction catalysis. *J. Am. Chem. Soc.* 139, 9544–9550. doi: 10.1021/jacs.7b02099

Artz, J., Mulder, D., Ratzloff, M., Peters, J., and King, P. (2020a). The hydricity and reactivity relationship in FeFe-hydrogenases [online]. [Preprint]. doi: 10.21203/rs.3.rs-77874/v1

Artz, J. H., Zadvornyy, O. A., Mulder, D. W., Keable, S. M., Cohen, A. E., Ratzloff, M. W., et al. (2020b). Tuning catalytic bias of hydrogen gas producing hydrogenases. *J. Am. Chem. Soc.* 142, 1227–1235. doi: 10.1021/jacs.9b08756

Bas, D. C., Rogers, D. M., and Jensen, J. H. (2008). Very fast prediction and rationalization of pKa values for protein-ligand complexes. *Proteins* 73, 765–783. doi: 10.1002/prot.22102

Beinert, H., Holm, R. H., and Münck, E. (1997). Iron-sulfur clusters: nature's modular, multipurpose structures. *Science* 277, 653–659. doi: 10.1126/science.277.5326.653

Birrell, J. A., Rodríguez-Maciá, P., and Hery-Barranco, A. (2021). A beginner's guide to thermodynamic modelling of [FeFe] hydrogenase. *Catalysts* 11:238. doi: 10.3390/catal11020238

Bominaar, E. L., Achim, C., Borshch, S. A., Girerd, J. J., and Münck, E. (1997). Analysis of exchange interaction and electron delocalization as intramolecular determinants of intermolecular electron-transfer kinetics. *Inorg. Chem.* 36, 3689–3701. doi: 10.1021/ic961298q

Brereton, P. S., Duderstadt, R. E., Staples, C. R., Johnson, M. K., and Adams, M. W. W. (1999). Effect of serinate ligation at each of the iron sites of the [Fe4S4] cluster of *Pyrococcus furiosus* ferredoxin on the redox, spectroscopic, and biological properties. *Biochemistry* 38, 10594–10605. doi: 10.1021/bi990671d

Brereton, K. R., Smith, N. E., Hazari, N., and Miller, A. J. M. (2020). Thermodynamic and kinetic hydricity of transition metal hydrides. *Chem. Soc. Rev.* 49, 7929–7948. doi: 10.1039/D0CS00405G

Brereton, P. S., Verhagen, M. F. J. M., Zhou, Z. H., and Adams, M. W. W. (1998). Effect of iron-sulfur cluster environment in modulating the thermodynamic properties and biological function of ferredoxin from *Pyrococcus furiosus*. *Biochemistry* 37, 7351–7362. doi: 10.1021/bi972864b

Bruice, T. C., Fife, T. H., Bruno, J. J., and Brandon, N. E. (1962). Hydroxyl group catalysis. II. The reactivity of the hydroxyl group of serine. The nucleophilicity of alcohols and the ease of hydrolysis of their acetyl esters as related to their pKa'*. *Biochemistry* 1, 7–12. doi: 10.1021/bi00907a002

Bullock, R. M., Appel, A. M., and Helm, M. L. (2014). Production of hydrogen by electrocatalysis: making the H–H bond by combining protons and hydrides. *Chem. Commun.* 50, 3125–3143. doi: 10.1039/c3cc46135a

Caserta, G., Papini, C., Adamska-Venkatesh, A., Pecqueur, L., Sommer, C., Reijerse, E., et al. (2018). Engineering an [FeFe]-hydrogenase: do accessory clusters influence O2 resistance and catalytic bias? *J. Am. Chem. Soc.* 140, 5516–5526. doi: 10.1021/jacs.8b01689

Cenens, J., Schoonheydt, R. A., and Voor, L. (1988). Visible spectroscopy of methylene blue on hectorite, Laponite B and Barasym in aqueous uspension. *Clay Clay Miner.*, 214–224. doi: 10.1346/CCMN.1988.0360302

Chen, J.-S., and Blanchard, D. K. (1984). Purification and properties of the H2-oxidizing (uptake) hydrogenase of the N2-fixing anaerobe *Clostridium pasteurianum* W5. *Biochem. Biophys. Res. Commun.* 122, 9–16. doi: 10.1016/0006-291X(84)90431-5

Chongdar, N., Birrell, J. A., Pawlak, K., Sommer, C., Reijerse, E. J., Rüdiger, O., et al. (2018). Unique spectroscopic properties of the H-cluster in a putative sensory [FeFe] hydrogenase. *J. Am. Chem. Soc.* 140, 1057–1068. doi: 10.1021/jacs.7b11287

Cornish, A. J., Gärtner, K., Yang, H., Peters, J. W., and Hegg, E. L. (2011). Mechanism of proton transfer in [FeFe]-hydrogenase from *Clostridium pasteurianum*. *J. Biol. Chem.* 286, 38341–38347. doi: 10.1074/jbc.M111.254664

Dörner, E., and Boll, M. (2002). Properties of 2-Oxoglutarate: ferredoxin oxidoreductase from *Thauera aromatica* and its role in enzymatic reduction of the aromatic ring. *J. Bacteriol.* 184, 3975–3983. doi: 10.1128/JB.184.14.3975-3983.2002

Duan, J., Senger, M., Esselborn, J., Engelbrecht, V., Wittkamp, F., Apfel, U.-P., et al. (2018). Crystallographic and spectroscopic assignment of the proton transfer pathway in [FeFe]-hydrogenases. *Nat. Commun.* 9:4726. doi: 10.1038/s41467-018-07140-x

Fasano, A., Land, H., Fourmond, V., Berggren, G., and Léger, C. (2021). Reversible or irreversible catalysis of H+/H2 conversion by FeFe hydrogenases. *J. Am. Chem. Soc.* 143, 20320–20325. doi: 10.1021/jacs.1c09554

Fourmond, V., Plumeré, N., and Léger, C. (2021). Reversible catalysis. Nature reviews. *Nat. Rev. Chem.* 5, 348–360. doi: 10.1038/s41570-021-00268-3

Frey, P. A. (2001). Review: strong hydrogen bonding in molecules and enzymatic complexes. *Magn. Reson. Chem.* 39, S190–S198. doi: 10.1002/mrc.953

Gauquelin, C., Baffert, C., Richaud, P., Kamionka, E., Etienne, E., Guieysse, D., et al. (2018). Roles of the F-domain in [FeFe] hydrogenase. *Biochim. Biophys. Acta* 1859, 69–77. doi: 10.1016/j.bbabio.2017.08.010

Ginovska-Pangovska, B., Ho, M.-H., Linehan, J. C., Cheng, Y., Dupuis, M., Raugei, S., et al. (2014). Molecular dynamics study of the proposed proton transport pathways in [FeFe]-hydrogenase. *Biochim. Biophys. Acta* 1837, 131–138. doi: 10.1016/j.bbabio.2013.08.004

Girbal, L., Abendroth, G. V., Winkler, M., Benton, P. M. C., Meynial-Salles, I., Croux, C., et al. (2005). Homologous and heterologous overexpression in *clostridium acetobutylicum* and characterization of purified clostridial and algal Fe-only hydrogenases with high specific activities. *Appl. Environ. Microbiol.* 71, 2777–2781. doi: 10.1128/AEM.71.5.2777-2781.2005

Hexter, S. V., Grey, F., Happe, T., Climent, V., and Armstrong, F. A. (2012). Electrocatalytic mechanism of reversible hydrogen cycling by enzymes and distinctions between the major classes of hydrogenases. *Proc. Natl. Acad. Sci.* 109, 11516–11521. doi: 10.1073/pnas.1204770109

Hosseinzadeh, P., and Lu, Y. (2016). Design and fine-tuning redox potentials of metalloproteins involved in electron transfer in bioenergetics. *Biochim. Biophys. Acta* 1857, 557–581. doi: 10.1016/j.bbabio.2015.08.006

Jumper, J., Evans, R., Pritzel, A., Green, T., Figurnov, M., Ronneberger, O., et al. (2021). Highly accurate protein structure prediction with AlphaFold. *Nature* 596, 583–589. doi: 10.1038/s41586-021-03819-2

King, P. W., Posewitz, M. C., Ghirardi, M. L., and Seibert, M. (2006). Functional studies of [FeFe] hydrogenase maturation in an *Escherichia coli* biosynthetic system. *J. Bacteriol.* 188, 2163–2172. doi: 10.1128/JB.188.6.2163-2172.2006

Knörzer, P., Silakov, A., Foster, C. E., Armstrong, F. A., Lubitz, W., and Happe, T. (2012). Importance of the protein framework for catalytic activity of [FeFe]-hydrogenases. *J. Biol. Chem.* 287, 1489–1499. doi: 10.1074/jbc.M111.305797

Lampret, O., Duan, J., Hofmann, E., Winkler, M., Armstrong, F. A., and Happe, T. (2020). The roles of long-range proton-coupled electron transfer in the directionality and efficiency of [FeFe]-hydrogenases. *Proc. Natl. Acad. Sci.* 117, 20520–20529. doi: 10.1073/pnas.2007090117

Liepinsh, E., and Otting, G. (1996). Proton exchange rates from amino acid side chains— implications for image contrast. *Magn. Reson. Med.* 35, 30–42. doi: 10.1002/mrm.1910350106

Long, H., King, P. W., and Chang, C. H. (2014). Proton transport in *Clostridium pasteurianum* [FeFe] hydrogenase I: a computational study. *J. Phys. Chem. B* 118, 890–900. doi: 10.1021/jp408621r

Morra, S., Giraudo, A., Di Nardo, G., King, P. W., Gilardi, G., and Valetti, F. (2012). Site saturation mutagenesis demonstrates a central role for cysteine 298 as proton donor to the catalytic site in CaHydA [FeFe]-hydrogenase. *PLoS One* 7:e48400. doi: 10.1371/journal.pone.0048400

Morra, S., Maurelli, S., Chiesa, M., Mulder, D. W., Ratzloff, M. W., Giamello, E., et al. (2016). The effect of a C298D mutation in CaHydA [FeFe]-hydrogenase: insights into the protein-metal cluster interaction by EPR and FTIR spectroscopic investigation. *Biochim. Biophys. Acta* 1857, 98–106. doi: 10.1016/j.bbabio.2015.10.005

Mulder, D. W., Guo, Y., Ratzloff, M. W., and King, P. W. (2017). Identification of a catalytic iron-hydride at the H-cluster of [FeFe]-hydrogenase. *J. Am. Chem. Soc.* 139, 83–86. doi: 10.1021/jacs.6b11409

Mulder, D. W., Peters, W. J., and Raugei, S. (2021). Catalytic bias in oxidation–reduction catalysis. *Chem. Commun.* 57, 713–720. doi: 10.1039/D0CC07062A

Mulder, D. W., Ratzloff, M. W., Bruschi, M., Greco, C., Koonce, E., Peters, J. W., et al. (2014). Investigations on the role of proton-coupled electron transfer in hydrogen activation by [FeFe]-hydrogenase. *J. Am. Chem. Soc.* 136, 15394–15402. doi: 10.1021/ja508629m

Mulder, D. W., Ratzloff, M. W., Shepard, E. M., Byer, A. S., Noone, S. M., Peters, J. W., et al. (2013). EPR and FTIR analysis of the mechanism of H2 activation by [FeFe]-hydrogenase HydA1 from *Chlamydomonas reinhardtii*. *J. Am. Chem. Soc.* 135, 6921–6929. doi: 10.1021/ja4000257

Olsson, M. H. M., Søndergaard, C. R., Rostkowski, M., and Jensen, J. H. (2011). PROPKA3: consistent treatment of internal and surface residues in empirical pka predictions. *J. Chem. Theory Comput.* 7, 525–537. doi: 10.1021/ct100578z

Pham, C. C., Mulder, D. W., Pelmenschikov, V., King, P. W., Ratzloff, M. W., Wang, H., et al. (2018). Terminal hydride species in [FeFe]-hydrogenases are vibrationally coupled to the active site environment. *Angew. Chem.* 130, 10765–10769. doi: 10.1002/ange.201805144

Poudel, S., Tokmina-Lukaszewska, M., Colman, D. R., Refai, M., Schut, G. J., King, P. W., et al. (2016). Unification of [FeFe]-hydrogenases into three structural and functional groups. *Biochim. Biophys. Acta* 1860, 1910–1921. doi: 10.1016/j.bbagen.2016.05.034

Puthenkalathil, R. C., and Ensing, B. (2021). Linear scaling relationships to predict pKa's and reduction potentials for bioinspired hydrogenase catalysis. *Inorg. Chem.* 61, 113–120. doi: 10.1021/acs.inorgchem.1c02429

Ratzloff, M. W., Artz, J. H., Mulder, D. W., Collins, R. T., Furtak, T. E., and King, P. W. (2018). CO-bridged H-cluster intermediates in the catalytic mechanism of [FeFe]-hydrogenase CaI. *J. Am. Chem. Soc.* 140, 7623–7628. doi: 10.1021/jacs.8b03072

Rodríguez-Maciá, P., Breuer, N., Debeer, S., and Birrell, J. A. (2020). Insight into the redox behavior of the [4Fe–4S] subcluster in [FeFe] hydrogenases. *ACS Catal.* 10, 13084–13095. doi: 10.1021/acscatal.0c02771

Rodríguez-Maciá, P., Kertess, L., Burnik, J., Birrell, J. A., Hofmann, E., Lubitz, W., et al. (2019). His-ligation to the [4Fe–4S] subcluster tunes the catalytic bias of [FeFe] hydrogenase. *J. Am. Chem. Soc.* 141, 472–481. doi: 10.1021/jacs.8b11149

Rodríguez-Maciá, P., Pawlak, K., Rüdiger, O., Reijerse, E. J., Lubitz, W., and Birrell, J. A. (2017). Intercluster redox coupling influences protonation at the H-cluster in [FeFe] hydrogenases. *J. Am. Chem. Soc.* 139, 15122–15134. doi: 10.1021/jacs.7b08193

Senger, M., Eichmann, V., Laun, K., Duan, J., Wittkamp, F., Knör, G., et al. (2019). How [FeFe]-hydrogenase facilitates bidirectional proton transfer. *J. Am. Chem. Soc.* 141, 17394–17403. doi: 10.1021/jacs.9b09225

Silakov, A., Kamp, C., Reijerse, E., Happe, T., and Lubitz, W. (2009). Spectroelectrochemical characterization of the active site of the [FeFe] hydrogenase HydA1 from *Chlamydomonas reinhardtii*. *Biochemistry* 48, 7780–7786. doi: 10.1021/bi9009105

Sommer, C., Adamska-Venkatesh, A., Pawlak, K., Birrell, J. A., Rüdiger, O., Reijerse, E. J., et al. (2017). Proton coupled electronic rearrangement

within the H-cluster as an essential step in the catalytic cycle of [FeFe] hydrogenases. *J. Am. Chem. Soc.* 139, 1440–1443. doi: 10.1021/jacs.6b12636

Søndergaard, C. R., Olsson, M. H. M., Rostkowski, M., and Jensen, J. H. (2011). Improved treatment of ligands and coupling effects in empirical calculation and rationalization of pKa values. *J. Chem. Theory Comput.* 7, 2284–2295. doi: 10.1021/ct200133y

Von Abendroth, G., Stripp, S., Silakov, A., Croux, C., Soucaille, P., Girbal, L., et al. (2008). Optimized over-expression of [FeFe] hydrogenases with high specific activity in *Clostridium acetobutylicum*. *Int. J. Hydrog. Energy* 33, 6076–6081. doi: 10.1016/j.ijhydene.2008.07.122

Yacoby, I., Tegler, L. T., Pochekailov, S., Zhang, S., and King, P. W. (2012). Optimized expression and purification for high-activity preparations of algal [FeFe]-hydrogenase. *PLoS One* 7:e35886. doi: 10.1371/journal.pone.0035886

Ye, M., Thompson, N. B., Brown, A. C., and Suess, D. L. M. (2019). A synthetic model of enzymatic [Fe4S4]–alkyl intermediates. *J. Am. Chem. Soc.* 141, 13330–13335. doi: 10.1021/jacs.9b06975

Zuris, J. A., Halim, D. A., Conlan, A. R., Abresch, E. C., Nechushtai, R., Paddock, M. L., et al. (2010). Engineering the redox potential over a wide range within a new class of FeS proteins. *J. Am. Chem. Soc.* 132, 13120–13122. doi: 10.1021/ja103920k

Conflict of Interest: All authors are employees of Alliance for Sustainable Energy, LLC, an M&O contractor of the U.S. Government.

Author Disclaimer: The views expressed in the article do not necessarily represent the views of the DOE or the U.S. Government.

Publisher's Note: All claims expressed in this article are solely those of the authors and do not necessarily represent those of their affiliated organizations, or those of the publisher, the editors and the reviewers. Any product that may be evaluated in this article, or claim that may be made by its manufacturer, is not guaranteed or endorsed by the publisher.

frontiers | Frontiers in Microbiology

TYPE Original Research
PUBLISHED 17 January 2023
DOI 10.3389/fmicb.2022.1073315

OPEN ACCESS

EDITED BY
Francesca Valetti,
University of Turin,
Italy

REVIEWED BY
Anna Rovaletti,
University of Milano-Bicocca, Italy
Gary Sawers,
Martin Luther University of Halle-Wittenberg, Germany

*CORRESPONDENCE
Maria Andrea Mroginski
✉ andrea.mroginski@tu-berlin.de

SPECIALTY SECTION
This article was submitted to Microbiological Chemistry and Geomicrobiology, a section of the journal Frontiers in Microbiology

RECEIVED 18 October 2022
ACCEPTED 23 December 2022
PUBLISHED 17 January 2023

CITATION
Dragelj J, Karafoulidi-Retsou C, Katz S, Lenz O, Zebger I, Caserta G, Sacquin-Mora S and Mroginski MA (2023) Conformational and mechanical stability of the isolated large subunit of membrane-bound [NiFe]-hydrogenase from *Cupriavidus necator*. *Front. Microbiol.* 13:1073315. doi: 10.3389/fmicb.2022.1073315

Conformational and mechanical stability of the isolated large subunit of membrane-bound [NiFe]-hydrogenase from *Cupriavidus necator*

Jovan Dragelj[1], Chara Karafoulidi-Retsou[1], Sagie Katz[1], Oliver Lenz[1], Ingo Zebger[1], Giorgio Caserta[1], Sophie Sacquin-Mora[1,2,3] and Maria Andrea Mroginski[1]*

[1]Institut für Chemie, Technische Universität Berlin, Berlin, Germany, [2]CNRS, UPR, Laboratoire de Biochimie Théorique, Université de Paris Cité, Paris, France, [3]Institut de Biologie Physico-Chimique-Fondation Edmond de Rotschild, PSL Research University, Paris, France

Comprising at least a bipartite architecture, the large subunit of [NiFe]-hydrogenase harbors the catalytic nickel–iron site while the small subunit houses an array of electron-transferring Fe-S clusters. Recently, some [NiFe]-hydrogenase large subunits have been isolated showing an intact and redox active catalytic cofactor. In this computational study we have investigated one of these metalloproteins, namely the large subunit HoxG of the membrane-bound hydrogenase from *Cupriavidus necator* (*Cn*MBH), targeting its conformational and mechanical stability using molecular modelling and long all-atom Gaussian accelerated molecular dynamics (GaMD). Our simulations predict that isolated HoxG is stable in aqueous solution and preserves a large portion of its mechanical properties, but loses rigidity in regions around the active site, in contrast to the MBH heterodimer. Inspired by biochemical data showing dimerization of the HoxG protein and IR measurements revealing an increased stability of the [NiFe] cofactor in protein preparations with higher dimer content, corresponding simulations of homodimeric forms were also undertaken. While the monomeric subunit contains several flexible regions, our data predicts a regained rigidity in homodimer models. Furthermore, we computed the electrostatic properties of models obtained by enhanced sampling with GaMD, which displays a significant amount of positive charge at the protein surface, especially in solvent-exposed former dimer interfaces. These data offer novel insights on the way the [NiFe] core is protected from de-assembly and provide hints for enzyme anchoring to surfaces, which is essential information for further investigations on these minimal enzymes.

KEYWORDS

hydrogenase, molecular modelling, Gaussian accelerated molecular dynamics, rigidity profile, electrostatic potential, dipole moment, IR spectroscopy, size exclusion chromatography

Introduction

Dihydrogen (H_2) is an important energy carrier that is extensively investigated in view of its potential interconnection with renewable energy sources. The development of affordable and efficient hydrogen-based technologies for energy storage and conversion (e.g., biofuel cells) took inspiration from the natural machinery involved in the H_2 activation, namely the hydrogenase enzymes, which use earth-abundant transition metals for H_2 production/oxidation (Ruff et al., 2018). Among them, [NiFe]-hydrogenases contain a heterobimetallic [NiFe] active site bound to the protein scaffold *via* four cysteine residues (Shafaat et al., 2013; Sickerman and Hu, 2019). Two of these cysteines bridge the Ni and Fe, the remaining two are bound terminally to the Ni while the coordination sphere of the Fe is completed by one CO and two CN-ligands (Rippers et al., 2012). Albeit the majority of [NiFe]-hydrogenases are strongly inhibited by molecular oxygen (O_2), a few organisms have been shown to host O_2tolerant enzymes enabling catalysis under oxic conditions. In our groups we have thoroughly investigated the membrane-bound hydrogenase (MBH) from *Cupriavidus necator* (*Cn*), formerly known as *Ralstonia eutropha* (Saggu et al., 2009; Goris et al., 2011) which belongs to the biotechnologically relevant subclass of O_2-tolerant [NiFe]-hydrogenases (Lenz et al., 2015; Caserta et al., 2022b). The MBH catalytic architecture comprises the HoxG large subunit, which harbors the $NiFe(CN)_2(CO)$ catalytic site, and the small subunit HoxK containing three different electron-transferring [FeS]-clusters (Caserta et al., 2022b). Given the rare trait of being O_2-tolerant, the MBH has been utilized for the development of various immobilization procedures on electrode surfaces to facilitate its applicability (Vincent et al., 2005; Utesch et al., 2013; Heidary et al., 2015; Harris et al., 2018). These procedures demand a detailed understanding of the structural, physical and chemical properties of the enzyme to ensure an efficient coupling between the biocatalyst and electrode surface (Utesch et al., 2013; Oteri et al., 2014b; Hitaishi, 2018).

More recently, [NiFe]-hydrogenase catalytic subunits have been successfully isolated independently of the small protein subunits (Hartmann et al., 2018; Kwon et al., 2018; Caserta et al., 2021, 2022a; Wang et al., 2021) and two of them from the model organism *C. necator* have been shown to host a redox-active O_2-stable $NiFe(CN)_2(CO)$ active site (Caserta et al., 2021, 2022a). These are the HoxC subunit from the regulatory hydrogenase (RH) and the HoxG from MBH, and both could activate molecular hydrogen to a little extent (Hartmann et al., 2018; Caserta et al., 2020a). While several crystal structures of heterodimeric [NiFe]-hydrogenases (*Cn*MBH included) have been reported (Fontecilla-camps et al., 2007; Fritsch et al., 2011; Frielingsdorf et al., 2014) and detailed information on the substrate/product routes are available (Kalms et al., 2016, 2018), the structure of an isolated catalytic subunit of such [NiFe]-hydrogenase that solely harbors the active [NiFe] site, has not been experimentally determined. Additionally, despite spectroscopy having provided detailed insights on the electronic and ligands arrangements of the [NiFe] cofactor (Caserta et al., 2020a, 2021, 2022a), little is known about the protein arrangement and the conformational changes of the catalytic subunit upon removal of the small protein subunit (Kwon et al., 2018). Several computational studies have been already performed on the heterodimeric hydrogenases [for data on *Cn*MBH see, e.g. (Teixeira et al., 2006; Utesch et al., 2013; Oteri et al., 2014a,b; Heidary et al., 2015; Kalms et al., 2018; Albareda et al., 2019)], however, only very few of them have focused on the isolated hydrogenase catalytic subunits (Albareda et al., 2019). In this work we focus on the conformational stability of the MBH catalytic subunit, the HoxG protein, which was investigated using molecular modeling and extensive Gaussian accelerated molecular dynamics (GaMD) (Miao et al., 2015). Accelerated MD is a computational approach used to enhance sampling of the conformational space of large molecular systems by artificially decreasing energy barriers of the potential energy surface that surpass a certain energy threshold. This allows the population of conformational states, which are inaccessible with conventional classical MD (cMD) simulations in the same time span (Hamelberg et al., 2004). In GaMD, the boost potential follows a near-Gaussian distribution that ensures simultaneous energetic noise reduction and free energy computations (Miao et al., 2015). These approaches can be used for investigating structural, mechanical, and electrostatic properties of large (bio)molecular systems in complex heterogeneous environments such as proteins attached to membranes (Tillmann, 2018) or immobilized on electrodes (Utesch et al., 2013; Heidary et al., 2015). By combining GaMD with Coarse-grained Brownian Dynamics (BD) simulations (Sacquin-Mora, 2014, 2016, 2018), we targeted the conformational space and predicted the mechanical properties as well as the structural stability of HoxG protein. Our computational work shows the consequences of reducing a whole enzyme to its catalytic unit. Finally, supported by biochemical and infrared spectroscopic data, we revealed a direct correlation between the HoxG oligomerization states and their influence on the active site stability. The atomistic information gained within this combined computational/experimental approach is essential not only for understanding the consequences of reducing an enzyme architecture to its catalytic unit but also for rationally designing new "smaller" constructs with comparable stability and, in turn, biological activity to the native system.

Materials and methods

In the following, models of the large subunit HoxG will be labelled as follows: $HoxG_m$: thermodynamically equilibrated monomeric form, $HoxG_d$: thermodynamically equilibrated homodimeric form, $HoxG_c$: isolated HoxG in crystallographic arrangement; $HoxG_{MBH}$: HoxG complexed with HoxK (small subunit) in crystallographic arrangement.

Structure preparation and modelling of the large subunit of MBH ($HoxG_m$)

The X-ray crystal structure of the heterodimeric MBH from *C. necator* (MBH; PDB code: 3RGW (Fritsch et al., 2011; Figure 1) was used to extract coordinates of the large subunit (HoxG) as a starting model. During the natural maturation of MBH, the HoxG subunit forms a heterodimer with HoxK only after insertion of the [NiFe] cofactor and cleavage of its C-terminal tail (Hartmann et al., 2018, 2020; Caserta et al., 2022a).

Therefore, this C-terminal peptide is not found in the heterodimeric crystal structure, and it is not present in our model targeting a fully mature HoxG subunit.

The HoxG protein is equipped with a Strep-tag II at its N terminus (Caserta et al., 2022a); therefore, we have used CHARMM software (Brooks et al., 2009) and CHARMM 36 Force-Field (MacKerell, 1998; Best et al., 2012) to model the affinity tag. After prediction using i-Tasser (Zhang, 2008; Roy et al., 2010; Yang et al., 2014), the Strep-tag II sequence has been modelled in a random coil conformation, followed by a geometry optimization in the dielectric medium ($\varepsilon = 4$) for 4,000 steps. Additionally, a short geometry optimization of Strep-tag II while keeping the coordinates of HoxG fixed was done with NAMD (Phillips et al., 2005) in vacuum for 10 ns. The protonation pattern has been computed with Karlsberg2$^+$ software (Rabenstein and Knapp, 2001; Kieseritzky and Knapp, 2008; Meyer and Knapp, 2015) at pH 7.0 and applied to titratable groups in all MD simulations (see SI; Supplementary Table S1). The resulting structure with modelled cofactors has been used as a basis for all further MD simulations, both conventional (cMD) and Gaussian accelerated (GaMD; Miao et al., 2015). Amino-acid numbering has been kept following that of the MBH crystal structure. Where necessary, the amino acid numbering of the Strep-tag II sequence has been included with the prefix "tag."

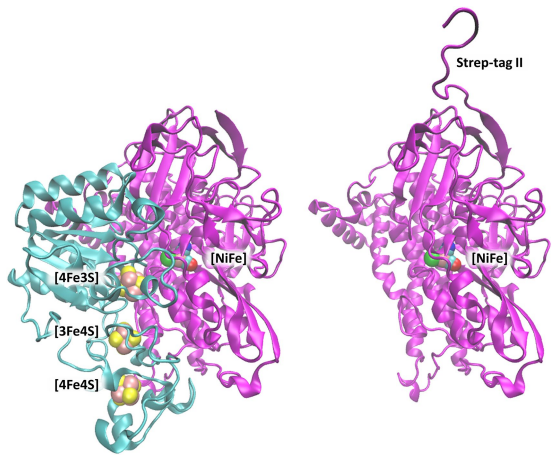

FIGURE 1
[NiFe]-hydrogenase from *C. necator* (PDB code: 3RGW (Fritsch et al., 2011)). **Left**: Heterodimer consisting of the small subunit (HoxK, colored cyan) and large subunit (HoxG, colored magenta). **Right**: Isolated large subunit (HoxG) with its Strep-tag II sequence located at the N terminus (Caserta et al., 2022a). [NiFe]-active site and [FeS]-clusters are shown as spheres and depicted with the following color code: Fe in pink, Ni in green, S (from Cys) in yellow, CN-and CO groups, cyan-blue and cyan-red, respectively.

Atomic partial charges and modelling of the [NiFe]-active site

The [NiFe] active site of MBH has been trapped in several redox states of the catalytic cycle (Sickerman and Hu, 2019; Apfel et al., 2020). For simplicity, we have chosen an EPR silent state, the Ni_a-S state (Ilina et al., 2019; Sickerman and Hu, 2019), which represents the presumed state accepting and releasing H_2. In the Ni_a-S state, both Ni and Fe are in a + 2 redox state, coordinated to four cysteine residues. The atomic partial charges have been taken from early works on similar enzymes (Teixeira et al., 2006), where electrostatic potential was computed quantumchemically with Gaussian (Frisch, 2016) and fitted with RESP (Cornell et al., 1993). During preparatory steps and MD simulations, the [NiFe] active site has been kept rigid with coordinates as in the crystal structure but with corrected ligand orientation [Rippers et al., 2012; PDB code: 3RGW (Fritsch et al., 2011)] by applying conformational restraints on bonds (force constant of 500 kcal), angles (force constant of 100 kcal) and dihedral angles (barrier of 1.0 kcal) with NAMD (Phillips et al., 2005), as in previous applications (Utesch et al., 2013; Heidary et al., 2015). Considering that the main goal of this study is to investigate the global dynamic properties of the large subunit, constraints on the [NiFe] active site will have little to no influence.

Molecular dynamics (MD) simulations

The prepared structure of the large subunit with the N-terminal Strep-tag II and crystal water molecules were solvated using a TIP3P (Jorgensen et al., 1983) water box with periodic boundary conditions *via* a PSFGEN VMD plugin (Humphrey et al., 1996) with an addition of NaCl ions (150 mM). A water box with slightly larger dimensions 102 Å x 121 Å x 93 Å was used to accommodate conformational changes stemming from Strep-tag II flexibility or other protein regions. All MD simulations (conventional and Gaussian accelerated) were performed with software NAMD (Phillips et al., 2005) with 2 fs time step using SHAKE (Ryckaert et al., 1977) fixing bond lengths of hydrogen atoms, Langevin dynamics at 300 K with small friction constant of $\beta = 1\ ps^{-1}$ avoiding slowing down of dynamics (Blumhagen et al., 1996) and particle-mesh Ewald method (Darden et al., 1993) for electrostatic interactions.

The solvated model system described above was energy minimized, then heated to 300 K for 20 ps while restraining the positions of all protein heavy atoms. During the 60 ps-long preequilibration step, the conformational restraints on the protein

atoms were gradually lifted except for the atoms constituting the [NiFe] active site including the three inorganic ligands and the side chains atoms (up to Cβ) of the coordinating cysteine residues. Finally, the entire system was thermally equilibrated for 45 ns *via* cMD. The preparatory steps before GaMD included a 2 ns extension of the cMD in order to collect potential statistics for the estimation of the GaMD (double boost) acceleration parameters and a 2 ns GaMD equilibration considering the previously calculated boost potential (Miao et al., 2015). GaMDs were run for 250 ns. During these simulations the upper limits of the standard deviation of the total boost potential and the dihedral boost potential were set to 5 kcal/mol. To enlarge the statistical sampling, both cMD and GaMD were repeated twice. Further in text, these simulations are referred to as simulation 1 and simulation 2.

Electrostatic energy and pK_A computations

The initial protonation pattern (Supplementary Table S1; SI) was determined based on the initial model [HoxG from the crystal structure 3RGW (Fritsch et al., 2011) with modelled N-terminal Strep-tag II as a random coil, Figure 1], by computing pK_A values with Karlsberg2$^+$ (KB2$^+$; Rabenstein and Knapp, 2001; Kieseritzky and Knapp, 2008; Meyer and Knapp, 2015), as in previous applications (Wolf et al., 2020; Dragelj et al., 2021a,b; Batebi et al., 2018). The pK_A values have been computed in the range from −10.00 to 20.00, not only for the starting model but also for the structures from GaMD trajectories obtained every 2 ns. The conformational stability of predicted structures was evaluated considering conformational energies from the time frames of GaMDs. Conformational energies were computed by solving the linearized PoissonBoltzmann (LPB) equation with the program "Adaptive Poisson-Boltzmann Solver" (APBS) (Baker et al., 2001). Water molecules and electrolytes were removed and replaced by an implicit ion concentration of 150 mM. The region out of the solvent accessible surface area was treated as a dielectric continuum with $\varepsilon = 80$ and protein volume was treated as a dielectric continuum with $\varepsilon = 4$. These conformational energies were computed using a grid resolution of 0.3 Å for frames taken every 4 ns from the resulting trajectories.

Computation of mechanical properties *via* coarse-grain simulations

Coarse-grained Brownian Dynamics (BD) simulations were run using the ProPHet (Probing Protein Heterogeneity, available online at https://bioserv.rpbs.univ-paris-diderot.fr/services/ProPHet/) program (Sacquin-Mora, 2014, 2016, 2018). In this approach, the protein is represented using an elastic network model (ENM). Unlike most common coarse-grained models where each residue is described by a single pseudo atom (Tozzini, 2005) ProPHet uses a more detailed representation (Zacharias, 2003) that involves up to 3 pseudo atoms per residue and enables different amino acids to be distinguished. Pseudo atoms closer than the cutoff parameter $R_c = 9$ Å are joined by Gaussian springs which all have identical spring constants of $\gamma_{struct} = 0.42\ N.m^{-1}$ ($0.6\ kcal.mol^{-1}.Å^{-2}$). The springs are taken to be relaxed for the initial conformation of the protein. The simulations use an implicit solvent representation *via* the diffusion and random displacement terms in the equation of motion, (Ermak and McCammon, 1978) and hydrodynamic interactions are included through the diffusion tensor (Pastor et al., 1988).

Mechanical properties are obtained from 200,000 BD steps at an interval of 10 fs and a temperature of 300 K. The simulations lead to deformations of roughly 1.5 Å root-mean-square deviation with respect to the protein starting conformation (which by construction corresponds to the system's equilibrium state). The trajectories are analyzed in terms of the fluctuations of the mean distance between each pseudo atom belonging to a given amino acid and the pseudo atoms belonging to the remaining protein residues. The inverse of these fluctuations yields an effective force constant k_i describing the ease of moving a pseudo atom with respect to the overall protein structure:

$$k_i = \frac{3k_BT}{\left\langle \left(d_i - \langle d_i \rangle\right)^2 \right\rangle},$$

where $\langle\rangle$ denotes an average taken over the whole simulation and $d_i = \langle d_{ij} \rangle j^*$ is the average distance from particle i to the other particles j in the protein (the sum over j^* implies the exclusion of the pseudo atoms belonging to residue i). The distance between the C_α pseudo atom of residue i and the C_α pseudo atoms of the adjacent residues i-1 and $i + 1$ are excluded since the corresponding distances are virtually constant. The force constant for each residue is the average of the force constants for all its constituent pseudo atoms i. We will use the term *rigidity profile* to describe the ordered set of force constants for all the residues of the protein.

Modelling and MD simulations of the homodimeric large subunit of MBH ($HoxG_d$)

Despite the experimental evidence that isolated preHoxG (i.e., a HoxG protein precursor equipped with an [NiFe] active site but still containing its C-terminal extension tail) can be found in different oligomerization states with a prevalent homodimeric fraction, no detailed structural information was available (Hartmann et al., 2018). The three-dimensional structure of the HoxG homodimer was constructed using the cartesian coordinates of the monomeric structure predicted with the lowest conformational energy during 20 ns of GaMD simulation. We used SymmDock Webserver (Schneidman-Duhovny et al., 2005a,b) to investigate the relative orientation of two $HoxG_m$ subunits. The SymmDock algorithm predicts protein complexes by geometry-based rigid docking,

whereby the scoring function considers both geometric fit and atomic desolvation energy of resulting constructs. In our protocol we requested the docking of two isolated HoxG units without distance constraints, nor the prior definition of a binding interface. Interestingly, out of the resulting top 10 suggested complexes more than half of them form dimer structures in which both HoxG monomers interact with each other *via* the HoxG-HoxK interface of the functional MBH heterodimer as seen in Figure 2. For simplicity, we have chosen a $HoxG_d$ model with the highest overall score as a starting model, as the prediction of reliable dimer poses can be computationally very demanding, and it is not the main objective of this work. The $HoxG_d$ model was prepared for MD simulations following the same protocols and conditions as described above for the $HoxG_m$ with an unchanged protonation pattern [determined by Karlsberg2$^+$ software (Rabenstein and Knapp, 2001; Kieseritzky and Knapp, 2008; Meyer and Knapp, 2015). $HoxG_d$ was solvated in a water box with dimensions of 121 Å x 114 Å x 114 Å. After 45 ns thermal equilibration at 300 K with cMD, boost parameters for GaMD were estimated for a 150 ns long GaMD of the $HoxG_d$ model.

Size exclusion chromatography

For the size exclusion chromatography experiments, the as-purified HoxG protein was investigated in various concentration ranges (0.5, 2.5, 12.5 and 60 mg/ml) in 50 mM K_iPO_4, 150 mM NaCl pH 7.4 (purification buffer). Measurements were run on an ÄKTA pure 25 using a Superdex 200 Increase 10/300 GL (Cytiva) column equilibrated with the purification buffer at 4 °C. A calibration curve was made by measuring six protein standards with known molecular weights between 12 and 670 kDa: Thyroglobulin (669 kDa, 9.34 ml), Apoferritin (443 kDa, 10.49 ml), β-Amylase (200 kDa, 11.8 ml), Bovine serum albumin (66 kDa, 14.1 ml), Carbonic anhydrase (29 kDa, 16.8 ml) and cytochrome C (12.3 kDa, 18.24 ml). Additionally, HoxC (the large subunit of the regulatory hydrogenase from *C. necator*) was included in the calibration series as its oligomerization profile was recently elucidated (Caserta et al., 2020a).

IR spectroscopy

HoxG protein solutions were transferred into a homemade, gas-tight, and temperaturecontrolled (10°C) transmission cell equipped with two sandwiched CaF_2 windows separated by a Teflon spacer with an optical pathlength of 50 µm. Spectra with a resolution of 2 cm^{-1} were recorded on a Tensor 27 Fourier-Transform spectrometer (Bruker) equipped with an MCT (liquid nitrogen-cooled mercury-cadmium-telluride) detector. The cell compartment was purged with dried air. For a single spectrum 200 individual scans were averaged. A buffer spectrum was used as reference for calculating the corresponding absorbance spectra. OPUS software version 7.5 from Bruker was used for data analysis. For the cofactor-stability experiments, IR spectra of as-isolated HoxG protein solution 35 mg/ml (500 µM) and a threefold higher concentrated sample were recorded consecutively for 7 h.

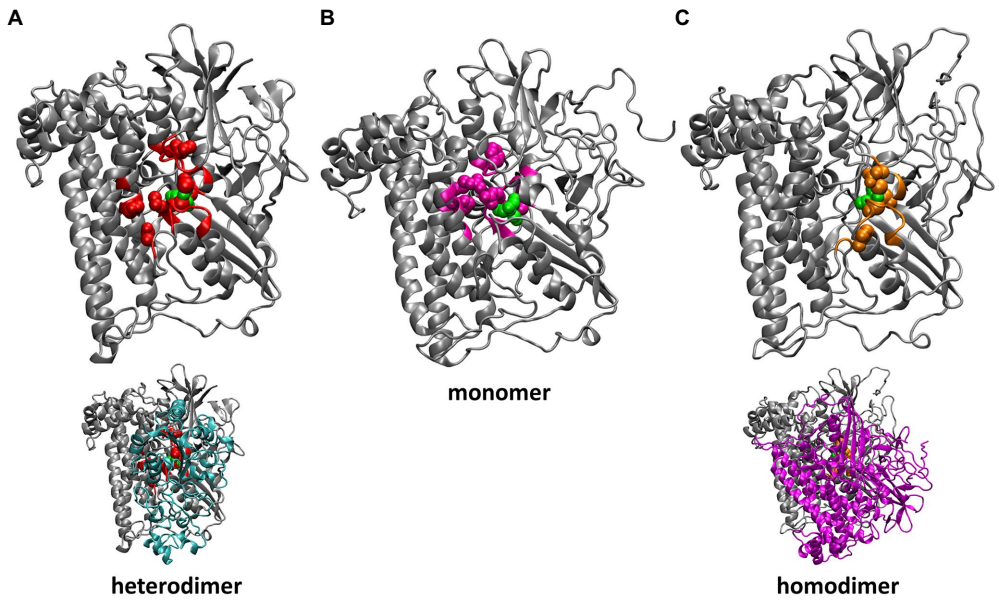

FIGURE 2
Residues of HoxG with highest rigidity constants (100kcal·mol^{-1}·Å^{-2}): in the crystal structure of *Cn*MBH, $HoxG_{MBH}$ (**A**, red), in a $HoxG_m$ structure taken from GaMD simulation 2 at 200ns (**B**, magenta) and in one monomer of the $HoxG_d$ structure taken from GaMD simulation at 150ns (**C**, gold). The structures of the entire *Cn*MBH heterodimer and the entire $HoxG_d$ are also displayed (**A**,**C**, bottom). The [NiFe] active site is shown in green. The protein backbone of residues with force constants less than 100kcal·mol^{-1}·Å^{-2} is shown in grey.

Results

Conformation of the isolated large subunit $HoxG_m$

The structures obtained from Gaussian accelerated molecular dynamics simulations were analyzed in order to get a deeper insight into the dynamics and stability of the $HoxG_m$ subunit. Special attention has been given to the quaternary structure, as well as the preservation of secondary structure elements. Root-meansquare deviation (RMSD), root-mean-square fluctuation (RMSF) of backbone atoms of protein, electrostatic conformational energy, and rigidity profile of the structure were computed.

The RMSF values of backbone Cα atoms from two GaMD simulations (shown in Supplementary Figure S1) are mostly low (below 2 Å), indicating a stable structure with some flexible loops. The highest flexibility is observed for the Strep-tag II affinity tag (Supplementary Figure S1), in line with the fact that this peptide fragment is seldom resolved in X-ray protein structures. In all simulations, no secondary structure elements could be assigned for Step-tag II, which exhibited multiple conformations relative to the HoxG structure (Supplementary Figure S2). Furthermore, the flexibility of the affinity tag may cause destabilization of the terminal β-sheet as seen in Figure 3 (residues 213, yellow). A reliable indicator of the structural stability is the root-mean-square deviation or RMSD value of the protein backbone, which was computed in all cases by excluding the mobile.

Strep-tag II (both from the alignment and the calculations). The RMSD values in cMD (Supplementary Figure S3) show a steady rise to about 2.0 Å. This was also observed for GaMD simulations, where RMSD values reached 3.0 Å (Figure 3B1). Moreover, when several flexible loops, identified based on RMSF values (residues 24–28, 171–191, 373–386, and 244–250), were excluded, the RMSD value was reduced to about 0.5 Å. The flexibility of loop regions is commonly observed in molecular dynamics simulations but it is noteworthy that residues from these loop regions form interactions with the small subunit (HoxK) in the heterodimeric MBH enzyme (Fritsch et al., 2011; Albareda et al., 2019). In contrast, these loops are solvent exposed in the $HoxG_m$. Interestingly, the loop containing residues 24–28 (Figure 3A3) hosts Glu27, which plays an important proton gate role and it is located in the center of the interface of the two subunits in MBH (Tombolelli and Mroginski, 2019).

Analysis with VMD (Humphrey et al., 1996) showed that the majority of the secondary structures are preserved during both GaMD simulations, supported by a relatively low reduced RMSD, hinting at the stability of HoxG even in the absence of the small subunit. Furthermore, the relative conformational energies of time frames extracted from GaMD simulations yield average values of 345 kJ/mol and 331 kJ/mol above the 28,000 kJ/mol baseline (Supplementary Figure S4) for simulations 1 and 2, respectively, with fluctuations up to 400 kJ/mol. Despite these large fluctuations of the conformational energy, there is no indication of either protein unfolding or large conformational changes in the structures derived from GaMD simulations.

Structural properties of the homodimer $HoxG_d$

$HoxG_d$ structure, predicted by SymmDock Webserver (Schneidman-Duhovny et al., 2005a,b) was subjected to cMD and GaMD simulations (see Materials and methods for details) in order to obtain a thermally equilibrated moiety for the analysis of structural features. RMSD and RMSF values (Supplementary Figures S5, S6) computed for backbone atoms indicate a high structural stability comprising a "closed" conformation and a preserved orientation of the two subunits. Computed relative conformational energies of time frames extracted from GaMD simulations yield and average value of 382 kJ/mol above the baseline value (Supplementary Figure S7), with fluctuations of around 350 kJ/mol, furthermore confirming the structural integrity of the predicted HoxG homodimer. The homodimer interface (Supplementary Figure S8) contains 52 residues (3,382 $Å^2$) and 49 residues (3,366 $Å^2$) belonging to HoxG-I and HoxG-II, respectively *via* 6 salt-bridges, 28 hydrogen bonds and 260 non-bonded contacts, as identified with PDBSum (Laskowski, 2009). Salt-bridges found in the thermally equilibrated $HoxG_d$ after 150 ns are: Arg62(I)-Glu21(II), Arg73(I)Glu27(II), Glu21(I)-Arg62(II), Glu27(I)-Arg73(II), Arg267(I)-Asp211(II) and Glu371(I)Arg384(II). Several important residues have been observed to play a role at the interface between two HoxG subunits. Residue Glu27 that plays an important role in proton transfer in MBH is involved in the formation of a stable salt-bridge with Arg62 in both HoxG subunits in the $HoxG_d$ structure (Dementin et al., 2004; Tombolelli and Mroginski, 2019). Cysteines 597 and 75, coordinating the Ni ion, are involved in interface interactions as well, albeit only observed in one subunit (HoxG-I; Supplementary Figure S8) in the $HoxG_d$.

Mechanical properties and rigidity profile of HoxG

Computation of mechanical properties and rigidity profiles may help identify the location of the active sites in proteins (Lavery and Sacquin-Mora, 2007; Sacquin-Mora, 2016) and were utilized in this work in order to identify stable regions of the catalytic (large) subunit of MBH (HoxG) in the absence of its small counterpart HoxK. Rigidity profiles were computed for both $HoxG_m$ and $HoxG_d$ models based on time frames from GaMD simulations, as well as, for the entire MBH structure [PDB code: 3RGW (Fritsch et al., 2011)] and its HoxG subunit extracted from 3RGW without further processing ($HoxG_c$, $HoxG_{MBH}$; Figure 4; Supplementary Figures S9, S10).

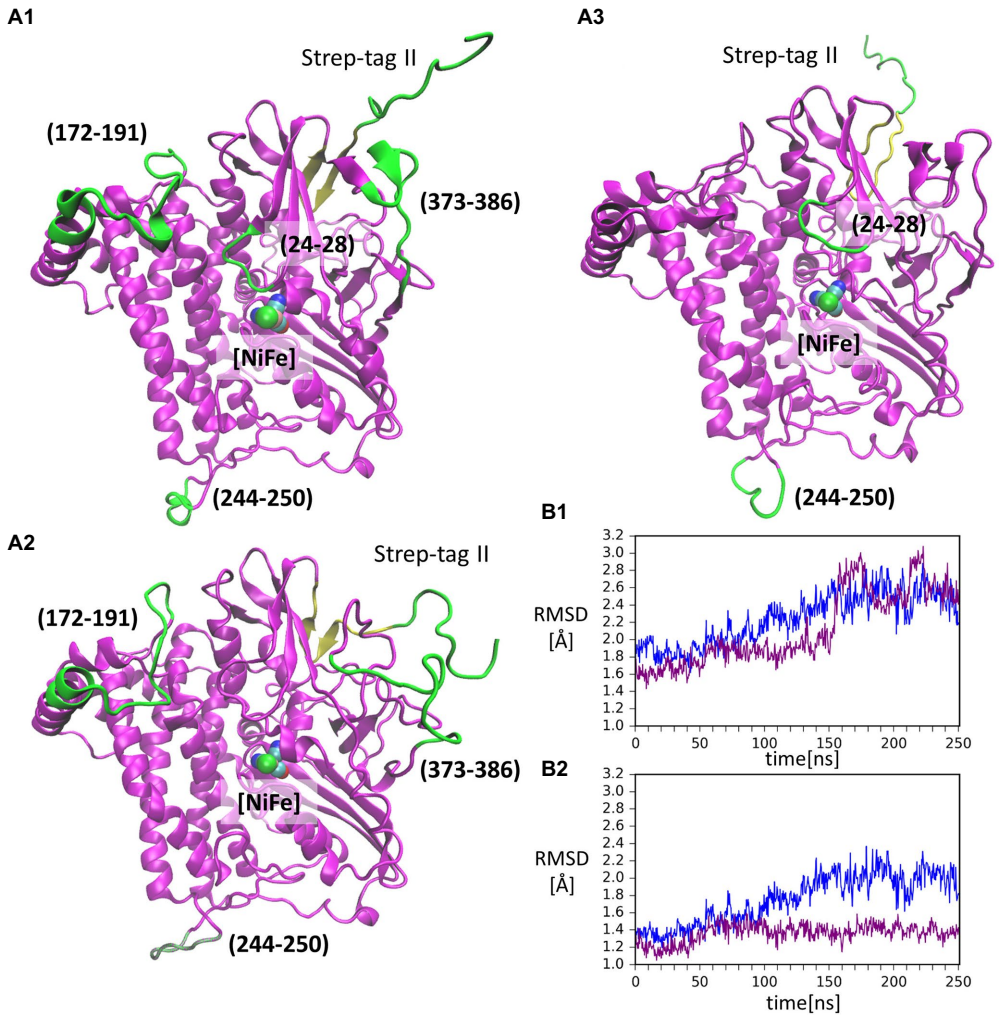

FIGURE 3
Conformations of the isolated large subunit, $HoxG_m$ from GaMD simulations: **(A1)** – initial modelled structure with N-terminal Strep-tag II. Flexible loops and structure elements that were excluded from RMSD calculation in **(B2)** are shown in green; **(A2)** – representation of mobility of Strep-tag II and loops with residues 171–191, 373–386, and 244–250, shown in time frame taken from simulation 2 after 199ns; **(A3)** – representation of mobility of Strep-tag II and loops with residues 24–28 and 244–250, shown in time frame taken from simulation 1 after 156ns. The β-sheet adjacent to the Strep-tag II is shown in yellow in all structures. [NiFe] active site is in vdW representation in all structures. Root-mean-square deviation (RMSD) of backbone atoms relative to the crystal structure [PDB code: 3RGW (Fritsch et al., 2011)] in GaMD simulations (blue – simulation 1, purple – simulation 2): **(B1)** – Strep-tag II was excluded from the calculation; **(B2)** – Strep-tag II and all flexible loops shown in **(A1)** were excluded from the calculation.

The rigidity profile obtained for $HoxG_{MBH}$ (Supplementary Figure S10) is qualitatively similar to those reported in an earlier study (Oteri et al., 2014a) for the soluble and membrane-bound [NiFe]-hydrogenases from *D. fructosovorans* and *A. aeolicus*, respectively. The highest force constant peaks obtained for the MBH structure are observed for residues coordinating the active site, i.e., Cys75, Cys78, Cys597 and Cys600 (Figure 4, red line), which is a common feature in proteins with cofactors (Yang and Bahar, 2005; Sacquin-Mora and Lavery, 2006; Sacquin-Mora et al., 2007). Despite the absence of HoxK, a similar trend is observed for $HoxG_c$ (Figure 4, black line) as well as in structures extracted from GaMD simulations (Figure 4, purple line), where peaks have different intensities. In the region of Cys75 and Cys78, the intensities of peaks decrease from about 700 kcal·mol^{-1}·Å^{-2} to just below 100 kcal·mol^{-1}·Å^{-2} and in the region of Cys597 and Cys600 the magnitude of the force constants is significantly reduced from *ca.* 300 kcal·mol^{-1}·Å^{-2} to half when comparing $HoxG_m$ to the $HoxG_{MBH}$. The loss of rigidity around active site cysteines is compensated by an increase in peak intensities around residues Gly412, Arg476 and Arg530. The highest peak (at 373 kcal·mol^{-1}·Å^{-2} in Figure 4, purple line) from GaMD simulations is assigned to Arg530, which is also very pronounced in the rigidity profile of $HoxG_{MBH}$. Arg530 forms a stable salt-bridge with Asp117 in several structures of *Cn*MBH [PDB codes: 3RGW (Fritsch et al., 2011), 4IUC, 4IUB, 4IUD (Frielingsdorf et al., 2014)] and it is maintained in cMD and GaMD simulations (Supplementary Figure S11).

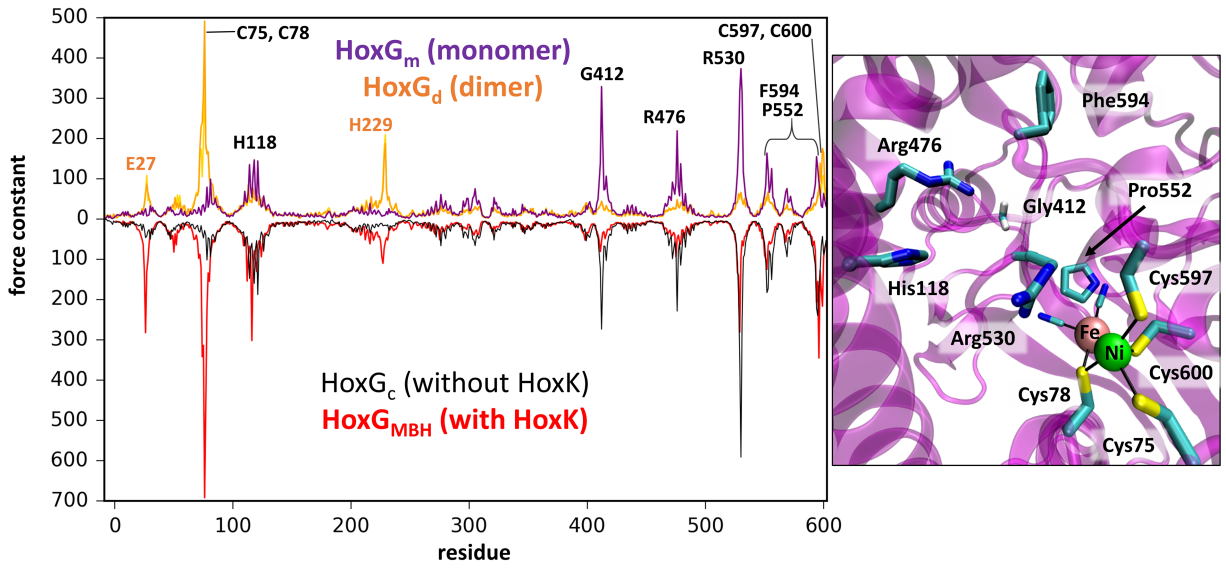

FIGURE 4
Left: Rigidity profiles of HoxG$_m$ and HoxG$_d$ (upper purple and yellow line, respectively) and HoxG$_c$, HoxG$_{MBH}$ [PDB code: 3RGW (Fritsch et al., 2011); black and red line, respectively]. Force constants (in units kcal·mol^{-1}·Å^{-2}) of HoxG$_m$ and HoxG$_d$ models were obtained using frames extracted after 200ns GaMD simulation (simulation 2 in case of HoxG$_m$). **Right**: Residues predicted with force constants of 100kcal·mol^{-1}·Å^{-2} or higher in the structures of HoxG$_m$ taken from GaMD simulation 2 at 200ns.

Generally, residues featured as peak-representatives are within 12 Å of the [NiFe] active site (Figure 4), thereby reflecting the stability of the protein core in the isolated HoxG (Figure 2). However, the [NiFe] active site in the HoxG$_m$ is somewhat less rigid than that in HoxG$_{MBH}$ with force constants of all cysteines below 100 kcal·mol^{-1}·Å^{-2}. Loss of rigidity around the active site may be the consequence of the solvent exposure of Ni^{2+}, Cys597 and Cys75 and the increased flexibility of the adjacent loop with residues 24–28 (Figure 3A3). These sites are located at the HoxG-HoxK interface in MBH that becomes solvent exposed when isolating the HoxG unit.

Interestingly, the rigidity encompassing the [NiFe] active site, which was lost in the HoxG$_m$ is partially regained in the HoxG$_d$ model (Figures 2, 4). Furthermore, the rigidity of Glu27 seems to be recovered as reflected by a force constant peak of approx. 108 kcal·mol^{-1}·Å^{-2}, which is similar to that observed in HoxG$_{MBH}$. His229, which interacts with the HoxK subunit in MBH, also contributes to the rigidity of the HoxG$_d$ with a force constant peak of approx. 209 kcal·mol^{-1}·Å^{-2}. Notably, the region encompassing the Arg530 and Phe594 appears less rigid. The change of mechanical properties in this region may also have consequences on the efficiency of substrate channeling and binding to the active site.

Electrostatic properties of HoxG$_m$

The electrostatic properties of proteins are crucial for understanding their interactions with other molecules and/or surfaces, e.g., of electrodes (Oteri et al., 2014b; Heidary et al., 2015). After separation from the HoxK subunit of MBH, the electrostatic properties of the HoxG$_m$ exhibit some differences compared to the HoxG$_{MBH}$. The pK$_A$ values (protonation states) initially determined with Karlsberg2$^+$ (Rabenstein and Knapp, 2001; Kieseritzky and Knapp, 2008; Meyer and Knapp, 2015), remain unchanged in all MD simulations (Supplementary Table S1). Remarkable is the significant change in the pK$_A$ value of Glu27 upon isolation of the HoxG subunit. This residue is located in the proximity of the [NiFe] center and is immersed in the protein matrix at the HoxG-HoxK interface. A very high pK$_A$ value (> 20) is predicted, indicating a neutral charge state. Upon removal of HoxK, Glu27 becomes solvent exposed and its pK$_A$ drops significantly down to *ca.* 4, suggesting the prevalence of its anionic form. Therefore, we propose that the mechanism by which protons are supplied to the active site is altered when the HoxK unit is detached from the MBH.

In order to better identify changes in the electrostatic properties arising from the removal of the small HoxK subunit, we also computed the electrostatic potential surface (EPS) of the HoxG$_c$ and that of HoxG$_m$ using APBS (Baker et al., 2001; Figure 5). The EPS of thermally equilibrated HoxG$_m$ (Figure 5B) shows a considerable number of positive charges at the solvent exposed interface (occupied by the HoxK subunit in MBH), where several Arg, Lys and His residues are present. A comparison of the computed EPS for *Cn*MBH and its HoxG subunit is shown in Supplementary Figure S12. In regions different from the former heterodimer interface we observed similar charge localizations patterns, with important exceptions in regions containing flexible loops and the Strep-tag II tag (Figure 6; Supplementary Figure S12). Here, the differences in charge distribution significantly depend on their local conformations and interactions.

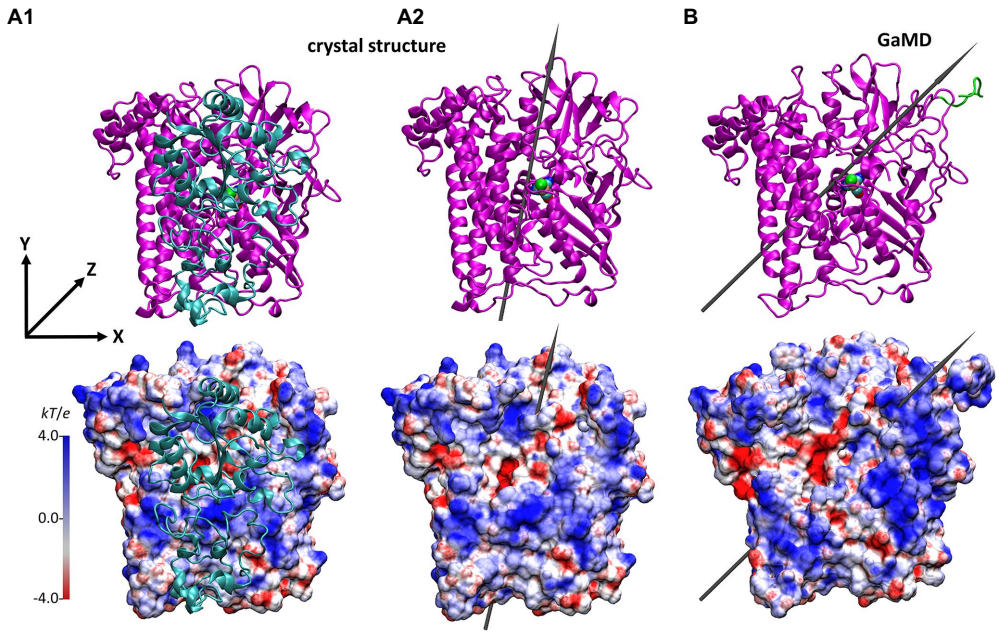

FIGURE 5
Structure and the electrostatic potential surface of the HoxG structures, showing the former dimer interface (other orientations are shown in Supplementary Figure S13). **(A)**: HoxG subunit from the MBH crystal structure 3RGW (Fritsch et al., 2011), with $HoxG_{MBH}$ **(A1)** and without $HoxG_c$ **(A2)** the small subunit HoxK. **(B)**: $HoxG_m$ structure taken from simulation 2 after 100ns. The upper panels show the secondary structure elements. The representation and color codes are taken from Figure 1. The electrostatic potential surface calculated with the APBS (Baker et al., 2001; grid resolution 0.3Å) is qualitatively displayed (range: −4 kT/e to 4 kT/e), where red and blue indicate negatively and positively charged regions, respectively. The grey arrows indicate the direction of the dipole moment in monomers $HoxG_c$ and $HoxG_m$, *ca.* 644 Debye **(A2)** and *ca.* 740 Debye **(B)**, respectively. Charges and radii were used as defined in the CHARMM Force-Field (MacKerell, 1998; Best et al., 2012). Comparison to the *Cn*MBH heterodimer is shown in the SI (Supplementary Figure S12).

The direction and magnitude of the dipole moment in $HoxG_m$ were evaluated over the course of GaMD simulations using VMD (Humphrey et al., 1996), with charges and atomic radii from CHARMM ForceField (MacKerell, 1998; Best et al., 2012). The dipole moment of the $HoxG_{MBH}$ oriented along the y axis, which was defined from Cα of Asn311 to Cα of Pro22 as reference (Figure 5A). In the course of the GaMD simulation, the total dipole moment of $HoxG_m$ rotates 25° with respect to its initial position. This is shown in Figure 5B as representative conformation, taken from simulation 2 after 100 ns. Thereby, $HoxG_m$ adopts an orientation similar to that in the heterodimer MBH (Supplementary Figure S12; Utesch et al., 2013; Heidary et al., 2015). Furthermore, moderate fluctuations of the magnitude and orientation of the dipole moment are predicted during the simulations (Supplementary Figure S14) like previously reported for other [NiFe]-hydrogenases (Oteri et al., 2014b).

During the GaMD simulations, the magnitude of the dipole moment of the $HoxG_m$ fluctuates moderately around 800 ± 250 Debye (Supplementary Figure S14) and decreases to around 677 ± 100 Debye upon exclusion of the Strep-tag II (Supplementary Table S2). Moreover, also the orientation of the dipole moment in HoxG shows some fluctuations, as the formed angle of the dipole moment computed for $HoxG_c$ in 3RGW (Fritsch et al., 2011) oscillates between 5° and 40° when the Strep Tag-II is taken into account and between 0° and 30° if the tag is absent (the related $HoxG_c$ does not contain a Strep-tag II; Fritsch et al., 2011). Thus, our calculations demonstrate that the presence of a flexible tag region, carrying charged Glu, His^+ and Lys residues, has a significant influence on the orientation and strength of the total dipole moment of HoxG protein and consequently, on the stability of the electrostatic interactions with potential reactions partners (e.g., proteins and surfaces).

Size exclusion chromatography

The oligomerization state of HoxG was investigated utilizing size exclusion chromatography. The protein was measured in various concentrations between 0.5 and 60 mg/ml. We observed that at concentrations below 12.5 mg/ml, the chromatographic profile of HoxG comprises mainly a monomeric form (R_V 15.34 ml). At higher protein concentrations, a significant amount of a dimeric form (R_V 14.1 ml) was detected (Figure 7).

The computational work predicted a stable $HoxG_d$ homodimer at the former HoxK interface. This structural arrangement is

supposed to contribute to the cofactor stability, protecting the solvent exposed $NiFe(CN)_2(CO)$ site from degradation. To elucidate whether the dimeric arrangement might confer stability to the active site, we used IR spectroscopy. Given that the CO and CN-diatomic ligands of the [NiFe] cofactor have specific spectroscopic signatures that vary with respect to changes in electron density at the active site, IR spectroscopy can provide detailed information on the hydrogenase cofactor monitoring redox changes, hydrogen bonding, protonation state of neighboring residues as well as stability of the [NiFe] site in the protein scaffold (Ash et al., 2017; Tai et al., 2021).

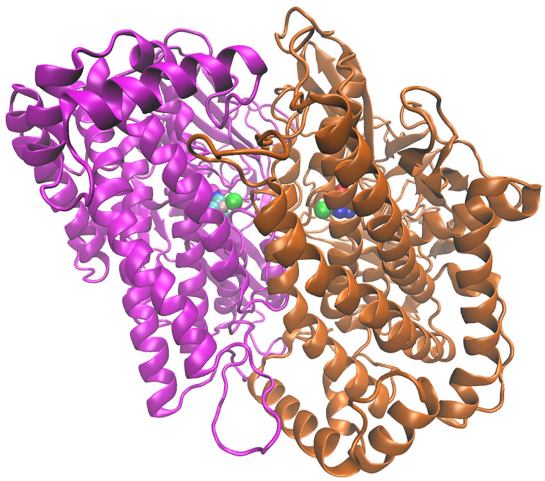

FIGURE 6
Structure of the HoxG homodimer ($HoxG_d$) taken from GaMD simulation at 150ns. 232 [NiFe]-active sites are depicted as spheres following the color code: Fe in pink, Ni in green 233 $CN^-$and CO groups, cyan-blue and cyan-red, respectively.

For this purpose, IR spectra of two HoxG samples (ca 30 mg/ml and 100 mg/ml, respectively) were recorded continuously for 7 h. These two protein concentrations were chosen such that, the first sample (between 12.5 and 60 mg/ml) has a higher monomer content, while the 100 mg/ml sample has a higher dimer content. Furthermore, the comparable high protein concentrations enable a clear detection of the active site absorption bands suitable for cofactor quantitation. The spectra were first normalized to the intensity of the amide II band (at *ca.* 1,551 cm^{-1}) and then the integral of the CO stretching bands region was calculated and plotted as a function of time (Figure 8A). The fully mature HoxG protein has been recently characterized (Caserta et al., 2022a) and its spectrum shows two main CO absorptions at 1,929 and 1,939 cm^{-1}, and a weaker band at 1953 cm^{-1} that was assigned to an unmatured portion of the protein still containing its C-terminal peptide extension (Hartmann et al., 2018; Caserta et al., 2022a).

By comparing the first (t_0) and last IR spectrum (t_{7h}) of the two HoxG samples (Figures 8A,B) and their time dependence (Figure 8C), we observed a more pronounced loss of the active site signals in the sample with higher monomer content. Given a strong correlation between the amount of dimeric HoxG and the increased stability of the active site signals, we propose that the dimerization occurs at the interface freed by the HoxK subunit. This is in line with the computational predictions, suggesting a recovery of the active site rigidity for the HoxG protein upon (homo)-dimerization.

Discussion

Biochemical, theoretical, and spectroscopic studies on [NiFe]-hydrogenases have focused on a small subset of these

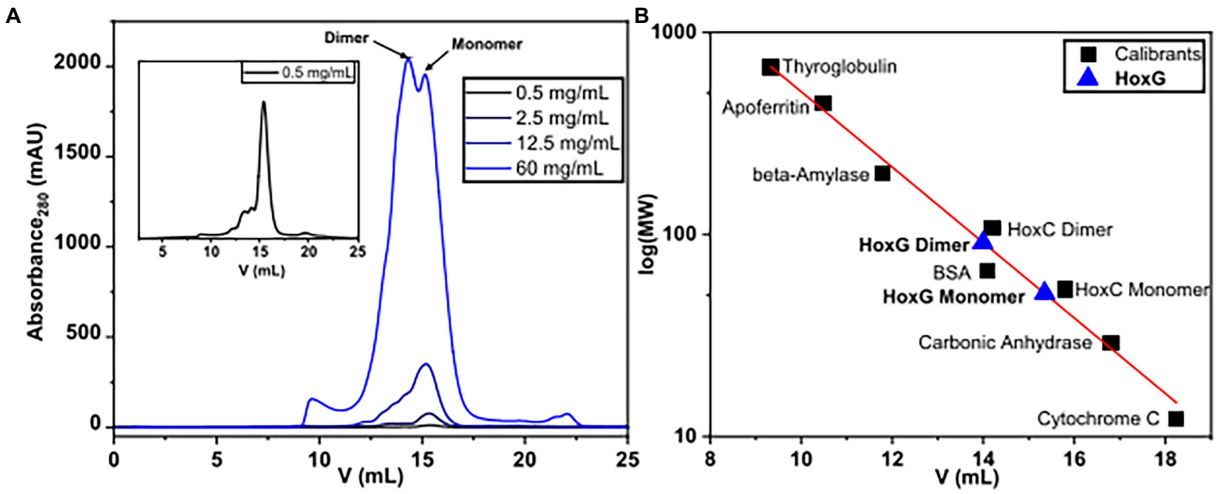

FIGURE 7
Size-exclusion chromatography measurements of HoxG in different protein concentrations **(A)** were performed in 50mM K_iPO4, 150mM NaCl, pH=7.4, T=4°C. Monomeric and dimeric forms were calculated based on reference proteins **(B)**.

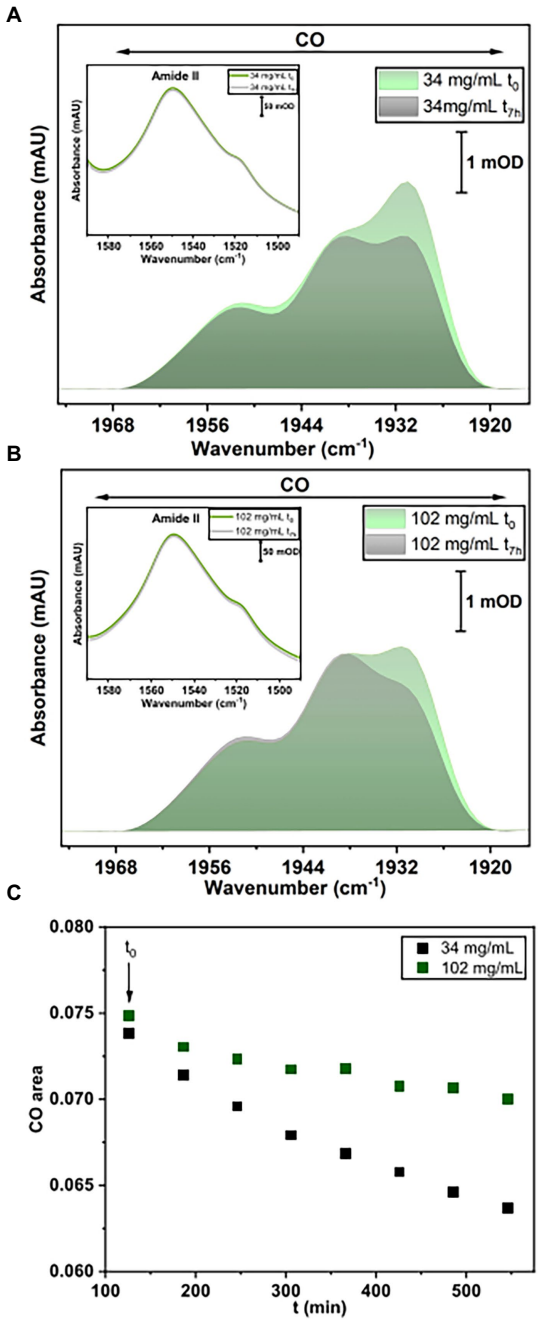

FIGURE 8
IR spectroscopy measurements. **(A)** Baseline-corrected IR spectra for HoxG sample (34mg/ml) at t_0 and after 7h accumulation. **(B)** Baseline-corrected IR spectra for HoxG sample (102mg/ml) at t_0 and after 7h accumulation. The spectral region in **(A,B)** displays bands related to the CO stretching vibrations of the active site. Shown spectra have been normalized to the intensity of the amide II band (see figure insets in **A,B**). **(C)** Time evolution of the integral of the [NiFe] active site CO absorption bands for the HoxG sample at 30 (black squares) and 100mg/ml (red squares), respectively. For an adequate comparison of the time evolution of the active site signals in **A,B**, we have chosen 120min (t_0=120min) as starting point for plotting the integral intensity of the CO absorptions.

enzymes, assuming that the knowledge gained herein would apply to all [NiFe]-hydrogenases (Sickerman and Hu, 2019). Recently, we have shown that it is possible to isolate hydrogenase catalytic subunits equipped with an intact and redox-active NiFe(CN)$_2$(CO) active site (HoxC and HoxG proteins from *Cn*RH and *Cn*MBH, respectively). This grants an exclusive spectral view on the hydrogenase active site without the interference from Fe-S cluster relay (Hartmann et al., 2018; Caserta et al., 2020a,b, 2021, 2022a). Albeit we suggest that these biophysical properties apply to all [NiFe] hydrogenases, the premature large subunit from *Thermococcus kodakarensis*, *Tk*HyhL (Kwon et al., 2018), was isolated exclusively in its apo-form while the catalytic subunit Pf$_\alpha$ from the cytoplasmic soluble [NiFe]-hydrogenase from *Pyrococcus furiosus* (*Pf*SHI) did not exhibit any biological and electrochemical properties (Chandrayan et al., 2015; Wang et al., 2021). Considering these recent observations and the fact that the HoxG protein has been isolated even at different stages of the biosynthetic maturation of the [NiFe] cofactor (Caserta et al., 2022a), we have undertaken an investigation of the structural and mechanical properties of this protein.

Upon removal of the small subunit HoxK from the heterodimeric MBH, the former dimer interface in the HoxG subunit becomes solvent accessible and with it, a small fraction of the catalytic site becomes exposed (Figure 2A). Alterations in the polarity of the protein environment may cause significant structural reorganization, specifically at the previous interface site. To verify this assumption, a series of classical MD simulations were performed. The changes in mechanical and electrostatic properties were evaluated using a coarse-grained Brownian dynamics approach and Poisson Boltzmann electrostatic calculations. An initial model structure for the HoxG subunit was extracted from the available crystallographic data on the heterodimeric MBH (3RGW; Fritsch et al., 2011), which was equipped with a Strep-tag II affinity tag at the N-terminus in line with the recent biochemical data (Caserta et al., 2022a). These models were thermally equilibrated with classical MD simulations and then subjected to Gaussian-Accelerated molecular dynamics GaMD (Miao et al., 2015).

Rigid docking approaches favored the formation of a HoxG homodimer (HoxG$_d$), built at the interface freed by the HoxK subunit. Such protein arrangement stabilizes/protects the active site by limiting solvent accessibility. Analysis of the thermally equilibrated structures derived from GaMD simulations demonstrate that the overall HoxG$_m$ structure remains stable over the course of simulations, substantiated by the relatively low RMSD (below 2.5 Å, after excluding the mobile Strep-tag II) and RMSF values (Figure 3; Supplementary Figure S1). Indeed, the core of the HoxG$_m$ protein matrix with its secondary structural elements are largely preserved in our MD simulations. To shed light on the structural stability and mechanical properties, rigidity profiles of the MBH heterodimer as well as HoxG structures extracted from GaMD simulations were computed (Figure 4). The rigidity profiles of HoxG$_m$ structures identified the residues

Gly412, Arg476, and Arg530 in the protein core as those with the largest force constants (Figure 4). In contrast, rigidity peaks in $HoxG_{MBH}$ are localized around active site cysteines (Cys75, Cys78, Cys597, and Cys600) consistent with those reported in earlier studies on hydrogenases (Oteri et al., 2014a). Our calculations suggest that the loss of rigidity at the [NiFe] active site of $HoxG_m$ upon detachment of the HoxK subunit was most likely caused by an increased solvent accessibility around the active site. Nonetheless, biochemical and spectroscopic data revealed a stable and redox active [NiFe] active site in isolated HoxC and HoxG proteins from *C. necator* (Hartmann et al., 2018; Caserta et al., 2020a,b, 2021, 2022a). Interestingly, our computational work predicts that the rigidity around the [NiFe] site is recovered in the $HoxG_d$ model, suggesting that a change in the oligomerization state of the HoxG subunit may be relevant to restore stability. These predictions were corroborated by experimental data. Indeed, size exclusion chromatography showed a concentration-dependent homodimerization of the HoxG protein and IR measurements revealed a strong correlation between the integrity of the active site and the aggregation state of the isolated HoxG (i.e., samples with higher dimer content exhibit longer remaining active absorptions as compared to the monomer counterpart). It is worth emphasizing that also other hydrogenase large subunits contain a certain amount of homodimer forms, which have not been rationalized so far (Sasaki et al., 2012; Hartmann et al., 2018; Kwon et al., 2018; Caserta et al., 2020a). Notable are in this context studies of the large subunit HyhL from *Thermococcus kodakarensis*, which was shown to form a complex at the active site interface with the Ni-inserting accessory protein HypA only upon enrichment of the large subunit monomeric form. These data suggest that the dimeric interface might be in proximity of the [NiFe] site also in *Tk*HyhL protein.

A closer look at the active site area in both $HoxG_m$ and $HoxG_d$ models revealed a salt-bridge between Arg530 and Asp117 that is conserved also in multiple MBH crystal structures (Fritsch et al., 2011; Frielingsdorf et al., 2014). The Arg530 has been shown to play a relevant functional and structural role in [NiFe] hydrogenases. Indeed, this Arg residue located above the free coordination site of the [NiFe]center (Supplementary Figure S11) has been proposed to act as general base triggering H_2 activation according to a frustrated Lewis pair mechanism (Evans et al., 2016). The Arg530 in $HoxG_m$ is associated with the highest peak in the rigidity profile, indicating that this residue plays a significant role in stabilizing the surrounding protein matrix.

In previous works done on the MBH heterodimer (Smith et al., 2012; Utesch et al., 2013; Heidary et al., 2015; Kalms et al., 2018), no large conformational changes of HoxG (or HoxK) were observed and our new simulations reveal preservation of the mechanical properties in $HoxG_m$. This statement is supported by the steady temporal evolution of the conformational energies of $HoxG_m$ structures obtained over the course of the GaMD simulations (Supplementary Figure S4). These data do not show drastic conformational changes in $HoxG_m$, which could eventually lead to protein unfolding. Moreover, the former heterodimer interface of $HoxG_m$ is largely hydrophilic as can be seen in the map of electrostatic potential (Figure 5). Herein, the positive charges from Lys, His^+ and Arg residues support the overall stability of the protein in aqueous solution.

In addition to the highly dynamic Strep-tag II (Supplementary Figure S1), several flexible loop regions (Figure 6A1) were identified on the edges of the new solvent-exposed interface. In the $HoxG_{MBH}$, residues from these flexible regions form non-covalent interactions with the small subunit HoxK (Albareda et al., 2019). Herein, we propose that the flexible regions could be relevant for interactions of the $HoxG_m$ with other molecular species such as maturase proteins involved in the biosynthesis of the [NiFe] cofactor (Lacasse and Zamble, 2016; Kwon et al., 2018) and may be used to facilitate the protein immobilization on electrode surfaces (Utesch et al., 2013). In the latter case, detailed information on the electrostatic potential surface can guide the optimization of protein immobilization strategies assuring an efficient electrochemical control. In this regard, early work on MBH heterodimer using (spectro) electrochemical techniques showed that immobilization of the enzyme can be controlled by changing the protonation of the self-assembled monolayer (SAM) of functionalized n-alkanethiols attached to the gold surface (Utesch et al., 2013).

In summary we have clearly shown that a Strep-tag II sequence, often included to enhance protein purity and homogeneity (Johar and Talbert, 2017), has a substantial effect on the electrostatic behavior of a macromolecule (Oteri et al., 2014b). In the case of the $HoxG_m$, this highly flexible positively charged sequence of amino acids is responsible for destabilizing the dipole moment and reducing its strength. However, the affinity tag does not control the dipole moment direction as much as the rest of the protein (Supplementary Figure S14). Generally, the direction of the dipole moment in $HoxG_m$ (avg. value *ca.* 833 Debye; Supplementary Table S2) as depicted in Supplementary Figure S12, is steady throughout the MD simulations.

Finally, our combined computational/experimental data revealed that the artificial isolation of the large subunit of MBH does not result in protein unfolding and the key mechanical properties are preserved. Various oligomers could be observed in $HoxG_m$ depending on the protein concentration, and we propose that homodimers are formed *via* the former HoxG-HoxK interface of the MBH. This arrangement confers mechanical stability to the active site and we hypothesize that the active site rigidity may be regained also through a specific and oriented immobilization of $HoxG_m$ on a functionalized surface, as previously observed in the case of similar enzymes (Oteri et al., 2014b). More importantly, we used thermally equilibrated structures from GaMD simulations to determine formerly unknown properties of $HoxG_m$, such as surface charge distribution and dipole moment strength and orientation. This information is essential for understanding the details of the hydrogenase maturation (Lacasse and Zamble, 2016; Hartmann et al., 2018; Caserta et al., 2020a, 2022a), achieving electrostatic control of these enzymes and more importantly boosting their applications.

Data availability statement

The original contributions presented in the study are included in the article/Supplementary material, further inquiries can be directed to the corresponding author.

Author contributions

JD and SS-M: calculations. CK-R, SK, and GC: experiments. JD, SS-M, SK, GC, IZ, and MM: analysis, writing—original draft preparation, and writing—review and editing. IZ, OL, and MM: funding acquisition. All authors contributed to the article and approved the submitted version.

Funding

This work was funded by the Deutsche Forschungsgemeinschaft (DFG, German Research Foundation) under Germany's Excellence Strategy – EXC 2008–390540038 (UniSysCat), further financial support was granted by the "Initiative d'Excellence" program from the French State (Grant "DYNAMO," ANR-11-LABX-0011-01).

Acknowledgments

We are grateful for the provided computer time from North German Supercomputing Alliance (HLRN) within the project bec00218 in 2020. We also acknowledge support by the German Research Foundation and the Open Access Publication Fund of TU Berlin.

Conflict of interest

The authors declare that the research was conducted in the absence of any commercial or financial relationships that could be construed as a potential conflict of interest.

Publisher's note

All claims expressed in this article are solely those of the authors and do not necessarily represent those of their affiliated organizations, or those of the publisher, the editors and the reviewers. Any product that may be evaluated in this article, or claim that may be made by its manufacturer, is not guaranteed or endorsed by the publisher.

Supplementary material

The Supplementary material for this article can be found online at: https://www.frontiersin.org/articles/10.3389/fmicb.2022.1073315/full#supplementary-material

References

Albareda, M., Pacios, L. F., and Palacios, J. M. (2019). Computational analyses, molecular dynamics, and mutagenesis studies of unprocessed form of [NiFe] hydrogenase reveal the role of disorder for efficient enzyme maturation. *Biochim. Biophys. Acta Bioenerg.* 1860, 325–340. doi: 10.1016/j.bbabio.2019.01.001

Apfel, U.-P., Weigand, W., Horch, M., Zebger, I., Lenz, O., and Fujishiro, T. (2020). *2. Hydrogen development*. eds. W. Weigand and U.-P. Apfel (Berlin: De Gruyter), 13–136.

Ash, P. A., Hidalgo, R., and Vincent, K. A. (2017). Proton transfer in the catalytic cycle of [NiFe] hydrogenases: insight from vibrational spectroscopy. *ACS Catal.* 7, 2471–2485. doi: 10.1021/acscatal.6b03182

Baker, N. A., Sept, D., Joseph, S., Holst, M. J., and McCammon, J. A. (2001). Electrostatics of nanosystems: application to microtubules and the ribosome. *Proc. Natl. Acad. Sci. U. S. A.* 98, 10037–10041. doi: 10.1073/pnas.181342398

Batebi, H., Dragelj, J., and Imhof, P. (2018). Role of AP-endonuclease (Ape1) active site residues in stabilization of the reactant enzyme-DNA complex. *Proteins: Struct. Funct. Genet.* 86, 439–453. doi: 10.1002/prot.25460

Best, R. B., Zhu, X., Shim, J., Lopes, P. E. M., Mittal, J., Feig, M., et al. (2012). Optimization of the additive CHARMM all-atom protein force field targeting improved sampling of the backbone φ, ψ and side-chain χ1 and χ2 dihedral angles. *J. Chem. Theory Comput.* 8, 3257–3273. doi: 10.1021/ct300400x

Blumhagen, K., Muegge, I., and Knapp, E. W. (1996). Diffusion of two different water models and thermal conductivity in a protein—water system. *Int. J. Quantum Chem.* 59, 271–279. doi: 10.1002/(SICI)1097-461X(1996)59:4<271::AIDQUA2>3.3.CO;2-R

Brooks, B. R., Brooks, C. L. III, Mackerell, A. D. Jr., Nilsson, L., Petrella, R. J., Roux, B., et al. (2009). CHARMM: the biomolecular simulation program. *J. Comput. Chem.* 30, 1545–1614. doi: 10.1002/jcc.21287

Caserta, G., Hartmann, S., Van Stappen, C., Karafoulidi Retsou, C., Lorent, C., Yelin, S., et al. (2022a). Active site assembly of [NiFe]-hydrogenase scrutinized on the basis of purified maturation. *ChemRxiv.* doi: 10.26434/chemrxiv-2022-jvtgw

Caserta, G., Lorent, C., Ciaccafava, A., Keck, M., Breglia, R., Greco, C., et al. (2020a). The large subunit of the regulatory [NiFe]-hydrogenase from Ralstonia eutropha – a minimal hydrogenase? *Chem. Sci.* 11, 5453–5465. doi: 10.1039/D0SC01369B

Caserta, G., Lorent, C., Pelmenschikov, V., Schoknecht, J., Yoda, Y., Hildebrandt, P., et al. (2020b). In vitro assembly as a tool to investigate catalytic intermediates of [NiFe]-hydrogenase. *ACS Catal.* 10, 13890–13894. doi: 10.1021/acscatal.0c04079

Caserta, G., Pelmenschikov, V., Lorent, C., Tadjoung Waffo, A. F., Katz, S., Lauterbach, L., et al. (2021). Hydroxy-bridged resting states of a [NiFe]-hydrogenase unraveled by cryogenic vibrational spectroscopy and DFT computations. *Chem. Sci.* 12, 2189–2197. doi: 10.1039/d0sc05022a

Caserta, G., Zuccarello, L., Barbosa, C., Silveira, C. M., Moe, E., Katz, S., et al. (2022b). Unusual structures and unknown roles of FeS clusters in metalloenzymes seen from a resonance Raman spectroscopic perspective. *Coord. Chem. Rev.* 452:214287. doi: 10.1016/j.ccr.2021.214287

Chandrayan, S. K., Wu, C.-H., McTernan, P. M., and Adams, M. W. W. (2015). High yield purification of a tagged cytoplasmic [NiFe]-hydrogenase and a catalytically-active nickel-free intermediate form. *Protein Expr. Purif.* 107, 90–94. doi: 10.1016/j.pep.2014.10.018

Cornell, W. D., Cieplak, P., Bayly, C. I., and Kollman, P. A. (1993). Application of RESP charges to calculate conformational energies, hydrogen bond energies, and free energies of solvation. *J. Am. Chem. Soc.* 115, 9620–9631. doi: 10.1021/Ja00074a030

Darden, T., York, D., and Pedersen, L. (1993). Particle mesh Ewald: an Nślog(N) method for Ewald sums in large systems. *JCP* 98, 10089–10092. doi: 10.1063/1.464397

Dementin, S., Burlat, B., de Lacey, A. L., Pardo, A., Adryanczyk-Perrier, G., Guigliarelli, B., et al. (2004). A glutamate is the essential proton transfer gate during

the catalytic cycle of the [NiFe] hydrogenase. *J. Biol. Chem.* 279, 10508–10513. doi: 10.1074/jbc.M312716200

Dragelj, J., Mroginski, A., and Ebrahimi, K. H. (2021a). *Hidden in plain sight: Natural products of commensal microbiota as an environmental selection pressure for the rise of new variants of SARS-CoV-2. Vol. 2.* 1–6.

Dragelj, J., Mroginski, M. A., and Knapp, E. W. (2021b). Beating heart of cytochrome c oxidase: the shared proton of Heme a 3 propionates. *J. Phys. Chem. B* 125, 9668–9677. doi: 10.1021/acs.jpcb.1c03619

Ermak, D. L., and McCammon, J. A. (1978). Brownian dynamics with hydrodynamic interactions. *J. Chem. Phys.* 69, 1352–1360. doi: 10.1063/1.436761

Evans, R. M., Brooke, E. J., Wehlin, S. A. M., Nomerotskaia, E., Sargent, F., Carr, S. B., et al. (2016). Mechanism of hydrogen activation by [NiFe] hydrogenases. *Nat. Chem. Biol.* 12, 46–50. doi: 10.1038/nchembio.1976

Fontecilla-camps, J. C., Volbeda, A., Cavazza, C., Nicolet, Y., and Fourier, J. (2007). "*Structure/function relationships of [NiFe]- and [FeFe]-hydrogenases*".

Frielingsdorf, S., Fritsch, J., Schmidt, A., Hammer, M., Löwenstein, J., Siebert, E., et al. (2014). Reversible [4Fe-3S] cluster morphing in an O 2-tolerant [NiFe] hydrogenase. *Nat. Chem. Biol.* 10, 378–385. doi: 10.1038/nchembio.1500

Frisch, M. J. (2016). "*Gaussian development version, revision I. 13; Gaussian, Inc*," Wallingford, CT.

Fritsch, J., Scheerer, P., Frielingsdorf, S., Kroschinsky, S., Friedrich, B., Lenz, O., et al. (2011). The crystal structure of an oxygen-tolerant hydrogenase uncovers a novel iron-Sulphur Centre. *Nature* 479, 249–252. doi: 10.1038/nature10505

Goris, T., Wait, A. F., Saggu, M., Fritsch, J., Heidary, N., Stein, M., et al. (2011). A unique iron-sulfur cluster is crucial for oxygen tolerance of a [NiFe]-hydrogenase. *Nat. Chem. Biol.* 7, 310–318. doi: 10.1038/nchembio.555

Hamelberg, D., Mongan, J., and McCammon, J. A. (2004). Accelerated molecular dynamics: a promising and efficient simulation method for biomolecules. *J. Chem. Phys.* 120, 11919–11929. doi: 10.1063/1.1755656

Harris, T. G. A. A., Heidary, N., Kozuch, J., Frielingsdorf, S., Lenz, O., Mroginski, M. A., et al. (2018). In situ Spectroelectrochemical studies into the formation and stability of robust Diazonium-derived interfaces on gold electrodes for the immobilization of an oxygen-tolerant hydrogenase. *ACS Appl. Mater. Interfaces* 10, 23380–23391. doi: 10.1021/acsami.8b02273

Hartmann, S., Frielingsdorf, S., Caserta, G., and Lenz, O. (2020). A membrane-bound [NiFe] hydrogenase large subunit precursor whose C-terminal extension is not essential for cofactor incorporation but guarantees optimal maturation. *Microbiol open.* 9, 1197–1206. doi: 10.1002/mbo3.1029

Hartmann, S., Frielingsdorf, S., Ciaccafava, A., Lorent, C., Fritsch, J., Siebert, E., et al. (2018). O2-tolerant H2 activation by an isolated large subunit of a [NiFe] hydrogenase. *Biochemistry* 57, 5339–5349. doi: 10.1021/acs.biochem.8b00760

Heidary, N., Utesch, T., Zerball, M., Horch, M., Millo, D., Fritsch, J., et al. (2015). Orientation-controlled electrocatalytic efficiency of an adsorbed oxygen-tolerant hydrogenase. *PLoS One* 10:e0143101. doi: 10.1371/journal.pone.0143101

Hitaishi, V. P. (2018). Controlling redox enzyme orientation at planar electrodes. *Catalysts* 8, 1–38. doi: 10.3390/catal8050192

Humphrey, W., Dalke, A., and Schulten, K. (1996). VMD: visual molecular dynamics. *J. Mol. Graph.* 14, 33–38. doi: 10.1016/0263-7855(96)00018-5

Ilina, Y., Lorent, C., Katz, S., Jeoung, J. H., Shima, S., Horch, M., et al. (2019). X-ray crystallography and vibrational spectroscopy reveal the key determinants of biocatalytic dihydrogen cycling by [NiFe] hydrogenases. *Angew. Chemie - Int. Ed.* 58, 18710–18714. doi: 10.1002/anie.201908258

Johar, S. S., and Talbert, J. N. (2017). Strep-tag II fusion technology for the modification and immobilization of lipase B from Candida antarctica (CALB). *J. Genet. Eng. Biotechnol.* 15, 359–367. doi: 10.1016/j.jgeb.2017.06.011

Jorgensen, W. L., Chandrasekhar, J., Madura, J. D., Impey, R. W., and Klein, M. L. (1983). Comparison of simple potential functions for simulating liquid water. *J. Chem. Phys.* 79, 926–935. doi: 10.1063/1.445869

Kalms, J., Schmidt, A., Frielingsdorf, S., Utesch, T., Gotthard, G., von Stetten, D., et al. (2018). Tracking the route of molecular oxygen in O 2-tolerant membranebound [NiFe] hydrogenase. *Proc. Natl. Acad. Sci.* 115:E2229. doi: 10.1073/pnas.1712267115

Kalms, J., Schmidt, A., Frielingsdorf, S., van der Linden, P., von Stetten, D., Lenz, O., et al. (2016). Krypton derivatization of an O2-tolerant membrane-bound [NiFe] hydrogenase reveals a hydrophobic tunnel network for gas transport. *Angewandte Chemie* 55, 5586–5590. doi: 10.1002/anie.201508976

Kieseritzky, G., and Knapp, E. W. (2008). Optimizing pKA computation in proteins with pH adapted conformations. *Proteins Struct. Funct. Genet.* 71, 1335–1348. doi: 10.1002/prot.21820

Kwon, S., Watanabe, S., Nishitani, Y., Kawashima, T., Kanai, T., Atomi, H., et al. (2018). Crystal structures of a [NiFe] hydrogenase large subunit HyhL in an immature state in complex with a Ni chaperone HypA. *Proc. Natl. Acad. Sci. U. S. A.* 115, 7045–7050. doi: 10.1073/pnas.1801955115

Lacasse, M. J., and Zamble, D. B. (2016). [NiFe]-hydrogenase maturation. *Biochemistry* 55, 1689–1701. doi: 10.1021/acs.biochem.5b01328

Laskowski, R. A. (2009). PDBsum new things. *Nucleic Acids Res.* 37, D355–D359. doi: 10.1093/nar/gkn860

Lavery, R., and Sacquin-Mora, S. (2007). Protein mechanics: a route from structure to function. *J. Biosci.* 32, 891–898. doi: 10.1007/s12038-0070089-x

Lenz, O., Lauterbach, L., Frielingsdorf, S., and Friedrich, B. (2015). *4 oxygen-tolerant hydrogenases and their biotechnological potential*, in M. Rögner Biohydrogen, Ed. Berlin, München, Boston: De Gruyter. 61–96.

MacKerell, A. D. (1998). All-atom empirical potential for molecular modeling and dynamics studies of proteins †. *J. Phys. Chem. B* 102, 3586–3616. doi: 10.1021/jp973084f

Meyer, T., and Knapp, E.-W. (2015). P K a values in proteins determined by electrostatics applied to molecular dynamics trajectories. *J. Chem. Theory Comput.* 11, 2827–2840. doi: 10.1021/acs.jctc.5b00123

Miao, Y., Feher, V. A., and McCammon, J. A. (2015). Gaussian accelerated molecular dynamics: unconstrained enhanced sampling and free energy calculation. *J. Chem. Theory Comput.* 11, 3584–3595. doi: 10.1021/acs.jctc.5b00436

Oteri, F., Baaden, M., Lojou, E., and Sacquin-Mora, S. (2014a). Multiscale simulations give insight into the hydrogen in and out pathways of [NiFe]-hydrogenases from aquifex aeolicus and desulfovibrio fructosovorans. *J. Phys. Chem. B* 118, 13800–13811. doi: 10.1021/jp5089965

Oteri, F., Ciaccafava, A., De Poulpiquet, A., Baaden, M., Lojou, E., and Sacquin-Mora, S. (2014b). The weak, fluctuating, dipole moment of membrane-bound hydrogenase from Aquifex aeolicus accounts for its adaptability to charged electrodes. *Phys. Chem. Chem. Phys.* 16, 11318–11322. doi: 10.1039/c4cp00510d

Pastor, R. W., Vanable, R. M., and Karplus, M. (1988). Brownian dynamics simulation of a lipid chain in a membrane bilayer. *J. Chem. Phys.* 89, 1112–1127. doi: 10.1063/1.455218

Phillips, J. C., Braun, R., Wang, W., Gumbart, J., Tajkhorshid, E., Villa, E., et al. (2005). Scalable molecular dynamics with NAMD. *J. Comput. Chem.* 26, 1781–1802. doi: 10.1002/jcc.20289

Rabenstein, B., and Knapp, E.-W. (2001). Calculated pH-dependent population and protonation of carbon-Monoxy-myoglobin conformers. *Biophys. J.* 80, 1141–1150. doi: 10.1016/S0006-3495(01)76091-2

Rippers, Y., Horch, M., Hildebrandt, P., Zebger, I., and Mroginski, M. A. (2012). Revealing the absolute configuration of the CO and CN-ligands at the active site of a [NiFe] hydrogenase. *ChemPhysChem* 13, 3852–3856. doi: 10.1002/cphc.201200562

Roy, A., Kucukural, A., and Zhang, Y. (2010). I-TASSER: a unified platform for automated protein structure and function prediction. *Nat. Protoc.* 5, 725–738. doi: 10.1038/nprot.2010.5

Ruff, A., Szczesny, J., Markovi, N., Conzuelo, F., Lubitz, W., and Schuhmann, W. (2018). A fully protected hydrogenase/polymer-based bioanode for high-performance hydrogen/glucose biofuel cells. *Nature communications* 9:106. doi: 10.1038/s41467-018-06106-3

Ryckaert, J.-P., Ciccotti, G., and Berendsen, H. J. (1977). Numerical integration of the cartesian equations of motion of a system with constraints: molecular dynamics of nalkanes. *J. Comput. Phys.* 23, 327–341. doi: 10.1016/00219991(77)90098-5

Sacquin-Mora, S. (2014). Motions and mechanics: investigating conformational transitions in multi-domain proteins with coarse-grain simulations. *Mol. Simul.* 40, 229–236. doi: 10.1080/08927022.2013.843176

Sacquin-Mora, S. (2016). Bridging enzymatic structure function via mechanics: a CoarseGrain approach. *Methods Enzymol.* 578, 227–248. doi: 10.1016/bs.mie.2016.05.022

Sacquin-Mora, S. (2018). Mechanical variations in proteins with large-scale motions highlight the formation of structural locks. *J. Struct. Biol.* 203, 195–204. doi: 10.1016/j.jsb.2018.05.006

Sacquin-Mora, S., Laforet, E. Milie, and Lavery, R. (2007). Locating the active sites of enzymes using mechanical properties. *Proteins*, 67, 350–359.

Sacquin-Mora, S., and Lavery, R. (2006). Investigating the local flexibility of functional residues in hemoproteins. *Biophys. J.* 90, 2706–2717. doi: 10.1529/biophysj.105.074997

Saggu, M., Zebger, I., Ludwig, M., Lenz, O., Friedrich, B., Hildebrandt, P., et al. (2009). Spectroscopic insights into the oxygen-tolerant membrane-associated [NiFe] hydrogenase of Ralstonia eutropha H16. *J. Biol. Chem.* 284, 16264–16276. doi: 10.1074/jbc.M805690200

Sasaki, D., Watanabe, S., Kanai, T., Atomi, H., Imanaka, T., and Miki, K. (2012). Characterization and in vitro interaction study of a [NiFe] hydrogenase large subunit from the hyperthermophilic archaeon Thermococcus kodakarensis KOD1. *Biochem. Biophys. Res. Commun.* 417, 192–196. doi: 10.1016/j.bbrc.2011.11.083

Schneidman-Duhovny, D., Inbar, Y., Nussinov, R., and Wolfson, H. J. (2005a). Geometry-based flexible and symmetric protein docking. *Proteins Struct. Funct. Genet.* 60, 224–231. doi: 10.1002/prot.20562

Schneidman-Duhovny, D., Inbar, Y., Nussinov, R., and Wolfson, H. J. (2005b). PatchDock and SymmDock: servers for rigid and symmetric docking. *Nucleic Acids Res.* 33, W363–W367. doi: 10.1093/nar/gki481

Shafaat, H. S., Rüdiger, O., Ogata, H., and Lubitz, W. (2013). [NiFe] hydrogenases: a common active site for hydrogen metabolism under diverse conditions. *Biochim. Biophys. Acta Bioenerg.* 1827, 986–1002. doi: 10.1016/j.bbabio.2013.01.015

Sickerman, N. S., and Hu, Y. (2019). "Hydrogenases," in *Methods in Molecular Biology. Vol. 1876* ed. Y. Hu (United States: Humana Press Inc.), 65–88.

Smith, D. M. A., Xiong, Y., Straatsma, T. P., Rosso, K. M., and Squier, T. C. (2012). Forcefield development and molecular dynamics of [NiFe] hydrogenase. *J. Chem. Theory Comput.* 8, 2103–2114. doi: 10.1021/ct300185u

Tai, H., Hirota, S., and Stripp, S. T. (2021). Proton transfer mechanisms in bimetallic hydrogenases. *Acc. Chem. Res.* 54, 232–241. doi: 10.1021/acs.accounts.0c00651

Teixeira, V. H., Baptista, A. M., and Soares, C. M. (2006). Pathways of H2 toward the active site of [NiFe]-hydrogenase. *Biophys. J.* 91, 2035–2045. doi: 10.1529/biophysj.106.084376

Tillmann, U. (2018). A computational modeling approach predicts interaction of the antifungal protein AFP from aspergillus giganteus with fungal membranes via its γcore motif. *Msphere* 3, e00377–e00318. doi: 10.1128/mSphere.0037718

Tombolelli, D., and Mroginski, M. A. (2019). Proton transfer pathways between active sites and proximal clusters in the membrane-bound [NiFe] hydrogenase. *J. Phys. Chem. B* 123, 3409–3420. doi: 10.1021/acs.jpcb.9b00617

Tozzini, V. (2005). Coarse-grained models for proteins. *Curr. Opin. Struct. Biol.* 15, 144–150. doi: 10.1016/J.SBI.2005.02.005

Utesch, T., Millo, D., Castro, M. A., Hildebrandt, P., Zebger, I., and Mroginski, M. A. (2013). Effect of the protonation degree of a self-assembled monolayer on the immobilization dynamics of a [NiFe] hydrogenase. *Langmuir* 29, 673–682. doi: 10.1021/la303635q

Vincent, K. A., Cracknell, J. A., Lenz, O., Zebger, I., Friedrich, B., and Armstrong, F. A. (2005). Electrocatalytic hydrogen oxidation by an enzyme at high carbon monoxide or oxygen levels. *Proc. Natl. Acad. Sci. U. S. A.* 102, 16951–16954. doi: 10.1073/pnas.0504499102

Wang, Y., Song, Y., Ma, H, C., Xia, Q., Wu, R., and Zhu, Z. (2021). Electrochemical characterization of a truncated hydrogenase from Pyrococcus furiosus. *Electrochim. Acta* 387:138502. doi: 10.1016/j.electacta.2021.138502

Wolf, A., Dragelj, J., Wonneberg, J., Stellmacher, J., Balke, J., Woelke, A. L., et al. (2020). The redox-coupled proton-channel opening in cytochrome c oxidase. *Chem. Sci.* 11, 3804–3811. doi: 10.1039/C9SC06463J

Yang, L. W., and Bahar, I. (2005). Coupling between catalytic site and collective dynamics: a requirement for mechanochemical activity of enzymes. *Structure* 13, 893–904. doi: 10.1016/j.str.2005.03.015

Yang, J., Yan, R., Roy, A., Xu, D., Poisson, J., and Zhang, Y. (2014). The I-TASSER suite: protein structure and function prediction. *Nat. Methods* 12, 7–8. doi: 10.1038/nmeth.3213

Zacharias, M. (2003). Protein-protein docking with a reduced protein model accounting for side-chain flexibility. *Protein Sci.* 12, 1271–1282. doi: 10.1110/ps.0239303

Zhang, Y. (2008). I-TASSER server for protein 3D structure prediction. *BMC Bioinformatics* 9, 1–8. doi: 10.1186/1471-2105-9-40

frontiers | Frontiers in Microbiology

TYPE Original Research
PUBLISHED 24 March 2023
DOI 10.3389/fmicb.2023.1151097

OPEN ACCESS

EDITED BY
Chris Greening,
Monash University,
Australia

REVIEWED BY
Philippe Constant,
Université du Québec,
Canada
Tobias Goris,
German Institute of Human Nutrition
Potsdam-Rehbruecke (DIfE),
Germany
Jan Zarzycki,
Max Planck Institute for Terrestrial
Microbiology,
Germany

*CORRESPONDENCE
Huub J. M. Op den Camp
✉ h.opdencamp@science.ru.nl

SPECIALTY SECTION
This article was submitted to
Microbiological Chemistry and
Geomicrobiology,
a section of the journal
Frontiers in Microbiology

RECEIVED 25 January 2023
ACCEPTED 08 March 2023
PUBLISHED 24 March 2023

CITATION
Hogendoorn C, Pol A, de Graaf R, White PB, Mesman R, van Galen PM, van Alen TA, Cremers G, Jansen RS, Jetten MSM and Op den Camp HJM (2023) "*Candidatus* Hydrogenisulfobacillus filiaventi" strain R50 gen. nov. sp. nov., a highly efficient producer of extracellular organic compounds from H_2 and CO_2.
Front. Microbiol. 14:1151097.
doi: 10.3389/fmicb.2023.1151097

"*Candidatus* Hydrogenisulfobacillus filiaventi" strain R50 gen. nov. sp. nov., a highly efficient producer of extracellular organic compounds from H_2 and CO_2

Carmen Hogendoorn[1], Arjan Pol[1], Rob de Graaf[1], Paul B. White[2], Rob Mesman[1], Peter M. van Galen[3], Theo A. van Alen[1], Geert Cremers[1], Robert S. Jansen[1], Mike S. M. Jetten[1] and Huub J. M. Op den Camp[1]*

[1]Department of Microbiology, RIBES, Radboud University, Nijmegen, Netherlands, [2]Department of Synthetic Organic Chemistry, IMM, Radboud University, Nijmegen, Netherlands, [3]Department of Systems Chemistry, IMM, Faculty of Science, Radboud University, Nijmegen, Netherlands

Production of organic molecules is largely depending on fossil fuels. A sustainable alternative would be the synthesis of these compounds from CO_2 and a cheap energy source, such as H_2, CH_4, NH_3, CO, sulfur compounds or iron(II). Volcanic and geothermal areas are rich in CO_2 and reduced inorganic gasses and therefore habitats where novel chemolithoautotrophic microorganisms for the synthesis of organic compounds could be discovered. Here we describe "*Candidatus* Hydrogenisulfobacillus filiaventi" R50 gen. nov., sp. nov., a thermoacidophilic, autotrophic H_2-oxidizing microorganism, that fixed CO_2 and excreted no less than 0.54mol organic carbon per mole fixed CO_2. Extensive metabolomics and NMR analyses revealed that Val, Ala and Ile are the most dominant form of excreted organic carbon while the aromatic amino acids Tyr and Phe, and Glu and Lys were present at much lower concentrations. In addition to these proteinogenic amino acids, the excreted carbon consisted of homoserine lactone, homoserine and an unidentified amino acid. The biological role of the excretion remains uncertain. In the laboratory, we noticed the production under high growth rates (0.034h^{-1}, doubling time of 20h) in combination with O_2-limitation, which will most likely not occur in the natural habitat of this strain. Nevertheless, this large production of extracellular organic molecules from CO_2 may open possibilities to use chemolithoautotrophic microorganisms for the sustainable production of important biomolecules.

KEYWORDS

acidophilic, autotroph, hydrogenase, amino acids, volcanic soil, *Hydrogenisulfobacillus*

Introduction

Fossil fuels, such as coal, natural gas and oil, are used in energy generation, transportation and for the production of chemicals and this contributes to more greenhouse gas emissions, global warming and an imbalanced global carbon cycle (SEI, 2021). To reduce global warming, usage of fossil fuels should be replaced by more sustainable resources, such as solar and wind

power. However, the production of chemicals still largely depends on fossil fuels. Alternatively, chemicals can be produced by fixing CO_2 into organic compounds. Methods to fix CO_2 are currently being explored and involve the chemical and biological fixation of CO_2 into larger molecules (Appel et al., 2013; Hepburn et al., 2019; Ullah et al., 2019).

Plants and several prokaryotic microorganisms can fix CO_2 for the production of organic compounds (biomass). Using plants for the production of chemicals will require massive amounts of land, ultimately resulting in competition between biomass production, agriculture and nature. Therefore, microorganisms, and more specifically photosynthetic microalgae, can be used for the production of starch, carotenoids, fatty acids, proteins, antioxidants and pigments (Mooij et al., 2013; Gangl et al., 2015). Fixing CO_2 to produce larger biomolecules requires energy. Photoautotrophic microorganisms use light as energy source for this activation. Chemolithoautotrophic microorganisms, can use reduced inorganic compounds, such as H_2, CH_4, NH_3, CO, sulfur compounds or iron(II) for activation of CO_2 (Friedrich and Schwartz, 1993; Khadem et al., 2011).

Volcanic and geothermal terrestrial soils are hot, acidic and emit several gasses, including high amounts of CO_2 and the reduced gasses H_2, CH_4, CO and H_2S (D'Alessandro et al., 2009; Magro et al., 2013; Bergfield et al., 2014; Gagliano et al., 2016). Despite the harsh conditions, these soils are home to a unique microbial community that can use the geothermal CO_2 for carbon fixation and the reduced gasses as energy source (Picone et al., 2020). Metagenomic studies of Yellowstone National Park hot springs have shown the presence of a microbial community, which is enriched in genes encoding for H_2 oxidation and CO_2 fixation (Lindsay et al., 2019). Metagenomics of the geothermal soils of Pantelleria Island identified a high variety of hydrogenase genes and H_2 consumption has already been observed in the top layers of geothermal soils (Gagliano et al., 2016; Picone et al., 2020).

Oxidation of H_2 is catalyzed by the enzyme hydrogenase, whereby H_2 is converted into two protons and two electrons. These enzymes are classified as [NiFe]-, [FeFe]- or [Fe]-hydrogenases depending on the metal ion in the active site (Lubitz et al., 2014). These hydrogenases can be further categorized into eight groups and 38 subgroups based on amino acid-based phylogenetic analyzes, metal-binding motifs, predicted genetic organization and reported biochemical characteristics (Greening et al., 2016). Uptake hydrogenases are involved in the oxidation of H_2, whereby the generated energy can be used to fix inorganic carbon.

So far, seven CO_2 fixation pathways have been discovered (Gong et al., 2016; Sánchez-Andrea et al., 2020). Three of these are involved in CO_2 fixation under mostly anaerobic conditions, including the Wood-Ljungdahl pathway, the dicarboxylate/4-hydroxybutyrate cycle and the reductive TCA cycle. The three more predominant aerobic CO_2 fixation pathways are the 3-hydroxypropionate cycle, the 3-hydroxypropionate-4-hydroxybutyrate cycle and the Calvin-Benson-Bassham (CBB) cycle. The widespread CBB cycle can be found among plants, algae, photosynthetic prokaryotes and many chemolithoautotrophic microorganisms. The key enzyme of the CBB cycle is the ribulose-1,5- bisphosphate carboxylase (cbb) composed of a large and a small subunit. In this pathway, three molecules of CO_2 are converted to glyceraldehyde 3-phosphate at the expense of nine ATP molecules and six NAD(P)H molecules, which makes it the highest energy-consuming pathway for CO_2 fixation (Berg, 2011; Erb and Zarzycki, 2018).

The aim of the present study was to enrich and isolate new thermoacidophilic, autotrophic microorganisms that serve as primary producers for the establishment of a microbial community and potentially produce extracellular compounds. To this end, we used aerobic chemostat cultivation with H_2 as limiting substrate and CO_2 as carbon source. A pure culture was obtained by serial dilution to extinction and resulted in the isolation of a novel bacterium of the phylum Bacillota, which we tentatively named "*Candidatus* Hydrogenisulfobacillus filiaventi" strain R50. "*Ca*. H. filiaventi" R50 is a chemolithotrophic microorganism that grows on H_2, CO_2 and O_2 and produces large amounts of extracellular organic compounds, mainly amino acids.

Materials and methods

Geological setting

Pantelleria Island is the largest volcanic satellite island of Sicily, characterized by phenomena related to hydrothermal activities as fumaroles and passive degassing from geothermal soils. The main active area is called Favara Grande, with soil temperatures up to 115°C at 5 cm of depth and soil pH values as low as 3. The geothermal field passively degasses CO_2, CH_4 and H_2 in order of magnitude of percent per volume unit. Soil samples were taken in June 2017 at Favara Grande from two sites, FAV1 (FAV1, 36°50′80"N; 11°57′170″E) and FAV2 (FAV2, 36°50′77"N; 11°57′160″E) (Gagliano et al., 2016), using a core sampler (diameter 1.5 cm), divided into subsections of 5 cm and stored in sterile 50 ml tubes.

Enrichment and isolation

Soil (top 10 cm composite sample of site FAV1) was mixed with sterile medium of pH 3, using a volume ratio of 1:1. The medium was composed of 0.5 mM $MgCl_2$, 0.5 mM $CaCl_2$, 1 mM Na_2SO_4, 2 mM K_2SO_4, 1 mM $(NH_4)_2SO_2$, and 1 mM NaH_2PO_4. The final trace element concentrations were 1 µM for $CoCl_2{\cdot}6H_2O$, $NaMoO_4$, Na_2SeO_3, $CeCl_3$, and $ZnSO_4$, 5 µM for $MnCl_2$ and $FeSO_4$, and 10 µM for $CuSO_4$ and $NiCl_2$. The pH was set to 3.0 by adding 1 M H_2SO_4. 4 ml of soil slurry was added to a bioreactor.

The bioreactor of 500 ml had a working volume of 325 ml and was stirred using a 4 cm stirring bar at 500 rpm. The reactor was operated at 75°C, pH 3.3 and supplied with a mixture of 80% CO_2(v/v), 10% CH_4 (v/v), 10% H_2 at a flow rate of 5 ml/min. The CH_4 flow was switched off after 4 weeks when it came apparent that CH_4 was not consumed by the microbial community. Air was supplied to the reactor to reach a dissolved oxygen concentration of 4% air saturation. Two days after inoculation, the air supply was controlled to maintain a dissolved O_2 concentration between 0.2 and 5% air saturation. After 12 days, the reactor was operated as chemostat with a dilution rate of 0.018 h^{-1}. After steady state was reached, the temperature was gradually increased to 85°C. After the temperature had reached 85°C, the microbial culture became inactive and the bioreactor was re-inoculated with effluent and the temperature of the chemostat was stepwise decreased to 65°C. This resulted in a

shift in population, as could be seen from microscopy. Coccoid cells disappeared and rod-shaped microorganisms started to appear. These microorganisms were further enriched and isolated using serial dilutions to extinction using 9 consecutive rounds. In the first six rounds, the reactor medium was used for the serial dilutions. From round seven onward, the medium was supplemented with 0.05 mM $Na_2S_2O_3$ as a source of sulfur. 10 ml of medium was added to a 120 ml bottle containing 10% H_2 (v/v), 10% CO_2 (v/v), 3% O_2 (v/v), and 77% N_2 (v/v) in the headspace. These bottles were incubated at 55°C and 200 rpm shaking.

Batch cultivation

Growth experiments were performed in 120 ml flasks with 20 ml medium. The headspace contained 10% (v/v) H_2, 5% (v/v) O_2, 5% (v/v) CO_2, and 80% (v/v) N_2. Bottles were incubated at 55°C, unless stated otherwise, in a shaking incubator operating at 200 rpm. To test the growth on organic substrates, H_2 was replaced by 25 mM of organic substrate (formate, acetate, butyrate, methanol, ethanol, propanol, butanol, glucose, galactose, fructose, maltose, and succinate) or yeast extract (1 g/l). To test nitrogen fixation, medium without ammonium was used. To test for growth on urea as nitrogen source, ammonium was replaced by 2 mM urea.

Batch and continuous cultivation in a bioreactor

Cultivation was performed in a 500 ml bioreactor (Applikon, Delft, Netherlands) with a working volume of 350 ml and the medium described above. The temperature was maintained at 55°C using a Peltier element. The pH was set to 3.0, measured by a pH electrode and maintained at pH 3.0 ± 0.1 by adding 0.2 M NaOH. The dissolved oxygen (DO) concentration was measured using a DO electrode, but remained 0% since the reactor was operated at O_2-limiting conditions, while supplied with 2 ml/min air. Temperature and pH were controlled using the My-Control process controller (Applikon, Delft, Netherlands). The reactor was stirred at 2,000 rpm using a stirrer with two Rushton impellers. The reactor was supplied with 10 ml/min CO_2: Argon (5%: 95%, v/v) and 3 ml/min H_2. The O_2-limited continuous cultivation was operated at a dilution rate of 0.034 h^{-1}.To determine to growth rate at different dissolved oxygen concentrations, the DO was set to 0.2, 0.5, 3.5, or 7.5% dissolved air saturation and the reactor was operated as batch.

Gas analysis

H_2 in the headspace of the bottles and the in- and outflow of the chemostat cultures was measured using a HP 5890 gas chromatograph (Agilent, Santa Clara, California) equipped with a Porapak Q column (1.8 m, ID 2 mm) and a thermal conductivity detector. For this analysis, 50–100 µl gas samples were injected. To determine the CO_2 and O_2 consumption, 25 µl gas was injected and measured on an Agilent series 6,890 GC–MS (Agilent, Santa Clara, California) and analyzed as described before (Ettwig et al., 2008).

Optical density, dry weight, total organic carbon, and total nitrogen

The optical density was measured using a Cary 50 UV–VIS spectrophotometer at a wavelength of 600 nm (Agilent, Santa Clara, California). Dry weight was determined by filtering 25 ml of culture over a pre-weighted 0.45 µm filter, drying at 60°C under vacuum and weight measurement. The total organic carbon and total nitrogen in the supernatant and in cell suspensions was determined using a TOC-L analyzer (Shimadzu, Kyoto, Japan) as described before (Mohammadi et al., 2017).

Untargeted metabolomics

Supernatant and blank culture medium were diluted five-fold in methanol:acetonitrile (1:1, v/v) and analyzed in triplicate on an Agilent 1,290 LC system coupled to a 6,546 Q-ToF high-resolution mass spectrometer (Agilent) as described (Jansen et al., 2020). In brief, 2 µl sample was injected onto a Diamond Hydride Type C column (Cogent) and subjected to a 0.4 ml/min gradient of water with 0.2% formic acid (A) in acetonitrile with 0.2% formic acid (B) (0–2 min: 85% B, 3–5 min: 80% B, 6–7 min: 75% B, 8–9 min: 70% B, 10–11 min: 50% B, 11–14: 20% B, 14–24: 5% B, followed by 10 min re-equilibration at 85% B). Detection was performed from m/z 50–1,200 in the positive ionization mode, using a continuously infused solution of purine, trifluoroacetic acid, and hexakis for reference mass calibration. The resulting data were converted to mzXML format using ProteoWizard software (Chambers et al., 2012) and the two sample groups were compared using XCMS online (Tautenhahn et al., 2012) using centWave feature detection (15 ppm, 10–60s peak width, SN threshold 6, integration method 2), and obiwarp retention time correction (profStep 0.5). The resulting peak table was filtered for features that were more abundant in the culture supernatant compared to blank medium (fold-change >5, value of p <0.05) and present at a high level (max intensity >10^6). From the resulting list of 12 features, 5 features representing isotopes or in-source fragments were manually removed, whereas the presence of one feature was not reproducible in subsequent analyzes. To identify the remaining 6 features, their accurate masses were queried in the metabolite database METLIN (Guijas et al., 2018).

NMR analysis

All spectra were recorded on a Bruker AVANCE III 500 MHz spectrometer equipped with a Prodigy BB probe. Samples were collected as either 10x or 50x freeze-dried concentrates and dissolved in D_2O containing TMSP as reference. ^{1}H spectra were acquired with composite-pulse presaturation water suppression, 32 scans and a relaxation of 3 s. Multiplicity-edited HSQC spectra were acquired with 1,024 t1 increments using 25% NUS (256 real FIDs) and 8 scans per increment. HMBC spectra were acquired with 1,024 t1 increments using 50% NUS (512 real FIDs), 32 scans per increment and a nJCH of 8 Hz. 1H-1H DQF-COSY spectra were acquired with 512 t1 increments using 25% NUS (128 real FIDs) and 16 scans per increment. ^{1}H-^{1}H presaturated TOCSY spectra were acquired with

1,024 t1 increments using 25% NUS (256 real FIDs), 32 scans per increment and 80 ms of spin-lock mix time.

Quantification of amino acids

An amino acid standard mixture containing 17 different L-amino acids at 1.25 and 2.5 μmoles/mL was obtained from Sigma Aldrich (AAS18-5 ml) and used to prepare calibration curves in blank culture medium for the Q-ToF LC–MS system described above. These calibration curves were used to calculate the concentration of the different amino acids in the supernatant of the R50 reactor. To this end, reactor supernatant was diluted 30x in culture medium. Of this solution 100 μl was diluted with 900 μl acetonitrile:methanol:water (40:40:20).

Membrane inlet mass spectroscopy

The kinetics of hydrogen consumption were determined by membrane inlet mass spectrometry MIMS (Hiden HPR-40, Hiden Analytical, Warrington, United Kingdom). Detection took place by pulsed ion counting (PIC). For highest sensitivity the emission current was set between 250 and 450 μA. As an inlet probe a 1/8 inch stainless steel (SS) tube was used. The inlet probe (tube 1/8 inch, internal diameter 2.8 mm) was perforated at the end over 2 cm. The holes were covered with a piece of Dow Corning Q7-4750 silicon tubing (1.96 outer diameter, 0.25 mm wall thickness; Freudenberg Medical, VWR International, Amsterdam, NL). To apply the silicon on the probe tube, isopropanol was used as a lubricant. The probe was connected to a water trap, consisting of a 10 cm diameter coil (1/4 inch stainless steel tube) that was cooled inside a Dewar flask with solid carbon dioxide. Connections were made by Swagelok Unions with Vespel (85%)/Graphite (15%) ferrules. After connecting the probe to the vacuum inlet, the MIMS system was operated for a few days to reach a low and stable background signal, after which the chamber experiments were started.

A 500 ml glass vessel with a water-jacket was used as incubation chamber. The stainless steel head plate of the chamber was clamped to the chamber with a Viton O-ring in between. The head plate had three ports with Omni-Lok inverted cone fittings for pieces of 1/16 inch capillary peek tubes (0.76 mm inner diameter). After filling the chamber completely with medium, gassing was done at 40 ml/min with a long stainless steel capillary tube (0.7 mm diameter) through one of the ports, while the central port was open, for at least 30 min with a mixture of Ar and CO_2 (95/5%) gas, and stirring with a stirrer bar (4 cm long) at 1000 rpm. Another port was used for adding deoxygenated medium, after the flushing procedure, by means of a 20 ml syringe. In this way all gas introduced during the gassing procedure was removed from the chamber. This port for gassing was later used as a capillary outlet for the medium when additions were done *via* the central tube by means of gastight glass syringes (Hamilton) fitted with 3 inch long needles (0.74 mm diameter). For calibrations and calculations, known amounts of hydrogen gas-saturated water were administered to the incubation chamber from 50 ml serum bottles containing 10 ml of water.

For measuring oxygen concentration in the chamber, an optical oxygen probe (DP-PST3) was used (PreSens - Precision Sensing, Regensburg, Germany). The probe was inserted through a 4 mm port that was sealed with a Viton O-ring. The sensor was connected to a Fibox 4 trace meter (PreSens). To adjust the initial oxygen concentration, oxygenated medium was added. For higher concentrations, pure oxygen gas was introduced. In the latter case, when the desired concentration was reached, the remaining gas was pushed out with medium from the 20 ml syringe. During the chamber incubations, the oxygen concentrations were maintained constant by adding oxygen saturated medium. Cells used for these experiments (250 μl) were obtained from a H_2-limited chemostat culture (5% AS; $OD_{600} = 1.6$).

Cryo EM

Cells were harvested from the O_2-limited bioreactor and kept at 55°C until freezing. For each sample, 2 μl cell suspension was mixed with 0.5 μl 10 nm Protein A gold solution (CMC, UMC Utrecht) on a glow discharged Quantifoil R2/2 grid (Cu, 200#, Quantifoil Gmbh) and plunge frozen in liquid ethane using a Vitrobot Mk4 (FEI/Thermo Fisher) with controlled humidity (100%) at blot-force 1 with a blot time of 2.5 s. Frozen grinds were imaged in low dose in a JEOL-JEM2100 operating at 200 kV using a Gatan high-tilt cryo-holder.

DNA sequencing and genome assembly

For DNA isolation, 2 ml cell suspension (OD_{600} 0.5–1.0) from the continuous culture was harvested by centrifugation (2 min, 14,000 x g) and resuspended in 100 μl sterile MQ water. DNA was extracted with the PowerSoil DNA isolation kit or the DNeasy Blood and Tissue kit according to the manufacturer's instructions (Qiagen Benelux B.V, Venlo, The Netherlands). The quality and quantity of the DNA were analyzed using the Qubit (Thermo Fisher, Waltham, Massachusetts) and the Agilent 2,100 Bioanalyzer (Thermo Fisher, Waltham, Massachusetts). The genome was reconstructed using a combination of short-read paired-end Illumina sequencing and long-read Nanopore sequencing. For Illumina library preparation, the Nextera XT kit (Illumina, San Diego, California) was used according to the manufacturer's instructions. Enzymatic tagmentation was performed starting with 1 ng of DNA, followed by incorporation of the indexed adapters and amplification of the library. After purification of the amplified library using AMPure XP beads (Beckman Coulter, Indianapolis, Indiana), libraries were checked for quality and size distribution using the Agilent 2,100 Bioanalyzer and the High sensitivity DNA kit. Quantitation of the library was performed by Qubit using the Qubit dsDNA HS Assay Kit (Thermo Fisher Scientific, Waltham, Massachusetts). The libraries were pooled, denatured, and sequenced with the Illumina MiSeq sequence machine (San Diego, California). Paired end sequencing of 2 × 301 base pairs was performed using the MiSeq Reagent Kit v3 (Illumina, San Diego, California) according to the manufacturer's protocol. For Nanopore library preparation, 1–1.5 μg of DNA was used. The input DNA was checked for high molecular DNA and absence of degradation by agarose (0.5%) gel electrophoresis. For Nanopore sequencing, the DNA Library construction was performed using the Ligation Sequencing Kit 1D (SQK-LSK108) in combination the Native barcoding Expansion Kit (EXP-NBD103 or EXP-NBD104) according

to the manufacturer's protocol (Oxford Nanopore Technologies, Oxford, United Kingdom). The libraries were loaded and sequenced on a Flow Cell (R9.4.1) and run on a MinION device (Oxford Nanopore Technologies, Oxford, United Kingdom), according to the manufacturer's instructions. Base calling after sequencing was done using the guppy_basecaller in combination with guppy_barcoder (Oxford Nanopore Technologies, Limited Version 2.3.7). The genome was assembled from Nanopore reads using Canu (v1.8) (Koren et al., 2017). Assembled contigs were first polished with Racon (v1.3.1) (Vaser et al., 2017) followed by two iterations of Pilon (v1.23) polishing with Illumina reads (Walker et al., 2014). The genome was annotated using the MicroScope platform (Vallenet et al., 2013) and annotations were checked manually. The genome of this strain is available from GenBank under accession number GCA_902809825.

RNA sequencing and RNA-seq analysis

For transcriptome analysis, triplicate samples of 10 ml cell suspension (OD_{600} = 0.5) from the continuous culture (55°C, pH 3.0 with 0.2% AS, 7.5% AS or O_2-limiting conditions) were harvested by centrifugation and mRNA was isolated using the RiboPure™-Bacteria kit according to the manufacturer's protocol (Thermo Fisher, Waltham, Massachusetts). The quality and quantity of the RNA were analyzed using the Qubit (Thermo Fisher, Waltham, Massachusetts) and the Agilent 2,100 Bioanalyzer (Thermo Fisher, Waltham, Massachusetts). The transcriptome libraries were constructed using the TruSeq® Stranded mRNA Library Prep protocol (Illumina, San Diego, California) according to the manufacturer's instructions. Total mRNA was used for library preparation and obtained libraries were checked qualitatively and quantitatively as described above. Pooled libraries were sequenced using the Illumina MiSeq sequence machine (Illumina, San Diego, California United States). For sequencing, the 151 bp sequence chemistry was performed using the MiSeq Reagent Kit v3 (Illumina, San Diego, California) according to the manufacturer's protocol in one direction. CLCBio software (version 10.1.1, Qiagen, Aarhus, Denmark) was used to perform RNA-seq analysis. Gene expression levels were compared by calculating the reads per kilobase per million reads (RPKM) values for the CDSs and calculating the log2-fold to median (Mundinger et al., 2019). The raw reads are available *via* project number PRJNA616204.

16S rRNA gene analysis

The 16S rRNA gene of bacteria was PCR amplified from isolated DNA using the primers 616F (5'-AGAGTTTGATYMTGGCTCAG-3′) and 1492R (5'-GGTTACCTTGTTACGACTT-3′) using the PCR program; 5 min 94°C, 30 cycles 40 s at 96°C, 40 s 55°C, 40 s 72°C and finally 10 min 72°C. The 16S rRNA gene of the Archaea was PCR amplified from isolated DNA using the primers Arch21F (5'-TTCCGGTTGATCCYGCCGG-3′) and Arch915R (5'-GTGCTCCCCCGCCAATTCCT-3′) using the PCR program; 5 min 94°C, 30 cycles 40 s at 96°C, 40 s 54°C, 900 s 72°C and finally 10 min 72°C. The amplicons were cloned into the pGEM-T Easy cloning vector (Promega) and transformed into competent *E. coli* cells. After growth of the cells, the 16S rRNA amplicon in the vector was PCR amplified, cleaned (GeneJET PCR purification kit, Thermo Fisher, Waltham, United States) and sequenced using the Sanger sequencing platform (BaseClear B.V., Leiden, The Netherlands).

Results

Enrichment and isolation

Geochemical analyzes and a metagenomic survey indicated the presence of high amounts of geothermal H_2 and many genes encoding hydrogenases (Gagliano et al., 2016; Picone et al., 2020) in volcanic soils of Pantelleria Island. Therefore, we set out to enrich and isolate novel aerobic H_2-oxidizing microorganisms using a continuous bioreactor with H_2 as limiting substrate. As inoculum, soil from the geothermal active area Favara Grande on the island of Pantelleria, Italy, was used. The primary growth temperature was 75°C. Under these growth conditions, microscopic analysis showed that this microbial culture was dominated by a coccoid-shaped microorganism (Supplementary Figure S1). Analysis of the microbial culture indicated that the 16S rRNA gene of this microorganism had a high identity with *Acidianus* sp. (97–99%) (Supplementary Figure S2). The enriched *Acidianus* sp. could be isolated in pure culture by serial dilution but grew poorly in bottles despite additions of sulfide, cysteine, thiosulfate, sulfur, or yeast extract. The temperature optimum of 70–75°C of the *Acidianus* sp. dominated enrichment culture was determined by stepwise increasing the temperature with 5°C steps and measuring the maximum growth rate. However, after the temperature had reached 85°C, the culture became inactive and the bioreactor was re-inoculated using the collected effluent. Then, the temperature was stepwise decreased, but after the temperature had reached 65°C, the microbial culture changed. The coccoid-shaped *Acidianus* sp. disappeared and now rod-shaped bacteria started to dominate the culture (Figure 1). Some cells were more elongated. These bacteria were isolated by means of serial dilution to extinction. Serial dilutions up to six rounds did not result in a pure culture. Only after adding thiosulfate as a sulfur source, three more serial dilutions series resulted in the isolation of strain R50.

Phylogeny

The genome of strain R50 was sequenced and assembled resulting in a closed genome of 2.6 Mb. The general features of this genome are compiled in Table 1. The four complete rRNA operons were highly similar. A total of 22 different tRNAs were identified, with 1 to 5 copies per tRNA type.

According to the GTDB classification (Chaumeil et al., 2019), strain R50 belongs to the phylum of *Bacillota* and to a new family [provisional R501 family (https://gtdb.ecogenomic.org/genome?gid=GCA_902809825.1)], but no genus or species could be attributed to this strain. Phylogenomic analysis of this strain shows that it falls outside of the genus *Sulfobacillus* (Figure 2). This is also supported by the Type (strain) Genome Server at DSMZ (Meier-Kolthoff and Göker, 2019; Supplementary Figure S3). The closest *Sulfobacillus* relative, *Sulfobacillus acidophilus* DSM 10332, shows 87% identity to the 16S rRNA gene of strain R50. No genomes or metagenome assembled genomes (MAGs) were found that are phylogenetically closer to strain R50 than members of the genus *Sulfobacillus*. To investigate if close relatives of this isolate can be found

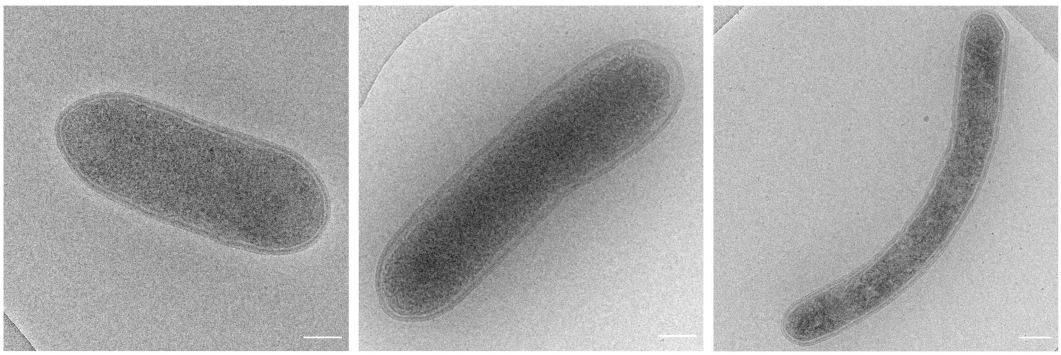

FIGURE 1
Cryo electron microscopy images of strain R50 (scale bar, 250nm).

TABLE 1 Genomic features of Strain R50.

Feature	Value
Genome size (bp)	2,570,337
DNA coding (bp)	2,273,977
DNA G + C (%)	70.55
Total genes	3,013
Protein coding genes	2,756
rRNA genes (4 operons)	12
tRNA genes	55
Genes assigned to COGs	15

in other environments, the 16S rRNA gene (4 copies in the genome) was compared to prokaryotic 16S rRNA gene amplicon datasets retrieved using the integrated microbial NGS (IMNGS; Lagkouvardos et al., 2016) platform. The retrieved 16S rRNA amplicon sequences that showed a high identity with the 16S rRNA gene of strain R50 could be found in metagenomes of acid copper mines and hot springs (Figure 3). Based on the extended phylogenetic analysis, our isolate is a representative of a novel genus within the *Bacillota* for which we propose the name "*Candidatus* Hydrogenisulfobacillus filiaventi" R50 gen. nov., sp. nov.

Description of "*Ca. Hydrogenisulfobacillus*" gen. nov.

"*Ca. Hydrogenisulfobacillus*" (*Hydrogenisulfobacillus*. N.L. n. *Hydrogeni*, Hydrogen; N.L. n. *bacillus* a small staff or rod; *Hydrogenisulfobacillus*, Hydrogen using microbe that is rod shaped and related to *Sulfobacillus* sp.).

Description of "*Ca. Hydrogenisulfobacillus filiaventi*" sp. nov.

"*Ca.* Hydrogenisulfobacillus filiaventi" [fi.li.a.ven.ti. N.L. n. *filia*, daughter (from L. *filiae*, daughter); N.L. n. *venti*, wind (from L. *ventum*, wind); N.L. n *filiaventi*, daughter of the wind. "*Ca.* Hydrogenisulfobacillus filiaventi] R50 is isolated from the geothermal soils of the island of Pantelleria. The name of the island originates from Arab name Bint al-Riyāh, which means "daughter of the winds."

Physiology

The optimal temperature and pH of "*Ca.* H. filiaventi" R50 were determined during batch experiments with H_2 as electron donor and CO_2 as carbon source. The strain had an optimal growth temperature of 55°C (Supplementary Figure S4A) and grew only in a narrow pH range, namely between pH 2.5 and 4.0, with an optimum pH of 3.0 (Supplementary Figure S4B). No growth at pH 3 on any of the following organic substrates was observed; formate, acetate, butyrate, methanol, ethanol, propanol, butanol, glucose, galactose, fructose, maltose, succinate, and yeast extract. It was tested whether amino acids could serve as energy and nitrogen source, but no growth was observed on the amino acids such as alanine, arginine, aspartic acid, cysteine, glycine, glutamic acid, leucine, lysine, methionine, phenylalanine, proline, threonine, tyrosine, or valine. Only NH_4^+ could be used as nitrogen source and no growth was observed using nitrite, nitrate, urea or N_2 as N-source. As S-source, sulfide, thiosulfate, tetrathionate, and cysteine could be used, but not sulfate. Cysteine could only be used as sulfur source, not as energy source. Spore formation was not observed.

To determine the stoichiometry of "*Ca.* H. filiaventi" R50, an O_2-limited chemostat ($D = 0.043\ h^{-1}$) was started. Based on dry weight, 1.4 g DW was produced per mole H_2 consumed. Under these conditions, 0.12 mol CO_2 per mol H_2 was fixed. Analysis of the total organic carbon showed that 0.54 mole organic carbon was excreted per mole CO_2 consumed. This means that only 0.46 moles of carbon were assimilated into cellular biomass per mole CO_2 consumed. Besides organic carbon, the total nitrogen could be determined. The N: C ratio of these organic compounds was 0.4. This narrows down the search of organic compounds that consists of carbon, nitrogen and most likely oxygen and hydrogen.

Excretion of organic compounds

To identify the dominant organic metabolites excreted into the supernatant, we performed LC–MS untargeted metabolomics on culture

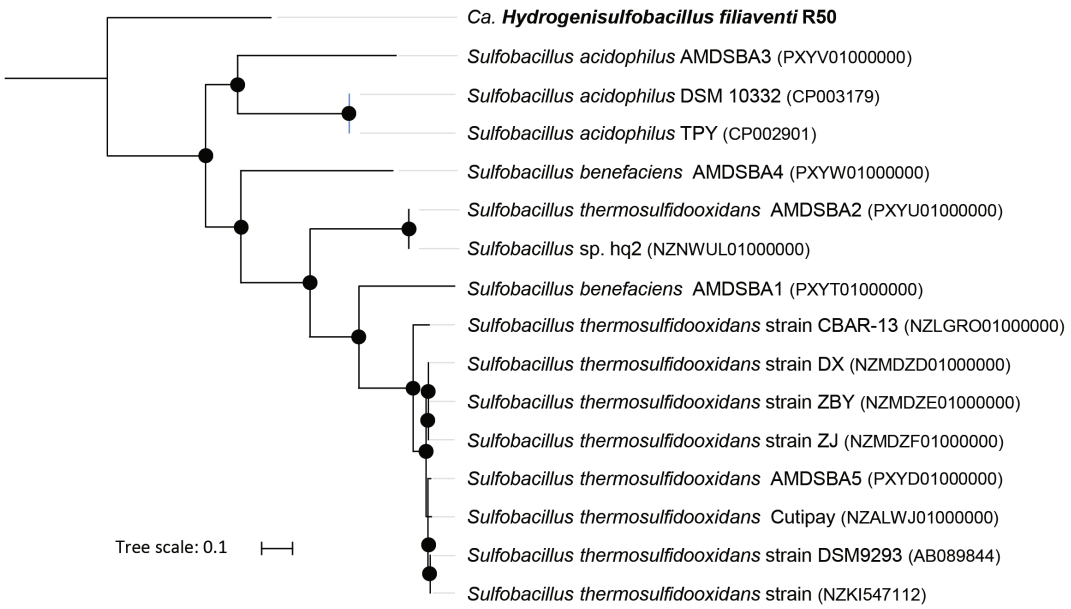

FIGURE 2
Up-to-date Bacterial Core Gene (UBCG) phylogenetic tree of strain R50 and members of the genus *Sulfobacillus*. *Hyphomicrobium denitrificans* was used to root the tree, but removed from the tree for clarity. The tree was constructed using RAxML. Bootstrap analysis was carried using 100 replications and percentage bootstrap values >95% are indicated by a black dot at the nodes.

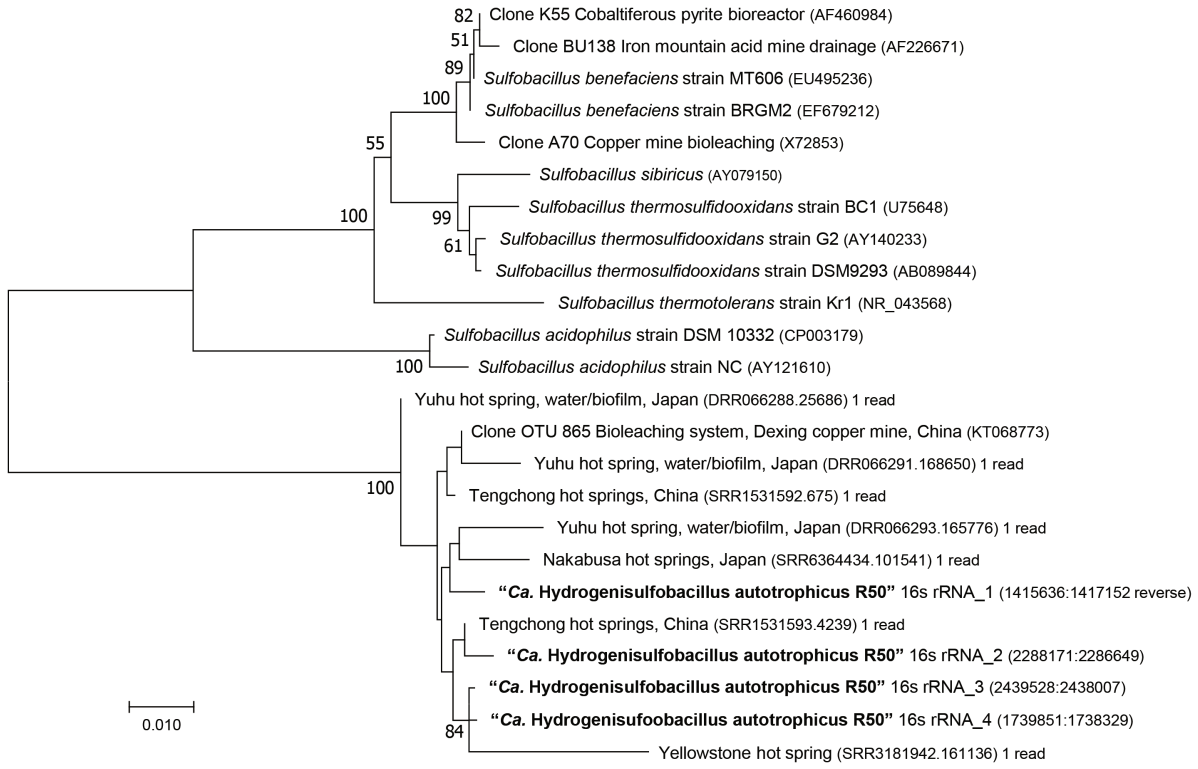

FIGURE 3
16S rRNA gene-based phylogenetic tree of Strain R50, representative *Sulfobacillus* species and environmental sequences. The evolutionary history was inferred using the Neighbor-Joining method. Bootstrap values above 50% (500 replicates) are shown next to the branches. Evolutionary distances were computed using the Jukes-Cantor method and the analysis was performed in MEGA7 (Kumar et al., 2016).

supernatant and blank culture medium. After filtering for abundance and presence in culture supernatant, the six most abundant features were selected for further identification. Using accurate mass searches in the metabolite database METLIN, we found that five of these features had masses matching amino acids (Phe, Tyr, Ile/Leu, Val, Hse/Thr), while one feature matched the mass of an amino acid derivative (Hse-lactone).

To corroborate these findings and extent the spectrum of excreted organic compounds, ^{1}H as well as ^{1}H-^{1}H and ^{1}H-^{13}C correlation 2D NMR spectra were recorded from the culture supernatant (Figures 4, 5). From the 1D ^{1}H spectrum, methyl-containing amino acids such as Val, Ala and Ile were immediately obvious. Similarly clear was the observation of the aromatic amino acids Tyr and Phe, albeit in much lower concentrations. Additionally, Lys and Glu/Gln were identified through their COSY and TOCSY ^{1}H-^{1}H correlations. While Lys was barely visible, Glu/Gln was relatively abundant. The assignment of Glu/Gln was complicated by the fact that they have very similar ^{1}H and ^{13}C chemical shifts but based on the LC–MS data, however, we assign the signal to Glu. Surprisingly, a large portion of the spectra could be assigned to the above proteinogenic amino acids. However, there were several sets of large resonances (Unk1-3) that appeared to have the structure of an amino acid but did not match the 20 proteinogenic amino acids. For Unk1-2, the large downfield chemical shifts for the γ ^{1}Hs and ^{13}Cs (Unk1: 3.85 ppm/60.4 ppm, Unk2: 4.4–4.6 ppm/70 ppm) suggested a structure with a directly attached O-atom, similar to Ser. Indeed, when comparing these sets of resonances to literature references for serine analogs and our LC–MS data, it could be concluded that Unk1 and Unk2 were homoserine (Hse) and homoserine lactone (Hse-lactone), respectively. This confirmed our LC–MS untargeted metabolomics results. The presence of Hse-lactone was intriguing because one would expect it to be unstable in the highly acidic growth medium, yet it was quite abundant. The hydrolysis product of Hse-lactone would be Hse, which could explain its presence. Together, Hse-lactone and Hse represent a major part of the excreted material. Another substantial species present was Unk3. HSQC and HMBC data revealed an amino acid backbone, however the side chain was revealed *via* COSY and TOCSY to be a simple ethyl group like homo-alanine (hAla) (Inada et al., 2019). Its presence could not be detected by LC–MS, so this metabolite remains unknown. Together, the LC–MS and NMR results thus provide a detailed overview, which shows that amino acids and their derivatives are the major excreted organic compounds.

To compare the identified excreted compounds with the total organic carbon, we quantified the excreted compounds using LC–MS (Table 2). Lysine, homoserine, homoserine lactone and unknown 3 were not quantified by LC–MS, but by comparison of NMR signals. Taken together, the amino acids detected by LC–MS and NMR represented 6.58 mM total carbon, which corresponds to 120% of the total excreted carbon determined by total organic carbon analysis.

Hydrogenases

The assembled genome was analyzed for hydrogenase genes. Genes encoding two [NiFe]-hydrogenases were found, one belonging to group 1b (*hynA* and *hynB*) and one belonging to group 1 h/5 hydrogenases (*hhyS* and *hhyL*) (Figure 6). Phylogenetic analysis revealed that these [NiFe]-hydrogenases cluster with hydrogenases of Bacillota, with *Sulfobacillus* species as closest relatives (66–89% identity). The hydrogenases are closely related (~50% identity) to the characterized Campylobacterota hydrogenases of *Wolinella succinogenes*, *Helicobacter pylori*, *Campylobacter,* and *Sulfurospirillum multivorans*. The large subunit of the 1b hydrogenase, hynB, contains the active site motifs L1 (QRxCGVTxxH) and L2 (DPCxGCxVH). This L1 motif is typical for group 1b hydrogenases; however, the L2 motif contains a glycine where often an alanine is found (Greening et al., 2016). The large subunit of the 1 h/5 hydrogenase, *hhyL*, contains the L1 motif (TSRICGICGDNH) and L2 motif (SFDPCLPCGVH), which are conserved in group 1 h/5 hydrogenases (Greening et al., 2016). The group 1b hydrogenase operon shows besides the two catalytic subunits' genes encoding HynC (cytochrome b subunit), HupD, HypC, a 4Fe-4S ferredoxin iron–sulfur-binding domain-containing protein, a conserved protein of unknown function, and

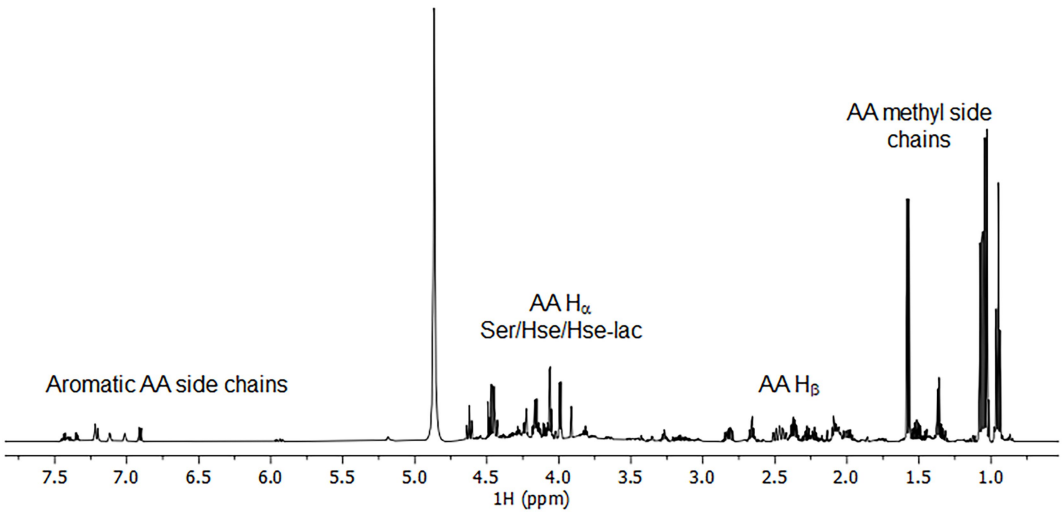

FIGURE 4
^{1}H spectrum of 50x concentrated bioreactor supernatant.

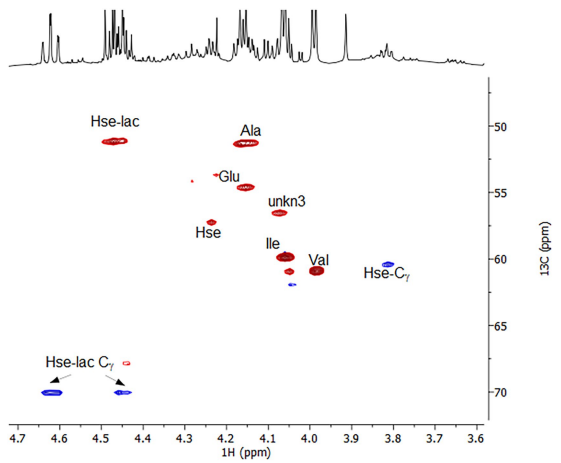

FIGURE 5
^{1}H-^{13}C multiplicity-edited HSQC spectrum highlighting the Hα-Cα correlations for the amino acids and the Hγ-Cγ correlations for Hse and Hse-lactone. Red corresponds to CH/CH_3s and Blue to CH_2s.

TABLE 2 Quantification of excreted compounds in culture supernatant.

Compound	Concentration (μM)
Ala	264[a]
Glu	15.0[a]
Ile	327[a]
Lys	23.4[b]
Phe	36.0[a]
Tyr	39.6[a]
Val	239[a]
Hse	93.3[b]
Hse-lactone	222[b]
Unknown 3	119[b]

[a]Determined by LC–MS, [b] Determined by NMR.

HypA. Upstream of the operon separate HypC, HypE, and a TatA proteins are encoded. The cytochrome b subunit (HynC) shows five transmembrane helices. The group 1 h hydrogenase operon starts with the two catalytic subunits followed by genes encoding a small unknown protein, HypC, HypD, HypE, HypA, HYpB, a Rieske domain-containing protein, and eight additional conserved proteins of unknown function. All genes in both operons are constitutively expressed (Supplementary Table S1). The small subunits of the 1b- and 1 h-type hydrogenases show C-terminal motifs for FeS cluster binding, H-x(2)-C-x(19)-C-x(5)-C-x(19)-C-P-x(5)-C-x(2)-C and H-x(2)-C-x(24)-C-x(5)-C-x(8)-C-P-x(17)-C-x(2)-C, respectively. The 1b-type small subunit does not have a tat signal at the N-terminus pointing to a cytoplasmic location.

Group 1b hydrogenases are classified as oxygen sensitive, whereas group 1 h/5 hydrogenases are oxygen tolerant (Greening et al., 2014; Mohammadi et al., 2017; Schmitz et al., 2020). It was tested if the expression of the group 1b hydrogenase was affected by the dissolved O_2 concentration and if, in turn, this would have an impact on the growth rate. The effect of O_2 on growth rate was tested in a bioreactor, whereby the dissolved oxygen concentration was controlled. Growing "*Ca*. H. filiaventi" R50 at low dissolved O_2 concentration (0.2% or 0.5% AS) resulted in a lower growth rate compared to the growth rate obtained at higher dissolved O_2 concentrations (3% or 7.5% AS), whereby a maximal growth rate of 0.14 h^{-1} (doubling time 5.0 h) was obtained (Figure 7). To test whether both hydrogenases were expressed and to see if the expression levels were influenced by the dissolved O_2 concentration, a transcriptome analysis was performed. This analysis showed that both hydrogenases (1b and 1 h/5) were constitutively expressed during growth in batch with 0.2 and 7.5% air saturation and during growth in a chemostat with O_2 as limiting substrate (DO 0%). No increase in the expression levels of the oxygen sensitive group 1b hydrogenase was observed with decreasing O_2 concentration.

Kinetics of H_2 consumption

"*Ca*. H. filiaventi" R50 possesses a high affinity group 1 h/5 hydrogenase, which are known for their extreme high affinity for H_2 (Schmitz et al., 2020). The test if "*Ca*. H. filiaventi" R50 cells have a high affinity for H_2, the kinetic parameters for H_2 consumption were measured using Membrane-Inlet Mass Spectrometry (MIMS) with cells from a H_2-limited chemostat (5% AS). Addition of H_2 resulted in immediate H_2 consumption. The V_{max} could only be determined accurately if H_2 was not consumed completely and oxygen concentrations were 0.3–0.4% AS (Figure 8). After the biomass had been without H_2, the $V_{(app)max}$ was reduced, but the $K_{(app)s}$ was not affected. Therefore, the $V_{(app)max}$ and the $K_{(app)s}$ could be determined after each other in the same experiment (Figure 8). The H_2 depletion followed Michaelis–Menten kinetics and resulted in a $V_{(app)max}$ of 953 ± 3 nM H_2/min/mg dry weight ($n = 4$) and strain R50 has a high affinity for H_2, since a $K_{(app)s}$ of 353 ± 4 nM ($n = 4$) was found.

Carbon fixation

"*Ca*. H. filiaventi" R50 uses the Calvin-Benson-Bassham (CBB) cycle for carbon fixation. The first enzyme of the CBB cycle is the ribulose-1,5- bisphosphate carboxylase (cbb) composed of a large chain (CbbL) and a small chain (CbbS). The genome encodes for three *cbbL* genes and two *cbbS* genes (Supplementary Table S1). Phylogenetic analysis of the genes encoding the large subunit (*cbbL*) showed that these genes cluster within the group I *cbbL* 70–84% identity, but might represent novel subgroups together with other thermophiles (Figure 9). Especially R50_v2_1596 even may belong to a different subgroup outside of Form IC/D, Transcriptomic analysis showed that only two *cbbL* genes (R50_v2_0264 and R50_v2_1688) and one *cbbS* gene (R50_v2_1687) were expressed during batch growth and growth under O_2 limitation in a chemostat (Table 2). The expression values of R50_v2_1596 (*cbbL*) and R50_v2_1595 (*cbbS*) are low under these conditions. All other CBB cycle genes were expressed, whereby glyceraldehyde-3-phosphate dehydrogenase (*gapA*, R50_v2_2224) fructose-bisphosphate aldolase (*fba*, R50_v2_1401), ribulose-5-phosphate 3-epimerase, (rpe, R50_v2_1689), and phosphoribulokinase (*prk*, R50_v2_1690) showed high expression values (Table 3).

CO_2 fixation through the CBB-cycle is the first step in the production of the excreted organic compounds. Extensive analysis with LC–MS and NMR demonstrates that these excreted compounds consist of amino acids, with Ile, Val and Ala being the most dominant.

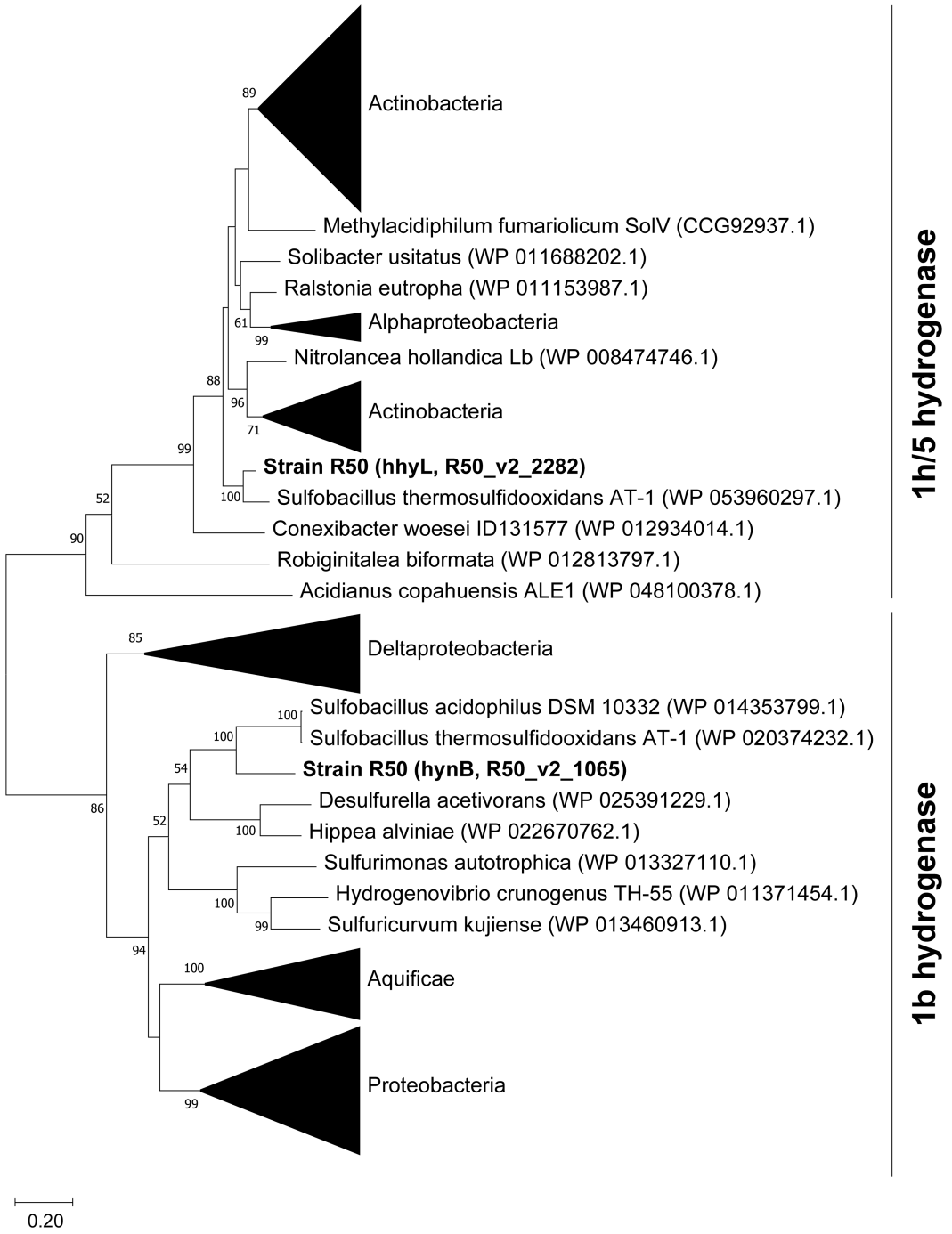

FIGURE 6
Phylogenetic analysis of the large subunits from group 1b and 1h/5 hydrogenases. The tree was constructed using the Maximum Likelihood method (Saitou and Nei, 1987). Bootstrap percentage values above 50% (1,000 replicates) are given at each node. Evolutionary distances were calculated using the Poisson correction method (Zuckerkandl and Pauling, 1965). The analysis was performed using MEGAX (Kumar et al., 2018). The amino acid sequence of the [Fe]-hydrogenase of *Methanothermococcus thermolithotrophicus* (WP_018153721.1) was used to root the tree, but the branch was removed for clarification.

All three amino acids are synthesized from pyruvate and their production share enzymatic conversions. The genome of H. filiaventi R50 encodes the whole valine, leucine, and isoleucine biosynthesis pathway (Supplementary Table S1). The valine, leucine, and isoleucine biosynthesis pathways were expressed under all tested conditions and the expression values of this pathway are comparable under all three different conditions (Table 3).

Metabolic potential

The substrate range that can be used by "*Ca.* H. filiaventi" R50 seems to be very narrow. Growth on sugars was not observed. Genome analysis revealed that sugar transporters are absent and the glycolysis and gluconeogenesis pathways are incomplete. Glucose-6-phosphate isomerase is missing, which catalyzes the reversible conversion of

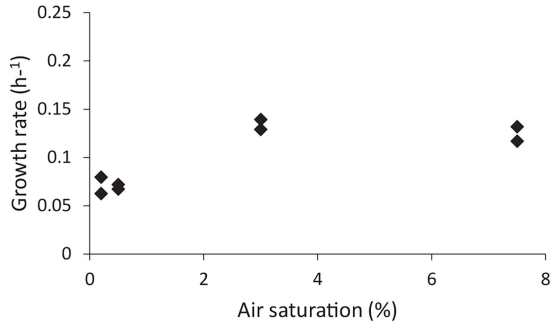

FIGURE 7
The effect of dissolved O_2 concentration on the growth rate.

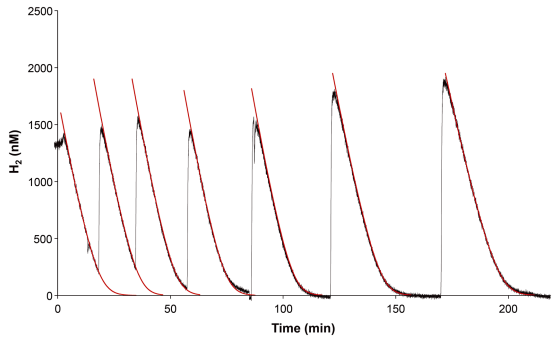

FIGURE 8
H_2 uptake by "*Ca*. H. filiaventi" R50 in the MIMS-system. The raw data are shown by the black lines. After each addition of new substrate (hydrogen) iterative curve fitting (1s time intervals) was performed (red lines). The substrate drop per second was calculated based on Michaelis–Menten kinetics. Each time interval (second) represents a new rate and will provide the substrate consumption over that period. The first part of each red line is virtual linear and as such represents $V_{(app)max}$. $V_{(app)max}$ and $K_{(app)s}$ in the kinetic formula were adapted to obtain the best fit through the raw data. The first four rounds of H_2 consumption were used to determine the $V_{(app)max}$, whereas the last four rounds of H_2 consumption were used to calculate the $K_{(app)s}$.

glucose-6-P into fructose-6-P. No genes were detected that encode for an enzyme that transfers fructose-6-P into fructose-1,6-P. The gene for the enzyme that catalyzes the reverse reaction, fructose-1,6-bisphosphatase could be detected (Supplementary Table S1). Transcriptome analysis showed that the expression values of the genes of the glycolysis and gluconeogenesis are low, unless these genes are shared with the CBB cycle (Table 3). The TCA cycle is complete and expressed under all tested growth conditions (Supplementary Tables S1). Genes encoding the enzymes of the glyoxylate shunt are not present in strain R50. The genes for pentose phosphate pathway enzymes were detected in strain R50 and expressed under all conditions tested (Supplementary Tables S1).

"*Ca.* Hydrogenisulfobacillus filiaventi" R50 used ammonium as nitrogen source. The genome contained three ammonium transporters of which all were expressed under the tested growth conditions. Glutamate dehydrogenase (R50_v2_0919) and glutamine synthetase (R50_v2_1125, R50_v2_2306) are used for primary ammonium assimilation. Nitrate, nitrite, urea and N_2 could not be used as nitrogen source during growth in batch, despite the presence of genes that should support growth on these compounds. The genome contains urease genes (*ureABCDG*, R50_v2_2255, R50_v2_2256, R50_v2_2259–2,261) and nitrogenase genes (*nifCDEHKXZ*, R50_v2_0452, R50_v2_0454–0459, R50_v2_0464). Genes for partial denitrification were detected, including a nitrate/nitrite transporter (R50_v2_1496), nitrate reductase (*narGHIJK*, R50_v2_1497, R50_v2_1497–1,501), nitrite reductase (*nirK*, R50_v2_1317), and nitric oxide reductase (*norB*, R50_v2_0576; Supplementary Table S1). However, no anaerobic growth on nitrate or nitrite was observed under the tested conditions, nor was there any physiological evidence for partial denitrification.

"*Ca*. H. filiaventi" R50 could not use sulfate as sulfur source, since the sulfate assimilation pathway is absent. Instead, the genome encodes for thiosulfate reductase (prsABC, R50_v2_1049–1,051), tetrathionate hydrolase (tth, R50_v2_2562), thiosulfate dehydrogenase (R50_v2_2558, R50_v2_2559), sulfur oxygenase/reductase (sor, R50_v2_0249, R50_v2_1684), and sulfite dehydrogenase (soeAB, R50_v2_0555, R50_v2_0556, R50_v2_1810, R50_v2_1811) to support the growth on thiosulfate, tetrathionate, and sulfur. Cysteine kinase (*cysK*, R50_v2_1277, R50_v2_1328) assimilates sulfide into cysteine (Supplementary Table S1). Also, cysteine can function as sulfur source, but not as energy source. Thiosulfate, tetrathionate, and sulfide could not be used as electron donor either.

Discussion

In this study, a novel aerobic, thermoacidophilic H_2-oxididizing bacterium "*Ca*. Hydrogenisulfobacillus filiaventi" R50 gen. nov., sp., nov., was isolated from the geothermal soil of the Favara Grande on Pantelleria Island, Italy. This strain was isolated using a continuous culture with H_2 as limiting substrate followed by serial dilution to extinction. "*Ca*. H. filiaventi" R50 used CO_2 as carbon source and converted half of the fixed CO_2 into biomass, whereas the other half was excreted as various amino acids. As a consequence of this excretion, the biomass yield on H_2 is much lower (1.4 g DW/mol H_2) compared to other "Knallgas" bacteria, such as *Ralstonia eutropha* (4.6 g DW/mol H_2) or *Methylacidiphilum fumariolicum* SolV (3.4 g DW/mol H_2), (Morinaga et al., 1978, Mohammadi et al., 2017). In all cases biomass yields were determined under oxygen-limited conditions but it should be considered that some variability may be caused by availability of H_2 and inorganic nutrients.

"*Ca*. H. filiaventi" R50 has an optimal growth temperature of 55°C and only grows between pH 2.5 and 4.0. These extreme conditions are observed in the soil where "*Ca*. H. filiaventi" R50 was isolated from (Gagliano et al., 2014). Interestingly, despite the fact that many "Knallgas" bacteria can grow on a variety of organic substrates (Bowien and Schlegel, 1981; Bonjour and Aragno, 1984; Friedrich and Schwartz, 1993; Reiner et al., 2018; Hogendoorn et al., 2020), "*Ca*. H. filiaventi" R50 cannot grow on sugar, volatile fatty acids or alcohols under the tested conditions. These organic substrates might not be available in great access in the natural habitat of "*Ca*. H. filiaventi" R50, which could have resulted in loss of the genetic blueprint to grow on these compounds. Despite having the genes that indicate that strain R50 could use N_2 and urea for growth, and is capable of partial denitrification, this could not be confirmed in batch cultivation experiments. Nitrogenases are O_2 sensitive and might only be active

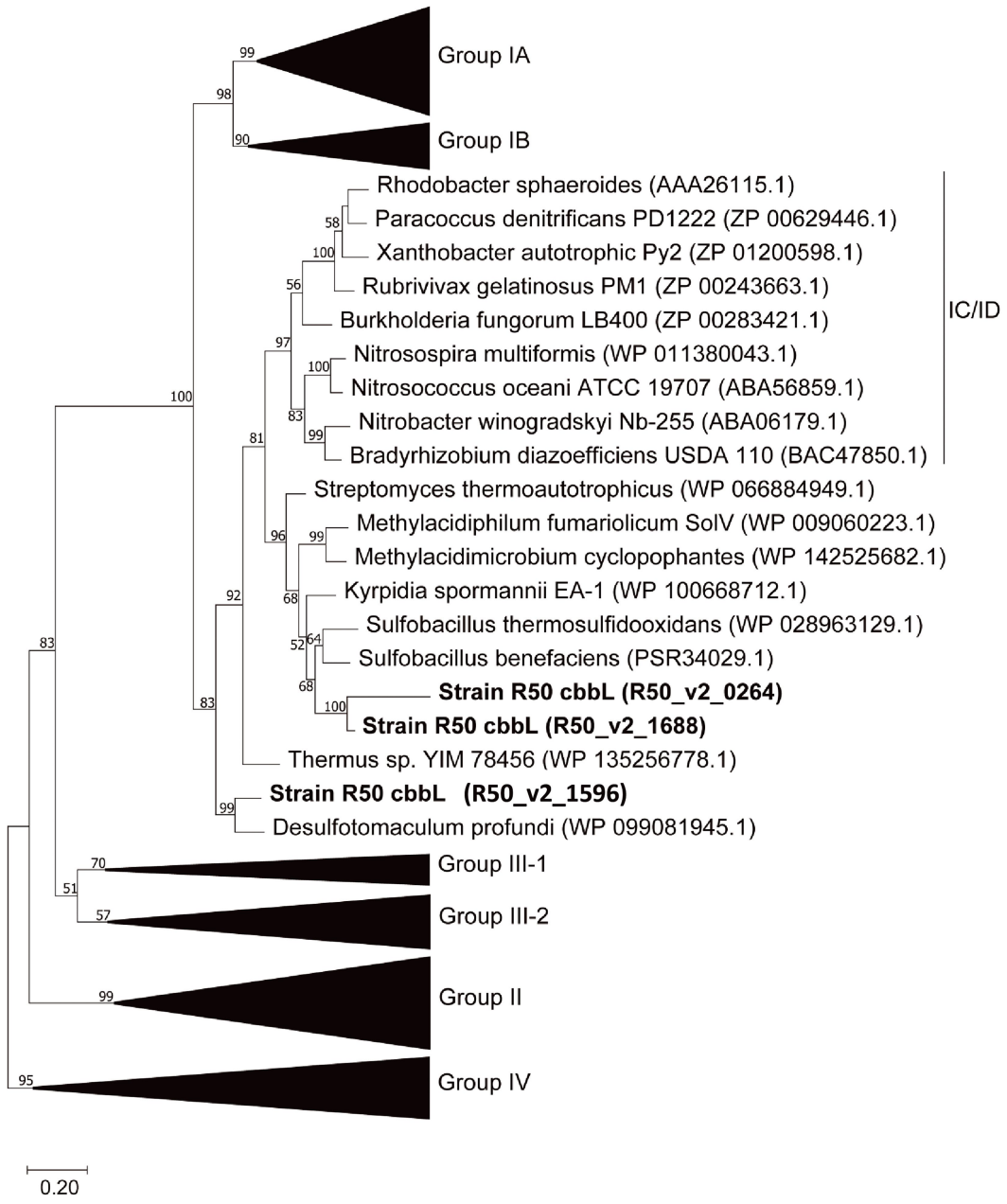

FIGURE 9
Phylogenetic analysis of the RubisCO large subunit (CbbL) using the classification as proposed by Tabita et al. (2007). The amino acid-based tree was constructed using the Maximum Likelihood method (Saitou and Nei, 1987). Bootstrap percentage values above 50% (1,000 replicates) are given at each node. Evolutionary distances were calculated using the Poisson correction method (Zuckerkandl and Pauling, 1965). The analysis was performed using MEGAX (Kumar et al., 2018). Group IV RuBisCO was used to root the tree.

at very low O_2 concentration, as was observed in *Methylacidiphilum fumariolicum* SolV (Khadem et al., 2011). Denitrification is often hampered at low pH and it might require a long time before the expression of denitrification genes is started (van den Heuvel et al., 2010).

The genome "*Ca*. H. filiaventi" R50 encodes for two hydrogenases, one classified as oxygen-sensitive group 1b hydrogenase and one as oxygen tolerant, high affinity, group 1 h/5 hydrogenase (Greening et al., 2016). Despite that the 1b hydrogenase is classified as oxygen sensitive, this hydrogenase was expressed under O_2-limited conditions, at 0.2% air saturation and 7.5% air saturation. This indicates that the expression of this hydrogenase is not controlled by oxygen concentration. The same was reported for transcription and translation of NiFe hydrogenases from *Sulfurospirillum multivorans* (Kruse et al., 2017). Furthermore, there is no physiological evidence that supports the oxygen sensitive character of this 1b hydrogenase. The growth rate of "*Ca*. H. filiaventi" R50 does not increase when the oxygen concentration is reduced. This is in contrast to *Methylacidiphilum fumariolicum* SolV that possesses besides a 1 h/5 hydrogenase, an oxygen-sensitive 1d hydrogenase. For *M. fumariolicum* SolV, the growth rate increased at lower oxygen concentration due to the increased activity of its oxygen-sensitive 1d

TABLE 3 Expression levels of the genes involved in H_2 oxidation and CO_2 fixation in strain R50.

Pathway	Product	Gene name	Identifier MicroScope	Expression level (RPKM)		
				Batch 0.2% AS	Batch 7.5% AS	Chemostat O_2-lim
1b H2ase	Hydrogenase formation chaperone	*hypC*	R50_v2_1061	297 ± 106	484 ± 146	452 ± 65
	Carbamoyltransferase, hydrogen maturation protein	*hypE*	R50_v2_1062	117 ± 45	205 ± 110	265 ± 77
	Hydrogenase small subunit	*hynA*	R50_v2_1064	101 ± 61	285 ± 201	402 ± 187
	Hydrogenase large subunit-group 1b	*hynB*	R50_v2_1065	125 ± 76	328 ± 231	413 ± 188
	Cytochrome b subunit	*hynC*	R50_v2_1066	233 ± 100	475 ± 219	531 ± 228
	Hydrogenase maturation protein	*hupD*	R50_v2_1067	279 ± 114	448 ± 196	466 ± 186
	Hydrogenase accessory protein	*hypC*	R50_v2_1068	107 ± 42	214 ± 129	166 ± 72
	Hydrogenase maturation factor	*hypA*	R50_v2_1072	177 ± 63	228 ± 75	287 ± 58
	Hydrogenase maturation factor	*hypB*	R50_v2_1,073	50 ± 17	66 ± 19	84 ± 13
1 h/5 H2ase	Hydrogen maturation factor	*hypB*	R50_v2_2276	34 ± 1 3	57 ± 49	46 ± 12
	Hydrogen maturation factor	*hypA*	R50_v2_2277	0.5 ± 0.5	0.25 ± 0.43	1 ± 0
	Carbamoyltransferase, hydrogen maturation protein	*hypE*	R50_v2_2278	18 ± 9	21 ± 16	26 ± 9
	Hydrogenase maturation factor	*hypD*	R50_v2_2279	61 ± 31	81 ± 63	85 ± 25
	Hydrogenase accessory protein	*hypC*	R50_v2_2280	124 ± 87	118 ± 75	164 ± 37
	Hydrogenase large subunit - group 1 h/d	*hhyL*	R50_v2_2282	462 ± 165	605 ± 427	696 ± 148
	Hydrogenase small subunit	*hhyS*	R50_v2_2283	3,432 ± 110	386 ± 130	550 ± 69
CBB cycle	Ribulose bisphosphate carboxylase large chain	*cbbL*	R50_v2_0264	214 ± 25	314 ± 31	183 ± 24
	Ribulose bisphosphate carboxylase small chain	*cbbS*	R50_v2_1595	8 ± 7	25 ± 16	3 ± 1
	Ribulose bisphosphate carboxylase large chain	*cbbL*	R50_v2_1596	9 ± 3	35 ± 25	5 ± 3
	Ribulose bisphosphate carboxylase small chain	*cbbS*	R50_v2_1687	245 ± 53	340 ± 87	193 ± 8
	Ribulose bisphosphate carboxylase large chain	*cbbL*	R50_v2_1688	48 ± 16	58 ± 28	48 ± 9
	Phosphoglycerate kinase	*pgk*	R50_v2_2223	8 ± 1	8 ± 2	12 ± 3
	Glyceraldehyde-3-phosphate dehydrogenase	*gapA*	R50_v2_2224	117 ± 10	120 ± 45	131 ± 17
	Triose phosphate isomerase	*tpiA*	R50_v2_2222	5 ± 1	5 ± 2	9 ± 2
	Fructose-bisphosphate aldolase	*fba*	R50_v2_1401	92 ± 20	118 ± 42	127 ± 18
	Fructose-bisphosphate aldolase	*fba*	R50_v2_1599	0.25 ± 0.43	0 ± 0	0 ± 0
	Fructose 1,6-bisphosphatase class II	*glpX*	R50_v2_0617	47 ± 23	29 ± 11	32 ± 6
	Transketolase	*tktA*	R50_v2_1691	24 ± 6	29 ± 11	42 ± 10
	Triose phosphate isomerase	*rpiB*	R50_v2_0628	97 ± 24	66 ± 13	81 ± 15
	Ribulose-5-phosphate 3-epimerase	*rpe*	R50_v2_1689	239 ± 85	137 ± 24	175 ± 36
	Phosphoribulokinase	*prk*	R50_v2_1690	452 ± 84	284 ± 32	353 ± 60
Valine/leucine/ isoleucine biosynthesis	Acetolactate synthase (large subunit)	*ilvB*	R50_v2_0814	30 ± 13	13 ± 4	25 ± 5
	Acetohydroxy-acid isomeroreductase (NADP-dependent)	*ilvC*	R50_v2_0811	58 ± 33	12 ± 5	54 ± 12
	Dihydroxy-acid dehydratase	*ilvD*	R50_v2_0815	35 ± 10	19 ± 7	32 ± 7
	Branched-chain-amino-acid aminotransferase	*ilvE*	R50_v2_0816	35 ± 13	23 ± 9	36 ± 7
	Branched-chain-amino-acid aminotransferase	*ilvE*	R50_v2_2305	35 ± 11	28 ± 13	38 ± 10
	Leucine dehydrogenase, NAD-dependent	*bcd*	R50_v2_1159	5 ± 1	8 ± 3	14 ± 4
	2-isopropylmalate synthase	*leuA*	R50_v2_0812	32 ± 22	11 ± 4	24 ± 8
	3-isopropylmalate dehydratase (large subunit)	*leuC*	R50_v2_1801	26 ± 7	15 ± 5	21 ± 6
	3-isopropylmalate dehydrogenase	*leuB*	R50_v2_0813	18 ± 9	6 ± 2	15 ± 3

The mRNA expression is shown as RPKM values ($n = 3 \pm$ standard deviation). RNA-seq was performed on a batch operated at 0.2% air saturation (AS), a batch at 7.5% air saturation and an O_2-limited chemostat culture.

hydrogenase (Mohammadi et al., 2017). Group 1 h/5 hydrogenases are known for their extremely high affinity for H_2 and are held responsible for atmospheric H_2 uptake. Atmospheric hydrogen gas (H_2) concentrations are only 0.53 ppmv (Novelli et al., 1999), but despite this low concentration, soil microorganisms can consume these trace amounts of H_2 (Schuler and Conrad, 1990; Conrad, 1996). Tropospheric H_2 concentrations can be scavenged by different soil microorganisms with a 1 h/5 hydrogenases, which gives them this extremely high affinity for H_2. "*Ca*. H. filiaventi" R50 has a high affinity for H_2, with a K_s of 353 nM. Such a high affinity is observed in different soil microorganisms, including the Acidobacteriota *Streptomycetes* (Constant et al., 2010) and *Acidobacterium ailaaui* (Myers and King, 2016), the Actinomycetota *Mycobacterium smegmatis* (Greening et al., 2014), the Chloroflexi *Thermomicrobium roseum* and *Thermogemmatispora* sp. T81 (Islam et al., 2019), and the Verrucomicrobiota *Methylacidiphilum fumariolicum* SolV (Schmitz et al., 2020). All of these microorganisms possess a group 1 h/5 hydrogenase. Geothermal environments are usually exposed to elevated H_2 concentrations, but the emitted H_2 concentration might fluctuate over time. Having a high affinity hydrogenase might not only sustain growth on H_2, but also be involved in persistence when the H_2 concentrations are too low to grow on (Greening et al., 2014, 2016; Schmitz et al., 2020).

"*Ca*. H. filiaventi" R50 uses the Calvin-Benson-Bassham (CBB) cycle for CO_2 fixation with the key enzymes ribuolose-1,5-bisphosphate carboxylase (RubisCO) and phosphoribulokinase. RubisCO incorporates CO_2 into ribulose-1,5-bisphosphate to produce two 3-phosphoglycerate molecules. Eventually, the CBB cycle yields one glyceraldehyde-3-phosphate at the expense of nine ATP equivalents and six NAD(P)H (Wildman, 2002; Berg, 2011). So far, four different forms of RubisCO have been described, whereby form I and form II play a role in autotrophic carbon fixation (Tabita et al., 2007). Form I is comprised a large and a small subunit, whereas form II consists of multimers of the large subunit. Furthermore, the role of these two RuBisCO forms differs. Form I is mainly involved in the carbon fixation for biomass production, whereas from II is involved in balancing the redox potential, whereby CO_2 is used as electron sink (Tabita, 1999; Dubbs and Tabita, 2004). "*Ca*. H. filiaventi" R50 encodes three different RubisCO large subunits and two different small subunits. All of these cluster closely to the group 1C/D RubisCO and are likely to be involved in CO_2 fixation for the production of larger molecules. Two of the three RubisCO large genes are expressed under the tested conditions. The expression of the different RubisCO genes might be dependent on CO_2 levels, as in the autotrophic hydrogen oxidizer *Hydrogenovibrio marinus*. This bacterium possess two copies of form I RubisCO and one copy of form II RubisCO. Form II is expressed at high (>15%) CO_2 concentrations, one of the form I RubisCO genes was expressed below 0.15% CO_2 and the other form I RubisCO was expressed in the intermediate CO_2 concentrations. Interestingly, at atmospheric CO_2 concentration, all three RubisCO genes are expressed in *Hv. marinus* (Yoshizawa et al., 2004).

Fixation of CO_2 by RubisCO is the first step in the production and excretion of the unknown organic compounds. Extensive chemical analysis revealed that these organic compounds are amino acids and Hse-lactone. It is remarkable, that there are so far no indications of feedback regulation found, since the production of these organic compounds from CO_2 is an energy intensive process. Transcriptome analysis showed expression of the valine/leucine/isoleucine pathways during batch growth and under O_2-limited conditions.

The ecological reason for the excretion of high amounts of organic compounds remains uncertain. It could be a compound that is involved in signaling, stimulates symbioses, or has antimicrobial properties (Berdy, 2005). The production of these molecules can be the results of electron balancing. In other words, the generated electrons during the oxidation of H_2 cannot all be transferred to O_2, hence these organic molecules are excreted to get rid of the electrons. Remarkably, we did not observe the metabolic potential for carbon (glycogen, PHB) and/or energy (polyphosphate) storage. Nevertheless, it is very likely that the growth conditions in the laboratory, are not the growth conditions that this strain faces in their natural habitat. In fact, it is likely that the strain is often in dormant state, rather than growing at high growth rate. It might be that under more natural growth conditions, these amounts of organic compounds are not excreted.

Using the CBB-cycle for CO_2 fixation, high input of ATP and reducing equivalents are needed. These come from the oxidation of the electron donor, in this case H_2. To use an autotrophic "Knallgas" bacterium for the economically feasible production of chemicals, the production of H_2 must be inexpensive. Furthermore, sustainable resources, such as solar and wind power cannot only be used for energy generation, but also for the production of H_2. In addition, CO_2 levels must be high enough to reach the highest CO_2 fixation rates. Special bioreactors must be developed in order to supply sufficient substrates (H_2, CO_2 and O_2) to the microbial culture, since these gasses dissolve poorly in water. Nevertheless, using this H_2 for the production of chemicals, while fixing CO_2, could be a sustainable alternative to the production of chemicals from oil or natural gas. However, more research will be needed to evaluate if our autotrophic "*Ca*. Hydrogenisulfobacillus filiaventi" strain R50 could provide a new sustainable alternative.

Data availability statement

The datasets presented in this study can be found in online repositories. The names of the repository/repositories and accession number(s) can be found in the article/Supplementary material.

Author contributions

CH, AP, MJ, and HC designed the projects and experiments. AP, CH, and HC sampled the geothermal soils. CH and AP performed the enrichment and isolation experiments. CH and AP conducted the physiology experiments, including MIMS. RM performed the electron microscopic analyzes. RG, PW, RM, PG, and RJ performed the NMR and untargeted metabolomics experiments. GC and TA sequenced the genome and transcriptome, reconstructed the genome, and analyzed the gene expression. CH, AP, and HC carried out the data analysis. CH, MJ, and HC wrote the manuscript. All authors contributed to revision of the manuscript, and read and approved the submitted version.

Funding

CH and HC were supported by the European Research Council (ERC Advanced Grant project VOLCANO 669371), MJ was supported by the European Research Council (ERC Advanced Grant project Eco_MoM 339880) and The Soehngen Institute of Anaerobic Microbiology (SIAM 024002002).

Conflict of interest

The authors declare that the research was conducted in the absence of any commercial or financial relationships that could be construed as a potential conflict of interest.

Publisher's note

Supplementary material

The Supplementary material for this article can be found online at: https://www.frontiersin.org/articles/10.3389/fmicb.2023.1151097/full#supplementary-material

References

Appel, A. M., Bercaw, J. E., Bocarsly, A. B., Dobbek, H., DuBois, D. L., Dupuis, M., et al. (2013). Frontiers, opportunities, and challenges in biochemical and chemical catalysis of CO_2 fixation. *Chem. Rev.* 113, 6621–6658. doi: 10.1021/cr300463y

Berdy, J. (2005). Bioactive microbial metabolites. *J. Antibiot. (Tokyo)* 58, 1–26. doi: 10.1038/ja.2005.1

Berg, I. A. (2011). Ecological aspects of the distribution of different autotrophic CO_2 fixation pathways. *Appl. Environ. Microbiol.* 77, 1925–1936. doi: 10.1128/aem.02473-10

Bergfield, D., Lowenstern, J. B., Hung, A. G., Shanks, W. C. P., and Evans, W. C. (2014). *Gas and Isotope Chemistry of Thermal Features in Yellowstone National Park*, Wyoming, US. Geological Survey Scientific Investigations Report.

Bonjour, F., and Aragno, M. (1984). *Bacillus tusciae*, a new species of thermoacidophilic, facultatively chemolithoautotrophic hydrogen oxidizing sporeformer from a geothermal area. *Arch. Microbiol.* 139, 397–401. doi: 10.1007/BF00408386

Bowien, B., and Schlegel, H. G. (1981). Physiology and biochemistry of aerobic hydrogen-oxidizing bacteria. *Annu. Rev. Microbiol.* 35, 405–452. doi: 10.1146/annurev.mi.35.100181.002201

Chambers, M. C., Maclean, B., Burke, R., Amodei, D., Ruderman, D. L., Neumann, S., et al. (2012). A cross-platform toolkit for mass spectrometry and proteomics. *Nat. Biotechnol.* 30, 918–920. doi: 10.1038/nbt.2377

Chaumeil, P.-A., Mussig, A. J., Hugenholtz, P., and Parks, D. H. (2019). GTDB-Tk: a toolkit to classify genomes with the genome taxonomy database. *Bioinformatics* 36, 1925–1927. doi: 10.1093/bioinformatics/btz848

Conrad, R. (1996). Soil microorganisms as controllers of atmospheric trace gases (H_2, CO, CH_4, OCS, N_2O, and NO). *Microbiol. Rev.* 60, 609–640. doi: 10.1128/mr.60.4.609-640.1996

Constant, P., Chowdhury, S. P., Pratscher, J., and Conrad, R. (2010). Streptomycetes contributing to atmospheric molecular hydrogen soil uptake are widespread and encode a putative high-affinity [NiFe]-hydrogenase. *Environ. Microbiol.* 12, 821–829. doi: 10.1111/j.1462-2920.2009.02130.x

D'Alessandro, W., Bellomo, S., Brusca, L., Fiebig, J., Longo, M., Martelli, M., et al. (2009). Hydrothermal methane fluxes from the soil at Pantelleria island (Italy). *J. Volcanol. Geotherm. Res.* 187, 147–157. doi: 10.1016/j.jvolgeores.2009.08.018

Dubbs, J. M., and Tabita, F. R. (2004). Regulators of nonsulfur purple phototrophic bacteria and the interactive control of CO_2 assimilation, nitrogen fixation, hydrogen metabolism and energy generation. *FEMS Microbiol. Rev.* 28, 353–376. doi: 10.1016/j.femsre.2004.01.002

Erb, T. J., and Zarzycki, J. (2018). A short history of RubisCO: the rise and fall (?) of Nature's predominant CO_2 fixing enzyme. *Curr. Opin. Biotechnol.* 49, 100–107. doi: 10.1016/j.copbio.2017.07.017

Ettwig, K. F., Shima, S., van de Pas-Schoonen, K. T., Kahnt, J., Medema, M. H., Op den Camp, H. J. M., et al. (2008). Denitrifying bacteria anaerobically oxidize methane in the absence of archaea. *Environ. Microbiol.* 10, 3164–3173. doi: 10.1111/j.1462-2920.2008.01724.x

Friedrich, B., and Schwartz, E. (1993). Molecular biology of hydrogen utilization in aerobic chemolithotrophs. *Annu. Rev. Microbiol.* 47, 351–383. doi: 10.1146/annurev.mi.47.100193.002031

Gagliano, A. L., D'Alessandro, W., Tagliavia, M., Parello, F., and Quatrini, P. (2014). Methanotrophic activity and diversity of methanotrophs in volcanic geothermal soils at Pantelleria (Italy). *Biogeosciences* 11, 5865–5875. doi: 10.5194/bg-11-5865-2014

Gagliano, A. L., Tagliavia, M., D'Alessandro, W., Franzetti, A., Parello, F., and Quatrini, P. (2016). So close, so different: geothermal flux shapes divergent soil microbial communities at neighbouring sites. *Geobiology* 14, 150–162. doi: 10.1111/gbi.12167

Gangl, D., Zedler, J. A. Z., Rajakumar, P. D., Martinez, E. M. R., Riseley, A., Włodarczyk, A., et al. (2015). Biotechnological exploitation of microalgae. *J. Exp. Bot.* 66, 6975–6990. doi: 10.1093/jxb/erv426

Gong, F., Cai, Z., and Li, Y. (2016). Synthetic biology for CO_2 fixation. *Sci. China Life Sci.* 59, 1106–1114. doi: 10.1007/s11427-016-0304-2

Greening, C., Berney, M., Hards, K., Cook, G. M., and Conrad, R. (2014). A soil actinobacterium scavenges atmospheric H_2 using two membrane-associated, oxygen-dependent [NiFe] hydrogenases. *Proc. Natl. Acad. Sci. U. S. A.* 111, 4257–4261. doi: 10.1073/pnas.1320586111

Greening, C., Biswas, A., Carere, C. R., Jackson, C. J., Taylor, M. C., Stott, M. B., et al. (2016). Genomic and metagenomic surveys of hydrogenase distribution indicate H_2 is a widely utilised energy source for microbial growth and survival. *ISME J.* 10, 761–777. doi: 10.1038/ismej.2015.153

Guijas, C., Montenegro-Burke, J. R., Domingo-Almenara, X., Palermo, A., Warth, B., Hermann, G., et al. (2018). METLIN: a technology platform for identifying knowns and unknowns. *Anal. Chem.* 90, 3156–3164. doi: 10.1021/acs.analchem.7b04424

Hepburn, C., Adlen, E., Beddington, J., Carter, E. A., Fuss, S., Mac Dowell, N., et al. (2019). The technological and economic prospects for CO_2 utilization and removal. *Nature* 575, 87–97. doi: 10.1038/s41586-019-1681-6

Hogendoorn, C., Pol, A., Picone, N., Cremers, G., van Alen, T. A., Gagliano, A. L., et al. (2020). Hydrogen and carbon monoxide-utilizing *Kyrpidia spormannii* species from Pantelleria Island, Italy. *Front. Microbiol.* 11:951. doi: 10.3389/fmicb.2020.00951

Inada, H., Shibuya, M., and Yamamoto, Y. (2019, 2019). Direct synthesis of free α-amino acids by telescoping three-step process from 1,2-diols. *Organ. Lett.* 21, 709–713. doi: 10.1021/acs.orglett.8b03910

Islam, Z. F., Cordero, P. R. F., Feng, J., Chen, Y. -J., Bay, S. K., Jirapanjawat, T., et al. (2019). Two *Chloroflexi* classes independently evolved the ability to persist on atmospheric hydrogen and carbon monoxide. *ISME J.* 13, 1801–1813. doi: 10.1038/s41396-019-0393-0

Jansen, R. S., Mandyoli, L., Hughes, R., Wakabayashi, S., Pinkham, J. T., Selbach, B., et al. (2020). Aspartate aminotransferase Rv3722c governs aspartate-dependent nitrogen metabolism in Mycobacterium tuberculosis. *Nat. Commun.* 11, 1960. doi: 10.1038/s41467-020-15876-8

Khadem, A. F., Pol, A., Wieczorek, A., Mohammadi, S. S., Francoijs, K.-J., Stunnenberg, H. G., et al. (2011). Autotrophic methanotrophy in Verrucomicrobia: *Methylacidiphilum fumariolicum* SolV uses the Calvin-Benson-Bassham cycle for carbon dioxide fixation. *J. Bacteriol.* 193, 4438–4446. doi: 10.1128/jb.00407-11

Koren, S., Walenz, B. P., Berlin, K., Miller, J. R., Bergman, N. H., and Phillippy, A. M. (2017). Canu: scalable and accurate long-read assembly via adaptive k-mer weighting and repeat separation. *Genome Res.* 27, 722–736. doi: 10.1101/gr.215087.116

Kruse, S., Goris, T., Wolf, M., Wei, X., and Diekert, G. (2017). The NiFe hydrogenases of the tetrachloroethene-respiring Epsilonproteobacterium *Sulfurospirillum multivorans*: biochemical studies and transcription analysis. *Front. Microbiol.* 8:444. doi: 10.3389/fmicb.2017.00444

Kumar, S., Stecher, G., Li, M., Knyaz, C., and Tamura, K. (2018). MEGA X: molecular evolutionary genetics analysis across computing platforms. *Mol. Biol. Evol.* 35, 1547–1549. doi: 10.1093/molbev/msy096

Kumar, S., Stecher, G., and Tamura, K. (2016). MEGA7: molecular evolutionary genetics analysis version 7.0 for bigger datasets. *Mol. Biol. Evol.* 33, 1870–1874. doi: 10.1093/molbev/msw054

Lagkouvardos, I., Joseph, D., Kapfhammer, M., Giritli, S., Horn, M., Haller, D., et al. (2016). IMNGS: a comprehensive open resource of processed 16S rRNA microbial profiles for ecology and diversity studies. *Sci. Rep.* 6:33721. doi: 10.1038/srep33721

Lindsay, M. R., Colman, D. R., Amenabar, M. J., Fristad, K. E., Fecteau, K. M., Debes, R. V. 2nd, et al. (2019). Probing the geological source and biological fate of hydrogen in Yellowstone hot springs. *Environ. Microbiol.* 21, 3816–3830. doi: 10.1111/1462-2920.14730

Lubitz, W., Ogata, H., Rüdiger, O., and Reijerse, E. (2014). Hydrogenases. *Chem. Rev.* 114, 4081–4148. doi: 10.1021/cr4005814

Magro, G., Gherardi, F., and Bayon, F. E. B. (2013). Noble and reactive gases of Palinpinon geothermal field (Philippines): origin, reservoir processes and geodynamic implications. *Chem. Geol.* 339, 4–15. doi: 10.1016/j.chemgeo.2012.09.036

Meier-Kolthoff, J. P., and Göker, M. (2019). TYGS is an automated high-throughput platform for state-of-the-art genome-based taxonomy. *Nat. Commun.* 10:2182. doi: 10.1038/s41467-019-10210-3

Mohammadi, S., Pol, A., van Alen, T. A., Jetten, M. S. M., and Op den Camp, H. J. M. (2017). *Methylacidiphilum fumariolicum* SolV, a thermoacidophilic 'Knallgas' methanotroph with both an oxygen-sensitive and -insensitive hydrogenase. *ISME J.* 11, 945–958. doi: 10.1038/ismej.2016.171

Mooij, P. R., Stouten, G. R., Tamis, J., van Loosdrecht, M. C. M., and Kleerebezem, R. (2013). Survival of the fattest. *Energy Environ. Sci.* 6, 3404–3406. doi: 10.1039/C3EE42912A

Morinaga, Y., Yamanaka, S., Ishizaki, A., and Hirose, Y. (1978). Growth characteristics and cell composition of *Alcaligenes eutrophus* in chemostat culture. *Agric. Biol. Chem.* 42, 439–444. doi: 10.1080/00021369.1978.10862993

Mundinger, A. B., Lawson, C. E., Jetten, M. S. M., Koch, H., and Lücker, S. (2019). Cultivation and transcriptional analysis of a canonical *Nitrospira* under stable growth conditions. *Front. Microbiol.* 10:1325. doi: 10.3389/fmicb.2019.01325

Myers, M. R., and King, G. M. (2016). Isolation and characterization of *Acidobacterium ailaaui* sp. nov., a novel member of *Acidobacteria* subdivision 1, from a geothermally heated Hawaiian microbial mat. *Int. J. Syst. Evol. Microbiol.* 66, 5328–5335. doi: 10.1099/ijsem.0.001516

Novelli, P. C., Lang, P. M., Masarie, K. A., Hurst, D. F., Myers, R., and Elkins, J. W. (1999). Molecular hydrogen in the troposphere: global distribution and budget. *J. Geophys. Res.* 104, 30427–30444. doi: 10.1029/1999jd900788

Picone, N., Hogendoorn, C., Cremers, G., Poghosyan, L., Pol, A., van Alen, T. A., et al. (2020). Geothermal gases shape the microbial community of the volcanic soil of Pantelleria, Italy. *mSystems* 5, e00517–e00520. doi: 10.1128/mSystems.00517-20

Reiner, J. E., Jung, T., Lapp, C. J., Siedler, M., Bunk, B., Overmann, J., et al. (2018). *Kyrpidia spormannii* sp. nov., a thermophilic, hydrogen-oxidizing, facultative autotroph, isolated from hydrothermal systems at Sao Miguel Island, and emended description of the genus *Kyrpidia*. *Int. J. Syst. Evol. Microbiol.* 68, 3735–3740. doi: 10.1099/ijsem.0.003037

Saitou, N., and Nei, M. (1987). The neighbor-joining method: a new method for reconstructing phylogenetic trees. *Mol. Biol. Evol.* 4, 406–425. doi: 10.1093/oxfordjournals.molbev.a040454

Sánchez-Andrea, I., Guedes, I. A., Hornung, B., Boeren, S., Lawson, C. E., Sousa, D. Z., et al. (2020). The reductive glycine pathway allows autotrophic growth of *Desulfovibrio desulfuricans*. *Nat. Commun.* 11:5090. doi: 10.1038/s41467-020-18906-7

Schmitz, R. A., Pol, A., Mohammadi, S. S., Hogendoorn, C., van Gelder, A. H., Jetten, M. S. M., et al. (2020). The thermoacidophilic methanotroph *Methylacidiphilum fumariolicum* SolV oxidizes subatmospheric H_2 with a high-affinity, membrane-associated [NiFe] hydrogenase. *ISME J.* 14, 1223–1232. doi: 10.1038/s41396-020-0609-3

Schuler, S., and Conrad, R. (1990). Soils contain two different activities for oxidation of hydrogen. *FEMS Microbiol. Ecol.* 73, 77–83. doi: 10.1111/j.1574-6968.1990.tb03927.x

SEI. (2021). *The Production Gap: Governments' Planned Fossil Fuel Production Remains Dangerously out of Sync with Paris Agreement Limits*. IISD, ODI, Climate Analytics, CICERO., and UNEP. Available at: http://productiongap.org/

Tabita, F. R. (1999). Microbial ribulose 1,5-bisphosphate carboxylase/oxygenase: a different perspective. *Photosynth. Res.* 60, 1–28. doi: 10.1023/A:1006211417981

Tabita, F. R., Hanson, T. E., Li, H., Satagopan, S., Singh, J., and Chan, S. (2007). Function, structure, and evolution of the RubisCO-like proteins and their RubisCO homologs. *Microbiol. Mol. Biol. Rev.* 71, 576–599. doi: 10.1128/mmbr.00015-07

Tautenhahn, R., Patti, G. J., Rinehart, D., and Siuzdak, G. (2012). XCMS online: a web-based platform to process untargeted metabolomic data. *Anal. Chem.* 84, 5035–5039. doi: 10.1021/ac300698c

Ullah, H., Mousavi, B., Younus, H. A., Khattak, Z. A. K., Chaemchuen, S., Suleman, S., et al. (2019). Chemical fixation of carbon dioxide catalyzed via cobalt (III) ONO pincer ligated complexes. *Commun. Chem.* 2:42. doi: 10.1038/s42004-019-0139-y

Vallenet, D., Belda, E., Calteau, A., Cruveiller, S., Engelen, S., Lajus, A., et al. (2013). MicroScope--an integrated microbial resource for the curation and comparative analysis of genomic and metabolic data. *Nucleic Acids Res.* 41, D636–D647. doi: 10.1093/nar/gks1194

van den Heuvel, R. N., van der Biezen, E., Jetten, M. S. M., Hefting, M. M., and Kartal, B. (2010). Denitrification at pH 4 by a soil-derived *Rhodanobacter*-dominated community. *Environ. Microbiol.* 12, 3264–3271. doi: 10.1111/j.1462-2920.2010.02301.x

Vaser, R., Sovic, I., Nagarajan, N., and Sikic, M. (2017). Fast and accurate de novo genome assembly from long uncorrected reads. *Genome Res.* 27, 737–746. doi: 10.1101/gr.214270.116

Walker, B. J., Abeel, T., Shea, T., Priest, M., Abouelliel, A., Sakthikumar, S., et al. (2014). Pilon: an integrated tool for comprehensive microbial variant detection and genome assembly improvement. *PLoS One* 9:e112963. doi: 10.1371/journal.pone.0112963

Wildman, S. G. (2002). Along the trail from fraction I protein to Rubisco (ribulose bisphosphate carboxylase-oxygenase). *Photosynth. Res.* 73, 243–250. doi: 10.1023/a:1020467601966

Yoshizawa, Y., Toyoda, K., Arai, H., Ishii, M., and Igarashi, Y. (2004). CO_2-responsive expression and gene organization of three ribulose-1,5-bisphosphate carboxylase/oxygenase enzymes and carboxysomes in Hydrogenovibrio marinus strain MH-110. *J. Bacteriol.* 186, 5685–5691. doi: 10.1128/jb.186.17.5685-5691.2004

Zuckerkandl, E., and Pauling, L. (1965). Molecules as documents of evolutionary history. *J. Theor. Biol.* 8, 357–366. doi: 10.1016/0022-5193(65)90083-4

frontiers | Frontiers in Microbiology

TYPE Original Research
PUBLISHED 27 March 2023
DOI 10.3389/fmicb.2023.1139276

OPEN ACCESS

EDITED BY
Stefan Frielingsdorf,
Technical University of Berlin,
Germany

REVIEWED BY
Wolfgang Buckel,
University of Marburg,
Germany
Christiane Dahl,
University of Bonn,
Germany

*CORRESPONDENCE
Myriam Brugna
✉ mbrugna@imm.cnrs.fr

†These authors share first authorship

SPECIALTY SECTION
This article was submitted to Microbial Physiology and Metabolism, a section of the journal Frontiers in Microbiology

RECEIVED 06 January 2023
ACCEPTED 09 March 2023
PUBLISHED 27 March 2023

CITATION
Kpebe A, Guendon C, Payne N, Ros J, Khelil Berbar M, Lebrun R, Baffert C, Shintu L and Brugna M (2023) An essential role of the reversible electron-bifurcating hydrogenase Hnd for ethanol oxidation in *Solidesulfovibrio fructosivorans*. *Front. Microbiol.* 14:1139276. doi: 10.3389/fmicb.2023.1139276

An essential role of the reversible electron-bifurcating hydrogenase Hnd for ethanol oxidation in *Solidesulfovibrio fructosivorans*

Arlette Kpebe[1†], Chloé Guendon[1†], Natalie Payne[1,2], Julien Ros[1], Manel Khelil Berbar[3], Régine Lebrun[3], Carole Baffert[1], Laetitia Shintu[2] and Myriam Brugna[1*]

[1]CNRS, Aix-Marseille Univ, BIP, Marseille, France, [2]CNRS, Aix-Marseille Univ, Centrale Marseille, ISM2, Marseille, France, [3]CNRS, Aix-Marseille Univ, Plate-forme Protéomique de l'IMM, FR 3479, Marseille Protéomique (MaP), Marseille, France

The tetrameric cytoplasmic FeFe hydrogenase Hnd from *Solidesulfovibrio fructosivorans* (formely *Desulfovibrio fructosovorans*) catalyses H_2 oxidation and couples the exergonic reduction of NAD^+ to the endergonic reduction of a ferredoxin by using a flavin-based electron-bifurcating mechanism. Regarding its implication in the bacterial physiology, we previously showed that Hnd, which is non-essential when bacteria grow fermentatively on pyruvate, is involved in ethanol metabolism. Under these conditions, it consumes H_2 to produce reducing equivalents for ethanol production as a fermentative product. In this study, the approach implemented was to compare the two *S. fructosivorans* WT and the *hndD* deletion mutant strains when grown on ethanol as the sole carbon and energy source. Based on the determination of bacterial growth, metabolite consumption and production, gene expression followed by RT-q-PCR, and Hnd protein level followed by mass spectrometry, our results confirm the role of Hnd hydrogenase in the ethanol metabolism and furthermore uncover for the first time an essential function for a *Desulfovibrio* hydrogenase. Hnd is unequivocally required for *S. fructosivorans* growth on ethanol, and we propose that it produces H_2 from NADH and reduced ferredoxin generated by an alcohol dehydrogenase and an aldehyde ferredoxin oxidoreductase catalyzing the conversion of ethanol into acetate. The produced H_2 could then be recycled and used for sulfate reduction. Hnd is thus a reversible hydrogenase that operates in H_2-consumption by an electron-bifurcating mechanism during pyruvate fermentation and in H_2-production by an electron-confurcating mechanism when the bacterium uses ethanol as electron donor.

KEYWORDS

hydrogenase, Hnd, *Desulfovibrio*, *Solidesulfovibrio*, ethanol, alcohol dehydrogenase, aldehyde ferredoxin oxidoreductase, flavin-based electron bifurcation

1. Introduction

Desulfovibrio are metabolically versatile sulfate reducing bacteria able to oxidize a wide range of electron donors, such as lactate, pyruvate, or formate in the presence of sulfate but also to ferment certain substrates such as pyruvate. Hydrogen plays a central role in the energy metabolism of these bacteria, since they can use H_2 as an energy source in the presence of sulfate,

or H_2 is produced during fermentation to dissipate excess reducing power (Fauque et al., 1988; Thauer et al., 2007; Rabus et al., 2013). Moreover, during growth on some substrates, H_2 is also produced but immediately re-consumed allowing the respiration of sulfate. Several models describing H_2 metabolism in *Desulfovibrio*, including the H_2 recycling model, have been proposed over the past 40 years (Odom and Peck, 1981; Lupton et al., 1984; Noguera et al., 1998; Keller and Wall, 2011; Rabus et al., 2013; Sim et al., 2013). Hydrogenases, the key enzymes of this metabolism, catalyze the conversion between H_2 and protons and electrons. These enzymes, which are functionally and structurally diverse, and widespread in prokaryotes, are classified into two main groups according to the metal content of their active site: FeFe-hydrogenases and NiFe-hydrogenases.

Solidesulfovibrio fructosivorans (formerly *Desulfovibrio fructosovorans*, Waite et al., 2020), our model organism, contains no less than six gene clusters encoding different hydrogenases: one membrane-bound of Ech-type, two periplasmic and three cytoplasmic hydrogenases, among which the [FeFe]-hydrogenase Hnd (Baffert et al., 2019). Marker-exchange mutagenesis was performed to determine the role of hydrogenases in the energy metabolism of the bacterium. However, the multiplicity and diversity of these enzymes makes their precise role difficult to establish probably due to compensation processes as the result of deletion of genes encoding one, two, or three hydrogenases (Rousset et al., 1991; Malki et al., 1997; Casalot et al., 2002a,b).

Hnd, a tetrameric enzyme, belongs to the A3 group of the Greening's FeFe-hydrogenase classification (Greening et al., 2016) which includes hydrogenases that bifurcate electrons. Flavin-based electron bifurcation (FBEB) is a recently discovered mechanism of energy coupling, widely distributed mainly in anaerobic prokaryotes, that couples an endergonic redox reaction to an exergonic redox reaction (for reviews, see; Buckel and Thauer, 2018a,b). Multimeric bifurcating FeFe-hydrogenases couple H_2 oxidation to the reduction of NAD^+ and a ferredoxin. Some of them have been shown to perform the reverse reaction and confurcate electrons to produce H_2 (Schut and Adams, 2009; Schuchmann and Müller, 2012; Wang et al., 2013; Zheng et al., 2014; Kpebe et al., 2018). Contrary to what was previously thought, Hnd reduces NAD^+ rather than $NADP^+$ and a ferredoxin from H_2 and it retains activity even when purified aerobically unlike other electron-bifurcating hydrogenases (Kpebe et al., 2018; Jacq-Bailly et al., 2020). It contains, in addition to the hydrogenase catalytic subunit (HndD) which is closely related to the CpI hydrogenase from *Clostridium pasteurianum*, a [2Fe-2S] subunit (HndA), a subunit homologous to the NuoF flavin subunit of complex I (HndC), and a fourth subunit (HndB) which probably does not contain any redox center (Malki et al., 1995; Kpebe et al., 2018). The recent structures obtained by cryo-EM of trimeric hydrogenases of this class has allowed to propose a mechanism of electron bifurcation for these hydrogenases (Furlan et al., 2022; Katsyv et al., 2023).

We have recently demonstrated, by comparing the WT strain and the SM4 mutant strain lacking Hnd (Δ*hndD*) (Malki et al., 1997) that this hydrogenase is involved in ethanol metabolism when *S. fructosivorans* grows fermentatively with pyruvate as energy source (Payne et al., 2022, 2023). Whereas under this condition, Hnd is not essential for bacterial growth, the deletion of *hndD* leads to a dramatic decrease in the expression of two genes involved in the conversion of acetate into ethanol: *adh* (DesfrDRAFT_3929) encoding an iron-containing alcohol dehydrogenase (Adh) and *aor* (DesfrDRAFT_2487) encoding an aldehyde ferredoxin oxidoreductase (Aor). The Δ*hndD* mutant strain is, under these conditions, affected in the production of H_2 and ethanol. We proposed a model in which the oxidation of H_2 by Hnd would allow, thanks to its electron bifurcation mechanism, the production of reducing power in the form of NADH and reduced ferredoxin necessary for the production of ethanol as a fermentation product by the two enzymes Adh3929 and Aor2487 (Payne et al., 2022). In addition, our NMR-based metabolomic analysis highlighted that, under these growth conditions, the metabolic reprogramming induced by the deletion of *hndD* leads to the upregulation of several NADP-dependent pathways, including succinate production and branched-chain amino acid biosynthesis pathways (Payne et al., 2023).

To further understand the precise role of Hnd and since this hydrogenase is involved in ethanol metabolism, the approach implemented in this study was to compare the two *S. fructosivorans* WT and SM4 Δ*hndD* strains when grown on ethanol as the sole carbon and energy source. Our results confirm the role of this electron-bifurcating hydrogenase in ethanol metabolism and furthermore uncover for the first time an essential function for a *Desulfovibrio* hydrogenase.

2. Materials and methods

2.1. Bacterial strains and growth conditions

The WT strain of *S. fructosivorans* JJ (Ollivier et al., 1988), the SM4 strain lacking Hnd, deleted of *hndD* encoding the hydrogenase catalytic subunit (Δ*hndD*, Cm^R) (Malki et al., 1997), and the complementation strain, containing the entire *hnd* operon on the plasmid pBGhnd6 (strain SM4/pBGhnd6, Cm^R, and Gm^R) (Kpebe et al., 2018) were used in this study. The ADH-CG1 mutant strain of *S. fructosivorans*, lacking Adh3929, obtained in this study was also used.

Strains were grown anaerobically at 37°C in different media, containing pyruvate as carbon and electron donor and sulfate as electron acceptor (PS2 and PS20 media described in Payne et al., 2022) or containing ethanol instead of pyruvate as carbon and electron donor, in the presence of 20 mM sulfate (ES20 medium) or in the absence of sulfate (ES0 medium). Ethanol was used at the concentration of 40 mM for the WT and complementation strains, whereas for the SM4 strain the concentration was 60 mM because of the addition of the antibiotics thiamphenicol that is dissolved in ethanol. Thiamphenicol (34 μg/mL) was added to the medium for the growth of SM4 and ADH-CG1 strains and gentamicin (20 μg/mL) was added for the growth of SM4/pBGhnd6 strain. The media were inoculated with 5–10% of fresh cultures grown in PS2 medium. Growth on molecular hydrogen was also tested in the same medium (but without pyruvate or ethanol) in the presence of 30 mM sulfate, 10 mM acetate and 1 bar pressure of H_2, in 90 mL of anaerobic medium in 100 mL serum bottles. The medium was bubbled 15 min with H_2 before the inoculation with cells.

2.2. Construction of the *adh* mutant (ADH-CG1 strain)

The strain, called ADH-CG1, lacking the *adh* gene (accession WP_005996817, locus tag DESFRDRAFT_RS19365, old locus tag

DesfrDRAFT_3929) was constructed for this study. In order to replace the entire *adh* gene by the chloramphenicol Cm^R cassette on the chromosome, a 1,087 bp and a 1,086 bp PCR fragments corresponding to the upstream and downstream region of *adh* gene were cloned in the pNot19Cm plasmid (Fiévet et al., 2011) surrounding the Cm^R gene. Upstream and downstream region of *adh* gene were amplified with the following primers: ADH3929-del-amont-slic-pnot-F (5′CTCTAGAGGCGCGCCACTAGTCAGAAAGCGAGGGACTACTTC3′), ADH3929-del-amont-slic-cm-R(5′AACAGGGAAGTGAGAACTAGGGTGCCAACCTCACTTGGGT3′), ADH3929-del-aval-slic-F(5′AAATTCGCAATTGAGATCTATACGGGACCAACGTGTCAAA3′), ADH3929-del-aval-slic-R (5′GACCATGATTACGCCAAGCTTCTCATGAATTCGACTCCCTC3′). The Cm^R gene (1,413 bp) was amplified with the following primers: Cm slic-del-ADH3929-F(5′ACCCAAGTGAGGTTGGCACCCTAGTTCTCACTTCCCTGTT3′), Cm slic-del-ADH3929-R (5′TTTGACACGTTGGTCCCGTATAGATCTCAATTGCGAATTT3′). The three fragments were cloned in the SpeI/ HindIII digested pNot19Cm plasmid using the NEBuilder HiFi DNA assembly mix from NEB according the instruction. The pNot19Cm is a derivative pUC19 vectors and do not replicate in sulfate-reducing bacteria, it is used as a suicide plasmid in *S. fructosivorans* to direct the marker exchange mutagenesis on the chromosome. The resulting plasmid pNot-Cm-adh3929 was introduced in the WT strain of *S. fructosivorans* using electrotransformation (Malki et al., 1997). The genotype of the chloramphenicol/thiamphenicol resistant strain was analyzed by PCR and DNA sequencing to confirm the deletion of *adh* gene.

2.3. Metabolite production and consumption

Strains were grown in 100 mL serum bottles containing 90 mL of medium. Each culture was done in triplicate. H_2 accumulation was followed as described previously using a gas chromatography system (Agilent 7820A, GS-Carbonplot 115–3,133 column) (Payne et al., 2022). The H_2 accumulation is expressed as micromoles of H_2 accumulated in the headspace. Ethanol consumption and acetate production were followed by HPLC as previously described (Payne et al., 2022). The analysis was performed on the same *S. fructosivorans* cultures as those used for the growth curves and as those used to measure H_2 production and sulfate consumption. The consumption of sulfate in the growth medium was followed using ionic chromatography. At different growth times, 1 mL of culture samples were collected, centrifuged 5 min at 14,100 × g to remove cells and stored at −20°C until used. Before injection, samples were diluted in 1% isopropanol up to 7.5 mL and 0.22 µm filter-sterilized. Samples were analyzed using a Metrohm (Herisau Switzerland) 925 ECO ion chromatograph equipped with a conductivity detector, Metrohm Suppressor Module (MSM), 250 µL injection loop with peristaltic pump, Metrohm high pressure pump with purge valve and 863 compact autosampler. The detection of SO_4^{2-} anions was investigated, at room temperature, in suppressor mode using the separation column "Metrosep A Supp 4" (250 mm × 4.0 mm) with a Metrohm IC precolumn cartridge PRP-2 (Metrosep RP2 Guard/3.5) and eluent 1.7 mM $NaHCO_3$/1.8 mM Na_2CO_3, 20% acetone. The eluent flow-rate was 1 mL/min. The calibration of the instrument was done by injecting standard solutions of sulfate. The instrument was operated with the MagIC Net Basic software, that controls and monitors the instrument, evaluates the recorded data and manages it in a database.

2.4. Protein extract preparation

Preparation of protein extracts was done as follows: *S. fructosivorans* cells, grown in 250 mL bottles containing 200 mL of medium were harvested at 3 days after the end of the exponential phase and resuspended in 4 mL of 20 mM Tris–HCl pH 7.5 supplemented with 2 mM sodium dithionite, protease inhibitor cocktail (SIGMAFAST™ tablet), Dnase I (Roche) and Lysozyme (Sigma-Aldrich). The cells were broken in an anaerobic glovebox (Jacomex) using a sonicator (Hielscher) with 15 cycles of 30 s. Non-disrupted cells and cellular debris were removed by a centrifugation at 20,000×*g* for 20 min. Total cell extract was ultracentrifuged at 200,000×*g* for 45 min at 4°C, then the soluble extract was recovered. For hydrogenase enzymatic assay, the same protocol is carried out except that cells were harvested at the beginning of the stationary phase, the pellet was resuspended in 100 mM Tris–HCl pH 8 buffer and that total protein extract was used in the tests. Proteins were quantified using the Bio-Rad protein assay based on Bradford dye binding method using bovine serum albumin as standard. The same soluble protein extracts were used for ethanol dehydrogenase enzymatic assays, SDS-PAGE, Western immunoblot, and mass spectrometry analysis.

2.5. SDS-PAGE and Western blot

Separation of proteins by 10% SDS-PAGE and Western immunoblot were described previously (Payne et al., 2022). Two identical 10% SDS-PAGE were performed in parallel with 15 µg of soluble protein extract. After migration, the first one was stained with a Coomassie blue solution and the second one was used for western blotting experiment. The primary anti-HndD antibody was used to detect HndD protein on the nitrocellulose membrane.

2.6. Cloning, production, and purification of proteins

Recombinant strep-tagged Hnd hydrogenase and FdxB ferredoxin, both from *S. fructosivorans*, were produced and purified as described previously (Kpebe et al., 2018). A concentration of 1.46 mg/mL for Hnd was determined using the Bio-Rad protein assay based on Bradford dye binding method using bovine serum albumin as standard. The concentration of the mature FdxB in oxidized form was estimated to be 233 µmol/L by spectrophotometry at 410 nm, corresponding to the absorption peak of iron sulfur clusters, using an absorption coefficient value of 24,000 M^{-1} cm^{-1}.

The same strategy for *fdx*B cloning was used for *pfor* gene cloning. The *pfor* gene encoding the pyruvate:ferredoxin oxidoreductase (accession WP_006919792.1, locus tag DESFRDRAFT_RS00590, old locus tag DesfrDRAFT_0121) was amplified using the following primers: Oligo1-PFOR-df-SLIC-F (5′GTTTATCTGTTACCCCGTAGGATCCATGGCCAAGAAGATGAAAAGC3′), Oligo2c-PFOR-strep-df-SLIC-R(5′ACTACCACCACC

ACTACCCCCGGGTTTTCCGGAGCGGCCTTCGT3′). The 3,687 bp PFOR PCR fragment was digested with *SmaI* and *BamHI* NEB enzymes and cloned into the *SmaI-BamHI* linearized pthl-Fd-LL-C-Tag plasmid (Gauquelin et al., 2018). The resulting pthl-PFOR-LL-C-Tag plasmid was checked by sequencing and introduced in the *E. coli* MG1655 Δ*iscR::kan* strain by electroporation. The resulting strain was then used to produce recombinant strep-tagged PFOR. Strain was grown aerobically at 37°C during 16 h in LB medium supplemented with 0.5% glycerol, 40 mM sodium fumarate, 0.1 g/l Fe(III) citrate, 40 mM MOPS, 50 μg/mL kanamycin and 100 μg/mL ampicillin. Cells pellet was washed and then resuspended in buffer W (Tris–HCl 100 mM pH 8.0, NaCl 150 mM) supplemented with SIGMAFAST protease Inhibitor Cocktail tablet (SIGMA) and DNaseI (Roche). All purification steps were done anaerobically in a glove box under nitrogen atmosphere (Jacomex). Cells were lysed by sonication (20 cycles of 30 s). After ultracentrifugation (45 min at 200,000 × g at 4°C), the supernatant was loaded on a 5 mL StrepTactin superflow (IBA) affinity column and purification was done according IBA instruction. PFOR was eluted with 2.5 mM desthiobiotin in buffer W, dialyzed and concentrated with a 30 kDa molecular mass cut-off Vivaspin 20 (Sartorius). The purity of the PFOR (133.4 kDa) was checked on a 10% SDS-PAGE (Supplementary Figure S1). The catalytic activity of recombinant PFOR was measured in an anaerobic quartz cuvette, at 30°C, under N_2 atmosphere, in 1 mL reaction mixture containing 1 mM $MgCl_2$, 2 mM thiamine pyrophosphate, 0.32 mM dithioerythritol, 10 mM sodium pyruvate, 0.1 mM Coenzyme A, 20 μM ferredoxin FdxB in 100 mM Phosphate buffer pH7. The reaction was started by the addition of PFOR in the cuvette and absorbance at 410 nm was followed (reduction of FdxB). An activity of 0.045 U/mg was determined.

2.7. Enzymatic assays

Hydrogenase activity, both H_2-oxidation and H_2-evolution, using the methylviologen as electron acceptor/donor, in total cell extracts was measured as described previously (Payne et al., 2022). One unit of hydrogenase activity corresponds to the uptake of 1 μmol of H_2/min and the production of 1 μmol of H_2/min, respectively.

Electron bifurcation activity of Hnd was determined as described in Kpebe et al. (2018). NADH- and Fd-dependent H_2-production activity of Hnd (electron confurcation assay) was assayed using gas chromatography (GC). A 800 μL mixture containing 100 mM Tris–HCl pH 8.0, 4 μM of FMN, 4 μM of FAD, 15 mM sodium pyruvate, 25 μM Coenzyme A, 1 mM $MgCl_2$, 2 mM thiamine pyrophosphate, 0.32 mM dithioerythritol, 2.4 mM NADH, 73 μM ferredoxin FdxB, 36 μg of PFOR was prepared in a glove-box (Jacomex) and placed in a 8 mL vial closed by a septum. The reaction mixture was let react at room temperature for 40 min to allow the maximum reduction of FdxB by the PFOR. The confurcation reaction was started by the addition of 14.6 or 43.8 μg of Hnd. Hundred microliter of headspace gas were removed periodically using a gastight syringe and injected into a gas chromatography system (Agilent 7,820) equipped with a thermal conductivity detector and a HP-plot Molesieve capillary column (30 m, 0.53 mm, 25 μm), using argon as the carrier gas, at a flow rate of 4.2 mL/min, an oven temperature of 30°C and a detector temperature of 150°C. H_2 was quantified according to a standard calibration curve. H_2 production rate was expressed as μmol of H_2 produced. The H_2 signal appears for a retention time of 2.1 min while O_2 retention time is 2.5 min. Thus we can discriminate between the signals of these two gases. Electron bifurcation and confurcation activities were measured using the same samples of Hnd and ferredoxin FdxB proteins.

Ethanol dehydrogenase activity was determined in soluble cell extract according to Ramos et al. (2015) except that the assays were not performed in an anaerobic glove box but the activity was measured using anaerobic spectrophotometric cuvette. As a control, NAD^+ reduction was followed without ethanol in the reaction mixture in order to determine the NAD^+ reduction independent of ethanol dehydrogenase activity, which reduction was systematically deduced from the value measured in the reaction with ethanol.

2.8. Real-time quantitative PCR

10^{10} cells were pelleted. Total RNA was extracted using the *Maxwell®* Instruments from PROMEGA. This automated nucleic acid purification platform can perform 16 samples simultaneously. The cells pellet was resuspended in the homogenizing solution (*Maxwell Promega kit*). The resuspended cells were mixed with 0.1 mm glass beads followed by two 45 s steps of 6.5 m/s in the QUICKPREP mode of the MP Biomedicals™ Instrument FastPrep-24™ 5G. The total RNA extraction was then carried out according to the supplier's protocol. An extra step, with *TURBO DNA free™ kit (Life technology)* was done to remove genomic DNA contamination of the total RNA. RNA concentration was determined with a NanoDrop 2000 spectrophotometer and purity was checked with the automated platform of Agilent 4200 TapeStation system. Reverse transcription was performed on 1 μg of total RNA by using the superscript VI reverse transcriptase and random primers (Invitrogen). The protocol and primers used were previously described by Payne et al. (2022).

2.9. Relative quantitative proteomic data analysis

The protein-containing SDS-PAGE stacking bands containing 60 μg of extracted proteins from cells of *S. fructosivorans* WT and SM4/pBGhnd6 strains cultured in PS2 and ES20 conditions and collected at stationary phase of growth, were treated in biological triplicates for proteomic analysis as previously described in Gérard et al. (2022) with slight modifications as follows. Eight hundred nanograms of peptides were injected for LC-MSMS analysis on nano liquid chromatography Ultimate 3,000 (Thermo Scientific) coupled to a Q-Exactive Plus mass spectrometer (Thermo Scientific). The spectra were processed by Proteome Discoverer software (ThermoFisher, version: 2.4.1.15) using the Sequest HT algorithm with the search following settings: *Solidesulfovibrio_fructosivorans* database (TxID 596151) extracted from Uniprot (4,161 sequence entries); trypsin enzyme (maximum 2 missed cleavages); fixed modification: carbamidomethyl (Cys); variable modification: oxidation (Met); mass values specific for monoisotopic; precursor mass tolerance: ± 10 ppm; fragment mass tolerance: ± 0.02 Da; spectrum files were recalibrated. Peptide validation was based on target/decoy strategy based on *q*-value, maximum Delta Cn 0.05 and Strict Target False Discovery Rate at 0.01. Proteins were identified if minimum 2 unique peptide sequences more than 6 amino acids passed the high confidence filter. Relative quantification of Adh3929 (E1K229), Hnd

(HndA, E1JRZ9; HndB, E1HS00; HndC, E1JS01; HndD, E1JS02) and Aor2487 (E1JXY8) between the different conditions was established based on the number of Peptide Spectral Matched (PSM) of a protein, normalized by the total number of PSM in each sample, and averaged by the biological triplicate. Comparison was performed against the proteins from the WT strain grown in PS2 condition, fixed at 100%.

3. Results

3.1. SM4 mutant phenotype in ethanol medium

Both *S. fructosivorans* strains, the WT strain and the SM4 mutant strain deleted of *hndD* encoding the catalytic subunit of the Hnd hydrogenase, were grown on media that contain only ethanol as a carbon and energy source in the presence of 20 mM sulfate (ES20 medium) and in the absence of sulfate (ES0 medium). Growth was monitored over time by measuring the OD of cultures at 600 nm (Figure 1). As expected, in the presence of sulfate, on ES20 medium, the WT strain was able to oxidize ethanol for growth. The culture reached the stationary phase of growth after 90 h and the doubling time was 12.1 ± 1.9 h. In contrast, when sulfate was absent, the WT strain did not grow. Indeed, the bacterium is not able to ferment ethanol (Ollivier et al., 1988). The SM4 mutant strain is unable to grow on ethanol in both media, either in the presence or in absence of sulfate. These findings demonstrate that the deletion of *hndD* makes it impossible for this mutant strain to grow on ethanol even in the presence of sulfate, therefore the Hnd hydrogenase is essential for the growth of *S. fructosivorans* on ethanol. It should be noted that the SM4 mutant strain grows well under other growth conditions, on pyruvate, lactate and fructose (Malki et al., 1997; Payne et al., 2022, 2023). The deletion of *hndD* does not affect the growth of the bacterium on H_2/sulfate medium (Supplementary Figure S2) which confirms the result obtained by Malki et al. (1997) who showed that the growth of a mutant lacking Hnd (Δ*hndC*) is not affected compared to the WT strain. Hnd is not essential for bacterial growth on H_2/sulfate.

To confirm that the observed phenotype is indeed caused by the *hndD* deletion, the SM4 mutant strain carrying a plasmid containing the *hnd* operon (strain SM4/pBGhnd6, Kpebe et al., 2018) was cultivated on the two media ES0 and ES20. We observed that this strain, like the WT strain, can grow on ethanol in the presence of sulfate (Figure 1) but not in its absence (not shown). While the highest optical density at 600 nm is similar for both strains, the doubling time of the SM4/pBGhnd6 complementation strain is 4 times higher than that of the WT strain (47.9 ± 4.1 h). These results indicate that the expression of *hnd* from the pBGhnd6 plasmid restores the growth in a medium containing ethanol as the only source of carbon and energy although the complementation strain does not grow as fast as the WT strain. These results confirm that Hnd is essential for ethanol oxidation in *S. fructosivorans*. It is of note that, for some unknown reasons, the growth curve of the complemented strain shows a significant lag, the maximal OD600 is reached at 92 h for the WT strain while it is only reached at 306 h for the complemented strain. Pre-cultures of the strains were done on pyruvate medium and it seems that the complementation strain needs an adaptation time when transferred to ethanol medium. A lag phase of 200–250 h was also observed for a hydrogenase mutant of *Desulfovibrio vulgaris* Hildenborough (DvH) when the strain is transferred from a lactate medium to an ethanol medium (Haveman et al., 2003).

3.2. Metabolite production and consumption

In order to determine the effect of *hndD* deletion on the production of major metabolites, acetate and H_2 production as well as ethanol and sulfate consumption were followed during growth (Figure 2). As expected, ethanol is consumed quite rapidly (in less than 100 h) by the WT strain on ES20 medium whereas in absence of sulfate, ethanol is not consumed at all. Ethanol oxidation is coupled to sulfate reduction. This respiration allows the growth of the bacterium while fermentation is not possible. The mutant strain does not consume ethanol on both ES20 and ES0 media, explaining why it does not grow under these

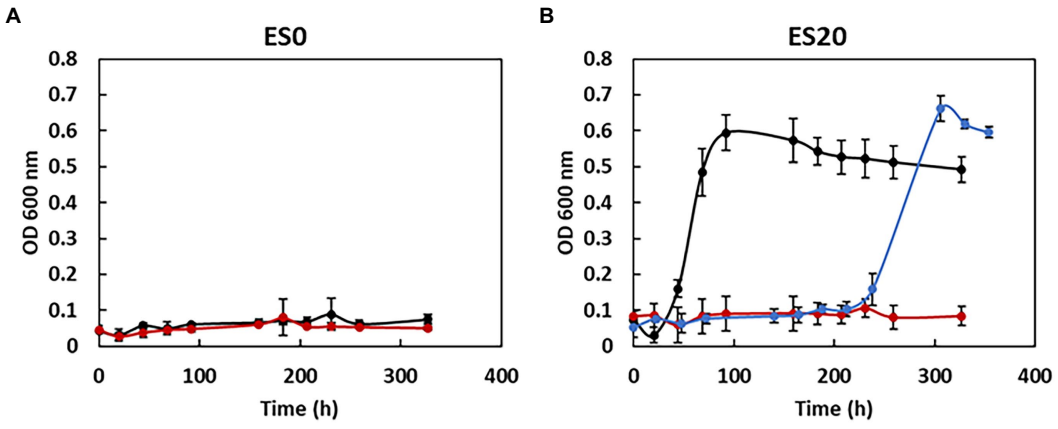

FIGURE 1
Growth curves of *Solidesulfovibrio fructosivorans* WT, SM4, and SM4/pBGhnd6 strains. Bacteria were grown in 100mL serum bottles containing 90mL of ES0 **(A)** and ES20 **(B)** media supplemented or not with 20mM sulfate, respectively, and 40 or 60mM ethanol as electron donor for the WT and the complementation strains, and the mutant strain, respectively. WT strain, black curves; SM4 strain, red curves; SM4/pBGhnd6 strain, blue curve. Data represent the averages of the results of three or four replicate growths. Error bars correspond to standard deviations.

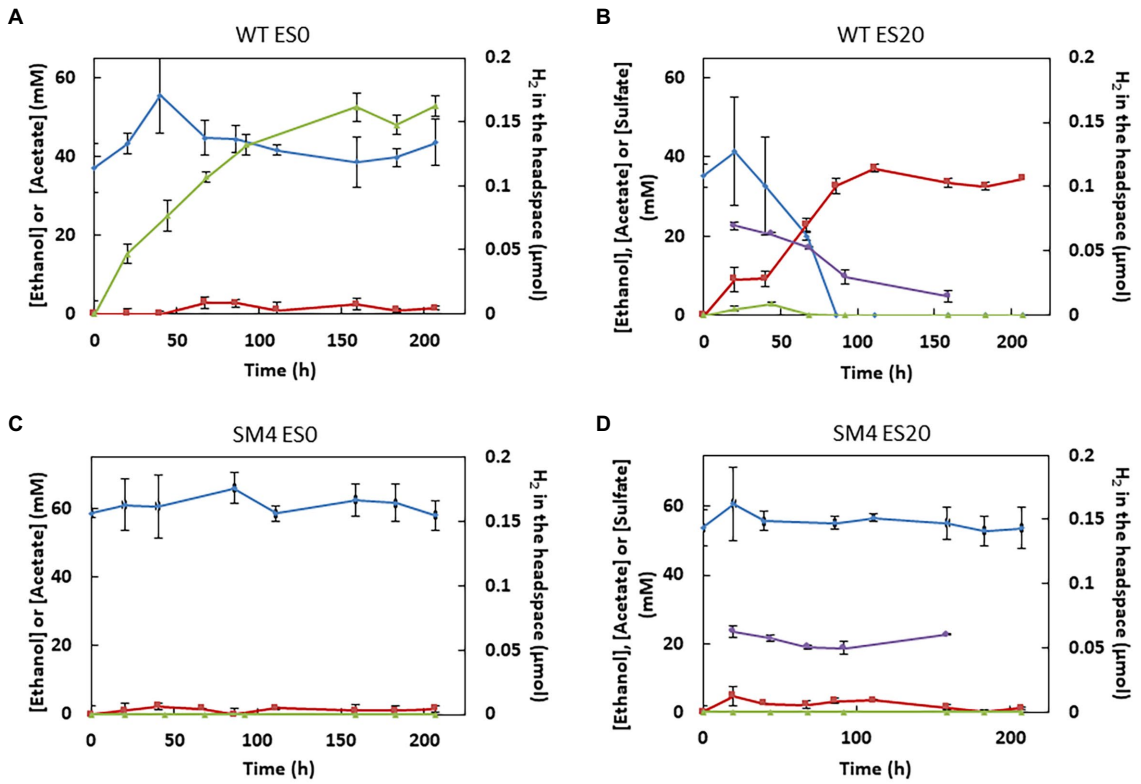

FIGURE 2
Acetate, ethanol, sulfate, and H_2 quantification. Acetate (red curves), ethanol (blue curves), and sulfate (purple curves) in the growth medium and H_2 in the headspace (green curves) were quantified by HPLC, ionic chromatography or GC during the growth of the *S. fructosivorans* WT strain **(A,B)** or the SM4 mutant strain **(C,D)** in the ES0 medium **(A,C)** or the ES20 medium **(B,D)**. Analyses were performed on the same *S. fructosivorans* cultures as those used for the growth curves. Data represent the averages of the results of three replicate growths. Error bars correspond to standard deviations.

conditions. Acetate is produced and sulfate is consumed only when ethanol is oxidized by the WT strain in ES20 medium.

H_2 accumulates in the gas phase when the WT strain grows in the absence of sulfate, showing that even though *S. fructosivorans* does not grow under these conditions, the bacteria from the inoculum are still able to survive and produce H_2. On ES20 medium, on the other hand, there is no accumulation of H_2 in the headspace although we observe a transient burst of H_2 at the beginning of the growth. In contrast, the SM4 mutant strain does not produce H_2 at all.

Taken together, these results lead us to propose that the Hnd hydrogenase catalyzes H_2 production when *S. fructosivorans* grows with ethanol as the only energy source in the presence of sulfate. It would therefore carry out the confurcation of electrons from NADH and reduced ferredoxin. We check the ability of Hnd to confurcate electrons *in vitro*. We determine an activity of 0.033 ± 0.015 U/mg. Although this activity is low compared to electron bifurcation activity (0.96 U/mg determined with the same protein sample), it shows that Hnd is able to produce H_2 *in vitro* from reduced FdxB ferredoxin and NADH (Supplementary Figure S3).

3.3. Impact of the carbon source and growth condition on Hnd level

Hnd production in the WT strain, followed by Western blot, was compared under pyruvate (fermentation or respiration) and ethanol (respiration) conditions (Figure 3A). As expected, in pyruvate medium, the amount of Hnd is much higher in fermentation (PS2) than in respiration (PS20) (Payne et al., 2022). Surprisingly, Hnd is much less abundant when the bacterium is growing in ethanol medium (ES20) than in PS2 medium, while it is essential for the growth of the bacterium when growing on ethanol as carbon source (Figure 1). To confirm this result, Hnd abundance was measured by quantitative proteomics using spectral counting from soluble extracts of the WT strain (Figure 3B) and an amount of Hnd 5 times lower was observed when bacteria were grown on ethanol medium (ES20) as compared to pyruvate fermentation medium (PS2). The expression of the *hndD* gene (locus tag DesfrDRAFT_0401), which was monitored by RT-qPCR, is more than twofold lower for the WT strain grown in ethanol medium (ES20) than in pyruvate medium (PS2) (Figure 3C). Expression of *hnd* is consistent with the results obtained at the Hnd protein level.

We measured the hydrogenase activity of H_2-consumption and H_2-production from total extracts of the WT and the SM4 mutant strains grown on the three media (PS2, PS20, and ES20) (Table 1). As shown previously, Hnd is responsible for the majority of the hydrogenase activity measured in the WT in PS2 medium since it is strongly reduced in the mutant SM4 strain (Payne et al., 2022). In PS20, the decrease in hydrogenase activity as compared to PS2 medium is explained by the drastic decrease in *hndD* expression (Payne et al., 2022). Interestingly, the activity of the WT strain is about 10 times lower on ES20 than on PS2 for H_2-oxidation and a half for

10.3389/fmicb.2023.1139276

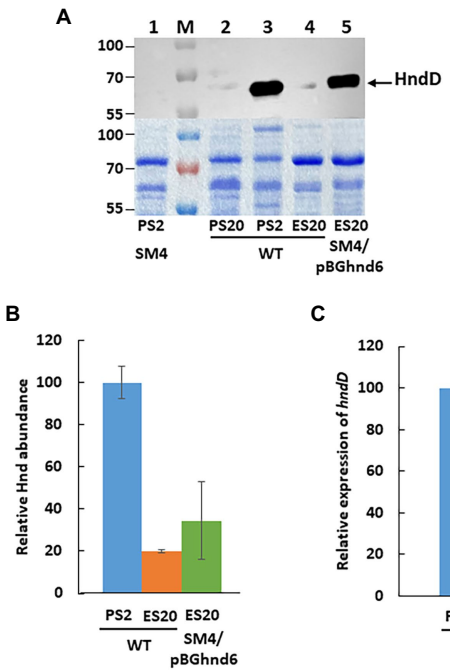

FIGURE 3
Hnd level in *S. fructosivorans* under pyruvate and ethanol conditions. **(A)** Western blot analysis of HndD production by WT (lanes 2–4), SM4 (lane 1) and SM4/pBGhnd6 (lane 5) cells of *S. fructosivorans* grown with pyruvate (PS2, lanes 1 and 3, or PS20, lane 2) or ethanol (ES20, lanes 4 and 5) as carbon source. Cells were harvested at stationary phase of growth and 15µg of total proteins from soluble extracts were separated by 10% SDS-PAGE and subjected to western blotting using an antibody raised against HndD. Molecular mass markers (lane M) are indicated in kDa. The SDS-PAGE below the western blot is a loading control. **(B)** Relative Hnd level determined by quantitative proteomics. *S. fructosivorans* WT and SM4/pBGhnd6 strains were grown with pyruvate (PS2) or ethanol (ES20) as carbon source and cells were collected at stationary phase of growth. Data represent the averages of the results of three experiments. Error bars correspond to standard deviations. **(C)** Relative expression of the *hndD* (DesfrDRAFT_0401) gene quantified by RT-qPCR. *S. fructosivorans* WT strain was grown with pyruvate (PS2) or ethanol (ES20) as carbon source and samples were collected at stationary phase of growth. Expression of the gene was normalized to that of the 16S rRNA gene. Data represent the averages of the results of three experiments. Error bars correspond to standard deviations.

TABLE 1 Hydrogenase activity in *S. fructosivorans*.

Growth medium		Hydrogenase activity ($U.mg^{-1}$)	
	S. fructosivorans strain	H_2-oxidation	H_2-production
PS2	WT	28.7 ± 6.0	8.4 ± 2.7
	SM4	0.4 ± 0.1	0.9 ± 0.1
PS20	WT	5.0 ± 1.6	1.6 ± 0.3
	SM4	2.7 ± 0.5	1.3 ± 0.5
ES20	WT	3.3 ± 1.0	4.3 ± 1.4
	SM4/pBGhnd6	6.9 ± 3.0	4.2 ± 1.2

H_2-production and H_2-oxidation were measured on the total extract of the WT, the SM4 mutant and the complementation SM4/pBGhnd6 strains grown with pyruvate (PS2 and PS20) or ethanol (ES20) as carbon source. Cells were harvested at the end of exponential phase of growth.

H_2-production. This sharp drop in both hydrogenase activities under ethanol compared to pyruvate fermentation conditions correlates with the significant decrease in the amount of the Hnd hydrogenase when the bacteria are growing on ethanol (Figures 3A,B).

The anti-HndD western blot on the complementation strain shows that, on ES20 ethanol medium, the amount of Hnd is similar to that of the WT strain, indicating that Hnd production is restored from the operon on the pBGhnd6 plasmid (Figure 3A). The same pattern is observed when the abundance of Hnd is determined by quantitative proteomics (Figure 3B). These results correlate with the fact that H_2 production and oxidation activities of the SM4/pBGhnd6 strain are comparable to those measured for the WT strain (Table 1).

Collectively, these results clearly show that the expression of the *hnd* operon as well as the amount of Hnd hydrogenase are much lower when the bacteria are growing under respiration (PS20 or ES20) than under fermentation (PS2). Unexpectedly, under respiratory condition, the nature of the carbon source, pyruvate or ethanol, has little effect on the expression of the hydrogenase while this enzyme is essential for the growth of the bacteria on ethanol but not on pyruvate (Payne et al., 2022).

3.4. Impact of the carbon source and growth condition on Adh and Aor levels

In a previous study, we have demonstrated that the deletion of the *hndD* gene, in the SM4 strain, leads to a drastic drop in the expression of the *adh*3929 gene (locus tag DesfrDRAFT_3929), coding for an alcohol dehydrogenase, and of the *aor*2487 (DesfrDRAFT_2487) coding for an aldehyde ferredoxin oxidoreductase (Payne et al., 2022). We therefore monitored Adh and Aor at the protein as well as the transcriptional levels under different growth conditions.

The amount of Adh3929 is so high in the cell in PS2 that it can be visualized directly on SDS-PAGE of cell extracts (Payne et al., 2022). Following Adh during bacterial growth shows that the enzyme accumulates in the cells (Supplementary Figure S4). Comparison of the amount of Adh in the stationary phase reveals that it is much more abundant in *S. fructosivorans* WT cells grown on PS2 than under respiration in PS20 medium as already shown (Payne et al., 2022) but also in ES20 medium (Figure 4A). Abundance of Adh was also measured by quantitative proteomics and confirms that the quantity of the enzyme is 3 times lower under ethanol respiration (ES20) than in pyruvate fermentation (PS2) for the WT strain (Figure 4B).

The ethanol dehydrogenase specific activity was determined on soluble extracts of the WT and the SM4 mutant strains (Table 2). The SM4 mutant shows no detectable ethanol dehydrogenase activity on pyruvate medium (PS2 and PS20). This is consistent with the fact that in this mutant the expression of *adh* is strongly reduced compared to the WT strain (Payne et al., 2022). More importantly, what was less expected is that in respiration, the ethanol dehydrogenase activity is similar on pyruvate medium (PS20) as on ethanol medium (ES20) for the WT strain. This activity is considerably lower when the bacteria are growing under ethanol respiration (ES20) than on pyruvate fermentation (PS2).

Similarly, the *adh* gene expression, measured by RT-qPCR, is extremely higher on PS2 than on ethanol medium (ES20) (Figure 4C). This result is consistent with the lower amount of Adh enzyme present on ES20 than on PS2 (Figures 4A,B) and also with the ethanol dehydrogenase activity measured under these two conditions

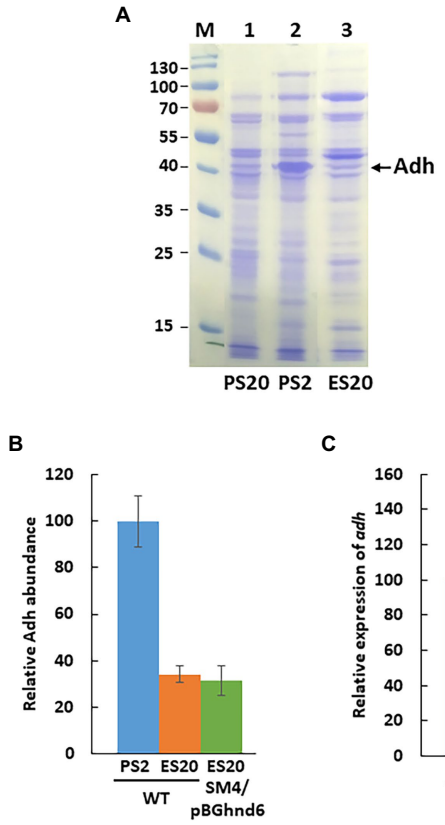

FIGURE 4
Adh level in *S. fructosivorans* under pyruvate and ethanol conditions. **(A)** Coomassie blue-stained SDS-PAGE of soluble proteins from *S. fructosivorans* WT strain grown with pyruvate (PS20, lane 1 or PS2, lane 2) or ethanol (ES20, lane 3) as carbon source. Cells were harvested at stationary phase of growth. Ten micrograms of soluble proteins were loaded in each lane of a 12% SDS-PAGE. Molecular mass markers (lane M) are indicated in kDa. Arrow indicates bands corresponding to Adh (3929). The theoretical molecular mass of Adh is 41.9kDa. **(B)** Relative Adh level determined by quantitative proteomics. *S. fructosivorans* WT and SM4/pBGhnd6 strains were grown with pyruvate (PS2) or ethanol (ES20) as carbon source and cells were collected at stationary phase of growth. Data represent the averages of the results of three experiments. Error bars correspond to standard deviations. **(C)** Relative expression of the *adh* (DesfrDRAFT_3929) gene quantified by RT-qPCR. *S. fructosivorans* WT strain was grown with pyruvate (PS2) or ethanol (ES20) as carbon source and samples were collected at stationary phase of growth. Expression of the gene was normalized to that of the 16S rRNA gene. Data represent the averages of the results of three experiments. Error bars correspond to standard deviations.

(Table 2). The presence of 40 mM of ethanol in the growth medium does not induce the overexpression of the *adh* gene at the transcriptional level.

The ethanol dehydrogenase activity for the complementation strain is very low in pyruvate media (PS2 and PS20) (Table 2) which is consistent with the fact that the complementation is only partial when the SM4/pBGhnd6 strain is growing on pyruvate (Payne et al., 2022). In contrast, when the complementation strain is grown on ethanol medium, expression of *hnd* operon from the plasmid restores Adh (both the amount of the enzyme and the ethanol dehydrogenase activity) suggesting that *adh* expression is restored (Figure 4B and Table 2).

TABLE 2 Ethanol dehydrogenase activity in *S. fructosivorans*.

Growth medium	*S. fructosivorans* strain	Ethanol dehydrogenase activity (mU.mg^{-1})
PS2	WT	375 ± 38
	SM4	N.D.
	SM4/pBGhnd6	4 ± 1
PS20	WT	18 ± 12
	SM4	N.D.
	SM4/pBGhnd6	1 ± 1
ES20	WT	22 ± 15
	SM4/pBGhnd6	51 ± 12

Ethanol dehydrogenase activity was measured on the soluble extract of the WT, the SM4 mutant and the complementation SM4/pBGhnd6 strains grown with pyruvate (PS2 and PS20) or ethanol (ES20) as carbon source. Cells were harvested at the stationary phase of growth. N.D., not detected.

Regarding Aor, quantitative proteomics and RT-qPCR experiments (Figures 5A,B) suggest that the level of Aor does not vary between the two conditions PS2 and ES20 and that the expression of the gene is even higher on ES20 than PS2 in stationary phase, contrary to what is observed for Adh. The amount of Aor is the same for the WT strain as for the complementation strain on ES20 (Figure 5A). These results suggest that different transcriptional regulators regulate the expression of the *adh* and *aor* genes, *adh* being more strongly expressed on PS2 while *aor* is more strongly expressed on ES20 leading to a similar amount of Aor enzyme on both media.

3.5. Growth analysis of the ADH-CG1 (Δ*adh*) mutant in pyruvate and ethanol media

We constructed the Adh-encoding gene deletion mutant, called the ADH-CG1 strain, and compared its growth to the WT strain (Figure 6). On pyruvate media, the ADH-CG1 strain grows well despite the fact that the generation time is higher than for the WT strain (30.9 ± 0.6 h for the mutant vs. 17.2 ± 0.9 h for the WT strain in PS2 medium and 28.0 ± 5.3 h for the mutant vs. 20.5 ± 0.3 h for the WT strain in PS20 medium) (Payne et al., 2022). On both media, the growth yield (OD_{600} max) is similar and is around 1 while it is slightly higher for the WT strain (between 1.2 and 1.4) (Payne et al., 2022). In contrast, on ES20 medium, the Δ*adh* mutant did not grow, indicating that Adh3929 is responsible for ethanol oxidation and that this enzyme is essential for bacterial growth under these conditions.

4. Discussion

In this work, we investigated the role of the electron-bifurcating Hnd hydrogenase in the physiology of *S. fructosivorans* by comparing the WT strain and SM4, the Hnd hydrogenase deletion mutant when the bacteria use ethanol as a carbon source. When Ollivier and colleagues characterized the *S. fructosivorans* species, they determined that it is able to oxidize ethanol in the presence of sulfate, much like related species from the *Desulfovibrio* genus (Ollivier et al., 1988). In

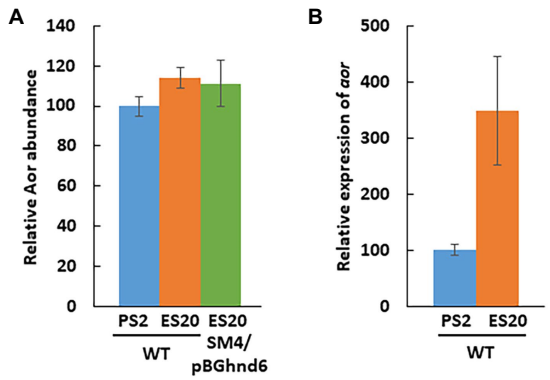

FIGURE 5
Aor level in *S. fructosivorans* under pyruvate and ethanol conditions. **(A)** Relative Aor level determined by quantitative proteomics. *S. fructosivorans* WT and SM4/pBGhnd6 strains were grown with pyruvate (PS2) or ethanol (ES20) as carbon source and cells were collected at stationary phase of growth. Data represent the averages of the results of three experiments. Error bars correspond to standard deviations. **(B)** Relative expression of the *aor* (DesfrDRAFT_2487) gene quantified by RT-qPCR. *S. fructosivorans* WT strain was grown with pyruvate (PS2) or ethanol (ES20) as carbon source and samples were collected at stationary phase of growth. Expression of the gene was normalized to that of the 16S rRNA gene. Data represent the averages of the results of three experiments. Error bars correspond to standard deviations.

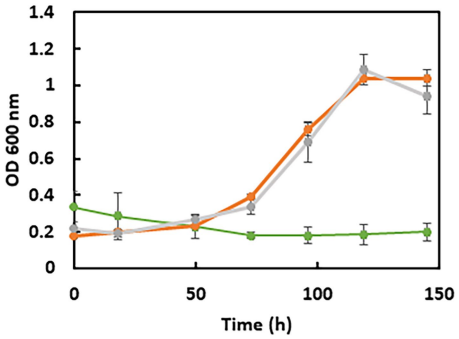

FIGURE 6
Growth curves of *S. fructosivorans* ADH-CG1 strain deleted of the Adh3929 encoding gene. Bacteria were grown in 100mL serum bottles containing 90mL of PS2 (orange curve), PS20 (gray curve) and ES20 (green curve) media. Data represent the averages of the results of three replicate growths. Error bars correspond to standard deviations.

low sulfate medium, the growth of *Desulfovibrio* is slight, and little of the ethanol is oxidized unless bacteria are co-cultured with an H_2-consuming organism (Bryant et al., 1977). This syntrophic association between two partners, a H_2-producing and a H_2-scavenging partner is particularly important in anaerobic environments. Moreover, the electron transfer could even take place between the two microorganisms of the co-culture, not only by interspecies H_2 transfer, but also directly as recently proposed by Zheng and colleagues, allowing the growth of *Desulfovibrio* in co-culture on ethanol in absence of sulfate (Zheng et al., 2021). As expected, we observed, in this study, that the WT strain is able to grow on a medium containing ethanol and sulfate but not on a medium containing ethanol only, while the growth of the SM4 mutant strain is completely prevented on both media, which confirms the involvement of Hnd in ethanol metabolism. Results obtained on the complementation strain indicate that contrary to what is observed on pyruvate media where the complementation is only partial in respiration (PS20) or in fermentation (PS2) (Payne et al., 2022), the presence of the *hnd* operon on the plasmid in the complementation strain restores the growth of the strain. These results also indicate that the amounts of the three enzymes Hnd, Adh and Aor are comparable in the two strains WT and SM4/pBGhnd6 and that the phenotype observed for the SM4 mutant strain is due to the *hndD* deletion. We have indeed shown previously that Hnd consumes, in a non-essential role, part of the H_2 produced during pyruvate fermentation and produces reducing equivalents in the form of NADH and reduced ferredoxin through the electron bifurcation mechanism. These reducing equivalents are used for ethanol production as a fermentative product (Payne et al., 2022, 2023). In this study, our results show that Hnd is essential for the growth of *S. fructosivorans* on ethanol, indicating the importance of its role and highlighting for the first time an essential role of a hydrogenase for the growth of a *Desulfovibrio*. Previous studies of *Desulfovibrio* hydrogenase deletion mutants have never demonstrated the essential character of a hydrogenase in these bacteria (Rousset et al., 1991; Malki et al., 1997; Casalot et al., 2002a,b; Haveman et al., 2003; Caffrey et al., 2007; Morais-Silva et al., 2013). Moreover, it is important to note that none of the five other hydrogenases of *S. fructosivorans* compensates for the loss of Hnd, not even Hnt, the trimeric FeFe hydrogenase whose genes were identified in the genome (Baffert et al., 2019) and whose structure is very similar to the trimeric FeFe flavin-based electron-bifurcating hydrogenase from *Thermotoga maritima* (Schut and Adams, 2009). This putative trimeric hydrogenase Hnt has never been purified and biochemically characterized in any *Desulfovibrio* species and no evidence concerning its possible physiological role is available.

Furthermore, although the WT strain does not grow in ES0, it survives and accumulates H_2 in the headspace whereas the SM4 mutant does not (Figure 2). A very small amount of ethanol must be consumed under these conditions to sustain this low H_2 production but it is probably too low to be detectable on Figure 2A and to allow the growth of the bacteria. Our results led us to propose that Hnd produces H_2 by an electron confurcation mechanism and regenerates the reducing equivalents, NADH and reduced ferredoxin, produced during ethanol oxidation by the two enzymes Adh which converts ethanol to acetaldehyde, and Aor which converts acetaldehyde to acetate (Figure 7). The H_2 produced could be used for cytoplasmic sulfate reduction, probably by the mechanism for energy coupling of H_2 cycling (Odom and Peck, 1981). Hnd is thus a reversible electron bifurcating hydrogenase that operates in H_2 consumption during pyruvate fermentation and in H_2 production when the bacterium uses ethanol as electron donor. Surprisingly, the expression of *hndD* in WT cells is much lower under pyruvate fermentation conditions than under ethanol oxidation conditions, which results in a lower amount of Hnd, although it is essential in the latter condition (Figure 3). The same is true for Adh3929 (Figure 4). We demonstrated that Hnd is able to catalyze H_2 production using electron confurcation *in vitro*. The specific activity measured is low compared to the electron bifurcation activity. This is probably due to the low specific activity (and the limited quantity that can be added in the assay) of the

10.3389/fmicb.2023.1139276

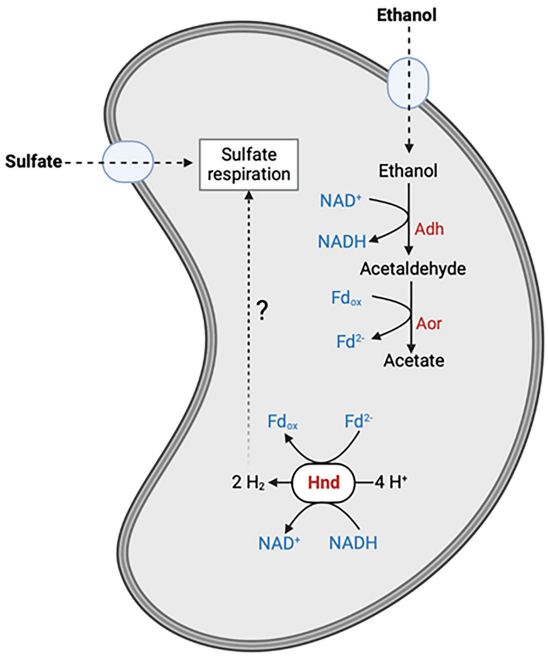

FIGURE 7
Model of the ethanol oxidation pathway in *S. fructosivorans*. Hnd hydrogenase is involved in the re-oxidation of NADH and reduced ferredoxin which are produced during ethanol oxidation by the enzymes Adh and Aor, through an electron confurcation mechanism. This leads to the production of H_2 which could be recycled for sulfate reduction. The question mark indicates that this electron transfer pathway is hypothetical. Adh, alcohol dehydrogenase; Aor, Aldehyde ferredoxin oxidoreductase; Fd_{ox}, oxidized ferredoxin; Fd^{2-}, reduced ferredoxin. This figure was created with BioRender.com.

PFOR used to generate reduced ferredoxin, that limits the overall confurcation activity. Moreover, we cannot directly compare the specific activities of electron confurcation vs. bifurcation because the driving force of the reactions is not the same and cannot be adjusted; it depends on the proportion of oxidized and reduced forms of the two electron donors/acceptors [on the Fdx(oxidized)/Fdx(reduced) ratio and on the NAD^+/NADH ratio]. These ratios are also unknown in bacterial cells. Although it is not possible to discuss the variation in Hnd amount in the light of confurcation/bifurcation activity *in vivo*, our results demonstrate that Hnd is a bidirectional hydrogenase.

Only a few bacterial electron-bifurcating FeFe hydrogenases have been purified and characterized and the role of some of them has been determined. In acetogenic bacteria, such as *Acetobacterium woodii* and *Moorella thermoacetica*, the electron-bifurcating hydrogenase is involved in H_2 consumption and produces NADH and reduced ferredoxin which are used for CO_2 reduction (Schuchmann and Müller, 2012; Wang et al., 2013). In glucose-fermenting bacteria, such as *Ruminococcus albus* and *T. maritima*, the trimeric hydrogenase is involved in the production of H_2 from NADH and reduced ferredoxin produced during fermentation through an electron confurcation mechanism to dissipate excess reducing power (Schut and Adams, 2009; Zheng et al., 2014; Greening et al., 2019).

The results obtained in this study and in our previous study clearly demonstrate that the *hnd* operon expression is strongly regulated at the transcriptional level. We have predicted the presence of a Rex-binding site in the promoter region of *hnd* and proposed that the expression of Hnd might be regulated by Rex, a transcriptional redox-sensing regulator controlled by the intracellular NAD^+/NADH ratio. Moreover, HydS, a putative H_2-sensing hydrogenase, whose mechanism has yet to be elucidated, might also be involved in the regulation of Hnd (Payne et al., 2022). When *R. albus*, a rumen bacterium, grows in co-culture with a hydrogenotrophic microorganism keeping the H_2 partial pressure very low, the trimeric electron-bifurcating hydrogenase is expressed and produces H_2. Its expression is tightly regulated, as is the expression of the two other hydrogenases of the bacterium, in response to H_2 partial pressure. It has been proposed that the Rex regulator as well as the HydS hydrogenase are involved in the regulation of the expression of this hydrogenase (Zheng et al., 2014; Greening et al., 2019).

The expression of *adh* is also regulated at the transcriptional level and surprisingly, under respiratory condition, it is not induced by ethanol but is dependent on *hnd*. Indeed, while the WT strain grows well on ES20 ethanol medium (Figure 1), the SM4 strain shows completely impaired growth suggesting that, as is the case on pyruvate (Payne et al., 2022), the deletion of *hndD* induces a drastic decrease in the expression of *adh* on ethanol medium, making it impossible for the deletion mutant to use ethanol. However, the mechanism of regulation involved remains to be elucidated. In DvH, the mutant strain deleted of the periplasmic FeFe-hydrogenase shows also a very drastic drop in the expression of the *adh* gene, whereas it is one of the most expressed in the WT strain. Moreover, *adh* is upregulated when DvH uses ethanol as electron donor instead of lactate, pyruvate, formate or H_2 indicating that the expression, unlike in *S. fructosivorans*, is induced by ethanol (Haveman et al., 2003). In this study, we also constructed the ADH-CG1 mutant strain deleted of the gene encoding Adh3929. The fact that this mutant strain does not grow on ethanol shows that Adh3929 is responsible for the oxidation of ethanol on ES20 and that this enzyme is essential for bacterial growth under these conditions. The counterpart of this Adh in DvH has also been shown to be responsible for the utilization of ethanol as the sole source of carbon and energy (Haveman et al., 2003). It is of note that although in the *S. fructosivorans* genome, 7 genes are annotated as "iron-containing alcohol dehydrogenase" in addition to the *adh*3929 gene (Supplementary Table S1), none of them compensates for the strong decrease of *adh*3929 expression in the *hndD* deletion mutant or for the lack of Adh3929 in the ADH-CG1 mutant to allow bacterial growth. This suggests that these *adh* genes are tightly regulated or that they code for alcohol dehydrogenases that do not use ethanol but other alcohols as a substrate. Interestingly, one of them, Adh1011, shows very strong homology to Adh 3929 (85% of protein sequence identity). However, the role of the other *adh* genes and the substrate specificity of the corresponding enzymes remain to be determined. Regarding *aor*, its expression profile is different compared to *hnd* and *adh* under ethanol condition while on pyruvate, the three genes followed the same profile (Payne et al., 2022). *aor* is over-expressed under ethanol condition as compared to pyruvate fermentation leading to a similar abundance of the enzyme under both conditions (Figure 5). These results again suggest that *aor* is regulated at the transcriptional level and that ethanol may be involved in the regulation of its expression.

For the three operon/genes *hnd*, *adh*, and *aor*, the mechanism of regulation of their expression remains to be elucidated. Surprisingly, ethanol is not involved in the regulation of *hnd* and *adh* expression, because their expression is not upregulated under these conditions.

In DvH, the enzyme complex Flx-Hdr (Flx for flavin oxidoreductase and Hdr for heterodisulfide reductase), proposed to also perform electron bifurcation, plays a role that strikingly resembles the role of the hydrogenase Hnd (Ramos et al., 2015). This soluble complex is composed of six subunits, the 3 Flx subunits are homologous to subunits of *Pyrococcus* soluble hydrogenases but without a hydrogenase catalytic subunit and the 3 Hdr subunits sharing sequence homology with the archaeal HdrABC enzyme. In methanogenic archaea, the HdrABC enzyme forms a complex with the MvhADG NiFe-hydrogenase that catalyzes heterodisulfide CoM-S-S-CoB reduction with H_2 coupled to the reduction of ferredoxin by flavin-based electron bifurcation (Thauer et al., 2008; Kaster et al., 2011; Wagner et al., 2017). The Flx-Hdr complex has been shown to be essential for ethanol oxidation in DvH by coupling the reduction of a ferredoxin and a disulfide (the DsrC protein) by NADH. In pyruvate fermentation, the Flx-Hdr complex is involved in ethanol production in a non-essential way by operating in reverse to reduce NAD^+. Contrary to what we have shown in *S. fructosivorans* for the *hnd* operon, the *flx-hdr* genes are increased in transcription during growth in ethanol-sulfate in DvH. DvH does not possess an electron bifurcating hydrogenase, so it is the Flx-Hdr complex that plays the same essential role as Hnd in the oxidation of ethanol in this bacterium. On the other hand, the genome of *S. fructosivorans* contains a cluster with seven genes sharing sequence homology with genes encoding the Flx-Hdr complex of DvH (locus tags DesfrDRAFT_3930–3936) but the role of this complex is still unknown in *S. fructosivorans*. It is noteworthy that the *flx-hdr* gene cluster in *S. fructosivorans* is located immediately downstream of the *adh*3929 gene, as is the case in DvH (Ramos et al., 2015), which could also indicate a role in ethanol metabolism in this bacterium. However, Flx-Hdr does not take over ethanol oxidation when the hydrogenase Hnd is deleted. Our results as well as the results of Ramos and colleagues (Ramos et al., 2015) demonstrating the essential role of Hnd in *S. fructosivorans* as well as of the Flx-Hdr complex in DvH for ethanol oxidation highlight the importance of electron bifurcation in the energy metabolism in *Desulfovibrio*.

In summary, the results obtained here on *S. fructosivorans* have provided conclusive evidence that the hydrogenase Hnd is essential for the growth on ethanol by oxidizing the reducing equivalents formed during ethanol oxidation and coupling this oxidation with H_2 production using an electron confurcation mechanism. Hnd is a reversible hydrogenase that operates in electron-bifurcating or -confurcating mechanism depending on the growth conditions.

Data availability statement

The raw data supporting the conclusions of this article will be made available by the authors, without undue reservation.

Author contributions

MB and AK involved in conception, design of the study, and writing of the manuscript. AK, CG, NP, JR, MKB, RL, CB, LS, and MB involved in acquisition, analysis, and interpretation of the data. All authors reviewed the manuscript and approved the submitted version.

Funding

This work was supported by the CNRS and Aix Marseille Université and the Région Sud (CR PACA – AAP Recherche 2020 volet général, projet No-O2). This project has received funding from the European Union's Horizon 2020 Research and Innovation Program under the Marie Skłodowska-Curie (grant agreement no. 713750). Also it has been carried out with the financial support of the Regional Council of Provence-Alpes-Côtes d'Azur and with the financial support of the A*MIDEX (no. ANR-11-IDEX-0001-02), funded by the Investissements d'Avenir project funded by the French Government, managed by the French National Research Agency (ANR).

Acknowledgments

The authors thank Marianne Guiral (BIP, CNRS) for fruitful discussions and help with ionic chromatography experiments and Yann Denis (IMM, CNRS) for RT-q-PCR experiments. The authors also thank I. Meynial-Salles (INSA, Toulouse) for kindly providing the plasmid pthl-Fd-LL-C-Tag.

Conflict of interest

The authors declare that the research was conducted in the absence of any commercial or financial relationships that could be construed as a potential conflict of interest.

Publisher's note

Supplementary material

The Supplementary material for this article can be found online at: https://www.frontiersin.org/articles/10.3389/fmicb.2023.1139276/full#supplementary-material

References

Baffert, C., Kpebe, A., Avilan, L., and Brugna, M. (2019). Hydrogenases and H_2 metabolism in sulfate-reducing bacteria of the *Desulfovibrio genus*. *Adv. Microb. Physiol.* 74, 143–189. doi: 10.1016/bs.ampbs.2019.03.001

Bryant, M. P., Campbell, L. L., Reddy, C. A., and Crabill, M. R. (1977). Growth of *Desulfovibrio* in lactate or ethanol media low in sulfate in association with H_2-utilizing methanogenic bacteria. *Appl. Environ. Microbiol.* 33, 1162–1169. doi: 10.1128/aem.33.5.1162-1169.1977

Buckel, W., and Thauer, R. K. (2018a). Flavin-based electron bifurcation, a new mechanism of biological energy coupling. *Chem Rev* 118, 3862–3886. doi: 10.1021/acs.chemrev.7b00707

Buckel, W., and Thauer, R. K. (2018b). Flavin-based electron bifurcation, ferredoxin, flavodoxin, and anaerobic respiration with protons (Ech) or NAD(+) (Rnf) as electron acceptors: A historical review. *Front. Microbiol.* 9:401. doi: 10.3389/fmicb.2018.00401

Caffrey, S. M., Park, H. S., Voordouw, J. K., He, Z., Zhou, J., and Voordouw, G. (2007). Function of periplasmic hydrogenases in the sulfate-reducing bacterium *Desulfovibrio vulgaris* Hildenborough. *J. Bacteriol.* 189, 6159–6167. doi: 10.1128/JB.00747-07

Casalot, L., De Luca, G., Dermoun, Z., Rousset, M., and de Philip, P. (2002a). Evidence for a fourth hydrogenase in *Desulfovibrio fructosovorans*. *J. Bacteriol.* 184, 853–856. doi: 10.1128/JB.184.3.853-856.2002

Casalot, L., Valette, O., De Luca, G., Dermoun, Z., Rousset, M., and de Philip, P. (2002b). Construction and physiological studies of hydrogenase depleted mutants of *Desulfovibrio fructosovorans*. *FEMS Microbiol. Lett.* 214, 107–112. doi: 10.1111/j.1574-6968.2002.tb11332.x

Fauque, G., Peck, H. D. Jr., Moura, J. J., Huynh, B. H., Berlier, Y., DerVartanian, D. V., et al. (1988). The three classes of hydrogenases from sulfate-reducing bacteria of the genus *Desulfovibrio*. *FEMS Microbiol. Rev.* 4, 299–344. doi: 10.1111/j.1574-6968.1988.tb02748.x

Fiévet, A., My, L., Cascales, E., Ansaldi, M., Pauleta, S. R., Moura, I., et al. (2011). The anaerobe-specific orange protein complex of *Desulfovibrio vulgaris* Hildenborough is encoded by two divergent operons coregulated by σ54 and a cognate transcriptional regulator. *J. Bacteriol.* 193, 3207–3219. doi: 10.1128/JB.00044-11

Furlan, C., Chongdar, N., Gupta, P., Lubitz, W., Ogata, H., Blaza, J. N., et al. (2022). Structural insight on the mechanism of an electron-bifurcating [FeFe] hydrogenase. *elife* 11:e79361. doi: 10.7554/eLife.79361

Gauquelin, C., Baffert, C., Richaud, P., Kamionka, E., Etienne, E., Guieysse, D., et al. (2018). Roles of the F-domain in [FeFe] hydrogenase. *Biochim. Biophys. Acta* 1859, 69–77. doi: 10.1016/j.bbabio.2017.08.010

Gérard, C., Lebrun, R., Lemesle, E., Avilan, L., Chang, K. S., Jin, E., et al. (2022). Reduction in Phosphoribulokinase amount and re-routing metabolism in *Chlamydomonas reinhardtii* CP12 mutants. *Int. J. Mol. Sci.* 23:2710. doi: 10.3390/ijms23052710

Greening, C., Biswas, A., Carere, C. R., Jackson, C. J., Taylor, M. C., Stott, M. B., et al. (2016). Genomic and metagenomic surveys of hydrogenase distribution indicate H_2 is a widely utilised energy source for microbial growth and survival. *ISME J.* 10, 761–777. doi: 10.1038/ismej.2015.153

Greening, C., Geier, R., Wang, C., Woods, L. C., Morales, S. E., McDonald, M. J., et al. (2019). Diverse hydrogen production and consumption pathways influence methane production in ruminants. *ISME J.* 13, 2617–2632. doi: 10.1038/s41396-019-0464-2

Haveman, S. A., Brunelle, V., Voordouw, J. K., Voordouw, G., Heidelberg, J. F., and Rabus, R. (2003). Gene expression analysis of energy metabolism mutants of *Desulfovibrio vulgaris* Hildenborough indicates an important role for alcohol dehydrogenase. *J. Bacteriol.* 185, 4345–4353. doi: 10.1128/JB.185.15.4345-4353.2003

Jacq-Bailly, A., Benvenuti, M., Payne, N., Kpebe, A., Felbek, C., Fourmond, V., et al. (2020). Electrochemical characterization of a complex FeFe hydrogenase, the electron-bifurcating Hnd from *Desulfovibrio fructosovorans*. *Front. Chem.* 8:573305. doi: 10.3389/fchem.2020.573305

Kaster, A. K., Moll, J., Parey, K., and Thauer, R. K. (2011). Coupling of ferredoxin and heterodisulfide reduction via electron bifurcation in hydrogenotrophic methanogenic archaea. *Proc. Natl. Acad. Sci. U. S. A.* 108, 2981–2986. doi: 10.1073/pnas.1016761108

Katsyv, A., Kumar, A., Saura, P., Pöverlein, M. C., Freibert, S. A., T Stripp, S., et al. (2023). Molecular basis of the electron bifurcation mechanism in the [FeFe]-hydrogenase complex HydABC. *J. Am. Chem. Soc.* 145, 5696–5709 doi: 10.1021/jacs.2c11683

Keller, K. L., and Wall, J. D. (2011). Genetics and molecular biology of the electron flow for sulfate respiration in *Desulfovibrio*. *Front. Microbiol.* 2:135. doi: 10.3389/fmicb.2011.00135

Kpebe, A., Benvenuti, M., Guendon, C., Rebai, A., Fernandez, V., le Laz, S., et al. (2018). A new mechanistic model for an O_2-protected electron-bifurcating hydrogenase, Hnd from *Desulfovibrio fructosovorans*. *Biochim. Biophys. Acta Bioenerg.* 1859, 1302–1312. doi: 10.1016/j.bbabio.2018.09.364

Lupton, F. S., Conrad, R., and Zeikus, J. G. (1984). Physiological function of hydrogen metabolism during growth of sulfidogenic bacteria on organic substrates. *J. Bacteriol.* 159, 843–849. doi: 10.1128/jb.159.3.843-849.1984

Malki, S., De Luca, G., Fardeau, M. L., Rousset, M., Belaich, J. P., and Dermoun, Z. (1997). Physiological characteristics and growth behavior of single and double hydrogenase mutants of *Desulfovibrio fructosovorans*. *Arch. Microbiol.* 167, 38–45. doi: 10.1007/s002030050414

Malki, S., Saimmaime, I., De Luca, G., Rousset, M., Dermoun, Z., and Belaich, J. P. (1995). Characterization of an operon encoding an NADP-reducing hydrogenase in *Desulfovibrio fructosovorans*. *J. Bacteriol.* 177, 2628–2636. doi: 10.1128/jb.177.10.2628-2636.1995

Morais-Silva, F. O., Santos, C. I., Rodrigues, R., Pereira, I. A., and Rodrigues-Pousada, C. (2013). Roles of HynAB and Ech, the only two hydrogenases found in the model sulfate reducer *Desulfovibrio gigas*. *J. Bacteriol.* 195, 4753–4760. doi: 10.1128/JB.00411-13

Noguera, D. R., Brusseau, G. A., Rittmann, B. E., and Stahl, D. A. (1998). A unified model describing the role of hydrogen in the growth of *Desulfovibrio vulgaris* under different environmental conditions. *Biotechnol. Bioeng.* 59, 732–746. doi: 10.1002/(SICI)1097-0290(19980920)59:6<732::AID-BIT10>3.0.CO;2-7

Odom, J. M., and Peck, H. D. Jr. (1981). Hydrogen cycling as a general mechanism for energy coupling in the sulfate-reducing bacteria, *Desulfovibrio* sp. *FEMS Microb. Lett.* 12, 47–50. doi: 10.1111/j.1574-6968.1981.tb07609.x

Ollivier, B., Cord-Ruwisch, R., Hatchikian, E. C., and Garcia, J. L. (1988). Characterization of *Desulfovibrio fructosovorans* sp. nov. *Arch. Microbiol.* 149, 447–450. doi: 10.1007/BF00425586

Payne, N., Kpebe, A., Guendon, C., Baffert, C., Maillot, M., Haurogné, T., et al. (2023). NMR-based metabolomic analysis of the physiological role of the electron-bifurcating FeFe hydrogenase Hnd in *Solidesulfovibrio fructosivorans* under pyruvate fermentation. *Microbiol. Res.* 268:127279. doi: 10.1016/j.micres.2022.127279

Payne, N., Kpebe, A., Guendon, C., Baffert, C., Ros, J., Lebrun, R., et al. (2022). The electron-bifurcating FeFe-hydrogenase Hnd is involved in ethanol metabolism in *Desulfovibrio fructosovorans* grown on pyruvate. *Mol. Microbiol.* 117, 907–920. doi: 10.1111/mmi.14881

Rabus, R., Hansen, T. A., and Widdel, F. (2013). "Dssimilatory sulfate- and sulfur-reducing prokaryotes" in *The prokaryotes*. eds. E. Rosenberg, E. F. DeLong, S. Lory, E. Stackebrandt and F. Thompson (Berlin: Springer), 309–404.

Ramos, A. R., Grein, F., Oliveira, G. P., Venceslau, S. S., Keller, K. L., Wall, J. D., et al. (2015). The FlxABCD-HdrABC proteins correspond to a novel NADH dehydrogenase/heterodisulfide reductase widespread in anaerobic bacteria and involved in ethanol metabolism in *Desulfovibrio vulgaris* Hildenborough. *Environ. Microbiol.* 17, 2288–2305. doi: 10.1111/1462-2920.12689

Rousset, M., Dermoun, Z., Chippaux, M., and Belaich, J. P. (1991). Marker exchange mutagenesis of the hydN genes in *Desulfovibrio fructosovorans*. *Mol. Microbiol.* 5, 1735–1740. doi: 10.1111/j.1365-2958.1991.tb01922.x

Schuchmann, K., and Müller, V. (2012). A bacterial electron-bifurcating hydrogenase. *J. Biol. Chem.* 287, 31165–31171. doi: 10.1074/jbc.M112.395038

Schut, G. J., and Adams, M. W. (2009). The iron-hydrogenase of *Thermotoga maritima* utilizes ferredoxin and NADH synergistically: A new perspective on anaerobic hydrogen production. *J. Bacteriol.* 191, 4451–4457. doi: 10.1128/JB.01582-08

Sim, M. S., Wang, D. T., Zane, G. M., Wall, J. D., Bosak, T., and Ono, S. (2013). Fractionation of sulfur isotopes by *Desulfovibrio vulgaris* mutants lacking hydrogenases or type I tetraheme cytochrome c_3. *Front. Microbiol.* 4:171. doi: 10.3389/fmicb.2013.00171

Thauer, R. K., Kaster, A. K., Seedorf, H., Buckel, W., and Hedderich, R. (2008). Methanogenic archaea: Ecologically relevant differences in energy conservation. *Nat. Rev. Microbiol.* 6, 579–591. doi: 10.1038/nrmicro1931

Thauer, R. K., Stackebrandt, E., and Hamilton, W. A. (2007). "Energy metabolism and phylogenetic diversity of sulphate-reducing bacteria" in *Sulphate-reducing bacteria environmental and engineered systems*. eds. L. L. Barton and W. A. Hamilton (New York, NY: Cambridge University Press), 1–37.

Wagner, T., Koch, J., Ermler, U., and Shima, S. (2017). Methanogenic heterodisulfide reductase (HdrABC-MvhAGD) uses two noncubane [4Fe-4S] clusters for reduction. *Science* 357, 699–703. doi: 10.1126/science.aan0425

Waite, D. W., Chuvochina, M., Pelikan, C., Parks, D. H., Yilmaz, P., Wagner, M., et al. (2020). Proposal to reclassify the proteobacterial classes *Deltaproteobacteria* and Oligoflexia, and the phylum *Thermodesulfobacteria* into four phyla reflecting major functional capabilities. *Int. J. Syst. Evol. Microbiol.* 70, 5972–6016. doi: 10.1099/ijsem.0.004213

Wang, S., Huang, H., Kahnt, J., and Thauer, R. K. (2013). A reversible electron-bifurcating ferredoxin- and NAD-dependent [FeFe]-hydrogenase (HydABC) in *Moorella thermoacetica*. *J. Bacteriol.* 195, 1267–1275. doi: 10.1128/JB.02158-12

Zheng, Y., Kahnt, J., Kwon, I. H., Mackie, R. I., and Thauer, R. K. (2014). Hydrogen formation and its regulation in *Ruminococcus albus*: Involvement of an electron-bifurcating [FeFe]-hydrogenase, of a non-electron-bifurcating [FeFe]-hydrogenase, and of a putative hydrogen-sensing [FeFe]-hydrogenase. *J. Bacteriol.* 196, 3840–3852. doi: 10.1128/JB.02070-14

Zheng, S., Li, M., Liu, Y., and Liu, F. (2021). *Desulfovibrio* feeding *Methanobacterium* with electrons in conductive methanogenic aggregates from coastal zones. *Water Res.* 202:117490. doi: 10.1016/j.watres.2021.117490

frontiers | Frontiers in Microbiology

TYPE Review
PUBLISHED 12 July 2023
DOI 10.3389/fmicb.2023.1179607

OPEN ACCESS

EDITED BY
Stefan Frielingsdorf,
Technical University of Berlin, Germany

REVIEWED BY
Francesca Valetti,
University of Turin, Italy
Jens Appel,
University of Kassel, Germany

*CORRESPONDENCE
Peter Lindblad
✉ peter.lindblad@kemi.uu.se
Gustav Berggren
✉ gustav.berggren@kemi.uu.se

†These authors share first authorship

RECEIVED 04 March 2023
ACCEPTED 09 June 2023
PUBLISHED 12 July 2023

CITATION
Schumann C, Fernández Méndez J, Berggren G and Lindblad P (2023) Novel concepts and engineering strategies for heterologous expression of efficient hydrogenases in photosynthetic microorganisms.
Front. Microbiol. 14:1179607.
doi: 10.3389/fmicb.2023.1179607

Novel concepts and engineering strategies for heterologous expression of efficient hydrogenases in photosynthetic microorganisms

Conrad Schumann[1†], Jorge Fernández Méndez[2†], Gustav Berggren[1*] and Peter Lindblad[2*]

[1]Molecular Biomimetics, Department of Chemistry - Ångström, Uppsala University, Uppsala, Sweden, [2]Microbial Chemistry, Department of Chemistry - Ångström, Uppsala University, Uppsala, Sweden

Hydrogen is considered one of the key enablers of the transition towards a sustainable and net-zero carbon economy. When produced from renewable sources, hydrogen can be used as a clean and carbon-free energy carrier, as well as improve the sustainability of a wide range of industrial processes. Photobiological hydrogen production is considered one of the most promising technologies, avoiding the need for renewable electricity and rare earth metal elements, the demands for which are greatly increasing due to the current simultaneous electrification and decarbonization goals. Photobiological hydrogen production employs photosynthetic microorganisms to harvest solar energy and split water into molecular oxygen and hydrogen gas, unlocking the long-pursued target of solar energy storage. However, photobiological hydrogen production has to-date been constrained by several limitations. This review aims to discuss the current state-of-the art regarding hydrogenase-driven photobiological hydrogen production. Emphasis is placed on engineering strategies for the expression of improved, non-native, hydrogenases or photosynthesis re-engineering, as well as their combination as one of the most promising pathways to develop viable large-scale hydrogen green cell factories. Herein we provide an overview of the current knowledge and technological gaps curbing the development of photobiological hydrogenase-driven hydrogen production, as well as summarizing the recent advances and future prospects regarding the expression of non-native hydrogenases in cyanobacteria and green algae with an emphasis on [FeFe] hydrogenases.

KEYWORDS

photobiological hydrogen, [FeFe] hydrogenases, [NiFe] hydrogenases, cyanobacteria, green algae, heterologous expression, genetic engineering, photosynthesis

1. Introduction

Sunlight is the most abundant and widespread energy source around the globe. Every year the sun irradiates Earth's surface with more than 7,000 times the current global energy consumption. On average 173 PW of energy strikes Earth's surface at any time, providing a virtually unlimited energy source that can be harvested locally. The conversion of solar energy into chemical energy, e.g., in the form of hydrogen (H_2), greatly facilitates storage, distribution

and applicability in a wide-range of settings. Presently H_2 is mainly produced via steam reforming (yielding so-called "grey" hydrogen), but truly fossil-free hydrogen production is increasing. Current fossil-free processes rely on electrolyzers driven by carbon-free electricity. Albeit efficient these technologies feature several limitations, e.g., high demand of electricity and scarce rare earth metals requirements. Renewable energies (which can yield green and yellow hydrogen) have become cost-competitive and their expected growth trends are astonishing [estimated annual growth rates of 8.4% for renewables (Novus-Light-Technologies, 2023)] during the next decade. Similarly, nuclear power (pink hydrogen) is expected to increase by 5.7% (Bussiness-Research-Company, 2023) in the same time period. Still, electricity demands are expected to increase significantly, up to 50%, during the electrification process towards a net-zero carbon emissions economy (IEA, 2021; Exxon-Mobil, 2022). It follows that electrochemical hydrogen production is likely to be limited to contexts where there is a frequent surplus of clean electricity generation. Consequently, novel hydrogen production technologies are required for global large-scale production, ideally integrated within other industrially relevant processes.

Biotechnological hydrogen gas production provides an inexpensive and scalable alternative technology for H_2 production. Indeed, our drive towards a hydrogen society is pre-dated by evolution, which has developed an efficient hydrogen economy involving biological machineries capable of hydrogen production without the requirement of rare-earth metals and avoiding heavy electricity consumption. Waste-to-hydrogen has been intensively explored as a sustainable alternative to conventional hydrogen production from fossil fuels. However, the demand of high-cost pre-treatment methods, the use of inconsistent feedstock as well as low energy conversion efficiencies are noteworthy constrictions of this technology (Lui et al., 2020). Also, the competition with well-established biogas production processes and the overall reduced energy content in waste limits its application for large-scale H2 production. Instead, oxygenic photosynthetic organisms stand out as ideal platforms for biological H_2 production as they are capable of direct solar-to-hydrogen (STH) energy conversion.

Cyanobacteria and green algae exhibit biological features that make them highly suitable for the engineering of hydrogenase based STH systems. They feature a highly specialized light harvesting machinery coupled to a complex photosynthetic electron transport chain (PETC). Briefly, protons (H^+) and electrons are extracted from the water splitting reaction at photosystem II (PSII). Subsequently, H^+ reduction to hydrogen can be performed by redirecting the high potential electrons via the PETC towards photosystem I (PSI) and then transferring them to a hydrogenase. Indeed, most cyanobacteria and green algae feature at least one native hydrogenase and certain strains are capable of native hydrogen production under specific conditions. Commonly, hydrogenases in cyanobacteria are used as a mechanism to recover energy from the H_2 produced as a byproduct of nitrogenase in nitrogen fixing strains (uptake hydrogenases). Additionally, hydrogenases also act as photoprotective electron valves during periods when metabolic electron sinks are inactive or cannot cope with a sudden increase in the reducing power supplied from photosynthetic apparatus (bidirectional hydrogenases). Important differences between both organisms are found in the light harvesting systems and internal cellular organization. While eukaryotic green algae harbor light harvesting complexes similar to plants, cyanobacteria are prokaryotes and feature phycobilisomes containing specific light harvesting phycobiliproteins not present in green algae. Still, both exhibit photosynthetic efficiencies and biomass production rates significantly higher than any plants. Previous reviews (Khanna and Lindblad, 2015; Kosourov et al., 2021; Touloupakis et al., 2021; Li et al., 2022; Redding et al., 2022) provide a broad picture of the STH paradigm, reviewing the most relevant photobiological H_2 production strategies reported to date.

Photobiological H_2 production can occur via two main mechanisms, employing either nitrogenases or hydrogenases. The former relies in co-occurring H_2 production during N_2-fixation. Moreover, nitrogenase H_2 production requires both ATP and reducing equivalents. Therefore, the maximum efficiency of nitrogenases is significantly lower than hydrogenase-based systems, which only require reducing equivalents from a compatible electron donor. Additionally, some hydrogenases have turnover numbers up to 1,000-fold greater than those of nitrogenases (Hallenbeck and Benemann, 2002). Thus, hydrogenases are undoubtedly better catalysts for the purpose of biotechnological STH conversion owing to its higher catalytic rates and more efficient energy utilization. Historically, hydrogenase derived H_2 production has attracted less attention due to a range of limitations, including the bidirectional nature and catalytic bias of the enzymes, and an apparent trade-off between turnover rates and O_2 tolerance. These perceived issues, in combination with an earlier lack of tools for extensive engineering of photosynthetic organisms and limited information about hydrogenase structure(s) and mechanism(s) has hindered the development of hydrogenase-driven STH production. However, during the last years, a number of multiple factors has unlocked the possibility of further development of hydrogenase based photobiological H_2 production.

Firstly, a deeper understanding of structural and functional principles of hydrogenases has been obtained. In addition, several novel hydrogenases have been discovered or engineered, exhibiting highly interesting features for biotechnological utilization. Secondly, a wider understanding of photosynthetic metabolism, cell physiology and regulation has been acquired during the last decades, enabling the development of more sophisticated genetic engineering and synthetic biology tools. In combination with a growing interest in photosynthetic microorganisms within the scientific community and industry, this has unlocked the possibility to further engineer photosynthetic organisms for photobiological hydrogenase-driven H_2 production. Current electrochemical STH technologies, feature energy conversion efficiencies ranging between 10 and 20% and production costs about 6 to 8 € · kg H_2^{-1} (Grimm et al., 2020). Maximum theoretical estimations for non-engineered photobiological hydrogen production indicate that efficiencies close to 10% could be achieved, being on-par with current electrochemical technologies (Kruse et al., 2005). We expect that further developments combining the different strategies summarized here will allow a dramatic increase of efficiency relative to current approaches. Depending on the obtainable STH conversion efficiencies and further bioprocess design, our production costs estimations may be as low as 5 € · kg H_2^{-1}, making photobiological H_2 production potentially cheaper than current STH electrochemical methods.

In the present review we provide a summary of the, in our opinion, most relevant achievements in the context of hydrogenase-based photobiological H_2 production systems, highlighting how these

efforts are bringing us closer towards the development of cost-effective photobiological hydrogen production technologies.

2. Hydrogenases overview

2.1. Hydrogenases for photosynthesis-coupled hydrogen production

Hydrogenases are an evolutionary convergent enzyme family of oxidoreductases that catalyze the reduction of protons into dihydrogen as well as the reverse oxidation of dihydrogen into two protons and two electrons. They are found in all domains of life, predominately present in Archaea and Bacteria and rarely in Eukarya (Vignais and Billoud, 2007; Greening et al., 2016). Hydrogenases are classified into [NiFe], [FeFe], and [Fe] hydrogenases based on their unique organometallic cofactors that facilitate reversible redox reactions (Lubitz et al., 2014; Berggren et al., 2022). [Fe] hydrogenases show comparably low catalytic rates and differ substantially from [NiFe] and [FeFe] hydrogenases in their reaction mechanism and substrates (Vogt et al., 2008). Therefore, they are not considered suitable for a photosynthesis-coupled hydrogen production and will not be discussed further. [NiFe] and [FeFe] hydrogenases on the other hand can achieve hydrogen turnover *in vivo* by using ferredoxin and NAD(P)H/NAD(P)$^+$ (among others) as redox partner which are closely linked to PSI and the photosynthetic machinery (Appel et al., 2020; Lupacchini et al., 2021) However, we note that the they are extremely diverse enzyme families, reflecting large variations in activity between different hydrogenases (Land et al., 2020; Berggren et al., 2022).

Efficient (photo-)biological hydrogen production is dependent on successful expression of active and robust hydrogenases. The oxygen (O_2) sensitivity of most [NiFe] and [FeFe] hydrogenases represent a particular challenge for coupling *in vivo* hydrogen production to the photosynthetic electron transport, as PS II produces molecular oxygen during the water oxidation. There are critical differences between hydrogenases in their reactivity towards O_2, but the terminology of oxygen tolerance and oxygen sensitivity can lead to misconceptions.

In the following, we will distinguish between oxygen-sensitive and oxygen-insensitive hydrogenases. Oxygen-insensitive enzymes are defined as functional under atmospheric oxygen concentration. Conversely, oxygen-sensitive hydrogenases are inhibited by oxygen, but can be further subdivided into oxygen-sensitive tolerant and oxygen-sensitive intolerant hydrogenases based on the reversibility of their oxygen-induced inhibition. It should be noted that these definitions are different as compared to the general hydrogenase literature, where the term O_2 tolerant is commonly used to describe what we would refer to as O_2 insensitive hydrogenases (see, e.g., Lubitz et al., 2014). Most [NiFe] hydrogenases reported to-date are oxygen-sensitive tolerant enzymes, i.e., they display reversible oxygen-induced inhibition. A few [NiFe] hydrogenases even stand out as oxygen-insensitive as their function under atmospheric oxygen concentrations is not impaired (Buhrke et al., 2005; Leroux et al., 2008; Liebgott et al., 2010; Schäfer et al., 2013; Grinter et al., 2023). In contrast, the majority of [FeFe] hydrogenases are oxygen-sensitive intolerant enzymes as the active site is irreversibly damaged when exposed to trace amounts of oxygen. Still, there are also reports of oxygen-sensitive tolerant [FeFe] hydrogenases (Morra et al., 2016; Corrigan et al., 2020; Winkler et al., 2021). Within these broad classifications, the kinetics of the inactivation and reactivation vary between enzymes (see for example Cracknell et al., 2008; Goldet et al., 2009; Lukey et al., 2011; Kubas et al., 2017; Koo and Swartz, 2018).

Most [NiFe] hydrogenases are dimeric enzymes, consisting of a "small" and a "large" subunit of which the latter one contains the active site with the catalytic [NiFe] cofactor. The small subunit harbors usually a chain of three FeS-clusters, denoted as proximal, medial and distal depending on their relative position to the [NiFe] active site, which ensures electron transport between protein surface and NiFe center. The medial cluster is often [3Fe-4S] while the proximal and distal clusters are [4Fe-4S] (Volbeda et al., 1995, 1996). Exceptions to this FeS-cluster arrangement have been observed, and include the soluble bidirectional cytoplasmatic [NiFe] hydrogenases found in different aerobic microorganisms such as the HoxFUYH complex from *Synechocystis* PCC 6803. The NAD(P)$^+$-reducing [NiFe] hydrogenase HoxFUYH is a multi-subunit complex with HoxH as catalytic (or "large") subunit. The accessory subunits HoxFUY build a complex electron relay where HoxY serves as the immediate electron transfer partner of HoxH, and can be considered equivalent to the small subunit, but features only a single [4Fe-4S] cluster (Carrieri et al., 2011). Other reported exceptions with changes to the electron relay clusters have been shown to influence oxygen tolerance and catalytic bias as further outlined below. [FeFe] hydrogenases often show substantially higher turnover rates than [NiFe] hydrogenases at the expense of being irreversibly inactivated by trace amounts of molecular oxygen (Goldet et al., 2009). [FeFe] hydrogenases are generally functional as monomers but can consist of several domains (Calusinska et al., 2010; Land et al., 2020). The H-domain is essential for the function as it contains the active site (H-cluster) which comprises a canonical [4Fe-4S] cluster ($[4Fe\text{-}4S]_H$) that is linked to the di-iron metal center via a bridging cysteine. [FeFe] hydrogenases commonly carry additional domains with FeS-clusters in the N- or C-terminus of the H-domain (Meyer, 2007). The modularity of these so-called F-domains ensures that they can provide the enzyme with different functions, e.g., ensuring efficient intra- or intermolecular electron transport between the highly conserved active site and redox partners (Gauquelin et al., 2018).

Even though [NiFe] and [FeFe] hydrogenases are not evolutionary related, they share certain key characteristics among their active sites. Both catalytic cofactors are dinuclear, and the metal ions bridged by thiol ligands. In the case of [NiFe] the thiols are derived from cysteine, while [FeFe] hydrogenases are dependent on a 2-aza-propane-dithiolate (adt) ligand that bridges the di-iron metal center. Furthermore, both feature Fe ions ligated by carbon monoxide and cyanide. These strong field ligands keep the Fe ions in a low-spin and low valent state, which enables the heterolytic splitting of H_2 or the dihydrogen formation. Considering their unique structures, the assembly and introduction of these organometallic active site cofactors unsurprisingly depend on hydrogenase-type specific maturation enzymes (Lubitz et al., 2014). Cyanobacteria express natively one or two [NiFe] hydrogenases, which either serve as sink for excess electrons from photosynthesis or are closely linked to the hydrogen uptake for nitrogenase activity. They rely on the expression of at least six [NiFe] cofactor maturation enzymes (HypABCDEF) which have been identified in *E. coli* but are known to be existent in all organisms that express [NiFe] hydrogenases. [FeFe] hydrogenases on the other

side are not present in any known cyanobacterial organism. So far [FeFe] hydrogenases and their specific cofactor maturation enzymes (HydEFG) have been exclusively found in algal organisms and non-cyanobacterial prokaryotes (Böck et al., 2006; Khanna and Lindblad, 2015). Consequently, heterologously expressed hydrogenases are only functional if either the expression host expresses natively the specific maturation enzymes or the maturation machinery is co-expressed (King et al., 2006; Wegelius et al., 2021). It was recently shown that maturation enzymes of [FeFe] hydrogenases require an additional auxiliary pathway providing a co-substrate, a glycine cleavage system generating methylated lipoyl-H-protein (Pagnier et al., 2022). However, this co-substrate may usually be regenerated by the native host metabolism.

2.2. Engineering of [Fe-Fe] hydrogenases

Several different approaches have been explored to achieve a photosynthesis-coupled hydrogen production. In the most cases, the work focused on coupling hydrogenases to electron carriers or PSI itself. Even though the high catalytic rates of [FeFe] hydrogenases exhibit a considerable potential for such applications the oxygen sensitivity and the irreversible inactivation are major obstacles as mentioned above. Therefore, it is necessary to explore possible ways to create oxygen-insensitive [FeFe] hydrogenases.

In the case of [NiFe] hydrogenases evolution has provided a number of different features identified to provide oxygen tolerance. Primarily these protection strategies appear to focus on the controlled reduction of O_2 to avoid reactive oxygen species (ROS) and/or limiting gas access to the O_2-sensitive active-site. These features could be considered for the generation of oxygen-insensitive [FeFe] hydrogenase. For several membrane bound oxygen-insensitive (originally referred as oxygen tolerant) [NiFe] hydrogenases an altered FeS cluster has been reported proximal to the di-nuclear metal center. This proximal [4Fe-3S]-6Cys cluster enables the oxygen-insensitive [NiFe] hydrogenases to rapidly transfer two electrons to the active site, ensuring detoxification of O_2 through reduction to water (Ogata et al., 2016). However, such an alteration of the [FeFe] active site is likely challenging as the proximal $[4Fe\text{-}4S]_H$-cluster is directly involved in the catalytic cycle. However, there are reports of F-clusters improving O_2 tolerance (Kubas et al., 2017). Still, we note that any protection mechanism depending on reduction of O_2 will result in loss of electrons towards unproductive process. Several studies also explored oxygen tolerance achieved by limiting mass transfer through the putative gas channels (Buhrke et al., 2005; Leroux et al., 2008; Liebgott et al., 2010). Buhrke et al. reported that in the H_2-sensing [NiFe] hydrogenase RH from *Ralstonia eutropha* bulky hydrophobic residues restrict the diffusion of molecular oxygen to the active site. A recent striking example of this mechanism at play is provided by the Huc hydrogenase from *Mycobacterium smegmatis*, which is capable of performing H_2 oxidation under fully aerobic conditions (Grinter et al., 2023). Molecular dynamics experiments of [FeFe] hydrogenases suggested that O_2 can only diffuse through hydrophobic gas channels whereas H_2 can also diffuse freely through temporary cavities in the flexible protein structure (Cohen et al., 2005). However, engineering approaches which aimed at modulating the gas transfer through the assumed main gas channel have not been successful so far (Lautier et al., 2011). Furthermore, a complete obstruction of the gas channels in [FeFe] hydrogenases is also not assumed beneficial, as the build-up of H_2 accumulation in the active site can inhibit the H_2 production (Fourmond et al., 2013).

The main protection mechanism against O_2-induced degradation of the [FeFe] hydrogenase cofactor identified to-date involves binding of thiol ligands at the open Fe-coordination site involved in catalysis. For sulphate-reducing bacteria *Desulfovibrio desulfuricans* and *Desulfovibrio vulgaris* Hildenborough, and their respective [FeFe] hydrogenases *Dd*HydAB and *Dv*HydAB, it has been shown that an extrinsic sulfide group can coordinate the substrate binding site. This protected state of the active site causes reversible inactivation but also oxygen-sensitve tolerant characteristics (Roseboom et al., 2006). Chemical treatments of purified [FeFe] hydrogenases with NaS_2 can induce this state *in vitro* under oxidizing conditions (Rodríguez-Maciá et al., 2018). More recently, a similar effect was reported through the binding of exogenous cyanide (Martini et al., 2023). However, in contrast to thiols, cyanide binding appears irreversible thus also causing inactivation of the enzyme. Up to now only one intrinsically oxygen-sensitive tolerant [FeFe] hydrogenase from *Clostridium beijerinckii* (*Cb*A5H/*Cb*HydA1) has been identified and characterized by Morra et al. (2016). An active site neighboring cysteine enables a reversible inactivation of the [FeFe] hydrogenases by coordinating the substrate binding site of the H-cluster with its thiol sidechain (Corrigan et al., 2020; Winkler et al., 2021). This coordination prevents the reduction of O_2 at the H-cluster and therefore also the formation of reactive oxygen species that could irreversibly damage the active site cofactor. Winkler et al. also reported that the interaction of individual distant residues around the loop region of the protective cysteine are crucial for an oxygen-protective conformation. In another recent study it was shown that one amino acid exchange on the surface of *Cb*HydA1 can modulate the transition rates between the inactivated and oxygen-sensitive state (Rutz et al., 2023). With the above-mentioned findings it stands out that protein engineering of characterized [FeFe] hydrogenases is of significant importance to develop more robust hydrogen-producing biocatalysts. In parallel, the identification and characterization of new [FeFe] hydrogenases are needed to explore more beneficial properties such as oxygen sensitivity (Morra, 2022).

Another aspect to consider when using hydrogenases is that they are bidirectional catalysts. However, the activity can be influenced by many parameters, and often the enzymes show a preference for either hydrogen production or oxidation. This kinetic discrepancy between the forward and reverse reaction is referred to as "catalytic bias." Amino acid side chains in the first coordination sphere of the organometallic cofactor can influence the catalytic bias (Land et al., 2020). Additionally, when present, the FeS clusters in the F-domains of [FeFe] hydrogenase have been shown to introduce a strong catalytic bias (Pandey et al., 2017; Birrell et al., 2021).

3. Improving photobiological H_2 production. Non-native hydrogenases and photosynthesis re-engineering in oxygenic photosynthetic microorganisms

Engineering efforts towards efficient photobiological H_2 production has focused into two main complementary paths. First,

removing native hydrogenases capable of H_2 uptake and optimizing the hydrogenase as the key component of the H_2 production system. In this context, heterologous, chimeric, or fully synthetic hydrogenases with improved features are over-expressed as a way to enhance hydrogen production. Importantly, enzyme expression also needs to be at high levels, as it has been documented that hydrogen production correlates with the abundance of active hydrogenase enzyme *in vivo* (Weiner et al., 2018). Secondly, significant efforts have been devoted at re-engineering different sub-systems within the complex bioenergetic machinery of PETC and/or light harvesting systems, aiming to enhance the overall electron supply and efficiently channel it towards the expressed hydrogenase.

3.1. Expression of non-native hydrogenases in cyanobacteria

During the last decades a deep understanding of cyanobacterial physiology has been acquired, giving rise to the development of an expanding synthetic biology toolbox for sophisticated strain engineering. These factors in combination with its generally faster growth rates, more flexible light harvesting machinery and engineering simplicity when compared to green algae makes them a very promising platform for developing highly efficient green cell H_2 producing factories. Table 1 provides a summary of achievements on H_2 production when expressing non-native hydrogenases in oxygenic photosynthetic microorganisms.

3.1.1. Expression and activation of [FeFe] hydrogenases in cyanobacteria

[FeFe] hydrogenases have been widely considered the most active and promising group for hydrogenase-catalyzed H_2 production. Unfortunately, cyanobacteria do not feature native [FeFe] hydrogenases, neither the maturation machinery required for its activation. This limitation has been overcome by the co-expression of an [FeFe] hydrogenase together with its maturation machinery (HydEFG). An [FeFe] hydrogenase from *Clostridium acetobutylicum* (HydA1) together with the HydEF and HydG maturation machinery from *Chlamydomonas reinhardtii* were introduced and expressed in the non-N_2-fixing unicellular cyanobacterium *Synechococcus elongatus* PCC 7942 (Ducat et al., 2011). The introduced enzyme showed an *in vivo* hydrogenase activity which connected to the light-dependent reactions of PETC under anoxic conditions. The heterologous hydrogenase supported limited growth in light using H_2 as the sole source of reducing equivalents. Moreover, the importance of adequate coupling between the non-native hydrogenases and the native electron carriers was noted, where an expression of a non-native ferredoxin improved the H_2 production. Comparably, the native [FeFe] hydrogenase operon from the bacterium *Shewanella oneidensis* MR-1 was expressed in heterocysts of the filamentous cyanobacterium *Nostoc* PCC 7120, leading to the assembly of an active enzyme (Gärtner et al., 2012). In a similar fashion, the native maturation machinery and of hydrogenase HydA of *Clostridium acetobutylicum* has been reported to yield an active [FeFe] hydrogenase in *Nostoc* PCC 7120 using the heterocyst specific *nifH* promoter. Furthermore, by co-expressing a GlbN cyanoglobin from *Nostoc commune* to decrease the oxygen levels, *in vivo* H_2 production was observed concomitantly with oxygenic photosynthesis in the vegetative cells of the filaments (Avilan et al., 2018). Earlier reports of active [FeFe] hydrogenases in cyanobacteria without the introduction of the specific [FeFe] hydrogenase maturation machinery (Asada et al., 2000; Berto et al., 2011) requires further confirmations.

However, it is possible to circumvent the biological maturation of [FeFe] hydrogenase by using a semi-synthetic activation approach. This procedure consists on the heterologous expression of the inactive [FeFe] apo-hydrogenase in living cells, followed by subsequent incubation with a synthetic $[2Fe]_H$ subcluster mimics, leading to the formation of an active H-cluster and rendering a mature holo-[FeFe] hydrogenase. Semi-synthetic [FeFe] hydrogenase maturation was first demonstrated in *E. coli* (Khanna et al., 2017). The mechanism by which the synthetic cofactor enters the cell and activates the enzyme remains to be elucidated, but it has been found to occur on a minute-time scale (Mészáros et al., 2018). Later work expanded its utilization to cyanobacteria (Wegelius et al., 2018, 2021). The resulting non-native, semisynthetic enzyme unmistakably links to the native metabolism of the photosynthetic cell and retain its H_2 production capacity for several days with an activity based on availability of electrons.

To date studies on [FeFe] hydrogenase expression in cyanobacteria has focused almost exclusively on representative examples of "prototypical" Group A [FeFe] hydrogenases. However, Wegelius et al. also reported on the variance in H_2 production arising from employing [FeFe] hydrogenases from different phylogenetic groups (Wegelius et al., 2021), and showed that the Group D enzyme *Thermoanaerobacter mathranii* HydS displayed distinct differences in its hydrogen gas production profile relative to the Group A enzymes from *C. reinhardtii* and *Solobacterium moorei*.

3.1.2. Expression of [NiFe] hydrogenases and hydrogenase fusion constructs in cyanobacteria

Heterologous expression of [NiFe] hydrogenases provides the possibility to take advantage of the native cyanobacterial [NiFe] hydrogenase maturation machinery. Thus, it circumvents the challenge of efficiently co-expressing the hydrogenase, together with its maturation machinery (HydEFG) required to obtain active [FeFe] hydrogenases. As such, it provides a potentially more straightforward way to study the effect of introducing enzymes with improved properties or to engineer fusion proteins between the native cyanobacterial [NiFe] hydrogenase and different components of the PETC, which in turn can guide efforts related to [FeFe] hydrogenase.

Early research reported the expression of heterologous [NiFe] hydrogenases from *Alteromonas macleodii* and the bidirectional [NiFe] hydrogenase from *Thiocapsa roseopersicina* in a mutant *Synechococcus elongatus* PCC 7942 lacking the native bidirectional hydrogenase structural genes (ΔHoxYH). Although the proteins did not show any activity *in vivo*, *in vitro* H_2 production confirmed the successful activation of the two hydrogenases, and the coupling of the catalytic subunits (HoxYH) from *T. roseopersicina* to the native diaphorase HoxEFU subunits. However, cloning of multiple hydrogenase accessory genes from native organisms was still required to achieve the assembly and activation of functional [NiFe] hydrogenases, highlighting the diversity of hydrogenase maturation mechanisms even within the realm of [NiFe] hydrogenases (Weyman et al., 2011).

In similar endeavors, O_2-tolerant, and NAD(H)-dependent hydrogenase from *Ralstonia eutropha* (*Re*SH) was expressed in

TABLE 1 Heterologous expression of hydrogenases in cyanobacteria and green algae.

Host	Implemented Strategy	Outcome and conclusion/Key findings	Reference
Cyanobacteria			
Synechococcus elongatus PCC 7942	IPTG- inducible heterologous expression of [FeFe] hydrogenases (HydA) and psba1 controlled expression of [FeFe] maturation machinery, *in vivo*	2.8 µmol $H_2 \cdot h^{-1} \cdot$ mg Chla^{-1}, ferredoxin-hydrogenases compatibility is crucial for efficient coupling to native redox metabolism	Ducat et al. (2011)
Anabaena/Nostoc PCC 7120	Heterologous expression of [FeFe] hydrogenase operon from *Shewanella oneidensis* MR-1 controlled by heterocyst-specific promoter *phetN*, deletion of native NiFe hydrogenases, *in situ*	1 µmol $H_2 \cdot h^{-1} \cdot$ mg Chla^{-1}in *in situ* experiments (supplemented with dithionite and MV)	Gärtner et al. (2012)
Anabaena/Nostoc PCC 7120	Heterologous expression of [FeFe] hydrogenases (HydA) and maturation machinery in heterocyst controlled by late-phase promoter, cyanoglobin expression under control of *patB* promotor *in vivo*	400 µmol $H_2 \cdot$ mg Chla^{-1} under argon atmosphere 13 µmol $H_2 \cdot$ mg Chla^{-1} under aerobic conditions O_2 level actively lowered by cyanoglobin GlbN in heterocyst, competition of nitrogenase and hydrogenase for reduced ferredoxin	Avilan et al. (2018)
Synechocstis PCC 6803	Expression of fusion protein PsaD-HoxYH (native NiFe hydrogenases and PSI subunit), deletion of *hoxEFUYH* and *psaD*	17-fold increase in H_2 concentration (546 µM) compared to WT. Higher temporary H_2 production rates than WT. H_2-uptake circumvented by avoiding backwards electron transfer to PSI. Limited rate of H_2 produced from oxygenic photosynthesis	Appel et al. (2020)
Green algae			
Chlorella sp. DT	Heterologous overexpression of clostridial [FeFe] hydrogenase (HydA) under control of two different promoters in aerobic and sulfur-supplied conditions	Native maturation of heterologous [FeFe] hydrogenase, H_2 production 10-fold higher than in WT strain, not proportional increase with protein expression level	Chien et al. (2012)
Chlamydomonas reinhardtii	Expression of a Fd-HydA1 fusion protein under control of the *psaD* promoter	Enhanced electron flow from PSI, leading to 4.5-fold higher hydrogen production than WT at low protein expression levels. Increased oxygen tolerance of the [FeFe] hydrogenase, probably due to Fd protection	Eilenberg et al. (2016)
Chlamydomonas reinhardtii	Screening for *Chlamydomonas reinhardtii* mutants overexpressing a Fd-HydA1 fusion integrated either in nuclear genome (*psaD* promoter) or chloroplasts chromosome (*psaA* promoter)	Sustained H_2 production that correlates linearly with active enzyme abundance. Enzyme showed 4.5-fold increase in hydrogenase activity compared to WT, even at high expression levels. Fd fusion limited hydrogenase activation, where up to 85% of the overexpressed hydrogenase chimera remained in the apo-form	Weiner et al. (2018)
Chlamydomonas reinhardtii	Expression of two different Fd-HydA1 chimeric proteins harboring a mutant Fd (D19A, D58A) with limited affinity towards FNR under a sulfur-limitation induced promoter	Chimeric protein expressed at comparable levels of HydA1 in WT. The Fd-HydA1 harboring a 25 aa linker exhibited better performance. Average production of 111.7 ± 3.4 ml $\cdot$ H_2 L^{-1}, a 4.6-fold increase in H_2 production compared to WT	Xiong et al. (2021)
Chlamydomonas reinhardtii	Design of a PSI-hydrogenase chimera by. Fusing the stromal PsaC subunit to either HydA1/HydA2 hydrogenases and *in vivo* expression in a Δ*psaC Chlamydomonas reinhardtii* mutant strain	Fusion chimeras were successfully activated by HydEFG maturases (>90% active protein), additionally, up to 60% of O_2-inactivated PSI-HydA chimeras could be reactivated after reducing O_2 concentration. Enhanced H_2 production was observed, mainly derived from indirect PETC regulation, lowered LET and O_2 production Average production of 14.0 ± 1.7 µmol $H_2 \cdot h^{-1} \cdot$ mg Chla^{-1} (for PSI-HydA2 chimera, expressed at 7 times lower levels than WT PSI, leading to reduced PSII activity and enabling sustaining H_2 production due to limited O_2 buildup). PSI-HydA1 chimera exhibited only 50% of PSI-HydA2 turnover rate. Its expression were 5 times higher than PSI-HydA2, restoring close-to-WT levels of PSII activity an increased O_2 production, leading to a 10-fold overall H_2 production compared to PSI-HydA2 chimera	Kanygin et al. (2020, 2022)

*Synechocystis*PCC 6803 featuring a knockout of the native hydrogenase (Lupacchini et al., 2021). In this study, the engineered strain was able to continuously produce H_2 under illumination at a higher rate than the wild-type (WT) and for up to 20 h under illumination. This result indicates that the native maturation machinery was sufficient to mature the heterologously expressed [NiFe] hydrogenase without the

requirement of its accessory *hyp*-genes. The sustained H_2 production was attributed with the higher O_2 tolerance of the *Re*SH. In addition, the *Re*SH expressing strain was able to use H_2 as sole electron source, enabling autotrophic growth, even when water oxidation at PSII was blocked by DCMU (3-(3,4-dichlorophenyl)-1,1-dimethylurea) addition. This indicates clear coupling between the introduced hydrogenase and the native cyanobacterial redox metabolism. However, due to the NAD(H) dependent nature of *Re*SH, a high intracellular NADH/NAD^+ ratio and efficient NADH supply are required for H_2 production. This was achieved by glucose supplementation and blocking of any other metabolic electron sinks such as nitrate or carbonate/CO_2 assimilation, where the cells were unable to produce H_2 in the absence of both conditions. In the absence of glucose supplementation and presence of the native electron sinks for assimilation pathways no H_2 production was observed. Overall, these results demonstrate the possibility of expressing heterologous O_2-tolerant hydrogenases in cyanobacteria, and how the native cyanobacterial maturation machinery can activate heterologous [NiFe] hydrogenases. Nonetheless, it is also clear that further engineering of the electron channeling towards the hydrogenase is required for the development of an efficient H_2 production system.

A complementary strategy is focused on enhancing the electron supply to the hydrogenase. PSI-hydrogenase fusion constructs have been considered an appealing solution. Critically this design could allow to intercept electrons from the PETC before they reach the Fd pool, thus avoiding the need for extensive engineering of hydrogenase coupling with the redox metabolism and competition with other native electron sinks. Following this principle, light-driven H_2 production from the *Desulfovibrio vulgaris* [NiFe] hydrogenases fused to cyt-c3 and PsaE subunit of PSI was reported *in vitro* (Ihara et al., 2006). This study highlighted the suitability of stromal PSI subunits as targets for PSI-Hydrogenase fusion proteins, as well as the importance of considering electron transport pathways from PSI to the fused hydrogenase moiety. More interestingly, the native [NiFe] hydrogenase of *Synechocystis* PCC 6803 (SynH) was fused to PSI PsaD subunit and overexpressed in a *Synechocystis* PCC 6803 mutant lacking the native hydrogenase (Appel et al., 2020). To date, this study reported the highest headspace H_2 concentration achieved using *Synechocystis* PCC 6803 (> 500 μM) and the only report of H_2 production *in vivo* using a PSI-hydrogenase fusion construct. The study shows how in spite of the reversible nature of SynH, H_2 uptake is virtually avoided in the engineered PSI-SynH system. This indicate that on the contrary to previous hydrogenase expression strategies, PSI-Hydrogenase fusion proteins can alter the enzyme's native bias by impeding reversed electron flow from the hydrogenase moiety back to PSI. Additionally, the study addressed the relevance of the PsaD-SynH fusion protein design, aiming to place the exposed external [4Fe4S] cluster of *Synechocystis* PCC 6803 native hydrogenase closer to the F_B and F_A [4Fe4S] clusters of the PSI PsaC subunit. The expressed SynYH hydrogenase corresponds only to the catalytic subunits of the native [NiFe] hydrogenase, reducing its ability to interact with native electron donors such as ferredoxin, thus reducing the possibility of hydrogen oxidation. The observed results indicate that a direct electron transfer from the [4Fe4S] clusters of the PSI PsaC subunit towards the [4Fe4S] cluster of the hydrogenase is the main, if not the only, electron source for the catalytic activity. These findings open the possibility of further engineering PSI-Hydrogenase systems where hydrogenases with desirable features are fused to PSI, as well as developing new fusion constructs with improved electron transfer properties. The latter could be achieved by reducing the distance between the PsaC [4Fe4S] donor clusters and the acceptor [4Fe4S] cluster of the hydrogenase (Appel et al., 2020) as well as via the introduction of electron carriers within the fusion construct's structure (Walters and Golbeck, 2020; Günzel et al., 2022). Similarly, coupling of the PSI PsaC subunit's F_B [4Fe4S] cluster to a *Clostridium acetobutylicum* HydA using a dithiol-based molecular wire has been reported (Lubner et al., 2011). The resulting biological/organic nanoconstruct exhibited a 2-fold increase in overall photosynthetic electron turnover in PSI and high light-driven H_2 production using an *in vitro* assay. These results demonstrate the relevance of PSI-Hydrogenase fusions as a promising way to overcome diffusional limitations of soluble redox carriers as well as limiting competition with other competing pathways. Undoubtedly, recent discoveries about hydrogenases' interactions with native electron carriers will help guiding more rational engineering designs (Rumpel et al., 2015).

It worth noting that these studies highlighted that their reported photobiological H_2 production titers where achieved in controlled experimental conditions avoiding O_2 inactivation. In this context, electrons are normally obtained from other sources of reducing equivalents (mainly glucose) and transferred to the PETC via fermentative pathways (Appel et al., 2020; Lupacchini et al., 2021). These findings accentuate the relevance of combining the described engineering strategies with further engineering in order to remove the limitations imposed by O_2 production in PSII.

3.2. Expression of hydrogenases and hydrogenase fusion constructs in green algae

Green algae harbor natively highly active [FeFe] hydrogenases and the associated HydEFG maturation machinery. Early studies of hydrogenase-driven H_2 production in green algae traditionally focused on developing cultivation protocols that shifts cell metabolism towards anoxygenic conditions thereby inducing H_2 production using nutrient-depleted media, as well as controlled pulse-illumination procedures (Melis et al., 2000; Kosourov et al., 2018). However, the growing availability of engineering tools developed during the last decade has led to several non-native hydrogenase expressions and other hydrogenase engineering strategies reported in green algae with promising results. Table 1 provides a summary of achievements on H_2 production when expressing non-native hydrogenases in oxygenic photosynthetic microorganisms.

Chien et al. reported an up-to 10-fold increase in H_2 production in engineered *Chlorella* DT strains. This was achieved by cloning and overexpression its principal native [FeFe] hydrogenase (Chien et al., 2012). Other engineering efforts focused on enhancing the redox coupling of the hydrogenase to PSI, aiming to reduce competition for PSI with Ferredoxin-$NADP^+$ reductase (FNR). A synthetic ferredoxin (Fd) - [FeFe] hydrogenase protein was designed by fusing native Fdx1 and HydA from *C. reinhardtii*. Strains expressing the fusion constructs showed 4.5-fold increase in specific H_2 production and surprisingly an enhanced O_2 tolerance (Eilenberg et al., 2016). A later report studied in deeper detail the *in vivo* performance of the Fdx1-HydA1 synthetic protein and aimed to enhance H_2 production by screening mutants overexpressing the fusion construct. Developed strains

exhibited higher protein expression levels and longer-lasting sustained H_2 production. However, this study also reported that up to 85% of the synthetic Fdx1-HydA1 fusion remained in the inactive apo-protein form, indicating inefficient *in vivo* hydrogenase maturation (Weiner et al., 2018). These findings highlight the importance of further synthetic protein engineering to optimize not only protein expression but also allow efficient hydrogenase maturation. More recently, a mutant ferredoxin with reduced electron transfer to FNR (Fdx1 D19A D58A) was fused to HydA1 using two different, 15 or 25 amino acids (aa), linkers. The obtained strains overexpressing the fusion constructs showed up to a 4.6-fold increase in H_2 production when compared with a strain expressing only HydA1 at comparable levels (Rumpel et al., 2014).

Similarly, to studies in cyanobacteria, PSI-hydrogenase fusion constructs have been expressed in green algae, leading to enhanced *in vivo* H_2 evolution. These efforts have primarily focused on *C. reinhardtii* which contains two native [FeFe] hydrogenases commonly denoted as HydA1 and HydA2. *In vitro* studies have suggested that HydA1 is primarily involved in H_2 production, while HydA2 appears more biased towards H_2 oxidation (Hambourger et al., 2008). In these studies, the stromal PsaC subunit of PSI was fused to *C. reinhardtii* HydA2. The engineered strain showed fermentative H_2 production, reaching approximately 60% of WT activity in anoxic dark conditions, indicating that the HydA2 moiety was still able to accept electrons from Fd. Furthermore, the strain showed a 7-fold lower abundance of the PSI-HydA2 construct compared to PSI in wild-type cells. The reduced PSI pool lead to a downregulation of native PSII activity which alters PETC regulation, mainly constraining the LET and consequently reducing the O_2 evolution. This lowered O_2 production may reduce the hydrogenase inactivation thereby increasing observed H_2 production. Overall, the expression of PSI-HydA2 fusion allowed a sustained H_2 production upon illumination at rates comparable to the transient H_2 production of the WT, arguably mainly due to the changes in PETC regulation. More recently, the potentially more efficient HydA1 was selected and a PSI-HydA1 fusion protein was designed and expressed in *C. reinhardtii* with the aim to increase H_2 production (Engelbrecht et al., 2021). The obtained strain accumulated 5-times more PSI-HydA1 protein than the previous PSI-HydA2 strain and exhibited a comparable interaction with native Fd in dark anoxic conditions. However, the turnover frequency of the PSI-HydA1 chimera turned out to be 50% of the previous PSI-HydA2 construct, and overall H_2 production by the fusion protein was 10-times lower than the previous PSI-HydA2 strain. These activities appear to conflict with the reported intrinsic biases of HydA1 of HydA2 (Engelbrecht et al., 2021). However, the results can largely be rationalized to higher abundance of PSI in the PSI-HydA1 fusion protein strains, releasing the constrains on PSII-driven O_2 evolution. Furthermore, the report shows how the native HydEFG machinery was able to activate the apo-PsaC-HydA1 chimera expressed before the induction of anoxic conditions, reaching turnover rates above 90% of the fully active form. Additionally, it was also shown that upon O_2 inactivation PSI-HydA1, the active site can be reinserted into the same PSI-HydA1 chimera by the maturases, inducing up to 60% of original hydrogenase activity recovery after 4 h of anaerobic adaptation (Kanygin et al., 2020, 2022).

It should be noted that in contrast to the [NiFe] hydrogenase-PSI fusion expressed in cyanobacteria (Appel et al., 2020), which was unable to produce H_2 under dark fermentative conditions, the fusion constructs expressed in green algae (Kanygin et al., 2020, 2022) exhibited H_2 production in darkness. Thus, it is unclear which is the main electron source of the hydrogenase. The reported dark fermentative H_2 production of the PSI-HydA1/2 engineered strains indicate that the ferredoxin docking site is probably still free in the fusion protein, allowing the hydrogenase to accept electrons from ferredoxin. Consequently, the enhanced H_2 production could be caused from the localization of the hydrogenase moiety in the proximal environment of PSI, thereby improving its access to reduced ferredoxin. Alternatively, it is also possible that the hydrogenase accepts electrons directly from the FeS cluster F_B of the proximal PsaC subunit, or even a combination of both formerly described mechanisms. Overall, in the case of PSI-hydrogenase fusions, proximity to the F_B [4Fe4S] cluster of the PSI PsaC subunit has been shown to be a critical requirement. The closeness to PSI ensures higher interaction with the reduced FeS clusters of the PsaC subunit or Fd and limits FNR coupling to PSI, broadening electron supply from Fd towards the hydrogenase (Moal and Lagoutte, 2012; Xiong et al., 2021).

3.3. Photosynthesis re-engineering strategies for improved photobiological H_2 production

Herein we describe the most relevant strategies and breakthroughs that has been reported to increase photobiological H_2 production beyond the expression of hydrogenases. In spite of the diversity of the different strategies, they can be grouped into three main focus areas: Light harvesting engineering, electron transport rewiring, and intracellular O_2 concentration reduction. Figure 1 provides a summary of discussed strategies and breakthroughs to increase photobiological production beyond the expression of hydrogenases.

3.3.1. Re-engineering light harvesting

As the ultimate driver of photobiological H_2 production is light energy, enhancing the cells ability to harvest and utilize light more efficiently could enhance the electron availability for hydrogen production. The main strategies have focused on three directions: Broadening the light spectra utilization, reducing the light harvesting antennas for efficient light distribution and stronger illumination tolerance as well as optimizing the electron transport chain and reducing photoprotective energy dissipation.

3.3.1.1. Introducing far-red chlorophylls

The far-red longest-wavelength absorbing chlorophyll known to date is chlorophyll F (Chl*f*). A Chl*f* synthase gene (*chlF*) of *Fischerella thermalis* PCC 7521 was heterologously expressed in *Synechoccocus elongatus* PCC 7002, leading to the incorporation of Chl*f* into the native PSI, functionally connected to the other pigments in the complex. Mutant strains lacking PSII and grown in far-red light achieved up to 50% of the Chl*f* content found in native far-red acclimated PSI. Although, the heterologous Chl*f* molecules were not as red-shifted as in their native environment, the assembly of a reduced amount of Chl*f* allowed to extend the photosynthetically active radiation up to 750 nm (Tros et al., 2020).

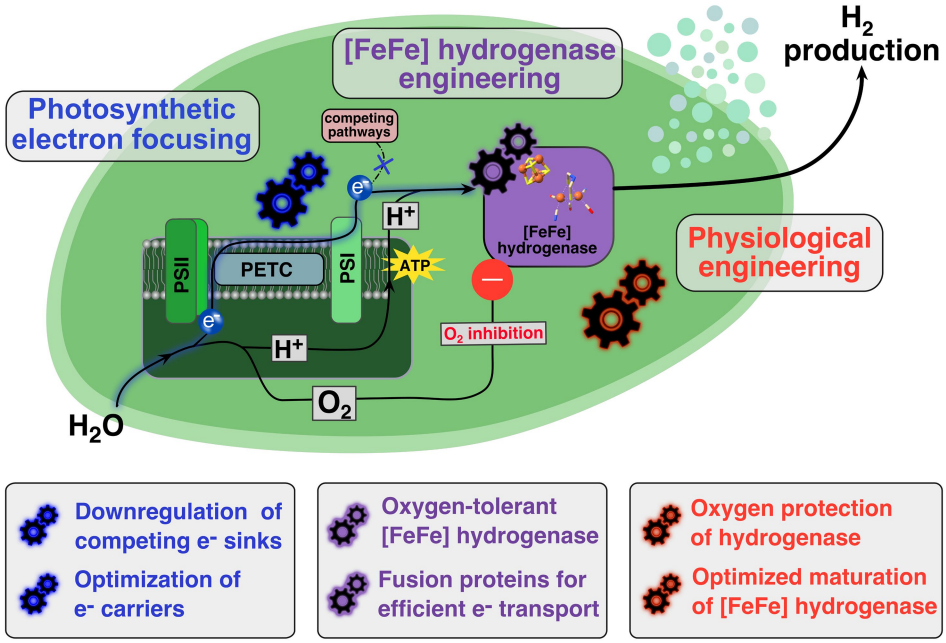

FIGURE 1
Schematic overview of engineering targets in photoautotrophic prokaryote for establishing efficient *in vivo* hydrogen production. Upon light-induced water splitting at photosystem II (PSII) oxygen is released and electrons are transferred *via* the photosynthetic electron transport chain (PETC) to photosystem I (PSI) where a cytoplasmatic electron carrier accepts these electrons. The photosynthetically-driven proton buildup in the thylakoids is enabling the ATP synthesis *via* ATP synthases at the thylakoid membrane. A heterologously expressed [FeFe] hydrogenase (purple box) uses the photosynthetically generated electrons and protons as substrates for a photobiological hydrogen production. To establish an efficient production system several features need to be targeted or introduced. Firstly, through photosynthetic electron focusing (blue gearwheels) the electrons transport from the photosynthetic machinery to the [FeFe] hydrogenase needs to be optimized. Secondly, the heterologously expressed [FeFe] hydrogenase has to be engineered (purple gearwheels) to work efficiently in the *in vivo* context. Especially, the oxygen-induced inhibition needs to be addressed by finding and introducing oxygen-insensitive or at least oxygen-sensitive tolerant enzyme variants into the *in vivo* system. Thirdly, physiological engineering efforts (red gearwheels) are necessary to assure that expressed [FeFe] hydrogenases can be activated and stay active for an extended period of time, as well as implementing further physiological modifications to protect the expressed hydrogenase from O_2.

3.3.1.2. Truncation of light harvesting complexes

Light-harvesting complexes have evolved to maximize solar energy capture. However, under strong illumination, the light-harvesting machinery absorb photons beyond the limits of photosystems capacity. Furthermore, large light-harvesting complexes also increase the shading effects in photobioreactors, causing to uneven light transfer.

It has been reported that truncation of light harvesting complexes in *Synechocystis* PCC 6803 leads to higher biomass accumulation and glycogen production while maintaining growth rates comparable to the WT. The effects were similar for deletion of phycocyanin (*Δcpc*) (Lea-Smith et al., 2014) or a phycobilisomes anchor protein (*ΔapcE*) (Joseph et al., 2014). Similar truncation strategies has also been reported to increase photosynthesis efficiency and biomass accumulation in green algae, extensively reviewed by Kumar et al. (2021). The potential influence of mutant cyanobacterial strains with unanchored phycobilisomes (*ΔapcE*), phycocyanin knockout (*Δcpc*), or whole phycobilisomes deletion (PAL mutant) have been studied. Overall antennae truncation lead to more resistant strains against light stress as well as reduced energy requirements for antenna synthesis and PSII repair. Additionally, mutants exhibited physiological adaptations upregulating linear electron transport (LET) and enhanced PSII expression and enhanced PSI turnover (Bernát et al., 2009). Nonetheless a higher number of PSII centers also leads to increased O_2 evolution, an effect that should be considered when coupling LET to O_2-sensitive hydrogenases.

3.3.1.3. Expression of proteorhodopsin as alternative light activated bioenergetic machinery

A potential strategy towards enhancing light energy utilization is the expression of proteorhodopsin - retinal complexes (PRrC). PRrC acts as light-driven proton pumps with maximum absorption peaks between 490 and 520 nm, matching with the fraction of light normally reflected by photosynthetic chlorophylls (450–550 nm). To date, PRrC systems have been successfully expressed in *Synechocystis*PCC 6803 and obtained strains were able to stimulate photoheterotrophic growth in a PSI deficient strain. Nonetheless further growth improvements were halted by the kinetic limitations of the native NDH-1 complex for reversed $NADP^+$ reduction. Surprisingly, although the provided additional PMF can increase the synthesis of ATP, thus enhancing LET via NADPH:ATP ratio balancing, during illumination with green light LET was reduced, mainly due to increased proton motive force (PMF) giving rise to cytochrome b6/f complex inhibition (Chen et al., 2017, 2019). This finding indicate that the integration of this systems should aim for a holistic comprehension of the overall bioenergetic context of the cells. In light of these findings, PRrC expression may expand the overall harvested light energy by filling the photosynthetic green gap with alternative light-driven proteins.

3.3.2. Rewiring electron channeling

Solar energy is harvested by the photosynthetic apparatus and converted into reducing power. However, in contrast to the fixed carbon which will be converted into different metabolites and can be stored, reducing power in the form of electrons must be used upon generation. In order to keep generation and demand(s) balanced they are channeled to available electron sinks. In photosynthetic microorganisms the four main electron sinks are: Carbon fixation (the Calvin–Benson–Bassham cycle, CBB), nitrate reduction pathways, oxygen reduction pathways (respiration or photoprotective mechanisms) and hydrogen production (Kosourov et al., 2021). Furthermore, it has been demonstrated that preferential channeling of photosynthetic electrons towards native growth supporting pathways (mainly carbon fixation) hinders hydrogen production and promote hydrogen uptake even before the O_2-driven hydrogenase deactivation takes place (Milrad et al., 2018). Therefore, rewiring the redox metabolism for a broader electron distribution towards hydrogen production is a crucial need for efficient photobiological H_2 production. Multiple strategies exist to address these requirements.

3.3.2.1. Inhibition of nitrogen metabolism

Nitrogen, specifically nitrate assimilation reactions account 16–20% of the photosynthetic electrons (Grund et al., 2019). Thus, inhibition of nitrate and nitrite reduction reactions has shown to translate into increased H_2 production (Gutthann et al., 2007). A *Synechocystis* PCC 6803 mutant with the nitrate and nitrite reductase genes knocked-out showed an up to 140-fold increase in H_2 production from the native bidirectional [NiFe] hydrogenase when compared to the WT cells. Interestingly, when cells where grown in media lacking nitrate, the engineered cells showed a 10-fold increase in H_2 production compared to WT cells. Since the transcript levels for the native hydrogenase where comparable between WT and the mutant strain, the increased H_2 production can be attributed to an increased availability of electrons (Baebprasert et al., 2011).

3.3.2.2. Elimination of oxygen reduction pathways and photoprotective oxygen reduction

Photoprotective mechanisms allows photosynthetic cells to cope with sudden changes in light irradiation and subsequent variations in reducing power generation. However, they are also responsible for significant energy dissipation. In fact, most of these enzymes catalyze O_2 reduction at the expense of H^+ and electron consumption which could be otherwise redirected to H_2 production. Several studies have reported the relevance of flavodiiron proteins (FDPs) (Santana-Sanchez et al., 2019) and terminal oxidases (Lea-Smith et al., 2013) as crucial mechanisms enabling cell survival in natural environments. Mutant strains lacking FDPs or terminal oxidases did not show significant growth defects when grown in controlled illumination conditions, highlighting their main role as electron-release valves under periods of reducing power overproduction.

Early studies in cyanobacteria showed improvements in H_2 production in a *Synechocystis* PCC 6803 mutant lacking a functional NAD(P)H dehydrogenase complex NDH-1. Mutant strains sustained significant H_2 production in the light. Since NDH-1 has been shown to be one of the major contributors to PMF formation by cyclic electron transport (CET) in *Synechocystis* PCC 6803 (Miller et al., 2021), the mutants are unable to pump protons, causing to severe alteration of PETC regulation and eventually increasing H_2 production due to the long-term accumulation a highly reduced NADPH pool during illumination, being sufficient to activate NADPH-dependent H_2 production by the native reversible hydrogenases (Cournac et al., 2004). Similarly, H_2 production in *Synechocystis* PCC 6803 knock-out strains for terminal cytochrome c oxidase (Δ*cox*), terminal quinol oxidase (Δ*cyd*), and alternative respiratory terminal oxidase (Δ*ARTO*) all exhibited increased H_2 production reaching up to 12-fold from WT levels for the triple mutant. Comparatively, the NDH-1 complex deficient mutant showed a 36-fold increase in total H_2 evolution but the production rate was lower when compared to previous mutant strains (Gutthann et al., 2007). While the mechanism behind the enhanced H_2 production in the terminal oxidase mutants seems to be mainly derived from enhanced electron supply to the hydrogenase, NDH-1 mutants may have other mechanisms. In the NDH1-mutants a lowered consumption of NADPH and reduced PMF derived from CET leads to an accumulation of NADPH which may be the main cause for enhanced production. Thus, it should be considered that altering the functioning of these respiratory photoprotective systems may not only increase H_2 production, but also have a profound impact in overall redox balance and PETC regulation specially in more complex hosts as green algae (Elman et al., 2022). Other studies showed how deletion of FDPs in green algae lead to up more than 2-fold increase in H_2 production under controlled pulse-illumination protocols. In addition, the lack of FDPs lead to a delayed activation of carbon fixation pathways (Jokel et al., 2019).

Considering these findings, deletion of respiratory and/or photoprotective electron sinks are powerful strategies to enhance H_2 production by the increasing electron availability. Nonetheless, the impact of these deletions on cell fitness and robustness should being considered. We note that potential fitness-rescue effects may be observed when deletions are combined with introduced engineered electron sink such as a hydrogenase.

3.3.2.3. Downregulation of carbon fixation pathways

Carbon fixation is essential for cell growth, where key reactions in the CBB cycle are energetically expensive consuming under ideal conditions 3 mol of ATP and 2 mol of NADPH per every mol of CO_2 fixed. Consequently, it is not surprising that early studies on hydrogenase-catalyzed H_2 production mainly focused on avoiding CBB activation via different physiological regulation mechanisms (Melis et al., 2000; Cournac et al., 2004). More recently, an RNA interference was used to downregulate expression of FNR in *Chlamydomonas reinhardtii*. Despite the small differences (12–18%) in autotrophic growth rates between WT and downregulated FNR mutants, a 60% reduction in Rubisco levels, 40% lower O_2 evolution at PSII, and up to 140% higher starch degradation rates were observed which lead to an earlier onset of anaerobiosis and increased electron supply to the hydrogenases, translating into a 2.5-fold increase in overall H_2 production (Sun et al., 2013). To our knowledge this is the only report of successful FNR regulation control in green algae via genetic engineering, leading to higher H_2 production. In a similar fashion, a petH gene merodiploid *Synechocystis* PCC 6803 mutant, also exhibited up to 4-fold higher photobiological H_2 production than the wild-type. In this study, the partial knock-out of the native FNR not only enhanced the H_2 production but also lead to a longer duration of the transitory hydrogen production (Gutekunst et al., 2014). In this light, FNR downregulation is another promising strategy to increase photobiological hydrogen production.

3.3.3. Engineering protective mechanisms against O_2-inactivaton

As the ultimate aim of STH is using sunlight to source H_2 from water, the process should mostly rely on LET where photosynthetic electrons are mostly sourced from water oxidation at PSII. However, increased PSII activity translates in higher O_2 production, impairing H_2 production due to the O_2-sensitive nature of most hydrogenases (Vuorijoki et al., 2017; Kanygin et al., 2020, 2022). Albeit the relevance of dealing with O_2 inactivation has been widely remarked, there are only a few studies reporting strategies tackling the O_2-sensitivity issue by other means than expressing more O_2-tolerant hydrogenases or anoxic cultivation conditions.

3.3.3.1. Spatial confinement of hydrogenases in anoxic compartments

One possibility consists in expressing hydrogenases within an anoxic environment. In this regard, the heterocysts of filamentous nitrogen-fixing cyanobacteria could be used (Gärtner et al., 2012; Avilan et al., 2018). Although most described strategies showed limited H_2 production, indicating that further engineering of the described systems is required. Similarly, expression of hydrogenases within anoxic bacterial microcompartments have already shown promising results in non-photosynthetic organisms. Particularly, carboxysomes are a very interesting scaffold for further engineering. Carboxysomes, present in all cyanobacteria, are polyhedral protein microcompartments that are selectively permeable to HCO_3^- and H^+ but not to O_2 or CO_2. Natively carboxysomes are formed by the self-assembly of different protein subunits, incorporating bicarbonate transporters, carbonic anhydrase and Rubisco (ribulose-1,5-bisphosphate carboxylase/oxygenase) within the compartment as a way to provide an anoxic environment and enhance carbon fixation. Interestingly, carboxysomes can be engineered to also incorporate heterologous enzymes within them. Due to the additional protection against O_2 they are emerging as promising scaffolds for improving hydrogenase activity. α-carboxysome shells have been engineered to co-encapsulate a protein fusion composed of the [FeFe] hydrogenase HydA1 from *Chlamydomonas reinhardtii* and its native Fd together with FNR from *E. coli*. In this system, NADPH is used as soluble electron donor and FNR enables NADPH dependent electron transfer to the hydrogenase. Interestingly, this system exhibited increased H_2 production under aerobic conditions both *in vivo* and *in vitro* (Li et al., 2020). Similarly, the catalytic subunits of the NADPH-dependent [NiFe] hydrogenase HyaAB from *E. coli* where expressed inside α-carboxysome shells. The assembled systems showed increased thermal stability and O_2 tolerance both *in vivo* and *in vitro* when compared with the free enzyme causing a significant increase in the measured H_2 production (Jiang et al., 2023). Nonetheless, this improvements in O_2 tolerance were more significant for the [NiFe] hydrogenase HyaAB than the [FeFe] hydrogenase HydA1. These results indicate that even when protected in a carboxysome shell, the hydrogenase intrinsic O_2 sensitivity still a critical factor in the catalytic system performance. Additionally, it should be noted that the dissolved O_2 levels in the aerobic cultures were significantly lower than atmospheric, due to the respiratory metabolism of *E. coli*. Because of this, although highly promising, whether these strategies can be transferred to photosynthetic microorganisms and efficiently coupled to native redox metabolism remains to be verified.

3.3.3.2. Implementation of O_2 consuming pathways

An artificial O_2 consumption pathway was integrated in *Chlamydomonas* chloroplasts, expressing *E. coli* pyruvate oxidase and *Synechococcus elongatus* PCC 7942 catalase under the control of a strong heat shock inducing promoter. The mutant strain exhibited higher oxygen consumption rate without significant growth defects or disruptions in the overall photosynthetic rate. The reduced intracellular O_2 concentration increased hydrogen production at moderate light intensities (30 μE) by 2-fold factor compared to WT. However, at higher light intensities (100 μE) O_2 production at PSII overcame the effects of the implemented O_2 consumption pathway, indicating the need of further refinement of the system (Xu et al., 2011). Recently, efficient O_2 consuming devices have been designed and characterized in *E. coli* (Pacheco et al., 2018). However, to our knowledge there are no reports about their implementation in any photosynthetic microorganism. In addition, respiration in photosynthetic organisms plays a key role in regulating intracellular O_2 (Shimakawa et al., 2020) and could potentially also be considered a potential engineering target. Eventually, the expression of oxygen-binding proteins has also been proven to reduce hydrogenase inhibition. The heterologous expression and assembly of the oxygen binding protein leghemoglobin from *Glycine max*, in chloroplasts of *C. reinhardtii* decreased the intracellular O_2 content and increased H_2 production rate up to 1.5-fold WT levels (Wu et al., 2010). Similar effects were observed for the expression of cyanoglobin in heterocysts of *Nostoc* PCC 7120 (Avilan et al., 2018).

3.3.4. Optimization of metal cofactors availability

Hydrogenases, their maturation machinery and electron carrier proteins all contain FeS clusters. Which is why it is expected that engineered strains overexpressing hydrogenases will feature a higher demand of FeS clusters. Therefore increasing native FeS cluster biosynthesis could potentially improve the system performance, as it has been already shown for nitrogenase enzymes (Li et al., 2016). In addition, as demonstrated by Akhtar and Jones (2008), deletion of *iscR* encoding the main FeS cluster biosynthesis pathway (ISC) repressor in *E. coli* increased hydrogenase activity and H_2 accumulation. Besides the common heterotrophic pathways, photosynthetic organisms use the sulfur utilization factor (SUF) pathway as the main FeS cluster biosynthesis route and exhibit up to a 10-fold higher FeS cluster biosynthesis than *E. coli* (Gao, 2020). Similar studies in *Synechocystis* PCC 6803, showed that deletion of the SUF pathway repressor under sufficient iron conditions (SufR) lead to an increased FeS cluster assembly while maintaining overall cell fitness (Vuorijoki et al., 2017). In the light of these findings, deregulation of FeS cluster biosynthesis may be used as a promising strategy alleviate limitations in FeS cluster availability for expressed heterologous hydrogenases and the accessory proteins required for its functioning.

3.3.5. Other engineering strategies

Future extensively engineered strains may exhibit limited growth, hindering the development of robust bioprocess design. This issue can be alleviated by implementing control systems for the expression of the introduced genetic elements. In this regard, the utilization of recently stationary phase promoters (Madsen et al., 2021) can drive the development of 2-stage cultivation strategies where initial growth is decoupled from further H_2 production (Burg et al., 2016;

Monshupanee et al., 2016). Additionally utilization of an O_2-inducible promoter (Immethun et al., 2016) could be used for fine-control of O_2 protective engineered systems.

4. Discussion

Future endeavors towards cost-effective photobiological H_2 production must rely on a holistic approach combining the strategies highlighted in this review. Three main engineering directions have been identified. Namely, the expression of non-native hydrogenase with improved features, extensive modifications of PETC for focusing electrons towards the heterologous hydrogenase, and further physiological engineering strategies to improve the overall performance of the producing strains and the expressed hydrogenase.

Firstly, H_2 productivity is highly dependent on the hydrogenase activity, requiring enzymes with displaced catalytic bias towards H_2 production combined with O_2 insensitivity. In this light [FeFe] hydrogenases are the most promising biocatalysts, for which recent research reported novel heterologous hydrogenases with intrinsic O_2 tolerance as well as engineered fusion hydrogenase proteins leading to improved H_2 production. Regarding fusion hydrogenases, it has been shown that protein design is critical. Any hydrogenase fusion protein must ensure efficient maturation of the hydrogenase H-domain and integration within the host bioenergetic machinery, ideally establishing unidirectional electron transport towards H_2 production.

Secondly, efficient focusing of photosynthetic electrons towards the hydrogenase can be achieved via the implementation of the formerly described strategies. Nonetheless, implementing multiple engineering strategies could significantly impact the overall photosynthesis physiology, leading to, e.g., alterations in PSI to PSII ratios and consequently the balance between PMF, LET and CET. These effects are especially relevant for PSI-hydrogenase fusion proteins and knock-out strains of respiratory terminal oxidases and FDPs. Due to potential synergistic effects this should be considered.

Likewise, it must be considered the physiological context of the producing strain. In this regard further host engineering should be implemented to ensure maximum hydrogenase activity. Therefore, establishing an efficient and orthogonal maturation systems is evidently required, especially in the case of [FeFe] hydrogenases expression in cyanobacteria. Moreover, O_2 protection strategies should be implemented to avoid irreversible hydrogenase inactivation, as this is likely to remain an issue even in designed enzymes.

Eventually, it is crucial to distinguish between H_2 production derived from the LET and other sources. Albeit many studies reported that reducing PSII activity correlated with higher H_2 production due to reduced intracellular O_2 concentrations this derives from overall lower water splitting at PSII and thus reduced LET, which ultimately limits the maximum theoretical STH H_2 production. This long-sustained paradox between LET activity and H_2 production may be overcome by the implementation of O_2 consuming device, pathway or the assembly of an O_2 protection mechanism *in vivo* thereby avoiding hydrogenase inactivation and efficiently coupling water splitting with H_2 production.

Finally, future efforts to improve photobiological H_2 production should use a combination of strategies highlighted in the study. These strategies include expressing and efficiently activating heterologous hydrogenases, avoiding its O_2-inactivation and levering the limitations of PETC towards increasing electron channeling to the hydrogenase. The described strategies can significantly impact overall photosynthesis physiology. Namely alterations in PSI to PSII ratios and balance between PMF, LET and CET. Thus, the interaction between the different engineering strategies must consider its synergistic effects towards the development of cost-effective photobiological H_2 production processes.

Author contributions

All authors contributed to conception and design of the review. CS and JF wrote the first draft of the manuscript. GB and PL contributed to read, revision and proof-reading of the manuscript drafts. CS contributed to the literature sources collection regarding hydrogenases. JF contributed to the literature sources collection of photosynthesis re-engineering and heterologous expression of hydrogenases. All authors contributed to the article and approved the submitted version.

Funding

This work was supported by the European Union Horizon Europe - the Framework Programme for Research and Innovation (2021–2027) under the grant agreement number 101070948 (project PhotoSynH2 to GB and PL) and The Swedish Energy Agency (project number 48574-1 to GB).

Conflict of interest

The authors declare that the research was conducted in the absence of any commercial or financial relationships that could be construed as a potential conflict of interest.

Publisher's note

References

Akhtar, M. K., and Jones, P. R. (2008). Deletion of iscr stimulates recombinant clostridial Fe-Fe hydrogenase activity and H_2-accumulation in *Escherichia Coli* Bl21(De3). *Appl. Microbiol. Biotechnol.* 78, 853–862. doi: 10.1007/s00253-008-1377-6

Appel, J., Hueren, V., Boehm, M., and Gutekunst, K. (2020). Cyanobacterial in vivo solar hydrogen production using a photosystem i–hydrogenase (Psad-Hoxyh) fusion complex. *Nat. Energy* 5, 458–467. doi: 10.1038/s41560-020-0609-6

Asada, Y., Koike, Y., Schnackenberg, J., Miyake, M., Uemura, I., and Miyake, J. (2000). Heterologous expression of clostridial hydrogenase in the cyanobacterium *Synechococcus* PCC7942. *Biochim. Biophys. Acta - Gene Struct. Expression* 1490, 269–278. doi: 10.1016/S0167-4781(00)00010-5

Avilan, L., Roumezi, B., Risoul, V., Bernard, C. S., Kpebe, A., Belhadjhassine, M., et al. (2018). phototrophic hydrogen production from a clostridial [FeFe] hydrogenase expressed in the heterocysts of the cyanobacterium *Nostoc* PCC 7120. *Appl. Microbiol. Biotechnol.* 102, 5775–5783. doi: 10.1007/s00253-018-8989-2

Baebprasert, W., Jantaro, S., Khetkorn, W., Lindblad, P., and Incharoensakdi, A. (2011). Increased H_2 production in the cyanobacterium *Synechocystis* sp. strain PCC 6803 by redirecting the electron supply via genetic engineering of the nitrate assimilation pathway. *Metab. Eng.* 13, 610–616. doi: 10.1016/j.ymben.2011.07.004

Berggren, G., Glover, S. D., and Cheah, M. H. (2022). "15.02 - hydrogenases and model complexes in bioorganometallic chemistry" in *Comprehensive Organometallic Chemistry Iv*. eds. G. Parkin, K. Meyer and D. O'hare (Oxford: Elsevier)

Bernát, G., Waschewski, N., and Rögner, M. (2009). Towards efficient hydrogen production: the impact of antenna size and external factors on electron transport dynamics in *Synechocystis* PCC 6803. *Photosynth. Res.* 99, 205–216. doi: 10.1007/s11120-008-9398-7

Berto, P., D'adamo, S., Bergantino, E., Vallese, F., Giacometti, G. M., and Costantini, P. (2011). The cyanobacterium *Synechocystis* sp. PCC 6803 is able to express an active [FeFe]-hydrogenase without additional maturation proteins. *Biochem. Biophys. Res. Commun.* 405, 678–683. doi: 10.1016/j.bbrc.2011.01.095

Birrell, J. A., Rodríguez-Maciá, P., Reijerse, E. J., Martini, M. A., and Lubitz, W. (2021). The catalytic cycle of [FeFe] hydrogenase: a tale of two sites. *Coord. Chem. Rev.* 449:214191. doi: 10.1016/j.ccr.2021.214191

Böck, A., King, P. W., Blokesch, M., and Posewitz, M. C. (2006). Maturation of hydrogenases. *Adv. Microb. Physiol.* 51, 1–71. doi: 10.1016/S0065-2911(06)51001-X

Buhrke, T., Lenz, O., Krauss, N., and Friedrich, B. (2005). Oxygen tolerance of the H_2-sensing [NiFe] hydrogenase from *Ralstonia eutropha* H16 is based on limited access of oxygen to the active site. *J. Biol. Chem.* 280, 23791–23796. doi: 10.1074/jbc.M503260200

Burg, J. M., Cooper, C. B., Ye, Z., Reed, B. R., Moreb, E. A., and Lynch, M. D. (2016). Large-scale bioprocess competitiveness: the potential of dynamic metabolic control in two-stage fermentations. *Curr. Opin. Chem. Eng.* 14, 121–136. doi: 10.1016/j.coche.2016.09.008

Bussiness-Research-Company (2023). Nuclear Electricity Global Market Report 2023 [Online]. Www.Thebusinessresearchcompany.Com: The Bussiness Research Company. Available at: https://www.Thebusinessresearchcompany.Com/Report/Nuclear-Electricity-Global-Market-Report [Accessed February 27, 2023].

Calusinska, M., Happe, T., Joris, B., and Wilmotte, A. (2010). The surprising diversity of clostridial hydrogenases: a comparative genomic perspective. *Microbiology* 156, 1575–1588. doi: 10.1099/mic.0.032771-0

Carrieri, D., Wawrousek, K., Eckert, C., Yu, J., and Maness, P.-C. (2011). The role of the bidirectional hydrogenase in cyanobacteria. *Bioresour. Technol.* 102, 8368–8377. doi: 10.1016/j.biortech.2011.03.103

Chen, Q., Arents, J., Ganapathy, S., de Grip, W. J., and Hellingwerf, K. J. (2017). Functional Expression of Gloeobacter Rhodopsin in Synechocystis sp. PCC6803. *Photochem. Photobiol.* 93, 772–781. doi: 10.1111/php.12745

Chen, Q., Arents, J., Schuurmans, J. M., Ganapathy, S., de Grip, W. J., Cheregi, O., et al. (2019). Combining retinal-based and chlorophyll-based (oxygenic) photosynthesis: Proteorhodopsin expression increases growth rate and fitness of a ΔPSI strain of Synechocystis sp. PCC6803. *Metabolic Engg.* 52, 68–76. doi: 10.1016/j.ymben.2018.11.002

Chien, L.-F., Kuo, T.-T., Liu, B.-H., Lin, H.-D., Feng, T.-Y., and Huang, C.-C. (2012). Solar-To-Bioh2 production enhanced by homologous overexpression of hydrogenase in green alga *Chlorella* sp. DT. *Int. J. Hydrog. Energy* 37, 17738–17748. doi: 10.1016/j.ijhydene.2012.09.068

Cohen, J., Kim, K., Posewitz, M., Ghirardi, M. L., Schulten, K., Seibert, M., et al. (2005). Molecular dynamics and experimental investigation of H_2 and O_2 diffusion in [Fe]-hydrogenase. *Biochem. Soc. Trans.* 33, 80–82. doi: 10.1042/BST0330080

Corrigan, P. S., Tirsch, J. L., and Silakov, A. (2020). Investigation of the unusual ability of the [FeFe] hydrogenase from *Clostridium beijerinckii* to access an O_2-protected state. *J. Am. Chem. Soc.* 142, 12409–12419. doi: 10.1021/jacs.0c04964

Cournac, L., Guedeney, G., Peltier, G., and Vignais, P. M. (2004). Sustained photoevolution of molecular hydrogen in a mutant of *Synechocystis* sp. strain PCC 6803 deficient in the type i Nadph-dehydrogenase complex. *J. Bacteriol.* 186, 1737–1746. doi: 10.1128/JB.186.6.1737-1746.2003

Cracknell, J. A., Vincent, K. A., Ludwig, M., Lenz, O., Friedrich, B., and Armstrong, F. A. (2008). Enzymatic oxidation of H_2 In atmospheric O_2: the electrochemistry of energy generation from trace H_2 by aerobic microorganisms. *J. Am. Chem. Soc.* 130, 424–425. doi: 10.1021/ja078299+

Ducat, D. C., Sachdeva, G., and Silver, P. A. (2011). Rewiring hydrogenase-dependent redox circuits in cyanobacteria. *Proc. Natl. Acad. Sci.* 108, 3941–3946. doi: 10.1073/pnas.1016026108

Eilenberg, H., Weiner, I., Ben-Zvi, O., Pundak, C., Marmari, A., Liran, O., et al. (2016). The dual effect of a ferredoxin-hydrogenase fusion protein in vivo: successful divergence of the photosynthetic electron flux towards hydrogen production and elevated oxygen tolerance. *Biotechnol. Biofuels* 9:182. doi: 10.1186/s13068-016-0601-3

Elman, T., Hoai Ho, T. T., Milrad, Y., Hippler, M., and Yacoby, I. (2022). Enhanced chloroplast-mitochondria crosstalk promotes ambient algal-H_2 production. *Cell Rep. Phys. Sci.* 3:100828. doi: 10.1016/j.xcrp.2022.100828

Engelbrecht, V., Liedtke, K., Rutz, A., Yadav, S., Günzel, A., and Happe, T. (2021). One isoform for one task? The second hydrogenase Of *Chlamydomonas reinhardtii* prefers hydrogen uptake. *Int. J. Hydrog. Energy* 46, 7165–7175. doi: 10.1016/j.ijhydene.2020.11.231

Exxon-Mobil (2022). Energy Demand: Three Drivers [Online]. Exxon Mobil. Available at: https://Corporate.Exxonmobil.Com/Energy-And-Innovation/Outlook-For-Energy/Energy-Demand#Industrial [Accessed February 27, 2023].

Fourmond, V., Baffert, C., Sybirna, K., Dementin, S., Abou-Hamdan, A., Meynial-Salles, I., et al. (2013). The mechanism of inhibition by H_2 of H_2-evolution by hydrogenases. *Chem. Commun.* 49, 6840–6842. doi: 10.1039/c3cc43297a

Gao, F. (2020). Iron–sulfur cluster biogenesis and iron homeostasis in cyanobacteria. *Front. Microbiol.* 11:165. doi: 10.3389/fmicb.2020.00165

Gärtner, K., Lechno-Yossef, S., Cornish, A. J., Wolk, C. P., and Hegg, E. L. (2012). Expression of *Shewanella oneidensis* Mr-1 [FeFe]-hydrogenase genes in *Anabaena* sp. strain PCC 7120. *Appl. Environ. Microbiol.* 78, 8579–8586. doi: 10.1128/AEM.01959-12

Gauquelin, C., Baffert, C., Richaud, P., Kamionka, E., Etienne, E., Guieysse, D., et al. (2018). Roles of the f-domain in [FeFe] hydrogenase. *Biochim. Biophys. Acta - Bioenerg.* 1859, 69–77. doi: 10.1016/j.bbabio.2017.08.010

Goldet, G., Brandmayr, C., Stripp, S. T., Happe, T., Cavazza, C., Fontecilla-Camps, J. C., et al. (2009). Electrochemical kinetic investigations of the reactions of [FeFe]-hydrogenases with carbon monoxide and oxygen: comparing the importance of gas tunnels and active-site electronic/redox effects. *J. Am. Chem. Soc.* 131, 14979–14989. doi: 10.1021/ja905388j

Greening, C., Biswas, A., Carere, C. R., Jackson, C. J., Taylor, M. C., Stott, M. B., et al. (2016). Genomic And metagenomic surveys of hydrogenase distribution indicate H_2 is a widely utilised energy source for microbial growth and survival. *ISME J.* 10, 761–777. doi: 10.1038/ismej.2015.153

Grimm, A., De Jong, W. A., and Kramer, G. J. (2020). Renewable hydrogen production: a techno-economic comparison of photoelectrochemical cells and photovoltaic-electrolysis. *Int. J. Hydrog. Energy* 45, 22545–22555. doi: 10.1016/j.ijhydene.2020.06.092

Grinter, R., Kropp, A., Venugopal, H., Senger, M., Badley, J., Cabotaje, P., et al. (2023). Energy extraction from air: structural basis of atmospheric hydrogen oxidation. *Nature* 615, 541–547. doi: 10.1038/s41586-023-05781-7

Grund, M., Jakob, T., Wilhelm, C., Bühler, B., and Schmid, A. (2019). Electron balancing under different sink conditions reveals positive effects on photon efficiency and metabolic activity of *Synechocystis* sp. PCC 6803. *Biotechnol. Biofuels* 12:43. doi: 10.1186/s13068-019-1378-y

Günzel, A., Engelbrecht, V., and Happe, T. (2022). Changing the tracks: screening for electron transfer proteins to support hydrogen production. *J. Biological Inorganic Chem.* 27, 631–640. doi: 10.1007/s00775-022-01956-1

Gutekunst, K., Chen, X., Schreiber, K., Kaspar, U., Makam, S., and Appel, J. (2014). The bidirectional nife-hydrogenase in *Synechocystis* sp. PCC 6803 is reduced by flavodoxin and ferredoxin and is essential under mixotrophic, nitrate-limiting conditions. *J. Biol. Chem.* 289, 1930–1937. doi: 10.1074/jbc.M113.526376

Gutthann, F., Egert, M., Marques, A., and Appel, J. (2007). Inhibition of respiration and nitrate assimilation enhances photohydrogen evolution under low oxygen concentrations in *Synechocystis* sp. PCC 6803. *Biochim. Biophys. Acta - Bioenerg.* 1767, 161–169. doi: 10.1016/j.bbabio.2006.12.003

Hallenbeck, P. C., and Benemann, J. R. (2002). Biological hydrogen production; fundamentals and limiting processes. *Int. J. Hydrog. Energy* 27, 1185–1193. doi: 10.1016/S0360-3199(02)00131-3

Hambourger, M., Gervaldo, M., Svedruzic, D., King, P. W., Gust, D., Ghirardi, M., et al. (2008). [FeFe]-Hydrogenase-catalyzed H_2 production in a photoelectrochemical biofuel cell. *J. Am. Chem. Soc.* 130, 2015–2022. doi: 10.1021/ja077691k

IEA (2021). Global Electricity Demand Is Growing Faster Than Renewables, Driving Strong Increase In Generation From Fossil Fuels [Online]. https://www.Iea.Org/: International Energy Agency. Available at: https://www.Iea.Org/News/Global-Electricity-Demand-Is-Growing-Faster-Than-Renewables-Driving-Strong-Increase-In-Generation-From-Fossil-Fuels [Accessed February 27, 2023].

Ihara, M., Nishihara, H., Yoon, K.-S., Lenz, O., Friedrich, B., Nakamoto, H., et al. (2006). Light-driven hydrogen production by a hybrid complex of a [NiFe]-hydrogenase and the cyanobacterial photosystem I. *Photochem. Photobiol.* 82, 676–682. doi: 10.1562/2006-01-16-RA-778

Immethun, C. M., Ng, K. M., Delorenzo, D. M., Waldron-Feinstein, B., Lee, Y.-C., and Moon, T. S. (2016). Oxygen-responsive genetic circuits constructed in *Synechocystis* sp. PCC 6803. *Biotechnol. Bioeng.* 113, 433–442. doi: 10.1002/bit.25722

Jiang, Q., Li, T., Yang, J., Aitchison, C. M., Huang, J., Chen, Y., et al. (2023). Synthetic engineering of a new biocatalyst encapsulating [NiFe]-hydrogenases for

enhanced hydrogen production. *J. Materials Chem.* B 11, 2684–2692. doi: 10.1039/D2TB02781J

Jokel, M., Nagy, V., Tóth, S. Z., Kosourov, S., and Allahverdiyeva, Y. (2019). Elimination of the flavodiiron electron sink facilitates long-term H_2 photoproduction in green algae. *Biotechnol. Biofuels* 12:280. doi: 10.1186/s13068-019-1618-1

Joseph, A., Aikawa, S., Sasaki, K., Matsuda, F., Hasunuma, T., and Kondo, A. (2014). Increased biomass production and glycogen accumulation in apce gene deleted *Synechocystis* sp. PCC 6803. *AMB Express* 4:17. doi: 10.1186/s13568-014-0017-z

Kanygin, A., Milrad, Y., Thummala, C., Reifschneider, K., Baker, P., Marco, P., et al. (2020). Rewiring photosynthesis: a photosystem i-hydrogenase chimera that makes H_2 in vivo. *Energy Environ. Sci.* 13, 2903–2914. doi: 10.1039/C9EE03859K

Kanygin, A., Smith, A., Nagy, V., Tóth, S. Z., and Redding, K. E. (2022). Interplay between hydrogen production and photosynthesis in a green alga expressing an active photosystem i-hydrogenase chimera. *Int. J. Hydrog. Energy* 47, 21969–21983. doi: 10.1016/j.ijhydene.2022.03.096

Khanna, N., Esmieu, C., Mészáros, L. S., Lindblad, P., and Berggren, G. (2017). In vivo activation of an [FeFe] hydrogenase using synthetic cofactors. *Energy Environm. Sci.* 10, 1563–1567. doi: 10.1039/C7EE00135E

Khanna, N., and Lindblad, P. (2015). Cyanobacterial hydrogenases and hydrogen metabolism revisited: recent progress and future prospects. *Int. J. Mol. Sci.* 16, 10537–10561. doi: 10.3390/ijms160510537

King, P. W., Posewitz, M. C., Ghirardi, M. L., and Seibert, M. (2006). Functional studies of [FeFe] hydrogenase maturation in an *Escherichia coli* biosynthetic system. *J. Bacteriol.* 188, 2163–2172. doi: 10.1128/JB.188.6.2163-2172.2006

Koo, J., and Swartz, J. R. (2018). System analysis and improved [FeFe] hydrogenase O_2 tolerance suggest feasibility for photosynthetic H_2 production. *Metab. Eng.* 49, 21–27. doi: 10.1016/j.ymben.2018.04.024

Kosourov, S., Böhm, M., Senger, M., Berggren, G., Stensjö, K., Mamedov, F., et al. (2021). Photosynthetic hydrogen production: novel protocols, promising engineering approaches and application of semi-synthetic hydrogenases. *Physiol. Plant.* 173, 555–567. doi: 10.1111/ppl.13428

Kosourov, S., Jokel, M., Aro, E.-M., and Allahverdiyeva, Y. (2018). A new approach for sustained and efficient H_2 photoproduction by *Chlamydomonas reinhardtii*. *Energy Environ. Sci.* 11, 1431–1436. doi: 10.1039/C8EE00054A

Kruse, O., Rupprecht, J., Mussgnug, J. H., Dismukes, G. C., and Hankamer, B. (2005). Photosynthesis: a blueprint for solar energy capture and biohydrogen production technologies. *Photochem. Photobiol. Sci.* 4, 957–970. doi: 10.1039/b506923h

Kubas, A., Orain, C., De Sancho, D., Saujet, L., Sensi, M., Gauquelin, C., et al. (2017). Mechanism of O_2 diffusion and reduction in FeFe hydrogenases. *Nat. Chem.* 9, 88–95. doi: 10.1038/nchem.2592

Kumar, V., Sharma, N., Jaiswal, K. K., Vlaskin, M. S., Nanda, M., Tripathi, M. K., et al. (2021). Microalgae with a truncated light-harvesting antenna to maximize photosynthetic efficiency and biomass productivity: recent advances and current challenges. *Process Biochem.* 104, 83–91. doi: 10.1016/j.procbio.2021.03.006

Land, H., Senger, M., Berggren, G., and Stripp, S. T. (2020). Current state of [FeFe]-hydrogenase research: biodiversity and spectroscopic investigations. *ACS Catal.* 10, 7069–7086. doi: 10.1021/acscatal.0c01614

Lautier, T., Ezanno, P., Baffert, C., Fourmond, V., Cournac, L., Fontecilla-Camps, J. C., et al. (2011). The quest for a functional substrate access tunnel in Fefe hydrogenase. *Faraday Discuss.* 148, 385–407. doi: 10.1039/C004099C

Lea-Smith, D. J., Bombelli, P., Dennis, J. S., Scott, S. A., Smith, A. G., and Howe, C. J. (2014). Phycobilisome-deficient strains of *Synechocystis* sp. PCC 6803 have reduced size and require carbon-limiting conditions to exhibit enhanced productivity. *Plant Physiol.* 165, 705–714. doi: 10.1104/pp.114.237206

Lea-Smith, D. J., Ross, N., Zori, M., Bendall, D. S., Dennis, J. S., Scott, S. A., et al. (2013). Thylakoid terminal oxidases are essential for the cyanobacterium *Synechocystis* sp. PCC 6803 to survive rapidly changing light intensities. *Plant Physiol.* 162, 484–495. doi: 10.1104/pp.112.210260

Leroux, F., Dementin, S., Burlat, B., Cournac, L., Volbeda, A., Champ, S., et al. (2008). Experimental approaches to kinetics of gas diffusion in hydrogenase. *Proc. Natl. Acad. Sci.* 105, 11188–11193. doi: 10.1073/pnas.0803689105

Li, T., Jiang, Q., Huang, J., Aitchison, C. M., Huang, F., Yang, M., et al. (2020). Reprogramming bacterial protein organelles as a nanoreactor for hydrogen production. *Nat. Commun.* 11. doi: 10.1038/s41467-020-19280-0

Li, S., Li, F., Zhu, X., Liao, Q., Chang, J.-S., and Ho, S.-H. (2022). Biohydrogen production from microalgae for environmental sustainability. *Chemosphere* 291:132717. doi: 10.1016/j.chemosphere.2021.132717

Li, X.-X., Liu, Q., Liu, X.-M., Shi, H.-W., and Chen, S.-F. (2016). Using synthetic biology to increase nitrogenase activity. *Microb. Cell Factories* 15:43. doi: 10.1186/s12934-016-0442-6

Liebgott, P.-P., Leroux, F., Burlat, B., Dementin, S., Baffert, C., Lautier, T., et al. (2010). Relating diffusion along the substrate tunnel and oxygen sensitivity in hydrogenase. *Nat. Chem. Biol.* 6, 63–70. doi: 10.1038/nchembio.276

Lubitz, W., Ogata, H., Rüdiger, O., and Reijerse, E. (2014). Hydrogenases. *Chem. Rev.* 114, 4081–4148. doi: 10.1021/cr4005814

Lubner, C. E., Applegate, A. M., Knörzer, P., Ganago, A., Bryant, D. A., Happe, T., et al. (2011). Solar hydrogen-producing bionanodevice outperforms natural photosynthesis. *Proc. Natl. Acad. Sci.* 108, 20988–20991. doi: 10.1073/pnas.1114660108

Lui, J., Chen, W.-H., Tsang, D. C., and You, S. (2020). A critical review on the principles, applications, and challenges of waste-to-hydrogen technologies. *Renew. Sust. Energ. Rev.* 134:110365. doi: 10.1016/j.rser.2020.110365

Lukey, M. J., Roessler, M. M., Parkin, A., Evans, R. M., Davies, R. A., Lenz, O., et al. (2011). Oxygen-tolerant [NiFe]-hydrogenases: the individual and collective importance of supernumerary cysteines at the proximal Fe-S cluster. *J. Am. Chem. Soc.* 133, 16881–16892. doi: 10.1021/ja205393w

Lupacchini, S., Appel, J., Stauder, R., Bolay, P., Klähn, S., Lettau, E., et al. (2021). Rewiring cyanobacterial photosynthesis by the implementation of an oxygen-tolerant hydrogenase. *Metab. Eng.* 68, 199–209. doi: 10.1016/j.ymben.2021.10.006

Madsen, M. A., Hamilton, G., Herzyk, P., and Amtmann, A. (2021). Environmental regulation of Pndba600, an auto-inducible promoter for two-stage industrial biotechnology in cyanobacteria. *Front. Bioeng. Biotechnol.* 8:619055. doi: 10.3389/fbioe.2020.619055

Martini, M. A., Bikbaev, K., Pang, Y., Lorent, C., Wiemann, C., Breuer, N., et al. (2023). Binding of exogenous cyanide reveals new active-site states in [FeFe] hydrogenases. *Chem. Sci.* 14, 2826–2838. doi: 10.1039/D2SC06098A

Melis, A., Zhang, L., Forestier, M., Ghirardi, M. L., and Seibert, M. (2000). Sustained photobiological hydrogen gas production upon reversible inactivation of oxygen evolution in the green alga *Chlamydomonas reinhardtii*. *Plant Physiol.* 122, 127–136. doi: 10.1104/pp.122.1.127

Mészáros, L. S., Nemeth, B., Esmieu, C., Ceccaldi, P., and Berggren, G. (2018). In vivo Epr characterization of semi-synthetic [FeFe] hydrogenases. *Angew. Chem. Int. Ed.* 57, 2596–2599. doi: 10.1002/anie.201710740

Meyer, J. (2007). [FeFe] hydrogenases and their evolution: a genomic perspective. *Cell. Molecul. Life Sci.* 64, 1063–1084. doi: 10.1007/s00018-007-6477-4

Miller, N. T., Vaughn, M. D., and Burnap, R. L. (2021). Electron flow through Ndh-1 complexes is the major driver of cyclic electron flow-dependent proton pumping in cyanobacteria. *Biochim. Biophys. Acta - Bioenerg.* 1862:148354. doi: 10.1016/j.bbabio.2020.148354

Milrad, Y., Schweitzer, S., Feldman, Y., and Yacoby, I. (2018). Green algal hydrogenase activity is outcompeted by carbon fixation before inactivation by oxygen takes place. *Plant Physiol.* 177, 918–926. doi: 10.1104/pp.18.00229

Moal, G., and Lagoutte, B. (2012). Photo-induced electron transfer from photosystem i to NaDP+: characterization and tentative simulation of the in vivo environment. *Biochim. Biophys. Acta - Bioenerg.* 1817, 1635–1645. doi: 10.1016/j.bbabio.2012.05.015

Monshupanee, T., Nimdach, P., and Incharoensakdi, A. (2016). Two-stage (photoautotrophy and heterotrophy) cultivation enables efficient production of bioplastic poly-3-hydroxybutyrate in auto-sedimenting cyanobacterium. *Sci. Rep.* 6:37121. doi: 10.1038/srep37121

Morra, S. (2022). Fantastic [FeFe]-hydrogenases and where to find them. *Front. Microbiol.* 13:853626. doi: 10.3389/fmicb.2022.853626

Morra, S., Arizzi, M., Valetti, F., and Gilardi, G. (2016). Oxygen stability in the new [FeFe]-hydrogenase from *Clostridium beijerinckii* Sm10 (Cba5h). *Biochemistry* 55, 5897–5900. doi: 10.1021/acs.biochem.6b00780

Novus-Light-Technologies (2023). Renewable Energy Market To Grow 8.4% Cagr Through 2030 [Online]. Www.Novuslight.Com: Novus Light Technologies Today. Available at: https://www.Novuslight.Com/Renewable-Energy-Market-To-Grow-8-4-Cagr-Through-2030_N12240.Html [Accessed February 27, 2023].

Ogata, H., Lubitz, W., and Higuchi, Y. (2016). Structure and function of [NiFe] hydrogenases. *J. Biochem.* 160, 251–258. doi: 10.1093/jb/mvw048

Pacheco, C. C., Büttel, Z., Pinto, F., Rodrigo, G., Carrera, J., Jaramillo, A., et al. (2018). Modulation of Intracellular O_2 Concentration in Escherichia coli Strains Using Oxygen Consuming Devices. *ACS Synthetic Bio.* 7, 1742–1752. doi: 10.1021/acssynbio.7b00428

Pagnier, A., Balci, B., Shepard, E. M., Yang, H., Warui, D. M., Impano, S., et al. (2022). [FeFe]-hydrogenase: defined lysate-free maturation reveals a key role for lipoyl-H-protein in dtma ligand biosynthesis. *Angew. Chem. Int. Ed.* 61:E202203413. doi: 10.1002/anie.202203413

Pandey, K., Islam, S. T. A., Happe, T., and Armstrong, F. A. (2017). Frequency and potential dependence of reversible electrocatalytic hydrogen interconversion by [FeFe]-hydrogenases. *Proc. Natl. Acad. Sci.* 114, 3843–3848. doi: 10.1073/pnas.1619961114

Redding, K. E., Appel, J., Boehm, M., Schuhmann, W., Nowaczyk, M. M., Yacoby, I., et al. (2022). Advances and challenges in photosynthetic hydrogen production. *Trends Biotechnol.* 40, 1313–1325. doi: 10.1016/j.tibtech.2022.04.007

Rodríguez-Maciá, P., Reijerse, E. J., Van Gastel, M., Debeer, S., Lubitz, W., Rüdiger, O., et al. (2018). Sulfide protects [FeFe] hydrogenases from O_2. *J. Am. Chem. Soc.* 140, 9346–9350. doi: 10.1021/jacs.8b04339

Roseboom, W., De Lacey, A. L., Fernandez, V. M., Hatchikian, E. C., and Albracht, S. P. J. (2006). The active site of the [FeFe]-hydrogenase from *Desulfovibrio desulfuricans*. Ii. redox properties, light sensitivity and co-ligand exchange as

observed by infrared spectroscopy. *J. Biol. Inorg. Chem.* 11, 102–118. doi: 10.1007/s00775-005-0040-2

Rumpel, S., Siebel, J.F., Diallo, M., Farès, C., Reijerse, E. J., and Lubitz, W. (2015). Structural Insight into the Complex of Ferredoxin and [FeFe] Hydrogenase from Chlamydomonas reinhardtii. *Chem. Bio. Chem.* 16, 1663–1669. doi: 10.1002/cbic.201500130

Rumpel, S., Siebel, J. F., Farès, C., Duan, J., Reijerse, E., Happe, T., et al. (2014). Enhancing hydrogen production of microalgae by redirecting electrons from photosystem i to hydrogenase. *Energy Environ. Sci.* 7, 3296–3301. doi: 10.1039/C4EE01444H

Rutz, A., Das, C. K., Fasano, A., Jaenecke, J., Yadav, S., Apfel, U.-P., et al. (2023). Increasing the O_2 resistance of the [FeFe]-hydrogenase Cba5h through enhanced protein flexibility. *ACS Catal.* 13, 856–865. doi: 10.1021/acscatal.2c04031

Santana-Sanchez, A., Solymosi, D., Mustila, H., Bersanini, L., Aro, E.-M., and Allahverdiyeva, Y. (2019). Flavodiiron proteins 1–to-4 function in versatile combinations in o_2 photoreduction in cyanobacteria. *elife* 8:E45766. doi: 10.7554/eLife.45766

Schäfer, C., Friedrich, B., and Lenz, O. (2013). Novel, oxygen-insensitive group 5 [NiFe]-hydrogenase in *Ralstonia Eutropha*. *Appl. Environ. Microbiol.* 79, 5137–5145. doi: 10.1128/AEM.01576-13

Shimakawa, G., Kohara, A., and Miyake, C. (2020). Characterization of light-enhanced respiration in cyanobacteria. *Int. J. Mol. Sci.* 22:342. doi: 10.3390/ijms22010342

Sun, Y., Chen, M., Yang, H., Zhang, J., Kuang, T., and Huang, F. (2013). Enhanced H_2 Photoproduction by down-regulation of ferredoxin-Nadp$^+$ reductase (Fnr) in the green alga *Chlamydomonas Reinhardtii*. *Int. J. Hydrog. Energy* 38, 16029–16037. doi: 10.1016/j.ijhydene.2013.10.011

Touloupakis, E., Faraloni, C., Silva Benavides, A. M., and Torzillo, G. (2021). Recent achievements in microalgal photobiological hydrogen production. *Energies* 14:7170. doi: 10.3390/en14217170

Tros, M., Bersanini, L., Shen, G., Ho, M.-Y., Van Stokkum, I. H. M., Bryant, D. A., et al. (2020). Harvesting far-red light: functional integration of chlorophyll f into photosystem i complexes of *Synechococcus* sp. PCC 7002. *Biochim. Biophys. Acta - Bioenerg.* 1861:148206. doi: 10.1016/j.bbabio.2020.148206

Vignais, P. M., and Billoud, B. (2007). Occurrence, classification, and biological function of hydrogenases: an overview. *Chem. Rev.* 107, 4206–4272. doi: 10.1021/cr050196r

Vogt, S., Lyon, E. J., Shima, S., and Thauer, R. K. (2008). The exchange activities of [Fe] Hydrogenase (iron–sulfur-cluster-free hydrogenase) from methanogenic archaea in comparison with the exchange activities of [FeFe] and [NiFe] hydrogenases. *J. Biol. Inorg. Chem.* 13, 97–106. doi: 10.1007/s00775-007-0302-2

Volbeda, A., Charon, M.-H., Piras, C., Hatchikian, E. C., Frey, M., and Fontecilla-Camps, J. C. (1995). Crystal structure of the nickel–iron hydrogenase from Desulfovibrio gigas. *Nature* 373, 580–587. doi: 10.1038/373580a0

Volbeda, A., Garcin, E., Piras, C., De Lacey, A. L., Fernandez, V. M., Hatchikian, E. C., et al. (1996). Structure of the [NiFe] Hydrogenase Active Site: Evidence for Biologically Uncommon Fe Ligands. *J. Am. Chem.l Soc.* 118, 12989–12996. doi: 10.1021/ja962270g

Vuorijoki, L., Tiwari, A., Kallio, P., and Aro, E.-M. (2017). Inactivation of iron-sulfur cluster biogenesis regulator sufr in *Synechocystis* sp. PCC 6803 induces unique iron-dependent protein-level responses. *Biochim. Biophys. Acta Gen. Subj.* 1861, 1085–1098. doi: 10.1016/j.bbagen.2017.02.020

Walters, K. A., and Golbeck, J. H. (2020). Designing a modified clostridial 2[4Fe–4S] ferredoxin as a redox coupler to directly link photosystem I with a Pt nanoparticle. *Photosynthesis Res.* 143, 165–181. doi: 10.1007/s11120-019-00679-w

Wegelius, A., Khanna, N., Esmieu, C., Barone, G. D., Pinto, F., Tamagnini, P., et al. (2018). Generation of a functional, semisynthetic [FeFe]-hydrogenase in a photosynthetic microorganism. *Energy Environ. Sci.* 11, 3163–3167. doi: 10.1039/C8EE01975D

Wegelius, A., Land, H., Berggren, G., and Lindblad, P. (2021). Semisynthetic [FeFe]-hydrogenase with stable expression and H_2 production capacity in a photosynthetic microbe. *Cell Rep. Phys. Sci.* 2:100376. doi: 10.1016/j.xcrp.2021.100376

Weiner, I., Shahar, N., Feldman, Y., Landman, S., Milrad, Y., Ben-Zvi, O., et al. (2018). Overcoming the expression barrier of the ferredoxin-hydrogenase chimera In *Chlamydomonas reinhardtii* supports a linear increment in photosynthetic hydrogen output. *Algal Res.* 33, 310–315. doi: 10.1016/j.algal.2018.06.011

Weyman, P. D., Vargas, W. A., Tong, Y., Yu, J., Maness, P. C., Smith, H. O., et al. (2011). Heterologous expression of alteromonas macleodii and *Thiocapsa roseopersicina* [NiFe] hydrogenases in *Synechococcus elongatus*. *PLoS One* 6:E20126. doi: 10.1371/journal.pone.0020126

Winkler, M., Duan, J., Rutz, A., Felbek, C., Scholtysek, L., Lampret, O., et al. (2021). A Safety cap protects hydrogenase from oxygen attack. *Nat. Commun.* 12:756. doi: 10.1038/s41467-020-20861-2

Wu, S., Yan, G., Xu, L., Wang, Q., and Liu, X. (2010). Improvement of hydrogen production with expression Of *Lba* gene in chloroplast of *Chlamydomonas reinhardtii*. *Int. J. Hydrog. Energy* 35, 13419–13426. doi: 10.1016/j.ijhydene.2009.11.118

Xiong, D., Happe, T., Hankamer, B., and Ross, I. L. (2021). Inducible high level expression of a variant Δd19a,D58a-ferredoxin-hydrogenase fusion increases photohydrogen production efficiency in the green alga *Chlamydomonas reinhardtii*. *Algal Res.* 55:102275. doi: 10.1016/j.algal.2021.102275

Xu, F.-Q., Ma, W.-M., and Zhu, X.-G. (2011). Introducing pyruvate oxidase into the chloroplast of *Chlamydomonas reinhardtii* increases oxygen consumption and promotes hydrogen production. *Int. J. Hydrog. Energy* 36, 10648–10654. doi: 10.1016/j.ijhydene.2011.05.130

Frontiers in Microbiology

Explores the habitable world and the potential of microbial life

The largest and most cited microbiology journal which advances our understanding of the role microbes play in addressing global challenges such as healthcare, food security, and climate change.

Discover the latest Research Topics

See more →

Frontiers

Avenue du Tribunal-Fédéral 34
1005 Lausanne, Switzerland
frontiersin.org

Contact us

+41 (0)21 510 17 00
frontiersin.org/about/contact